MICROSTRUCTURE AND FRACTURE TOUGHNESS OF Mn-STABILIZED CUBIC TITANIUM TRIALUMINIDE

by

Leszek Zbroniec

A thesis
presented to the University of Waterloo
in fulfilment of the
thesis requirement for the degree of

Doctor of Philosophy

in
Mechanical Engineering

Waterloo, Ontario, Canada, 1999

The University of Waterloo requires the signatures of all persons using or photocopying this thesis. Please sign below, and give address and date.

ABSTRACT

This thesis project is related to the fracture toughness aspects of the mechanical behavior of the selected Mn-modified cubic $L1_2$ titanium trialuminides.

Fracture toughness was evaluated using two specimen types: Single- Edge- Precracked- Beam (SEPB) and Chevron- Notched- Beam (CNB). The material tested was in cast, homogenized and HIP-ed condition. In the preliminary stage of the project due to lack of the ASTM Standard for fracture toughness testing of the chevron- notched specimens in bending the analyses of the CNB configuration were done to establish the optimal chevron notch dimensions.

Two types of alloys were investigated: a) boron-free and boron doped low-Mn (9at.% Mn), as well as (b) boron-free and boron-doped high-Mn (14at.% Mn). Toughness was investigated in the temperature range from room temperature to 1000°C and was calculated from the maximum load. It has been found that toughness of coarse-grained "base" 9Mn-25Ti alloy exhibits a broad peak at the 200- 500°C temperature range and then decreases with increasing temperature, reaching its room temperature value at 1000°C. However, the work of fracture (γ_{WOF}) and the stress intensity factor calculated from it (K_{IWOF}) increases continuously with increasing temperature. Also the fracture mode dependence on temperature has been established.

To understand the effect of environment on the fracture toughness of coarse-grained "base", boron-free 9Mn-25Ti alloy, the tests were carried out in vacuum (~1.3×10^{-5} Pa), argon, oxygen, water and liquid nitrogen. It has been shown that fracture toughness at ambient temperature is not affected by the environments

containing moisture (water vapor). It seems that at ambient temperatures these materials are completely immune to the water- vapor hydrogen embrittlement and their cause of brittleness is other than environment.

To explore the influence of the grain size on fracture toughness the fracture toughness tests were also performed on the dynamically recrystallized "base", boron-free 9Mn-25Ti material with the average grain size of 45 μm. Further refinement of the grain size was obtained by ball-milling of powders in order to obtain a nanostructure material. These were subsequently consolidated by hot pressing with the objective of retaining the nanostructure to the largest extent possible. The estimated grain size of the powder compact was ~50- 200 nm. The indentation microcracking fracture toughness measurements were performed on the powder compacts. It has been found that fracture toughness is independent of the grain size in the range ~1300- 45 μm and that for the finest grains (~50- 200 nm) it drops substantially and is equal to half of that for coarse- grained material.

A beneficial effect of boron doping, high-(Mn+Ti) concentration and combination of both, on the fracture toughness was observed at room and elevated temperatures. The addition of boron to a "base" 9at.% Mn- 25at.% Ti trialuminide improves the room temperature fracture toughness by 25- 50%. Addition of boron to a high (Mn+Ti) trialuminide improves the room temperature fracture toughness by 100% with respect to a "base" 9Mn- 25Ti alloy. Depending on the Mn+Ti concentrations and the level of boron doping, improvements of fracture toughness at 200- 600°C and 800- 1000°C ranges are also observed.

ACKNOWLEDGEMENTS

I would like to thank my supervisor, Professor Robert A. Varin for his guidance, tireless support and continual encouragement throughout this work. It has been a rewarding experience for me working with him and I would like to express my deepest respect and appreciation to him.

I would also like to express my appreciation to the members of my examining committee, Prof. S.Kumar (external examiner from Brown University), Prof. A.Plumtree, Prof. G.Glinka and Prof. J.Corbett for their valuable suggestions.

I wish to express my appreciation for the assistance I received from my colleagues and staff technicians in Materials Laboratory and machine shops.

DEDICATION

To

my Parents

and my Wife

CONTENTS

APPENDICES

LIST OF FIGURES

LIST OF TABLES

1 INTRODUCTION

The expanding interest in intermetallic compounds is driven by the quest to achieve higher operating temperatures and to reduce the weight of systems that will yield higher energy efficiency. The aerospace industry is therefore looking forward to the development of materials which would be lighter, stronger and having a higher temperature potential, compared to the presently available alloys. Among the various potential high temperature materials, intermetallic- based alloys are prime candidates for "alternative" materials. However, the lack of both ductility and toughness is often the "Achilles' heel" in intermetallics.

The focus of much of the recent work has been on improving the ambient temperature ductility of a few selected compounds. That is, to make them behave more like "real metals". Until quite recently no concerted effort had been made to understand the significance of real requirements for ambient temperature ductility of a material that will actually be used at elevated temperature where it is relatively ductile, but which exhibits very limited "forgiveness" at ambient temperature.

There also is concern that alloying to improve ductility may alter the fundamental characteristics of intermetallics to such an extent that their other attractive properties, such as density, modulus and elevated strength, may be seriously compromised. Thus, it is important to seek design solutions to ameliorate the effects of brittleness in addition to the ongoing modifications of the materials to make them less brittle. Therefore, it becomes essential to establish the minimum acceptable values of these other affected properties to be sure that a net gain is being realized. Intermetallics represent a new class of materials and will function in

a new domain of strength and ductility if they are implemented. Until very recently there has been only a limited amount of effort expended in understanding the design implications of this new domain.

For example, both monolithic and composite titanium aluminides have significant potential for application in the Integrated High Performance Turbine Engine Technology Initiative. The IHPTET goal is to double turbine propulsion capability by the turn of the century. The approach to achieve this goal focuses on three key areas: aerothermodynamics (more efficient combustion and hotter flow path), structures (radical new designs), and high-temperature, light weight materials. In the overall scheme, the role of advanced materials is crucial, for improvements in both aerodynamics and structural design are dependent on the continued development and implementation of advanced materials. Of the numerous material classes being contemplated for structures, titanium aluminides are of primary importance in the 600°C to 1000°C temperature range.

Hypersonic vehicles (designed to achieve velocities greater than Mach 5) represent another key requirement for advanced monolithic and composite titanium aluminide materials. Although hypersonic vehicles have been the subject of research for a number of years, recent investments by the United States in the National Aerospace Plane (NASP) program have catapulted investigations in hypersonic flight into the forefront of current aerospace research. The goal of the NASP program is to develop and demonstrate the technology necessary to build an experimental hypersonic vehicle capable of taking off from a runway and achieving earth orbit with a single stage, air-breathing propulsion system. This goal requires the development of high-temperature, lightweight honeycomb or truss core airframe panel structure. Titanium aluminides in thin-sheet form, both monolithic

and composite, are the prime candidate materials for large structural areas of the vehicle.

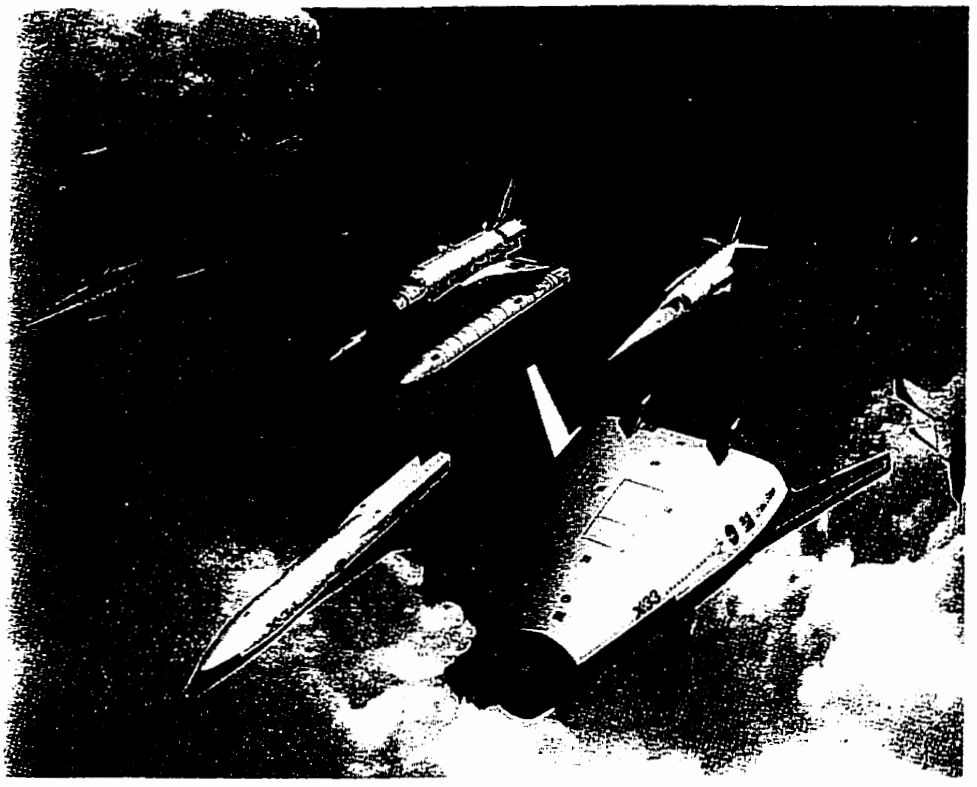

Figure 1.1 AeroMat's (Aerospace Materials) raison d'etre was dramatized by this illustration, titled "Advanced Materials: Enabling Technology for Generations of Aerospace Vehicles" which was provided by NASA Langley Research Center at ASM International's 8th Advanced Aerospace Materials & Processes Conference & Exposition in 1997.

There is a general need to achieve high material performance standards while insuring reliability of the structure throughout the design life. Generally, monolithic and composite titanium aluminide materials are intended for applications requiring good high temperature strength and creep resistance, while maintaining "adequate" ductility, fracture toughness, fatigue behavior, and impact crack resistance at RT and, for hydrogen fueled hypersonic vehicles, cryogenic temperatures. Moreover, the materials must be microstructurally stable over the design life of the structure,

and effects of a service environment (e.g., air, combustion gases, hydrogen) must not seriously degrade the material over its intended life.

The key to achieving successful design in these materials appears to lie in toughness, rather than in ductility [1]. Roughly, the distinction is that ductility is the ability to resist formation of a crack while toughness is the ability to resist propagation of a (pre- existing) crack. A material with adequate toughness should be able to survive the presence of a crack even if its ductility is inadequate to prevent the formation of one.

2 LITERATURE REVIEW ON CUBIC TITANIUM TRIALUMINIDES

2.1 General Properties of Titanium Trialuminides

The need for a lightweight, oxidation- resistant high temperature material has led to extensive investigation of aluminum-rich intermetallics of the type Al_3X (referred to as trialuminides), where X is usually Ti, Zr, Hf, V, Nb, or Ta. These compounds crystallize with the tetragonal DO_{22} (or DO_{23}) structure, and in attempt to enhance their low- temperature ductility, theoretical and experimental efforts have been expended to transform the DO_{22} structure to the related, more symmetric, cubic $L1_2$ structure.

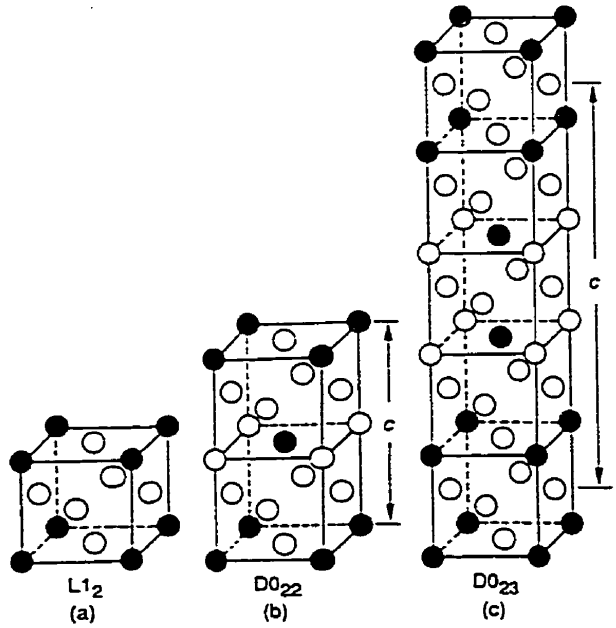

Figure 2.1 Structures of the types (a) $L1_2$, (b) DO_{22}, and (c) DO_{23} [2].

The DO_{22} structure is derived from the $L1_2$ structure by introducing an antiphase boundary (APB) with a displacement vector of a a/2<110> on every (001) plane (Fig.2.1b). Al_3Ti crystallizes into this $L1_2$-derivative, long-period superlattice structure. The DO_{23} structure is formed by introducing the APB on every second (001) plane (Fig.2.1c). Al_3Zr and Al_3Hf (at low temperatures), which are akin to Al_3Ti, possess this structure. In Al_3Ti the conversion from the DO_{22} structure to the $L1_2$ can be done if an appropriate number of d electrons are removed from the Ti sites. The removal of d electrons from the Ti sites can be accomplished by decreasing the charge transfer from Al to Ti, that is, by replacing an appropriate amount of Al with other less electro-positive elements which act as electron acceptors and thereby suppress the charge transfer from aluminum to titanium. This suggests that the crystal structure of Al_3Ti can be changed to the $L1_2$ structure by alloying with elements such as late period transition metals. Of the various $L1_2$ ternary trialuminides, the Al- X- Ti (X=Cu, Ni, Fe, Cr, Mn) have received the most attention, although the Al-Cu-Zr, Al-Fe-Zr, and Al-Mn-Zr systems have also been examined [3].

There have been numerous studies on these $L1_2$ trialuminides over the past few years, which have been summarized in several overviews [4,5,6,7]. However, there are still numerous disagreements and inconsistencies in the published literature regarding mechanical properties and even dislocation-dissociation schemes for a particular compound. These differences stem from a variety of sources, including inadequate knowledge of the size and shape of the $L1_2$ phase field, its variation with temperature and the sluggish kinetics of phase decomposition in these systems. Frequently, "nominally" single- phase materials as observed by optical microscopy contain second phases that are resolvable only at the TEM level.

Likewise, the role of stoichiometry within the single- phase field in influencing the mechanical properties and dislocation schemes is not well understood.

Two research groups independently reported the occurrence of ternary Al-rich $L1_2$ compounds in the Al- Cr- Ti and Al- Mn- Ti systems [8,9,10]. These compounds, $Al_{66}Cr_9Ti_{25}$ and $Al_{67}Mn_8Ti_{25}$ (at.%), were shown to exhibit improved compressive ductility relative to $Al_{66}Fe_9Ti_{25}$ and even some bend ductility at room temperature. The variation in compressive yield strength with temperature for these compounds in the polycrystalline form, with various stoichiometries has been reported in several reports [8,9,11]. Compressive- creep studies have also been conducted on these materials [12,13] in the 1000 K- 1200 K range and the response has been shown to be strongly grain- size dependent.

Bend test on $Al_{66}Cr_9Ti_{25}$ and $Al_{67}Mn_8Ti_{25}$ as a function of temperature revealed finite plastic strain in the Mn- based material at 298 K but not in the Cr- based counterpart up to 623 K [11] in contradiction to reports of ambient bend ductility in $Al_{66}Cr_9Ti_{25}$ [8,13].

Uniaxial tension tests on buttonhead specimens of forged $Al_{67}Cr_8Ti_{25}$ and $Al_{66}Mn_9Ti_{25}$ have been performed in air in the 298 K- 1073 K temperature range [14,15]. Isothermal oxidation- resistance of three of these $L1_2$ compounds ($Al_{67}Cr_8Ti_{25}$, $Al_{67}Ag_8Ti_{25}$, and $Al_{66}Mn_9Ti_{25}$) was compared against binary Al_3Ti and TiAl [16], and at 1273 K, all of the trialuminides were superior to TiAl. The compound $Al_{67}Cr_8Ti_{25}$ appeared to be the only one that formed Al_2O_3 and no TiO_2 and was better than $Al_{66}Mn_9Ti_{25}$, although at a lower temperature of 1073 K, they exhibited comparable resistance. Cyclic oxidation- resistance (1473 K/air/200 cycles, 1 h each) of the Cr- containing $L1_2$ compound was shown to be superior to

the Mn- based counterpart [17] although in a later study [18] it was shown that at lower temperatures, the two compounds exhibited comparable resistance.

In general, there are many possible causes of low ductility of ordered intermetallics. These include large Burgers vector of dislocations due to the ordered superlattice structure of the intermetallic alloys, insufficient number of deformation modes, planar slip and strain localization, lack of effective dislocation sources, difficulty of dislocation multiplication, poor cleavage strength and low surface energy, and grain boundary weakness. It is clear that some of the ordered intermetallics are brittle for more than one reason.

While there are many examples of intermetallic compounds which are brittle because of one or a combination of factors mentioned above (e.g. NiAl because it lacks five independent slip systems) there are others which should- by criteria used to judge metals and disordered alloys- be ductile, but are not. For example, the $L1_2$ trialuminides appear to have many of the requirements for good ductility: they slip on {111}<110>, i.e. they have five independent slip systems, they are not particularly strong or hard at room temperature indicating that dislocation generation and movement are not difficult in these materials; and, because they do not in general fracture intergranularly, they appear not to have weak grain boundaries. Yet they are without exception quite brittle. Microstructural and mechanistic understanding of this "soft and brittle" behavior of $L1_2$ trialuminides (Al_3Sc as well as Al_3Ti- base alloys) is at present elusive.

Table 2.1 shows the measured and calculated elastic moduli of some $L1_2$ trialuminides. It can be seen that the trialuminides all have unusually low values of Poisson's ratio, ν, which for most metals ranges between 0.25 and 0.35.

Table 2.1 Measured (room temperature) and calculated (0 K) elastic moduli and density of trialuminides. E (Young's modulus), G (Shear modulus), K (Bulk modulus), and ν is Poisson's ratio.

Alloy (at.%)	E [GPa]	G [GPa]	K [GPa]	ν	ρ [g/cm³]	Ref.
$Al_{67}Ni_8Ti_{25}$	200	82	116	0.22	-	19[1]
$Al_{67}Ni_8Ti_{25}$	-	-	-	-	3.8	20[2]
$Al_{67}Mn_8Ti_{25}$	174	79	74	0.11	-	8[1]
$Al_{67}Fe_8Ti_{25}$	192	84	89	0.14	-	21[1]
$Al_3Ti(L1_2)$	175	71	118	0.20	-	22[2]
$Al_3Ti(DO_{22})$	-	-	-	-	3.3	20[2]
$Al_{67}Fe_8Zr_{25}$	166	68	103	0.22	-	21[1]
$Al_{62}Cu_{13}Ti_{25}$	-	-	-	-	4.0	20[2]
$Al_{66}Zn_9Ti_{25}$	-	-	-	-	3.9	20[2]
Al_3Sc	166	68	99	0.22	-	23[1]
Al_3Sc	164	68	92	0.20	-	23[1]
Al_3Sc	-	-	-	-	3.0	20[2]

[1] Measured; [2] Calculated.

2.2 Microstructure/ (Tensile-Compressive) Relationships in Cubic Titanium Trialuminides

The mechanical properties of $L1_2$ trialuminides have most commonly been characterized by compression or hardness tests. These tests, while they provide valuable information on deformation behavior, are not as useful in characterizing fracture behavior. To date, the only uniaxial tensile tests have been done by Kumar and Brown [14,15,24] on the Mn- and Cr- modified compounds.

Compression tests performed on the medium size- grained $Al_{67}Cr_8Ti_{25}$ and $Al_{66}Mn_9Ti_{25}$ alloys [11] (grain size ~50 μm) showed that the yield strength exhibited

a plateau between 600 K and 1000 K. The material was obtained by isothermal forging of the cast ingots. The microstructure was essentially a single $L1_2$ phase with small amount of a second phase (unidentified) having a whisker (fibrous) morphology. The strength at any given temperature compared well with the results of Zhang et al. [25] on $Al_{67}Cr_8Ti_{25}$ and $Al_{67}Mn_8Ti_{25}$ alloys obtained by casting, homogenizing and HIP-ing. In contrast, the higher strength and a prominent peak in strength at 900 K was reported by Mabuchi [9] on $Al_{67}Cr_8Ti_{25}$ obtained by powder processing.

At room temperature, most $L1_2$ trialuminides apparently show ductile behavior in compression, usually with a macroscopic fracture strain of more than 10%. This apparent ductility has been recognized to be accompanied by profuse microcracking [19,26,27]. The precise strains at which these cracks first start to form during testing at room temperature are not known, but extensive internal and external cracking is observed at compressive strains as low as 2% [19]. Microcracks are also observed after low strains, on the order of 0.2% with pores as preferential sites for nucleation [28]. It is not known yet what fraction of the measured compressive ductility is due to microcracking and what fraction is due to dislocation activity. The development of microcracking at high temperatures is considerably less pronounced than that at RT. At high temperatures, the microcracks start forming at much higher compressive strains (several percent), the longest cracks observed after several percent of deformation at high temperature are much shorter than their counterparts developed at RT at much lower strains and the number of microcracks formed at high temperatures at corresponding strains is considerably smaller than the number of microcracks formed at RT at much lower strains. Also, there is a reduction in the frequency of secondary crack formation

(branching) at compressive failure strains with increasing test temperature and at 900°C, failure occurs by the propagation of one primary crack parallel to the compression axis [28].

Very often, the total crack length around a Vickers indent or the maximum crack-free load is used as a measure of relative ductility and/or the relative cracking resistance [29, 30, 31, 32]. The Vickers hardness of these materials decreases with load [33] down to a plateau value [34].

Winnicka and Varin [32] investigated the influence of boron on cracking characteristics of Cu- modified Al_3Ti compound. They found that boron- doped alloy exhibited many, relatively short cracks propagating from the indentation, as opposed to pure Cu- modified alloy which showed few but very long cracks originating from the indentation. The sensitivity of boron- doped compound to cracking at low indentation loads was much higher than that of its boron- free counterpart. At high indentation loads the opposite was true. The fracture modes of both boron- free and boron- doped alloys at room and slightly elevated temperatures were transgranular cleavage (TGC). However, the fracture surfaces of boron-doped samples appeared entirely different than the fracture surfaces of boron-free specimens. The fracture features occurred on a much finer scale than for the cleavage fracture in boron-free alloy. The cracks were formed by fracture of brittle boride particles. It was also observed in favor of this fracture mechanism that a large number of fine cracks was formed around the Vickers hardness indentation. It is intriguing how boron affects the fracture toughness of cubic ($L1_2$) titanium trialuminides especially at high temperatures where the major mode of fracture is intergranular failure (IGF). In Ni_3Al which has the same $L1_2$ crystallographic structure as cubic titanium trialuminides boron doping improves fracture toughness

by alleviating intergranular fracture [35]. Cubic titanium trialuminides fracture at room temperature by transgranular cleavage [15,19]. Therefore, the effect of boron at ambient temperature does not seem to be as direct as in $L1_2$ Ni_3Al. Nevertheless, taking into account rather distinct fracture behavior of Cu-stabilized titanium trialuminide [32] it is important to explore this avenue in the hope of improving fracture toughness. However, the fracture mode in titanium trialuminide changes to intergranular fracture (IGF) at high temperatures [15]. Therefore if boron segregates to grain boundaries it might have a beneficial effect at elevated temperatures by suppressing IGF. Therefore, tests were performed in the present study on boron-doped low- and high- Mn alloys in the temperature range from RT to 1000°C.

The influence of Mn and Ti content on the bending properties of Mn- modified $L1_2$ compound was investigated by Mabuchi et al. [36]. They observed an increase of the fracture strain from ~0.05% to 0.4% by increasing Mn content from 9% to 14% (keeping Ti content constant, 25%). The fracture stress was very similar in both cases. On changing Ti content from 25% to 29% (keeping Mn at constant level, 14%) they obtained a substantial increase in fracture stress from ~370 MPa to ~640 MPa and the fracture strain remained at the high (0.4%) level. Such a combination of fracture stress and strain is a highly desired material property from the point of view of fracture toughness. These results [36] encouraged the author of the present work to concentrate on the fracture toughness testing of the alloys with a high (Mn + Ti) concentration. As mentioned above, with the hope of obtaining even higher toughness especially at higher temperatures, the alloys with a high (Mn + Ti) concentration were also boron doped to the levels of 0.24% B and 0.65% B.

Kumar and Brown [14,15,24] were able to measure a finite (0.2%) amount of plastic tensile deformation at ambient temperatures and 1.3% at 623 K on the Mn-

modified Al_3Ti. A ductility minimum was reached for both materials at 773 K, followed by a tensile elongation increase to 5% for the Mn- modification and 19% for the Cr- modification at 1073 K. One explanation proposed for the ductility drop was based on the decrease in mobility of the matrix dislocations caused by dislocation tangling and pile- ups at the grain boundary. This decrease in mobility provides an opportunity for solute atmospheres to diffuse to the dislocations and pin them. Other factors that could cause a decrease in intermediate temperature ductility, a characteristic seen in $L1_2$ Ni_3Al and Co_3Ti [37,38], was attributed to dynamic oxygen embrittlement [39], where atomic bonds weakened by oxygen chemisorption, together with stress concentration at grain boundaries, cause grain-boundary microcracking. The overall decrease in ductility was attributed to continuous embrittlement of fresh crack tips and propagation of the crack along the boundary. Fracture mode changes from transgranular cleavage at ambient temperatures to a mixed cleavage plus intergranular failure at 623 K and to a predominantly intergranular mode at 923 K and higher. Small amounts of intergranular fracture were observed at temperature as low as 473 K. At this temperature fracture was predominantly transgranular cleavage, but the intergranular failure was typically observed at the periphery of the fracture surface, lending some credibility to the environmental embrittlement theory. It is possible that kinetics of chemisorption is maximum around 773 K, leading to ductility minimum. However, the temperature corresponding to the tensile ductility minimum is not in agreement with the temperature for the onset of intergranular fracture. The recovery in ductility at higher temperatures was attributed to a combination of possible dynamic recrystallization and enhancement of slip transfer across grain boundaries.

The existence of a yield stress anomaly, i.e. an increase of yield stress with temperature, does not seem to correlate with alloying additions to Al_3Ti. A relatively well- defined anomalous behavior for the Fe- modified Al_3Ti was observed by Kumar and Pickens [40], but very small one by Wu et al. [41]. Likewise, anomalous behavior was found in compression for the Mn- and Cr- modified Al_3Ti [9,25] but in other studies was not observed [42].

In bending tests on the Cr- and Mn- modified compounds a very small but definite plastic strain has been observed [13,29]. While a large number of branched microcracks are accumulated in specimens tested in compression, specimens tested in bending contain almost no microcracks [27,43]. This is because once a crack is formed in the tensile side of a bending tests specimen, it propagates catastrophically through the specimen.

The models of strain- induced nucleation of microcracks by dislocation pile- ups [44,45] were applied for trialuminides and it was calculated [46], that at the stress approaching 0.2% offset stress, only 200 to 400 dislocations are required in a pile-up to nucleate microcracks with the length 10 to 45 μm in the $L1_2$ Ti- trialuminides. These calculated crack lengths are within the size range of microcracks observed experimentally in the $L1_2$ Ti- trialuminides after about 0.2- 0.4% deformation in compression [28].

2.3 Fracture Toughness of Cubic Titanium Trialuminides

Toughness requirements are dependent on working stress levels, and static and impact analysis suggest that the fracture toughness (in $MPa\sqrt{m}$) should be about one-third the numerical value of the working stress (in MPa) [1]. As mentioned by

Ashby [47], a value of $K_{IC} \approx 20$ MPa$\sqrt{m}$ is often quoted as a minimum for conventional design. Also, Jackson et al. [48] stated that a working hypothesis has been offered that once a material exceeds a threshold of ≈20 MPa$\sqrt{m}$, toughness in the make-and-assemble stages is not a major issue. This threshold may eventually be relaxed as further experience is gained. Therefore, an important goal is optimising the structure of many intermetallic alloys to obtain the value of K_{IC} at least about 20 MPa$\sqrt{m}$, if not better.

Fracture toughness tests reported are only those of Brown and Kumar [49] on the Cr- and Mn- modified Ti trialuminides as a function of temperature in the range from RT to 1000 K. Three point bend single- edge- notched- beam specimens with a notch tip radius of ~50 μm were tested with a crosshead speed of 2.1×10^{-3} mm/s. Fracture toughness increased monotonically from ~3.5 MPa$\sqrt{m}$ at RT to ~11 MPa$\sqrt{m}$ and 13 MPa$\sqrt{m}$ at 1000 K for the Mn- and Cr- modified materials, respectively, and a ductility minimum in uniaxial tension at ~773 K [14,15] was not evident in the toughness- temperature profile.

Tests done on notched bend specimens at 973 K using crosshead speed 4×10^{3} times faster than the toughness tests, still produced fully intergranular failure when tested in air as well as in vacuum (1.3×10^{-3} Pa), i.e. fracture mode at 973 K remained intergranular independent of strain rate and environment. However, there are no numerical values of toughness for these materials tested in vacuum in the study reported in Ref. [49] or in any other environment at all. It is intriguing what is the toughness vs. temperature profile in different environments, especially in correlation with tensile behavior of these materials with temperature described above. As mentioned earlier, Kumar and Brown [49] conducted their toughness

tests to 1000 K. In the present work the testing temperatures are extended to 1273K.

Though very sparse, the most comprehensive experimental data on fracture toughness of single phase and multiphase ordered intermetallics have been summarized by Vehoff [50]. Unfortunately, this overview does not contain the group of alloys which are of interest in this work.

2.4 Intrinsic and Extrinsic Factors in the Fracture of Intermetallics and their Applicability to Cubic Titanium Trialuminides

2.4.1 Extrinsic Factors- Environmental Effects

Considering first extrinsic factors, the presence of impurities has been ruled out as a major contributor to the brittle fracture of trialuminides on the basis of Auger analyses of fracture surfaces [21].

There are two types of environmental degradation observed in intermetallics. One is hydrogen- induced embrittlement occurring at ambient temperature. The other is oxygen- induced embrittlement in air at elevated temperature. In both cases, the embrittlement is due to a dynamic effect involving generation and penetration of an embrittling agent (i.e., hydrogen or oxygen) during testing.

In the last several years it has been found that some ordered cubic (or near- cubic) intermetallics are prone to a very peculiar type of embrittlement caused by moisture- containing environments such as, for example, air. As reported in the literature, the moisture- induced embrittlement can result in both intergranular failure and transgranular cleavage. For example, under tensile or bending loading conditions a polycrystalline, ordered ($L1_2$) Ni_3Al fails by intergranular fracture [51] but a polycrystalline, ordered (B2), Al- lean FeAl compound fails by transgranular

cleavage [52]. The embrittlement mechanism is thought to involve reaction of reactive metallic M, with water vapor in air, resulting in the generation of atomic hydrogen [52,53]:

$$M + H_2O \rightarrow M - O + H$$

Atomic hydrogen penetrates into crack tips causing embrittlement and premature failure. However, the details of this water vapor- hydrogen embrittlement are still not completely understood.

In terms of hydrogen-induced environmental degradation, ordered intermetallics can be grouped into two categories: (a) alloys containing no reactive elements, and (b) alloys containing reactive elements (e.g., Al or Si). For the first category, the alloys are severely embrittled only when being charged with hydrogen, such as by cathodical charging. For the second category, the alloys themselves are capable of generating hydrogen from hydrogen-containing environments at ambient temperature. The most striking is severe embrittlement of iron aluminides in moist air at room temperature.

Some authors reported that compression tested specimens of most cubic titanium trialuminides contain numerous internal cracks, which are not in contact with the external environment [19] and this can lead to the assumption that environmental embrittlement is not a major factor controlling fracture behavior. However, the surface cracks can be in contact with the environment and hence, this assumption might not be quite correct. Additionally, there was no discernible change in the fracture mode (namely, cleavage) after in-situ fracture in the ultrahigh vacuum of the Auger microprobe ($<2x10^{-8}$ Pa) [21]. It should be recognized however that a range of ductilities is possible for a given fracture mode.

An interesting case of the influence of the environment such as hydrogen on the slip properties has also been presented [54]. When the material is exposed to hydrogen at a fugacity f_0 and mechanically loaded at the same time, hydrogen may facilitate its entry into the material by riding with the dislocations emitted from a surface crack. If n hydrogen atoms per unit length of dislocation can lower their fugacities from f_0 to some value f by residing in the emitted dislocations, the energy barrier for the emission process is lowered by $nKln(f_0/f)$ per unit length of dislocation. A larger effect is expected in the case of high fugacity hydrogen such as atomic hydrogen absorbed from moisture in air at the crack tip. However, the effect of hydrogen on fracture behavior of some intermetallic alloys (especially Long Range Ordered) is just opposite. It does not enhance the crack tip plasticity by making the dislocations more mobile. Instead, it weakens the atomic bonds in already highly stressed crack tip region, thereby lowering the fracture toughness. Usually the effect of hydrogen on the fracture behavior of some intermetallic compounds is such that it degrades the fracture toughness through weakening the cohesive strength of grain boundaries. In effect, it changes the ductile, transgranular fracture mode to brittle intergranular mode.

As mentioned earlier, cubic titanium trialuminides have low yield strength and hardness. They are still brittle in tension although they show quite a substantial apparent ductility in compression. This soft- brittle behavior is the most peculiar phenomenon which makes the cubic titanium trialuminides extremely interesting from the scientific point of view. The exact causes of such a behavior are not well understood. However, by analogy to what is said above, it could also be possible that the environment (e.g. water vapor) might somehow be responsible, if only partially, for the embrittlement of the ternary cubic ($L1_2$) titanium trialuminides.

Tensile tests on the Cr- modified Al_3Ti showed possible influence of environment on ductility [14]. Specimens protected by an Au film and tested at 773 K exhibited >1% ductility although the fracture mode at this temperature remained predominantly transgranular cleavage. In the specimens without the protective film, ductility was not measurable at 773 K. However, the enhancement in ductility afforded by a protective film may also arise from a source that is not environment related. It was shown that such a film provides an interface that acts as a dislocation source [55], thereby enabling slip and enhanced plastic deformation. Such a mechanism cannot be ruled out in interpreting the results without tests in vacuum or an inert environment.

Bending tests of Kumar and Brown [56] on Cr- modified Al_3Ti conducted in both air and diffusion- pump oil at 473K revealed the likely absence of environmental embrittlement. In both cases the specimens fractured at identical strains. Morris et al. [57], on the other hand, suggested that environment was responsible for intergranular fracture extending some distance into the tensile edge of the bend specimens. Coatings used in their studies have not been able to inhibit such an environmental effect. It was concluded that perhaps environment plays its role already during sample polishing.

To understand the effect of environment on the fracture toughness of these intermetallics, a testing of the $L1_2$ Mn- modified Al_3Ti in bending has been carried out in the present work in air, vacuum, argon, water and liquid nitrogen.

2.4.2 Intrinsic Factors- Crack Tip Plasticity and Low Cleavage Strength

Intrinsic factors which can cause brittle transgranular cleavage fracture in metals include [7]:

1. Insufficient number of "slip systems".
2. High yield strength.
3. High strain rate sensitivity.
4. Inhibited dislocation emission from crack tips.
5. Poor cleavage strength.

The above factors will be now discussed as applied to the brittle behavior of cubic titanium trialuminides.

Recently, a study of the mechanical properties of single crystals of Al_3Ti in the $L1_2$ form (alloyed with Fe and Cr) has been made with the aim to investigate whether the brittleness is related to some unusual slip properties. The following are the major results [41]:

1. The critical resolved shear stress (CRSS) for (111)[101] slip is low and is only mildly temperature dependent over a broad range of temperatures between 300 and 1100 K, but it increases sharply with decreasing temperature below 300 K.
2. The CRSS for (111)[101] slip obeys Schmid's law over the entire temperature range.
3. The CRSS for (111)[101] slip is only mildly strain rate dependent.
4. There is no shortage of slip systems. Slip occurs on all {111}<101> systems.
5. No compressive ductility is possible below 1000 K.

Based on findings 1-4, Al_3Ti could be expected to be a reasonably tough material, but it is seen from result 5 that it is in fact quite brittle. Cubic titanium trialuminides do not have an unusually high yield strength (σ_y for the Mn-modified Al_3Ti is ~60 MPa [28]). The strain rate sensitivity at RT in the strain rate regime 10^{-4} to 10^{-2} s^{-1} is low for the Ni- modified Al_3Ti [19] and modest increase (~17%) in the

RT yield strength of the Fe- modified Al_3Ti was observed when strain rate increased from ~10^{-4} to 10^{-3} s^{-1} [27]. Thus dislocations are able to respond to the rapidly changing stress fields associated with propagating cracks. Also the bending tests on Cr- modified Al_3Ti compound [56] showed that ductility was fairly constant over a large range of crosshead speeds ($4.2x10^{-5}$ mm/s to 0.85 mm/s). However, increasing the loading rate from 0.85 mm/s to 4.2 mm/s caused the ductility drop from 0.55% to zero and also very substantial drop of fracture load. One plausible explanation of the ductility loss could be a limitation in dislocation velocity which could result in incomplete crack- tip shielding.

In order to understand the intrinsic, atomic level deformation characteristic of Al_3Ti in the $L1_2$ phase, dislocation core structures were investigated for a model $L1_2$ compound with a high antiphase boundary (APB) energy and performed using the Finnis- Sinclair- type many- body potentials [58] and their results suggest that the cores of screw dislocations in Al_3Ti in the $L1_2$ phase are always sessile, spread onto two intersecting {111} planes of the <101> common direction. This explains the strong temperature dependence of the yield stress at low temperatures but suggests that at temperatures higher than 300 K, the material should be ductile, because thermal activations are sufficient at these temperatures to render the dislocations with non- planar cores glissile. Hence, no atomic level structural reason for the "quasi- brittleness" has been identified.

Now, the discussion will be focused on crack tip plasticity, in particular the emission from the crack tip and its models relevant to cubic titanium trialuminides. There is lack of general understanding in the areas of crack-tip plasticity, fracture toughness and notch sensitivity and it was specifically mentioned in the discussion of the NATO Advanced Research Workshop on Ordered Intermetallics [59].

TEM studies of Kumar and Brown [15] on thin foils of $Al_{66}Mn_9Ti_{25}$ clearly showed that dislocations were emitted at the crack tip. However, they found several boundaries at 298 K which were able to absorb but unable to emit dislocations readily into the adjacent grain, thereby causing a pile- up in the first grain. This led to rapid work- hardening and increase in flow stress above that for cleavage, leading to low ductility. It was suggested that at higher temperatures (473 and 623K), even though the material work-hardens rapidly in the initial stages, the subsequent rate drops due to easier dislocation transfer through grain boundaries. Morris et al. [57] in their studies on thin foils of $Al_{67}Mn_8Ti_{25}$ observed that stress and strain relaxation near tip of a cleavage crack could occur by the emission of mobile dislocations in the form of relatively intense slip bands. However, the amount of strain relaxation that occurred appeared to be limited by the relatively small number of slip bands that were produced. Also, the dislocations present in the material before mechanical testing were immobile and unable to assist the stress relaxation process. Similar conclusion was reached by Kumar and Brown [56] in their studies of effect of prestrain on bend ductility of $Al_{66}Cr_9Ti_{25}$ compound. They found that prestraining the polycrystalline $L1_2$ compound, either at low (298 K) or elevated temperature (1273 K) was unsuccessful in improving the bend ductility; instead the available ductility in the well- annealed material was lost. The authors argued that in $L1_2$ compounds, a prestrain at elevated temperatures may incorporate APB- dissociated dislocations on the cubic planes as well as dislocations with a<100> Burgers vectors that are likely to be immobile at room temperature and do not contribute necessarily to enhancing plasticity, but may contribute to work hardening. Additionally, the fact that in some $L1_2$ compounds such as Co_3Ti the dislocation dissociation scheme changes not only with

temperature but also with applied stress [60] led the authors to the conclusion that the dislocations from the prestrain may not be mobile under the influence of the applied stress unless they can reverse their dissociation behavior readily. It is worth noting here for comparative purpose that the beneficial effect of prestraining body-centered cubic metals to increase the mobile dislocation density that can assist in blunting crack tips, increase ductility and lower the brittle- to- ductile transition temperature is well established [61] (see also the model of Ashby and Embury in the following section).

It is known that the tendency to SISF dissociation could be favored under conditions of low temperature straining or high deformation speed, that is where thermal activation is limited [62]. Such high speed deformation conditions apply precisely near a propagating crack tip, which could thus perhaps favor such SISF dissociation and lead to the creation of poorly mobile dislocations.

2.4.2.1 Rice- Thomson General Model of Crack Tip Plasticity- Dislocation Emission

A conventional understanding that a solid will either be ductile or truly brittle depending upon the ratio of theoretical shear strength to theoretical tensile strength was refined by Rice and Thomson (referred to as the "R-T model") [63]. According to them a correct description of this competition should include actual dislocation processes at cracks, since the ductile response of the solid must produce dislocations in order to yield. The model will be presented because of its fundamental concepts and importance in the field.

The stress is highly localized in the vicinity of the crack tip. By geometrical necessity, localized shear on a plane intersecting the crack tip caused by the high shear stresses there, matched to a non- sheared region at greater distances on the

same plane, where the stress is below the theoretical strength simply defines a dislocation. Hence, a blunting reaction at the crack tip requires the production of dislocations.

Crystals for which dislocation emission is spontaneous can be expected to be good candidates for essentially plastic opening of the crack. Crystals for which there exists a large energy barrier for this emission can be expected to be good candidates for brittle cleavage. In order for a dislocation to blunt a crack, it is necessary for the Burgers vector to have component normal to the crack plane, and for the slip plane to intersect the crack line (or crack front) along its whole length, i.e. the line must be contained within the slip plane (Fig.2.2). The most likely plane that passes through a crack tip for dislocation emission is one that makes an angle of $\theta \approx 70.5°$ with the crack plane. The shear stress component of $\sigma_{r\theta}$ of a mode I crack in an elastic solid is $\sigma_{r\theta}=[K_I/\sqrt{(\pi\rho)}]\sin\theta\cos(0.5\theta)$, thus from $\partial\sigma_{r\theta}/\partial\theta=0 \Rightarrow \theta=70.5288°$ [64].

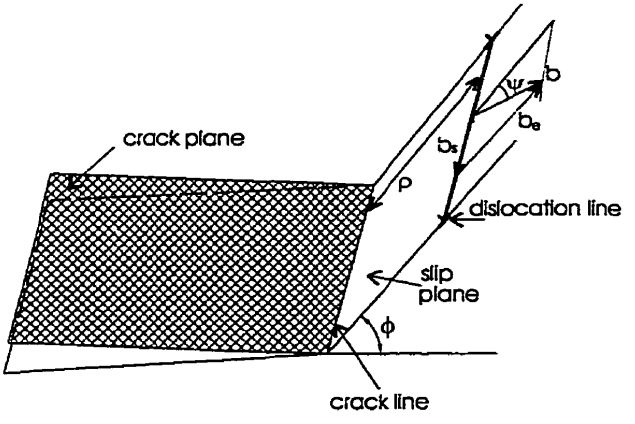

Figure 2.2 Crack configuration and geometry of the dislocation [63].

The model contains detailed description of force balance. The forces operating between a crack and a dislocation in two dimensions are:

1) the force on a dislocation due to the stress field surrounding the crack,

2) the surface tension force caused by creating more surface at the blunted crack,

3) the image force of the dislocation in the free surface of the crack.

The first term repels the dislocation, and the latter two attract it toward the crack tip, giving rise to the possibility of a position of unstable equilibrium. The critical distance, ξ_c, at which a straight dislocation is in unstable equilibrium under these three forces is given by the solution of:

$$f_{tot} = Gb\left[-\frac{1}{4\pi\xi}\frac{1-\nu\sin^2\psi}{1-\nu} - \frac{2}{\pi\eta^2\beta'}\frac{\alpha}{\xi^2+\alpha^2} + \frac{1}{\eta\beta}\left(\frac{1}{2\pi(1-\nu)\xi}\right)^{1/2}\right] = 0 \qquad (2.1)$$

$$\frac{1}{\beta} = \cos\psi\sin\phi\cos\phi/2$$

$$\frac{1}{\beta'} = \cos\psi\sin\phi$$

$$\alpha = e^{3/2}\xi_0/2$$

$$\xi = \rho/b$$

$$\eta^2 = Gb/\gamma$$

ξ_0 is the dislocation core cut off,

b is the Burgers vector,

G is the shear modulus,

ρ is the distance of the dislocation from the crack front,

ν is the Poisson's ratio,

γ is the true surface energy.

After some estimations $\xi_c \approx 0.1Gb/\gamma$.

If the equilibrium point, ξ_c, is larger than the core cut- off, then there is an energy hump for the dislocation to jump in order to be emitted from the crack. In this case it will be impossible for a uniform straight line to be emitted from the crack.

Instead, local fluctuations in the form of an irregular loop will be formed which, beyond the saddle point configuration, will expand under the external stress.

By substitution of the empirical values into Gb/γ for many materials and by relating the resulting number to the material's behavior, the authors arrived at the "semiempirical" condition which states that for $Gb/\gamma>7.5-10$, the crack will remain sharp and material will fail in the brittle manner and for $Gb/\gamma<7.5$ ductile fracture will occur. The essential weakness in this model is the argument that the dislocation is assumed to be suddenly well formed and no allowance is made for its gradual build- up [65]. For this reason no reliable estimate of the activation energy of the dislocation formation can be made. Schoeck [65] described such a build- up of the emerging dislocation and determined more realistically the critical stress intensity K_e for which spontaneous dislocation emission occurs at zero temperature and the energy barrier per unit length (in 2D) for the emission when $K<K_e$. The shape of the incipient dislocation is described by a single parameter w- the dislocation width (Weertman [64] treats the discrete crystal dislocations as a smeared continuum of infinitesimal dislocations).

Apart from a numerical factor of less than unity, the result obtained by Schoeck [65] is nearly identical to the corresponding equation of Rice and Thomson model. Again, the main difference in the formulation of the problem was that the dislocation core cut- off, r_0 was replaced by the well defined dislocation width.

An alternative view from that of Rice and Thomson [63] on brittle to ductile transition is presented in a model by Ashby and Embury [66]. This model explains the beneficial influence of the increased dislocation density in many bcc metals on fracture toughness. It is assumed in this model that the crack will run without crack tip plasticity (by the motion of the pre-existing dislocations) if the stress falls below

τ_p (the lattice resistance for dislocation motion) in a distance from the crack tip which is greater than the dislocation spacing, giving a low energy fracture. If, instead, dislocations are always within reach of the crack tip then a higher energy fracture will result. Eventually, the model gives the analytical dependence of the ductile-to-brittle temperature, T_C, on the dislocation density taking into account the effects of crack velocity and work hardening. The result shows that large increase in dislocation density produces a gentle decrease in T_C. However, at a very large value of dislocation density (roughly 10^{18} m/m^3) the work hardening contribution to the local flow stress becomes so great that plasticity and blunting is inhibited, and T_C rises steeply.

2.4.2.2 Dislocation Emission Models Applied to Intermetallic Compounds

In addition to predicting the average fracture mode at low temperatures, dislocation emission models can be used to make a variety of detailed predictions. These include predictions of fracture- mode transition temperatures and predictions of the effect of grain orientation on fracture mode. Cleavage fracture in materials possessing a high critical resolved shear stress (CRSS) is relatively easy to understand: the high resistance to slip inhibits crack tip plasticity, resulting in cleavage fracture. However, many intermetallic alloys that fail by cleavage fracture posses low to moderate values of CRSS, requiring an alternate explanation for cleavage fracture.

Turner, Powers and Wert [19] first applied the R-T model to cubic titanium trialuminides. They showed that the R-T model was consistent with cleavage fracture of $Al_{67}Ni_8Ti_{25}$, a trialuminide intermetallic stabilized by Ni. Room-temperature plastic deformation of $Al_{67}Ni_8Ti_{25}$ in compression was shown to occur

by the glide of undissociated a<110>{111} superlattice dislocations [19,67] which permitted direct application of the R-T model. Other intermetallic alloys with the $L1_2$ crystal structure were found to deform by the glide of dissociated superlattice dislocations, [68-72] complicating application of the original R-T model.

Subsequent observations have shown that several $L1_2$ intermetallic alloys with dissociated superlattice dislocations exhibit cleavage fracture [21, 62], contrary to the suggestion of Turner et al. [19].

Bartholomeusz and Wert (BW model) [73-77] extended the R-T analysis to treat emission of dissociated superlattice dislocations from crack tips in $L1_2$ and B2 intermetallic alloys. Therefore, they considered emission of concentric, semicircular, superlattice partial dislocation loops, shown schematically in Fig.2.3.

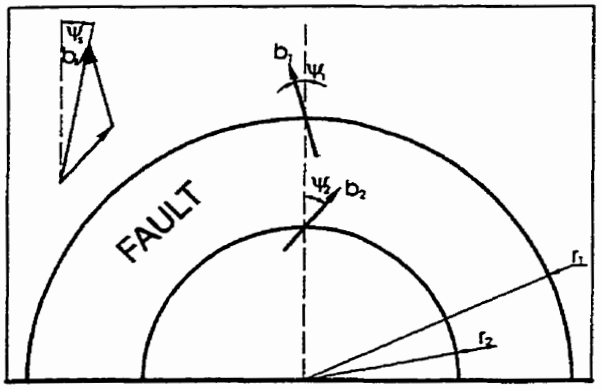

Figure 2.3 Geometry of a dissociated superlattice dislocation on the slip plane [73].

In the case of a dissociated superlattice dislocation, the total energy of the dislocation as a function of distance ahead of the crack tip is dependent on five material and two geometrical parameters. The material parameters are: shear modulus, G; Burgers vector, b; true fracture surface energy, γ; bulk modulus, K; and stacking fault energy, Γ. Two geometrical parameters are: ϕ- the angle between the

slip plane and the crack plane, and ψ_s–the superlattice Burgers vector orientation relative to the crack.

If U_{act} (activation energy for dislocation emission) is equal to zero, there is no energy barrier to superlattice dislocation emission, plastic crack blunting occurs. For a given material, it is possible to determine U_{act} as a function of ϕ and ψ_s, the parameters describing the slip system orientation relative to the crack tip. Variation of ϕ and ψ_s accounts for the variety of grain orientations encountered along a crack front. Figs.2.4 and 2.5 represent combinations of ϕ and ψ_s corresponding to

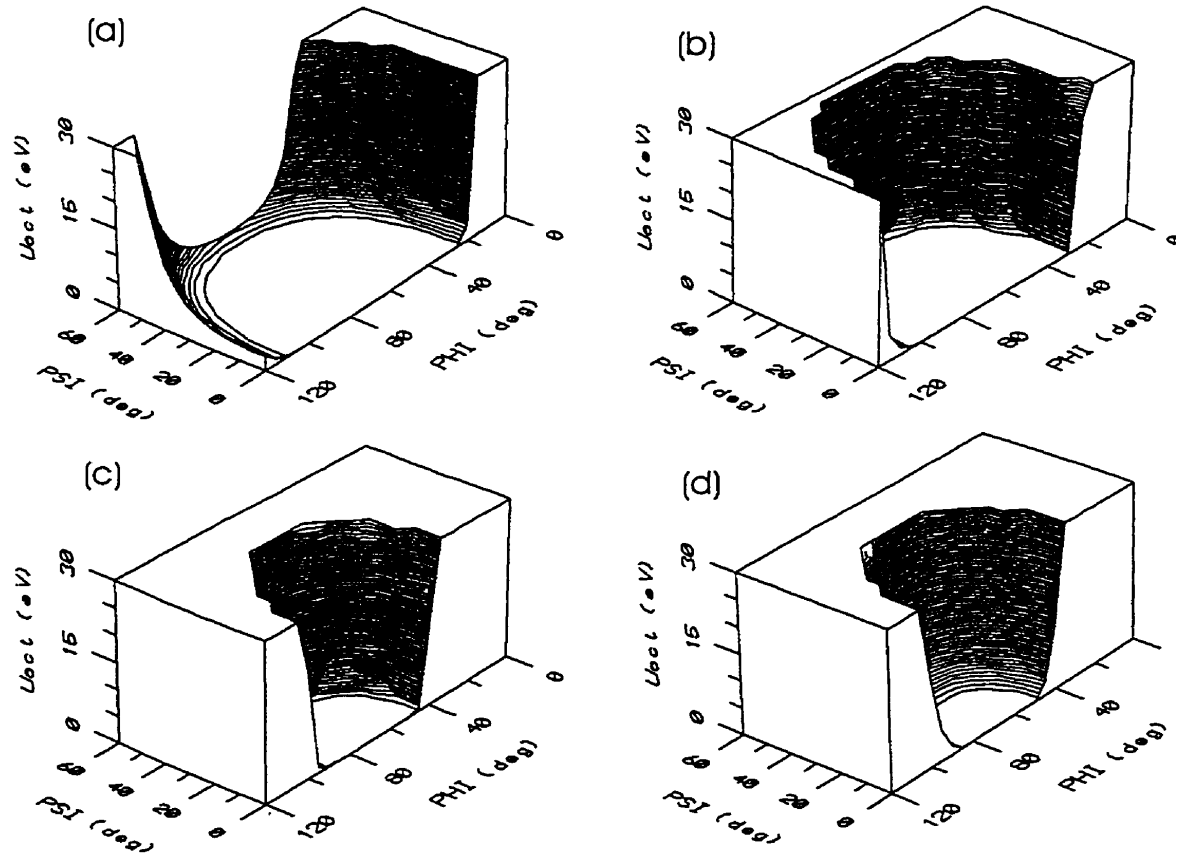

Figure 2.4 Activation energy for emission of a dissociated superlattice dislocation as a function of slip system orientation in several $L1_2$ intermetallic alloys exhibiting APB– type dissociation. a) Cu_3Au, b) Ni_3Al, c) Al_3Sc, d) $Al_{67}Ni_8Ti_{25}$ [73].

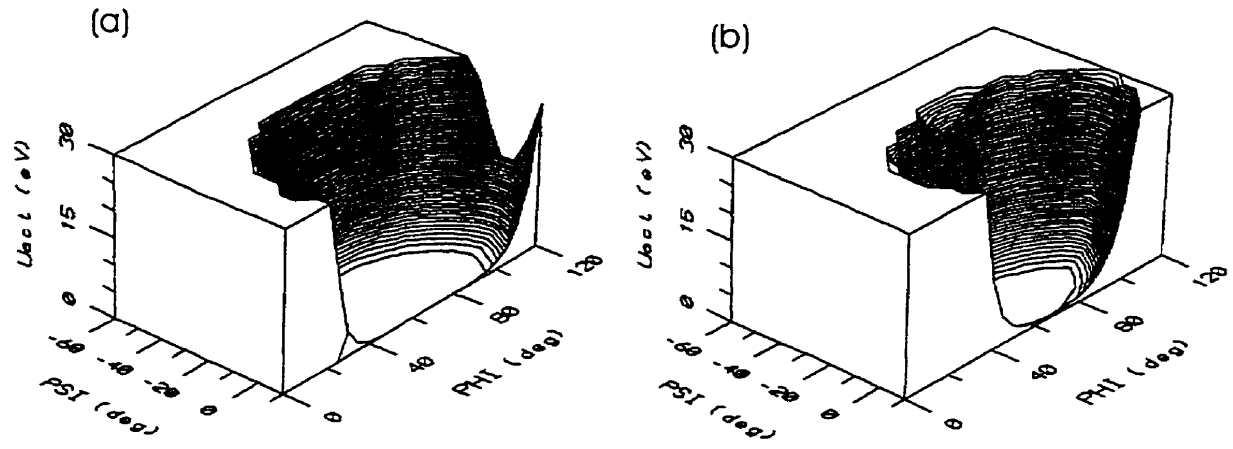

Figure 2.5 Activation energy for emission of a dissociated superlattice dislocation as a function of slip system orientation in two $L1_2$ intermetallic alloys exhibiting SISF- type dissociation. a) Zr_3Al, b) $Al_{66}Fe_6Ti_{23}V_5$ [73].

spontaneous emission of dissociated superlattice dislocations. The plateau at 1 eV represents the range of slip systems orientations for which spontaneous or thermally activated dislocation emission can occur at room temperature (it is assumed that at RT, there is enough thermal energy available to the dislocation half loop to overcome an energy barrier of 1 eV). The parameter $\xi(293)$ describes the fractional angular ranges of ϕ and ψ_s corresponding to spontaneous or thermally activated emission of dislocations at room temperature for a given material. Fractional implies the solid angle of all possible orientations of a superlattice dislocation. Angular ranges for ϕ and ψ_s are (-180 to +180) and (-90 to +90), respectively. The gradient of the surface represented by contour lines is related to the potential for significant thermal activation effects. Decreasing steepness of the sides of the activation energy well indicates a greater sensitivity to thermal activation. The model predicts that materials having a value of $\xi(293)$ greater than 0.08 are resistant to cleavage fracture. Reducing the magnitude of the Burgers vector renders dislocation emission from a crack tip more energetically favorable.

This can be accomplished either by dissociation of superlattice dislocations or by a change in slip vector. The emission of APB coupled superlattice partial dislocations is more energetically favorable than emission of undissociated superlattice dislocations. According to Bartholomeusz and Wert [74] lowering the APB energy is a possible means of inducing resistance to cleavage failure in intermetallic alloys at ambient temperatures. In contrast to this, lowering the SISF energy does not have a significant effect on $\xi(293)$ and is not expected to affect the fracture mode. Lowering the APB energy for $L1_2$ and B2 intermetallic alloys can generate sufficient spontaneous or thermally activated emission of dissociated superlattice dislocations to avoid cleavage fracture at room temperature (direct evidence has not yet been reported). The Bartholomeusz and Wert [74] model also predicts that crack tip plasticity is more sensitive to variations in the shear modulus than equivalent variations in the bulk modulus. Reducing the shear modulus increases resistance to cleavage fracture.

Very recently, Wang [78] proposed a model of dislocation emission using a newly introduced solid state physics parameter– the unstable stacking energy, γ_{us}. The starting point of the model is that if the critical energy release rate required for dislocation nucleation from the crack tip (G_{disl}) is lower than the critical crack extension force required for cleavage or decohesion of the solid (G_{cleav}) then dislocation emission occurs first, blunting a crack tip and as a result the solid is intrinsically ductile. If, however, $G_{disl}>G_{cleav}$ then cleavage occurs before dislocation emission, and the solid is intrinsically brittle.

There are two types of dissociation of superdislocations in $L1_2$ lattice [79,80], that is, the antiphase boundary-coupled (APB) a/2<110>{111} dissociation:

$$a\,[110] \rightarrow a/2\,[110] + APB(1\bar{1}1) + a/2\,[110]$$

and the superlattice intrinsic stacking fault (SISF)- coupled a/3<211>{111} dissociation:

$$a\,[110] \rightarrow a/3\,[21\bar{1}] + SISF(1\bar{1}1) + a/3\,[121]$$

Each of the a/3<211> superpartials can dissociate further to three a/6<211> Shockley partials with an APB and a complex stacking fault (CSF). Such a reaction is shown below for a a/3[211] superpartial:

$$SISF(1\bar{1}1) + a/3\,[21\bar{1}] \rightarrow SISF(1\bar{1}1) + a/6\,[1\bar{1}\bar{2}] + APB(1\bar{1}1) + a/6\,[21\bar{1}] + CSF(1\bar{1}1) + a/6\,[121]$$

The model considers incipient dislocation nucleation in the CSF-coupled scheme and assumes that cross slip of the screw segment is not activated so that the nucleated partials are glissile.

The model correctly predicts, for example, that Ni_3Al intermetallic alloy is less ductile than Ni. It also predicts that Ni_3Al single crystals are more ductile than bicrystals. However, the model also shows some inconsistency with the prediction of the brittle/ductile transition for Ni_3Al. It predicts that for the APB-coupled a/2<110>{111} slip the ratio $G_{disl}/G_{cleav}>1$ which means that Ni_3Al would be intrinsically brittle, and which is obviously in contradiction of the observed ductility of Ni_3Al (when tested in vacuum). The most frequently observed dislocation dissociation mode in Ni_3Al is through the APB-coupled superpartials [81-83]. According to the model, the CSF-dissociation renders Ni_3Al ductile.

A model of brittle- to- ductile transition temperature (BDTT) was proposed by Khantha et al. [84] (so called "KPV model"). In this model the BDTT is not described as a thermally activated phenomenon in the usual sense, but rather a thermally driven instability that results in a sudden large increase in the dislocation density.

The unstable dislocation generation is cooperative, which is totally unlike the case in the nucleation- based models, which consider the independent generation of single dislocations [84]. The principal feature of the model is a cumulative temperature- and stress- dependent dislocation screening effect caused by the interactions between many dipole nuclei that coexist at any temperature. The screening becomes stronger with increase in temperature and ultimately enables a collective dislocation instability to occur above a certain temperature, identified as the BDTT. This effect is physically distinct from the usual dislocation shielding of the crack tip stress field and does not exist if thermal fluctuations are not taken into account explicitly.

Very recent atomistic simulations on NiAl intermetallic [85] of crack response showed that when the emitted dislocations are sessile and stay in the immediate vicinity of the crack tip the emitted dislocations can actually lead to brittle failure. The observed cleavage is related to the effect of high density of dislocations in the tip region. The results were rationalized in terms of adding an effective mode I stress intensity by the emitted dislocations which is opposite in sign to that applied and therefore the generally accepted shielding character of emitted dislocations.

2.4.2.3 Low Cleavage Strength

George et al. [21,86] proposed low cleavage fracture strength as the cause of cleavage fracture in $L1_2$ trialuminide alloys. Their arguments were based on calculations showing that Al_3Sc has a significantly lower cohesive strength on {011} than Ni_3Al and that {011} is the cleavage plane of Al_3Sc. However, George at al. [86] pointed out that if low cohesive strength is the cause of brittle fracture, Al_3Sc should cleave on {111}, which is calculated to have lower cohesive strength than

{011}. Explanation of the brittleness on the basis of poor cleavage energy and strength [21] seems also to be unsatisfactory. On the one hand, comparing the surface energy γ of brittle Al_3Sc with that of ductile Ni_3Al, gives 1.7 vs. 3.0 J/m^2 for the (100) cleavage plane [87] (or the ideal cleavage strength of 19 GPa vs. 30 GPa) but on the other hand, γ of Al_3Sc compared with γ of ductile aluminum gives 1.7 vs. 1.2 J/m^2. However, what distinguishes the brittle trialuminides from ductile aluminum is their significantly higher shear moduli (G) which are two and a half to three times that of aluminum. The brittle behavior has also been interpreted in terms of the directional bonding within the trialuminide, which leads to low cleavage surface energies and low bulk moduli relative to the shear moduli [21,87,88,89] (K/G). The bonding hybridization also results in rather high values of APB and SISF energies [7]. It was suggested [5] that an important way to improve the toughness of the trialuminides, that is to achieve much greater generation of dislocation activity around cracks, is to decrease the value of the fault energies [73,74,77], particularly the APB energy, significantly below the values attained to-date. However, the reported APB energy (γ^{APB}) values are spread in the broad range depending on the researcher. Kumar and Hemker [90] determined $\gamma^{APB}=305\pm35$ mJ/m^2 for $Al_{66}Cr_9Ti_{25}$ at RT whereas Miura and Watanabe [91] reported 175 mJ/m^2 for $Al_{67.5}Cr_{7.5}Ti_{25}$ at RT. The energy γ^{APB} becomes lower at elevated temperatures- 150 mJ/m^2 at 523 K and 130 mJ/m^2 at 773 K [91]. At 623 K the Cr- modified titanium trialuminide had 0.2% tensile ductility whereas at 773 K it dropped to zero [14]. Therefore, it seems that the onset of tensile ductility is not completely reliant on the APB energy. Similar conclusion can be reached for Mn- modified alloy for which the tensile ductility was reported to increase with temperature not monotonically.

It appears that none of the normally- used criteria explain why the trialuminides cleave so easily. Pope [92] suggests that some other mechanism operates, e.g. the crack tip shear mechanism of Jokl et al. [93].

2.5 Grain Size Effect on Ductility and Fracture Toughness of Intermetallics

Armstrong [94] developed a general model relating the critical stress intensity factor, K_C, to the grain size of metallic material. The dependence is of the Hall-Petch type:

$$K_C = Cs^{1/2}\left[\sigma_0 + kd^{-1/2}\right] \qquad (2.2)$$

where C is a constant of proportionality, s is the plastic zone size, σ_0 is a measure of the lattice frictional stress and k is the microstructural stress intensity.

A reasonable agreement with this dependence was achieved in a number of investigations [95,96] on steel materials tested at relatively low temperatures. The inverse square root dependence of fracture toughness on grain size was also obtained from ductile fracture toughness measurements reported for a microalloyed ferritic steel [97]. In this case, the K values were obtained from multiplying J_{IC} by the elastic modulus, E. Very interesting consequence of reaching the lower limit of grain size (approximately equal to the plastic zone size (s)) is the triggering of the reverse (negative) slope of Hall-Petch dependence. According to Armstrong [94] in this case the equation 2.2 becomes:

$$K_C = C\left[\sigma_0 d^{1/2} + k\right] \qquad (2.3)$$

Very recently, Mercer and Soboyejo [98] tested gamma titanium aluminides and their results also clearly showed that a direct linear relationship exists between

fracture toughness and $d^{-1/2}$, indicating a Hall-Petch behavior. They observed a small increase of toughness from 25 to ~32 MPa$\sqrt{m}$ by refining the grain size from 88 to 72μm for Ti-48Al-1.5Cr (at.%), and from ~6 to ~8 MPa$\sqrt{m}$ by changing the grain size from 88 to 20μm for Ti-48Al-2Mn (at.%). Higher increase of toughness was obtained in binary Ti-48Al. Refining the grain size from 33 to 8 μm resulted in toughness increase from ~12 to ~20 MPa$\sqrt{m}$. Comparably high increase in toughness was measured in Ti-48Al-1.4Mn. By refining the grain size from 44 to 10μm, toughness increased from 5 to 20 MPa$\sqrt{m}$. Similar dependence was also obtained for both yield strength and ultimate tensile strength indicating that the average grain size is a primary microstructural parameter that controls a range of mechanical properties of gamma-based alloys. On the other hand, Gnanamoorthy et al. [99] reported lack of toughness dependence on grain size for gamma base titanium aluminides. Their 200μm equiaxed grains of Ti-50Al heat treated material gave toughness value of 14.7 MPa$\sqrt{m}$, whereas for 25μm grains the toughness was 15.3 MPa$\sqrt{m}$.

Chan [100] analyzed fracture process using a J-integral approach. He assumed that the initial flaw size is related to the grain size (the same as the grain size) and varies accordingly as the grain size changes. He also assumed that toughness (the critical stress intensity factor at the point of catastrophic failure) is independent of grain size. This assumption is difficult to confirm or criticize based on the experimental data found in the literature. Further, he assumed that the yield properties are independent of the grain size (which is unlikely). The analyses [100] showed that the fracture strain or ductility increases as the grain size is reduced, for a variety of materials with a range of values of fracture toughness. The important conclusion is the steady increase in strain to failure as the grain size is

reduced, with a dramatic increase once the grain size reaches a value characteristic for each material. Morris [101] refined the analyses of Chan [100] by considering the strong yield stress dependence of grain size. He also simplified the analyses to materials which are brittle, i.e. where a classical fracture toughness approach can be taken as sufficiently close to describe the behavior. An essential point of analyses by Morris [101] is a comparison of the evolution of the critical crack length as the grain size changes, for material of a given fracture toughness level. It was shown that for the materials exhibiting fracture toughness of 3 and 5 MPa$\sqrt{m}$ and the Hall-Petch exponent n of 0.5, the brittle to ductile transition takes place for the grain size in the range 300-30μm. According to Morris, any subsequent reduction of grain size, from the order of 1-10μm to below 100nm has almost no effect on fracture behavior. However, experimental results obtained by Morris and Leboeuf [102] showed just the opposite to that which was presented in the theoretical analysis [101]. The atomised and atomised and milled powders of the composition Ti-48Al-2Mn-2Nb (at.%) with carbon additions of 0.06 and 0.6 at.% were consolidated by HIP-ing. The TiAl alloys with the grain size in the range from 100μm (for conventional, HIP-ed material) to ~300nm (for powder compacts) exhibited the negative Hall-Petch slope for toughness. Fracture toughness decreased slightly (12-10 MPa$\sqrt{m}$) as the grain size was reduced over the 100-5μm range, and then fell rapidly (10-5MPa$\sqrt{m}$) for smaller grain sizes. In other study, by Hoffman and Birringer [103] it was shown that the fracture stress decreased substantially upon grain refinement from 100 to 25nm. In general, the difficulty in improving fracture toughness of nanocrystalline materials could possibly be attributed to two factors [101]:

a) The powder processing/ consolidation procedure might not be adequate and the harder nanocrystalline materials may be less than perfectly manufactured;
b) Changing material hardness dominates behavior over changes of material toughness and intrinsic structure-property relations prevent any tendency to toughening or to ductilization.

It was also suggested [101] that nanostructured materials will have better toughness since they are considered to show high strain rate sensitivity [104]. However, as was noted by Morris [101] it is not clear, whether such effects, measured under fairly slow strain rates, can be extrapolated to consider deformation in front of a rapidly propagating sharp crack.

3 OBJECTIVES OF RESEARCH

The complexity of dealing with the brittleness problem of cubic ($L1_2$) intermetallics is paramount. Therefore, a logical approach would be to eliminate the influence of some of the factors and concentrate on others that are most probably determining the mechanical behavior.

There is a lack of studies on the effect of environment on the fracture toughness and fracture behavior of the ternary cubic titanium trialuminides. Therefore, it is considered of importance to conduct fracture toughness tests on these alloys in vacuum and other environments.

Research concentrated on the following aspects:

1. Development of a suitable methodology of fracture toughness testing of small intermetallic specimens.
2. Fundamental understanding of the nature of the fracture process and resulting fracture toughness of cubic ($L1_2$) titanium trialuminides. In particular, the assessment of the following factors on the fracture behavior and toughness of cubic titanium trialuminides:
   - The effect of environment (moisture at ambient temperatures and oxygen at high temperatures)
   - The effect of grain size (refinement of grain size will be achieved by dynamic recrystallization of a coarse-grained cast ingot and controlled ball-milling of powders; more details will be given in the following section)
   - The effect of boron addition
   - The effect of higher Mn (14at.%) and Ti (28-31at.%) concentrations also in combination with boron doping.

4 EXPERIMENTAL PROCEDURES

4.1 Alloy Preparation, X-ray and Microstructure Techniques

All the alloys were prepared from pure elements- aluminum (99.99999%), titanium (99.9%), manganese (99.9%), and Al-3.2 wt.% boron master alloy, and one alloy was prepared from boron powder (95% purity). The elements were melted in a low porosity alumina crucible which was placed inside a boron nitride coated graphite crucible. The ingot that was prepared with addition of boron powder was prepared according to the following procedure. The raw elements (i.e. Al, Mn, and Ti) were placed in the crucible. The amount of boron powder in excess of ~0.15at.% above the boron concentration target was added on the top of the raw elements. Subsequently the entire crucible was shaken in order for the powder to settle down evenly throughout the crucible volume.

The melting process was identical for boron-free and boron-doped alloys. A high frequency induction furnace with high- purity argon atmosphere was used for this purpose. According to the supplier specifications, the argon purity was 99.998% and it contained less than 20vppm impurities. One cast block of the material weighing ~220g, used for cutting specimens was prepared by first melting two ingots of ~110g each, that were solidified in the crucible. Subsequently, this 220g block was cast by melting the two smaller ingots at a temperature ~50°C above melting point (i.e. above 1340°C), and pouring the molten alloy into a heated austenitic (316 grade) stainless steel mold. The temperature of the mold was chosen in the way as to obtain compromise between the quality of the external

surface (the higher the temperature the larger the air voids) and the propensity of the ingot to fracture caused by internal stresses (the lower the temperature the higher the stresses). This temperature ranged between 450–600°C.

The temperature of the melt was measured within accuracy of ±5°C by a W–5%Rh and W–25%Rh thermocouple inserted into the crucible just above the melt level. The cast ingots were wrapped with stainless pouches (Sen/Pak heat treatment containers) and homogenized for 100h at 1000°C under a high–purity argon atmosphere in a tubular furnace. All the ingots were subsequently HIP–ed at 1250°C for 2h under 170 MPa pressure.

To reveal the grain size in the HIP–ed materials, the following etchant was used: 100 ml H_2O + 5 ml HNO_3 + 0.5 ml HF.

Melting and casting procedure was done according to the following steps:

1. Evacuating the chamber of the induction furnace to 0.05 atm,
2. Heating up to ~400°C in vacuum,
3. Evacuating again to 0.05 atm. or below,
4. Pressurizing the chamber with high purity argon gas (1.7×10^{-2} MPa),
5. Heating the stainless steel mold to ~500°C,
6. Heating the raw elements up to 50°C above T_m (1390°C),
7. Holding at 1390°C for 15 min., pouring into a heated mold,
8. Cooling the furnace chamber.

Fig.4.1a shows the ceramic and graphite crucibles used for melting. Figs.4.1b and 4.1c show the graphite and austenitic stainless steel molds used for casting. The graphite molds were used at the procedure developmental stage and finally were replaced by more suitable austenitic stainless steel molds. One additional procedure at the developmental stage included the mechanical vibrating of the melt

during its solidification in order to decrease the shrinkage void. It did not bring the expected results.

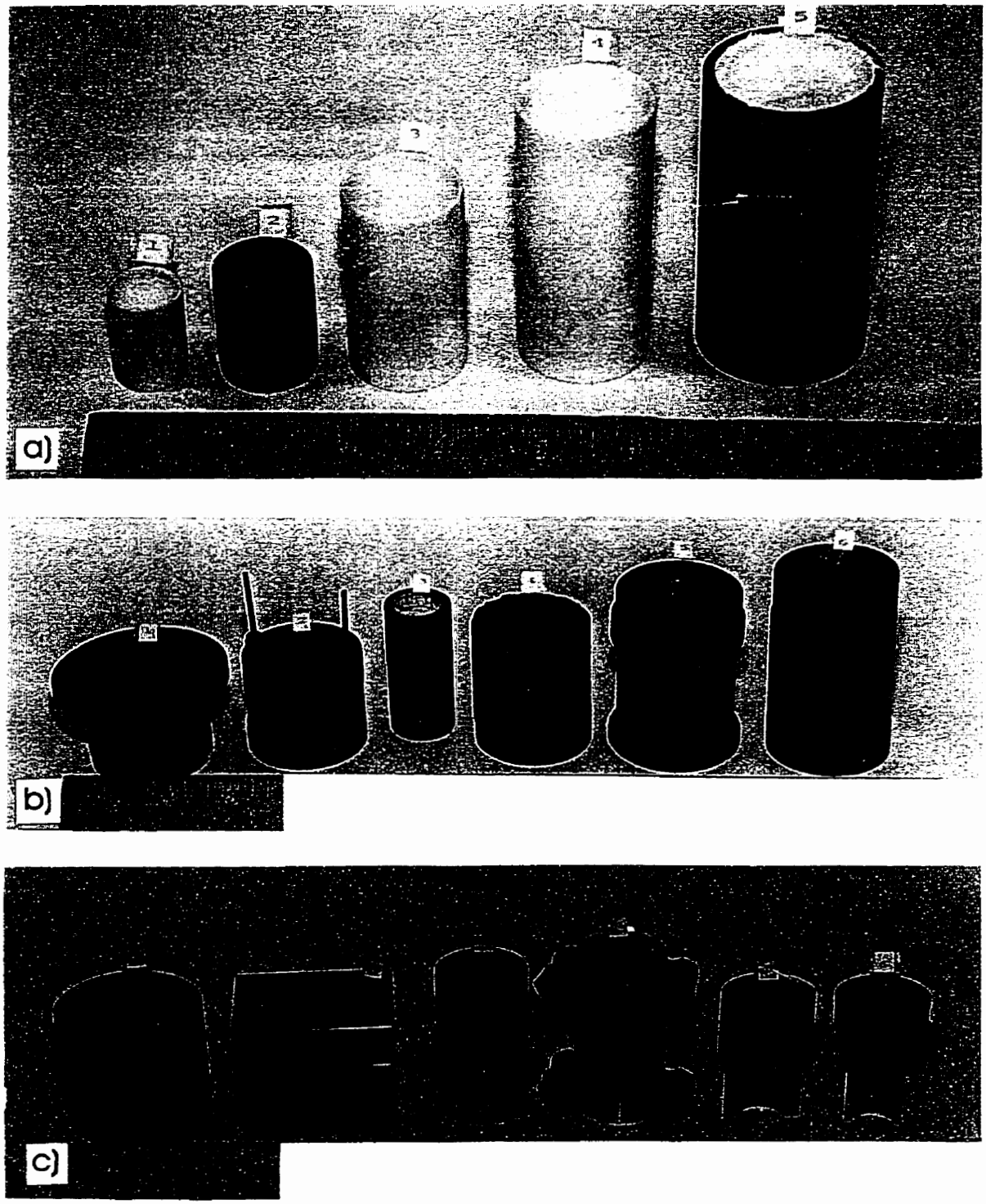

Figure 4.1 a) Ceramic and graphite crucibles, b) graphite molds, c) austenitic stainless steel molds.

Optical microscope equipped with the Nomarski interference contrast was used to investigate the microstructure. JEOL JSM-840 scanning electron microscope was used to observe fracture surfaces and to determine the composition of alloys. The composition was measured by a fully quantitative (elemental standards of purity better than 99.9% and the ZAF (Z-atomic number, A-absorption, F-fluorescence) correction program) X-ray dispersive spectroscopy (EDS) using QX2000Link system. The accelerating voltage of the probe was 20kV. Boron concentrations were measured using the neutron activation analysis by the Becquerel Labs Inc. (Mississauga, Ont.). X-ray diffraction profiles from the boron-free and boron-doped 14Mn alloys were recorded on a Siemens D500 diffractometer equipped with a nickel filter and a graphite monochromator using Cu-$K_{\alpha 1}$ radiation (λ=0.15406 nm). The operating parameters were 30mA, 50kV, speed 2 deg/min and step size 0.02 deg. The lattice parameters of 14Mn-type alloys were calculated by plotting the lattice parameter, (a) against an extrapolation function $\frac{1}{2}(\cos^2\theta/\sin\theta+\cos^2\theta/\theta)$ which holds down to low values of θ (taken in radians) [105].

The Atomic Force Microscope (AFM) scan of the crack tip in the 9Mn alloy specimen was obtained on the Digital Instruments Nanoscope IIIA MultiMode AFM at the University of Toronto.

4.2 Hot- Work at High Temperatures

The cast, homogenized and HIP-ed ingots comprised coarse grains. The purpose of the hot working was to refine the grain structure through dynamic recrystallization. As mentioned earlier, fracture toughness tests were performed on both coarse and medium size-grained material (recrystallized) in order to establish the toughness dependence on grain size.

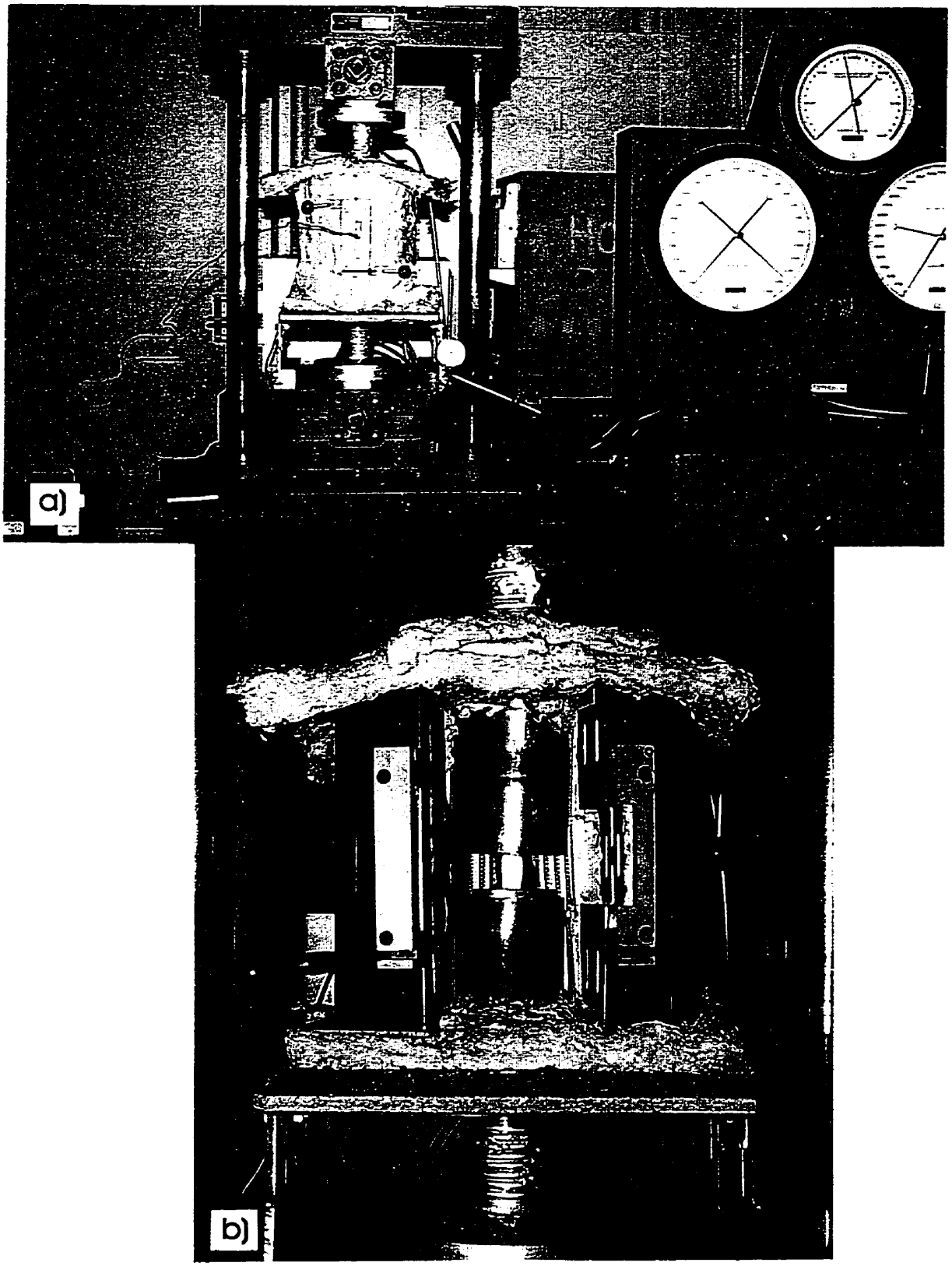

Figure 4.2 Set-up used for compression of $Al_3Ti(Mn)$ alloy at 1000°C, a) overall view, b) close-up of the specimen placed between pushing rods.

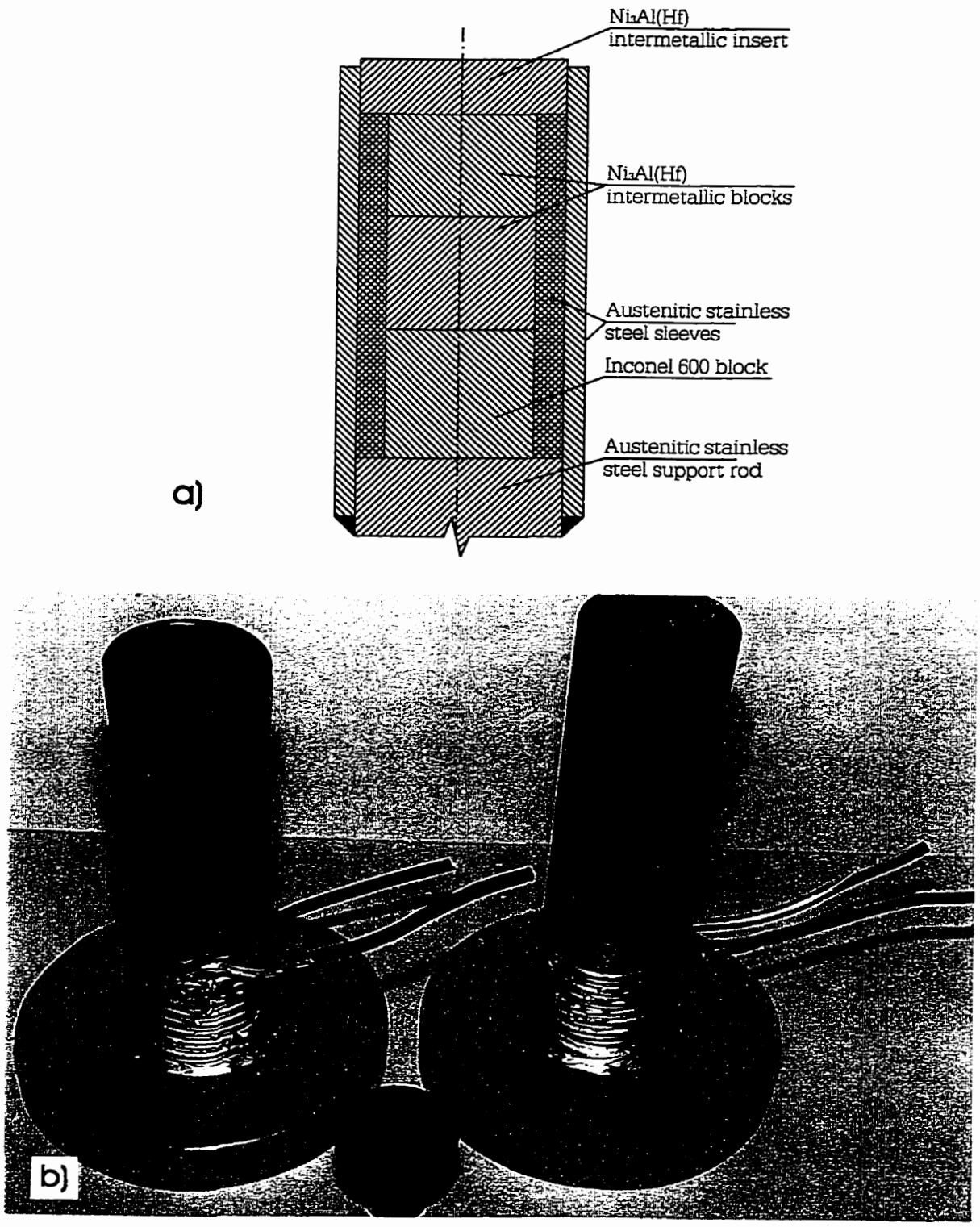

Figure 4.3 a) Details of the design, b) real appearance.

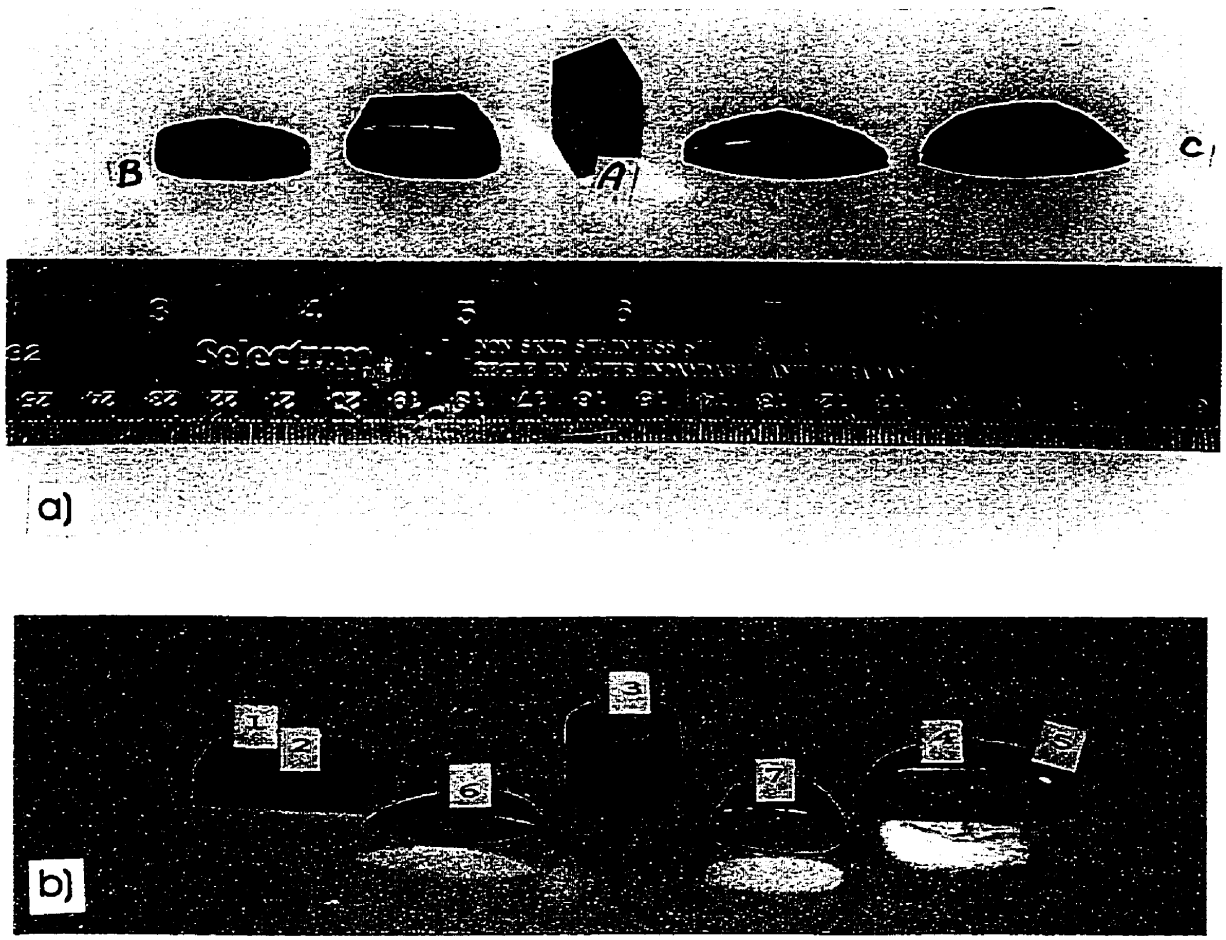

Figure 4.4 $Al_3Ti(Mn)$ material deformed in compression at 1000°C (top picture); a) the initial block of material, b) the block deformed to ~50%, c) the block deformed to ~75%. Bottom picture 1-Inconel insert; 2-the specimen pushed- in into the insert; 4,5- the same as 1 and 2; 3,6,7- specimen deformed different amounts.

Two blocks of initial size of ~12x12x25 mm were cut on Electro- Discharge Machine (EDM) from two different ingots. The blocks were deformed on Tatnal hydraulic press of load capacity 60000 lbs at 1000°C for several hours giving the deformation rate of $\sim 10^{-4}\ s^{-1}$. Fig.4.2 and Fig.4.3 show set-up for compression and pushers, respectively. The bottom picture of Fig.4.4 shows, unintentionally, the superiority of the light intermetallic to Inconel alloy in the resistance to high temperature deformation. The Inconel inserts are heavily deformed (indented).

These inserts were used in the early development stage of the compression set-up. In the subsequent stages they were replaced by Ni_3Al+Hf inserts which were cast in our laboratory; 4at.% of hafnium was added to Ni_3Al (75at.% Ni, 21at.% Al, 4at.% Hf) in order to obtain solid solution strengthening. Such a material is superior to the base Ni_3Al [83]- it has much higher yield strength which is required from inserts for high-temperature compression.

4.3 Powders

As discussed in Section 2.5 refinement of the grain size may be a possible way to improve the fracture toughness of the cubic titanium trialuminides. The most effective method of refining the grain size of intermetallics is mechanical milling (ball milling) [106]. Therefore, in the present work the ball milling was employed in order to refine the grain structure of the low- Mn alloys. Subsequently the indentation fracture toughness tests were performed on the consolidated powders.

4.3.1 Powder Production and Measurement Techniques

Two ingots, approximately 200g each, were induction melted from pure elements (Al- 99.99999%, Ti- 99.7% and Mn- 99.9%) under high purity argon and cast into a steel mold. Subsequently, the ingots were homogenized at 1000 °C for 100h. The compositions of the homogenized ingots were estimated by a fully quantitative (elemental standards and the ZAF correction program) energy dispersive X-ray spectroscopy (EDS). The results are given in Table 5.1 (ingots no.14 and 15). Compositions of both ingots correspond to a single $L1_2$ phase field in the ternary Al- Mn- Ti system [107]. Homogenized ingots were crushed into coarse particles and chunks by a heavy sledge- hammer and then pulverized in a steel mortar using

a steel pestle. A 20g charge of coarse particle material was loaded into the ball-milling vials of the ball- mill developed by Calka et al. [108] (Fig. 4.5) which was set up in a shearing mode. In this mode the balls both rotate and oscillate around an equilibrium position at the bottom of the milling cylinder in a strong magnetic field provided by the external magnets [108].

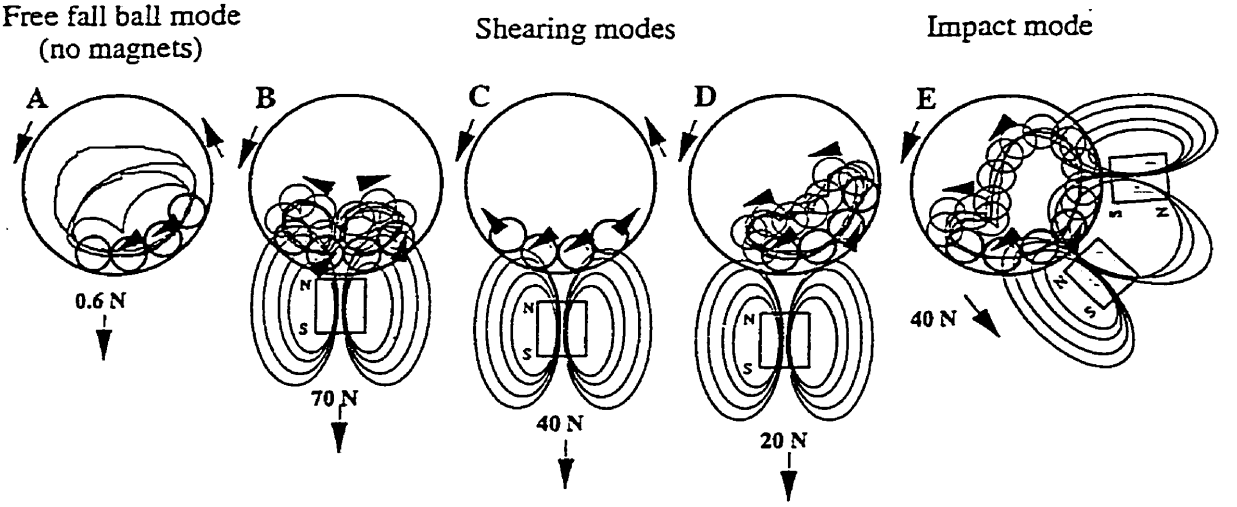

Figure 4.5 Schematic of ball-milling under controlled conditions [108].

In this mode the powder particles trapped between the rolling balls are mostly affected by shearing. Four hardened steel balls, 64g each, were loaded together with a pulverized ingot charge. This rendered a ball- to- charge weight ratio of around 8: 1. Milling was carried out in a pressure- tight vial filled up with an inert gas.

X-ray diffraction profiles from the milled powders were recorded on a Philips diffractometer coupled with a Philips X- ray Generator (PW 1730). The radiation used was CuK_{α} (λ=O.1542 nm) at operating parameters of 20 mA, 40 kV, speed 2 deg/min and step size 0.02 deg. Some scans were also made at 0.05 deg step size but from the experience the 0.02 deg step size is particularly recommended for calculating the profile breadths of annealed powders and standards (optimally narrow peaks are obtained).

The average crystallite (grain) size of the milled powders was calculated from the full width at half maximum (FWHM) of each selected Bragg peak. The FWHM values were calculated by the computer software TRACES™ developed by Diffraction Technology Ltd. (Canberra, Australia) (Dr. A.Calka, University of Wollongong). Two approaches to estimating crystallite size were used. The first one was a simple Scherrer formula [105]:

$$D = \frac{0.9\lambda}{(\Delta FWHM)\cos\theta} \tag{4.1}$$

where D is the nanocrystallite size, λ is the wavelength of X- ray radiation and ΔFWHM is determined by the TRACES™ by subtracting the FWHM of the unbroadened peak of a standard sample from the FWHM of the broadened (calculated) peak (milled powder). This approach takes into account the instrumental broadening.

The second approach was based on the approximation of strain broadening by a Gaussian function, whereas the nanocrystalline size broadening was approximated by a Cauchy function [105,109]. Assuming that the "pure" profile breadth is approximately equal to ΔFWHM the following equation describes both the broadening from the crystallite size and lattice strain broadening

$$\frac{(\Delta FWHM)^2}{\tan^2\theta_0} = \frac{0.9\lambda}{D}\left[\frac{(\Delta FWHM)}{\tan\theta_0 \sin\theta_0}\right] + 16e^2 \tag{4.2}$$

where θ_0 is the position of the analyzed peak maximum. Any available orders of a given reflection may be used to construct a linear plot of $(\Delta FWHM)^2/\tan^2\theta_0$ against $(\Delta FWHM)/\tan\theta_0\sin\theta_0$. From the slope $0.9\lambda/D$ and ordinate intercept $16e^2$, the crystallite size, D, and distortion parameters (strain), e, in a direction normal to the

diffraction planes may be determined. The four strongest FCC peaks: (111), (200), (220) and (311) (isotropic case [109]) were used for calculations.

For metallographic, chemical composition (EDS) and microhardness investigations the milled powders were mounted in conductive bakelite and carefully ground and polished according to the following procedure: 2400 and 4000 grade SiC paper (wet) backing on glass plate, then 6 μm and 1 μm diamond polish and finally 0.06 μm colloidal silica. This is the only polishing procedure which did not result, as was found, in a substantial pull out or damage to powder particles in the mount. Finally, a light etching for 15s using a mixture of 1% HF + 10% HNO_3 + 89% H_2O was applied to the surface.

Vickers microhardness measurements were made on the mounted and polished powders, as described above under a load of 10g (HV 0.01) and a dwell time 15s. Morphology of the milled powders was studied by SEM.

4.3.2 Powder Processing

Fine milled powders of Al_3Ti(Mn) alloys were processed at various conditions. The process consisted of two stages: first - pre-compaction on Tatnal hydraulic press at high pressure at RT; second - hot pressing of RT pre-compacted powders using various temperature and pressures. Fig.4.6 presents the set-up for RT pressing of the powders. The purpose of using a split sleeve in this set-up is the easy removal of the compacted powder button from the steel ring. Without this split sleeve it is impossible to remove the button from the ring undamaged (in one piece). This is due to high residual stresses that powder imposes on the walls of the steel ring. After pressing the split sleeve is punched out of the steel ring using a hand press without damaging the button. A thin copper foil is used to prevent the powder particles to enter the spaces between the four pieces of the split sleeve. The usage

of this foil also prevents damaging of the button during its removal from the steel ring. The high- temperature powder compaction was done using hydraulic Instron testing machine. The set-up is shown in Fig. 4.7. The usage of ceramic inserts caused low friction between loading rods and these inserts. An unstable high oil pressure induced mechanical vibrations which were transferred to the entire set-up. Therefore, there was a need to use the centering sleeves which keep the entire set-up in place. This problem was not encountered in RT pressing since the tungsten carbide inserts and plunger imposed higher friction and also the vibrations on the Tatnal press were much lower than on the Instron testing machine.

In a first design of the high-temperature set-up the die was made from Ni_3Al (75at.% Ni, 25at.% Al) (which was cast in our laboratory) as a single ring. During the test, however, the powder imposed such a high pressure on the die, that it fractured. Additionally, the yield strength of Ni_3Al die was not sufficient since its walls also deformed plastically under pressure imposed by compressed powder. The fracture was partially caused by unfavorable grain orientations in the die which was radial. Subsequently, tungsten carbide was used as a die. Because of limited material availability, this die was strengthened by the Ni_3Al ring.

The compacted buttons had ~8mm in diameter and ~0.8mm in thickness. Vickers microhardness measurements of compacted buttons were conducted at various loads from 10g to 2000g.

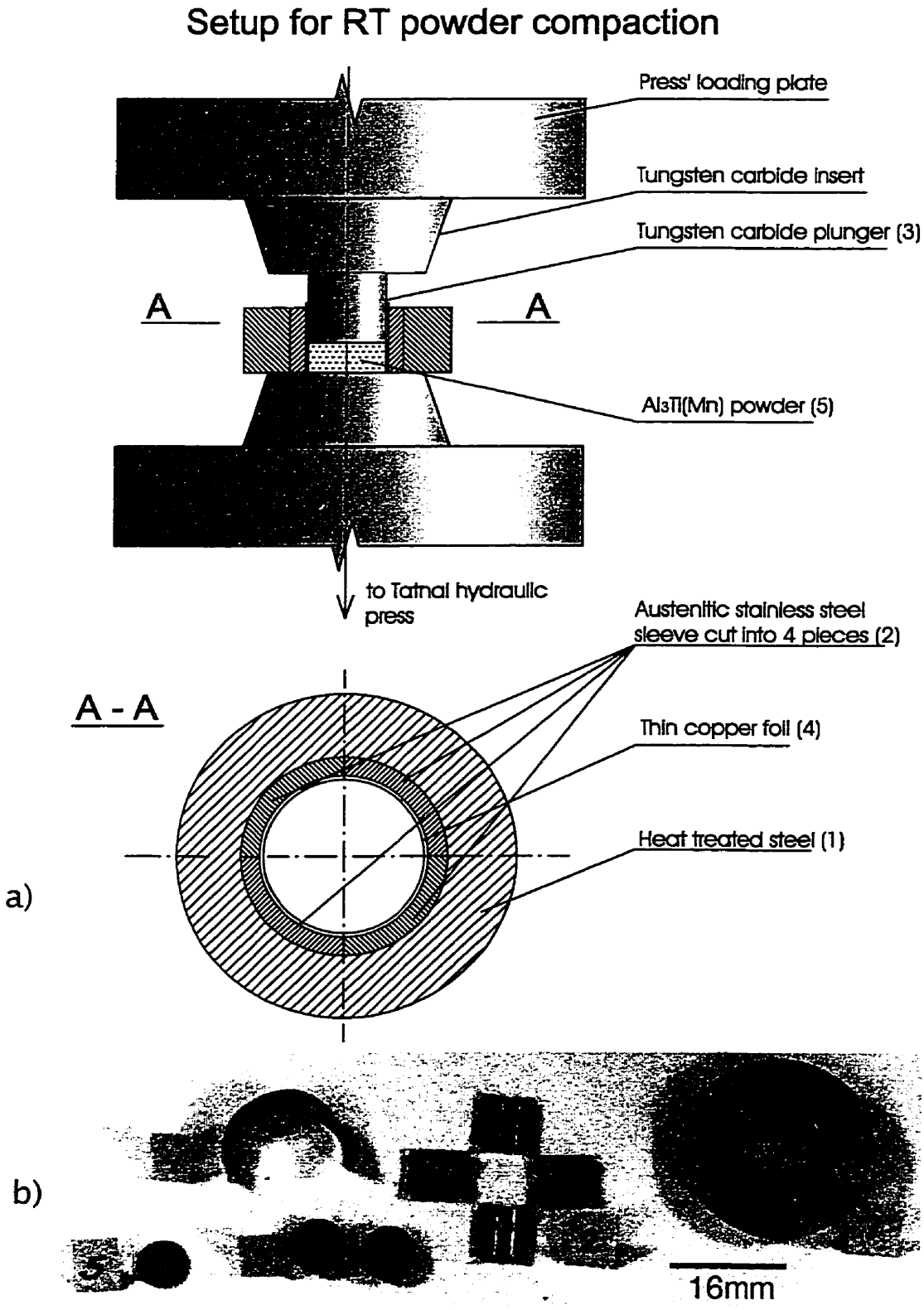

Figure 4.6 a) Set-up for cold (RT) pressing of powders, b) a photograph of the parts from (a). The numbers in (a) and (b) designate the same parts.

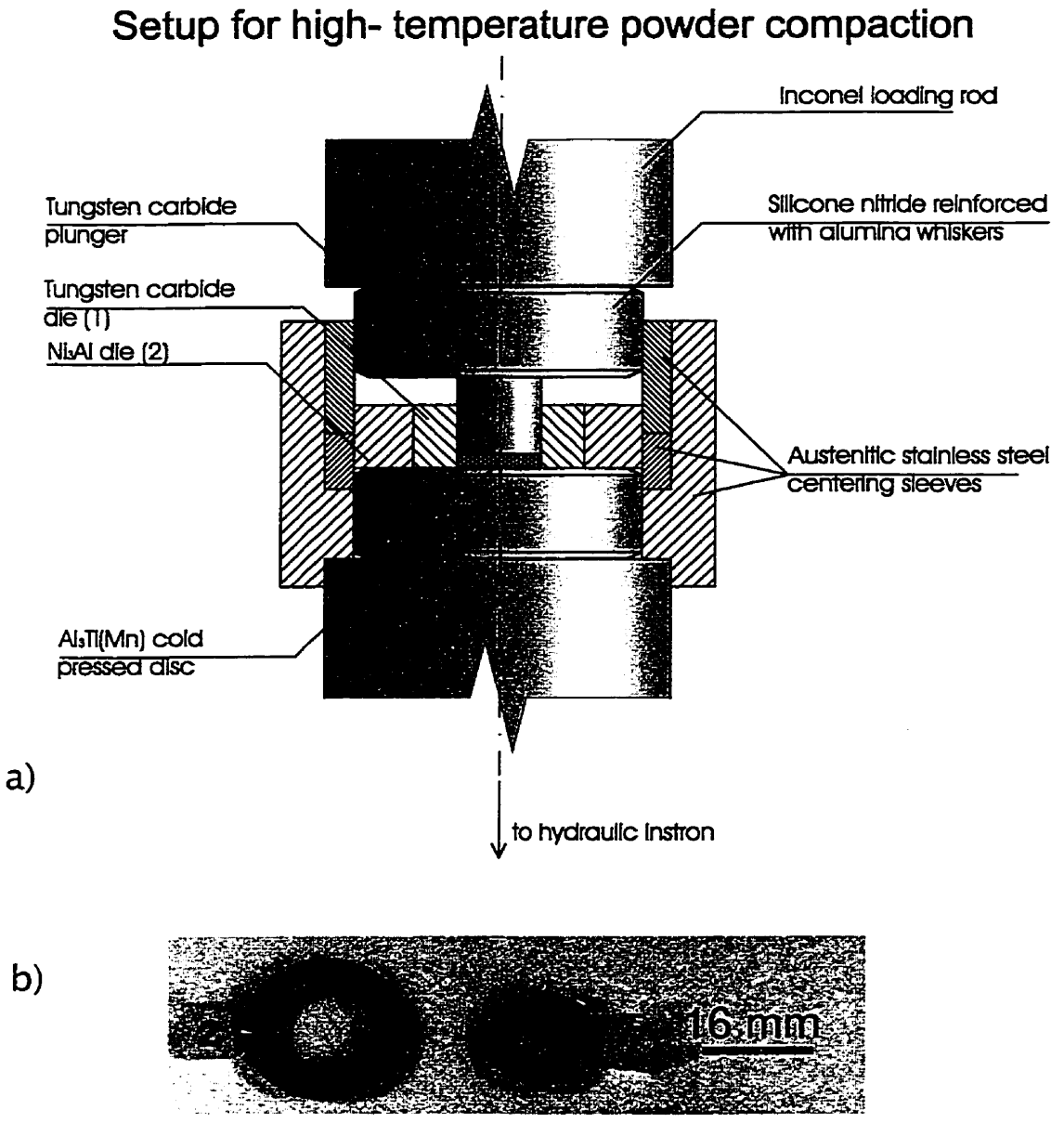

Figure 4.7 a) Set-up for hot pressing of powders, b) a photograph of the parts from (a). The numbers in (a) and (b) designate the same parts.

4.4 Fracture Toughness Testing

4.4.1 Selection of Fracture Toughness Testing Technique

None of the experimental methods of fracture toughness characterization customarily expressed as the critical stress intensity factor, K_{IC}, are utilized more extensively than others for a variety of reasons, including the ease of sample preparation and also the simplicity of the measurements. However, the widespread acceptance, simplicity or the extensive use of a single technique, does not necessarily indicate the superiority of that method over the others. The acceptance of any single technique must also be validated by its reproducibility and determined by other valid test methods.

The critical stress intensity factor is usually measured at slow loading rates. The values obtained can then be applied to failure prediction for the equivalent in-service loading rates.

The technique selection depends on both the measurement temperature and the material porosity [110]. For non- porous materials, pre- cracks can be readily detected using dye penetrants, thermal tinting or optical observations. Hence, the conventional techniques can be used at ambient temperature without difficulty- whichever is most convenient in terms of material availability, machining capabilities, test facilities, and pre- cracking facility. For elevated temperature measurements, the test procedure imposes additional constraints. Additional restrictions, equally important, come from the complicated setup design used in this study, which allows testing in the wide temperature range from RT - 1000 °C and at the same time in various environments - high vacuum (~ 1.5×10^{-7} Torr), oxygen, argon or any other environment. The chain of constraints imposed on the specimen design and mode of loading is as follows:

The clearance between the bottom and loading frame of the testing machine → the internal diameter of the tubular furnace and its height → the dimensions of the environmental chamber → the length of the loading rods (important at high temperatures) and the size of the specimen. It is almost imperative that specimens which use compressive loading should be used.

Many types of specimens, such as the Single- Edge- Notch- Beam (SENB) specimen, the double torsion, the double cantilever beam, and the surface flawed specimens are currently used. These specimens have either blunt notches produced by saw cutting, or cracks produced by wedge loading or by local thermal shock. Specimen with blunt notch can overestimate K_{IC}. Precracked specimens are difficult to prepare in a reproducible manner, and the initial crack front often cannot be seen on the fracture surface after testing, making it nearly impossible to measure the initial crack length. To overcome these difficulties Barker [111] has proposed a specimen with a chevron notch (CN). This type of specimen was first used by Nakajama [112] and later on by Tatterstall and Tappin [113] in bend tests for obtaining an average fracture surface energy. In the present work there were two fracture toughness specimen types used: Single- Edge- Precracked- Beam (SEPB) type specimen and Chevron- Notched- Beam (CNB) type specimen. The specimens' geometry and testing procedures were based on the ASTM recommendations [114,115]. The choice of the loading mode was dictated by high temperatures used in tests. The SEPB specimens, even though more difficult to prepare than CNB specimens, were chosen to assure a high crack sharpness. However, the difficulty in obtaining the reproducible precracks required a larger number of specimens be prepared and the fracture toughness be represented as a function of the remaining ligament length. Toughness values of all the specimens that satisfied plain strain requirement were

considered as valid K_{IC} values. This is because the other requirement imposed by the ASTM Standard [114] regarding the amount of plasticity developed in the specimen was satisfied for all the specimens tested, even at 1000°C.

The CNB specimens were chosen primarily because they were easier to prepare and provided better reproducibility of the notch dimensions. Also the required by ASTM Standard E1304-97 [115] on chevron-notched rod and bar in tension, thickness B of CNB specimens is twice smaller than that of SEPB type specimens to satisfy the plain strain condition. However, the problems encountered with the applicability of the equations of fracture toughness calculation for this type of specimens prevented CNB specimens from being the sole source of fracture toughness data. Later, after obtaining and comparing fracture toughness values for both specimen types in the entire temperature range from RT to 1000°C it became obvious that both methods of toughness testing give the results in the same bound of scatter. Therefore, after assuring that CNB specimens produce valid K_{QVM} [115] toughness values, the majority of toughness tests was performed using the CNB specimen configuration.

4.4.2 Set-up and Testing Procedure

Fig.4.8 presents the self-aligning universal setup especially designed in-house for fracture toughness testing. Tests were performed in bending mode. Experiments were done in air in the temperature range from RT - 1000°C, in high- vacuum (~1.5×10^{-7} Torr) in the temperature range from RT - 1000°C, in high- purity argon (according to supplier specifications 99.998%, less than 20 vppm impurities) in the temperature range from RT - 1000°C, in oxygen (99.5%, less than 6vppm moisture) at room temperature, in water, and in liquid nitrogen.

The experiments were performed in displacement control mode using a screw driven Instron testing machine. The 100 kG capacity load cell was used with the sensitivity range set to the desired value according to the expected load values.

Load and cross-head displacement were digitally recorded and stored in a computer. Testing at high temperature prevented the use of any displacement gages that could be placed close to the supporting and loading pins. Therefore, the cross- head displacement was considered as the load- line- displacement (LLD). This approach is valid because first, the compliance of the small and notched bend bar is much greater than that of the test jig/machine and second, the compliance of the jig is constant at the same testing temperature. Therefore the influence of the jig/machine compliance on the crack stability and work of fracture should be minimal (as discussed later).

Fig.4.9 shows the pictures of some parts of the set-up from Fig.4.8. The parts that are particularly exposed to contact stresses especially at high temperatures were fabricated from Ni_3Al (75at.% Ni, 25at.% Al) intermetallic also cast in our laboratory.

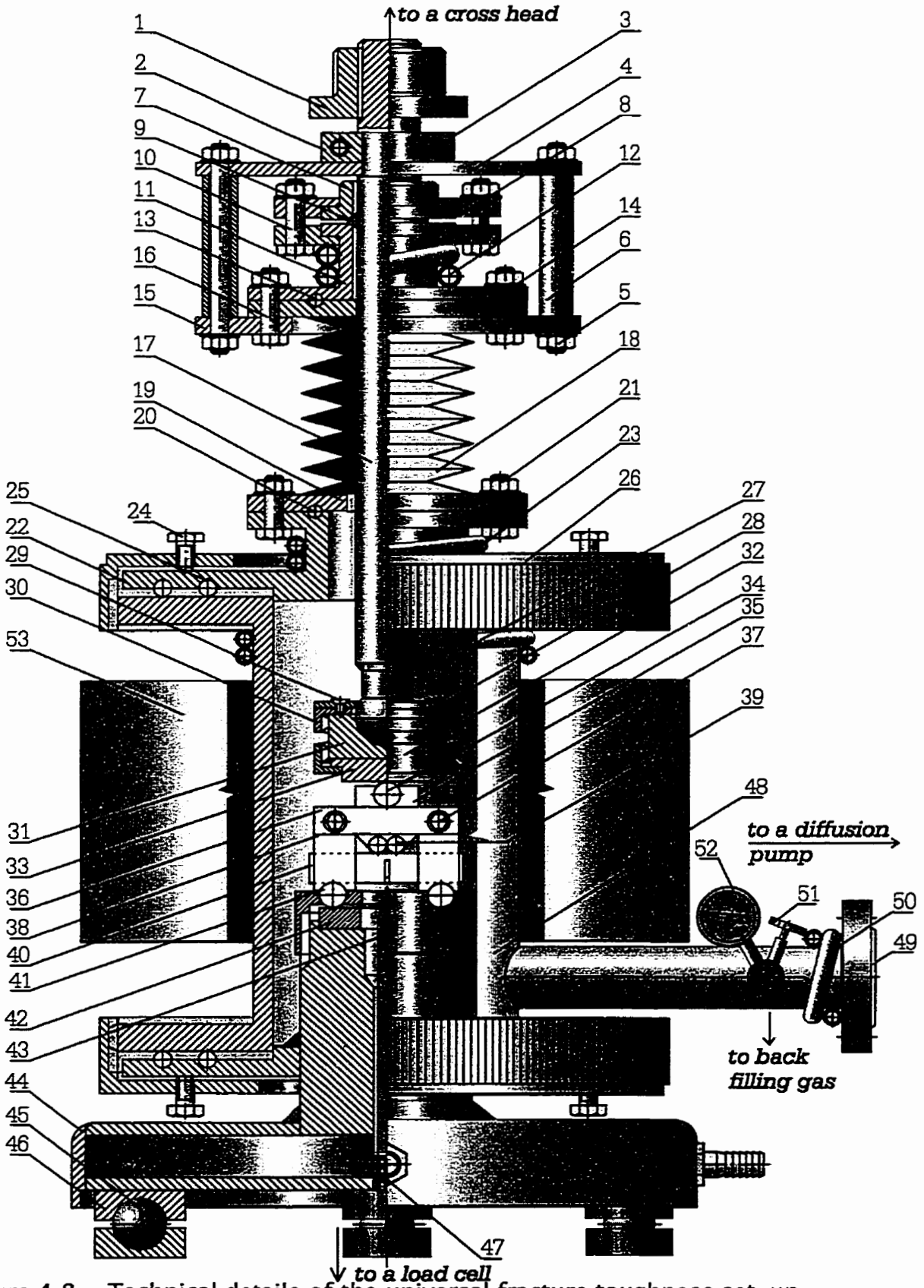

Figure 4.8 Technical details of the universal fracture toughness set-up.

Parts list:

1 - adapter
2 - clamp collar
3 - clamp collar bolt
4, 15 -bellow fixing plates
5 - bellow fixing bolts
6 - distance sleeve
7, 11 - flanged sleeves
8 - clamp
9 - "o"- ring closing environmental chamber from the top
10 - bolts squeezing the last "o"- ring
12, 23, 27, 51 - water- cooling coils
13 - "o"- ring sealing upper flange of the bellow
14 - upper flange of the bellow
16 - "o"- ring squeezing and bellow's upper flange fixing bolts
17 - loading rod
18 - thin walled, copper bellow
19 - lower flange of the bellow
20 - "o"- ring sealing lower flange of the bellow
21 - bolts squeezing the lower flange "o" ring
22 - flanged sleeve
24 - bolts squeezing the "o"- rings sealing vacuum chamber
25 - "o"- rings
26 - nut
28 - fixing collar
29 - bolt
30 - nut holding intermediate insert
31 - intermediate insert
32 - nut holding Ni_3Al intermetallic insert
33 - Ni_3Al intermetallic insert
34 - Al_2O_3, ceramic main loading rod
35 - Ni_3Al intermetallic loading block
36 - strip positioning loading rod
37 - bolt
38 - nut
39 - Al_2O_3, ceramic loading rollers
40 - fracture toughness specimen

41 - Al_2O_3, ceramic support rollers
42 - Ni_3Al intermetallic support insert
43 - thermocouple
44 - water container
45 - balls allowing the load to be transferred uniformly to the load cell
46 - ball's positioning block
47 - vacuum seal
48 - environmental chamber
49 - "o"- ring, sealing connection between environmental chamber and diffusion pump
51 - vacuum valve
52 - pressure gage
53 - tubular furnace

This setup has the following advantages:

- each rubber "o"- ring is protected by water cooling which allows for high-temperature testing up to 1000°C,
- well sealed small environmental chamber and powerful diffusion pump allows for obtaining vacuum of ~1.5×10^{-7} Torr in short time,
- possibility of back filling with gas such as oxygen, argon, etc.,
- accurate temperature measurement because the thermocouple is placed right below the specimen,
- easy adjustment for changing the mode of bending (3pt. and 4 pt. bending) and upper and lower spans,
- stable base due to support on three heat treated steel balls (three supporting points are always in one plane, therefore they form a stable base),
- low sensitivity to misalignment due to application of a ball joint at the loading insert,
- preparations and testing can be performed by one person.

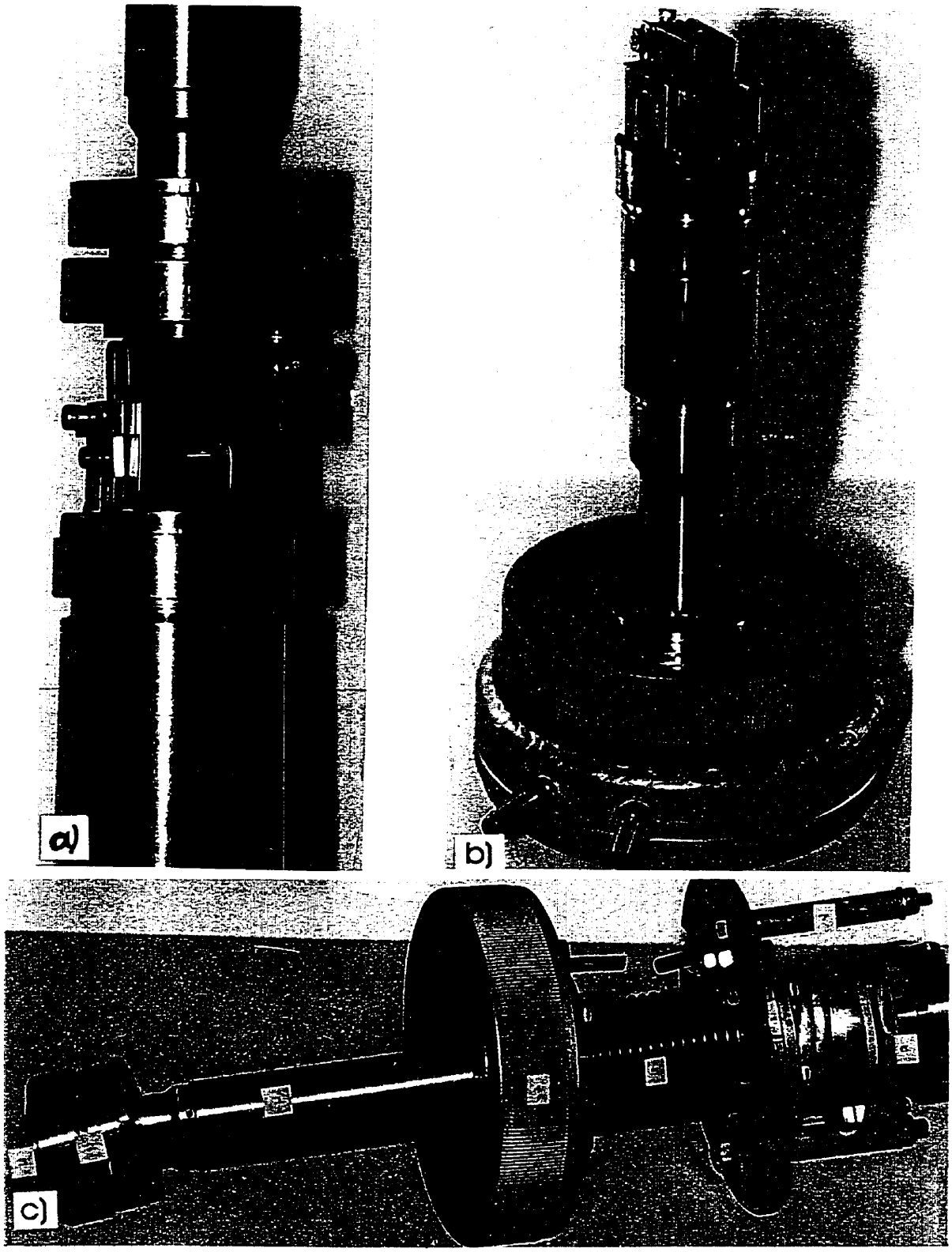

Figure 4.9 a) specimen under 4pt. loading, b) supporting rod with the cap closing the chamber from the bottom, c) loading rod with the cap closing the chamber from the top.

Fig.4.10 shows the set-up fully connected to Instron machine.

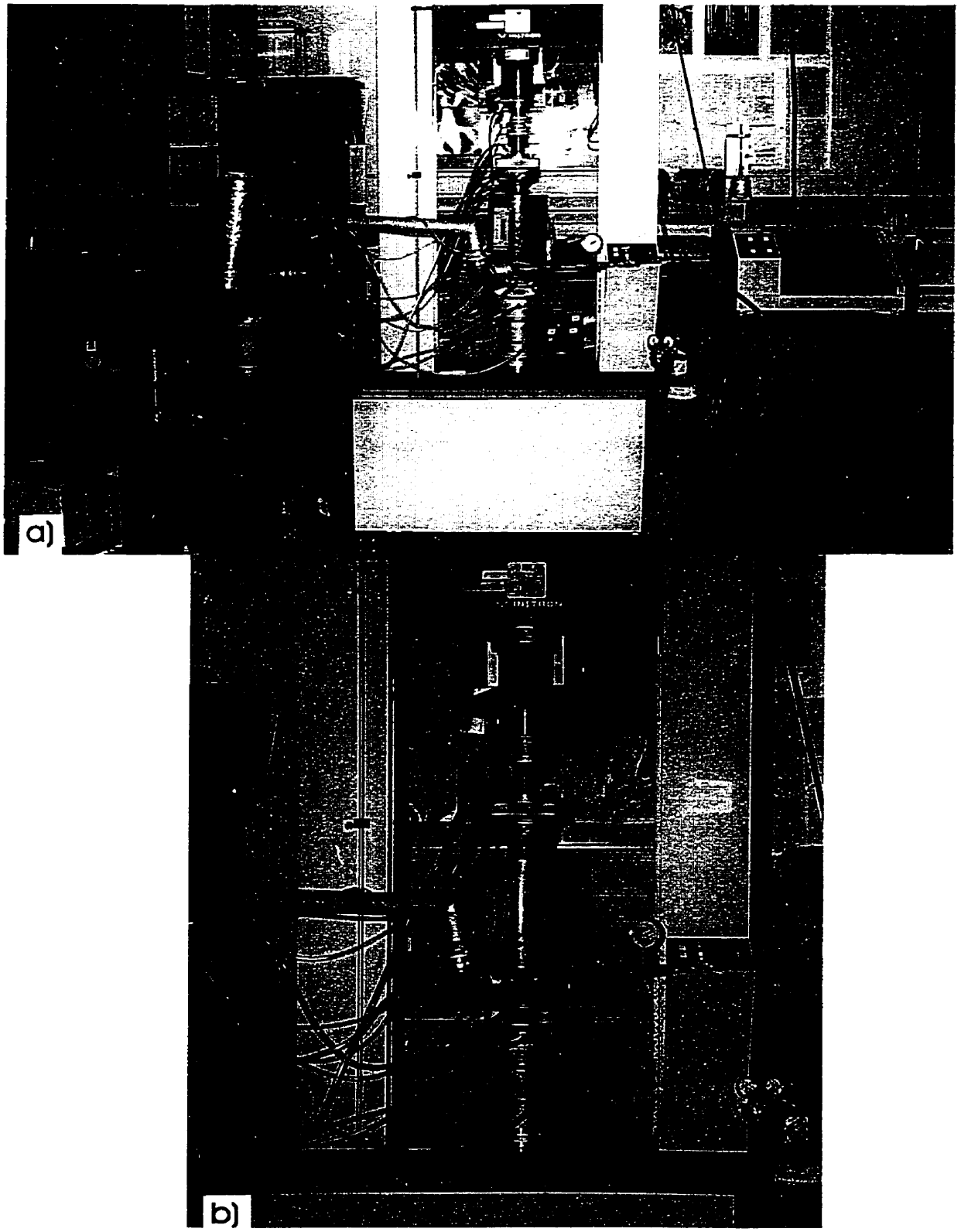

Figure 4.10 a) Overall view of the set-up ready for testing, b) close-up of the loading frame and the environmental chamber.

4.4.3 Specimen Types

Single- Edge- Precracked- Beam (SEPB) Type Specimen

Bending bars were cut from the block of cast and HIP-ed material into desired dimensions using Electro- Discharge- Machining (EDM). Subsequently the bars were ground with emery papers and polished using 1.0 and 0.3 micron alumina powder. The surface finish in this type of specimens is particularly important. One reason is to enable the observation of a stably growing crack during the precracking procedure. The second is to avoid possible scratches or/and cracks serving as notches in the precrack region. It was found that if the finishing paper was too rough, the specimen surface was left with the dense network of surface cracks. These cracks could interfere with the main crack during testing. Bend bars were subsequently notched with 0.1 mm copper wire, leaving the slot width ranging from 0.11 to 0.16 mm, depending on the specimen and electrical current used for notching.

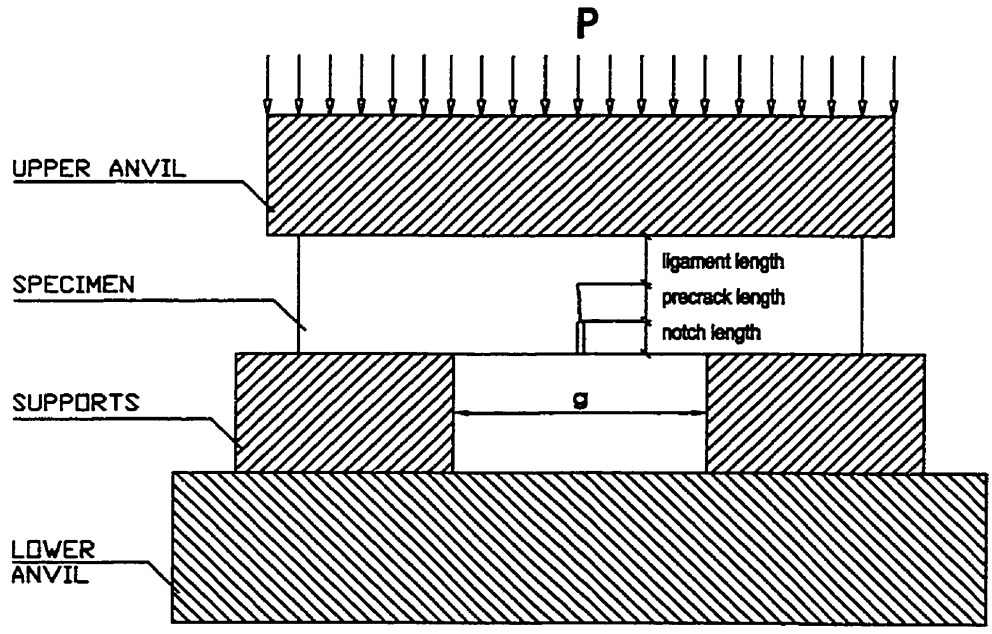

Figure 4.11 Jig used for precracking notched specimens [116].

Precracking procedure was done using the method introduced by Nose and Fuji [116] for ceramic materials. This method gave K_{IC} values almost identical with those of the fatigue- cracked- beam method [116]. The setup is shown in Fig.4.11.

A critical requirement for straight and planar precracks is the parallelism of the bar's sides and precisely machined bridge. Even fulfilling this does not guarantee good results. Precracks were marked by thermal tinting at 800 °C for ~2 min and measured after tests using Java System [117]. At temperatures other than RT, it was much easier to determine the precrack length due to changing mode of fracture with temperature.

The parameters influencing the length of the precrack or even the stability of the precrack are: applied load, specimen cross- sectional dimensions, distance between the supports in the bridge and the notch length. If the specimen is stiff (at given B and W it means the notch is too short and/or the span is too narrow) the crack has the propensity to grow stably. However, if the load is too high, a network of cracks (most probably throughout the entire volume of the specimen) is formed along the main pre-crack (Fig.4.12a) (the center) and at the contact surfaces of supports and the bar (Fig.4.12b,c). Extensive plastic deformation is also seen at the support/bar contact points. On the other hand, if the bar is too compliant (the span too wide and/or notch too deep), the precrack can easily jump long distance, very often close to the back side of the specimen, leaving the remaining ligament length not sufficient for determination of valid toughness values.

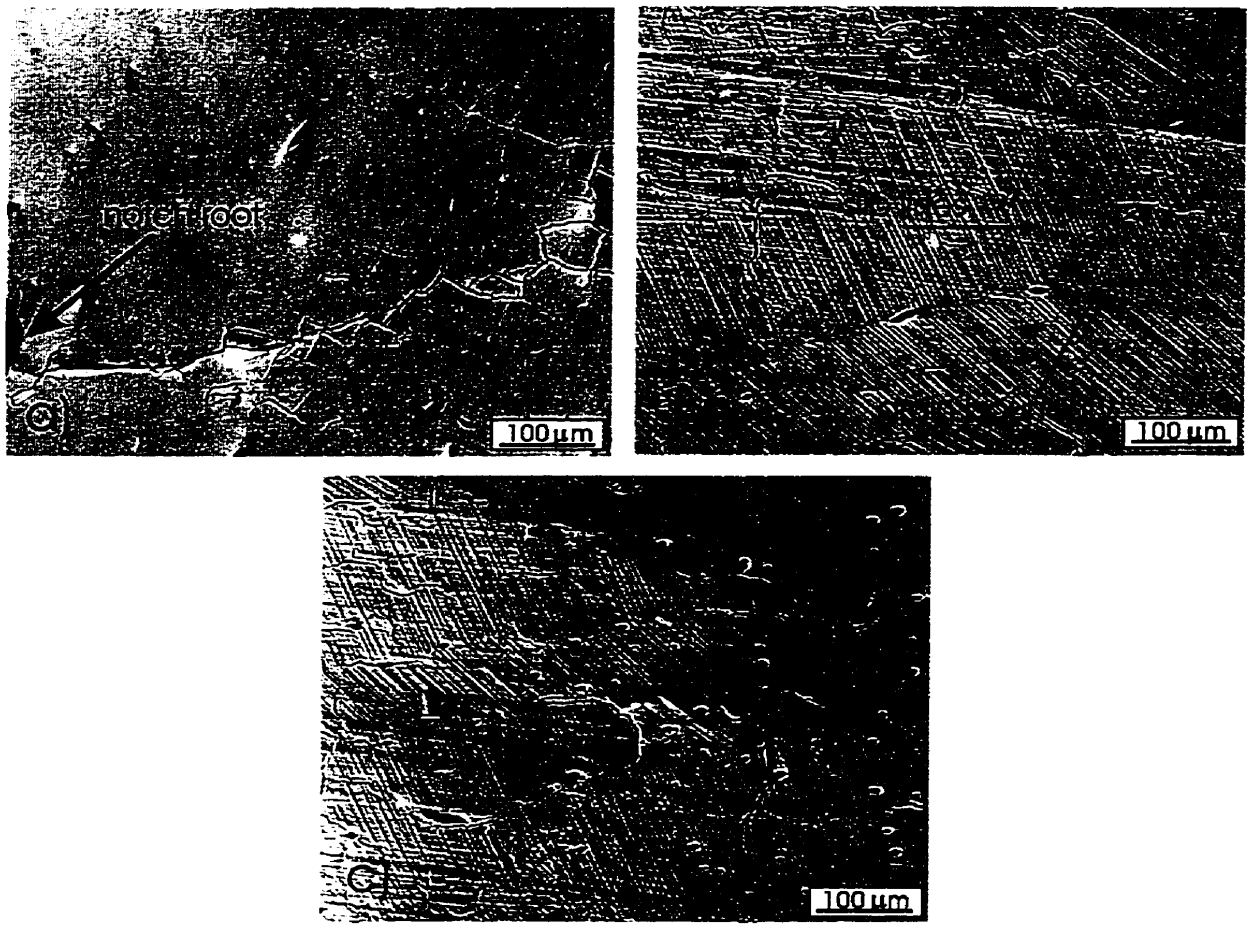

Figure 4.12 Precracking of the notched specimen: a) network of cracks formed around the main crack when the span is short and specimen overloaded, b) dual mode of deformation in the region of supports–plastic deformation and cracking (boron–free "base" 9Mn–25Ti alloy).

Fig.4.13 shows the cut notch and the precrack emanating from the tip of the notch and Fig.4.14 shows the fracture surface with pertaining dimensions.

Figure 4.13 a) SEM photograph of the SEPB specimen, b) optical photograph of the end of the notch and the entire precrack.

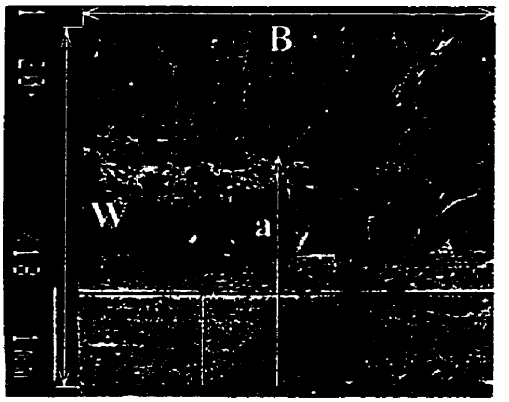

Figure 4.14 SEM photograph of the fracture surface of the SEPB specimen and its dimensions, a_0– notch length, a–notch + precrack length, W– width, B– thickness of the specimen.

A small jig (Fig.4.15) was used to observe in the SEM the precrack loaded to various progressive stress intensities. Specimen was loaded manually in 3pt. bending by torqueing a screw in four steps. After each loading step the strained tip of the precrack was carefully observed in the SEM. The purpose of this experiment was to explore the nature of the strained crack tip deformation and hopefully the size of the plastic zone of the precrack strained close to the critical stress intensity.

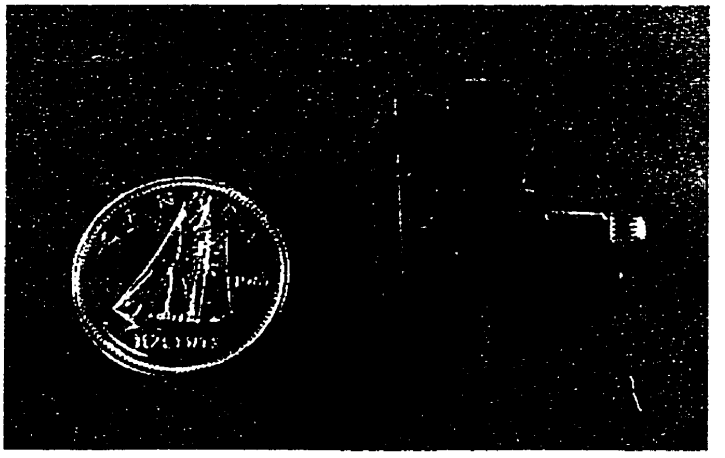

Figure 4.15 Jig used for straining of the SEPB specimen.

Chevron- Notched Specimens

The bending bars were prepared the same way as SEPB bars. The surface finish is not that critical as for SEPB type specimens because the fracturing material is deeply "hidden" inside the bulk of a bar. The chevron notches were cut using the jig shown in Fig.4.16. The general dimensions of the notch are shown in Fig. 4.17. α_1 parameter was kept ≈ 1 and α_0 could be approximately set to the desired value (geometrical parameters will be discussed in more detail in the following section).

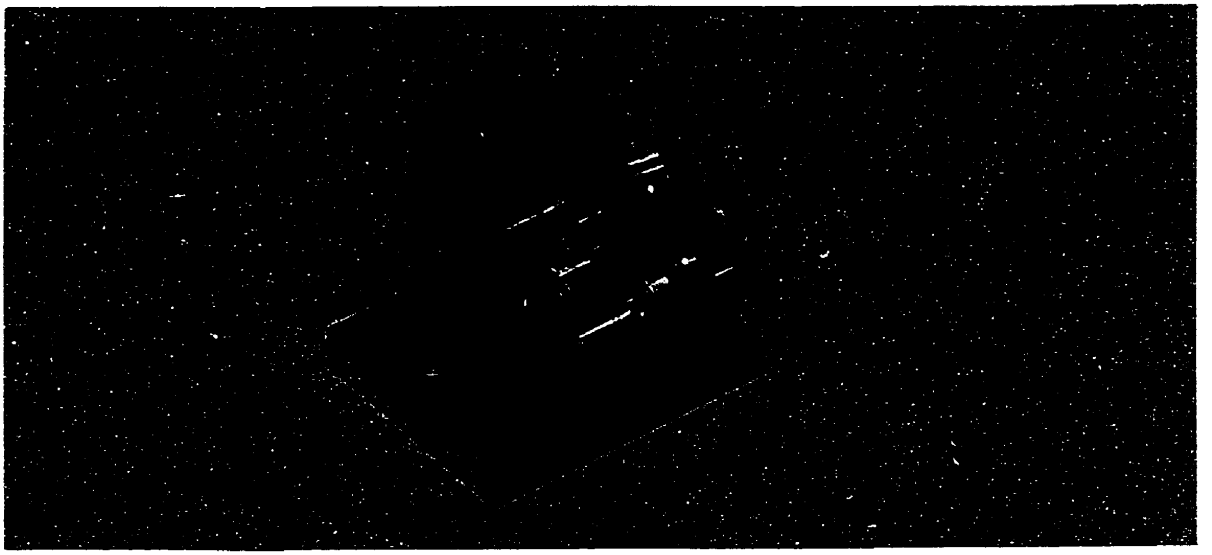

Figure 4.16 Jig used for cutting chevron notches.

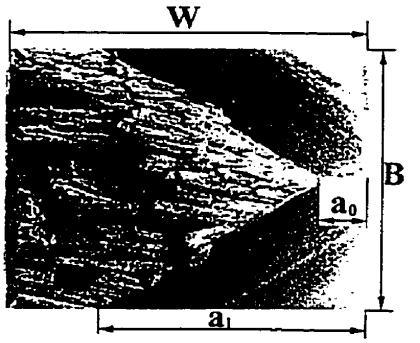

Figure 4.17 Fracture surface of the CNB specimen and its dimensions, a_0- notch depth, a_1- side dimension of the notch, W- width, B-thickness of the specimen.

A few CNB specimens were also precracked using the same bridge as for SEPB type specimens. Obtaining the stable cracks seems to be easier than in SEPB bars but it is more difficult to obtain short precracks ($\alpha_{pr} \leq \alpha_m$ - the critical crack length, for the definition see Section 4.4.5), since the propagating crack cannot be seen.

4.4.4 Critical Stress Intensity Factor Calculations

Fracture toughness calculations for SEPB specimens were done according to equations given in [114]. In the cases where S/W ratios were much different from 4, the calculations were performed according to equations given in [118]. The relevant equations for SEPB specimens are given in the Appendix A.

No more consideration of this type of specimen is given here because the procedure is straightforward (even P_Q load values [114] did not have to be determined due to linearly rising load up to the maximum load in the entire temperature range). Instead, more attention is directed towards CNB type specimens.

Existing stress intensity solutions [119,120] for chevron notched bend bars have been derived mainly with the use of Bluhm's slice model [121]. This requires the analysis of complex integral functions which can often be solved only by the use of powerful numerical techniques. The analyses are geometry specific and their complexity inhibits their application to different loading conditions and specimen geometries. This problem can be solved by utilizing approximate trigonometrical functions [122].

Bluhm divides the specimen with its trapezoidal crack/notch into slices of uniform thickness, i.e. slices in the straight- through portion of the trapezoid, and slices in the tapered portion. K_{QV} is given by (subscript v stands for chevron- notch)

$$K_{QVM} = \frac{P_M}{BW^{1/2}} Y^*_{\min} \tag{2.3}$$

Y^* is given by

$$Y^* = \left[\frac{1}{2}\frac{dC_V(\alpha)}{d\alpha}\left(\frac{\alpha_1 - \alpha_0}{\alpha - \alpha_0}\right)\right]^{1/2} \tag{2.4}$$

P_M– is the maximum test force;

α, α_0 and α_1 are normalized depths: $\alpha=a/W$, $\alpha_0=a_0/W$, $\alpha_1=a_1/W$;

$C_V(\alpha)$ is the compliance of the testpiece.

Final form of $C_V(\alpha)$ is:

$$\frac{1}{C_V(\alpha)} = \left[\frac{\alpha - \alpha_0}{\alpha_1 - \alpha_0}\right]\left[\frac{1}{\gamma + \beta\tan^2\left(\frac{\pi\alpha}{2}\right)}\right] + \frac{k}{(\alpha_1 - \alpha_0)(\gamma - \beta)} \times$$

$$\left\{(\alpha_1 - \alpha) - \frac{2}{\pi}\left(\frac{\beta}{\gamma}\right)^{1/2}\left[\arctan\left\langle\left(\frac{\beta}{\gamma}\right)^{1/2}\tan\left(\frac{\pi\alpha_1}{2}\right)\right\rangle - \arctan\left\langle\left(\frac{\beta}{\gamma}\right)^{1/2}\tan\left(\frac{\pi\alpha}{2}\right)\right\rangle\right]\right\} \tag{2.5}$$

Where k is the interlaminar shear factor

$$k = \begin{cases} 1 + 0.444(\alpha_1)^{3.12} & \text{for} \quad \phi \geq 1 \\ 1 + (\alpha_1)^{3.12}(2.236\phi - 4.744\phi^2 + 4.699\phi^3 - 1.77\phi^4) & \text{for} \quad \phi \leq 1 \end{cases}$$

where

$$\phi = 0.5(\pi - 6)$$

with

$$\beta = 2.7\left(\frac{S_1 - S_2}{W}\right)^2$$

and

$$\gamma = \left(\frac{S_1 - S_2}{W}\right)^2\left[\frac{S_1 + 2S_2}{4W} + \frac{(1+\upsilon)W}{2(S_1 + S)}\right]$$

θ is the included angle of the chevron notch in radians, ν is Poisson's ratio, S_1 and S_2 is the lower and upper span, respectively, γ is the nondimensional compliance of a specimen without a notch.

Simpler method of K_{QV} calculation is by using straight- through crack assumption (STCA). It is assumed that for a specimen with a chevron notch, the derivative of the compliance with respect to α is the same as for a specimen with a straight- through crack. According to this method

$$K_{QVM} = \frac{P_M}{BW^{1/2}} Y \left[\frac{\alpha_1 - \alpha_0}{\alpha - \alpha_0}\right]^{1/2} \tag{2.6}$$

and

$$Y^* = Y \left[\frac{\alpha_1 - \alpha_0}{\alpha - \alpha_0}\right]^{1/2} \tag{2.7}$$

where Y is the stress intensity coefficient factor for the straight- through- crack specimen.

Whether or not the Bluhm's slice model in fact improves upon STCA method of estimating the dimensionless stress intensity factor coefficient for the four point bend CNB specimen has not been substantiated by careful experimental compliance measurements. The difference, however, decreases with increasing α_0 [120].

In order for a test result to be valid in accordance with ASTM E1304 Standard Test Method [115], it is required that the specimen's lateral dimension, B, equals or exceeds $1.25(K_{QV}/\sigma_Y)^2$ where σ_Y is the material's 0.2% offset yield strength.

In the present study, calculations were performed according to Bluhm's slice model, i.e. equations (2.3) to (2.5) using Waterloo Maple Software.

4.4.5 Methodology of Testing and Specifics of Chevron Notch Design

Chevron notch test introduced by Barker [111] (short bar) is at present, generally accepted as a convenient method for measuring the plane strain critical stress intensity factor. The growing crack in the CNB specimen is stable in the long range due to the nature of the specimen geometry. A guiding notch imposes constraints on the crack path. This type of specimens has the advantage that a sharp crack is produced during loading, making it necessary only to measure the maximum load. The functional relation between the maximum load (P_M), the specimen geometry, and K_{QVM}, however, must be known. Many authors [111,123,124] pointed out by using analytical analysis that stable crack extension can be realized in CNB specimens, so that tiresome (or even impossible) fatigue precracking of specimens can be eliminated.

The ASTM E 1304- 97 Standard [115] for chevron-notch bar and rod in tension (there is no ASTM Standard for bending) defines the conditional fracture toughness calculated from maximum load, K_{QVM}, using equation 2.3. If $B>1.25(K_{QVM}/\sigma_Y)^2$ and if the actual crack surface does not deviate from the intended crack plane more than 0.04B when the width of the crack front is one third B, and if the values of P_M do not occur before a point corresponding to the slope ratio $1.2r_c$ (r_c- the unloading slope ratio at the critical crack length) then $K_{QVM}=K_{IVM}$ (plane strain chevron-notch fracture toughness).

According to this Standard, the critical crack length, α_m, in a chevron specimen is that at which the specimen's stress intensity factor coefficient, Y^* (symbol * stands for CNB type specimen), is a minimum, or equivalently, the crack length in a chevron specimen at which the maximum load would occur in a purely linear elastic fracture mechanics test. At the critical crack length, the width of the crack front is

approximately one third the dimension B. Barker [125] developed an inflatable bladder flatjack loading method on a short- rod specimen. The flatjack is placed inside the thin slot of the specimen, and the specimen is loaded by pressurizing the flatjack. It has been shown that pressure becomes maximum at certain crack length a_c which depends only on the specimen geometry, not the material. Therefore, crack location at the peak load is constant for certain geometry.

In other words, fracture toughness is calculated from the load required to advance the crack when crack is at the critical crack length. The fracture toughness determination from P_M of a chevron notched specimen therefore, is always for an ideally sharp crack.

The above described method of calculating K_{QV} from maximum load is correct for materials with flat K_R resistance curve. However, if K_R increases as Δa increases, K_{IVM} is overestimated. It is so because maximum load and Y^*_m do not occur coincidently at α_m. The load peaks, instead, at a relative crack length greater than α_m. This results in some error in the calculation of K_{IVM} at maximum load because the corresponding value of crack length is unknown.

Sometimes the load-displacement records exhibit pop-ins. This may be due to characteristic feature of a material or due to notch preparation technique. EDM cutting results in machined layers on the CN surfaces. Their structures are different from the matrix. The toughness of these layers may be higher than the toughness of matrix. Hence, the load needed to initiate a crack at the tip of CN may be high enough to extend the crack into matrix to some length a, that will cause a pop- in. If the crack length a is smaller than critical length a_m, the crack will continue to grow stably until it reaches the critical length. Therefore, the pop- in may not affect the maximum load P_M and the measurements of K_{QV}. In this sense the pop- in is

treated differently in CNB specimen than in SENB or SEPB specimen. In the latter case, the load at sufficiently long pop- in is taken for calculating K_{IC}. Therefore, preparation method of chevron notch may affect the crack growth mode of CNB specimen. Load- displacement record should always be obtained during test, unless it can be assured that the specimen definitely exhibits stable crack growth before rapid fracture.

The allowable CNB specimen size is twice smaller than that for SENB or SEPB type specimen. It is because the toughness is measured at approximately the midline of the specimen, and only in the material covered by the crack's lateral extent. This causes that the entire crack front is under plane strain condition (which is based on numerical calculations).

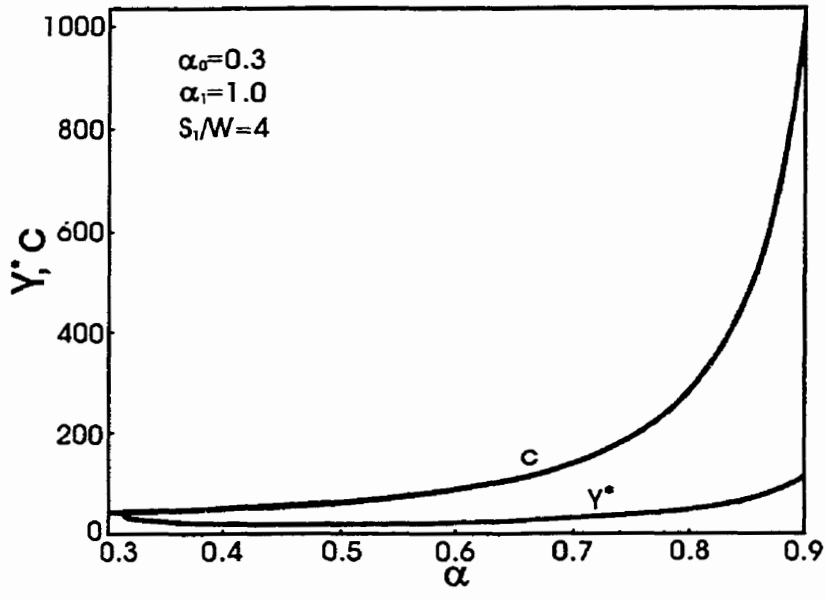

Figure 4.18 Nondimensional compliance C and stress intensity factor coefficient Y* dependences on crack length for chevron notch specimen.

The change of nondimensional compliance C and stress intensity factor coefficient Y^* with crack length are shown in Fig.4.18.

Graphs given below show the influence of notch parameters on the shape and position of the curves in Y^*, α coordinates. They are calculated for $B/W \approx 1$, $S_1/W \approx 4$, $S_1/S_2=4$ (or otherwise shown on the graph).

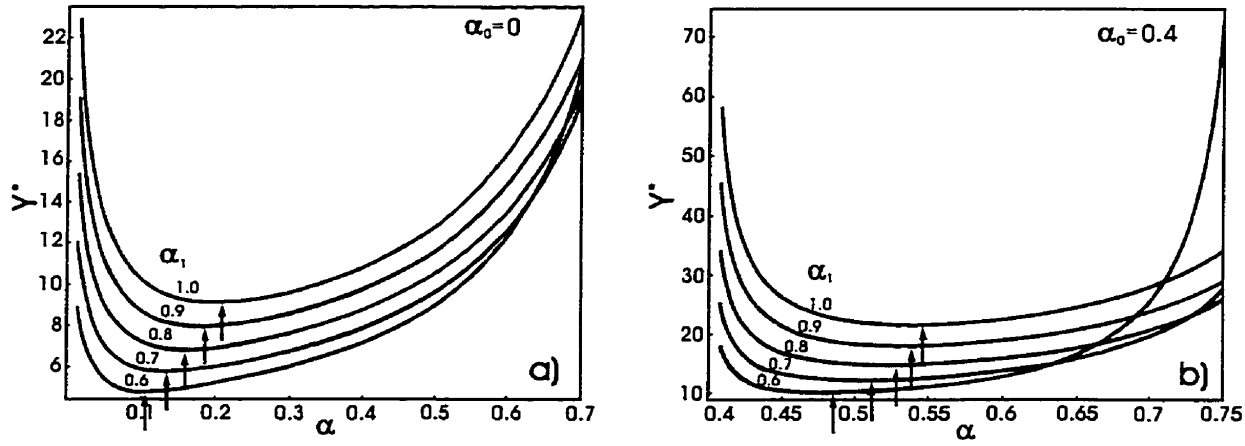

Figure 4.19 Stress intensity factor coefficient Y^* dependence on crack length α, a) for various α_1 values and $\alpha_0=0$, b) for various α_1 values and $\alpha_0=0.4$.

From Fig.4.19 it can be seen that keeping $\alpha_0=0$ and changing α_1 from 0.6 to 1.0 shifts the curve upward and Y^*_m towards longer cracks. For more deeply introduced notches, $\alpha_0=0.4$, the above is also true. However, the curves are much flatter before and after Y^*_m. As also can be seen deeper notches give higher values of Y^* (and at the same time higher compliance). Similar analysis is presented in Fig.4.20 but keeping constant α_1.

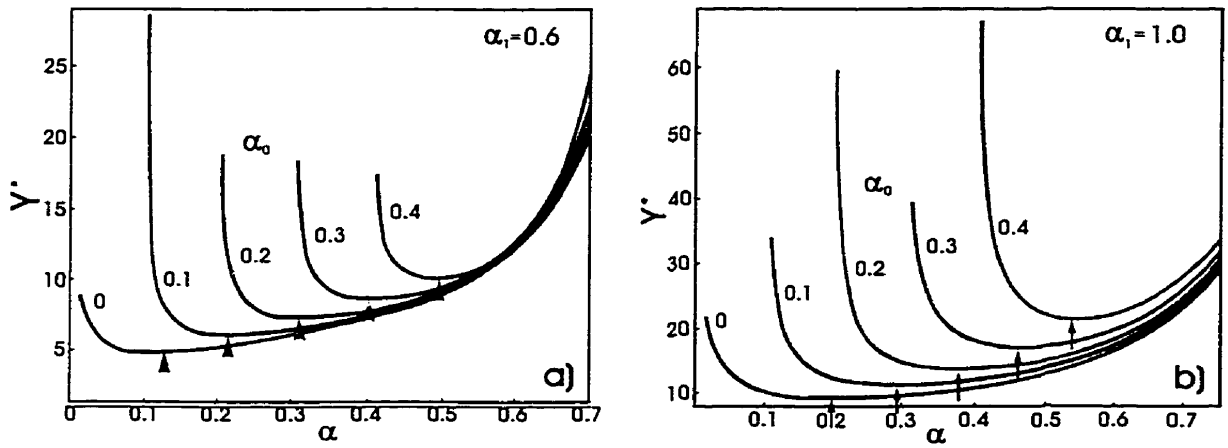

Figure 4.20 Stress intensity factor coefficient Y^* dependence on crack length α, a) for various α_0 values and α_1=0.6, b) for various α_0 values and α_1=1.0.

In Fig.4.20a by changing α_0 from 0 to 0.4 and keeping α_1=0.6, not only the Y^*_m is shifted to the right and upwards but also the shape of the curves is changing. The main difference comes from the fast increasing steepnes after Y^*_m for larger α_0. The main difference between graphs for α_1=0.6 and α_1=1.0 (Fig.4.20b) arises from the fact that for α_1=1.0, Y^*_m occurs at larger α_m and of course the curves are also shifted upward for α_1=1.0 with respect to α_1=0.6. For the same reason compliance is also higher.

Graph in Fig.4.21a shows the change in Y^* vs. α for α_0 and α_1 both increasing and graph in Fig.4.21b for α_0 increasing and α_1 decreasing. The latter causes the Y^*_m to remain at constant level. However, the Y^*_m is being shifted towards larger α_m, although the crack length of the flat portion of Y^* function before and after Y^*_m becomes shorter. There is no advantage to follow this path in notch design. Rather preferable direction is shown on graph in Fig.4.21a. It will be rationalized later by taking into account real loading system and response of a specimen with specific geometry.

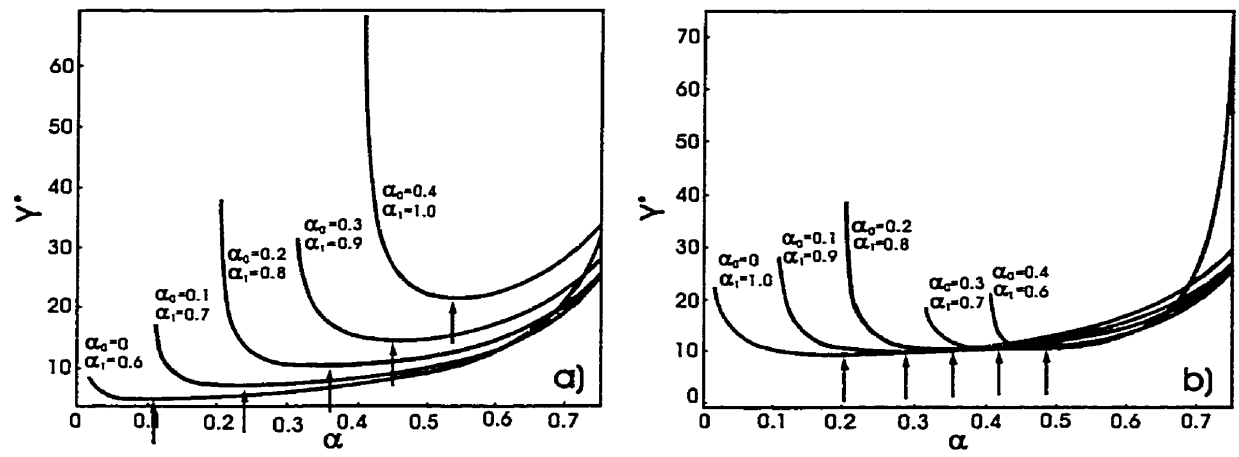

Figure 4.21 Stress intensity factor coefficient Y^* dependence on crack length α, a) for various α_0 and α_1 values both increasing b) for α_0 increasing and α_1 decreasing.

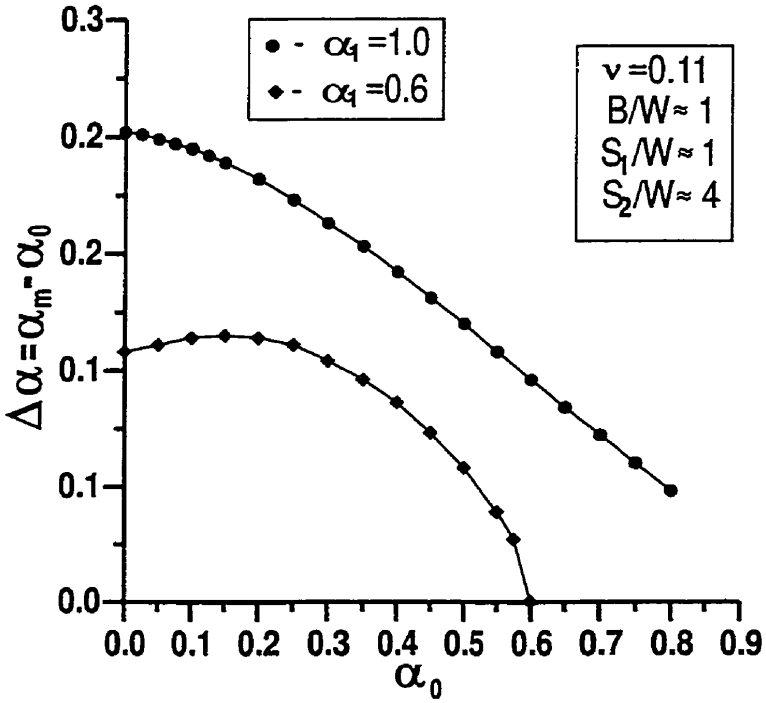

Figure 4.22 Dependence of $\Delta\alpha=\alpha_m-\alpha_0$ on the notch depth α_0.

One more important characteristic feature of the CNB configuration is the dependence of $\Delta\alpha=\alpha_m-\alpha_0$ on α_0 and α_1 (Fig.4.22). For $\alpha_1=1.0$ there is a monotonic drop of $\Delta\alpha$ with α_0, whereas for $\alpha_1=0.6$, $\Delta\alpha$ shows a maximum. The values of $\Delta\alpha$ are much higher for $\alpha_1=1.0$ than for $\alpha_1=0.6$. $\Delta\alpha$ is an important parameter in the notch design because the larger the $\Delta\alpha$ the higher the propensity for stable fracture.

From the description of the CNB configuration presented in this chapter some light can be shed and directions can be given for designing suitable notch parameters for fracture toughness determination.

As was mentioned earlier, subcritical crack growth is required for K_{QV} determination with CNB specimen. The shape of the load- displacement curve depends on the amount of the elastic energy stored in both testing machine and specimen, and also on material and notch parameters. From this point of view a hard machine is desired (low elastic energy stored).

The stored elastic energy is proportional to the square of the load, so it is particularly advantageous to shape the specimen so that fracture begins at small load. It is somehow to the contrary of the direction given by Y^* change with α for a given cross sectional dimensions B and W. Keeping B and W constant and choosing, say 4 pt. loading mode, in order to increase the compliance of that configuration, specimen must be notched deeply $\rightarrow$ large α_1 and α_0. From the graph in Fig.4.22 it is seen that the preferred geometry (from Y^* changes point of view) is $\alpha_1=1.0$ and $\alpha_0=0$. In this case the critical crack length $\Delta\alpha$ is longest, and this gives the highest propensity for subcritical crack growth for all the notch geometries.

In summary- in order to achieve a stable chevron-crack extension at low loads, two major testing requirements must be met. First, the elastic energy stored in both testing machine and specimen must be relatively low. This requirement would be met with a "hard" machine (screw driven) and a high compliance of the testpiece. The latter is equivalent to large values of the chevron-notch normalized geometry parameters α_1 and α_0. Second, the $\Delta\alpha=\alpha_m-\alpha_0$ should be relatively large (it occurs at large α_1 and small α_0 values). The second requirement of small α_0 is in obvious contradiction to the first requirement of large α_0 for a high compliance. Usually, a

compromise is made by choosing $\alpha_1 \approx 0.8-1.0$ and $\alpha_0 \approx 0.2-0.4$ [126-128]. Hence, in the present work α_1 was set at about 0.8-1.0 and α_0 at about 0.2-0.4.

In the case of a material with rising R- curve, however, $\alpha_1=1.0$ and large α_0 is recommended. In this case $Y^*(\alpha)$ must increase rapidly after $\Delta\alpha_m$ so that K_{QV} is not overestimated when K_R increases with increasing $\Delta\alpha$, i.e. the notch must be deep. $\Delta\alpha_m$ must be also relatively large (greater than 2ρ, where ρ is the notch tip radius- one-half of the notch width) to avoid the influence of the finite notch tip radius [129].

Also the notch tip angle must be relatively sharp to provide the propensity for stable crack growth. Again, it must be compromised with the high compliance requirement.

Using two methods: slice model and STCA (Straight- Through- Crack- Assumption) model for Y^*_m calculations it was shown [119] that slice model gave slightly higher Y^*_m values than STCA model (14% for $\alpha_0=0$ and 5% for $\alpha_0=0.5$).

For α_1 in the range 0.5-1.0, K_{QV} computed using the STCA decreases monotonically. Using the slice model, K_{QV} shows a minimum. For $\alpha_1 \approx 1.0$, both models predict similar values [119]. An effect of α_1 on K_{QV} was observed for the CNB specimen due possibly to inaccuracies in the shear transfer coefficient in Bluhm's model (see Section 4.4.4) for $\alpha_1<1$. Therefore, $\alpha_1=1.0$ is the preferred geometry. The Y^*_m values obtained from the STCA were within 3.5% of the Y^*_m values obtained from the experimental compliance. In case of precracking of CNB specimen, the above assumption should not be used to determine Y^* values other than Y^*_m since the agreement with experimental results is poor, particularly at smaller crack length to width ratios [123].

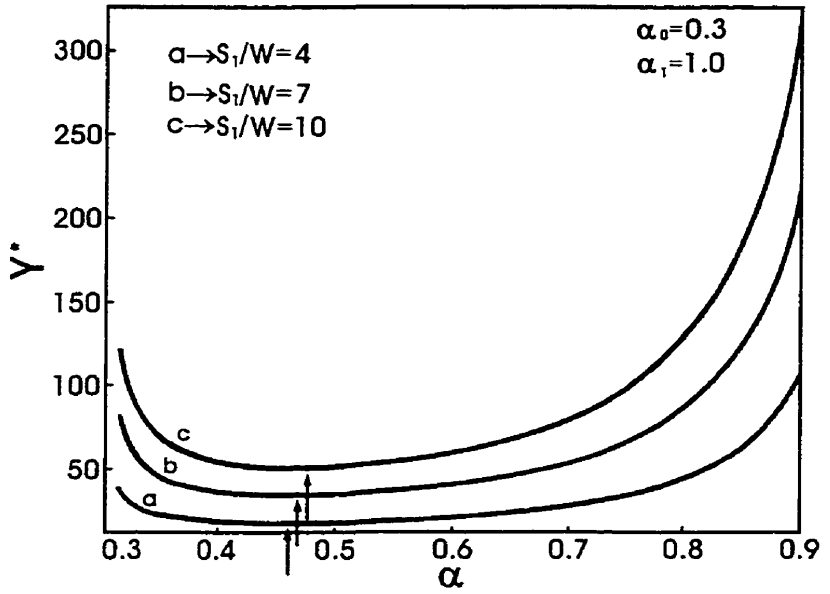

Figure 4.23 Stress intensity factor coefficient Y^* dependence on crack length α for three different S_1/W ratios.

Fig.4.23 shows the influence of S_1/W ratio in 4 pt. bending on the change of Y^*_m with crack length α. Character of Y^* has not been changed substantially. The main effect is shifting the curve towards higher Y^*_m values and higher compliance.

At the very beginning of this work, the author after obtaining linear load to fracture, went intuitively to highly compliant specimen by choosing high $S_1/W \approx 10$ and $S_1/S_2 \approx 12.5$ ratios. Unfortunately, stable crack growth was not obtained. Also, specimens with very sharp notch angles were tested with the same result.

In closing experiments of this work, some precracked CNB specimens were tested in 4 pt. bending in order to substantiate the obtained data for catastrophic fracture. Even though the $S_1/W=4$ and $S_1/S_2=4$ ratios were very low (propensity for low compliance) in one specimen with deeply precracked chevron- notch, the long pop-ins were observed. It happened despite the fact that the precrack length was larger than the critical crack length, but that could be the effect of a large grain size with respect to the notch surface area.

4.4.6 Work of Fracture

The work of fracture, γ_{wof}, is defined simply as the total energy, W_{wof}, consumed to produce a unit area of fracture surface during the complete fracture process [130,131], i.e.

$$\gamma_{wof} = W_{wof} / 2S \tag{2.8}$$

where S is the projected cross- sectioned area of the unnotched remaining ligament of the test specimen.

The key point in equation (2.8) is that none of the assumptions of linearity for the test specimen are made for the fracture process. It is possible to calculate γ_{wof} in the absence of any information on the stress intensity factor K_I, the notch tip accuity, the notch front geometry (straight through or chevron), etc. This fact is an important advantage in the analysis of very complicated fractures. However, the details of the physical meaning of γ_{wof} as the fracture surface energy, becomes somewhat ambiguous for fracture processes exhibiting prominent plastic deformation, phase transformation, microcracking induced residual stresses in the wake region, and strong crack bridging systems.

A critical issue is that the fracture process is usually far removed from an ideal state. A number of additional energy absorbing processes can occur during primary crack extension, even in the most brittle materials like ceramics. Even in the fracture surface of single crystals there are numerous imperfections including dislocations, twin deformation, cleavage steps and lines. In some materials, not only is crack branching evident in the frontal process zone, but also the zone shielding by microcracking and compressive residual stresses in the following wake region, as well as crack bridge shielding in the crack surface contact region occurring behind the running crack tip. All of these fracture processes add increments of energy consumption to the intrinsic surface energy (γ_0) [132].

5 EXPERIMENTAL RESULTS

5.1 Chemical Composition and Microstructure of Alloys

Table 5.1 contains the chemical composition obtained from a fully quantitative X-ray energy dispersive spectroscopy (EDS) (QX2000 LINK system) analysis of most of the HIP-ed ingots used in this study (at least 5 readings were made for the average; standard deviations are also shown). Boron content and overall chemical compositions of the specimens designated 9Mn-0.25B, 9Mn-0.66B, 14Mn-0.24B and 14Mn-0.65B (numbered 10, 11, 12, and 13 in Table 5.1, respectively) were determined using neutron activation analysis in Becquerel Labs. Inc. (Mississauga, Ont.). Boron content was also determined by this method in the 9Mn-0.004B alloy (no.9 in Table 5.1).

Compositions of the low- Mn ingots which were used for cutting fracture toughness specimens (~9at.% Mn, designated 9Mn) numbered 1, 2, 3, 4, 5, 6, 7, 9,10, 11, 14, 15, 18 and 19 in Table 5.1 are very similar and correspond essentially to a single $L1_2$ phase field [107]. Material in the as-cast condition contained very small amount of second phase (unidentified) (Fig.5.1a). This phase was completely dissolved during homogenization. Fig.5.1b shows characteristic needles most probably resulting from the presence of the interstitial impurities in the pure elements used for the preparation of the alloys. These needles were tentatively identified as Ti_2AlC [14] and Ti_2AlN [133]. Volume fraction of these needles is below 1% (Table 5.2, p.92). Porosity level after homogenization and HIP-ing is below 1%

(Fig.5.2a).

Table 5.1 Overall chemical composition of the ingots after HIP-ing.

ALLOY DESIGNATION	INGOT	SPECIMENS	Al (at.%)	Ti (at.%)	Mn (at.%)	B (at.%)
9Mn	1	4pt bending, CNB, small	66.5±0.2	25.0±0.2	8.5±0.1	-
	2	4pt bending, CNB, large	66.2±0.2	24.7±0.2	9.2±0.2	-
	3	3pt bending, CNB	65.8±0.1	25.0±0.1	9.2±0.2	-
	4	3pt bending, SEPB (air- series 1)	65.7±0.2	25.2±0.1	9.2±0.2	-
	5	3pt bending, SEPB (air- series 2)	66.0±0.1	24.9±0.1	9.1±0.1	-
	6	3pt bending, SEPB (argon)	66.1±0.2	24.9±0.2	9.0±0.2	-
	7	3pt bending, SEPB (vacuum, liquid N_2, water)	67.1±0.2	24.0±0.2	8.9±0.2	-
14Mn	8	4pt bending, CNB, high-Mn	56.4±0.1	29.4±0.1	14.2±0.1	-
9Mn-0.004B	9	4pt bending, CNB, B-doped	65.8±0.1	25.5±0.1	8.8±0.1	.004±0.001
9Mn-0.25B	10	4pt bending, CNB, B-doped	66.7±2.1	24.2±1.0	8.9±0.3	.25±0.007
9Mn-0.66B	11	4pt bending, CNB, B-doped	65.1±2.1	25.2±1.0	9.0±0.3	.66±0.02
14Mn-0.24B	12	4pt bending, CNB, B-doped	57.6±1.9	28.5±1.1	13.7±0.4	.24±0.007
14Mn-0.65B	13	4pt bending, CNB, B-doped	53.6±1.8	31.9±1.2	13.8±0.4	.65±0.02
9Mn	14	POWDER	66.4±0.2	24.2±0.3	9.4±0.2	
	15	POWDER	65.7±0.5	25.7±0.7	8.6±0.4	
	18	RECRYSTALLIZED (50% DEFORMED)	65.3±0.2	25.7±0.2	9.1±0.1	
	19	RECRYSTALLIZED (70% DEFORMED)	64.8±0.2	25.4±0.3	9.1±0.1	

Fig.5.3 shows the thermally etched, grainy structure of different grain morphologies corresponding to different locations in the ingot. Grain size is similar in all the ingots. Size of the equiaxed grains is ~0.2- 0.5 mm (Figs.5.2b, 5.3a, 5.4b, 5.7a, 5.9b, 5.10) (a few specimens had very large grains, ~1300 μm). Thickness and length of columnar grains change from ~0.15 to 0.3 mm (also grains as fine as ~0.05 mm were found) and ~2 to 5 mm, respectively (Figs.5.3b and 5.7b).

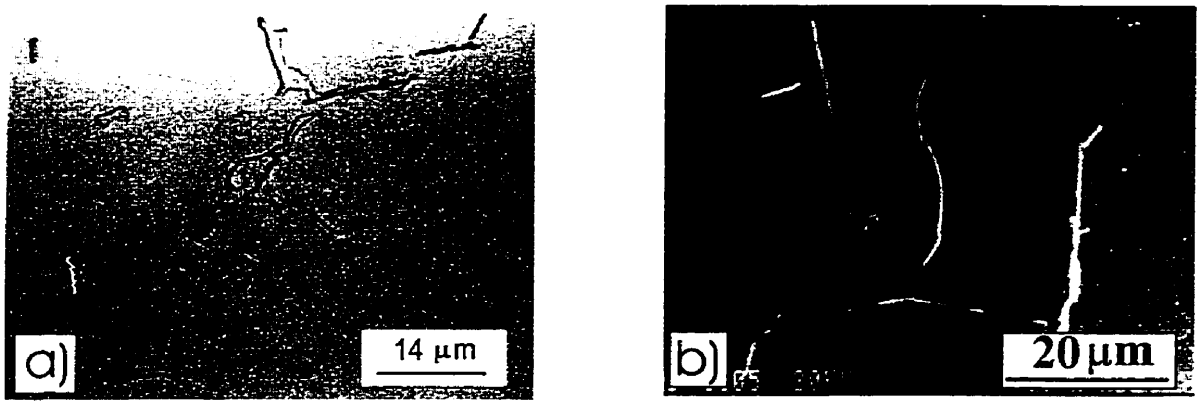

Figure 5.1 a) Optical micrograph of low- Mn alloy in as-cast condition (etched), b) after HIP-ing (SEM).

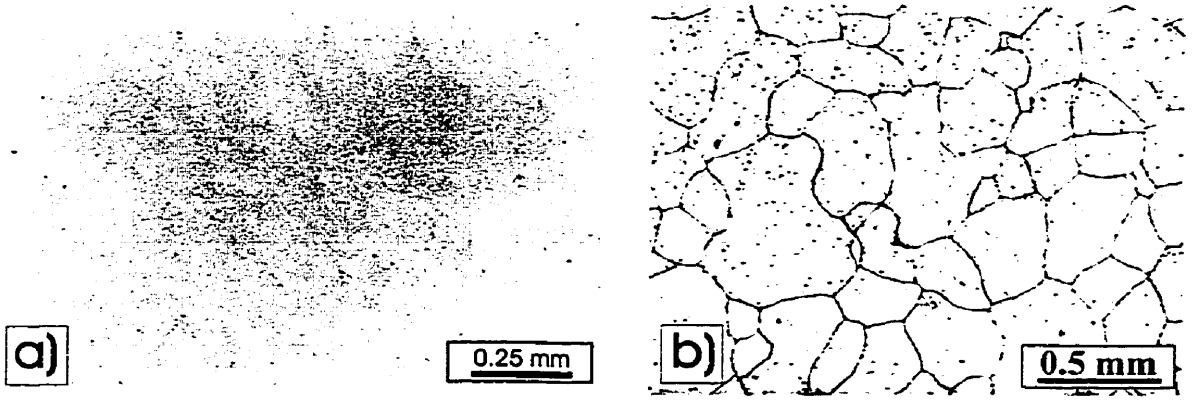

Figure 5.2 Optical micrographs of the HIP-ed, low- Mn material; a) low porosity (below 1%) (unetched), b) chemically etched boundaries of equiaxed grains (specimens tested in air).

Specimens tested in argon (Fig.5.4) have very similar microstructure to those tested in air.

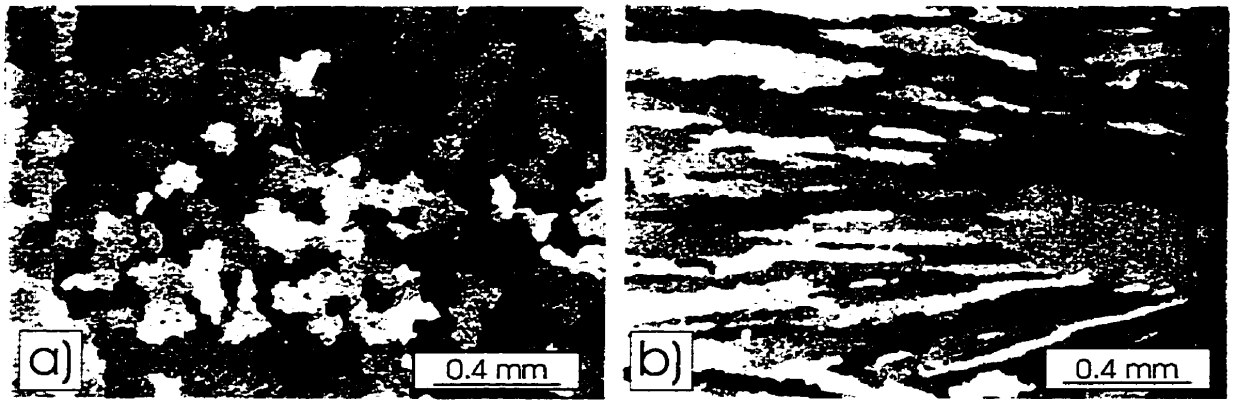

Figure 5.3 Optical micrographs of the HIP-ed, low- Mn material (thermally etched); a) equiaxed grains, b) columnar grains.

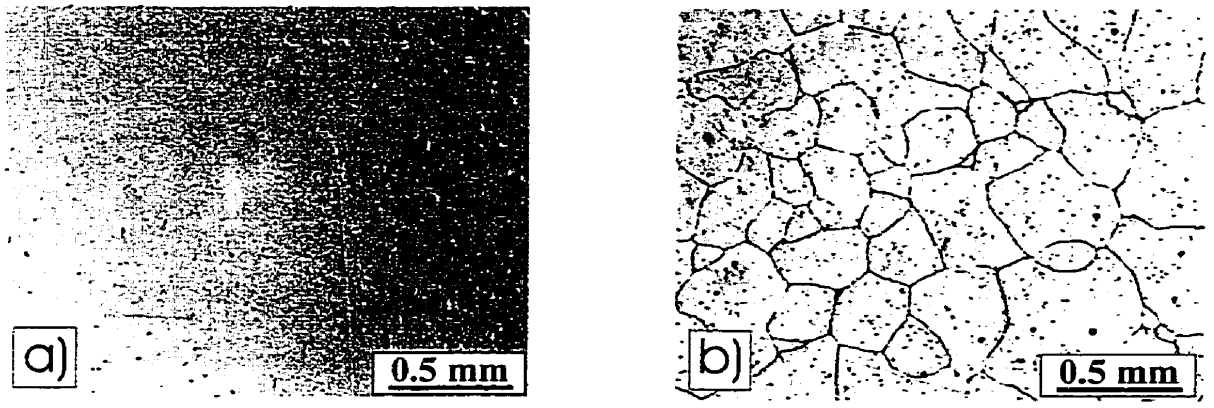

Figure 5.4 Optical micrographs of the HIP-ed, low- Mn material; a) low porosity (below 1%) (unetched), b) chemically etched boundaries of equiaxed grains (specimens tested in argon).

The microstructure of the as- cast, boron- doped (0.004 at.% B) alloy is shown in Fig.5.5. Second phase content was similar to the low- Mn, boron- free alloy. After homogenization, porosity was higher than in boron- free alloy but was reduced to ~1% after HIP-ing (Fig.5.6) (the size of pores and volume fraction was reduced). The equiaxed and columnar grains of the 9Mn-0.004B alloy are shown in Fig.5.7.

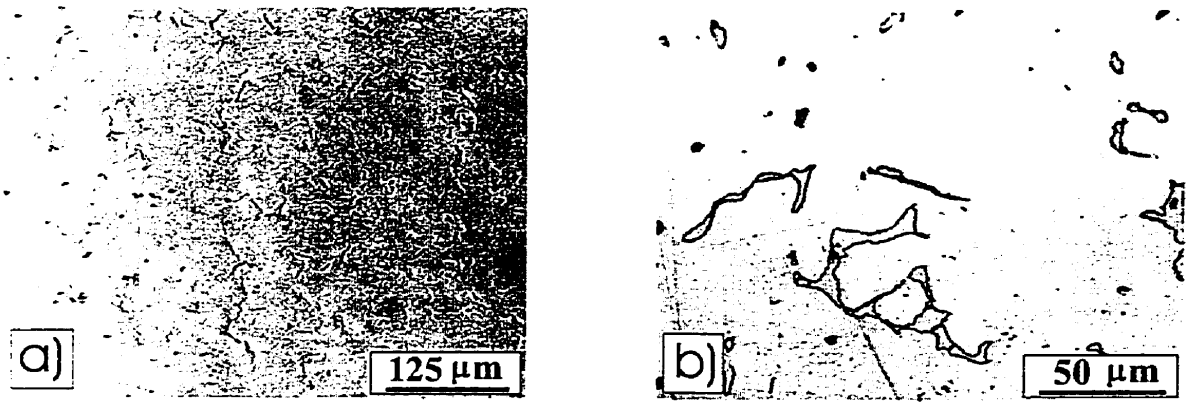

Figure 5.5 Optical micrographs of the 9Mn-0.004B as-cast alloy showing some content of the second phase (etched).

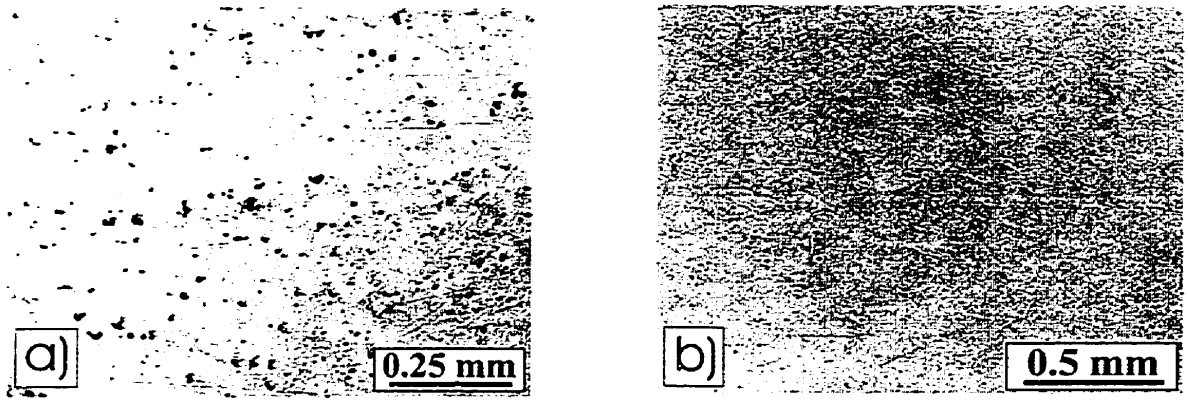

Figure 5.6 Optical micrographs of the a) homogenized and b) homogenized and HIP-ed 9Mn-0.004B alloy (unetched).

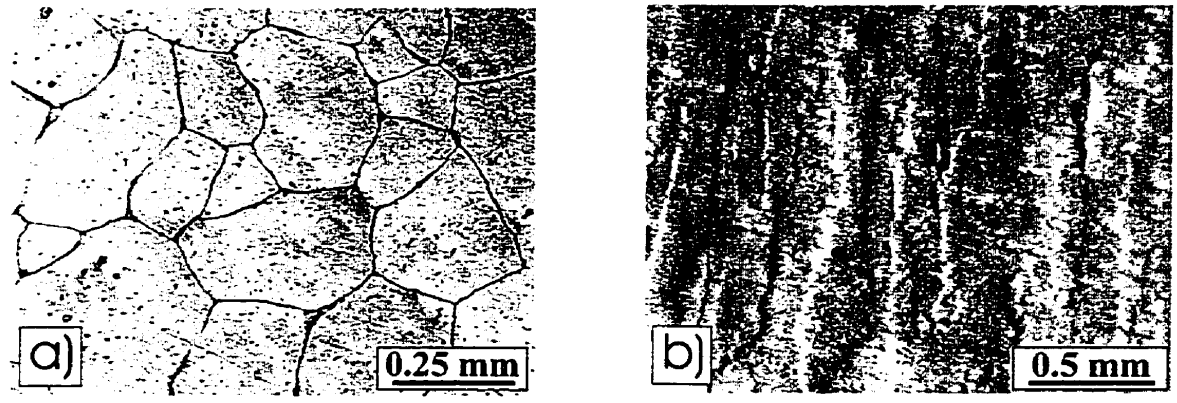

Figure 5.7 Optical micrographs of the homogenized and HIP-ed 9Mn-0.004B alloy; a) equiaxed (etched) and b) columnar grains (unetched).

The as-cast microstructure of the alloy with high- Mn content (14 at.% Mn) (ingot no. 8 in the Table 5.1) exhibits higher content of second phase (Fig.5.8) than the

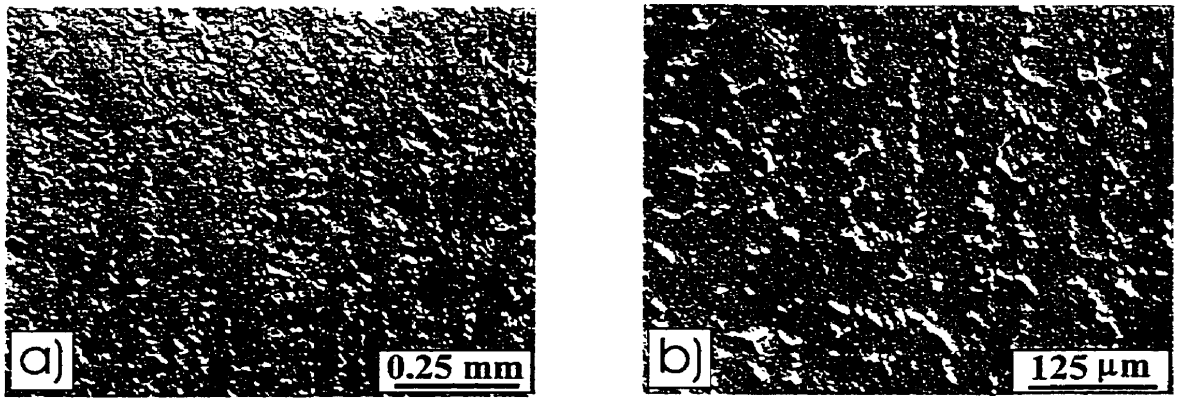

Figure 5.8 Optical micrographs of second phase in the as-cast high- Mn alloy (14% Mn) (unetched).

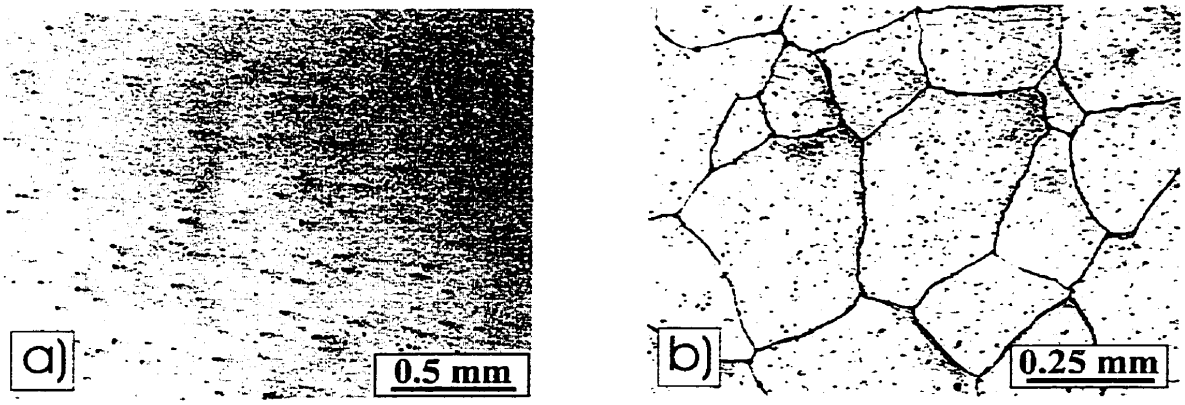

Figure 5.9 Optical micrographs of the homogenized and HIP-ed high- Mn alloy; a) porosity (~2%) (unetched), b) equiaxed grains (etched).

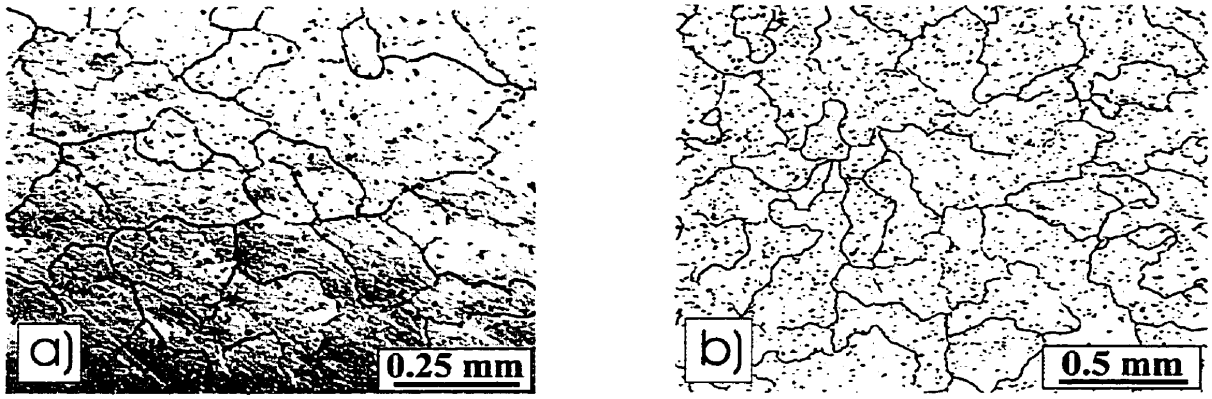

Figure 5.10 Optical micrographs of the homogenized and HIP-ed high- Mn alloy (etched) showing different morphology of "equiaxed" grains (appearing also in other alloys).

9Mn alloys. Homogenization dissolved entirely the second phase. After HIP-ing porosity was ~2% (Fig.5.9a), slightly higher than that in the 9Mn alloys. Figs.5.9b and 5.10 show the morphology of grains in high- Mn alloy.

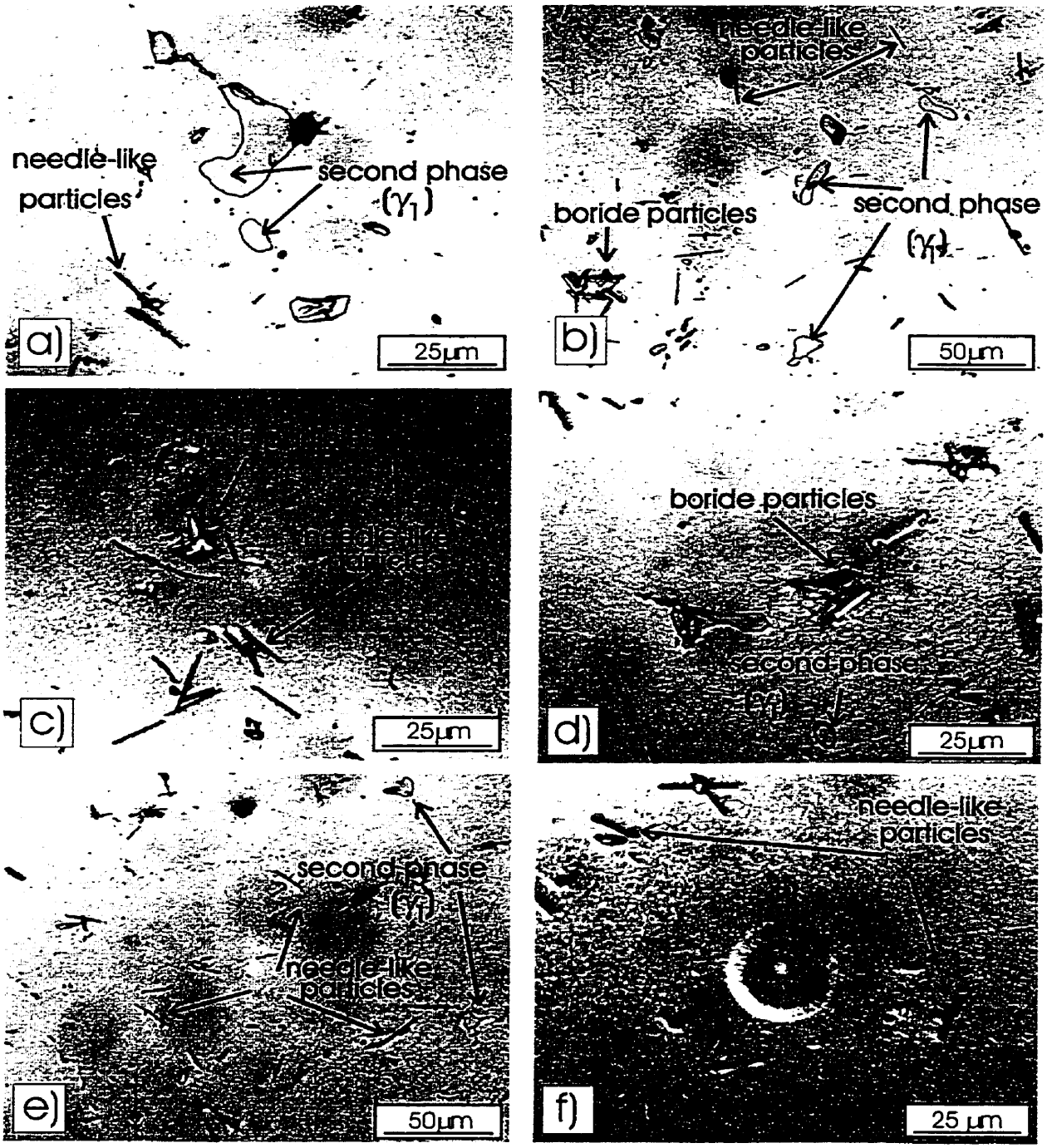

Figure 5.11 Optical micrographs of the microstructure of the homogenized and HIP-ed 14Mn-0.24B alloy (etched).

Alloys numbered 10, 11, 12, and 13 in Table 5.1 contain boron. Boron concentration around 0.2- 0.6 at.% is the optimal amount used in Ni_3Al to improve mechanical properties [134]. This amount of boron in Ni_3Al does not cause the

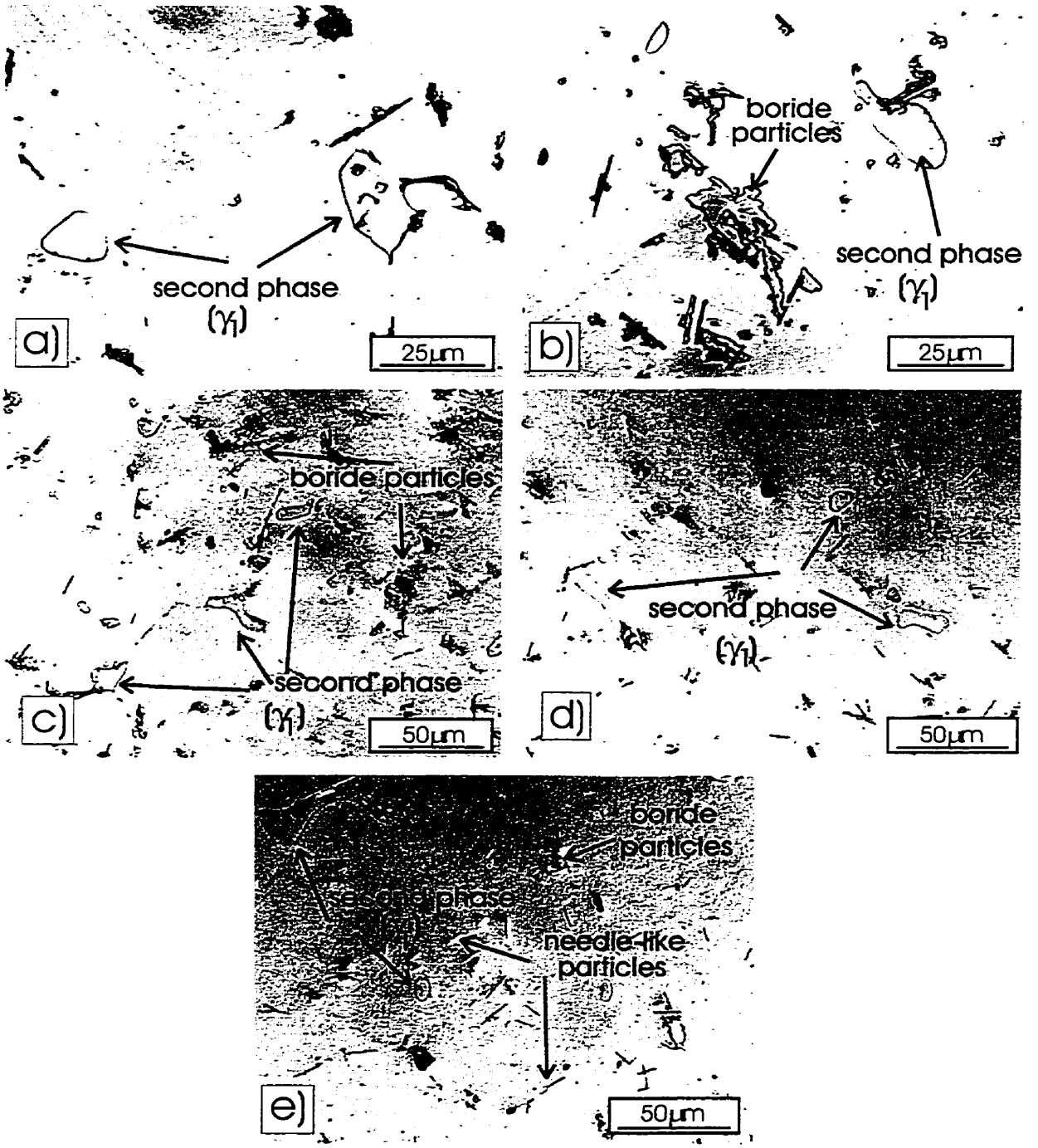

Figure 5.12 Optical micrographs of the microstructure of the homogenized and HIP-ed 14Mn-0.65B alloy (etched).

formation of borides. However, in the present alloys this amount of boron is sufficient for forming borides. Microstructures of the 9Mn-0.25B, 9Mn-0.66B, 14Mn-0.24B and 14Mn-0.65B alloys are shown in Figs.5.11, 5.12, 5.13, and 5.14, respectively.

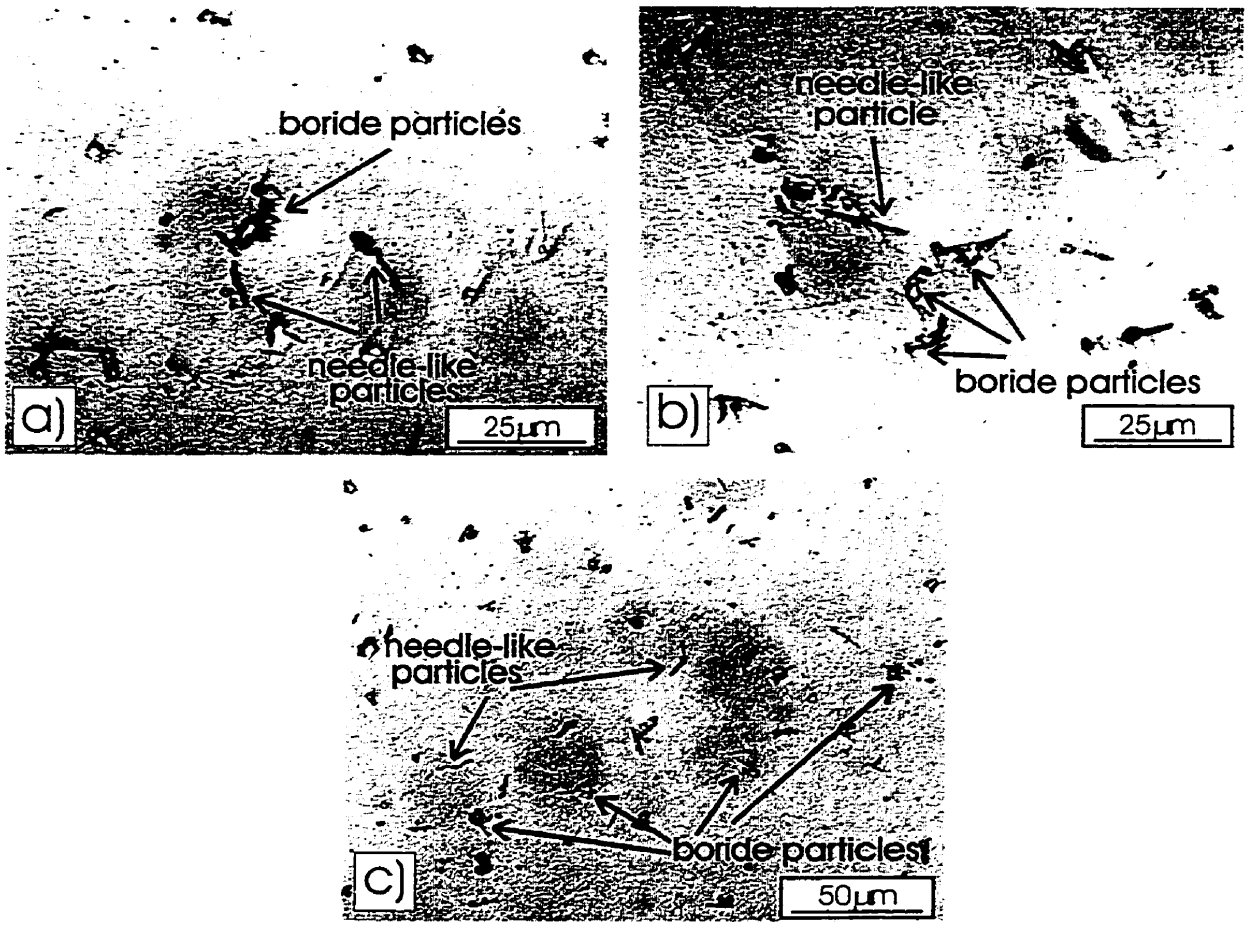

Figure 5.13 Optical micrographs of the microstructure of the homogenized and HIP-ed 9Mn-0.25B alloy (etched).

The microconstituents in these alloys are: the $L1_2$ matrix, the second phase of the composition Al: 41.2±0.8 at.%, Ti: 33.3±0.3 at.%, Mn: 25.5±0.5 at.% in the amount of 0.96±0.87% (the highest for 14Mn-0.65B alloy), the characteristic needles (~1%) and finally borides. Volume fraction of needles in high- Mn (14% Mn) alloy is higher than in the low- Mn alloys (9% Mn) (alloys containing no boron) but still is below

1%. The volume fraction of needles+borides in boron- doped alloys is higher for alloys containing higher amount of boron. Figs.5.15a and b show SEM photographs of boride particles in 14Mn-0.24B and 14Mn-0.65B alloys, respectively.

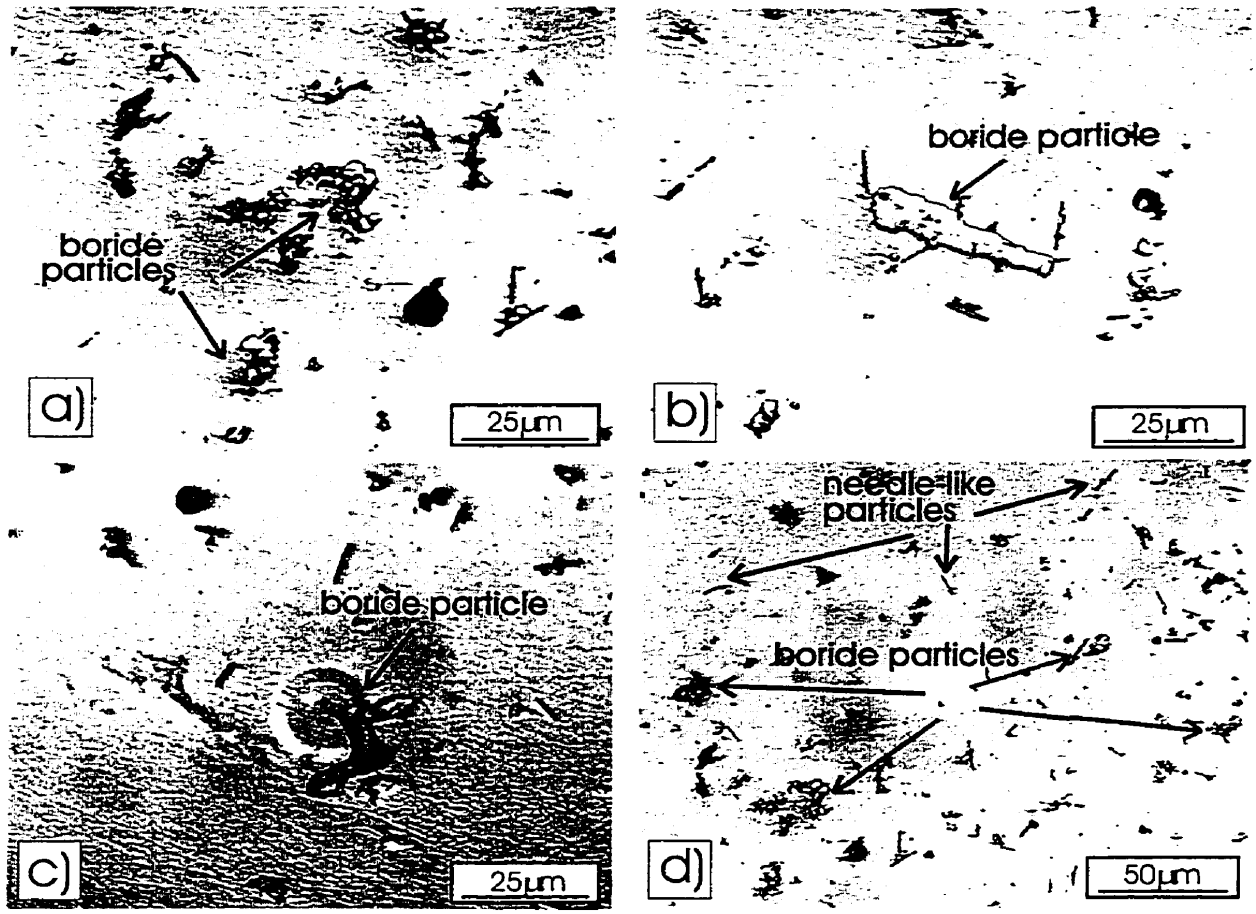

Figure 5.14 Optical micrographs of the microstructure of the homogenized and HIP-ed 9Mn-0.66B alloy (etched).

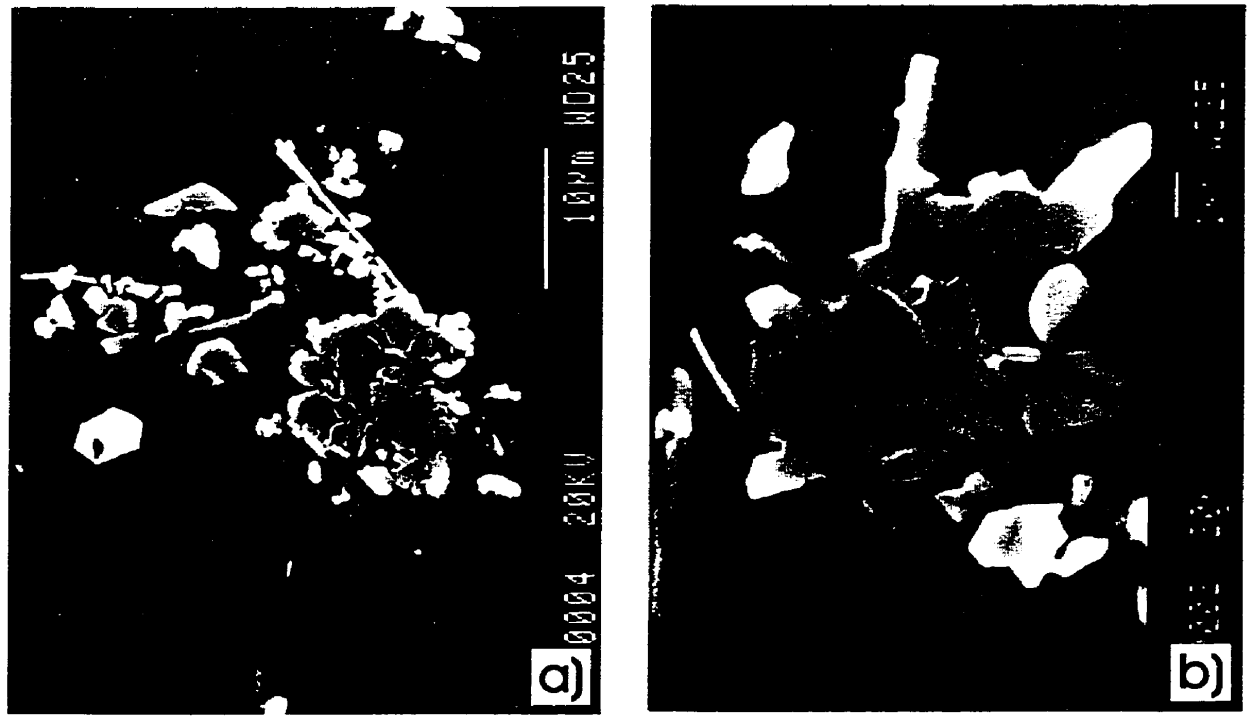

Figure 5.15 SEM photographs of boride particles in a) 14Mn-0.24B alloy, b) 14Mn-0.65B alloy.

The volume fraction of the microconstituents in the alloys was measured by extracting the measured constituent from digital image and applying Java image analysis package by Jandel Scientific [117] to calculate the amount of this constituent. This method is presented in Fig.5.16. Second phase content in 14Mn-0.65B alloy was determined by analyzing 20 digital images. The amount of borides+needles was determined by processing 10 images for each specimen and amount of needles in high Mn alloy (no.9) was determined by processing 5 digital images.

Porosity was measured on unetched specimens and there was no need for extraction because these were the only features in the image and Java package could be applied directly. Details of the microstructural features are given in Table 5.2.

Table 5.2 Composition and microstructural characterization of cubic titanium trialuminide alloys used for fracture toughness testing.

Alloy	Composition							Vol. fraction of sec. phase (γ_1) (%)	Vol. fraction of needles + borides + porosity (%)	Vol. fraction of needles (%)	Porosity (%)
	Overall (at. %)				Matrix (at. %)						
	Al	Ti	Mn	B	Al	Ti	Mn				
9Mn*)	66.2±0.2	24.7±0.2	9.2±0.2	-	-	-	-	-	No borides	<1.0	<1
9Mn-0.004B	65.8±0.1	25.5±0.1	8.8±0.1	0.004±0.001	-	-	-	-	No borides	<1.0	<1
9Mn-0.25B	66.7±2.1	24.2±1.0	8.9±0.3	0.25±0.007	65.7±0.3	25.0±0.2	9.3±0.2	-	2.2±0.2	<1.0	?
9Mn-0.66B	65.1±2.1	25.2±1.0	9.0±0.3	0.66±0.02	65.4±0.3	25.1±0.5	9.5±0.1	-	3.4±0.4	<1.0	?
14Mn*)	56.4±0.1	29.4±0.1	14.2±0.1	-	56.1±0.2	29.0±0.1	14.9±0.2	<0.5	No borides	1.0±0.1	<2
14Mn-0.24B	57.6±1.9	28.5±1.1	13.7±0.4	0.24±0.007	56.3±0.4	29.2±0.1	14.4±0.4	<0.5	3.5±0.6	<1.0	?
14Mn-0.65B	53.6±1.8	31.9±1.2	13.8±0.4	0.65±0.02	55.2±0.2	30.3±0.3	14.5±0.4	1.0±0.9	4.3±0.7	<1.0	?

*) Obtained from EDS; the other overall compositions obtained from neutron activation analysis by the Becquerel Labs. Inc. (Mississauga, Ont.). All matrix compositions are obtained from EDS.

?- Could not be measured by Java because of the similar appearance of the boride particles and pores.

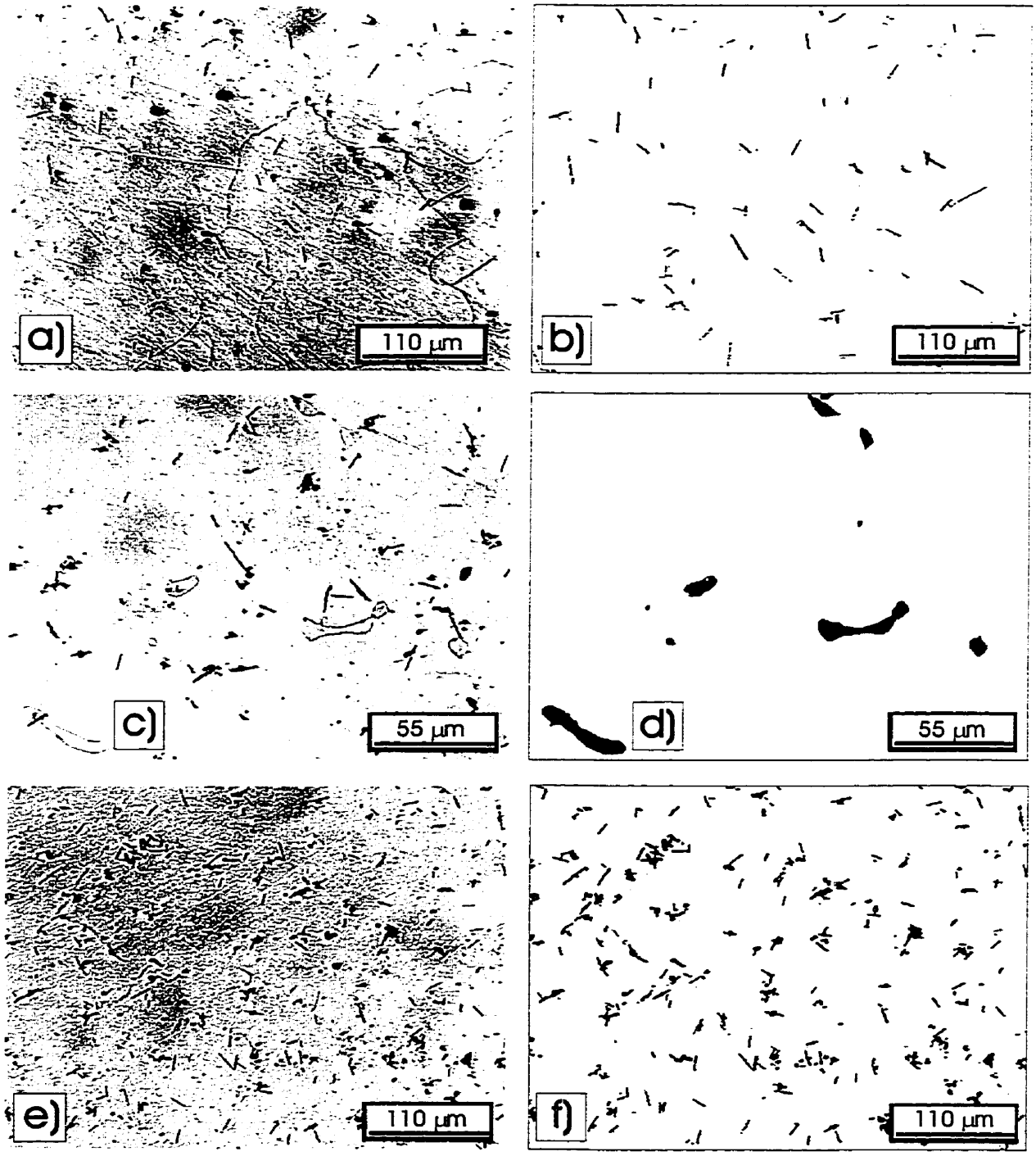

Figure 5.16 Digital image processing: a) and b) High- Mn alloy (14Mn) and extracted needle- like particles, respectively; c) and d) 14Mn-0.65B alloy and extracted second phase, respectively; e) and f) 14Mn-0.24B alloy and extracted needle- like particles + borides, respectively.

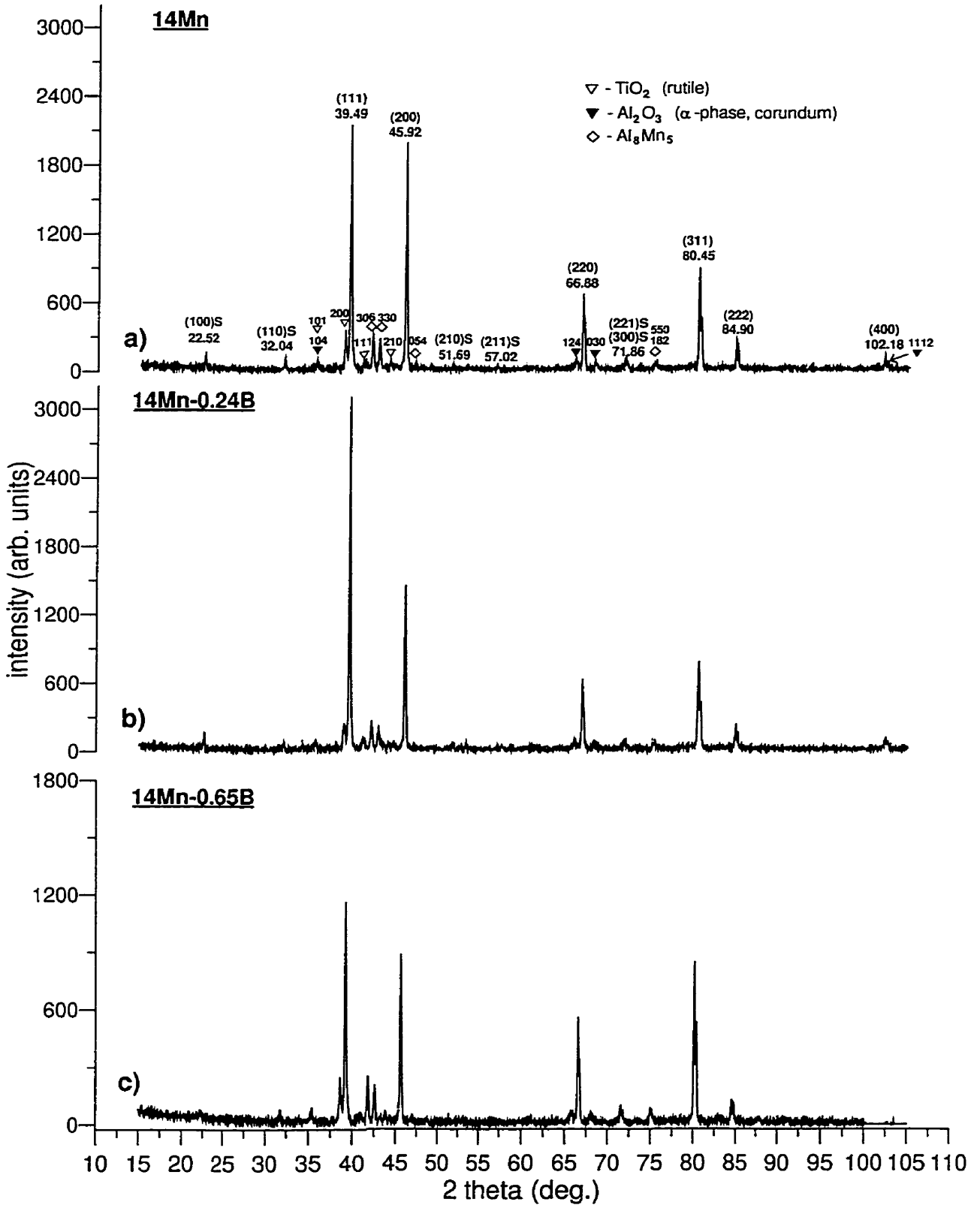

Figure 5.17 X-ray diffraction patterns of the alloys: a) boron-free, 14Mn, b) 14Mn-0.24B, c) 14Mn-0.65B.

X-ray diffraction patterns obtained from alloys 14Mn, 14Mn-0.24B and 14Mn-0.65B are shown in Fig.5.17. It can be seen that all the diffraction patterns contain additional peaks. Majority of these peaks was identified as oxide peaks (TiO_2 and Al_2O_3). The bulk samples were crushed and subsequently pulverized in a ceramic mortar using a ceramic pestle. In order to remove strains the powders were sealed in an evacuated tube and annealed at 1000°C for 1h. Oxidation of the powders took

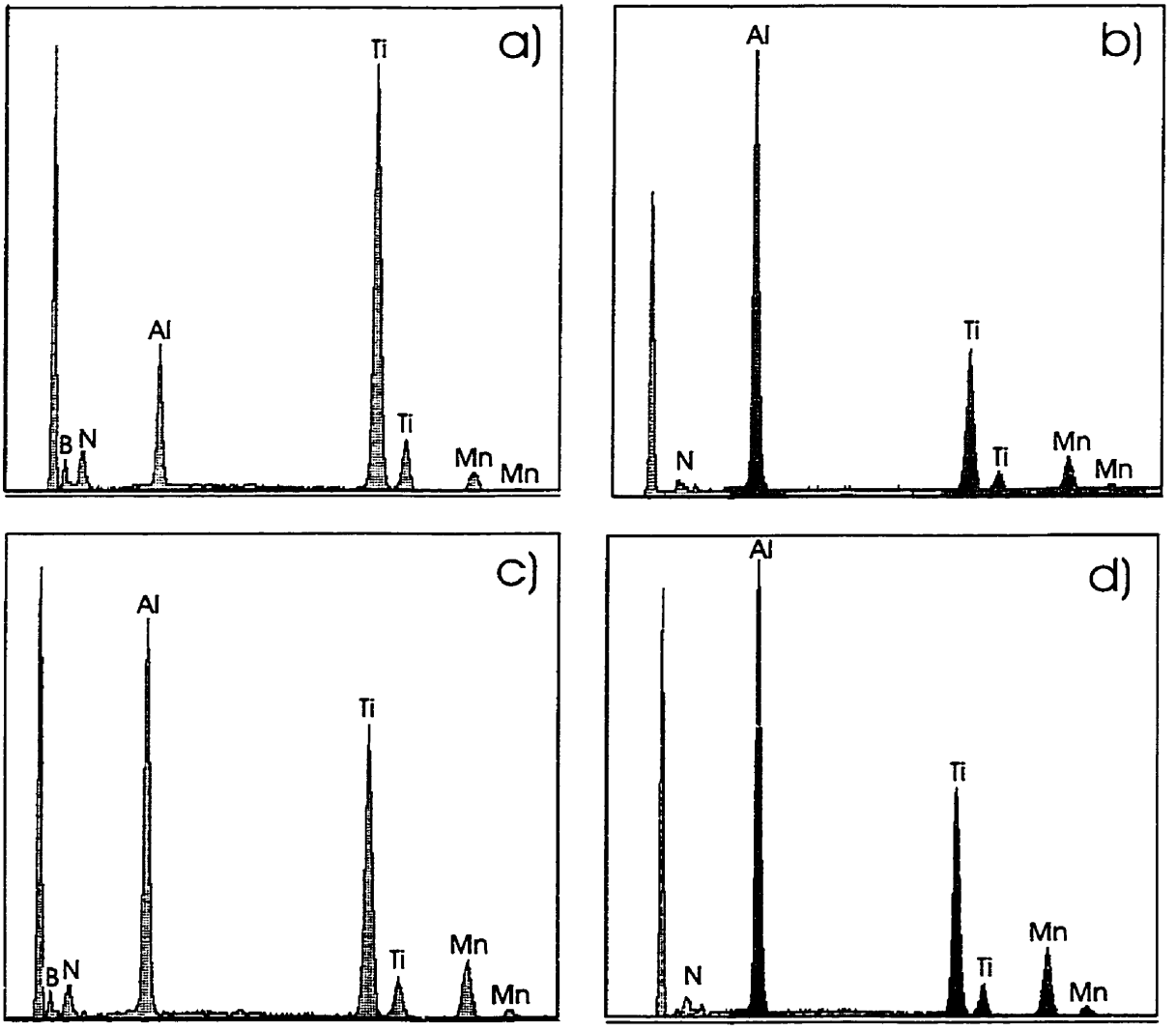

Figure 5.18 EDS energy spectra from boride particles in (a) 9Mn-0.66B and (c) 14Mn-0.65B as well as from the $L1_2$ matrix in (b) 9Mn-0.66B and (d) 14Mn-0.65B.

place during annealing due to insufficient vacuum in the quartz tube and/or due to a high annealing temperature. Also the peaks from the Al_8Mn_5 phase were detected.

It seems that this phase was formed during annealing due to depletion in Ti concentration (because of the TiO_2 formation) (Appendix B, Fig.B.1). It can also be seen (Fig.5.17b,c) that neither boride nor γ_1 particles were detected by x-ray diffraction. Additional X-ray spectrum obtained from a crushed and pulverized 14Mn alloy (without any annealing to eliminate the oxide peaks) showed only peaks arising from the $L1_2$ structure.

The calculated lattice parameters for boron-free 14Mn, 14Mn-0.24B and 14Mn-0.65B alloys are 0.3958 nm, 0.3953 nm, and 0.3959 nm, respectively.

The presence of boron in particles from Fig.5.15 is confirmed by a windowless EDS analysis (Fig.5.18a,c). It is quite obvious that they are borides. Unfortunately, their stoichiometry could not be obtained from a windowless (qualitative) EDS analysis. The EDS analysis of the $L1_2$ matrix (Fig.5.18b,d) shows no presence of boron in the matrix of the boron-doped specimens. Most probably, the boron level is below detectability limit of a windowless EDS. After all, the presence of borides in the alloys with 0.24-0.25at.% B and their absence in the alloy with 0.004at.% B (Table 5.2) indicate, rather convincingly, that the solid solubility limit of boron in the $L1_2$ matrix is somewhere between 0.004 and 0.24at.%. These numbers are definitely below the detectability limit of a windowless EDS. Additionally, some amount of boron in the matrix might have segregated to the grain boundaries depleting the matrix.

As can be seen in Fig. 5.18 the EDS energy spectra show the presence of the nitrogen (N) peak in both borides and matrix. This peak has always been observed in each alloy fabricated in this work regardless of its composition. Most surprisingly, the N peak has also been observed in a specimen taken from a master aluminum-boron alloy (Al-3.2wt.% B) obtained from a supplier. Therefore, the

origin of this N peak is not well understood at the present moment. However, because it is observed in all the alloys, its potential effect (if any) on the properties can be neglected.

5.2 Load-Load Line Displacement (P-LLD) Curves from Bending Fracture Toughness Testing

The following section shows the correlation of the appearance of the fracture surface obtained in fracture toughness testing of bend specimens and the corresponding load (P)- load-line displacement (LLD) curves. The purpose of the analysis presented here is to show the general trends in fracture response of the specimens whose fracture surfaces are characterized by various features.

P-LLD curves for 9Mn alloy, SEPB-type specimen look similar for all specimens tested in air, water, argon, and vacuum (Figs.5.19a and 5.20). Their similarity stems from the fact that almost always the loading is linear to its maximum value. Just one specimen showed a small amount of a subcritical crack extension when tested at RT (Fig.5.20b no.3). This type of smooth crack extension was occurring more frequently at the highest testing temperatures, 800°C- 1000°C (Figs.5.19a no.6 and 5.20a no.6). Very characteristic for specimens tested in liquid nitrogen is the saw-toothed appearance of the initial P-LLD curves (Fig.5.20b; no.6). This is most probably caused by the dimensional instability of the loading jig due to difficulty in equilibrating the temperature.

As in the case of the SEPB specimens, the CNB type specimens mainly fractured in a catastrophic manner, although even at RT a few specimens popped- in before final fracture (Fig.5.19b no.1). Pop- ins were more often occurring at high temperature 600°C- 1000°C (Figs.5.19b no.5,6, and 7). A feature that is common to both types of specimens is a rapid load drop after reaching the maximum load for the range of low to intermediate temperatures. Parameters that seem to control the amount of load drop are: test temperature, specimen's stiffness and grain morphology (equiaxed vs. columnar- having effect at high temperature due to changing mode

of fracture). Still some other fracture mechanisms are responsible for different behavior of specimens no.1 and 2 in Fig.5.19b. The two specimens posses almost identical stiffness, loads to fracture and fracture toughness values but they fracture

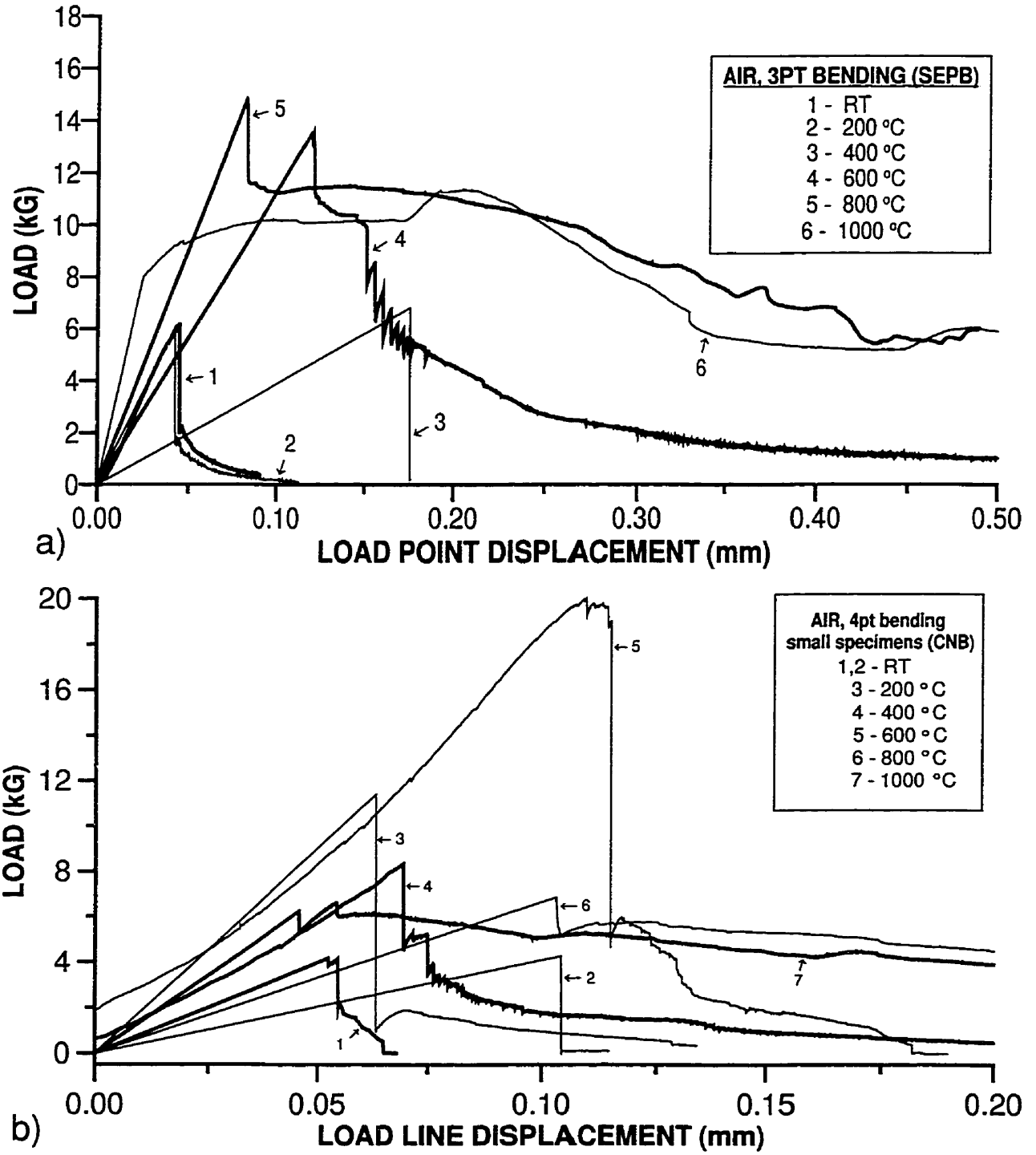

Figure 5.19 Load vs. load- line displacement for: a) SEPB, b) CNB specimens of the 9Mn alloys.

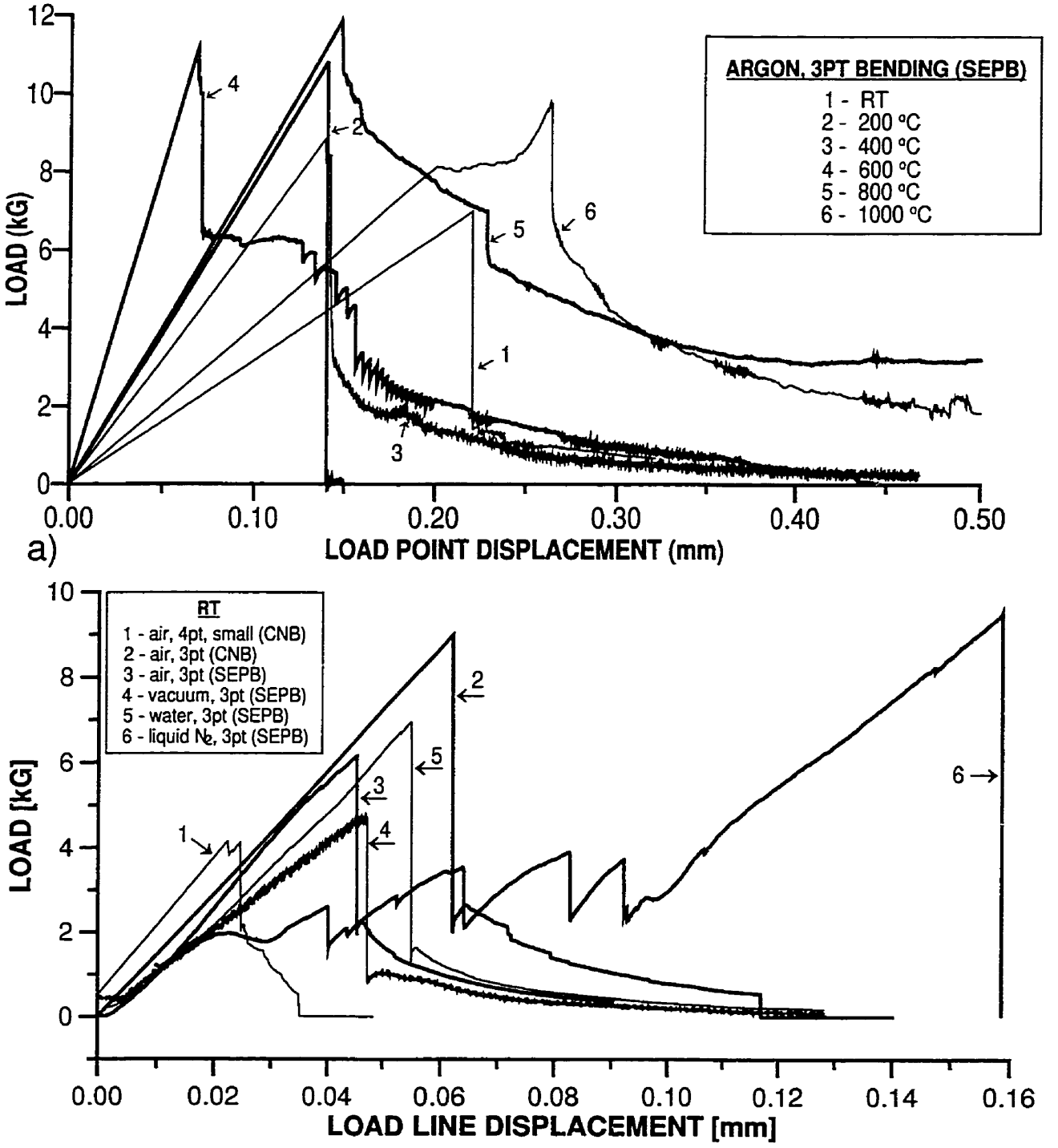

Figure 5.20 Load vs. load- line displacement for: a) SEPB specimens tested in argon, b) RT tests in various environments and loading modes (9Mn alloys).

differently. Possible explanation could be that specimen no.2 developed much more branching due to larger misorientation angles between grains which caused the

crack to propagate in a controlled manner after a rapid load drop. At high temperatures the amount of rapid load drop seems to decrease to a minimum (Figs.5.19a no.6 and 5.29b no. 6 and 7) and the curves display continuous change of the load during fracturing . Their fracture surface is in general very rough and non- planar due to IGF.

P-LLD curves for boron-free 14Mn specimens in the range from RT to ~400°C (Fig.5.21a) and most of 9Mn+B and 14Mn+B specimens regardless of test temperature, exhibited numerous crack pop-ins on the initial portion of the curve (examples for 9Mn-0.66B, 14Mn-0.65B, and 9Mn-0.25B are shown in Figs.5.22, 5.24, and 5.26, respectively). The occurrence of these pop-ins is essentially beneficial because they provide a very sharp crack tip, most probably sharper than the one formed from an initial notch slot. Such a sharp tip satisfies a principal requirement of linear elastic fracture mechanics (LEFM). Curves for boron-free 14Mn alloy at temperatures >400°C showed no pop-ins, but relatively smooth and linear behavior up to P_M followed by a small load drop and a pronounced "tail" past P_M (Fig.5.21b).

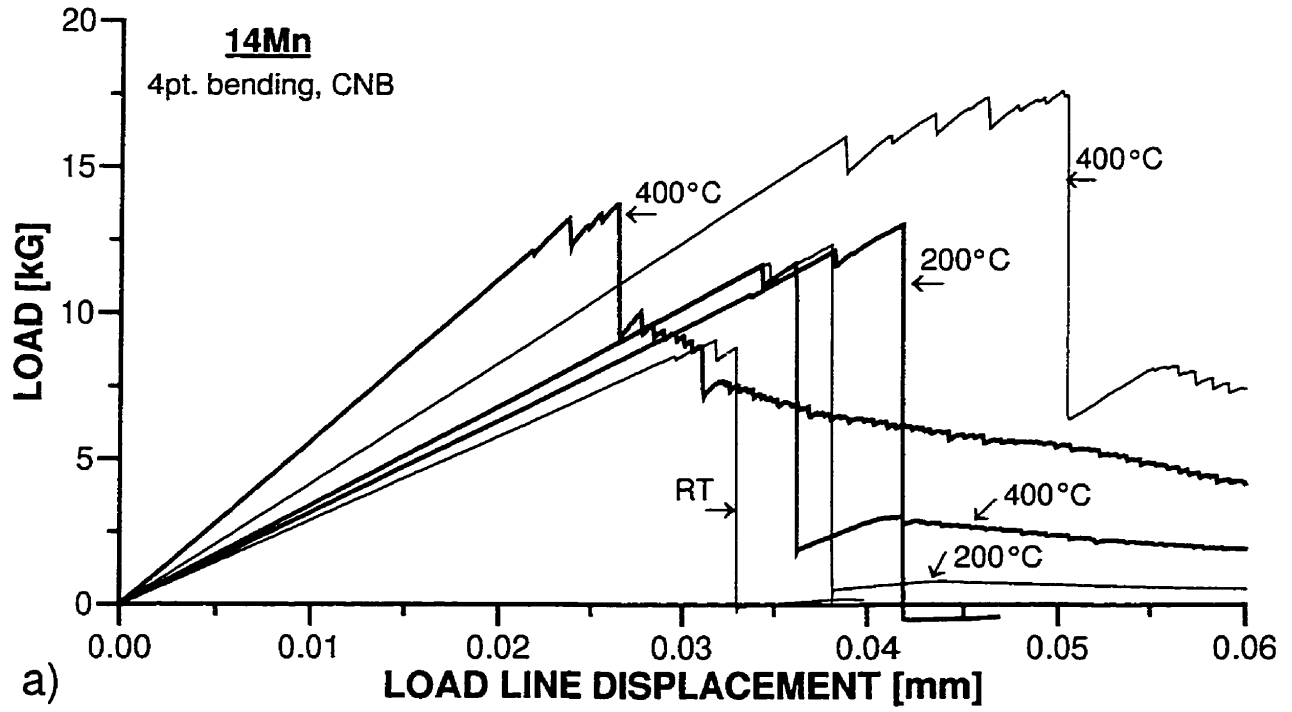

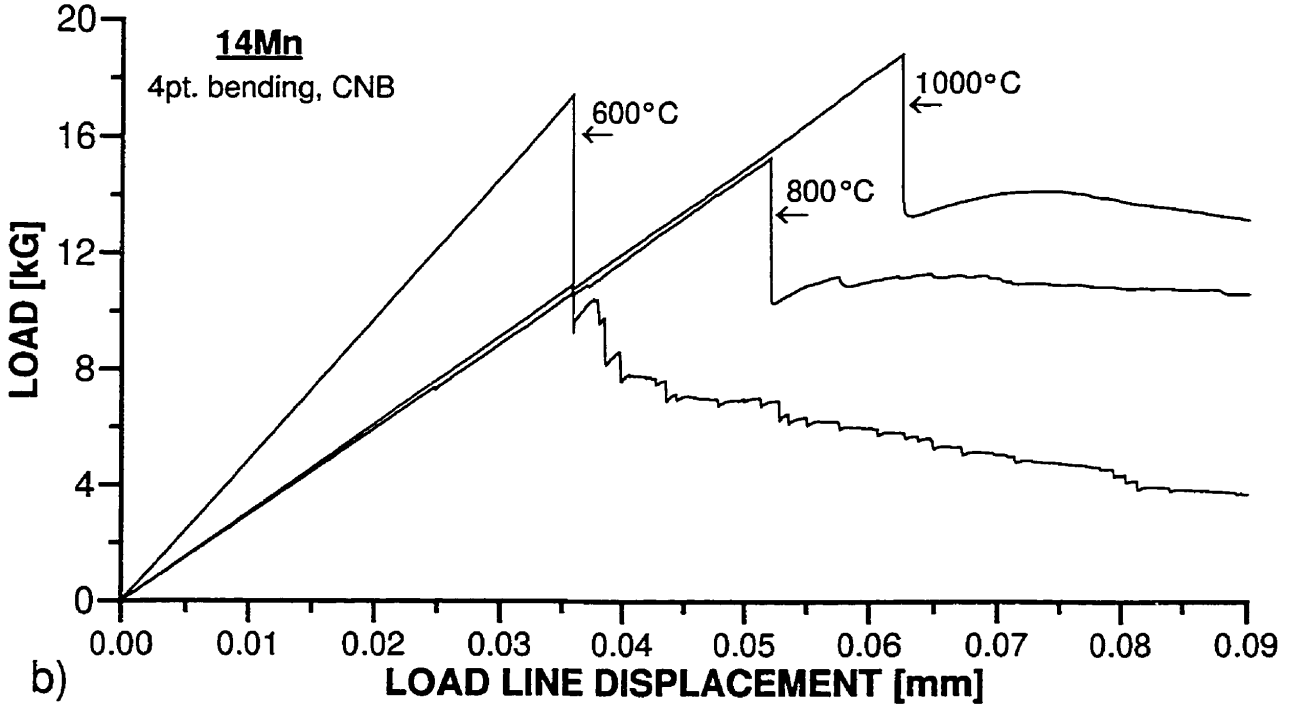

Figure 5.21 Load vs. load- line displacement for CNB specimens of 14Mn alloy.

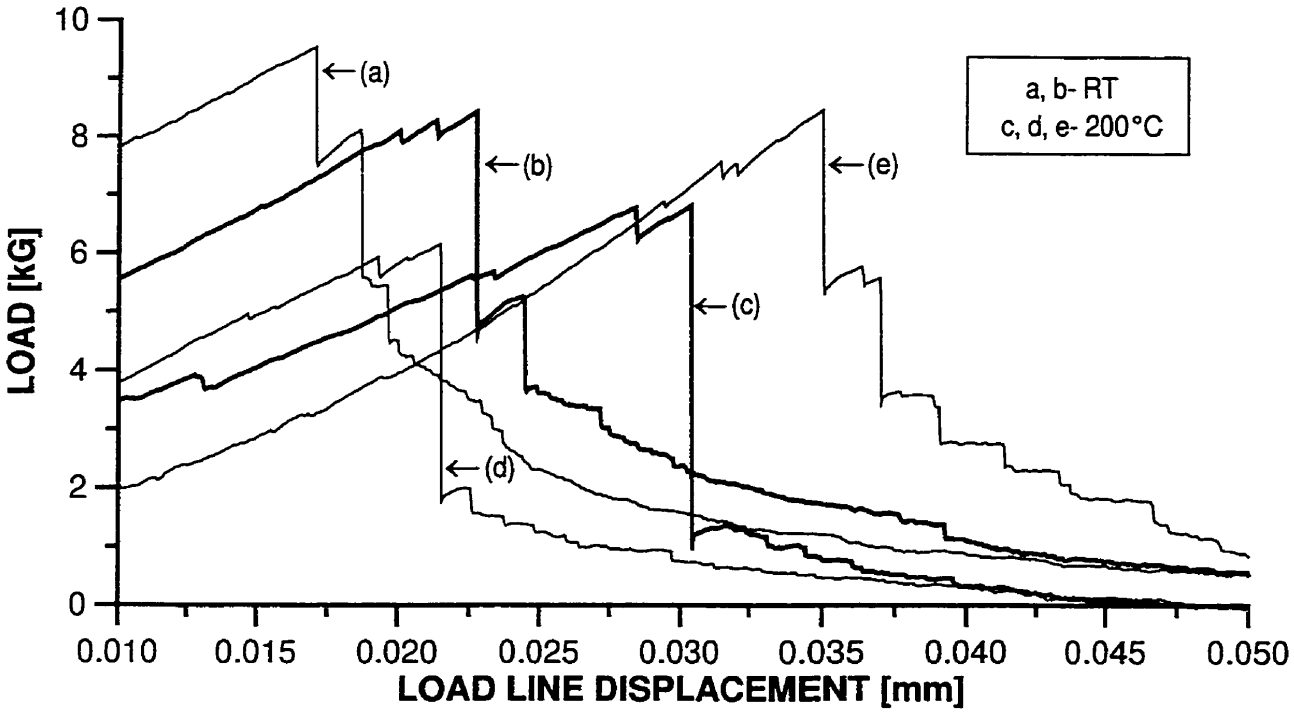

Figure 5.22 Load vs. load- line displacement for 9Mn-0.66B specimens tested at: a) and b) RT; c), d) and e) 200°C.

All the specimens of 9Mn-0.66B alloy in Fig.5.22 followed a fracturing pattern with numerous pop-ins. These short crack jumps are usually caused by the cleavage areas placed close to the notch tip (this statement is supported by analyses of P-LLD curves and corresponding fractographs of 38 low- and high- Mn boron-doped specimens). Fig.5.23 shows examples of the corresponding fractographs. Frames a1 and d1 show CN crack tip at higher magnification. They were not recorded for the specimen (a) but their existence is not excluded. The tip of this specimen is well branched and this could give rise to very fine pop- ins beyond the detection resolution of the measuring equipment used in this study. The deep secondary crack in the specimen (a) (Fig.5.23a) possibly contributed to a gradual load drop by slowing down the crack propagation. Similarly, splitting of the grains also slows down the fracture. In this case, a relatively large grain which was common to both

halves of the specimen was cleaved dividing the grain into pieces and leaving the appearance of fracture surface as shown in Fig.5.23e.

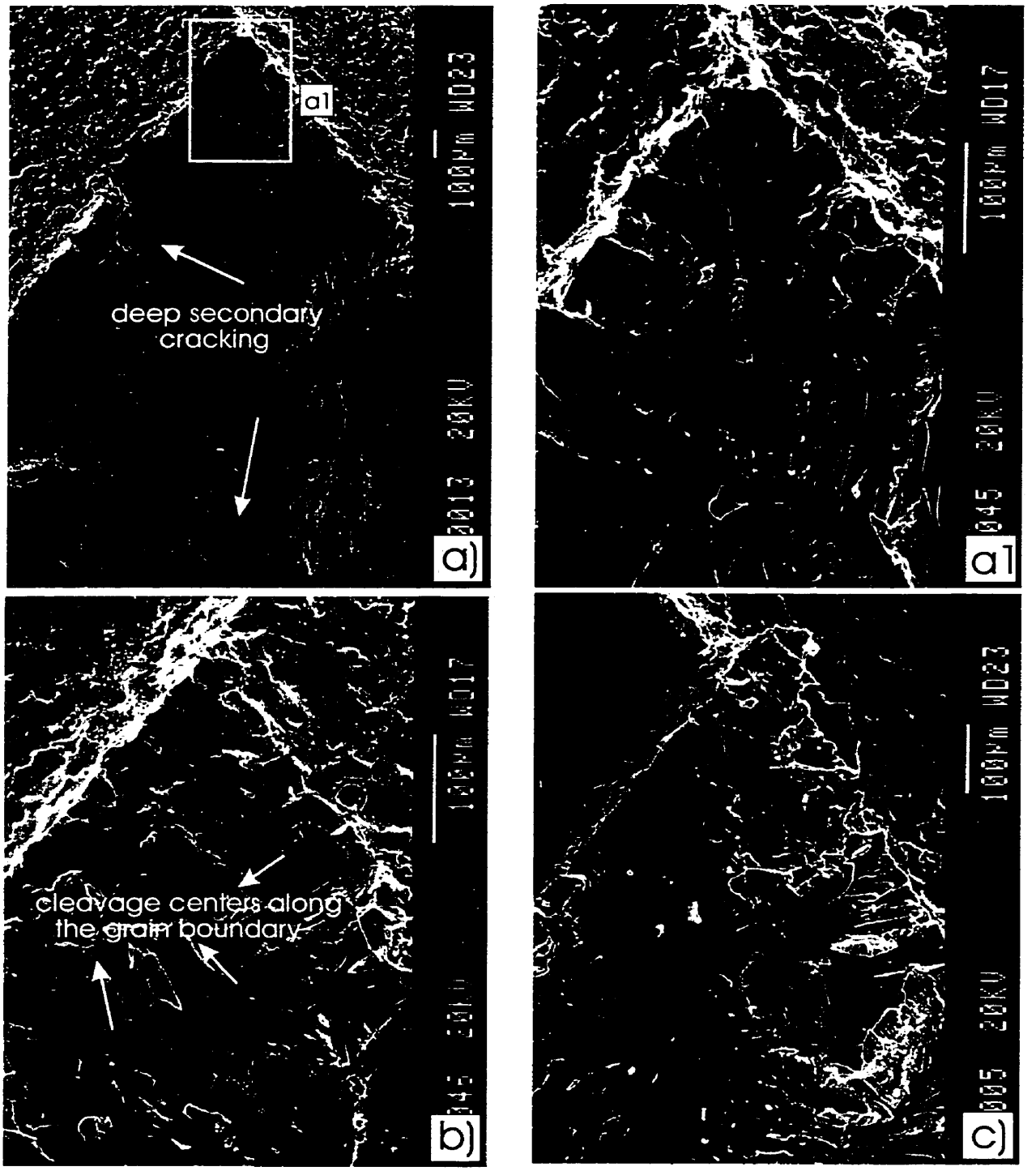

Figure 5.23 SEM fractographs of the specimens tested at: a) (higher magnification of the frame a1 is also shown), and b) RT; c), d) (higher magnification of the frame d1 is also shown), and e) 200°C (9Mn-0.66B alloy).

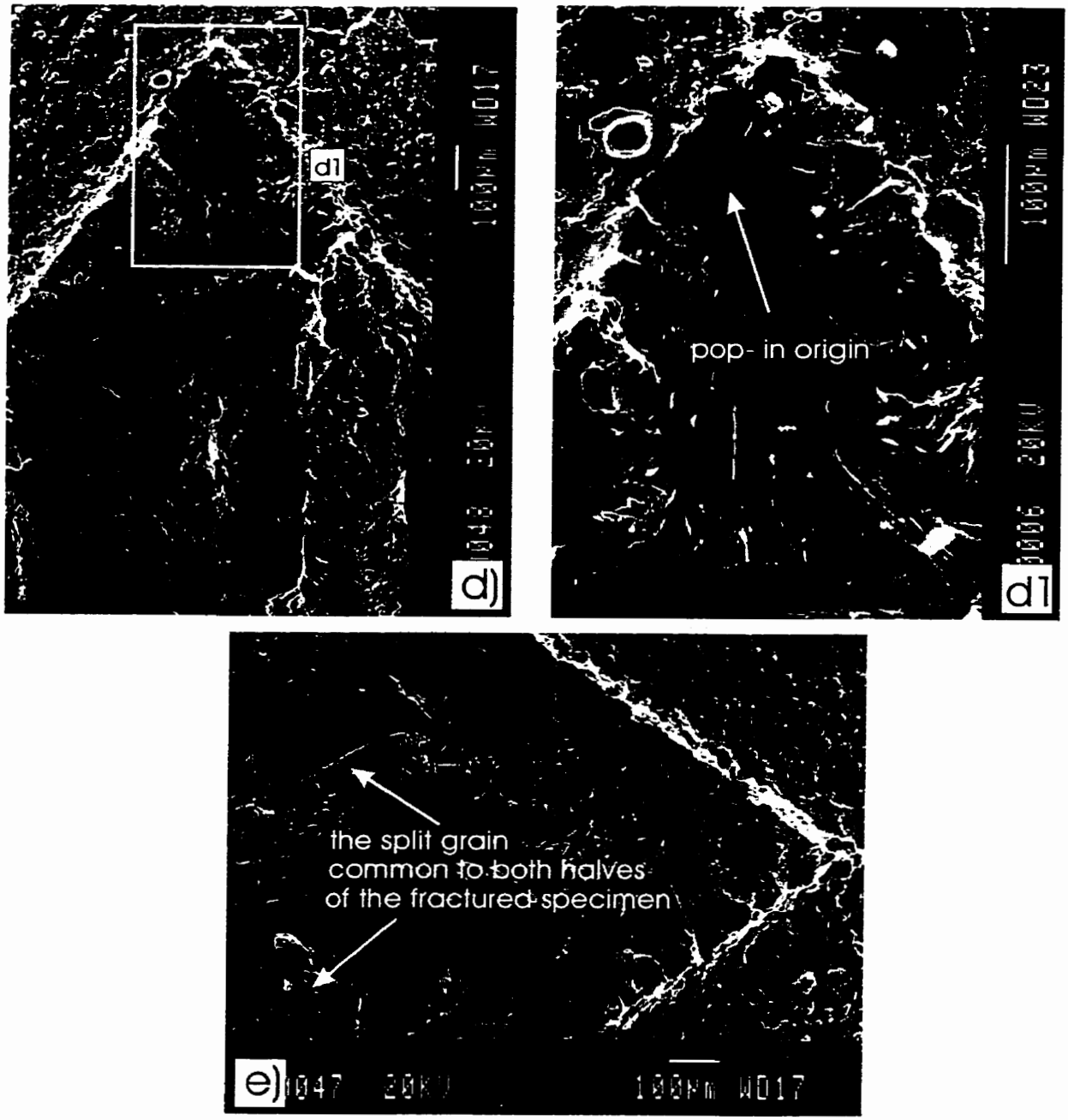

Figure 5.23 Contd.

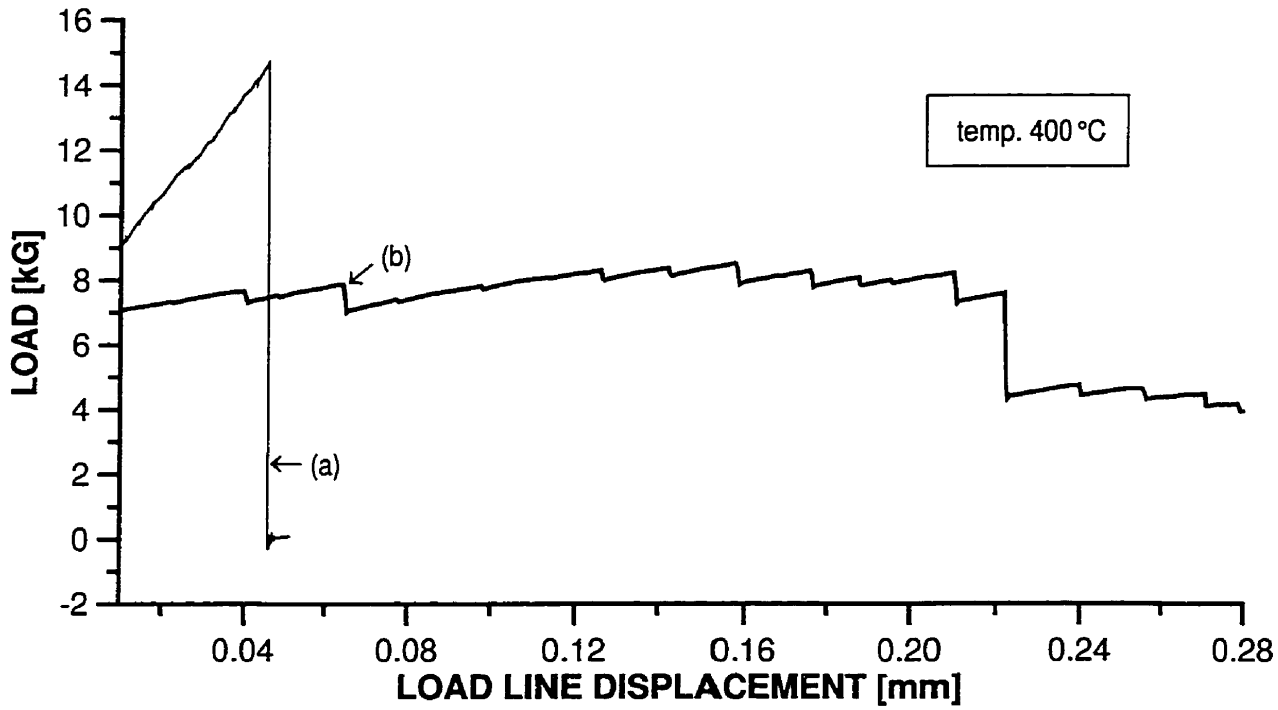

Figure 5.24 Load vs. load- line displacement for 14Mn-0.65B specimens tested at 400°C.

An example of different fracture behavior is shown in Fig.5.24 for two specimens of the same 14Mn-0.65B alloy tested at 400°C. Specimen (a) (Fig.5.24a and corresponding fractograph in Fig.5.25a) failed catastrophically down to zero load. In contrast, specimen (b) fractured through numerous pop- in events, supporting the load at its maximum level for long crack extension. Interestingly enough, both specimens had almost identical stiffness (their Y_{min} values differed by ~3%), yet they failed at much different loads; specimen (a) at 14.7 kG and specimen (b) at 8.5 kG resulting in toughness values of 9.4 and 5.7 MPa$\sqrt{m}$, respectively. Specimen (a) showed a deep secondary crack at the notch tip (Fig.5.25a) and specimen (b) fractured on different, parallel cleavage planes at the tip (Fig.5.25b). The short crack jumps in specimen (b) could be caused by extensively developed branching emanating from the edge of the cleaved plane in a direction roughly perpendicular

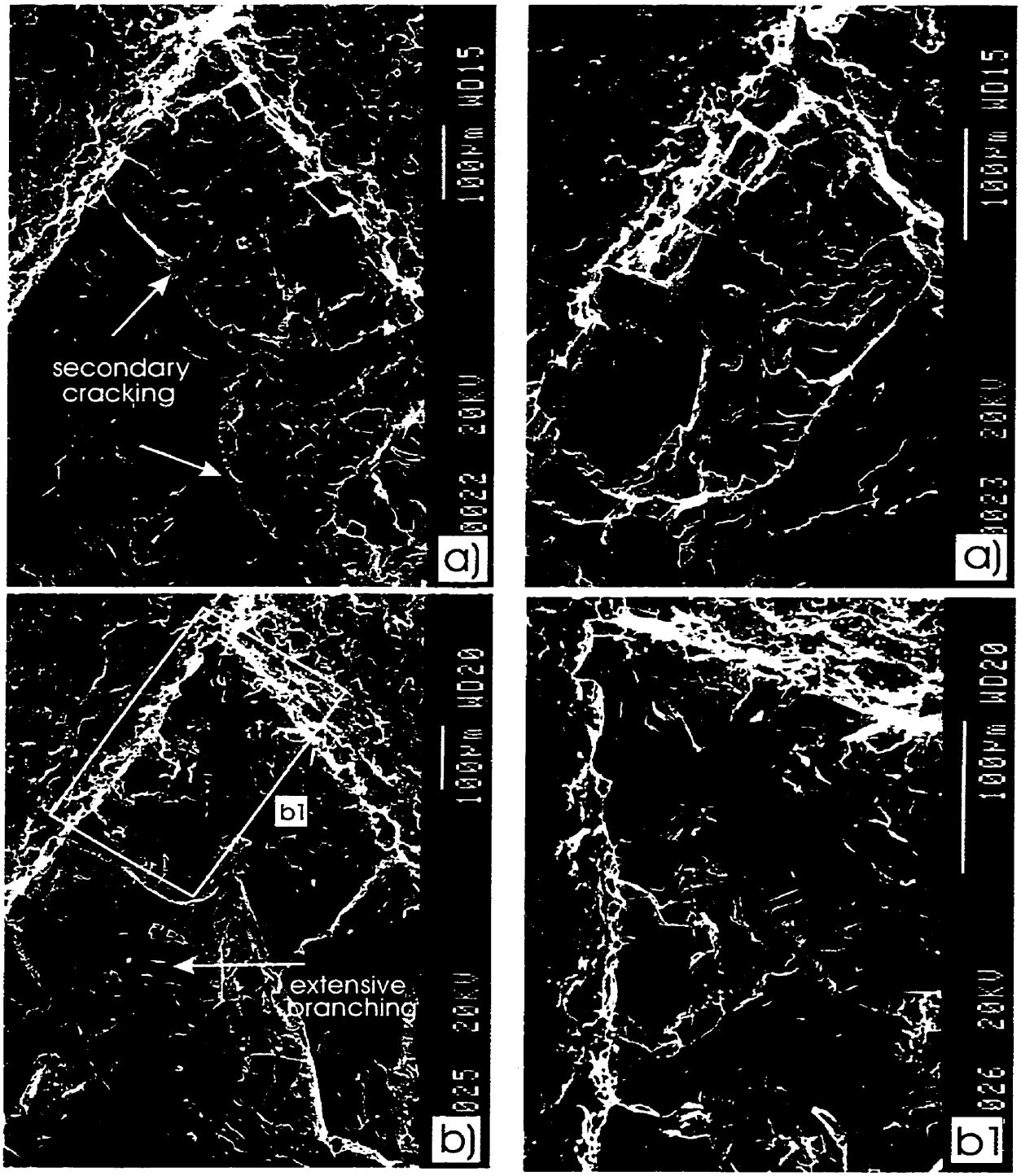

Figure 5.25 SEM fractographs of the specimens (a) and (b) from Fig.5.24 tested at 400°C (14Mn-0.65B alloy). Fractographs (a) represent two halves of the same specimen. b1 shows a high magnification frame of the crack tip.

to the macroscopic crack propagation. No further reasonable explanation for the different behavior could be given by comparing fracture surfaces of both specimens.

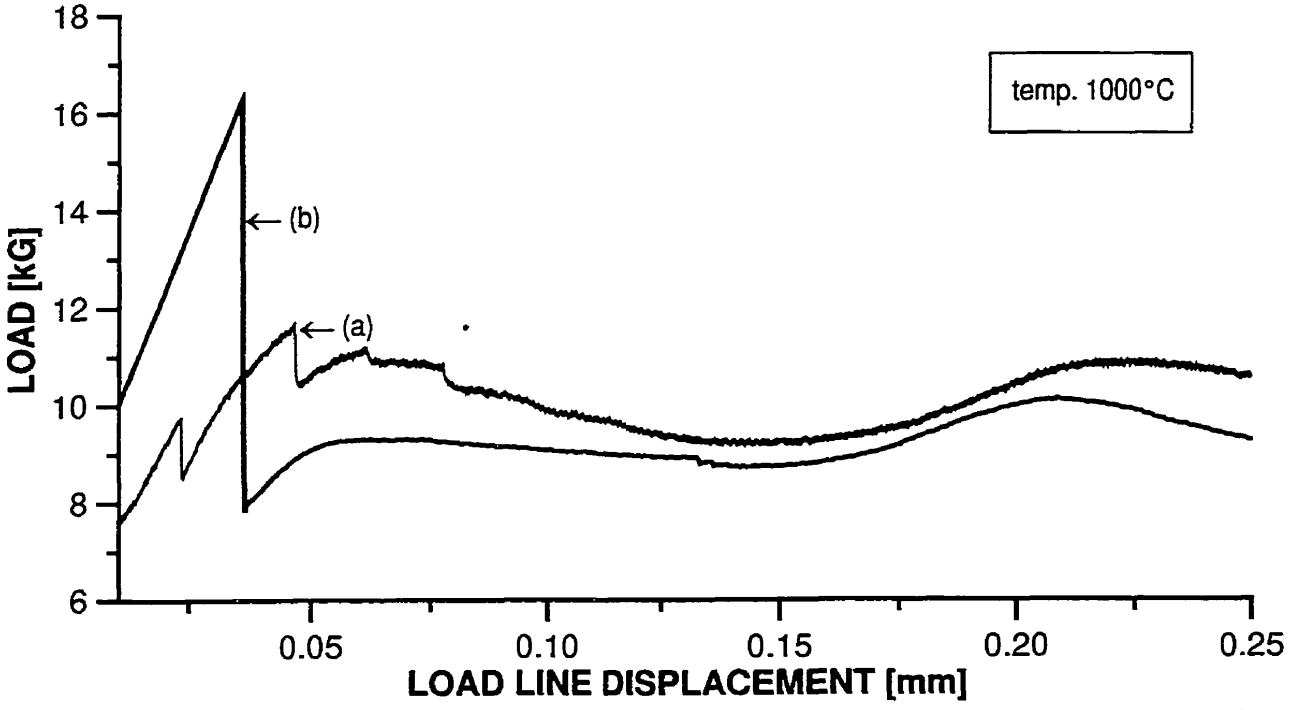

Figure 5.26 Load vs. load- line displacement for 9Mn-0.25B specimens tested at 1000°C.

Another example of different fracture behavior is shown in Fig.5.26. Two 9Mn-0.25B alloy specimens were tested at 1000°C. The two specimens, (a) and (b) (Figs.5.26a,b and corresponding fractographs in Fig.5.27a,b), differ in grain morphology. The equiaxed grains of specimen (a) make the fracture surface highly non- planar. In combination with 'unlocking' mechanism (for explanation see Section 6.2.2 in Discussion chapter) it makes the specimen capable of supporting ~90% peak load up to very long crack extensions. The small cleaved area at the notch tip was the crack initiation point and caused the occurrence of the crack jumps before reaching maximum load. The orientation of columnar grains (perpendicular to the crack propagation direction) in specimen (b) gave rise to ~50%

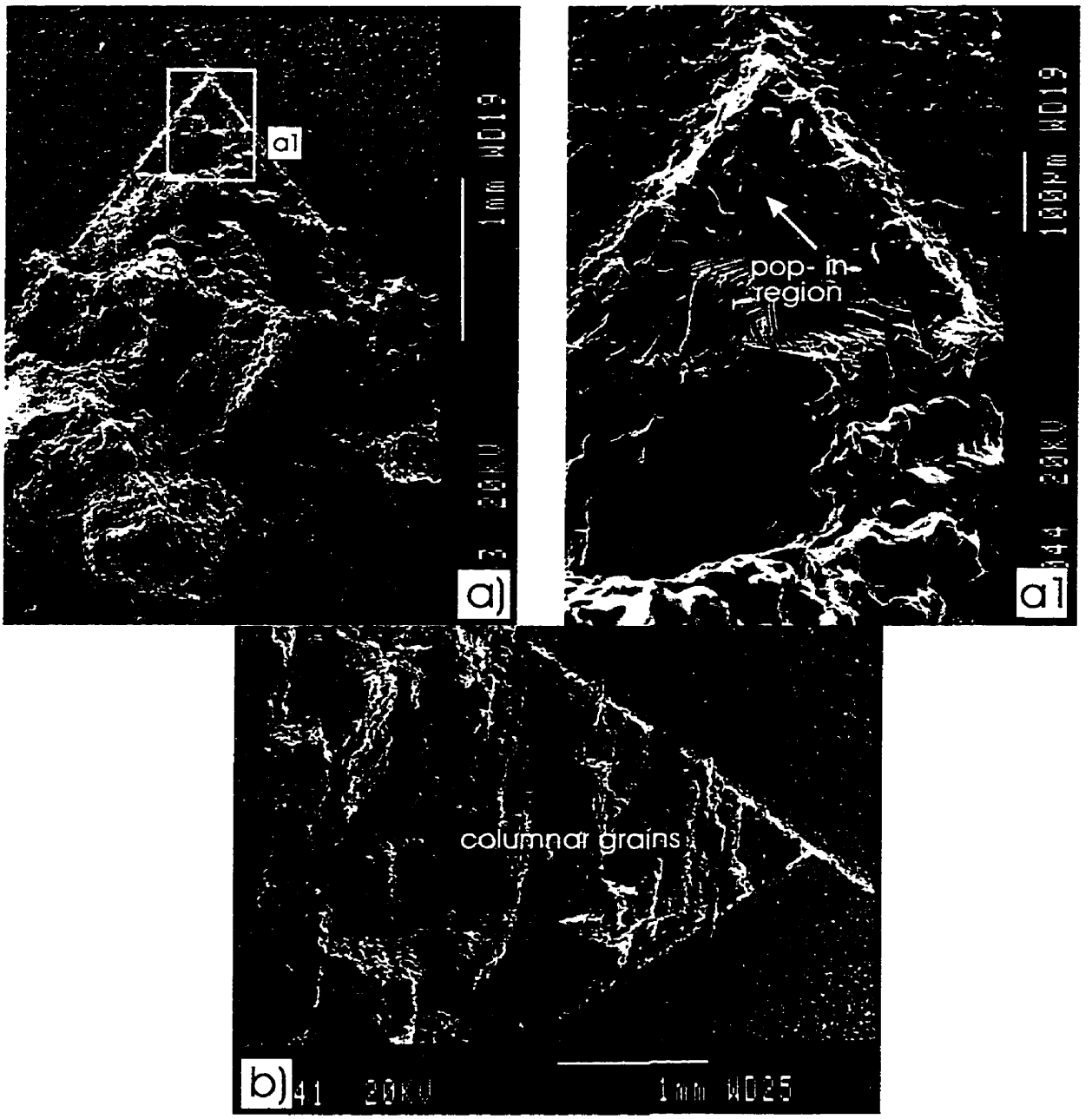

Figure 5.27 SEM fractographs of the specimens tested at 1000°C (9Mn-0.25B alloy) from Fig.5.26. a1 shows a high magnification frame at the crack tip.

rapid load drop. Further loading of already much more compliant specimen (much lower stress intensity increase K) caused very stable crack propagation. Again, the specimen (b) exhibiting a load drop has much higher fracture load than specimen (a) resulting in fracture toughness values of 12.2 MPa$\sqrt{m}$ and 7.0 MPa$\sqrt{m}$, respectively.

5.3 Dependence of Fracture Behavior and Fracture Toughness on the Grain Size in the Medium to Coarse Grain Range

Two low- Mn ingots (boron-free "base" 9Mn-25Ti) (no.18 and 19 in the Table 5.1) of very similar composition and microstructure were deformed at 1000°C at the deformation rate ~10^{-4} s^{-1} in order to induce dynamic recrystallization as described in the Experimental Procedures section. The one deformed ~50% underwent partial recrystallization (Fig.5.28) and the other deformed ~70% completely recrystallized (Fig.5.29).

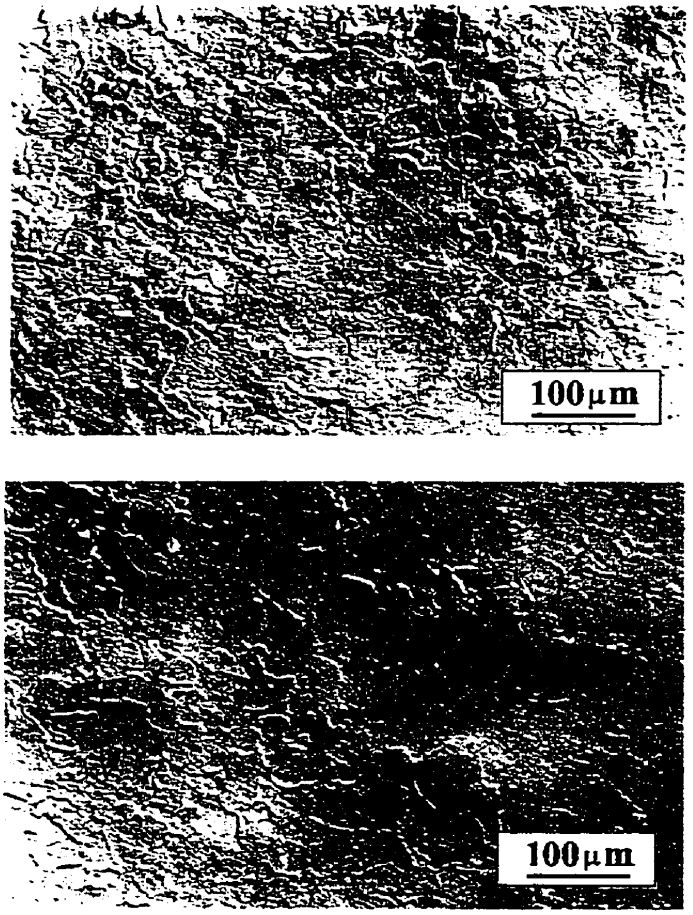

Figure 5.28 Optical micrograph of the partially dynamically recrystallized structure of the low- Mn alloy (boron-free "base" 9Mn-25Ti) (etched).

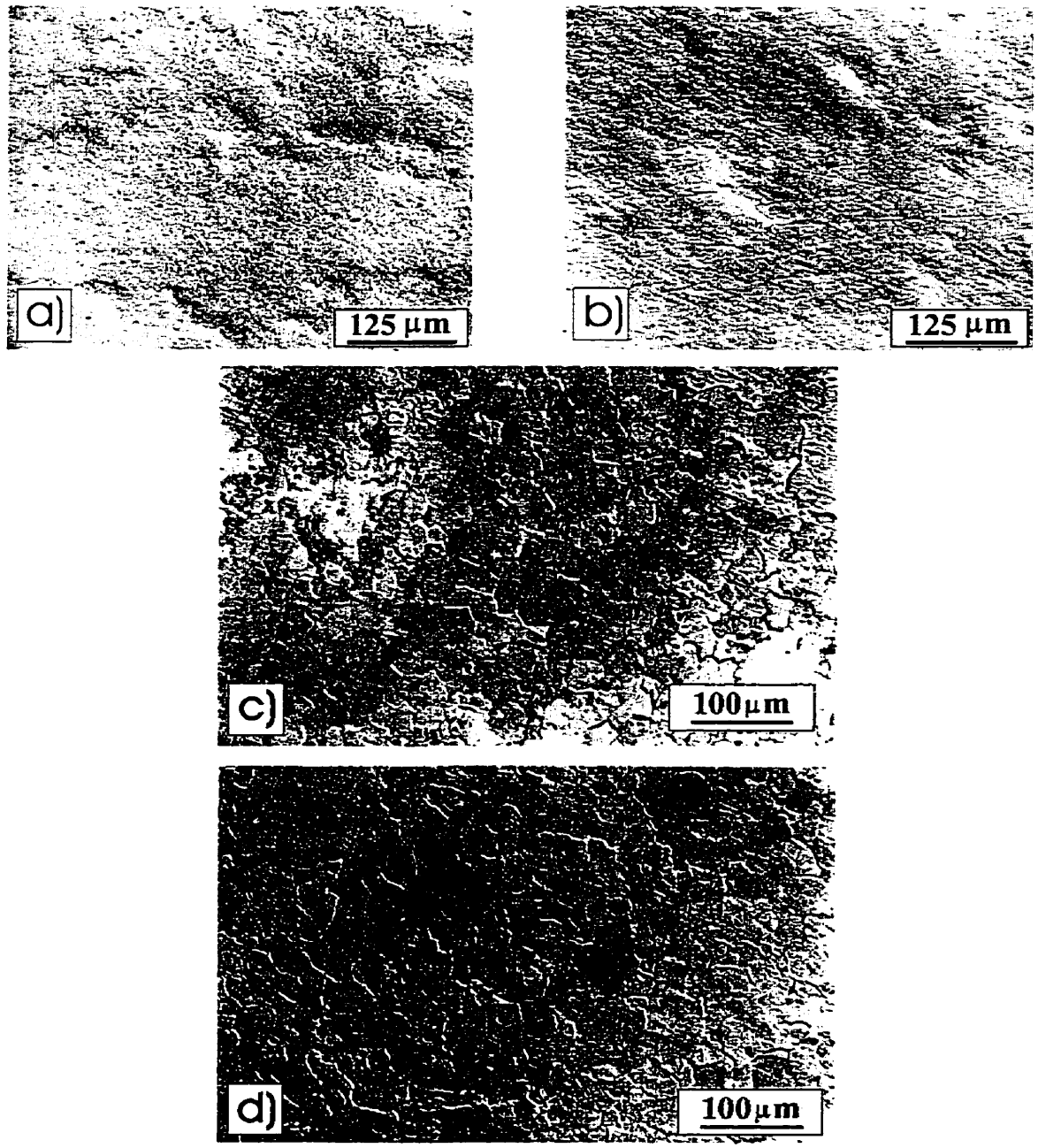

Figure 5.29 Optical micrograph of the completely dynamically recrystallized structure of the low- Mn alloy; a) and b) low level of porosity (unetched), c) and d) recrystallized grains (etched).

SEPB specimens were used for measuring fracture toughness at room temperature and a CNB specimen was used at 1000°C. Fracture mode for both fully and partially recrystallized materials was 100% TGC at room temperature (Figs.5.30a and 5.31a). For both alloys, however, a very small region of intergranular fracture (IGF) (approx. equal in size to the area shown in Figs.5.30b and 5.31b) was found. The specimen

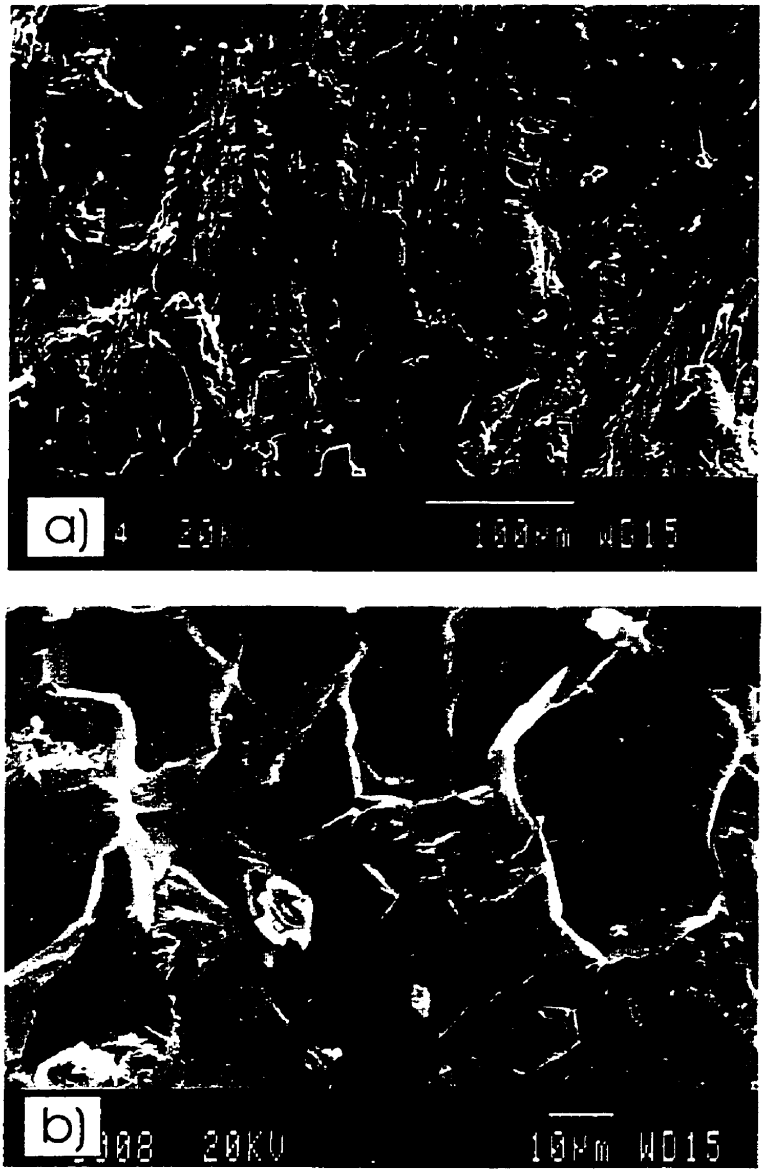

Figure 5.30 SEM fractographs of the dynamically recrystallized SEPB specimen (deformed ~50%) and tested at room temperature; a) TGC region, b) higher magnification of IGF region.

tested at 1000°C was partially dynamically recrystallized (~50% deformation). The fracture mode shown in Fig.5.32 is 100% IGF. It can be seen in Fig.5.32a that the

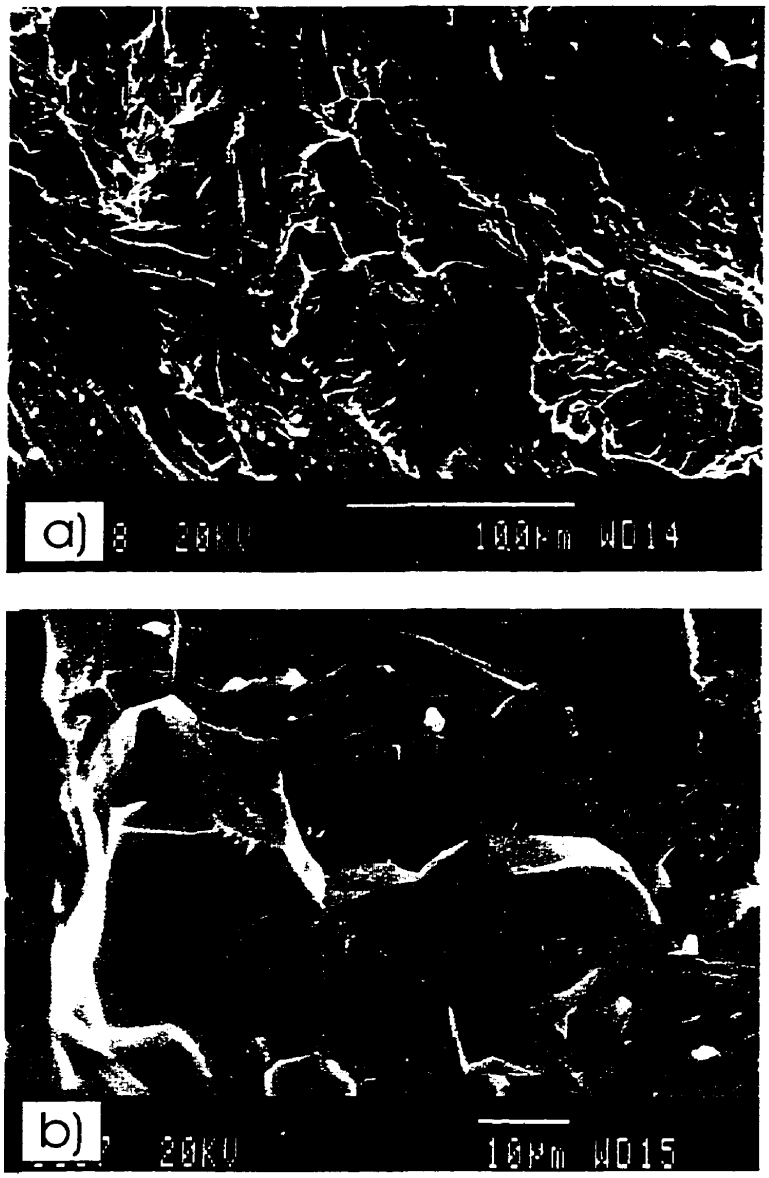

Figure 5.31 SEM fractographs of the dynamically recrystallized SEPB specimen (deformed ~70%) and tested at room temperature; a) TGC region, b) higher magnification of IGF region.

columnarity of the cast alloy is still observed in the fracture surface of the recrystallized material. Fig.5.32b and c show higher magnification of the recrystallized equiaxed grains.

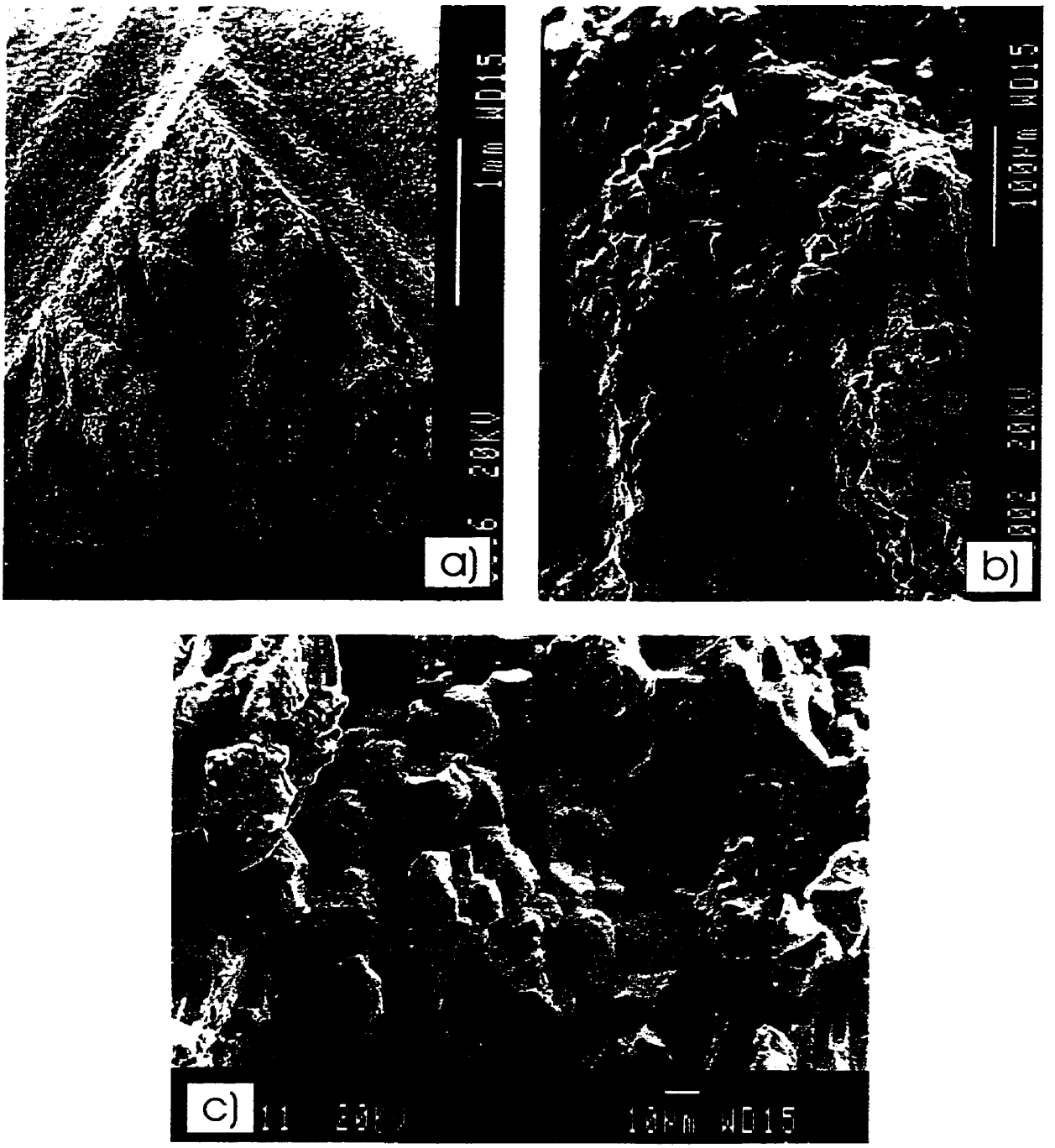

Figure 5.32 SEM fractographs of the partially dynamically recrystallized CNB specimen deformed ~50% and tested at 1000°C; a) columnarity of the fracture surface, b) and c) higher magnifications of the recrystallized, equiaxed grains.

As mentioned earlier, SEPB specimens were used for testing fracture toughness at ambient temperature and CNB was used at higher temperature (see Fig.5.32). The dependence of toughness on the remaining ligament length (RLL) for SEPB specimens for dynamically recrystallized material is shown in Fig.5.33. Partially recrystallized material (deformed to ~50% engineering strain) gives much weaker dependence than the entirely recrystallized material (deformed to ~70% engineering strain).

It is now important to establish which fracture toughness values in Fig.5.33 obey the requirement of the plane strain condition. Calculation of this type requires the knowledge of the yield strength of the dynamically recrystallized material. Since it was not tested in tension/compression due to a very limited amount of material available, data from the literature could be taken for a similar alloy. Zhongjie et al. [135] reported a Hall-Petch dependence of yield strength for $Al_{65}Mn_{10}Ti_{25}$ alloy given by equation: $\sigma_y=\sigma_0+k_y d^{-1/2}$, where $\sigma_0=171$ MPa and $k_y=370$ MPa$\mu m^{-1/2}$. Substituting the average grain size of 45μm estimated for the dynamically recrystallized material in the present work, the yield strength $\sigma_y=226$ MPa is obtained. Substituting this value into equation for the minimum RLL required [114] for the plain strain condition: $RLL \geq 2.5(K_Q/\sigma_{ys})^2$, and taking $K_Q=4$ MPa$\sqrt{m}$, one obtains RLL$\geq$783μm (line no. 1 in Fig.5.33). Now, the RLL value must be recalculated by taking new $K_Q=5.5$ MPa$\sqrt{m}$ value which is the average of K_Q values to the right of the line no.1. This new value RLL(5.5)$\geq$1476μm (line no.2) leaves only two data points with valid plain strain fracture toughness $K_{IC}=4$ MPa$\sqrt{m}$ and 5.6 MPa$\sqrt{m}$. However, Kumar et al. [42] reported much higher values of yield strength $\sigma_y=320$ MPa for 50μm grain sized material. Repeating the procedure for finding valid K_{IC} values for $\sigma_y=320$ MPa (described above) and assuming first $K_Q=4$MPa$\sqrt{m}$, the

RLL(4)=390μm is obtained (line no.3). This result is inherently inconsistent because all the data points in Fig.5.33 should be taken as K_{IC} but they are strongly dependent on the RLL. Taking new K_Q=5.6 MPa√m (there are only two potential values for K_{IC}, 4 and 5.6 MPa√m from Fig.5.33), the RLL(5.6)=765μm is obtained. As it was for the previous case, this result is also incorrect. Therefore, it seems that the value of the yield strength σ_Y=320 MPa given in Ref. [42] is too high for the alloy in the present work. For further considerations, 4.8 MPa√m is taken as the valid plain strain toughness at RT for a fully recrystallized material with ~45μm grain size.

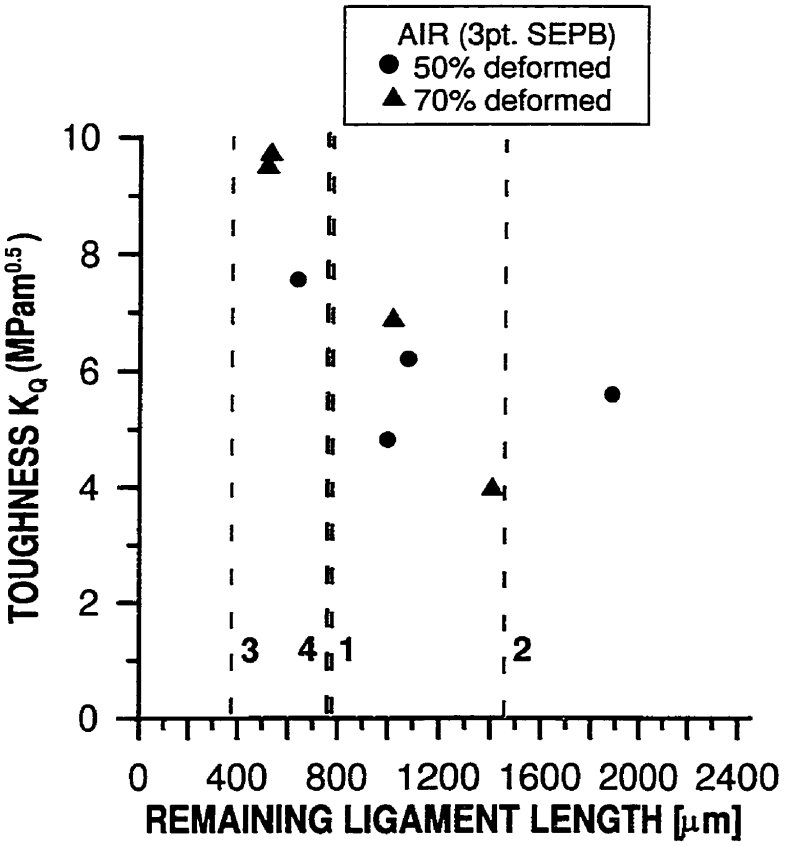

Figure 5.33 Dependence of the fracture toughness of the dynamically recrystallized low- Mn alloy on the remaining ligament length.

Valid fracture toughness (K_{IC}) at RT for specimens with various coarse as-cast grain sizes (assuming yield strength of 160 MPa [28] for a coarse-grained $L1_2$

trialuminide) are compiled in Table 5.3 (one data point corresponds to one SEPB specimen tested) and also presented in a graphical form in Fig.5.34. It seems, that valid plane strain fracture toughness values at RT do not show a dependence on the grain size in the wide range of grain sizes, 45– 1270 μm (Table 5.3 and Fig.5.34).

Table 5.3 K_{IC} values for various grain sizes.

GRAIN SIZE (μm)	K_{IC} (MPam$^{0.5}$)	PROCESSING METHOD	ALLOY
1270	3.7	as-cast, homogenized and HIP-ed	65.7±0.2, 9.2±0.2, 25.2±0.1 (no.4 in Table 5.1)
690	4.8	as-cast, homogenized and HIP-ed	65.7±0.2, 9.2±0.2, 25.2±0.1 (no.4 in Table 5.1)
350	4.2	as-cast, homogenized and HIP-ed	65.7±0.2, 9.2±0.2, 25.2±0.1 (no.4 in Table 5.1)
45	Average value 4.8	dynamically recrystallized (70% deformed) (50% deformed)	64.8±0.2, 9.1±0.3, 25.4±0.3 (no.19 in Table 5.1) 65.3±0.2, 9.1±0.1, 25.7±0.2 (no.18 in Table 5.1)

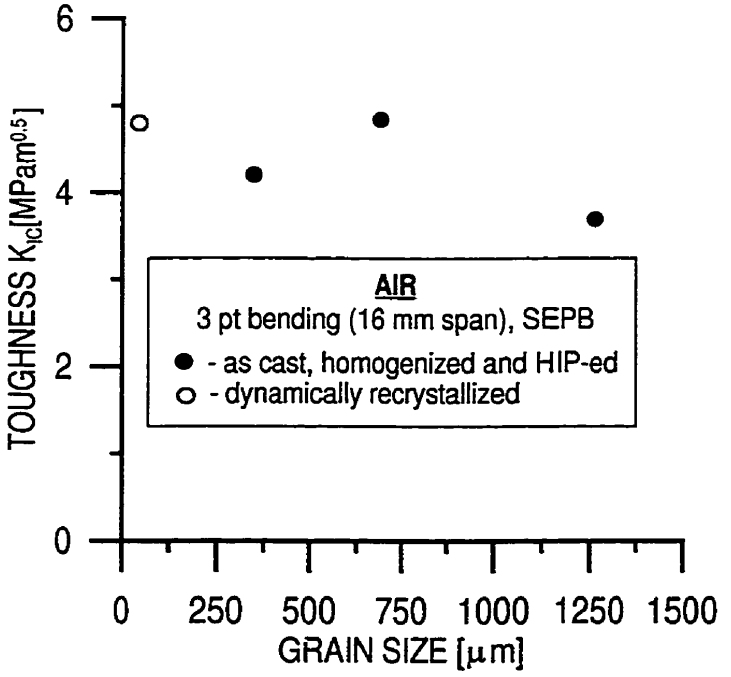

Figure 5.34 Plane strain fracture toughness values vs. grain size.

Much more substantial grain refinement (nanostructure?) might be necessary before any improvement in fracture toughness would be achieved. This is experimentally explored in the section on toughness of powder compacts (Section 5.9). Only one specimen (CNB) partially recrystallized (Fig.5.32) was tested at 1000°C giving K_{QVM}=7.8 MPa$\sqrt{m}$. The average recrystallized grain size is from 10 to 50 μm. Despite this limited data it seems that the refinement of grain size increases slightly the fracture toughness at 1000°C with respect to a very coarse-grained material exhibiting on the average ~4 MPa$\sqrt{m}$ (see the following section).

5.4 The Effect of Environment and Temperature on Fracture Behavior and Fracture Toughness of Coarse- Grained Boron Free Low- Mn Alloys.

5.4.1 Fracture Behavior (Fractographs).

Room temperature fracture is 100% transgranular cleavage (TGC) in all alloys tested. Characteristic features of this mode of fracture are presented in Figs.5.35, 5.36 and 5.37 for boron-free, "base" 9Mn-25Ti alloy. Typical features are: extensive crack branching, very well developed cleavage steps, jagged flakes and secondary cracking. Precrack surface was usually much flatter and contained lower amount of various features. The kind of steps shown in Figs.5.36d and 5.37a but different from those in Figs.5.37b,c and d, is characteristic to pre-crack surface region. These cleavage steps resemble real steps with the edge in most cases being perpendicular to the direction of the crack spreading (Fig.5.36d). The steps characteristic of fast fracture region resemble the edges of plates or flakes on the fracture surface (Figs.5.35b, 5.36c, 5.37b,c, and d). Transition from precrack to the fast region of fracture in most cases was similar to the one shown in Figs.5.35a and 5.37a. Starting from ~200°C the fracture mode becomes mixed with a very low fraction of IGF which increases with increasing temperature. Fig.5.38 shows mixed mode of failure at various temperatures. Fig.5.39 shows that in some cases cracks in the mixed mode of fracture originated at grain boundaries.

Fig.5.40 shows dimpled and oxidized area of the grain boundary facet. The specimen was tested at 1000°C. Such dimples were very rare and fraction of the dimpled surface was minimal on the grain boundary facets. The size of the dimples is much larger (~ order of magnitude) than the size of the dimples appearing on the fractured grain boundary facets of the specimen tested in argon (Fig.5.44). That

fact may also contribute to a high work of fracture obtained in tests in air (will be discussed in Section 5.5.3).

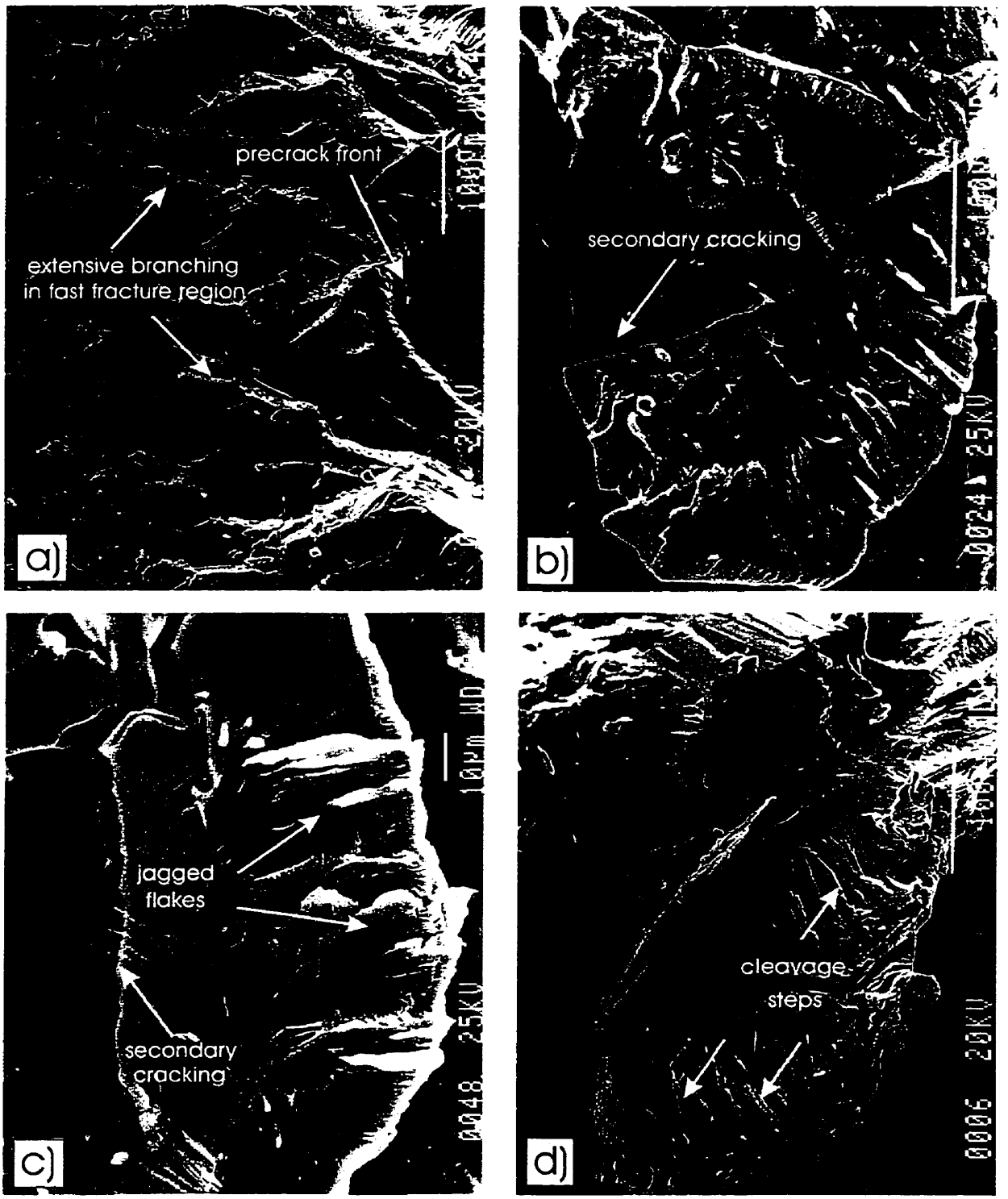

Figure 5.35 Fracture surface features of the low- Mn boron-free, "base" 9Mn-25Ti specimens tested at room- temperature.

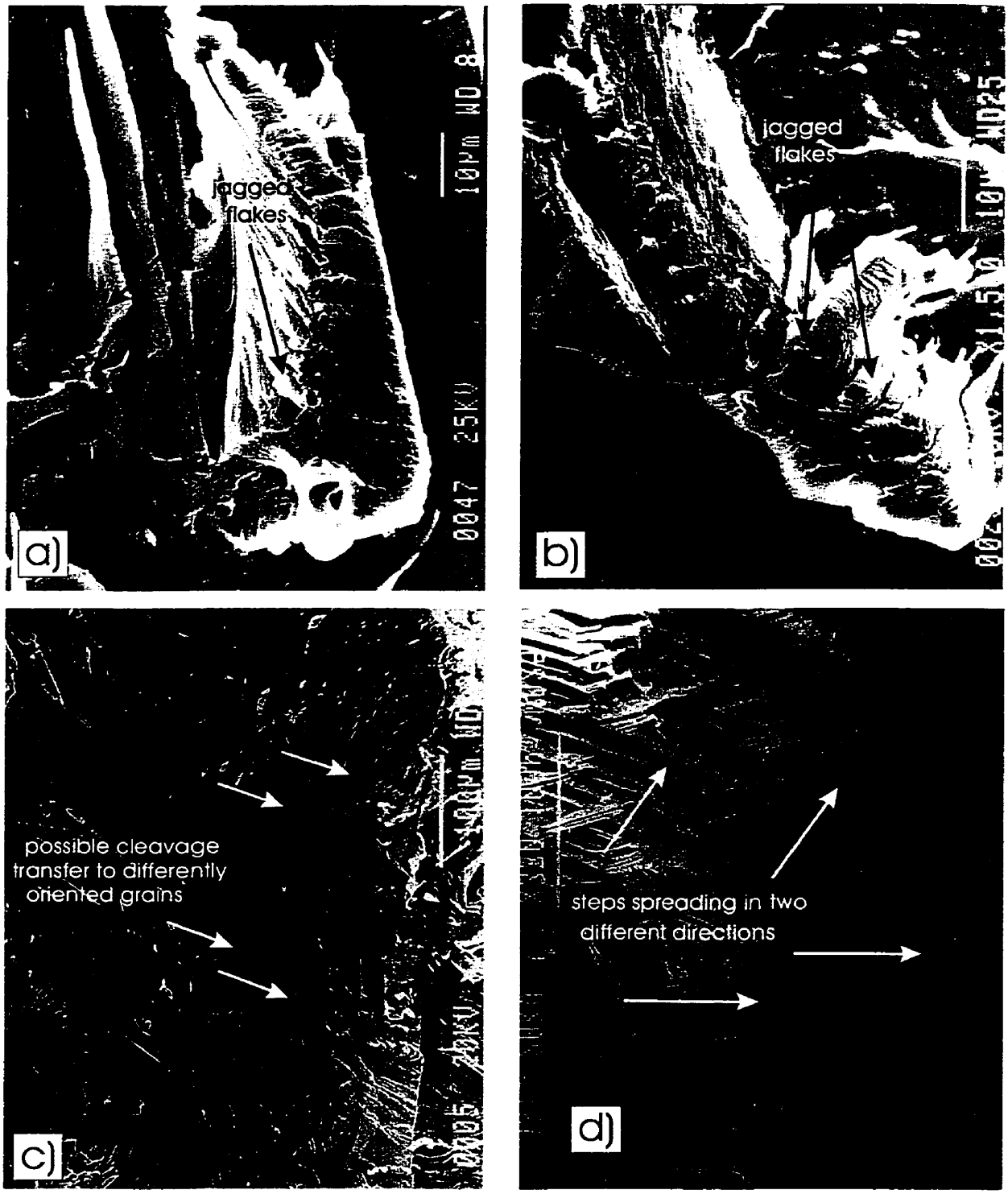

Figure 5.36 Fracture surface features of the low- Mn boron-free, "base" 9Mn-25Ti specimens tested at room- temperature.

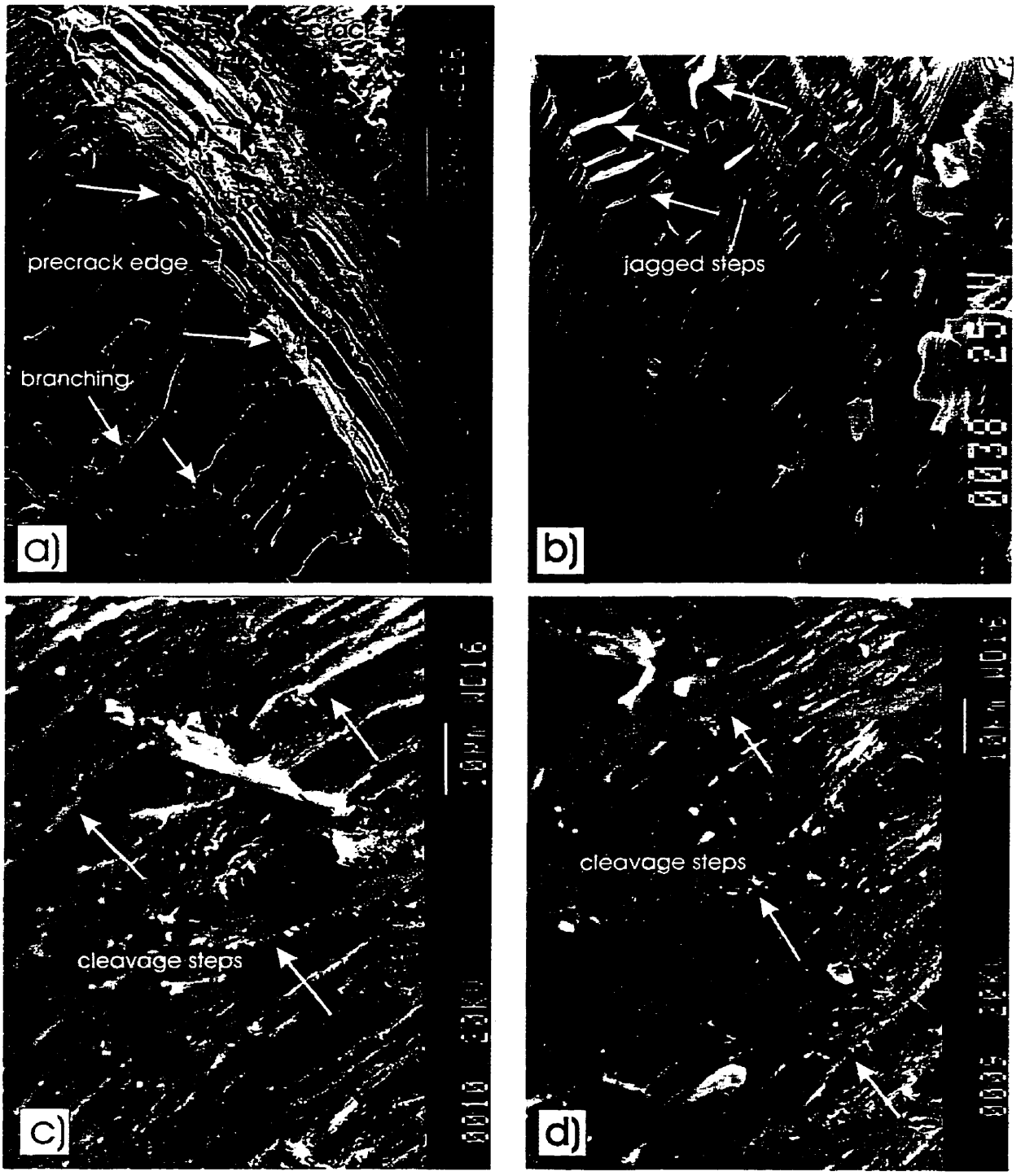

Figure 5.37 Fracture surface features of the low- Mn boron-free, "base" 9Mn-25Ti specimens tested at: a) and b) room- temperature; c) and d) 500°C.

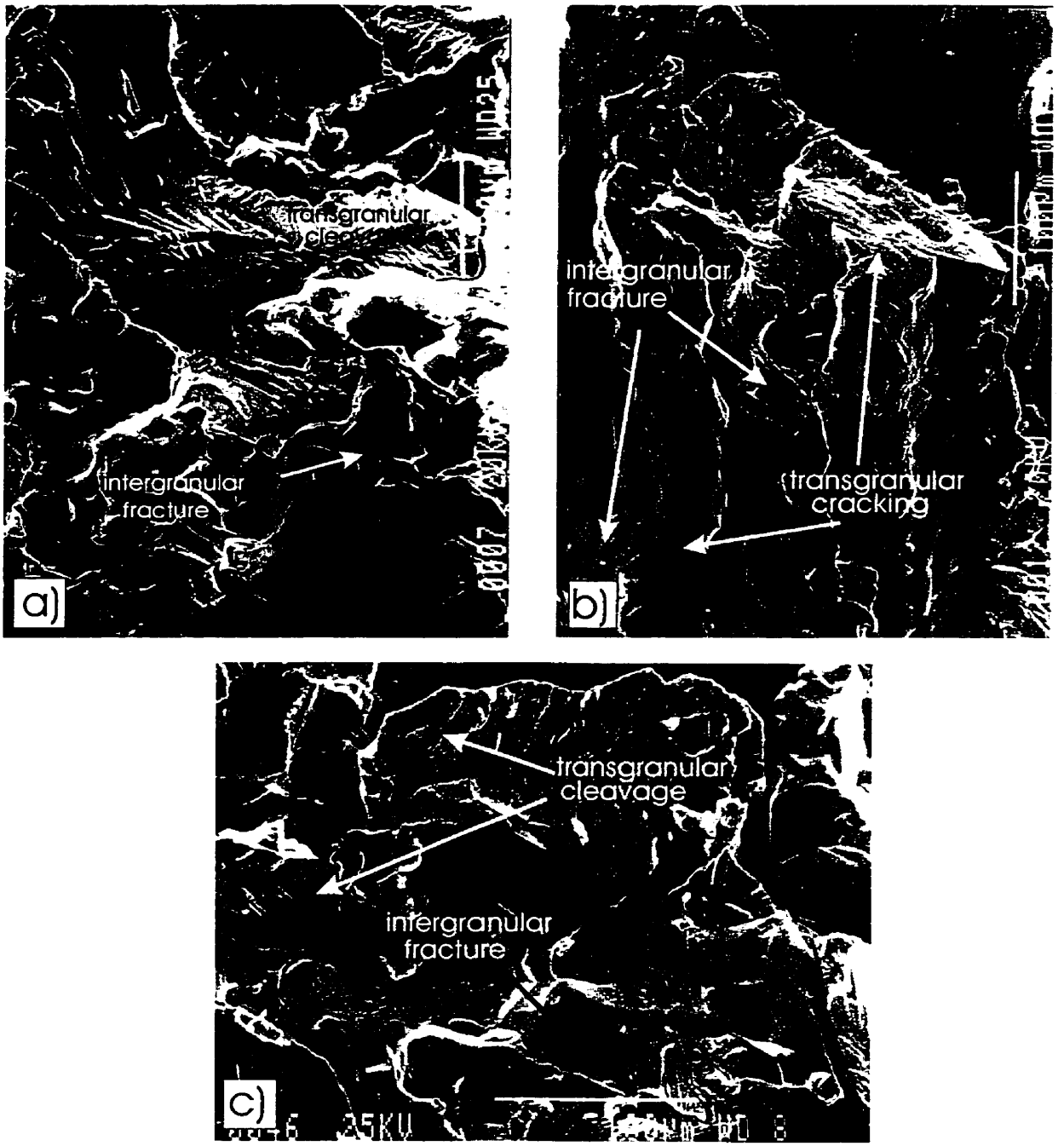

Figure 5.38 Mixed mode of fracture at higher temperatures, a) 400°C, b) 600°C and c) 800°C (low- Mn boron-free, "base" 9Mn-25Ti alloy).

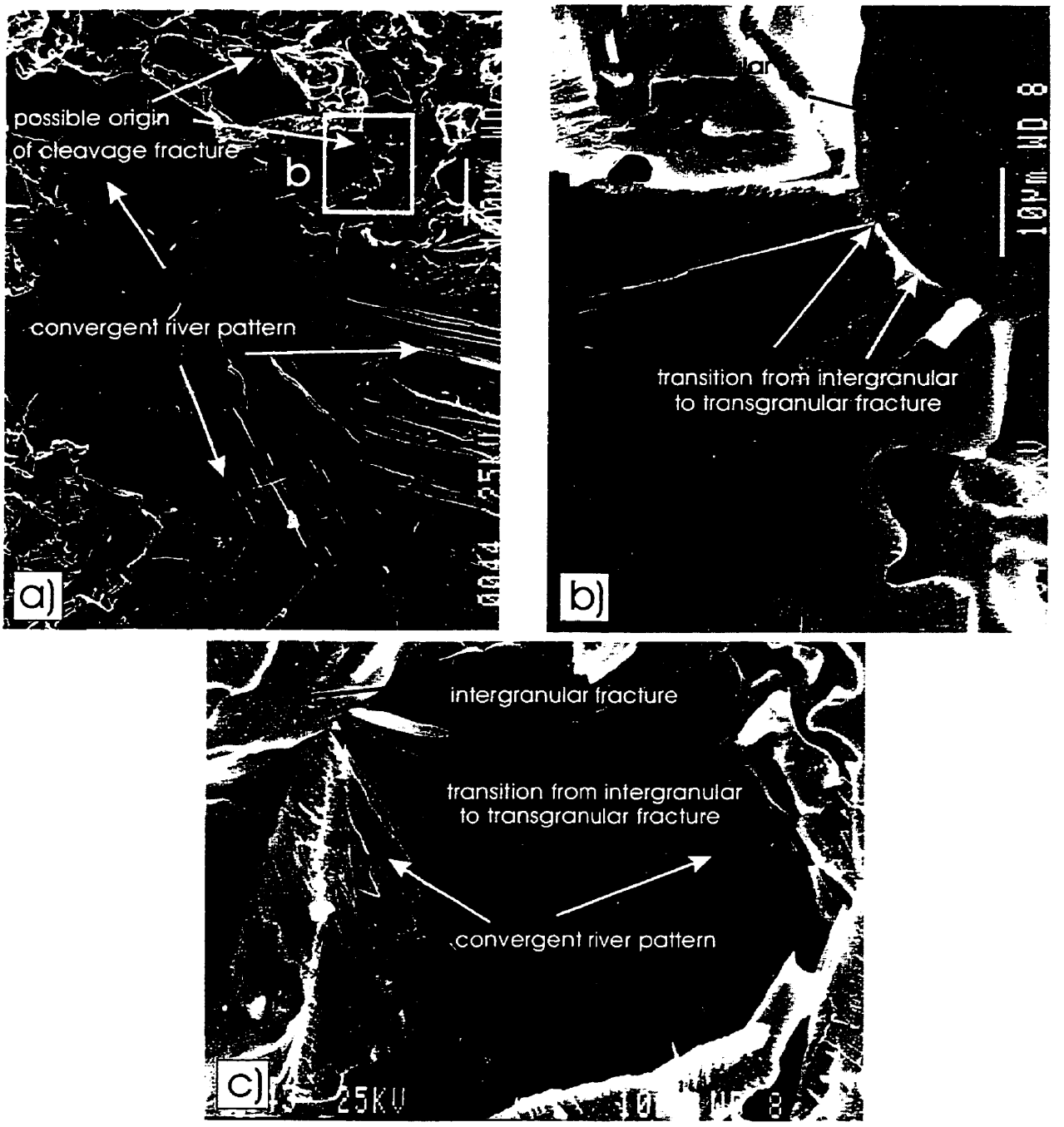

Figure 5.39 Failure at elevated temperature (800°C) in the mixed mode (low- Mn boron-free, "base" 9Mn-25Ti alloy) (higher magnification of the frame b is also shown).

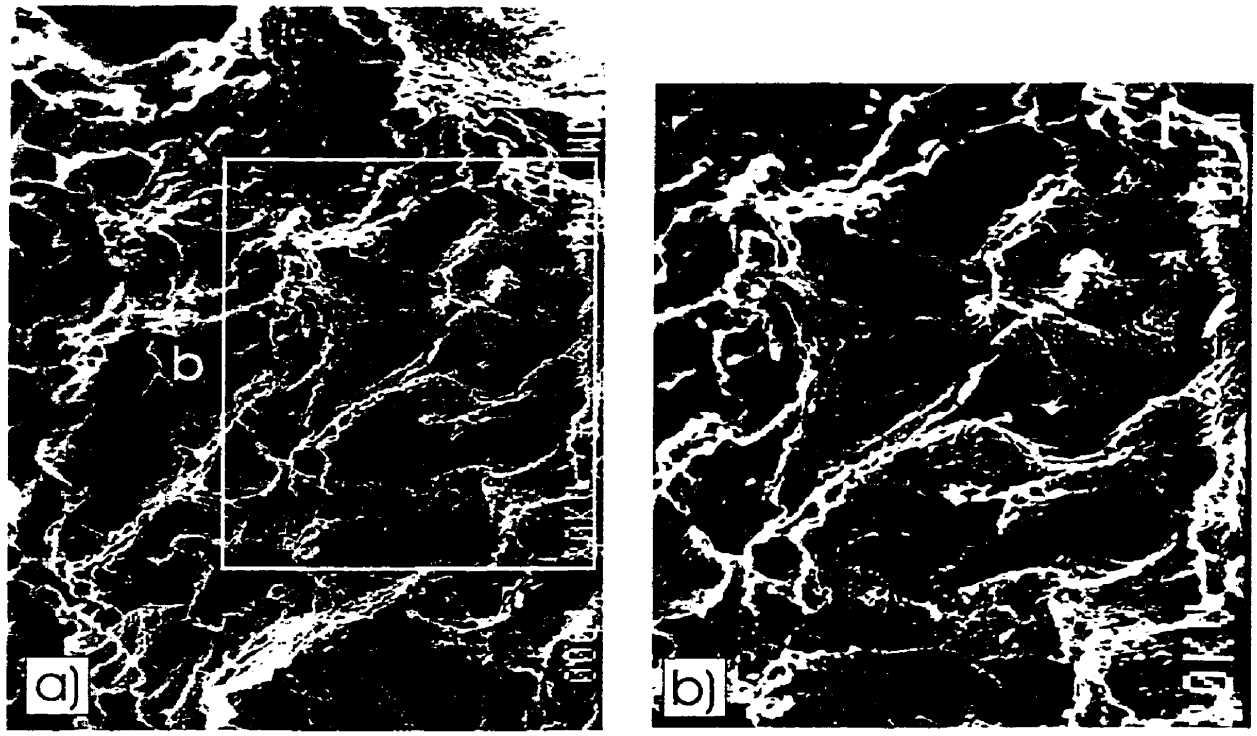

Figure 5.40 Dimpled and oxidized grain boundary facets of the specimen tested at 1000°C (low- Mn boron-free, "base" 9Mn-25Ti alloy).

Usually, the specimens tested in air showed some degree of oxidation. In some cases there is heavy oxidation (usually of the dimpled areas as in Fig.5.40). Cleaved surfaces never showed evidence of oxidation. Only exposed grain boundary facets were oxidized. There was no rule found in oxidizing the grain boundary surfaces. Sometimes they oxidized and in other cases they did not.

Fig.5.41 shows fractographs of specimen tested in dry oxygen at room temperature. Figs.5.42 to 5.44 show fractographs of specimens tested in argon at various temperatures. No visual change is seen in the appearance of fracture surface of the specimens tested at room temperature in dry oxygen (Fig.5.41) and in argon (Fig.5.42), with respect to those tested in air. However, at 1000°C, the specimen tested in argon shows in contrast to the specimens tested in air, the oxidation- free dimples (Fig.5.44). On the other hand, the specimen tested in

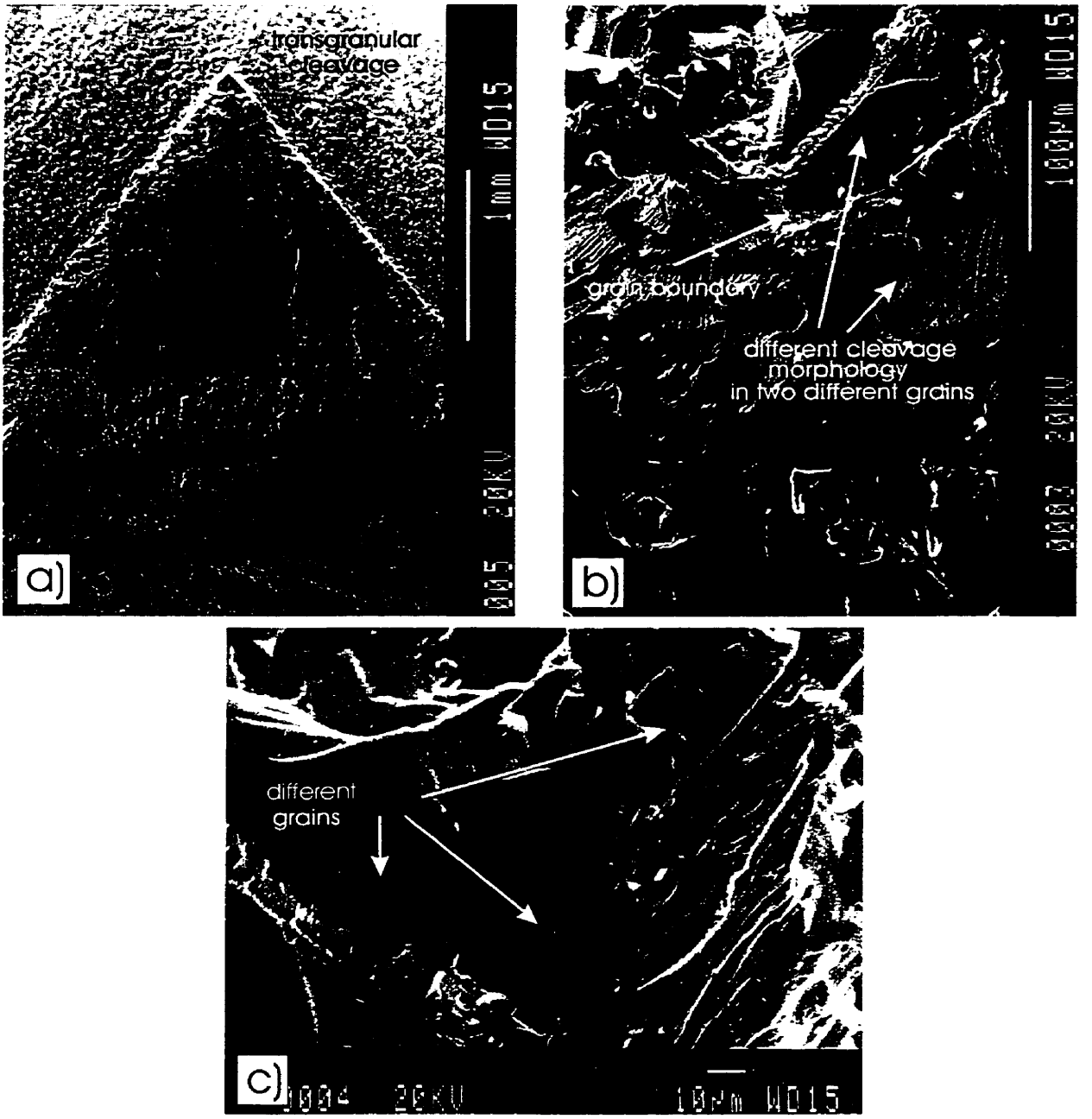

Figure 5.41 Low-Mn alloy tested in dry oxygen at room temperature.

vacuum at 950°C (the highest temperature for these tests) did not show any formation of dimples (fractographs not shown here). In general, the formation of dimples on the grain boundary facets takes place only at the highest temperature (1000°C) and preferably occurs after some crack extension where the crack propagation rate is relatively low.

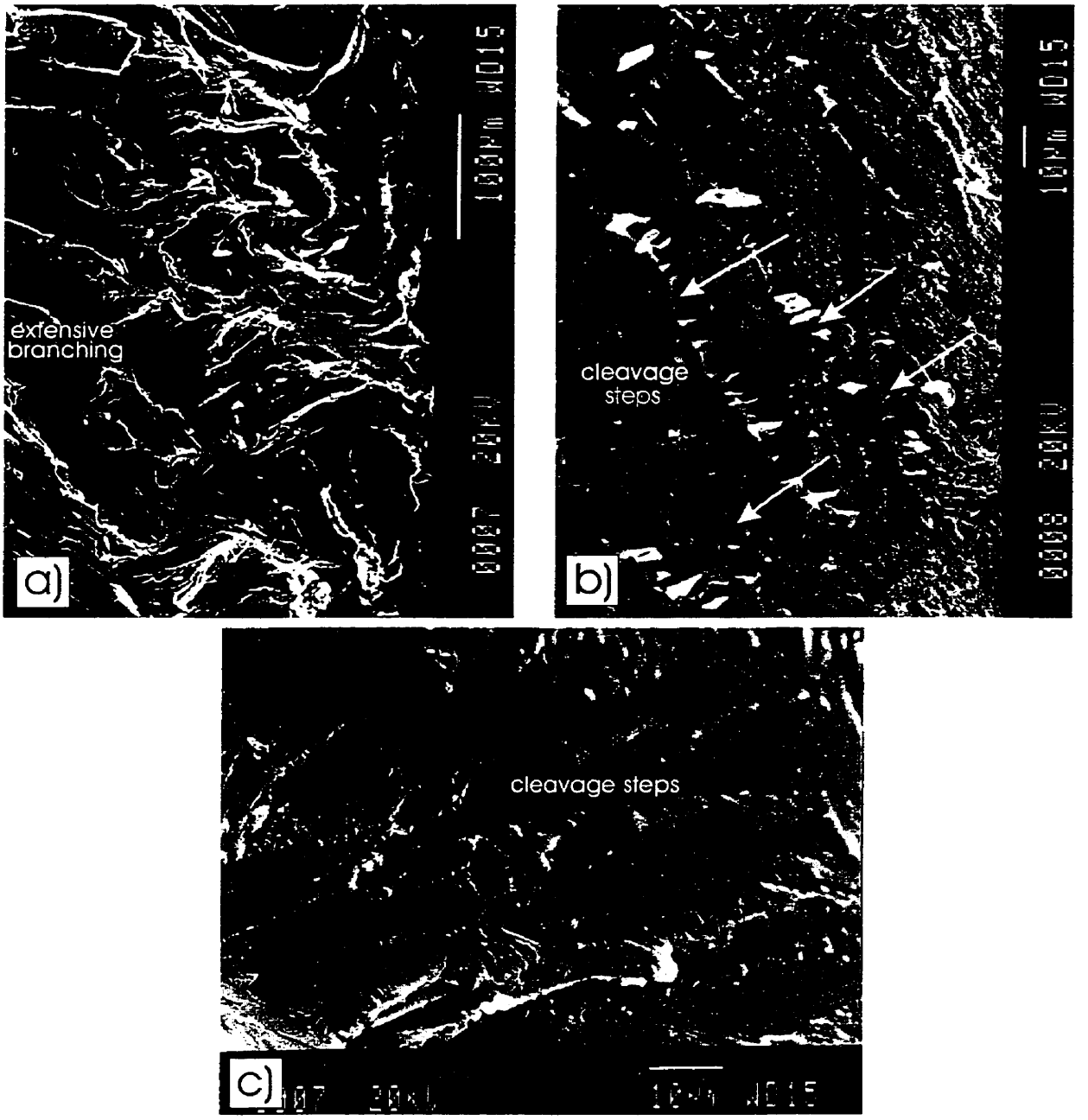

Figure 5.42 Characteristic appearance of fracture surface of the low-Mn alloy tested in argon at: a) RT; b) and c) 500°C.

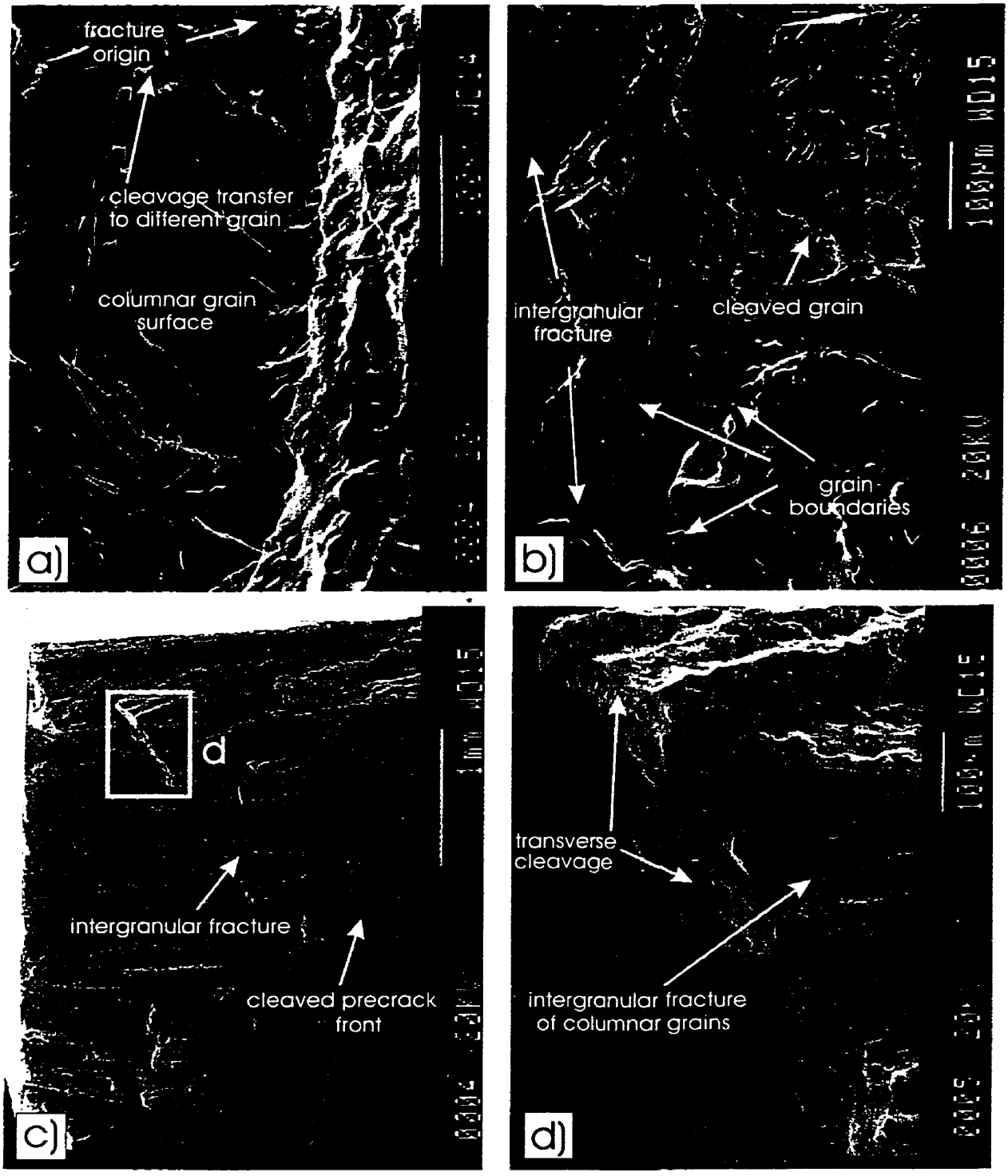

Figure 5.43 Fracture surface of the low-Mn boron-free, "base" 9Mn-25Ti alloy tested in argon at a) 600°C-columnar grains, b) 600°C- equiaxed grains, c) 1000°C- columnar grains, d) higher magnification of cleaved columnar grains at 1000°C.

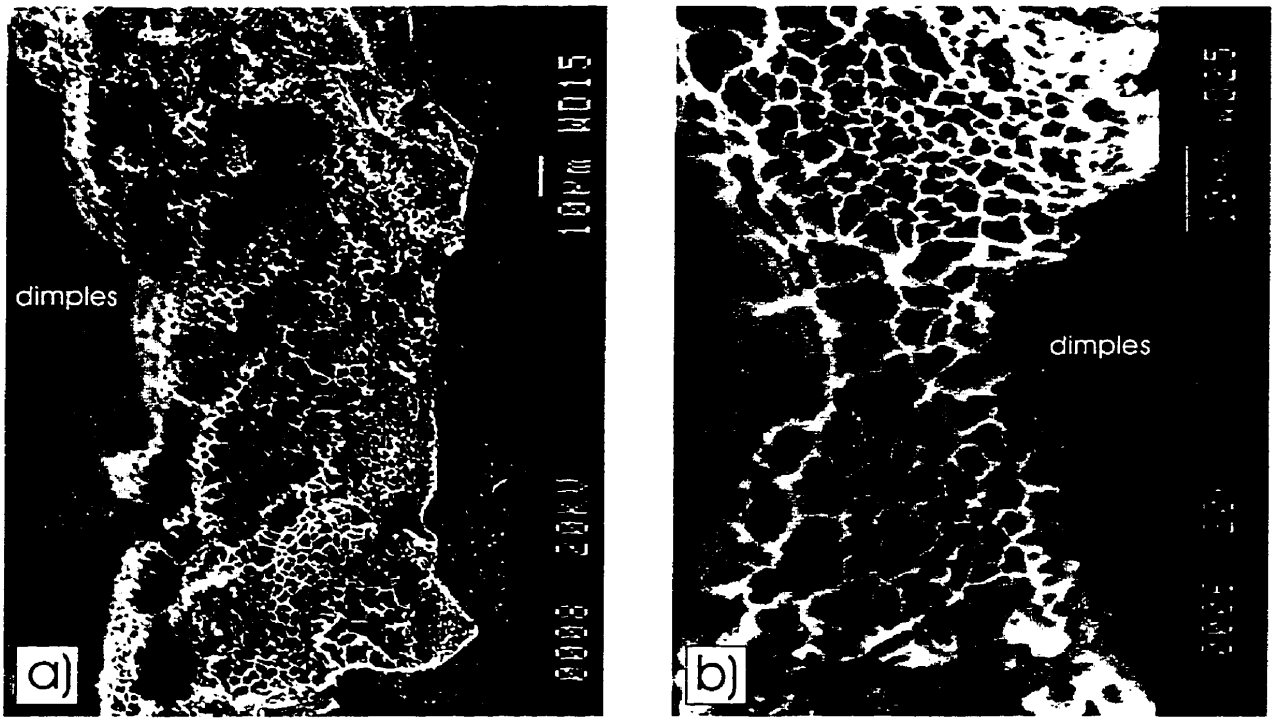

Figure 5.44 Oxidation- free dimples in the low-Mn alloy tested in argon at 1000°C.

One additional characteristic feature of fracture surfaces of specimens tested in argon at 1000°C is that if the specimen has columnar grains and if those grains are long enough with respect to the specimen width they can cleave in transverse direction (Figs.5.43c and d) even though the overall mode of fracture is intergranular.

To summarize, the mode of fracture for low- Mn boron-free, "base" 9Mn-25Ti alloy changes with temperature gradually but continuously and is entirely TGC at room temperature and 100% IGF at 1000°C. At around 500°C it is half transgranular and half intergranular as shown in Fig.5.45 for CNB specimens tested in 4pt. bending in air.

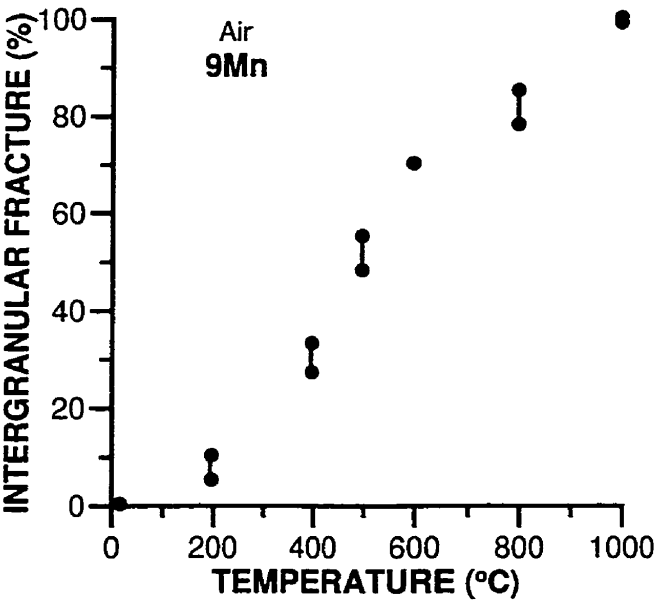

Figure 5.45 Fracture mode dependence on temperature for low- Mn (9Mn-25Ti) alloy tested in air (CNB specimens in 4pt. bending).

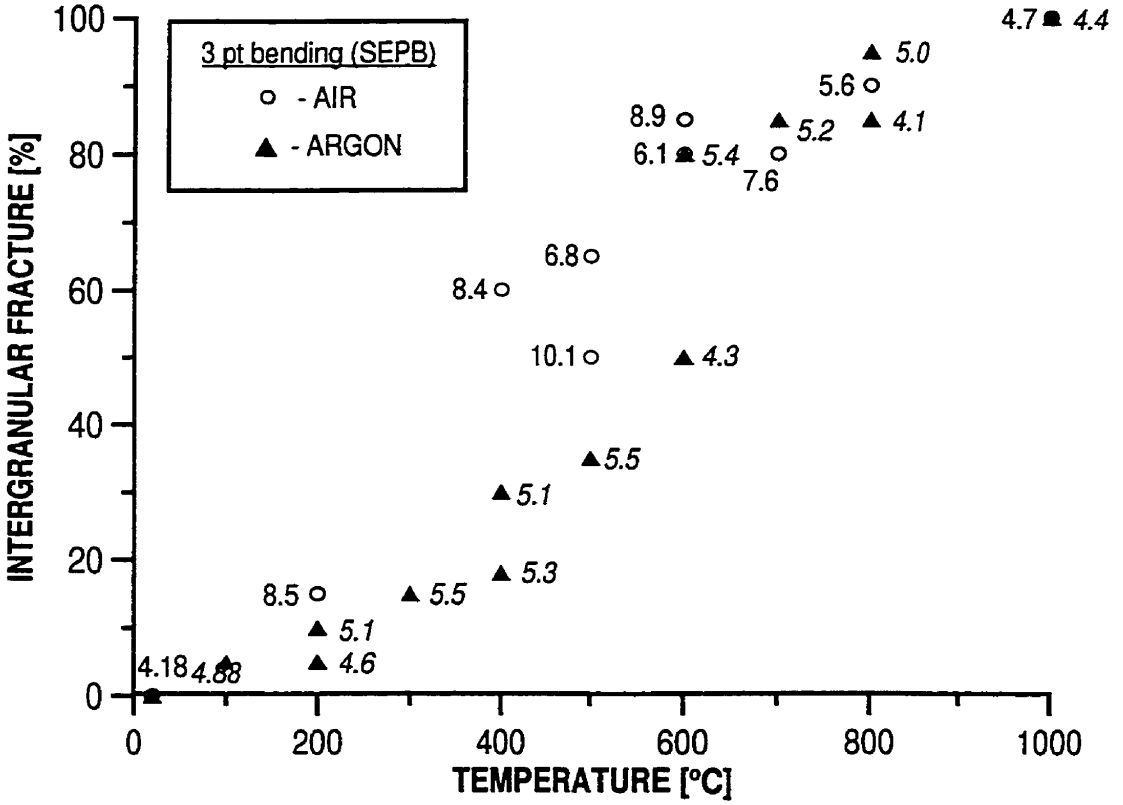

Figure 5.46 Fracture mode dependence on temperature for low- Mn (9Mn-25Ti) alloy tested in air and in argon (SEPB). Number beside each data point shows fracture toughness.

Low- Mn boron-free, "base" 9Mn-25Ti alloy tested in argon showed lower percentage of intergranular fracture in the temperature range 300°C- 600°C than that tested in air (Fig.5.46). At other temperatures in the range RT- 1000°C the modes of fracture in air and argon are similar. The numbers beside the data points designate toughness values. It must be added that the fracture mode dependence on temperature in air is similar for SEPB and CNB specimens.

5.4.2 Fracture Toughness

All the details regarding fracture toughness testing- modes of loading, test temperatures, tests environments, specimen dimensions and notch geometry, and the results of testing are given in the Appendices D, E, F, and G.

Fracture toughness tests were performed on two different types of specimens: single-edge-precracked-beam (SEPB) and chevron-notch-beam (CNB) specimens. The reason is to have more confidence in the obtained results. There are no restrictions regarding mode of loading for CNB specimens- 3pt. bending (according to E 399 Standard for SEPB type of specimens) or 4pt. bending. However, as will be seen, 3pt. bending of CNB specimens produced toughness results much different from those obtained in 4pt. bending on CNB specimens and 3pt. bending on SEPB specimens (the latter two gave very similar results in the entire temperature range). Therefore, not much attention will be given to 3pt. bending of CNB specimens due to this discrepancy. The use of the variety of the specimens tested- variety in specimen size, in notch geometry, and in S_1/S_2 ratios is justified by curiosity of the results of such configurations, sometimes by the material availability and still in other cases by the intention of (for example) changing the character of fracture process, i.e. the desire to obtain subcritical crack growth (in CNB type specimen).

One could get easily confused by this variety and have difficulty in accepting the results as being universal. This problem is solved by applying the plane strain validity check on conditional fracture toughness K_Q (for SEPB specimens) and K_{QV} (for CNB specimens). If the test conditions satisfy such a check, the K_{QV} values are treated as universal plane strain fracture toughness values (i.e. they are fully comparable). In some cases there was no confidence in the results due to different behavior of fracture toughness with temperature, then the specimens were cut into two halves and tested again. Such tests confirmed the results obtained on bigger specimens. The methodology of testing was such that one specimen was tested at the given temperature in the entire temperature range (usually with the temperature interval of 100°C or 200°C depending on the number of specimens available). Subsequent calculations of provisional fracture toughness K_Q and K_{QV} allowed determination of the temperature at which additional tests should be performed. Similar approach was applied to toughness testing in various environments, especially in argon (it will be justified later on). If not stated otherwise, the results presented were obtained on boron-free "base" 9Mn-25Ti single phase intermetallic alloy.

For SEPB specimens, fracture toughness depends on the remaining ligament length (RLL) (Fig.5.47). If the minimal value of the RLL (RLL=W-a) is calculated by taking $K_Q \approx 4.0$ MPa$\sqrt{m}$ and $\sigma_{ys} \approx 160$ MPa [28], then it follows that: RLL $\geq 2.5(K_Q/\sigma_{ys})^2 \approx 1560\mu m$ [114]. The RLL dependence of toughness at temperatures from 100°C to 1000°C is not that obvious as that at RT and seems to disappear at high temperatures (Fig.5.48).

The temperature dependence of toughness for SEPB and CNB specimens tested in air is presented in Figs.5.49 and 5.50, respectively. A broad peak of toughness

determined with the SEPB specimens appears in the temperature range ~200-500°C (Fig.5.49) and its existence is also confirmed by toughness tests on CNB specimens in four point bending (Fig.5.50).

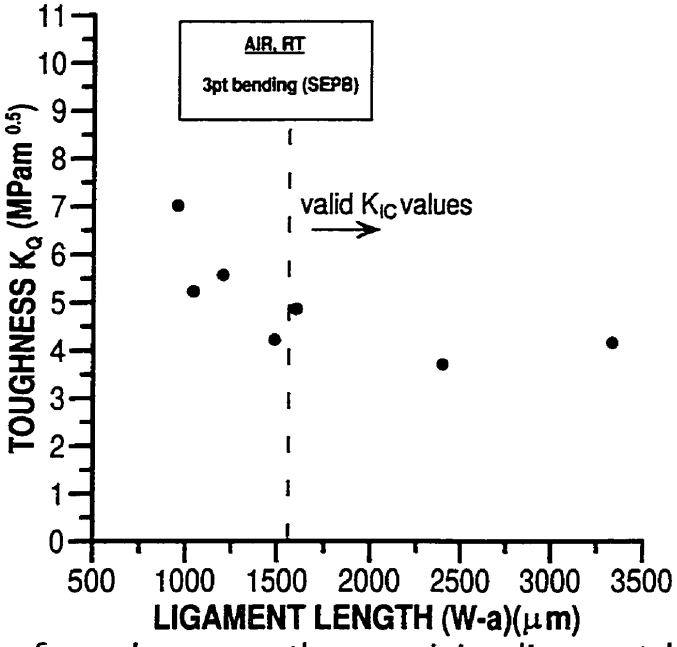

Figure 5.47 Dependence of toughness on the remaining ligament length (RLL) at room temperature (RT).

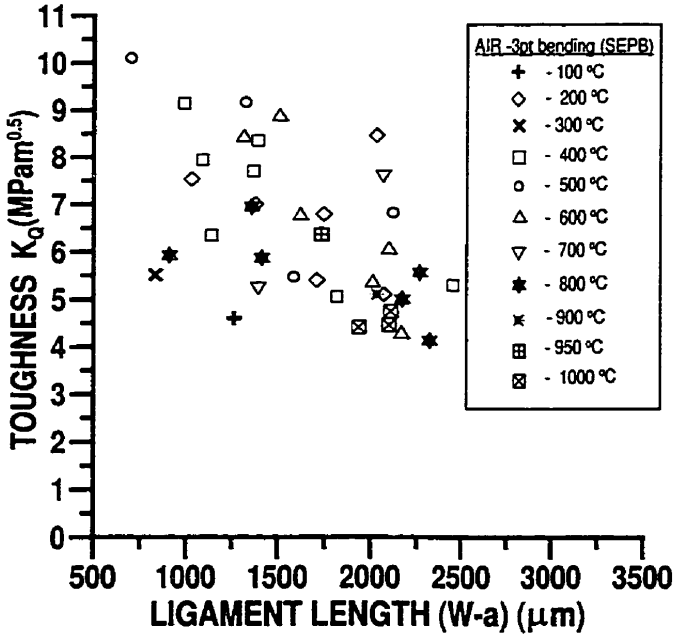

Figure 5.48 Fracture toughness dependence on the RLL in the temperature range from 100°C to 1000°C.

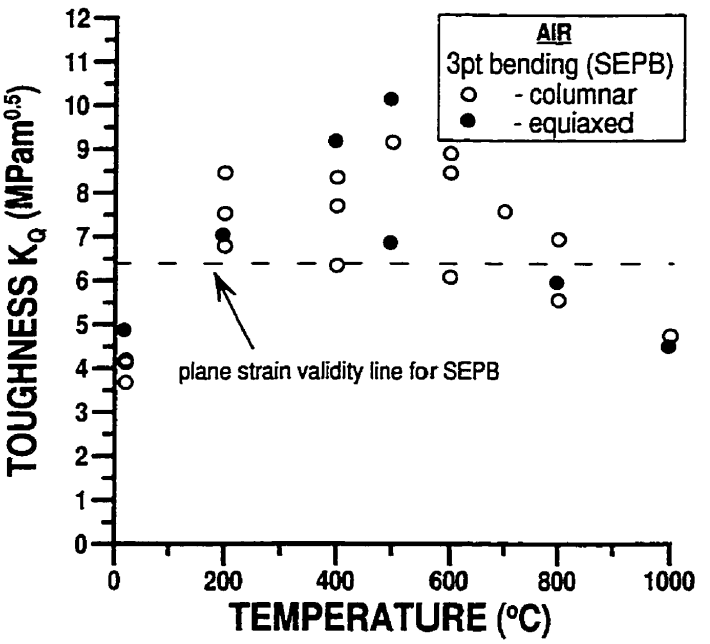

Figure 5.49 Temperature dependence of fracture toughness for SEPB specimens in air.

Plane strain validity lines are also shown in Figs.5.49 and 5.50a. They were calculated from the standard equations: $B \geq 2.5\ (K_Q/\sigma_{ys})^2$ (or alternatively $K_{IC} \leq \sqrt{(B\sigma_{ys}^2/2.5)}$ for the SEPB specimens [114] and $B \geq 1.25\ (K_{QVM}/\sigma_{ys})^2$ (or alternatively $K_{QVM} \leq \sqrt{(B\sigma_{ys}^2/1.25)}$ for the CNB specimens [115]. K_{QVM} is the fracture toughness for chevron notch specimen calculated from the maximum load as described in Section 4.5.4. The yield strength σ_{ys}=160 MPa [28] (almost constant in the entire temperature range from room temperature to 1000°C) for a coarse-grained Mn-stabilized titanium trialuminide and specimen thickness B=4 mm were taken for SEPB specimens, B=4.8 mm for large CNB and B=2.5 mm for small CNB specimens (see Tables C.2, C.3, and C.4 with the dimensions in Appendix C).

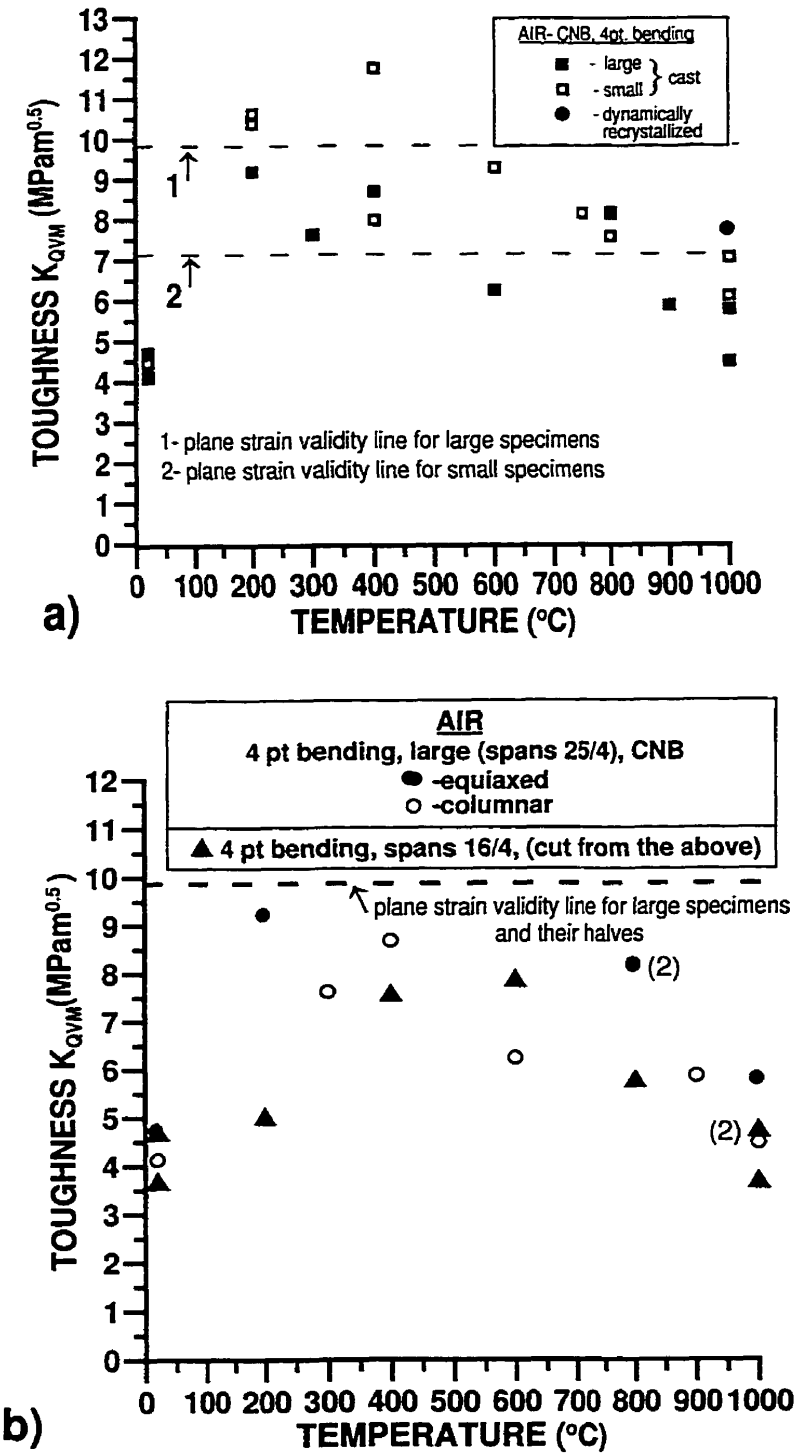

Figure 5.50 Temperature dependence of fracture toughness for CNB specimens in air: a) large and small, b) large specimens and their halves.

It seems that most of the K_Q values for SEPB specimens in the 200– 600°C range are not valid plane strain K_{IC} values (Fig.5.49) but still the remaining values close to and below the validity line show the peak in the temperature range 200°C– 600°C, although much shallower. However, Fig.5.50 shows that all the K_{QVM} values for large CNB specimens lie below their validity line.

Similar analysis can be applied to the small CNB specimens. Strict condition for the plane strain fracture toughness requires that valid values lie below the line no.2 in Fig.5.50a which makes an impression that most of the K_{QVM} values in the 200–600°C range are not valid. However, because all the K_{QVM} values for the small CNB specimens lying below the line no.1 in Fig.5.50a fall into the same scatter band as the large CNB specimens, then also K_{QVM} values for small specimens could be considered as valid values.

Material parameters that could affect the toughness values are the grain size and grain morphology. The grain size effect was already discussed in Section 5.4 and the grain morphology influence on toughness is shown in Figs.5.49 and 5.50b. The fracture toughness values of the specimens with equiaxed and columnar grains are contained in the same scatter band and there is no dependence of toughness on the morphology of grains.

The reasons of higher values of toughness obtained with the CNB specimens in three point bending (Fig.5.51) are not known. The huge scatter could possibly be the result of misalignment for each test (3pt. bending is more susceptible for misalignment than 4pt. bending). However, the alignment within 0.5 mm is easily achieved here and that would cause just a minimal scatter in K_{QVM} values.

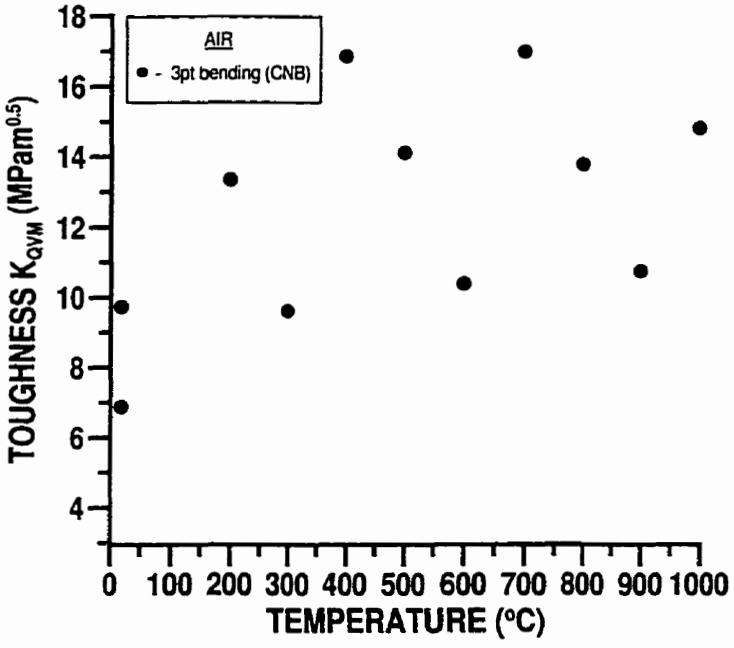

Figure 5.51 Fracture toughness dependence on temperature for CNB specimens in 3pt. bending, tested in air.

Fracture toughness dependence on the RLL in vacuum (~1.5x10^{-7} Torr) at room and the entire temperature range is presented in Figs.5.52 and 5.53, respectively). It is clear that K_Q depends on RLL at room temperature. The lack of dependence of toughness on the ligament length at higher temperatures is possibly related to the increasing fraction of intergranular fracture with increasing temperature. Fracture toughness vs. temperature in vacuum is shown in Fig.5.54. Therefore, the peak of toughness which is observed at ~400 °C in Fig.5.54 can be considered as a true peak.

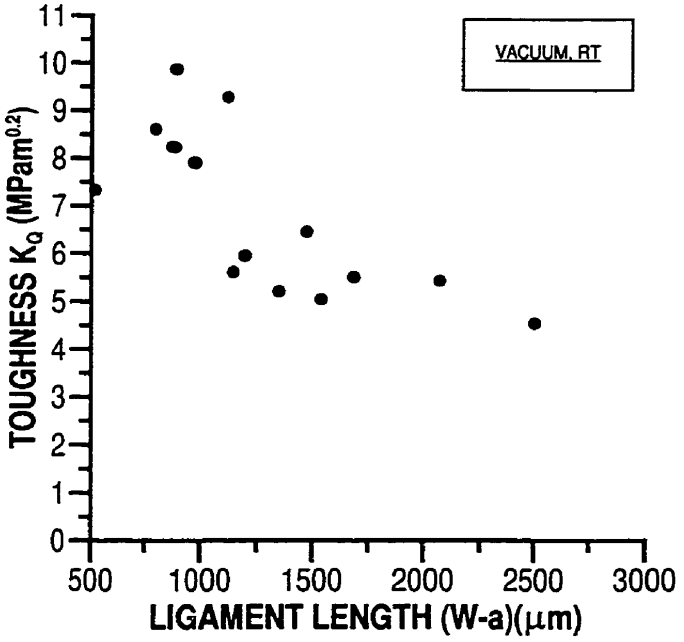

Figure 5.52 Toughness vs. ligament length at room temperature in vacuum (SEPB).

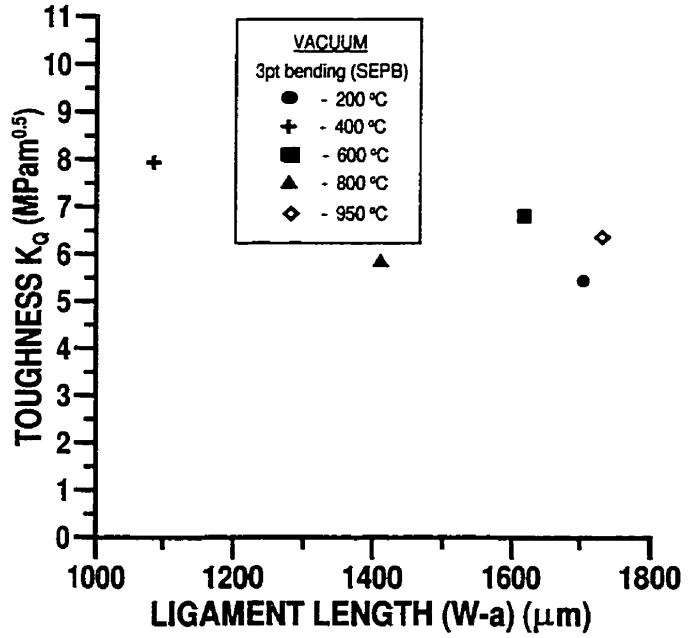

Figure 5.53 Toughness vs. ligament length in vacuum in the temperature range 200°C- 1000°C (SEPB).

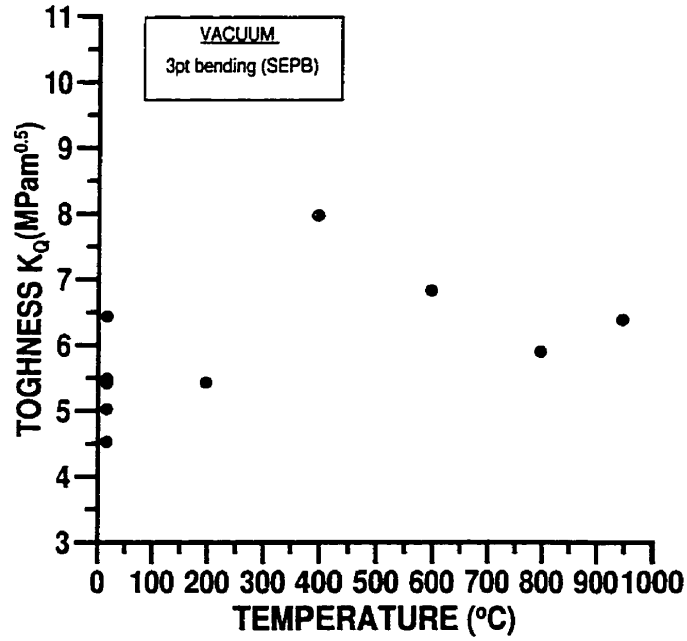

Figure 5.54 Toughness vs. temperature in vacuum.

Toughness obtained in argon (Fig.5.55) does not show any dependence on the remaining ligament and it remains almost constant in the entire temperature range (Fig.5.56).

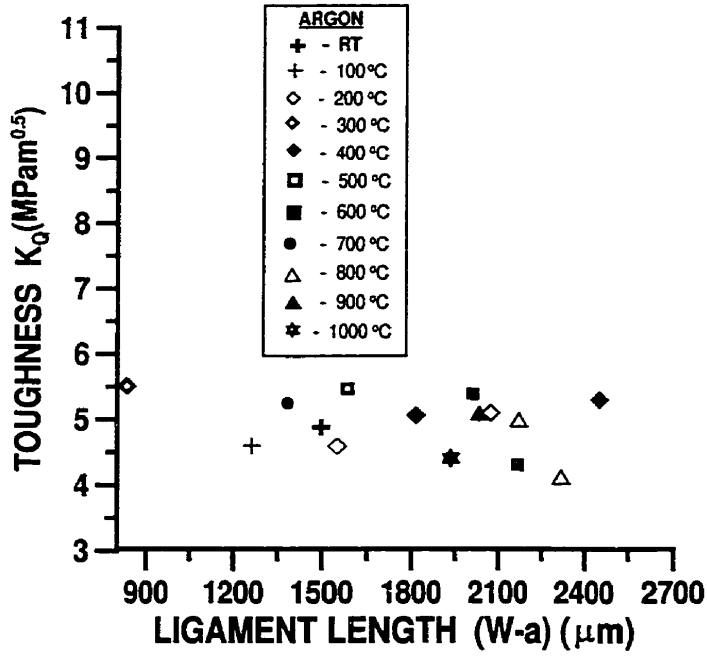

Figure 5.55 Toughness vs. ligament length in argon at various temperatures.

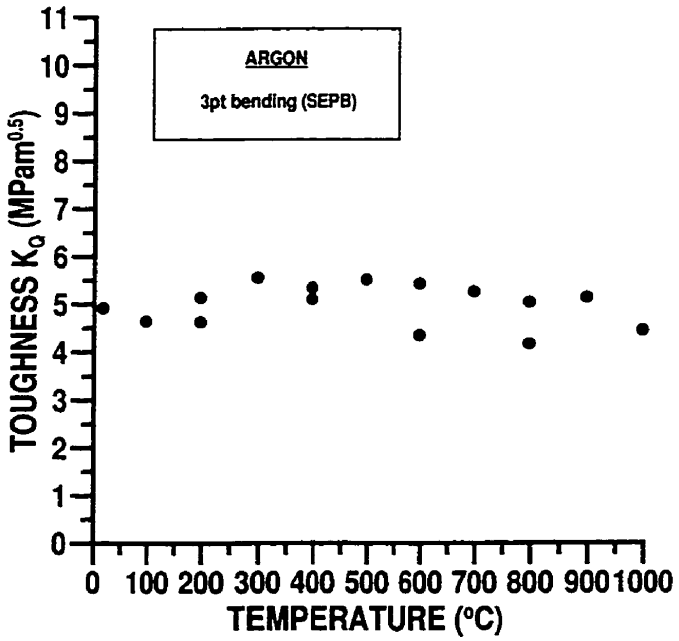

Figure 5.56 Toughness vs. temperature in argon at various temperatures.

The synthesis of toughness results in various environments for SEPB specimens in 3pt. bending is shown in Fig.5.57. Fig.5.57a shows a strong dependence of fracture toughness, K_Q, on the remaining ligament length but no clear dependence on the environment at ambient and liquid nitrogen temperature. It seems that the $L1_2$ titanium trialuminide is completely immune to the water vapor- hydrogen embrittlement and its cause of brittleness at ambient temperatures is other than environment.

Another interesting and rather striking feature of the toughness results observed in Fig.5.57b is that the peak of toughness is not observed in argon, i.e. K_Q in argon is essentially independent of temperature up to 1000°C. The lack of the broad toughness peak at the 200- 600°C range in argon also confirms unequivocally that the peak observed in air and vacuum is unrelated to the plane strain validity of the results but is a true fracture toughness peak. Additionally, toughness seems to be

insensitive to the length of the remaining ligament at all the temperatures in the range of ligaments tested (Fig.5.58).

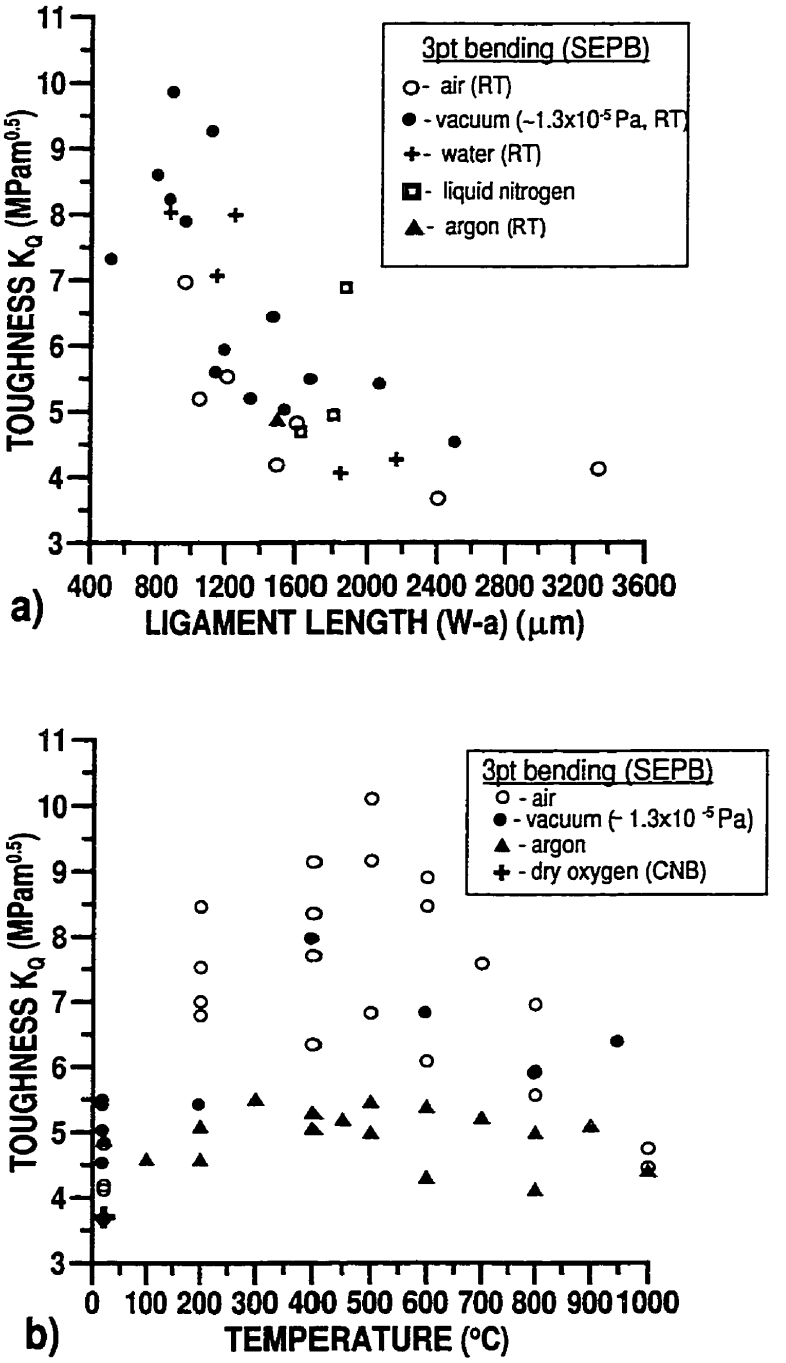

Figure 5.57 Fracture toughness, K_Q, as a function of a) remaining ligament length at room temperature and b) temperature for various environments.

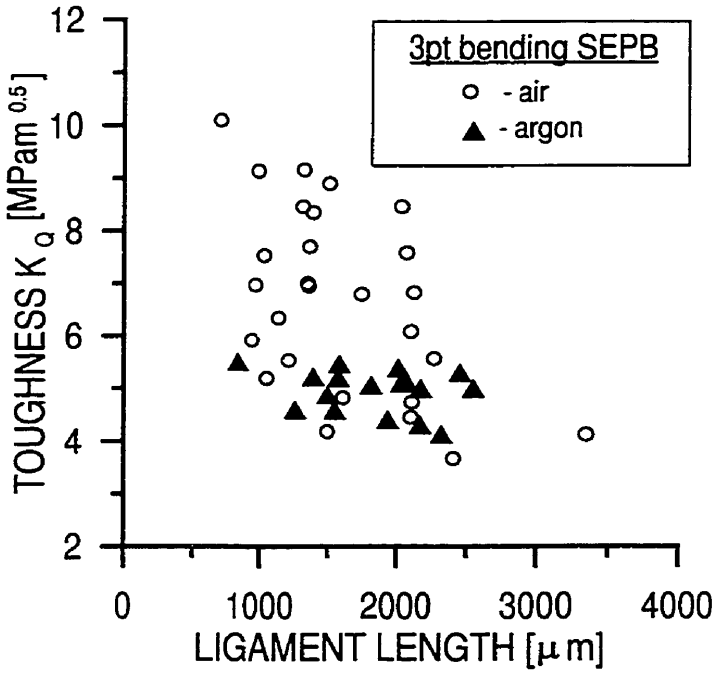

Figure 5.58 Toughness dependence on the remaining ligament length in air and argon for the entire temperature range RT- 1000°C.

Before getting into a discussion concerning interpretation of the obtained toughness results it is necessary to consider how trustworthy are the measured values of fracture toughness employing CNB specimens. A customary plane strain validity check as described in several preceding sections (Sections 4.5.4 and 5.5.2) indicates that most of the CNB (K_{QVM}) values obtained at the RT-200°C and 800-1000°C ranges are valid plane strain fracture toughness values. However, as shown in Section 5.3 the registered P-LLD curves in most cases of testing at ambient and elevated temperature did not exhibit a typical region corresponding to a stable crack extension which is a salient requirement of the CN testing methodology. A criterion for validity is the appearance on the loading curve, a smooth change in specimen compliance which is indicative of the stable crack extension. In contrast a sharp drop in the load usually indicates dynamic pop- in, and may take place at loads which would yield K_{QV} values significantly higher than that measured on the

same material by other techniques. This behavior is interpreted to mean that no sharp crack occurred in the chevron until a load was reached such that the crack poped- in to a position beyond the point at which it is stable. The lack of evidence of a stable crack extension preceding P_M in this work as shown by P-LLD curves in Section 5.3 is contrary to the expectations resulting from the theoretical approach to the chevron-notch geometry. However, such a behavior is not unique and has also been observed for chevron-notch testing for intermetallic, metallic and ceramic materials by other researchers [33,36,39,40,44-46]. The reported values of fracture toughness were rather conservative despite that no measurable crack extension preceded P_M.

A comparison of the provisional fracture toughness values obtained using CNB specimens (K_{QVM}) and SEPB specimens (K_Q) for titanium trialuminide alloy at RT (because of the lowest scatter of data) shows very similar values (Figs.5.49 and 5.50). This fact proves the applicability of the CNB method for fracture toughness measurements in this alloy. There is not much published literature regarding this matter and one is that by Withey and Bowen [136]. Lack of publications is most probably caused by extreme difficulty in introducing proper precracks in brittle materials for comparative purposes. Withey and Bowen [136] indicated that in brittle materials ($K_{QV} \leq 4.0$ MPa$\sqrt{m}$) it appears that valid toughness values may be obtained even without any indication of non- linear compliance changes prior to failure.

Interestingly, stable crack growth (very often until final fracture) can be easily obtained in ceramic material if the notch is designed properly (i.e. small notch width, large $\alpha_1 \approx 1$ and $\alpha_0 \approx 0.2$-0.3) for this purpose.

Sung and Nicholson [137] showed that ceramic specimens were overloaded in fracture tests using CN method. Tests on the precracked CNB specimens (precracking was done at very low loading rate of 0.01 mm/min) showed that the specimens were fracturing at lower loads (giving lower K_{IC} valid values) [137]. Any extent of precracking < α_m was judged in their work by the occurrence of a subsequent stable crack- growth region.

In this work, additional tests were performed on CNB precracked specimens in order to exclude the possibility that the blunt chevron-notches are responsible for catastrophic fracture. The precracks in CNB specimens were thermally tinted by exposure to a high temperature (~800°C) for ~2min (they followed the same procedure as SEPB specimens). Subsequently, the specimens were tested in 4pt. bending. After tests, the notch dimensions and the precrack lengths were measured under optical microscope using Java software. For each tested specimen, the stress intensity factor coefficient function Y^* was calculated on the basis of the specimen and notch dimensions, and S_1/S_2 ratio as a function of the normalized crack length. Figs.5.59 and 5.60 show the Y^* curves for pre-cracked 9Mn-0.004B (alloy no.9 in Table 5.1) and base 9Mn-25Ti alloy, respectively. Table E.1 shows the specimen specifications and K_{QVM} values.

The parameters α_m and α_{pr} in Figs.5.59 and 5.60 are the critical normalized chevron-crack length ($\alpha_m=a_m/W$) , corresponding to the minimum stress intensity factor coefficient, Y^*_{min}, and normalized chevron-precrack length ($\alpha_{pr}=a_{pr}/W$), respectively. The α_m values were calculated from the condition $\alpha_m=dY^*(\alpha)/d\alpha=0$ and Y_{min} from equation $Y_{min}=Y^*(\alpha_m)$. The normalized precrack length, α_{pr}, for each specimen is also shown on the graphs of Y^* vs. α in Figs.5.59 and 5.60. In those specimens in which $\alpha_{pr}<\alpha_m$ the K_{QVM} was calculated according to equation 2.3 in

Section 4.5.4. However, for specimens in which $\alpha_{pr}>\alpha_m$ the K_{QVM} was calculated according to the same equation but Y_{min} was replaced by the actual value of the stress intensity factor coefficient $Y_{\alpha pr}(\alpha_{pr})$.

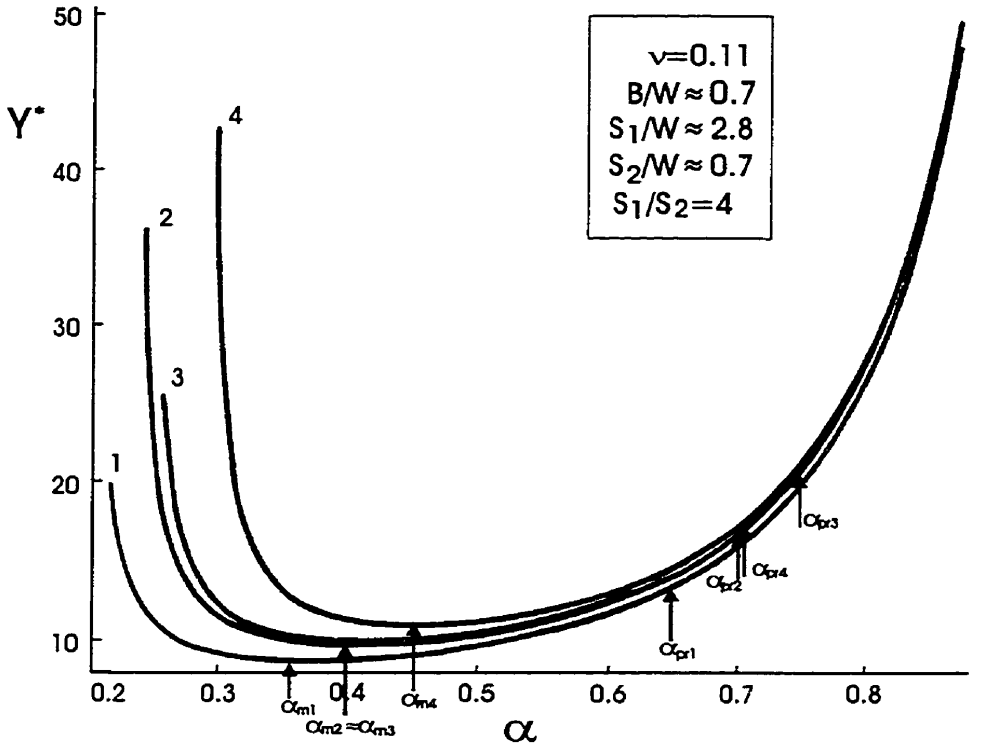

Figure 5.59 Crack length dependence of Y^* for CNB specimens of the 9Mn-0.004B alloy. Number beside each curve designates the Y^* function for each specimen tested.

For 9Mn-0.004B alloy, the calculated K_{QVM} values are in the 4.5- 6.3 MPa$\sqrt{m}$ range (Table E.1) and are very similar to those obtained using unprecracked notches for this alloy (Tables C.6 and C.7), even though the precracked specimens were quite wide with respect to the support span S_1 (low ratio $S_1/W=2.8$).

Fig.5.60 shows Y^* vs. α for the pre-cracked CNB specimens of alloy no.4 in Table 5.1. For curves 1-4, the ratio $S_1/W\approx2.8$. For this alloy and specimen configurations the calculated fracture toughness values are higher than those obtained on unprecracked CNB specimens of similar 9Mn-25Ti, base alloy (Table C3). This

difference can not be attributed to the fact that calculations of toughness for long precracks bear high errors in Y^* values due to the steepnes of the Y^* curves, because Y^* curves are quite flat (Fig.5.60, curves 1-4). Reasonable explanation for higher toughness obtained on the precracked CNB specimens than on the unprecracked CNB specimens of the similar alloy (Tables E.1 and C.3) could be the low $S_1/W=2.8$ ratio. Short specimens were used due to lack of material left. However, as was shown earlier for 9Mn-0.004B alloy, the toughness obtained on the precracked CNB specimens was comparable to that obtained on unprecracked CNB specimens despite the low $S_1/W=2.8$ ratio. Therefore, it seems that using the low S_1/W ratio in 4pt. bending of CNB specimens is unreliable for fracture toughness measurements.

For curves 5 and 6 in Fig.5.60 the ratio $S_1/W=5.2$ and 6.0, respectively and is relatively high but still the toughness calculated for the specimens 5 and 6 is higher than that obtained on unprecracked CNB specimens of similar 9Mn-25Ti, base alloy (Tables E.1 and C.3). However, Y^* curves for specimens 5 and 6 are very steep past α_m due to the high ratio of S_1/S_2 and this steepnes could contribute to high errors in toughness calculation because small variation in precrack length measurements cases large variations in $Y^*(\alpha_{pr})$.

For the type of study presented above, short precracks are preferable ($\alpha_{pr}<\alpha_m$). However, they are difficult to obtain. One reason is that they can not be observed. It can be concluded that the presence of a sharp crack in CNB specimen does not assure valid (when compared to K_{IC} values obtained by SEPB specimens, Table C.2) K_{QVM} values. This could be due to either low S_1/W ratio or the long precracks or due to both simultaneously.

For the purpose of comparison of fracture toughness obtained on unprecracked and precracked CNB specimens, the SEPB specimens of the B- doped alloy (no.9)

were also tested. The K_Q values in this case should be presented as a function of the remaining ligament length (RLL) (Fig.5.61). Valid K_{IC} values are those for which the plane strain condition is fulfilled: $B \geq 2.5(K_{IC}/\sigma_Y)^2=2.95$ mm, taking $K_{IC}\approx 5.5$ and $\sigma_Y=160$ MPa [28].

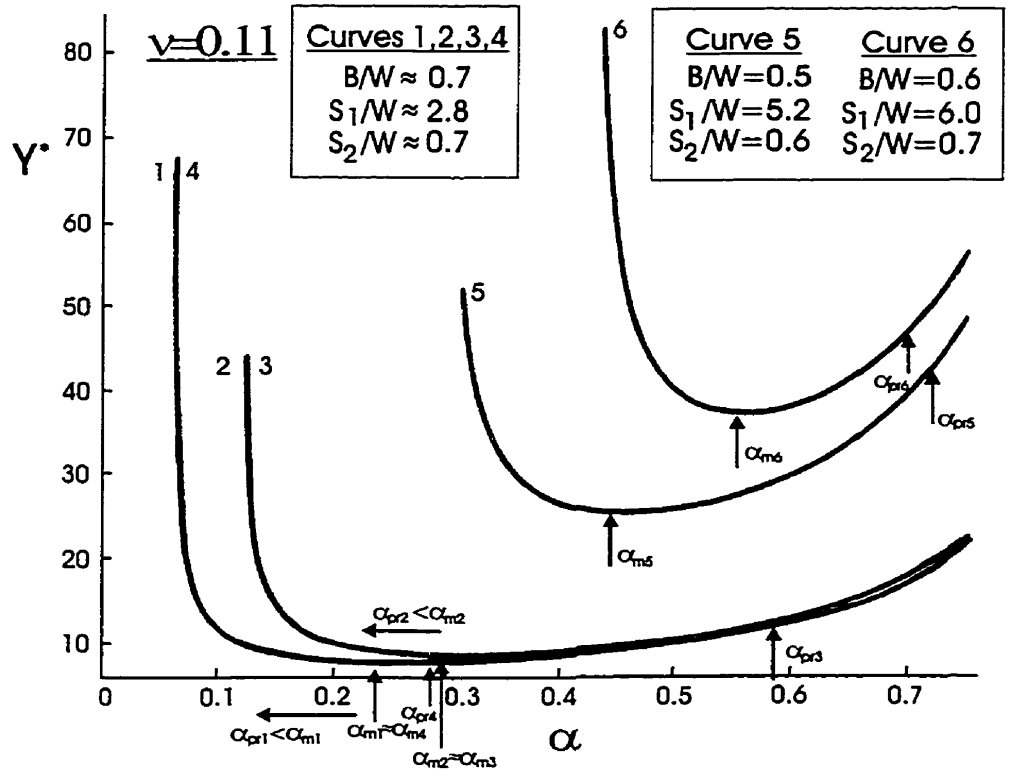

Figure 5.60 Crack length dependence of Y^* for CNB specimens of the 9Mn alloy.

Valid K_{IC} values are in the 5.2- 5.9 MPa$\sqrt{m}$ (Table E.1) range and are very similar to those obtained with unprecracked CNB specimens for this alloy (Tables C.6 and C.7), even though the S/W≈2.8 ratio is lower than the recommended ratio, S/W=4 (ASTM E399). These K_{IC} values are also similar to the K_{QVM} values obtained on the precracked CNB specimens (Table E.1) of the same alloy.

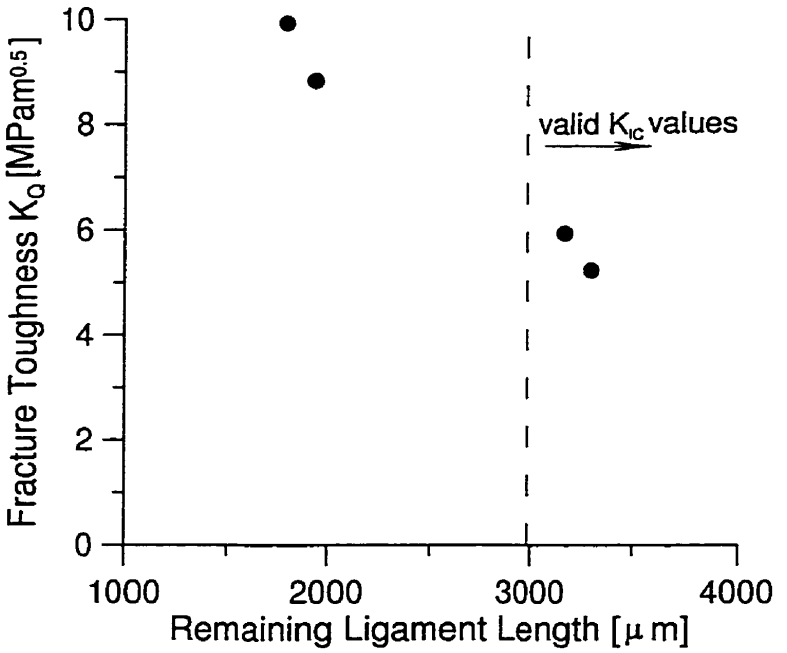

Figure 5.61 Fracture toughness dependence on the RLL in SEPB specimens of the 9Mn alloy.

5.4.3 Relationship Between Work of Fracture and Fracture Toughness

Figs.5.62a and b show the work of fracture versus RLL at RT and in the temperature range from 100°C to 1000°C, respectively. It is seen that there is lack of dependence of work of fracture on the RLL.

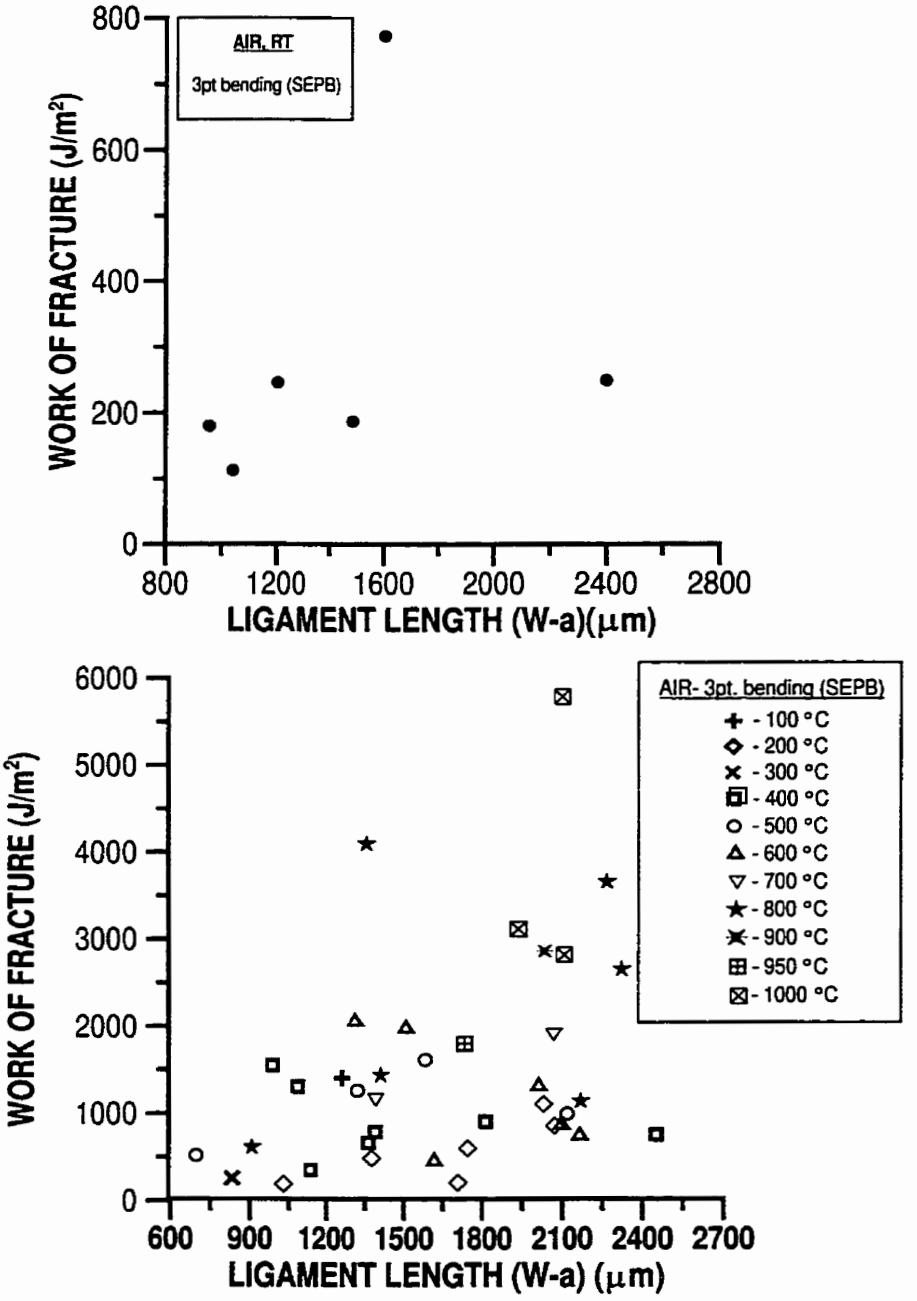

Figure 5.62 Dependence of work of fracture on the RLL, a) at RT, b) in the 100°C to 1000°C temperature range.

The temperature dependence of the work of fracture is presented in Figs.5.63 and 5.64 for SEPB and CNB specimens, respectively.

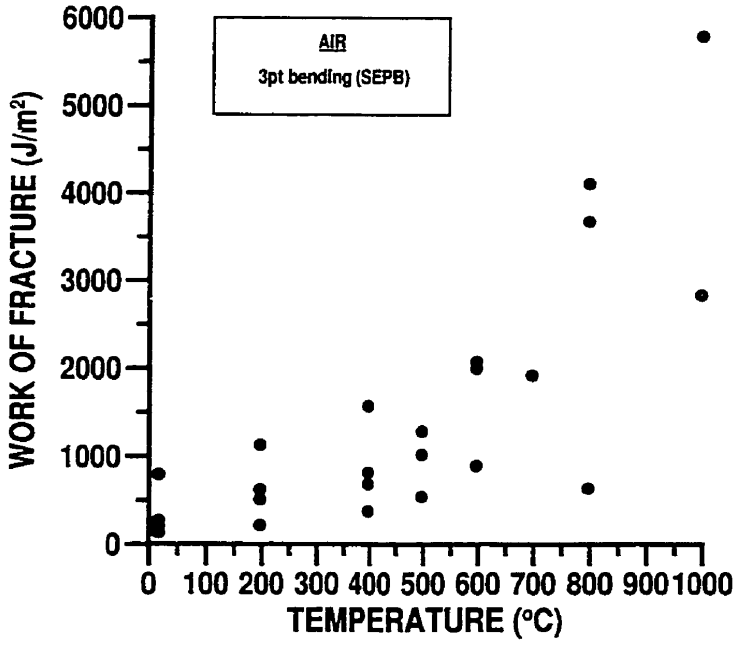

Figure 5.63 Temperature dependence of the work of fracture for SEPB specimens.

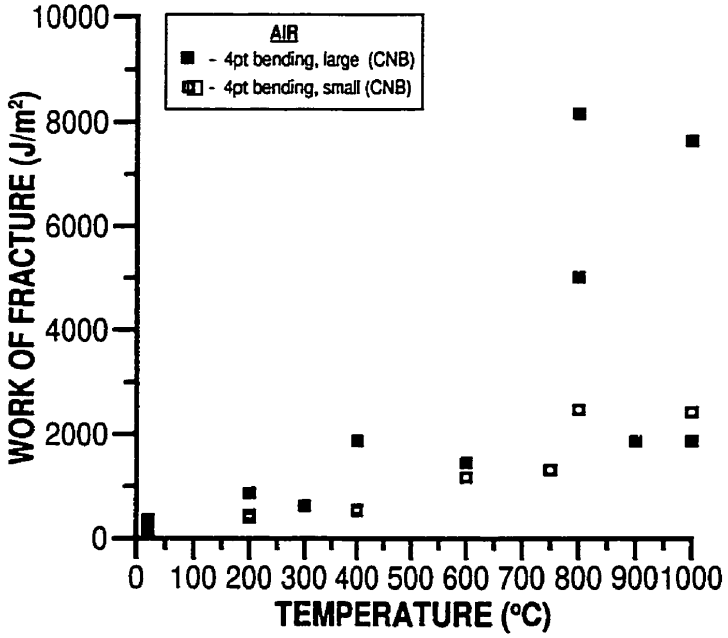

Figure 5.64 Work of fracture dependence on temperature for 4pt. bending of CNB specimens.

Regardless of the specimen type (SEPB vs. CNB) used for testing the work of fracture shows different dependence on temperature than toughness. It increases slowly but

continuously and shows abrupt increase at ~800°C. Increasing work of fracture can be attributed to increasing fraction of intergranular mode of fracture with temperature which means high work required to overcome friction between grains being pulled out (this will be discussed in more detail in Discussion chapter) and also possibly to the decrease of Young's modulus with increasing temperature (through the equation $\gamma_{WOF}=K^2/E$ [138], assuming that the elastic modulus decreases much faster with temperature than K).

Fig.5.65 shows the stress intensity calculated from the work of fracture (K_{IWOF}) according to the following equation [138-140]:

$$K_{IWOF} = (2E'\gamma_{WOF})^{1/2}$$

where γ_{WOF}- the work of fracture and E' is the effective elastic modulus, i.e. E'=E for the plane stress and $E'=E/(1-\nu^2)$ for the plane strain. Since for the $L1_2$ $Al_3Ti(Mn)$ intermetallics the value of Poisson's ratio, ν, is barely 0.11 [8] then the term can be practically neglected. The values of elastic modulus, E, of $L1_2$ $Al_3Ti(Mn)$ at a given test temperature were calculated assuming that it had the same temperature dependence as the elastic modulus of TiAl reported by Nakamura [141]:

$$E_T = E_0 - 0.0342\,T \qquad \text{at} \quad (25-935°C)$$

where the elastic modulus for $L1_2$ $Al_3Ti(Mn)$ at room temperature E_0=174 GPa [8] and T is temperature in °C.

A comparison of Figs.5.49 and 5.50 with Fig.5.65 shows that for every test temperature the stress intensity factor calculated from the γ_{WOF}, $K_{IWOF} > K_Q$ (or K_{QVM}), calculated from the maximum load. Tables 5.4 and 5.5 show the average stress intensity factor K_{IWOF} and work of fracture γ_{WOF} for large CNB (4pt.) and SEPB (3pt.) specimens, respectively.

Table 5.4 Average stress intensity factor and work of fracture for large CNB (4pt.).

	DESIG-NATION	T [°C]	K_{IWOF} [MPam$^{0.5}$]	W_F [J/m^2]
1.	ALTIL1	RT	11	350
2.	ALTIL9	RT	6.5	121
3.	ALTIL2	200	17	865
4.	ALTIL10	300	14.2	615
5.	ALTIL5	400	24.5	1870
6.	ALTIL7	600	21	1442
7.	ALTIL12	800	38.3	5004
8.	ALTIL14	800	49	8189
9.	ALTIL11	900	23	1857
10.	ALTIL6	1000	22.8	1860
11.	ALTIL13	1000	46.2	7632

Table 5.5 Average stress intensity factor and work of fracture for SEPB (3pt.).

	DESIG-NATION	T [°C]	K_{IWOF} [MPam$^{0.5}$]	W_F [J/m^2]
1.	1sh16	RT	9.3	246
2.	12sh16	RT	16.4	770
3.	18sh16	RT	6.2	109
4.	19sh16	RT	9.2	243
5.	20sh16	RT	8	184
6.	21sh16	RT	7.8	177
7.	5sh16	200	19.2	1107
8.	13sh16	200	12.7	487
9.	30sh16	200	8	193
10.	31sh16	200	14.1	602
11.	6sh16	400	14.6	662
12.	15sh16	400	22.3	1548
13.	22sh16	400	15.9	792
14.	29sh16	400	10.7	355
15.	9sh16	500	19.9	1260
16.	14sh16	500	12.8	519
17.	23sh16	500	17.7	997
18.	16sh16	600	25.1	2054
19.	24sh16	600	24.6	1976
20.	27sh16	600	16.3	871
21.	25sh16	700	23.9	1900
22.	8sh16	800	34.6	4093
23.	17sh16	800	13.4	615
24.	28sh16	800	32.7	3658
25.	4sh16	1000	28.1	2820
26.	11sh16	1000	40.2	5785

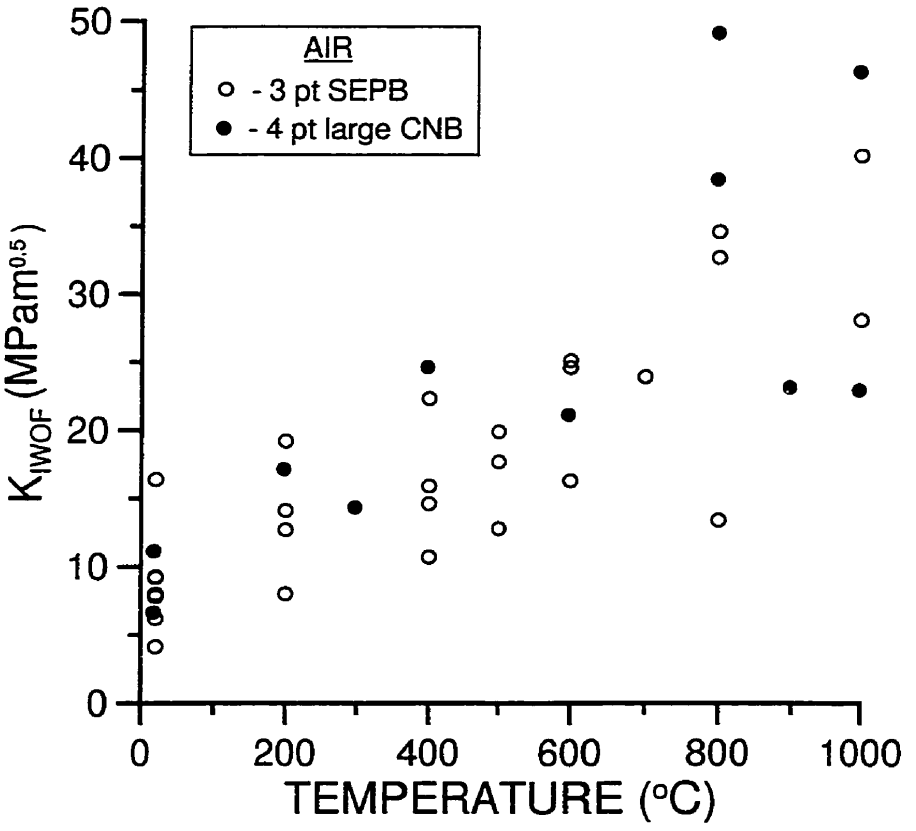

Figure 5.65 Stress intensity K_{IWOF} dependence on temperature.

SEM fractographs shown in Figs.5.66a, b, and c represent specimens with the upper bound of work of fracture ~6000 J/m² (for specimens shown in Figs.5.63 and 5.64). Fractographs d) and e) represent specimens exhibiting identical and rather low values of work of fracture ~2000 J/m², and specimen f) tested in argon showed intermediate, ~3000 J/m² value of work of fracture. All the specimens which exhibited very high work of fracture are characterized by a very well developed and non- planar fracture surface with, most probably, equiaxed grain structure whereas those which exhibited low work of fracture values show much flatter fracture surface with preserved columnar structure of grains, lying in the plane of fracture.

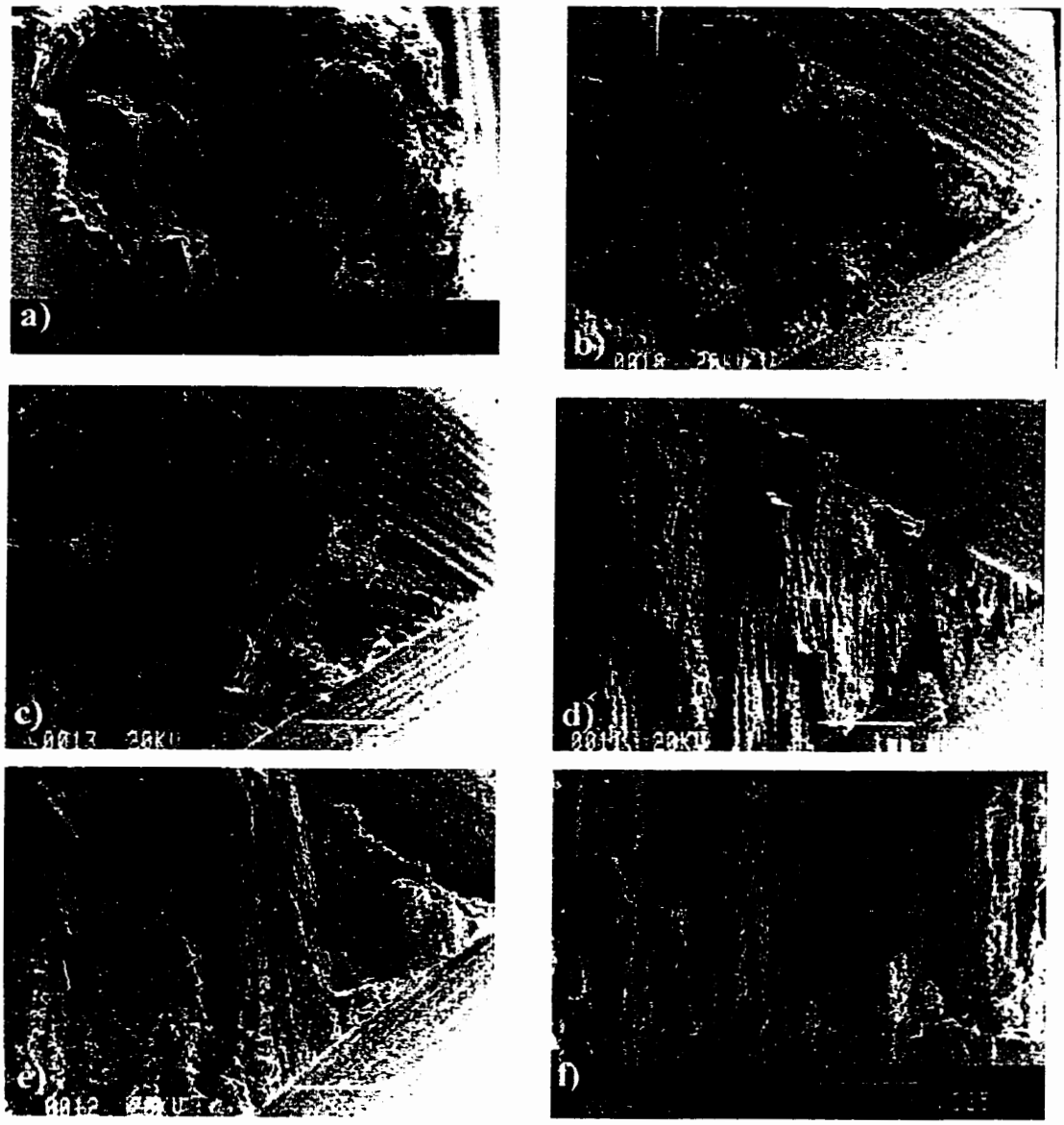

Figure 5.66 Fracture surfaces of the specimens tested at: a)3pt. SEPB (γ_{WOF}=5785 J/m²), b)4pt CNB (γ_{WOF}=7632 J/m²) and d) (γ_{WOF}=1860 J/m²) 1000°C in air, c) 4pt. CNB (γ_{WOF}=8189 J/m²) 800°C in air, e) 4pt. CNB (γ_{WOF}=1857 J/m²) 900°C in air, f) 1000°C in argon (3pt. SEPB) (γ_{WOF}=3113 J/m²).

5.5 The Effect of Grain Orientation on Fracture Toughness in Air

Set- up description.

Electron Back Scatter Pattern (EBSP) was used to determine the crystallographic orientation of grains. EBSP is a microtexture facility for obtaining electron diffraction data from bulk samples in the scanning electron microscope (SEM). The measurements were done on a Philips XL30 SEM. Fig.5.67 shows a photograph of the EBSP hardware set- up for an XL30 SEM.

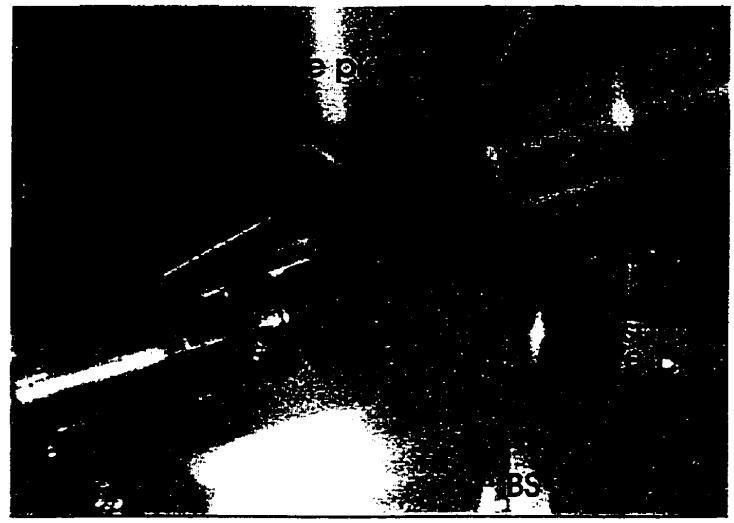

Figure 5.67 EBSP hardware set- up for a Philips XL30 SEM.

Information from EBSP appears as bright bands, geometrically arranged on a monitor or photographic film (Fig.5.68). The arrangement of these bands (Kikuchi lines) is unique to a certain crystallographic orientation and crystal symmetry. Crystals of the same structure will thus show different patterns when oriented differently. Fig.5.68 shows the schematics of formation of pairs of Kikuchi lines and the components of an EBSP system. In a typical EBSP investigation first the standard calibration routine is carried out to align the microscope/ specimen/

diffraction pattern geometry. Then, regions of interest on the specimen are identified (for example every grain in a specific area as illustrated schematically on Fig.5.69) and a stationary probe sited on each selected sampling point, whereupon an EBSP is obtained and can be 'indexed' by a computer. Data from each grain is finally stored for further processing or output.

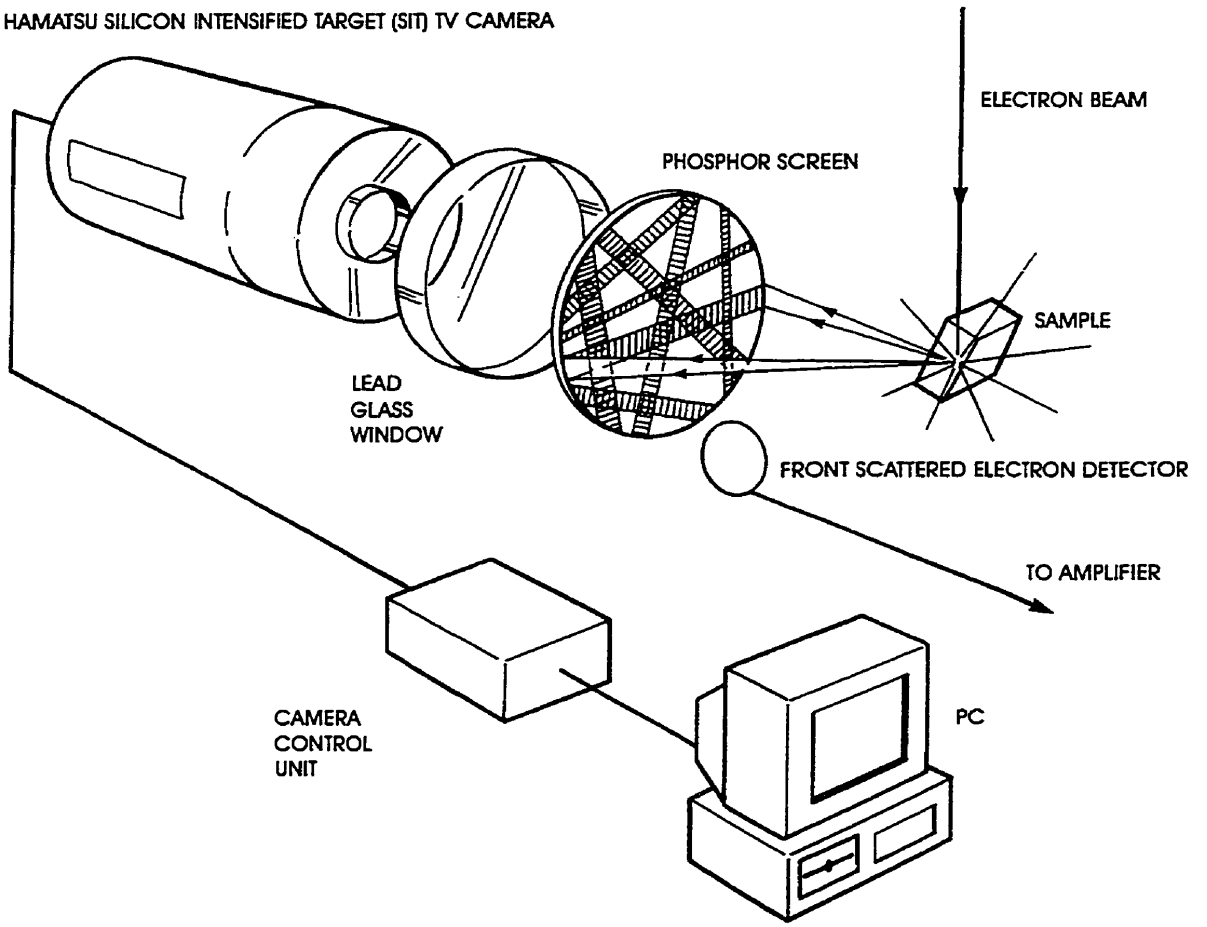

Figure 5.68 Components of an EBSP system.

The orientation data are made available in many different formats such as absolute orientations, misorientations, pole figures, inverse pole figures and Euler angles. All these different formats are derived from the orientation matrix, i.e., the orientation measurement expressed as 3x3 matrix. This matrix defines a three- dimensional orientation of crystal axes [100], [010] and [001] with respect to some reference axes, usually directions related to macroscopic or microscopic features recognized

in the specimen (e.g. grain shape). The orientation of these features with respect to the microscope stage (X_s, Y_s, and Z_s) must be specified in Crystal Orientation Software.

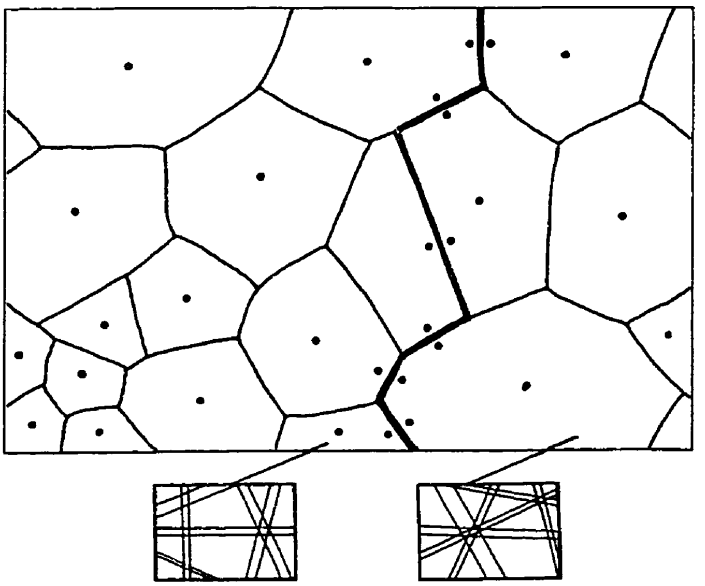

Figure 5.69 Schematic illustration showing a polycrystalline microstructure which contains a crack. Typical EBSP sampling sites are marked. EBSPs arising from two of the sampled sites are depicted.

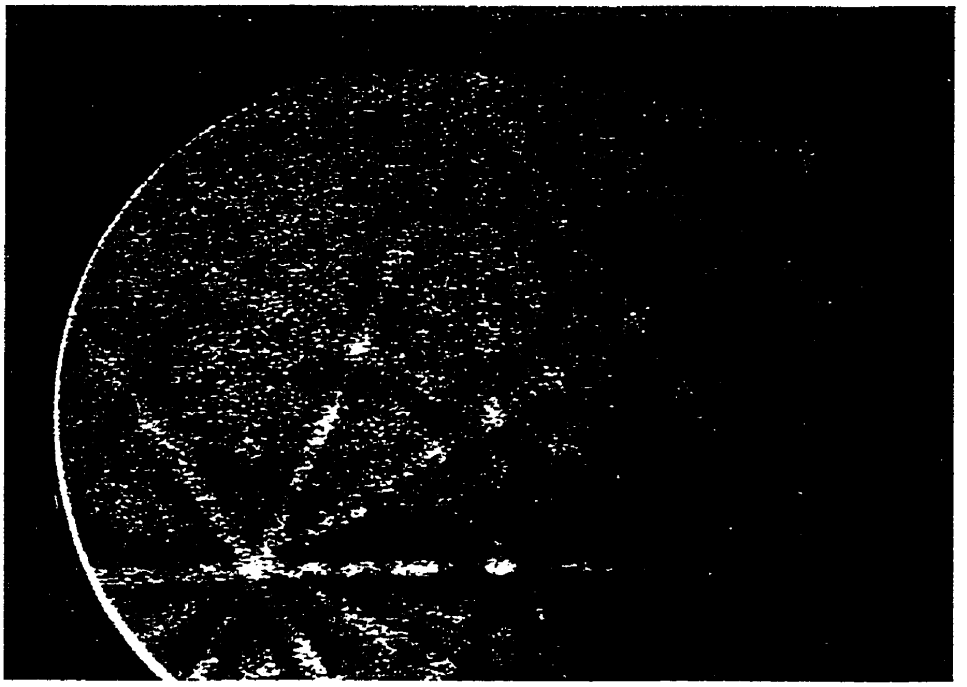

Figure 5.70 EBSP pattern obtained from $L1_2$ 9Mn-25Ti titanium trialuminide $Al_3Ti(Mn)$.

Specimen preparation.

The bend- test specimens of boron-free "base" 9Mn-25Ti alloy were prepared for EBSP analysis using the following method. Half of each broken specimen was mounted in a phenolic metallographic mount such that a transverse face of the bend specimen was exposed for grinding and polishing. The exposed transverse face of the specimen was subsequently ground, polished and chemically etched to reveal grain boundaries.

The transverse section of each specimen was oriented such that the surface normal was inclined at 68 deg relative to the incident electron beam. The spot size used was 6.0. When the electron beam was focused on one grain on the polished surface, an EBSP was obtained and the crystal orientation within the grain was determined (Fig.5.70). Crystal- orientation information was stored in the form of an orientation matrix prescribing the orientation of the crystal axes relative to the specimen axes. To identify the crystal orientation of fractured grains, EBSPs were obtained from those grains that were exposed on both the polished surface and on the fracture surface, as, for example the grains labeled 4 through 7 in Fig.5.71. When the EBSP analyses were complete, conventional SEM micrographs were taken of the polished and etched plane near the fracture surface and of all other spots in which crystal orientations had been determined.

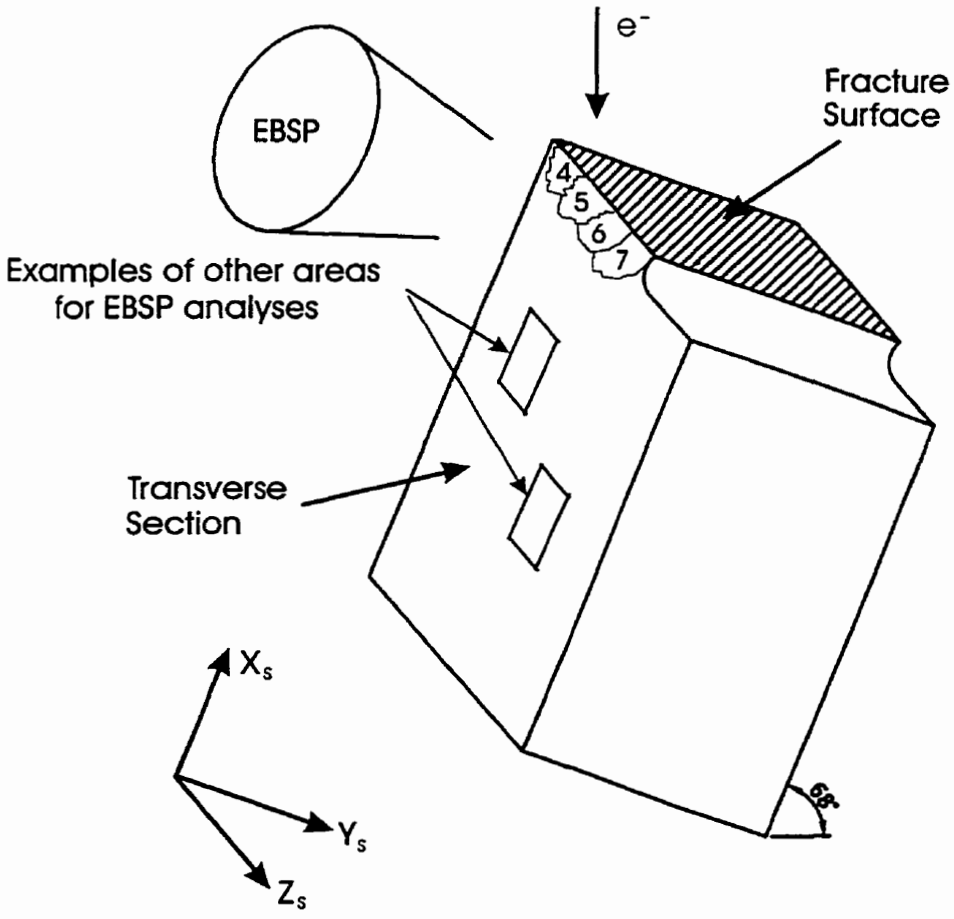

Figure 5.71 Schematic diagram showing specimen geometry used for local grain orientation determination during EBSP measurements.

Crystal orientation analysis.

Examples of grain orientation determination are shown in Figs.5.72, 5.73, and 5.74. The columnar grains in those figures are additionally elongated because the specimens were tilted ~70° for EBSP and the obtained images were not corrected. The results of orientation determination for all the grains and for the fractured grains (numbered 43–47 in Fig.5.74) are presented in the synthetical form (pole figures) in Fig.G.5 for the specimen tested at 1000°C. Additional pole figures for specimens tested at RT, 200°C, 400°C, 600°C and 800°C are presented in Fig.5.75 and Figs.G.1, G.2, G.3 and G.4, respectively (Appendix G).

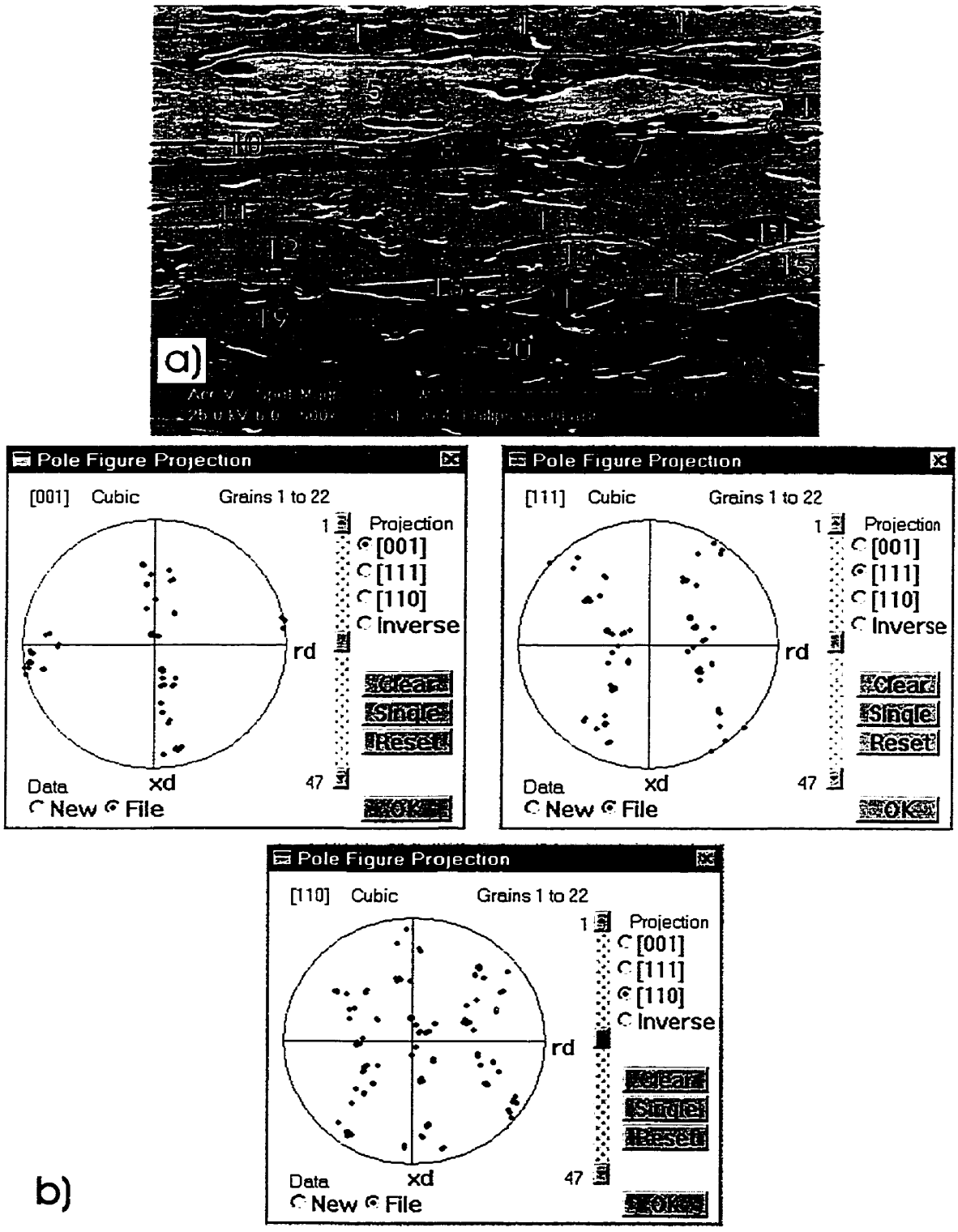

Figure 5.72 Schematics of the grain orientation determination in the specimen of the 9Mn alloy tested at 1000°C, a) SEM photograph (not corrected for tilt) with numbered columnar grains, b) pole figures for grains in (a).

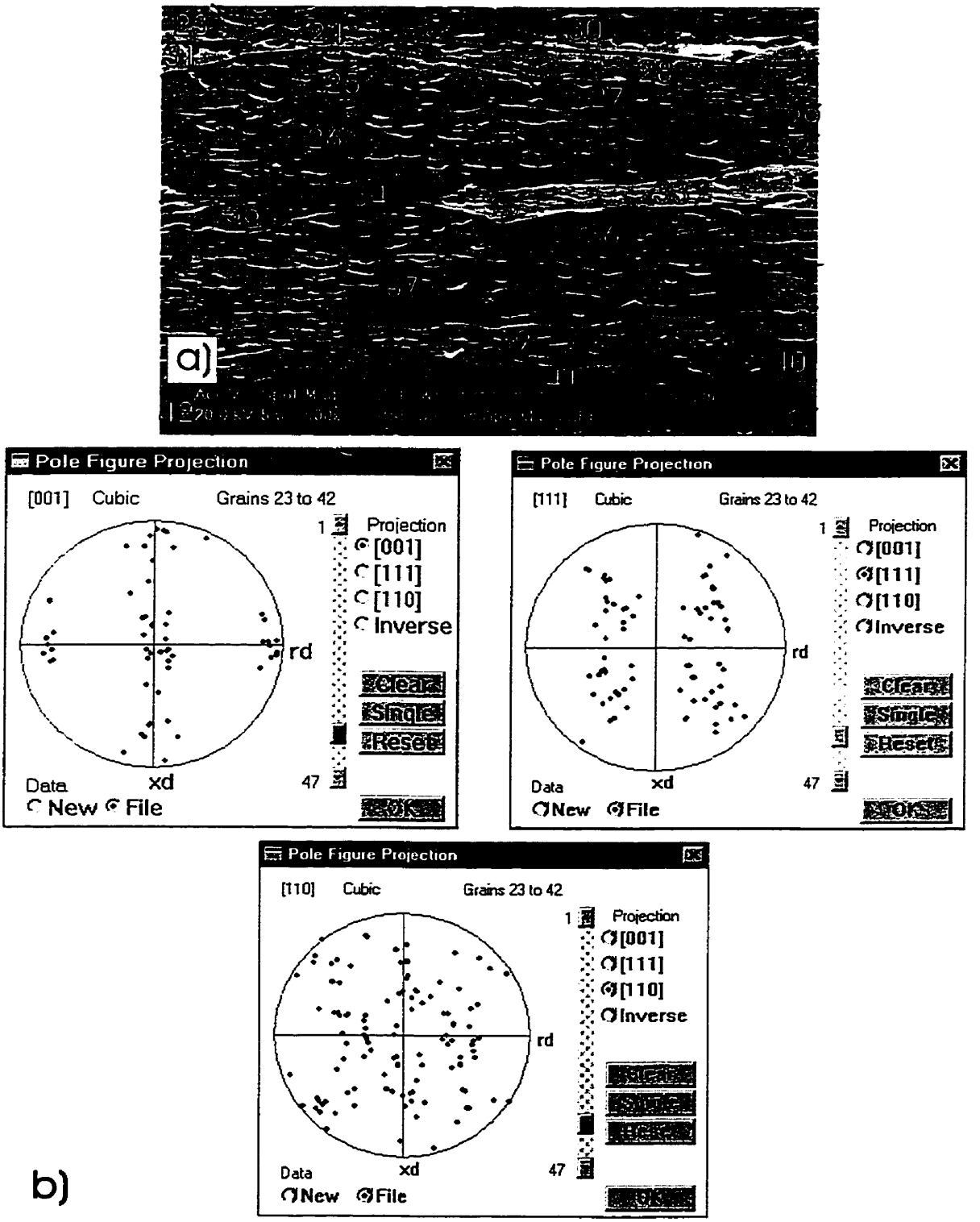

Figure 5.73 Schematics of the grain orientation determination in the specimen of the 9Mn alloy tested at 1000°C, a) SEM photograph (not corrected for tilt) with numbered columnar grains, b) pole figures for grains in (a).

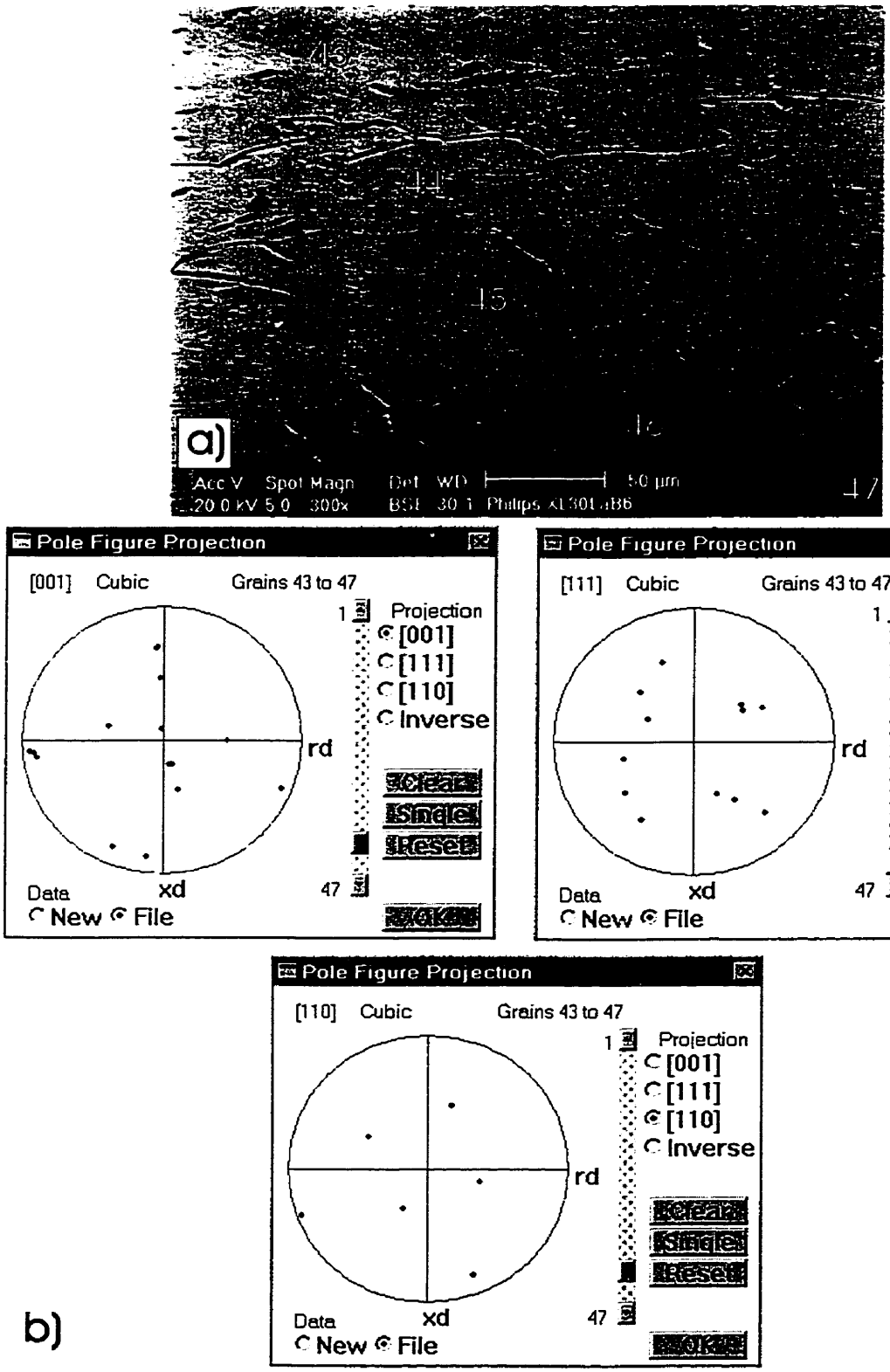

Figure 5.74 Schematics of the grain orientation determination in the specimen of the 9Mn alloy tested at 1000°C, a) SEM photograph (not corrected for tilt) with numbered columnar grains, b) pole figures for grains in (a).

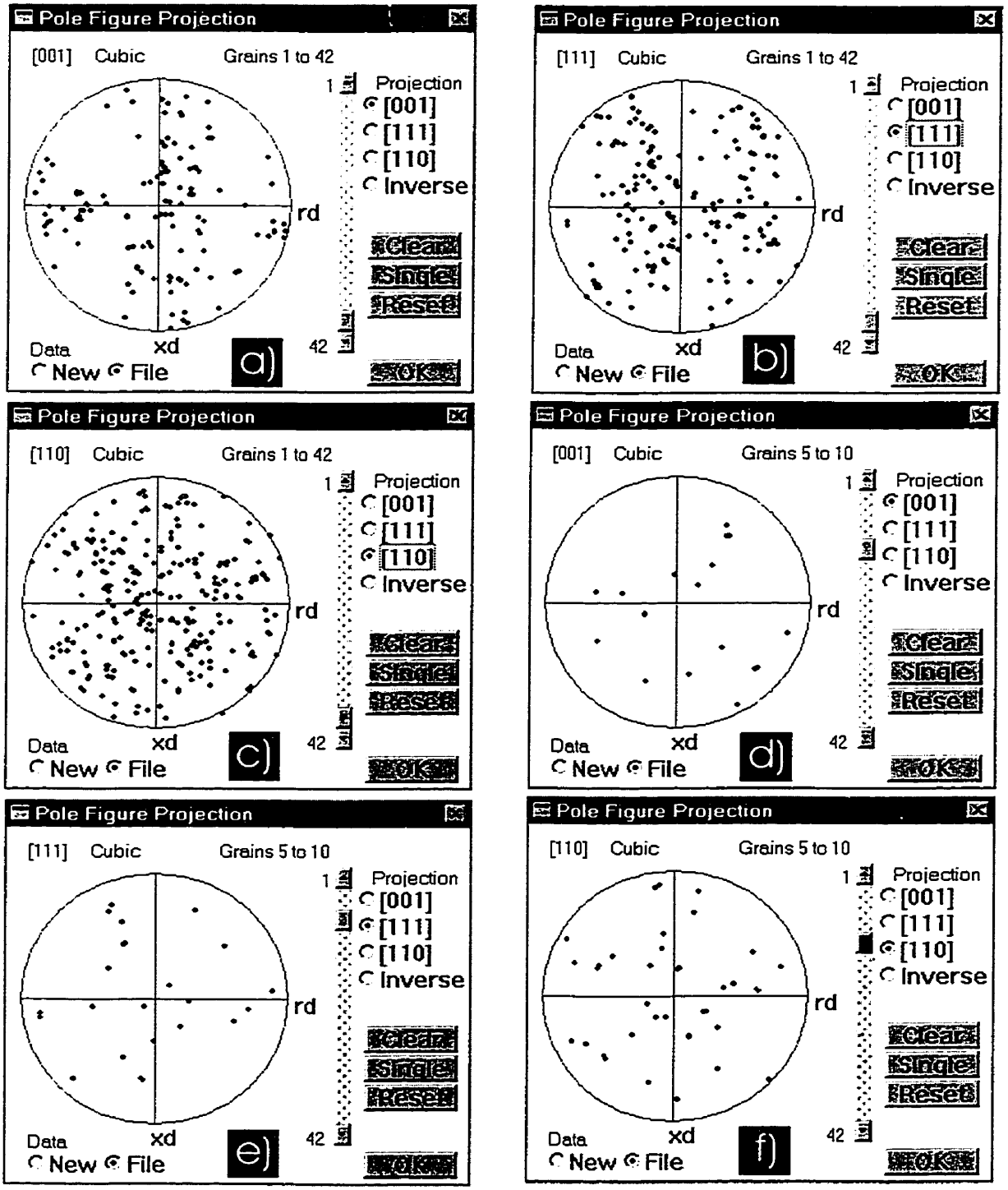

Figure 5.75 Pole figures for grains in the specimen of the 9Mn alloy tested at RT; a), b), and c) for all the grains measured; d), e), and f) for the fractured grains.

It is known that FCC metals usually have columnar grains with [100] normal to the mold wall [142]. The $L1_2$ titanium trialuminide specimens tested in this work comply with this general rule. In all the cases studied, the axis of columnar grains were parallel to [100] direction. This texture is clearly seen in Figs.5.72, 5.73 and G.5 where [001] projections are placed in a relatively narrow band at 90° to the rd-grains axis direction [100]. In the [111] projections the poles are located along a band at an angle 54° 44′ from the rd [100] direction.

The pole figures for the fractured grains no.5-10, 1-6, 1-7, 1-4, 1-8, and 43-47 are shown in Fig.5.75d,e,f and G.1- G.5 (d,e,f), respectively. The central portions of the fracture toughness beams (the fracture region) contained equiaxed grains and there was no texture present. Therefore, the equiaxed grains were randomly oriented. There were also many toughness specimens that contained columnar grains in the fracture region. However, these cases were not studied here.

The graphs already presented in Figs.5.49 and 5.50b show that toughness is independent of grain morphology. Since the EBSP studies have shown conclusively that columnar grains are strongly textured and equiaxed grains are randomly oriented, then one can conclude that there is no fracture toughness dependence on grain orientation.

Using grain orientation matrices, misorientation calculations of two (adjacent) crystals about their common axis were performed. Figures 5.76, 5.77, and 5.78 show the misorientation angle distribution for the grains whose boundaries were well etched (and thus the common boundaries of grains could be determined) of the specimens tested at RT, 200°C and 1000°C, respectively. It is seen that most of the boundaries are the high- angle grain boundaries.

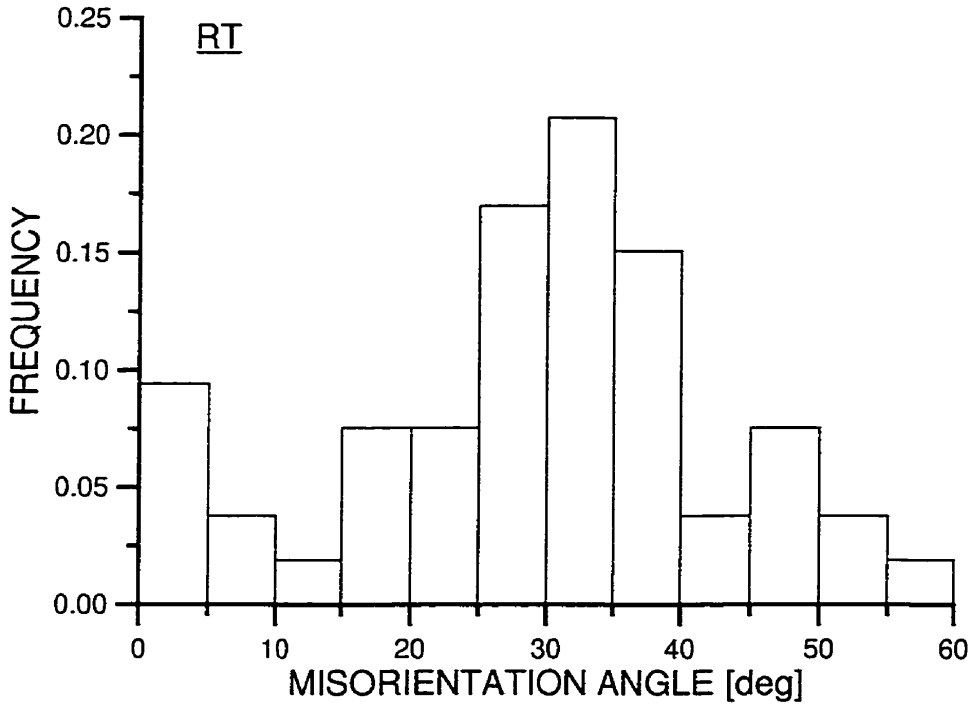

Figure 5.76 Misorientation angle distribution for the specimen of the 9Mn alloy tested at RT .

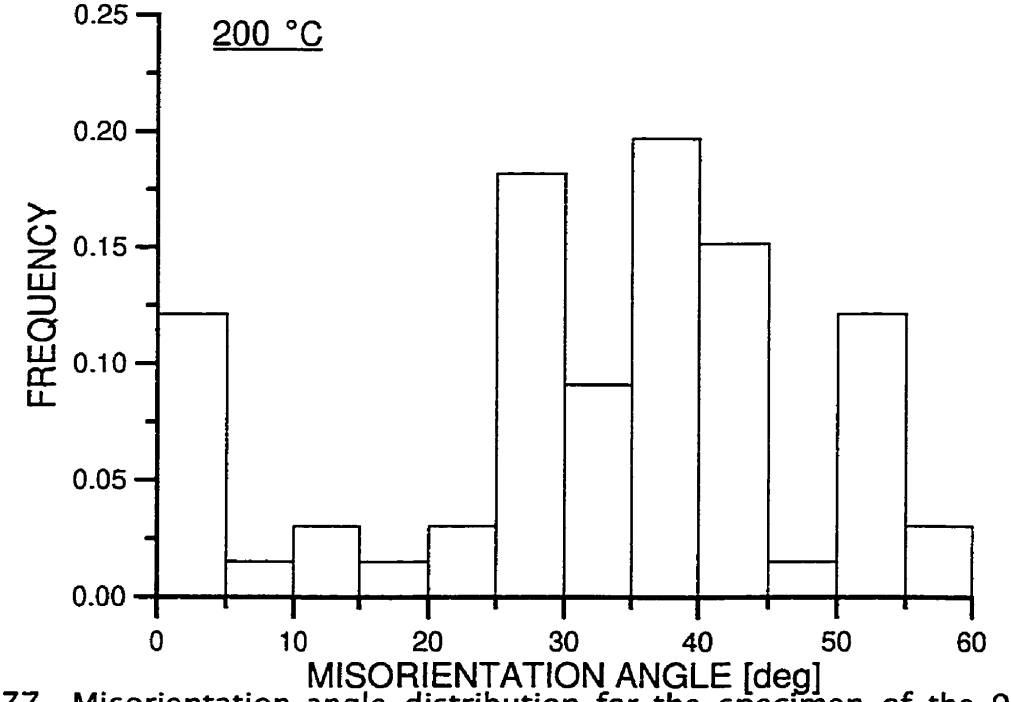

Figure 5.77 Misorientation angle distribution for the specimen of the 9Mn alloy tested at 200°C.

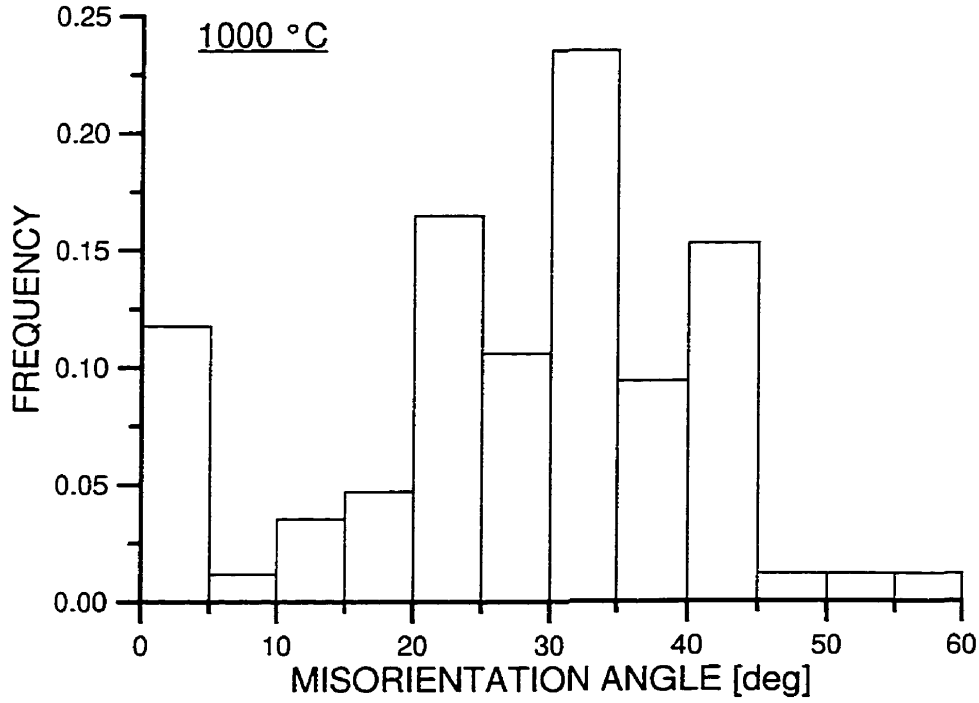

Figure 5.78 Misorientation angle distribution for the specimen of the 9Mn alloy tested at 1000°C.

5.6 The Effect of Boron and (Manganese + Titanium) Concentrations on Vickers Microhardness and Toughness

Table 5.6 shows the average microhardness values (HV2) of the alloys studied. The average microhardness of the high-(Mn+Ti) alloys is 50- 70% higher than their low-(Mn+Ti) counterparts. This increase in microhardness does not seem to be the result of boron doping. The 9Mn-type alloys having almost constant Ti concentration (≈25 at%) exhibit only a very small increase of hardness when doped with 0.25 and 0.66 at% B. Therefore, the higher hardness of boron-free and boron-doped 14Mn-type alloys might be the result of increasing Ti concentration, or a combined effect of Ti+Mn (this problem will be discussed later on).

Table 5.6 Vickers microhardness at 2000g load and the Ti concentration in the matrix (Table 5.2 in Section 5.1) of cubic trialuminide alloys.

Alloy	HV2 [kg/mm²]	Ti concentration in the matrix from Table 5.2 [at.%]
9Mn	163±4	24.7±0.2
9Mn-0.004B	164±6	25.5±0.1
9Mn-0.25B	170±3	25.0±0.2
9Mn-0.66B	171±4	25.1±0.5
14Mn	244±3	29.0±0.1
14Mn-0.24B	246±7	29.2±0.1
14Mn-0.65B	294±12	30.3±0.3

All the details relevant to fracture toughness testing of boron-doped alloys are given in the Appendix C. Table 5.7 shows the average CNB specimen dimensions (B and W) and spans (S_1 and S_2) for the alloys tested, compiled on the basis of data from Appendix C.

Table 5.7 Dimensions of CNB fracture toughness specimens.

Alloy	B [mm]	W [mm]	Span S1 [mm]	Span S2 [mm]
9Mn	4.8±0.2/4.8±0.2*	5.7±0.8/5.1±0.3*	25/16	9/4
9Mn-0.004B	5.8/3.8±0.3*	8.3/5.8*	25/16	4.5/4
9Mn-0.25B	4.5±0.2	5.7±0.1	25	4.5
9Mn-0.66B	4.5±0.1	5.4±0.5	25	4.5
14Mn	4.1±0.1/4.1±0.1*	4.1±0.1/5.1±0.1*	16/16	4/4.5
14Mn-0.24B	4.5±0.1	5.8±0.1	25	4.5
14Mn-0.65B	4.4±0.2	5.6±0.3	25	4.5

* Specimens with two sets of dimensions

As described in Section 5.2, a characteristic feature of the load (P)-load line displacement (LLD) curves for boron-free "base" 9Mn alloy up to about 800°C, was a linear behavior up to the maximum load (P_M) and then a sudden drop of the load. At room temperature (RT) this drop is essentially related to an unstable crack propagation and a catastrophic fracture of a specimen. However, at higher temperatures, a characteristic "tail" appears on the P-LLD curve after an initial crack pop-in (Figs.5.19a, no. 5 and 5.19b, no. 7). This indicates that the further crack extension is stable up to a final failure [138,143-146].

P-LLD curves for boron-free 14Mn specimens in the range from RT to ~400°C and most of 9Mn+B and 14Mn+B specimens regardless of test temperature, exhibited numerous crack pop-ins on the initial portion of the curve (examples are presented in Section 5.2). The occurrence of these pop-ins is essentially beneficial because they provide a very sharp crack tip, most probably sharper than the one formed from an initial notch slot. Curves for boron-free 14Mn alloy at temperatures >400°C showed no pop-ins, but relatively smooth and linear behavior up to P_M and a pronounced "tail" past P_M.

By analogy to ASTM E1304-97 on testing of chevron-notched bar and rod in tension, the conditional value of chevron-notch fracture toughness of boron-doped

alloys was calculated in a similar way as for boron-free alloys using the maximum load according to Eq.2.3 in Section 4.4.4. If a plane strain validity criterion $B \geq 1.25(K_{QVM}/\sigma_{YS})^2$ from ASTM E 1304-97 is met then $K_{QVM}=K_{IVM}$, the latter being "plane-strain chevron-notch (CN) fracture toughness".

Using the smallest specimen thickness $B \approx 4$ mm from Table 5.7 and the yield strength $\sigma_{YS} \approx 160$ MPa [28] for boron-free "base" 9Mn-25Ti alloys, one obtains valid CN fracture toughness values ≤ 9 MPam$^{1/2}$. Obviously, thicker specimen, e.g. 5.8 mm in Table 5.7 will have the higher validity limit ≈ 11-12 MPam$^{1/2}$. Since σ_{YS} of "base" 9Mn-25Ti alloys is practically independent of temperature, at least up to 950°C [28], then these validity criteria are essentially correct for the entire testing temperature range employed in this work. Furthermore, hardness of boron-free and boron-doped 14Mn-type alloys is higher than that of "base" 9Mn-25Ti alloys (Table 5.6). Therefore, their yield strength (not tested yet) would, most probably, be higher than about 160 MPa for "base" 9Mn-25Ti alloys. As a result, the plane-strain CN fracture toughness validity limit for 14Mn-type alloys would be much higher than the one estimated for 9Mn-25Ti alloys. Taking the above into account as well as the linear character of the P-LLD curves up to P_M, it is most likely that all the K_{QVM} values are indeed valid CN fracture toughness values (K_{IVM}).

Figures 5.79 and 5.80 show measured CN fracture toughness values (K_{QVM}) as a function of test temperature for boron-doped 9Mn-25Ti as well as for both boron-free and boron-doped 14Mn-type alloys, respectively. For comparison, the shaded bands represent the ranges of CN and SEPB fracture toughness data for coarse-grained, boron-free "base" 9Mn-25Ti alloys, replotted from Section 5.4.2. It is seen, that boron doping to the 9Mn-type alloy in the range 0.004-0.66at.%, improves room-temperature fracture toughness from about 4 MPam$^{1/2}$ to 5-6

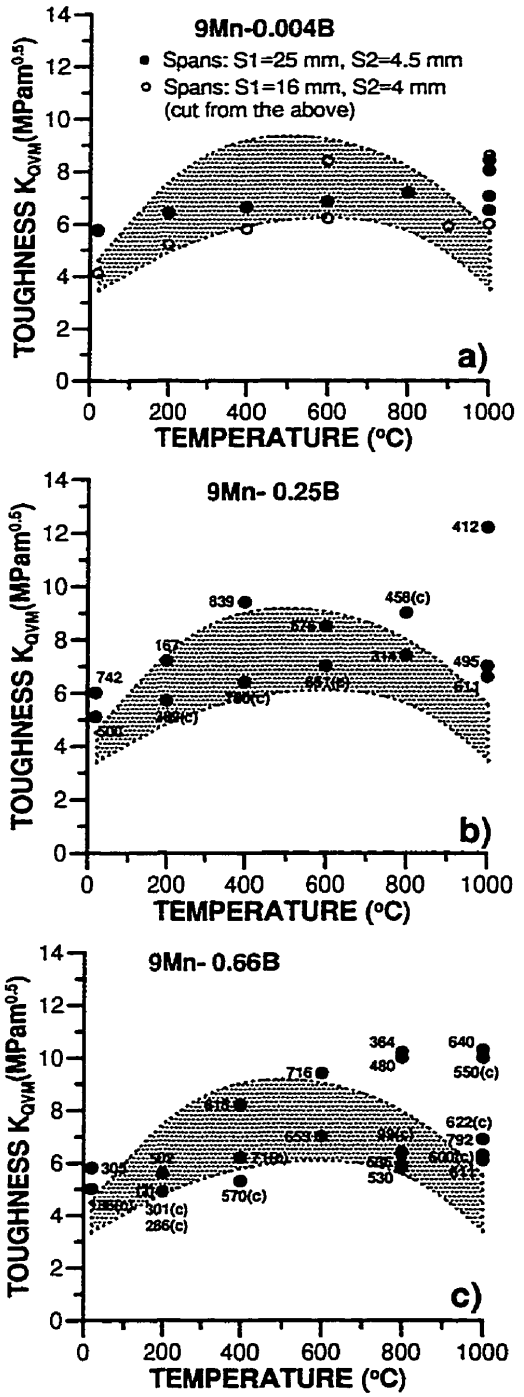

Figure 5.79 Chevron-notch fracture toughness of boron-doped 9Mn-type alloys as a function of temperature. (a) 9Mn-0.004B, (b) 9Mn-0.25B, and (c) 9Mn-0.66B. Number beside each data point shows grain size in μm (c-columnar). Shaded bands represent data ranges for boron-free 9Mn alloys replotted from Section 5.4.2.

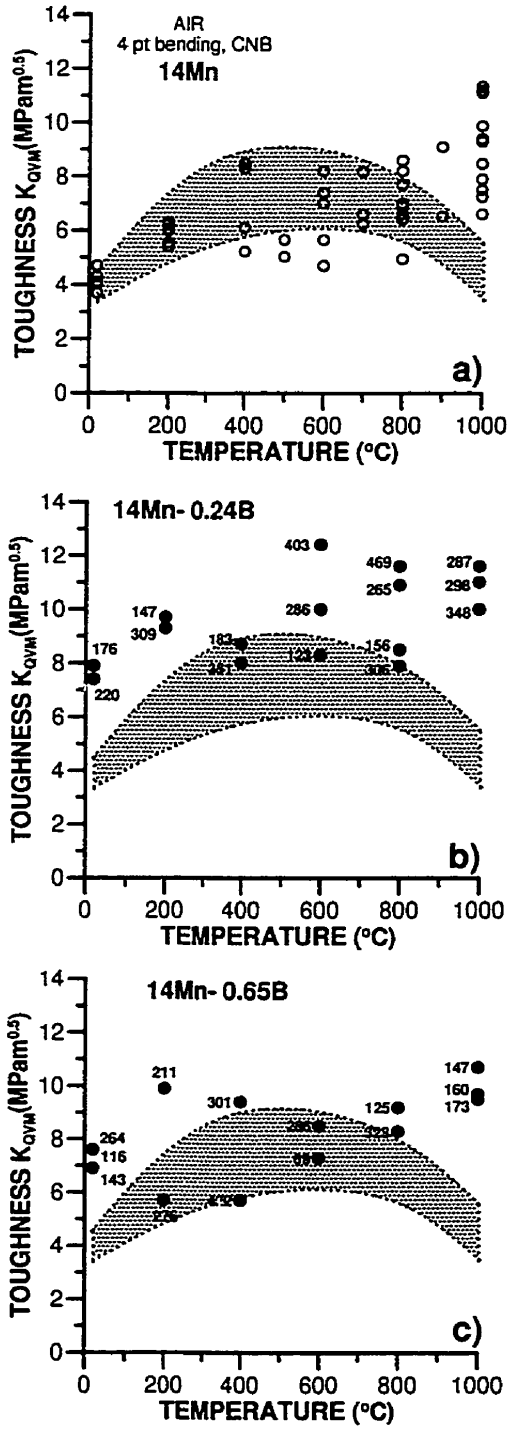

Figure 5.80 Chevron-notch fracture toughness of 14Mn-type alloys as a function of temperature. (a) Boron-free 14Mn, (b) 14Mn-0.24B, and (c) 14Mn-0.65B. Number beside each data point shows grain size in μm. Shaded bands represent data ranges for boron-free 9Mn alloys replotted from Section 5.4.2.

$MPam^{1/2}$, i.e. 25-50%. The fracture toughness in the intermediate temperature range (200-600°C) is essentially unchanged by boron doping (Fig.5.79). However, the fracture toughness at 1000°C is measurably improved by about 50-100% from about 4 $MPam^{1/2}$ to the range of 6-12 $MPam^{1/2}$, although quite a large scatter of results at 1000°C is still observed (Fig.5.79).

The most pronounced improvement of fracture toughness is observed for 14Mn-type alloys (Fig.5.80). Boron-free 14Mn alloys show increase of toughness at 1000°C to the range of 7-11 $MPam^{1/2}$ as compared to about 4 $MPam^{1/2}$ for "base" 9Mn alloys (Section 5.4.2). However, their toughness at room and intermediate temperatures is not improved. The alloys containing 0.24 and 0.65 at% B exhibit 100% improvement in the room temperature fracture toughness up to 8 $MPam^{1/2}$ without any pronounced scatter of data. Their toughness at intermediate temperatures and 800-1000°C is also improved to 8-12 $MPam^{1/2}$, i.e. by 100-200%, with much lower scatter than that for boron-free 14Mn alloy. In particular, a doping with 0.24 at% B seems to be an optimal level of doping. It results in the fracture toughness of 8 $MPam^{1/2}$ at room temperature with a minimal scatter of data, the 8-12 $MPam^{1/2}$ range for intermediate temperatures and about 10-12 $MPam^{1/2}$ at 800-1000°C (Fig.5.80b). The observed improvement of fracture toughness for 14Mn-29Ti-0.24B alloy in the entire test temperature range from room to 1000°C, is quite remarkable, taking into account that the alloy possesses an unoptimized, coarse- grained microstructure.

The number beside each data point in Figs.5.79 and 5.80 shows the average grain size of the tested specimen and a small letter "c" designates "columnar" grain morphology. As can be clearly seen, neither the grain size nor morphology

(equiaxed vs. columnar) affects fracture toughness. Similar observation was made for coarse- grained, boron-free, "base" 9Mn-25Ti alloys (Section 5.4.2).

Fracture mode observed in the present work changes from entirely transgranular cleavage (TGC) at room temperature to progressively more intergranular failure (IGF) with increasing temperature. Figures 5.81 and 5.82 show the variations of the surface area of IGF (measured on the projection of fractured surface) as a function of temperature (from data in Appendix F). The shaded bands represent the data ranges for boron-free "base" 9Mn-25Ti alloys replotted from Section 5.4.2. It is quite clear that the addition of boron to 9Mn-25Ti alloys (Fig.5.81) does not alter in any measurable way this behavior observed for boron-free "base" 9Mn-25Ti alloys as shown in Section 5.4.2. Other researchers observed the same fracture mode transition from TGC to IGF with increasing temperature in both tension [4,14] and bending [49,147] in cubic titanium trialuminides. As can be seen in Fig.5.81 for boron-doped 9Mn-25Ti alloys, the transition temperature from TGC to IGF (TGC/IGF transition temperature or "TGC/IGF TT" in short) begins at about 200°C and then the fraction of IGF increases gradually with increasing temperature, as also reported for boron-free "base" 9Mn-25Ti alloys in Section 5.4.2. On the other hand, Fig.5.82 shows that there is a substantial effect of high-(Mn+Ti) concentrations in 14Mn-type alloys on the TGC/IGF transition. First, the TGC/IGF TT is shifted towards much higher temperature of about 600°C. Second, the surface fraction of IGF for boron-free 14Mn alloy is substantially reduced at the high temperature ranges 600-1000°C (Fig.5.82a). At 1000°C the IGF surface fraction is only 40-50%, i.e. a half of that for a boron-free "base" 9Mn-25Ti alloy. Third, the boron doping to 14Mn-type alloys seems to increase slightly the IGF fraction but it does not shift the TGC/IGF TT which is still at around 600°C (Fig.5.82b,c).

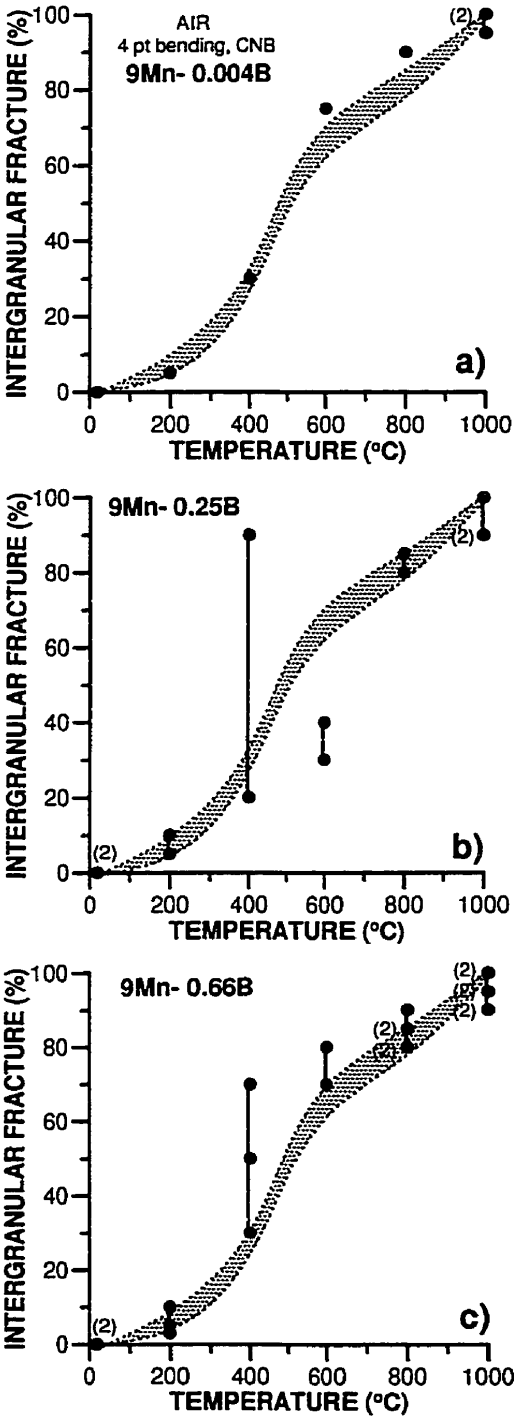

Figure 5.81 Surface fraction of intergranular failure of chevron-notched (CN) specimens for boron-doped 9Mn-type alloys as a function of temperature. (a) 9Mn-0.004B, (b) 9Mn-0.25B, and (c) 9Mn-0.66B. Shaded bands represent data ranges for boron-free 9Mn alloys replotted from Section 5.4.2.

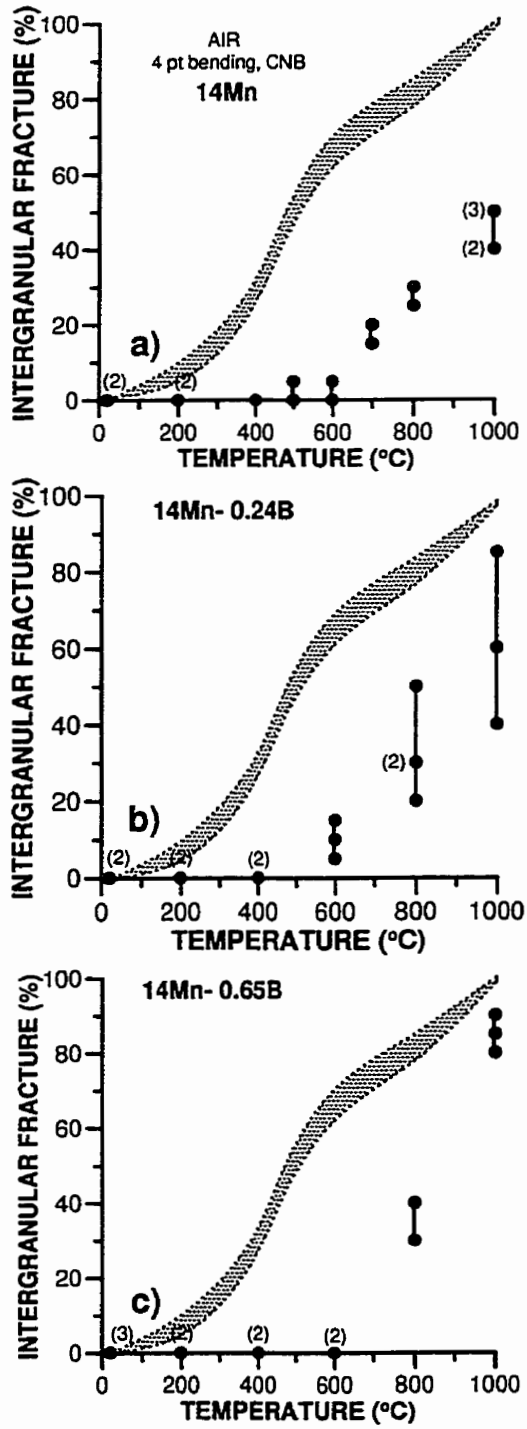

Figure 5.82 Surface fraction of intergranular failure of CN specimens for 14Mn-type alloys as a function of temperature. (a) boron-free 14Mn, (b) 14Mn-0.24B, and (c) 14Mn-0.65B. Shaded bands represent data ranges for boron-free 9Mn alloys replotted from Section 5.4.2.

Examples of fractographs of 14Mn alloy tested at RT and 1000°C are shown in Fig.5.83. Pictures (a) and (b) show the extensive crack branching at RT and pictures (c) and (d) the oxidation at 1000°C. It can be seen in picture (c) that cleavage crack resumed at discrete points along the grain boundary.

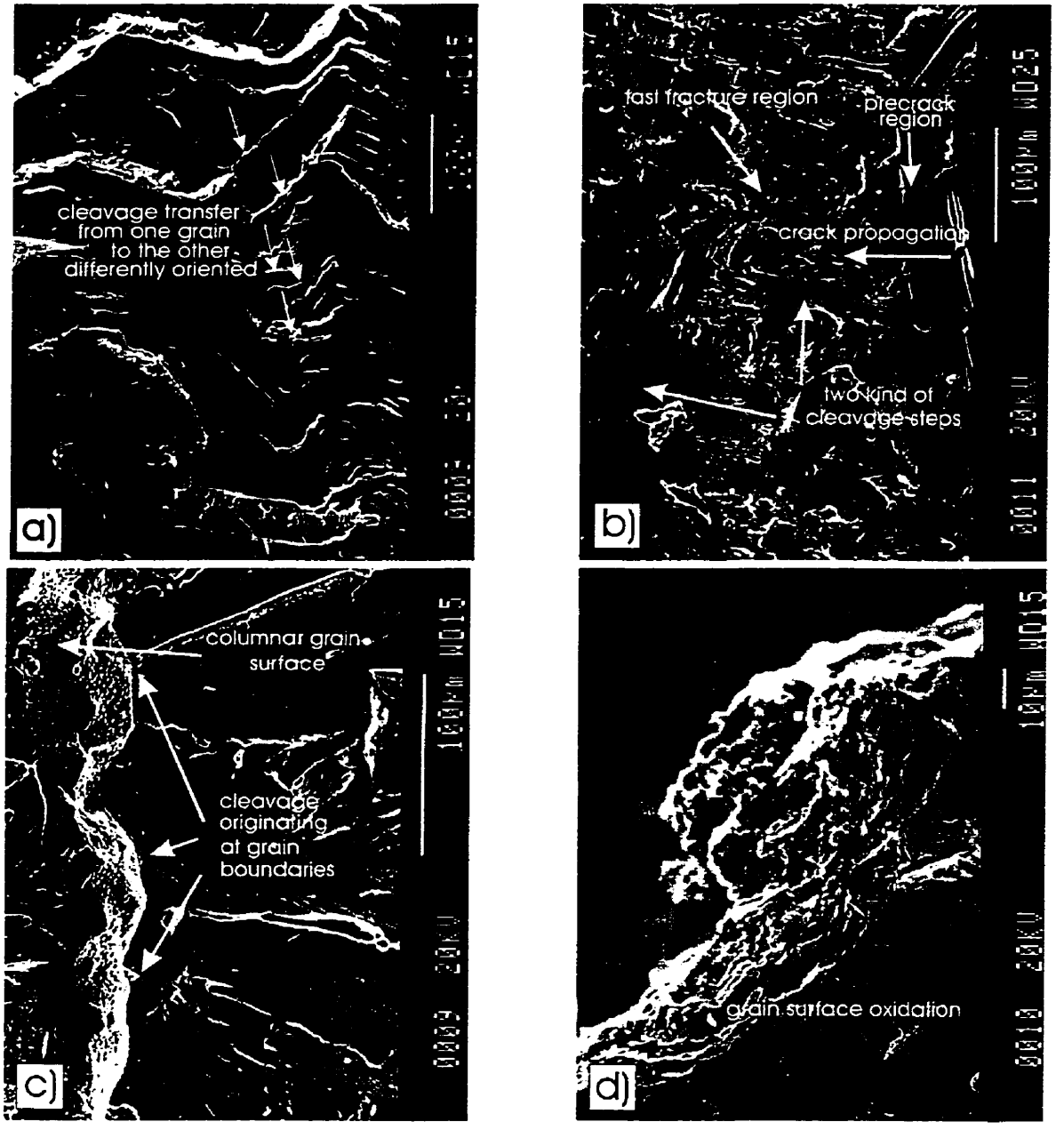

Figure 5.83 High- Mn alloy (14 at.% Mn) tested at: a) and b) RT (100% transgranular failure), c) and d) 1000°C (combination of ~50% transgranular and ~50% intergranular fracture).

5.7 Observation of Surface Cracks

This section describes in a pictorial way the characteristic features of cracks formed on the sides of the SEPB specimens made from low-Mn ("base" 9Mn-25Ti) alloy. Specimens were polished before the precracking procedure. This sequence of specimen preparation allows all the features formed during precracking and in some cases during further crack extension to be preserved, photographed and analyzed. Three techniques were used for analysis. Optical microscopy with Nomarski contrast was used to photograph the precracks. Scanning Electron Microscopy (SEM) was used to perform in- situ straining of the precracked specimens, observe and photograph the crack tip response. Finally, at the highest resolution level, Atomic Force Microscopy was used to obtain digital topology of the very tip of a precrack.

Many precracks shown in this section are not of good quality since they are formed at an angle to the notch instead of straight ahead of it. However, the quality of the precracks in the SEPB specimens used for fracture toughness testing was much better. The latter specimens were precracked in a high-precision jig using ceramic inserts as supporters. These inserts were accidentally damaged after all the toughness tests were done. Therefore, the SEPB specimens used in this section for precracks observations were obtained in the jig using less precisely finished tool steel supporters.

5.7.1 Optical Microscopy of Precracks in SEPB Specimens

First image of each precrack presented is a top, overall view of the precrack. A letter beside each window in such an image designates the picture label which is a high magnification optical image.

In Fig.5.84, precrack originated not from the notch root but from the opposite side of the specimen. It is the only observed case of such anomaly. However, in this case, a very extensive plastic strain field in the form of slip lines is present at the

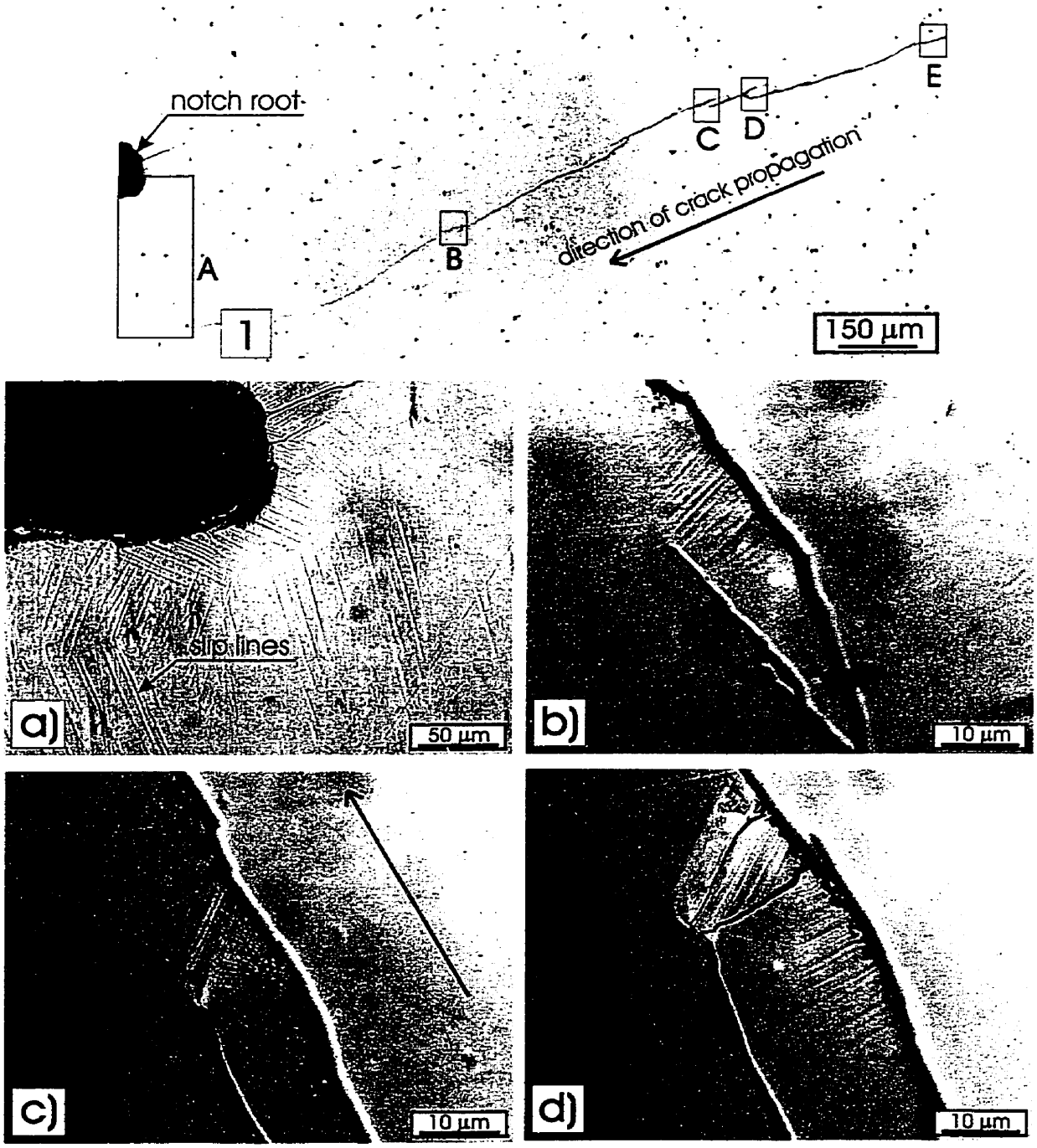

Figure 5.84 Plastically deformed regions of the branched precrack. 9Mn–25Ti alloy.

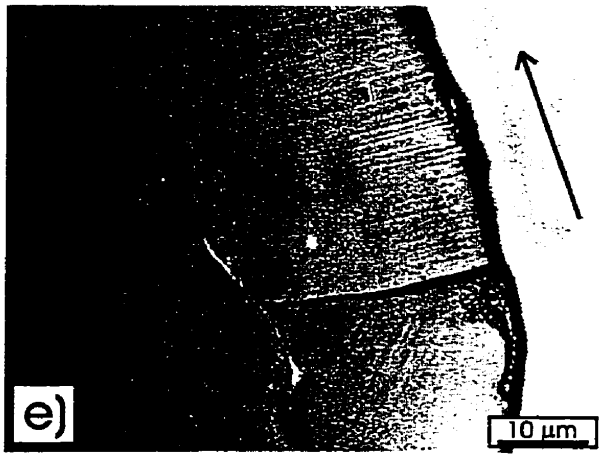

Figure 5.84 Contd.

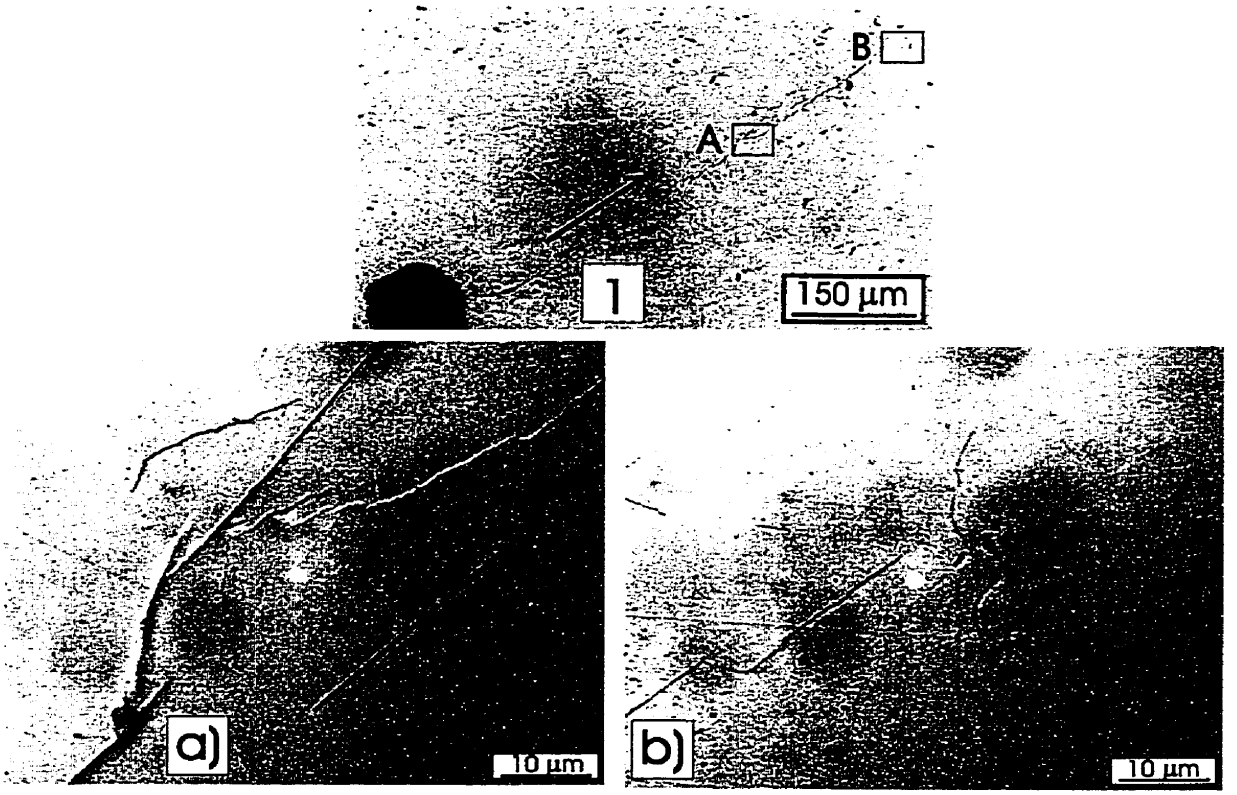

Figure 5.85 a) Very limited plastic deformation developed at the end of stopped crack and the beginning of the resumed crack, b) no surface deformation noticeable at the tip of the precrack. 9Mn–25Ti alloy.

notch root. It spreads from the notch root and also from the side of the notch towards the end of precrack (window A). Almost always where there was some crack branching along the path of a main crack some extent of plastic deformation was taking place. In most cases it was very difficult to see beside the slip lines also the

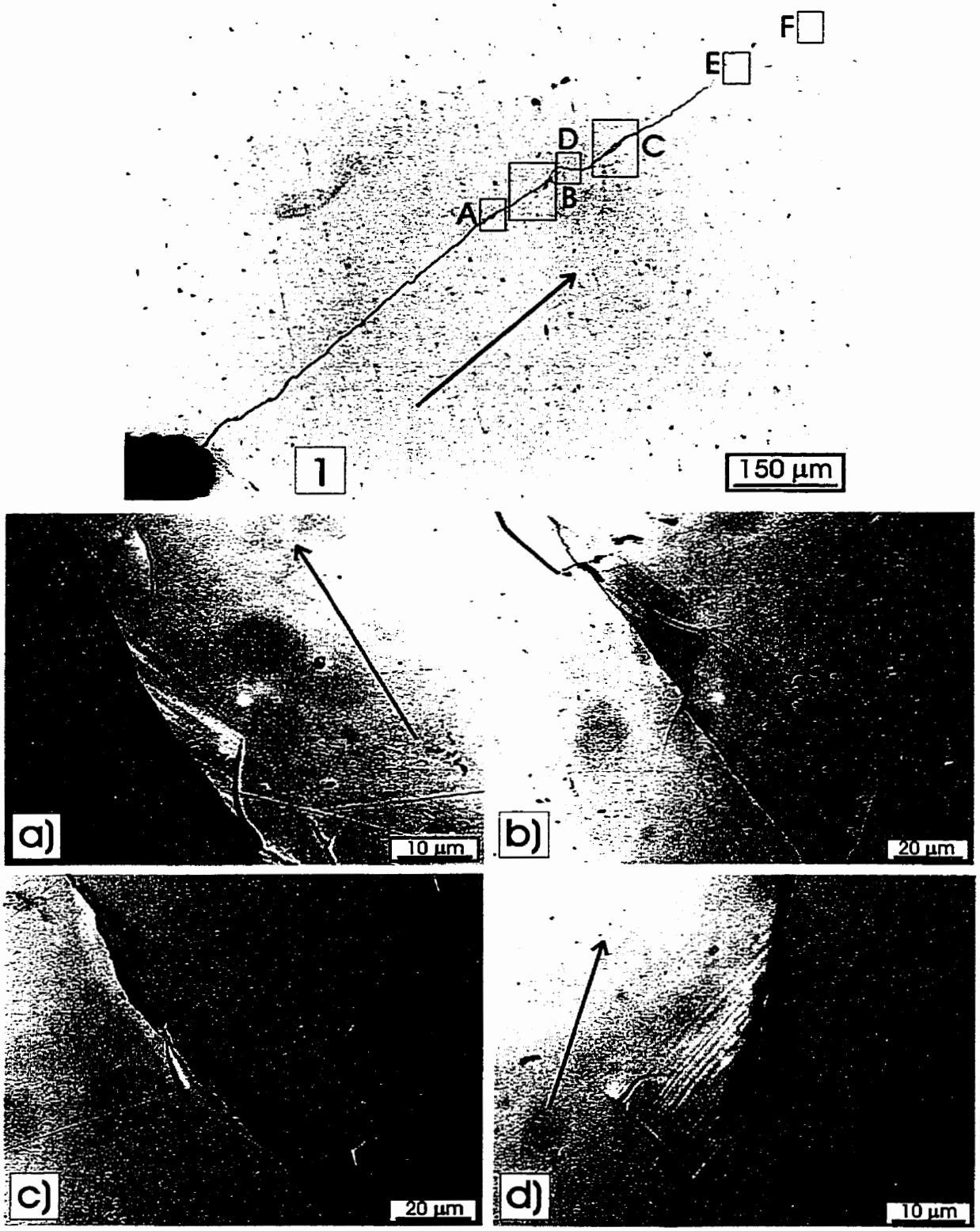

Figure 5.86 a), b), d), and e) Deformation transfer between branches of the precrack, c) deformed region between stopped and resumed precrack, f) small deformation at the very crack tip. 9Mn–25Ti alloy.

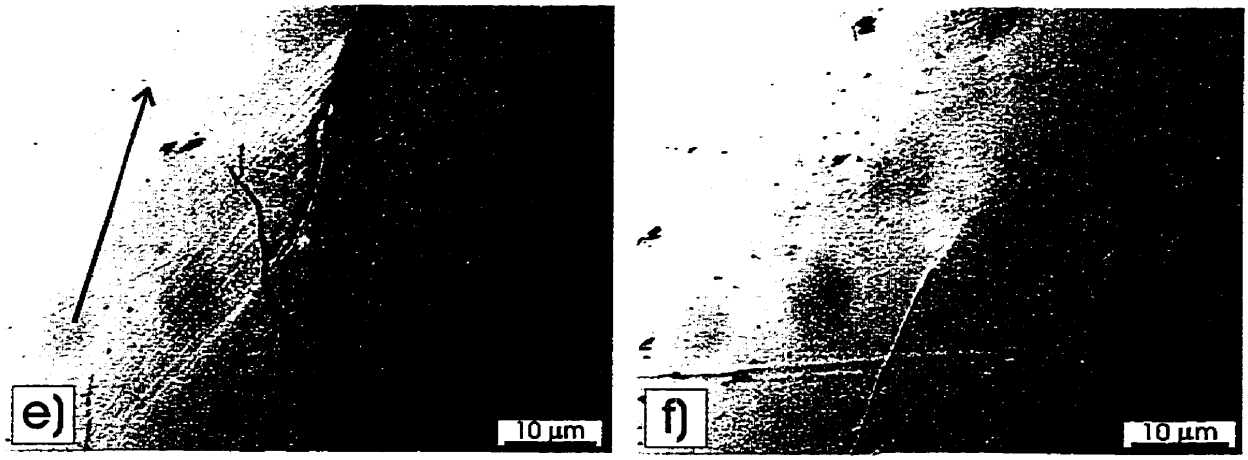

Figure 5.86 Contd.

surface topography. However, playing with the illumination (light direction and polarization) sometimes revealed the topography. Good examples are shown in Fig.5.84c and d where the surface deflection at the tip of a branched crack can be easily noticed.

On many occasions, the crack tips did not show any noticeable plastic deformation (Fig.5.85) or very little deformed regions as in Figs.5.86f, 5.87c, and 5.88c where plastically deformed front is confined to a very narrow band ahead of crack tip.

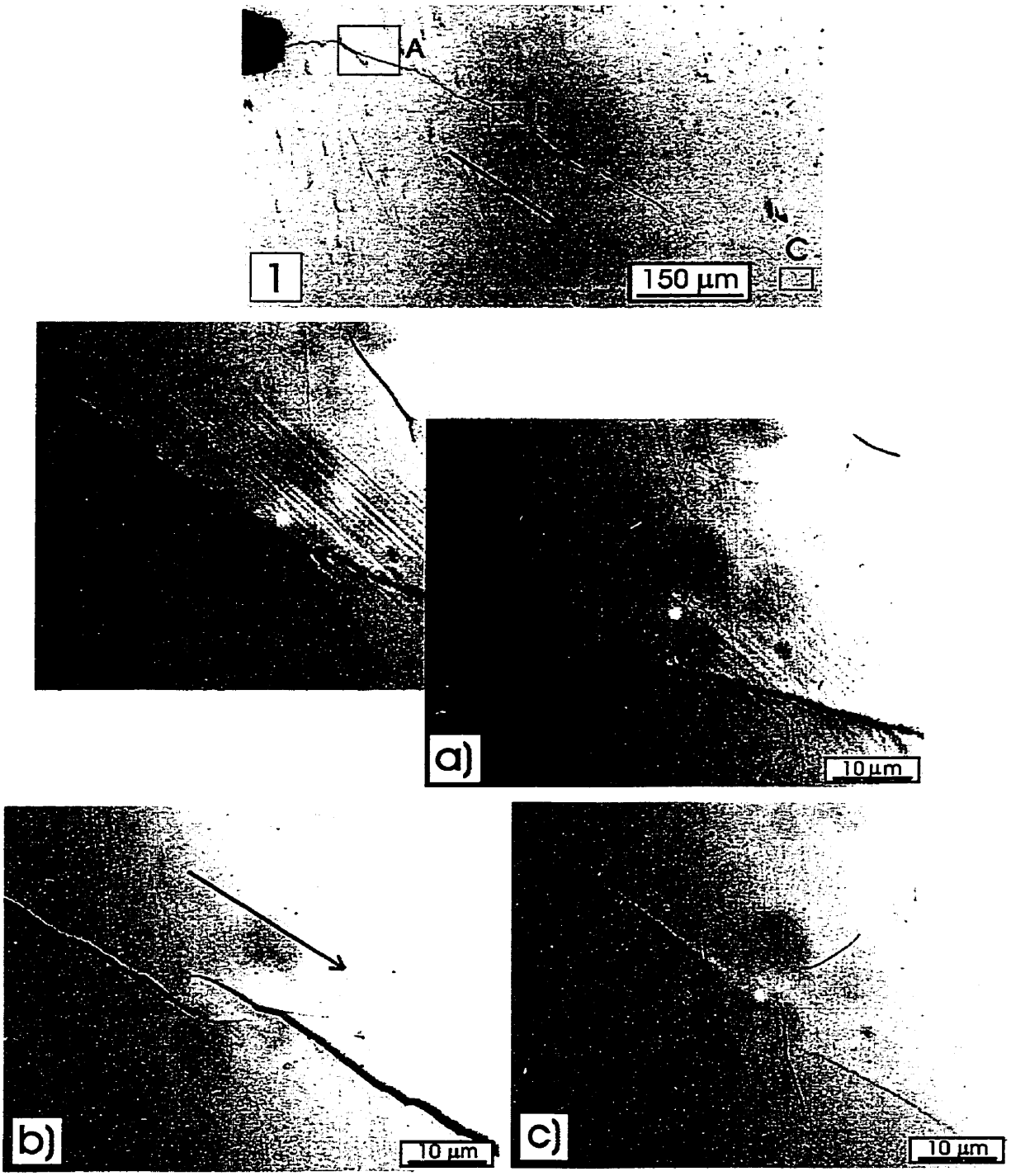

Figure 5.87 a) Very extensive plastic field between main crack and its branch, b) extremely small deformation at the tips of two parallel cracks, c) small deformation at the tip of the main crack. 9Mn-25Ti alloy.

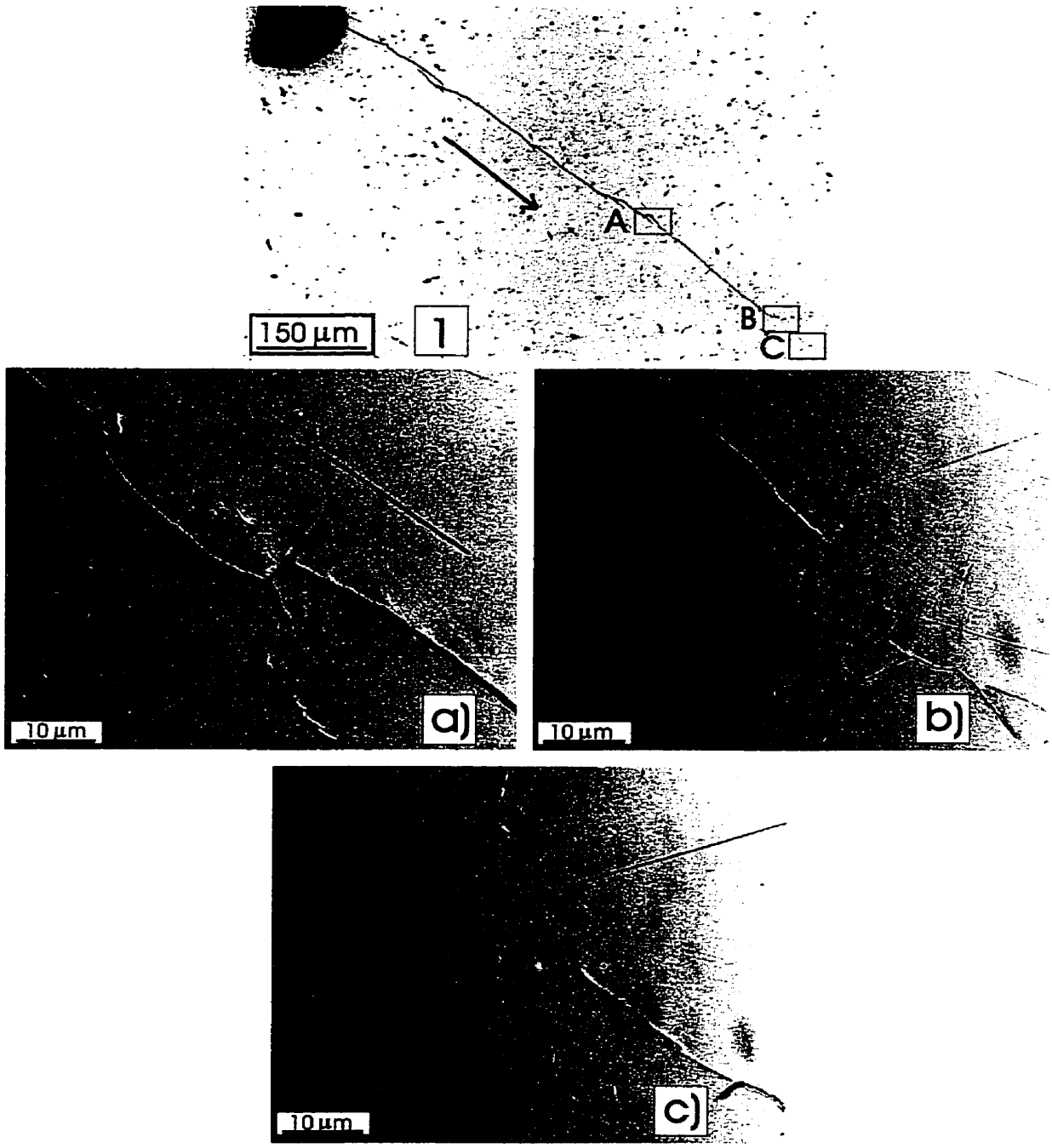

Figure 5.88 a) and b) Plastic deformation between main crack and a branch, c) small plasticity developed at the tip of the main crack. 9Mn-25Ti alloy.

Only one specimen among 16 tested showed extensive plasticity developed at the crack tip (Fig.5.89b). Interestingly enough, the same crack did not develop any plastic deformation at the tip on the other side of the specimen.

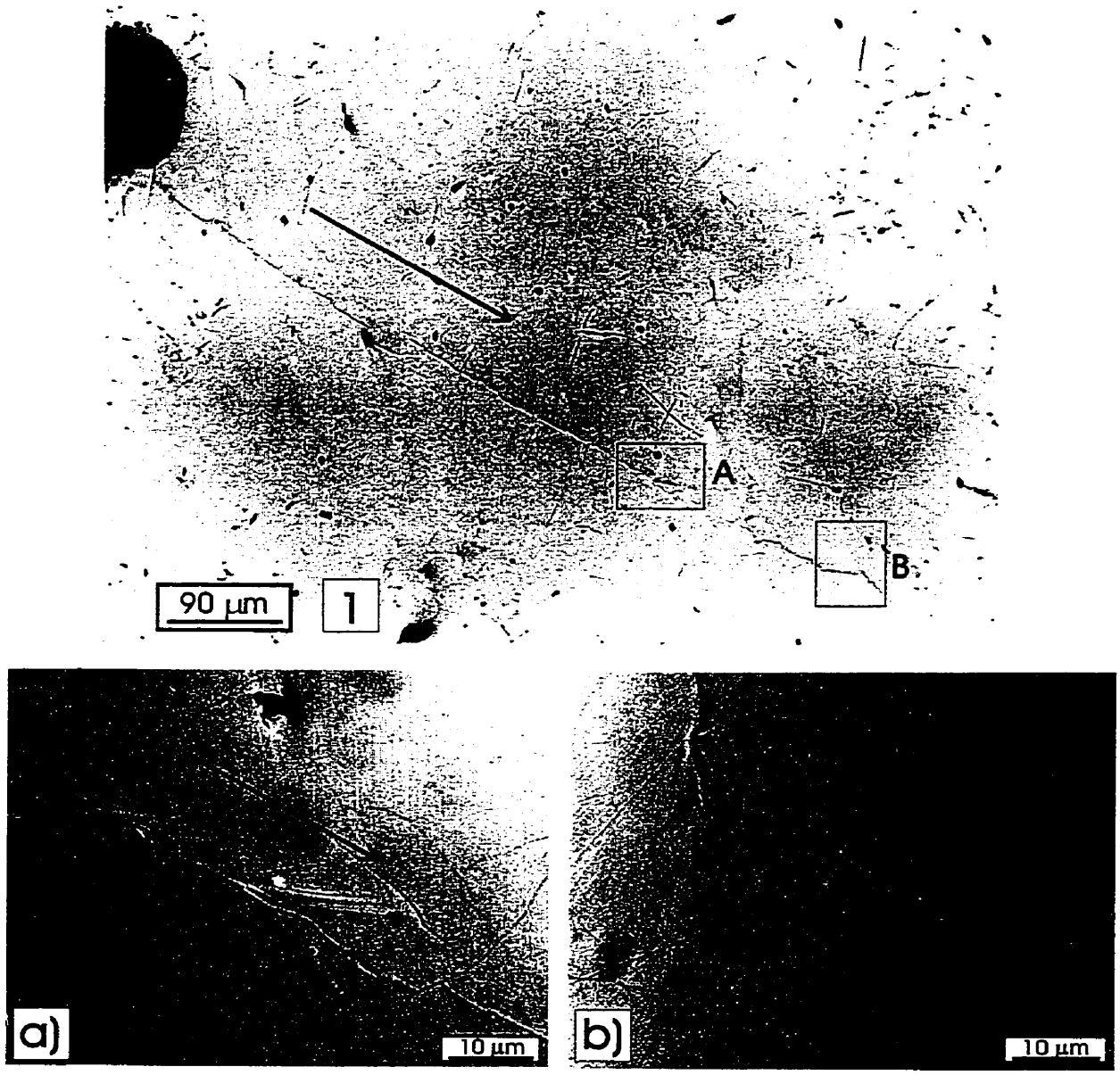

Figure 5.89 Symmetrical slip lines in the vicinity of the straight, main crack (very rarely occurring), b) extensive plasticity developed at the very crack tip. 9Mn-25Ti alloy.

There are various patterns of slip lines configurations lying in the close vicinity of branched cracks or cracks deviating from their paths. Sometimes these lines are perpendicular to the parallel cracks (Fig.5.84a in the vicinity of the precrack, and Fig.5.84b and d), and in other cases they are inclined ~45° (Fig.5.84a in the vicinity of the side of the notch, and Fig.5.84c and d). Still in some other cases these lines

were either parallel to the crack propagation direction or inclined at some angle (Figs.5.86, 5.87a, 5.88a,b, 5.89, H.1b, and H.2). It seems that in general, the inclination of the slip lines depends among other parameters on the relative crack velocities and interaction between dynamic strain fields of the moving cracks. Worth noting is the fact that if not disturbed (by crack branching or changes in path), the slip lines are symmetrical about the straight crack and inclined to it at an angle ~30- 35° (Figs.5.89a and H.2b). In effect, these lines are not included in the maximum shear stress planes on which the dislocation activity is being promoted. However, to be closer to correct interpretation, 3D geometrical analysis would be required with consideration of possibly high elastic anisotropy of the material.

5.7.2 Scanning Electron Microscopy of Precracks in the Pre- Strained SEPB Specimen

One precracked SEPB specimen of boron-free "base" 9Mn-25Ti alloy was strained in the small jig (Fig.4.15) in 3pt. bending to four different levels. After each strain increment the specimen mounted in the jig was placed into the SEM and the crack tip was photographed (Figs.5.90-5.93).

Plane stress plastic deformation zone shown in Fig.5.90a and b was formed during precracking procedure. Tearing ligaments became visible in the first stage of loading. The very tip of the crack was still obscure. The result of second stage of loading was formation of the crack extension trace (Fig.5.91). During third stage, the plane stress plastic zone became more round in shape with more pronounced boundary (Fig.5.92). The Crack Opening Displacement became larger. No noticeable changes were occurring to the very tip. However, at the third stage, the tiny and short lines in the tip region started to appear. As became obvious in the last stage of loading, these were microcracks scattered around the end of the main crack

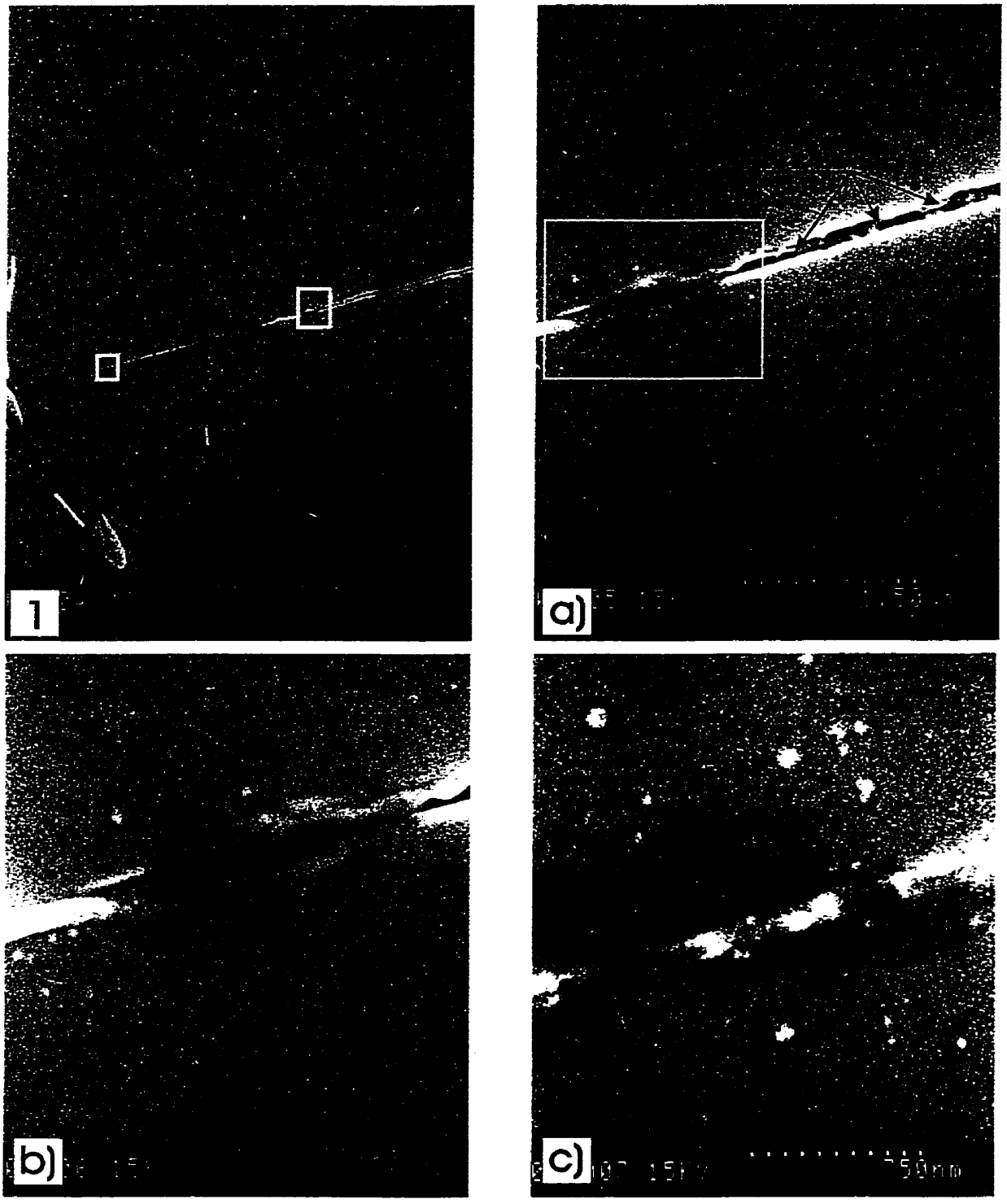

Figure 5.90 The tip of the crack in the first stage of straining.

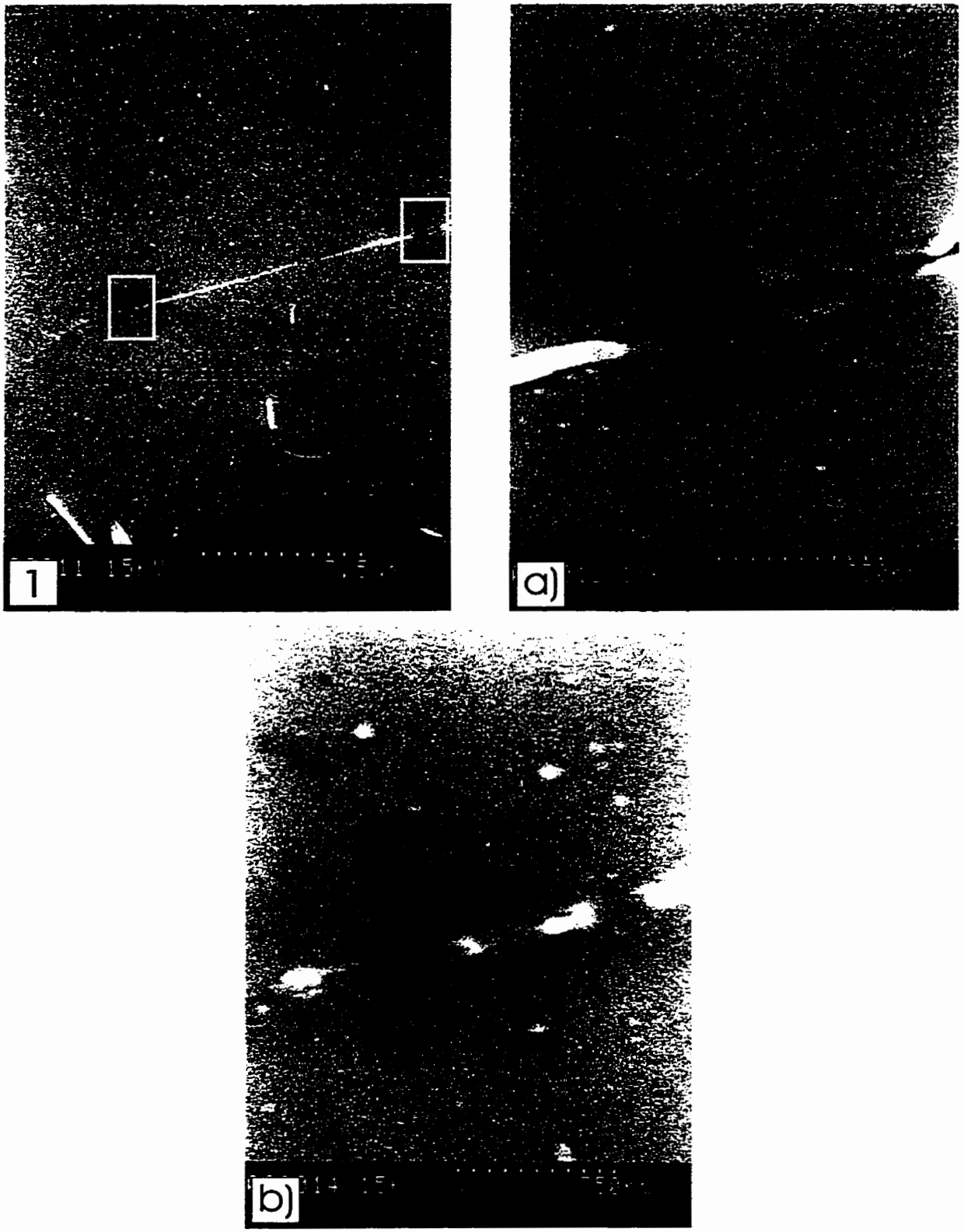

Figure 5.91 Second stage of straining.

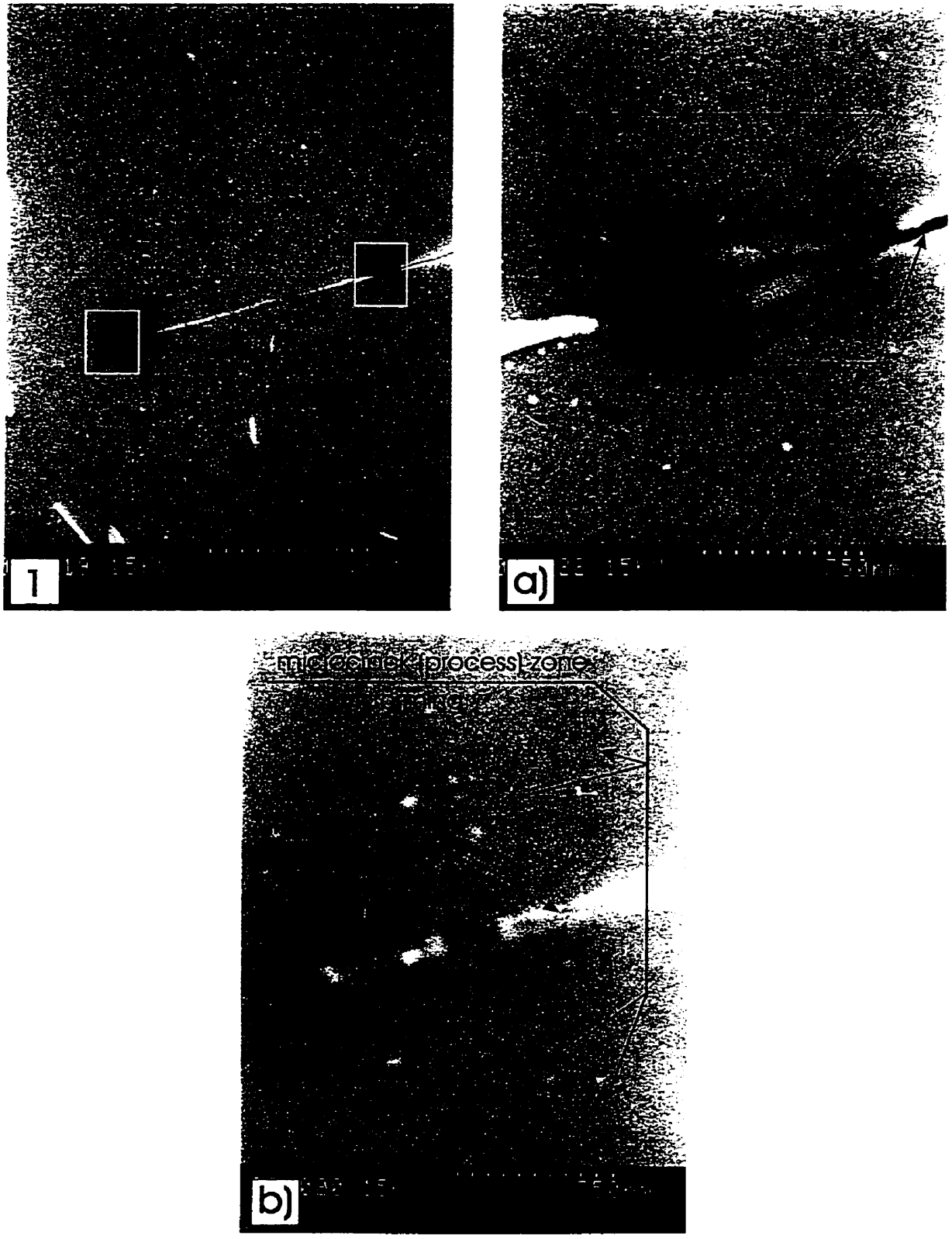

Figure 5.92 Third stage of straining.

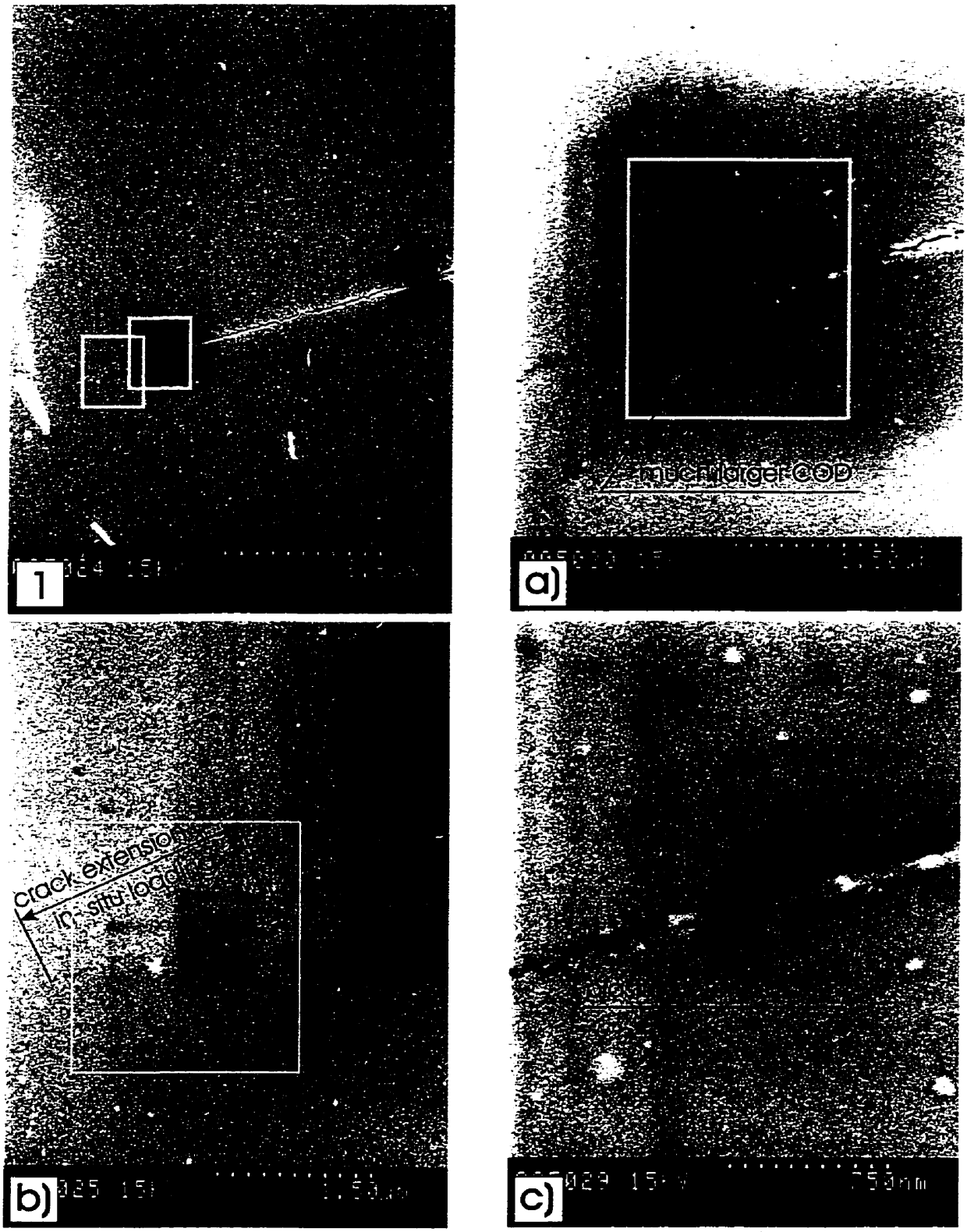

Figure 5.93 Fourth and final stage of straining.

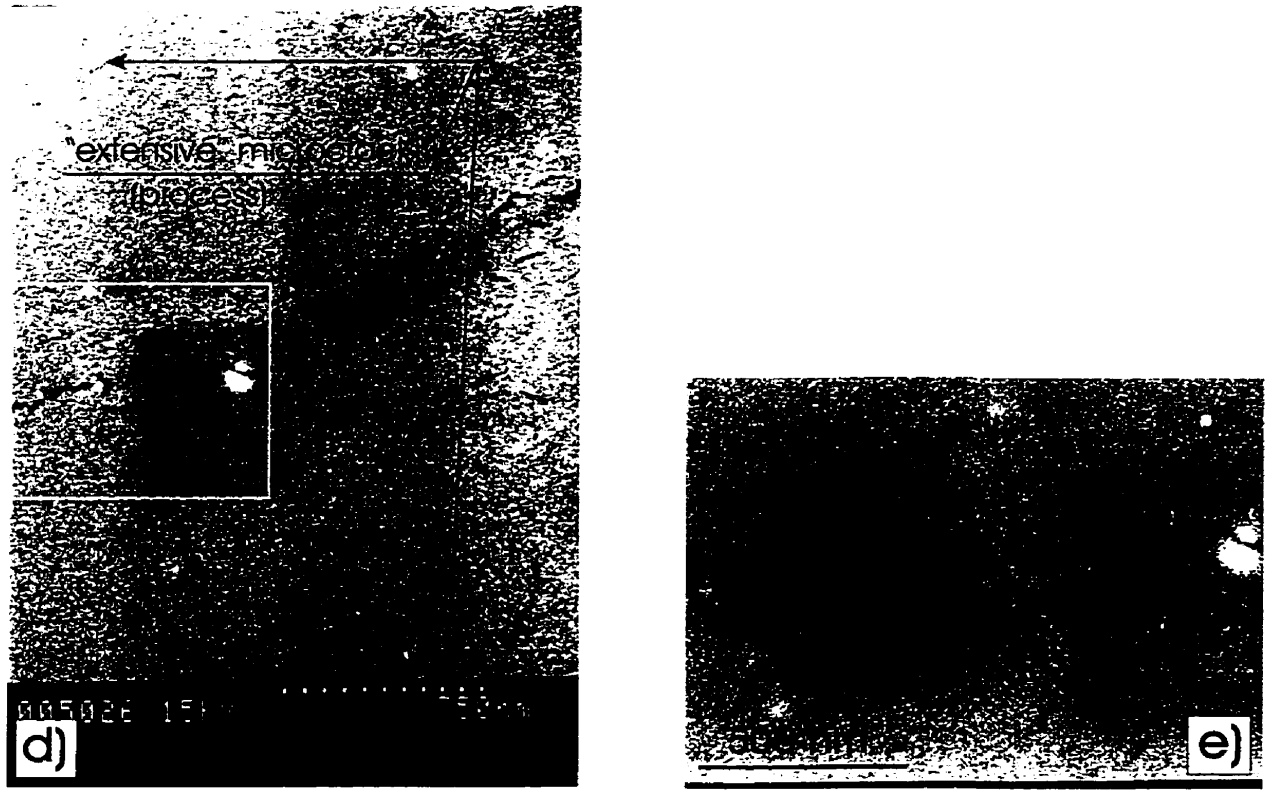

Figure 5.93 Contd.

(Fig.5.93d,e). The COD became larger once again and most importantly the crack propagated forward a small amount. The most striking feature of this crack extension and of the whole experiment was the appearance of the extended crack. It was very wavy in shape, spread at least into two branches and surrounded by the network of microcracks. It is difficult to seek for any rationale explaining this behavior, especially in the light of so many pictures showing the plastic deformation formed along the crack path. Obviously, there is a difference in magnification scale between optical and SEM pictures and moreover the slip lines or plastic deformation are difficult to notice unless observed at low angles but still it is unlikely that this kind of crack propagation could be accompanied by some plastic deformation. The microcrack process zone is known to shield or release the far field stresses at the crack tip. This phenomenon usually occurs in such brittle materials like ceramics or rocks. It is not known how much shielding could be

achieved in the experiment presented here. It is even not known whether there is an increase or degradation in toughness. Roughly it could be assessed considering the relative extent of the zone and the crack size (and microcrack density) and also taking into account the remaining ligament length. By comparing to the results of [148] on ceramics composite, most probably there is some toughness enhancement through this mechanism of fracture. Fig.5.94 shows the enormous bridging in ceramic material developed at 1500°C (this amount of bridging resulted obviously in toughness degradation). At lower temperature (~1200°C) this zone was substantially smaller and caused toughness increase.

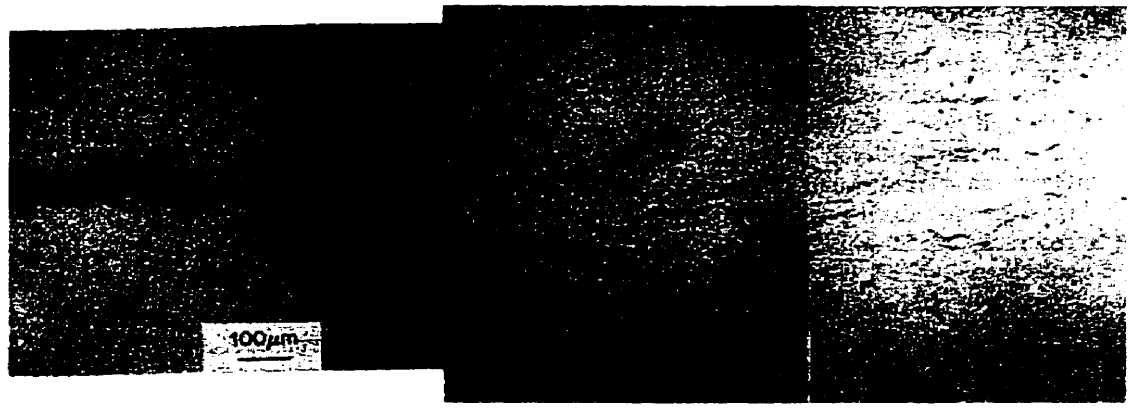

Figure 5.94 Extensive crack bridging causing toughness degradation in ceramic composite (formed at very high temp. ~1500°C). [148]

The other example of crack extension imaged in SEM is shown in Figs.5.95a and b. This time the extended crack is straight and again there is no noticeable plasticity accompanying the process. Very similar image (Fig.5.95c) was obtained for another very brittle intermetallic compound NiAl exhibiting toughness of ~2 MPa$\sqrt{m}$ [149]. SEM image of the extensive plasticity ahead of the crack tip formed during precracking procedure of "base" 9Mn-25Ti alloy is shown in Fig.5.96. The same tip is shown in optical photograph in Fig.5.89b.

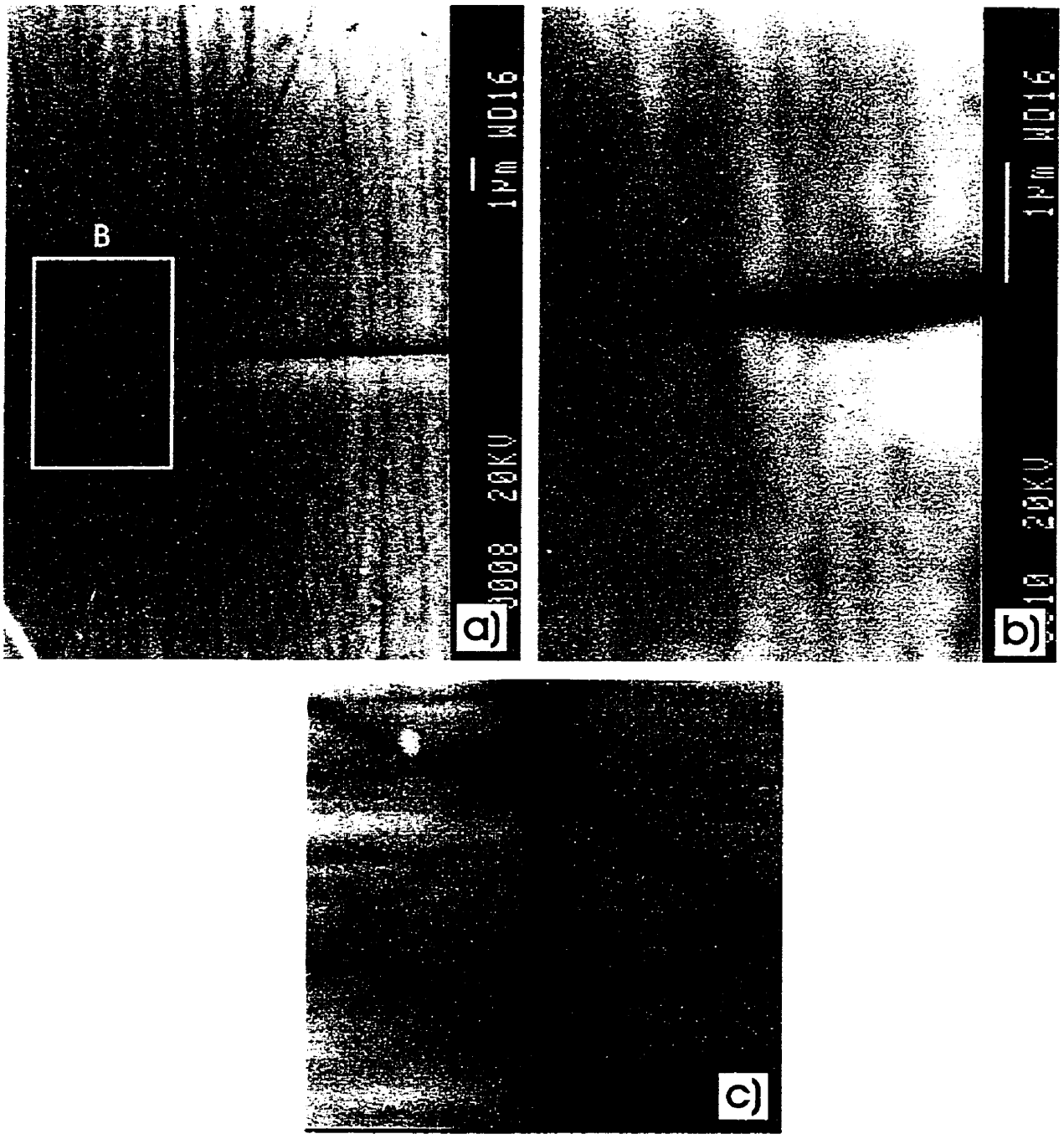

Figure 5.95 a) and b) Crack extension obtained in this study, c) in NiAl [149].

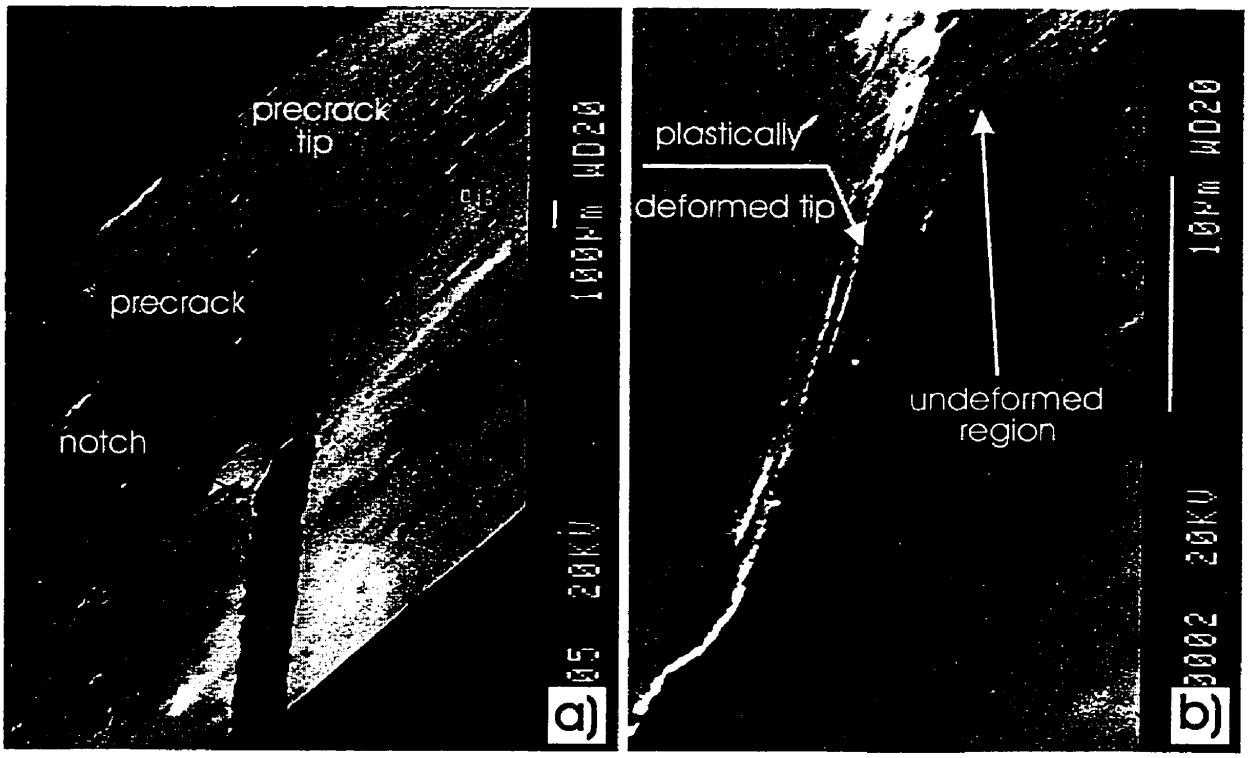

Figure 5.96 Extensive plasticity formed during precracking. "Base" 9Mn-25Ti alloy.

For the purpose of comparison, Fig.5.97 shows the surface deformation at the crack tip in Ni_3Al and Ni_3Al + B [35]. It represents plane stress deformation zone. The entire zone is plastically deformed in contrast to titanium trialuminide where the plastic deformation also extends in front of the crack but it is confined to plastically deformed, parallel bands leaving some regions undeformed.

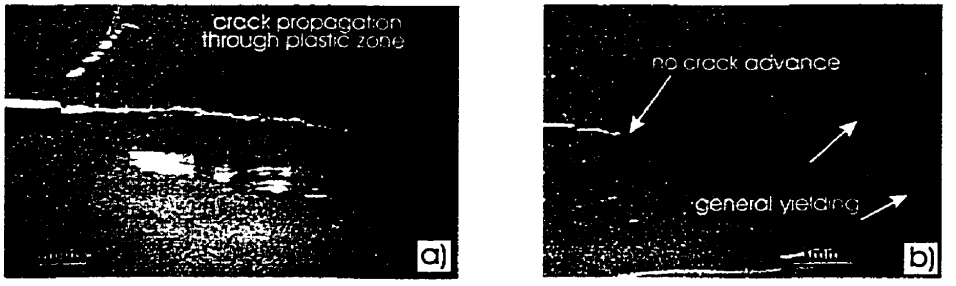

Figure 5.97 Surface deformation at the crack tip in: a) Ni_3Al; b) Ni_3Al + B [35].

5.7.3 Atomic Force Microscopy Digital Imaging of a Crack Tip

The AFM is a very powerful tool in imaging. It could be used very successfully in the in- situ fracture experiments. The stress intensity can be applied to the crack tip in a remotely controlled manner using a piezoelectric stage. The instantaneous crack tip response can be scanned, digitized and stored in a computer memory. This kind of an experiment can serve to establish the relationship between the applied stress intensity and the number of dislocations emitted from the crack tip [149]. An example of the AFM image of the crack tip in NiAl intermetallic alloy is shown in Fig.5.98.

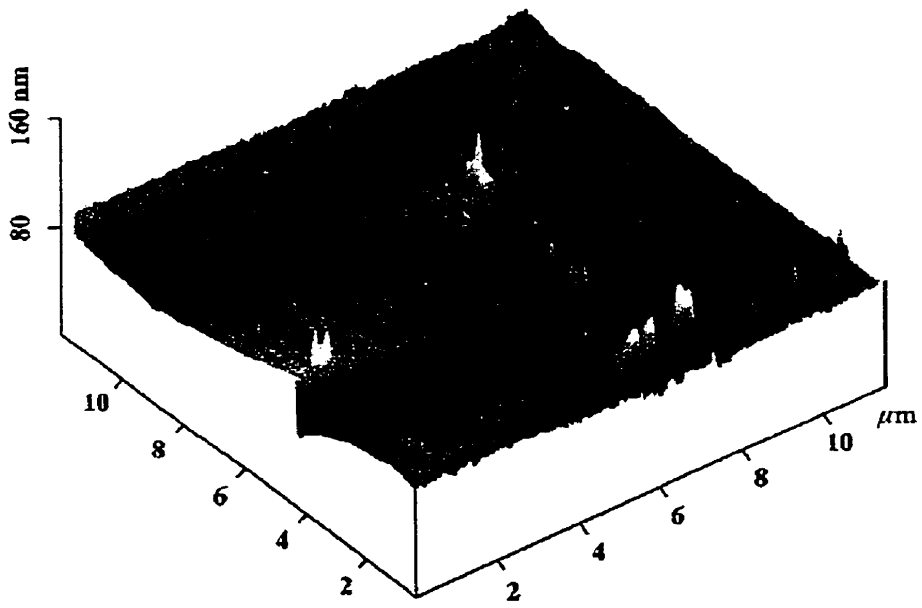

Figure 5.98 AFM crack tip image obtained in the in- situ straining on NiAl intermetallic alloy [149].

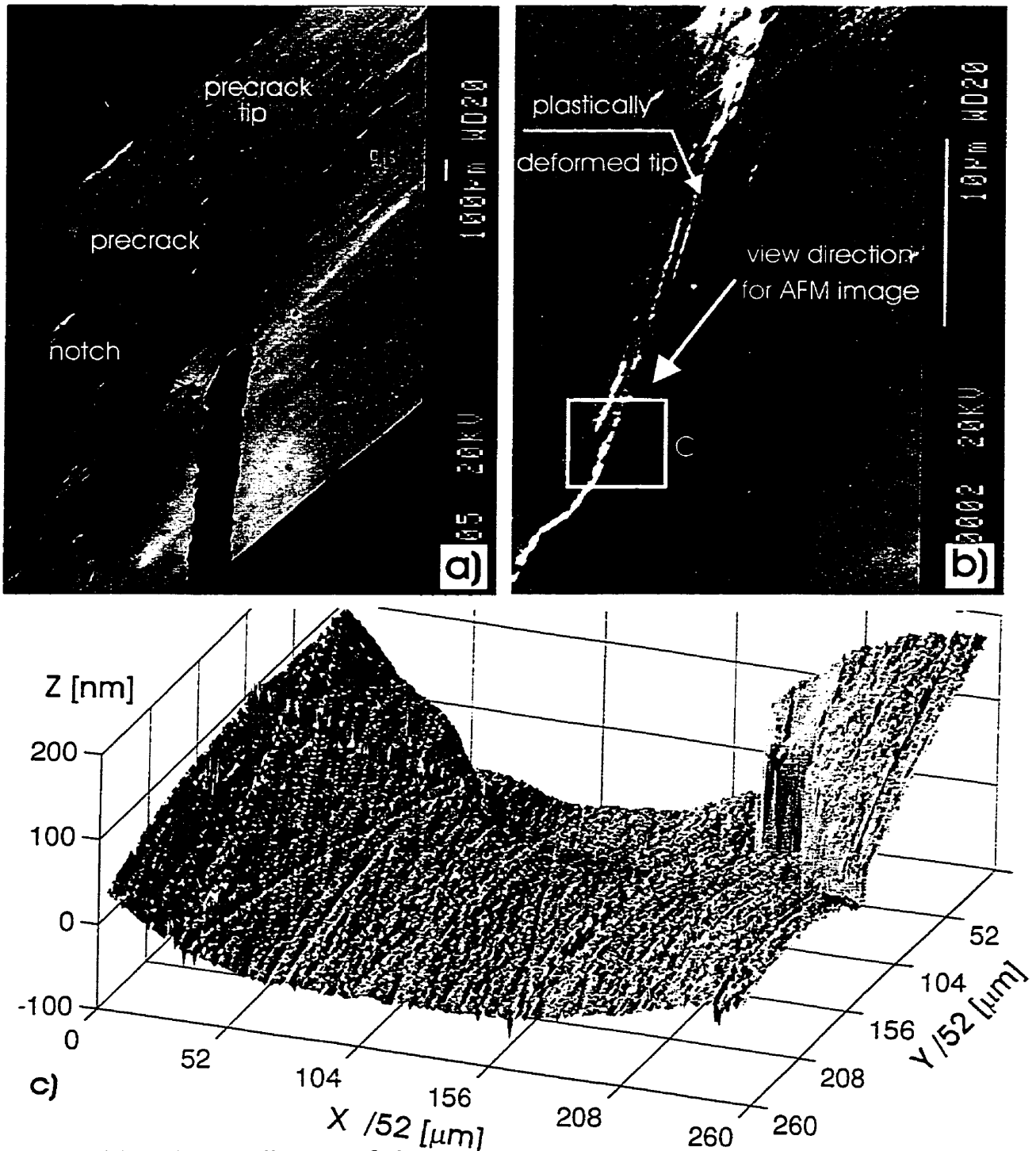

Figure 5.99 a) Overall view of the notch and precrack in SEPB specimen (SEM), b) plastic zone at the tip, c) AFM digital image of the window C area in (b).

Fig.5.99a,b shows the SEM photograph of the plastically deformed crack tip (the same as in Fig.5.96 and also shown on an optical micrograph in Fig.5.89). AFM

image in Fig.5.99c shows that plastically displaced material at the very tip of the precrack has a form of a very steep fold of a height of ~200- 250 nm on one side of the tip and very gradually and evenly spread deformation on the other side. Fig.5.100 shows the same image but levels of the same height are represented by the same color.

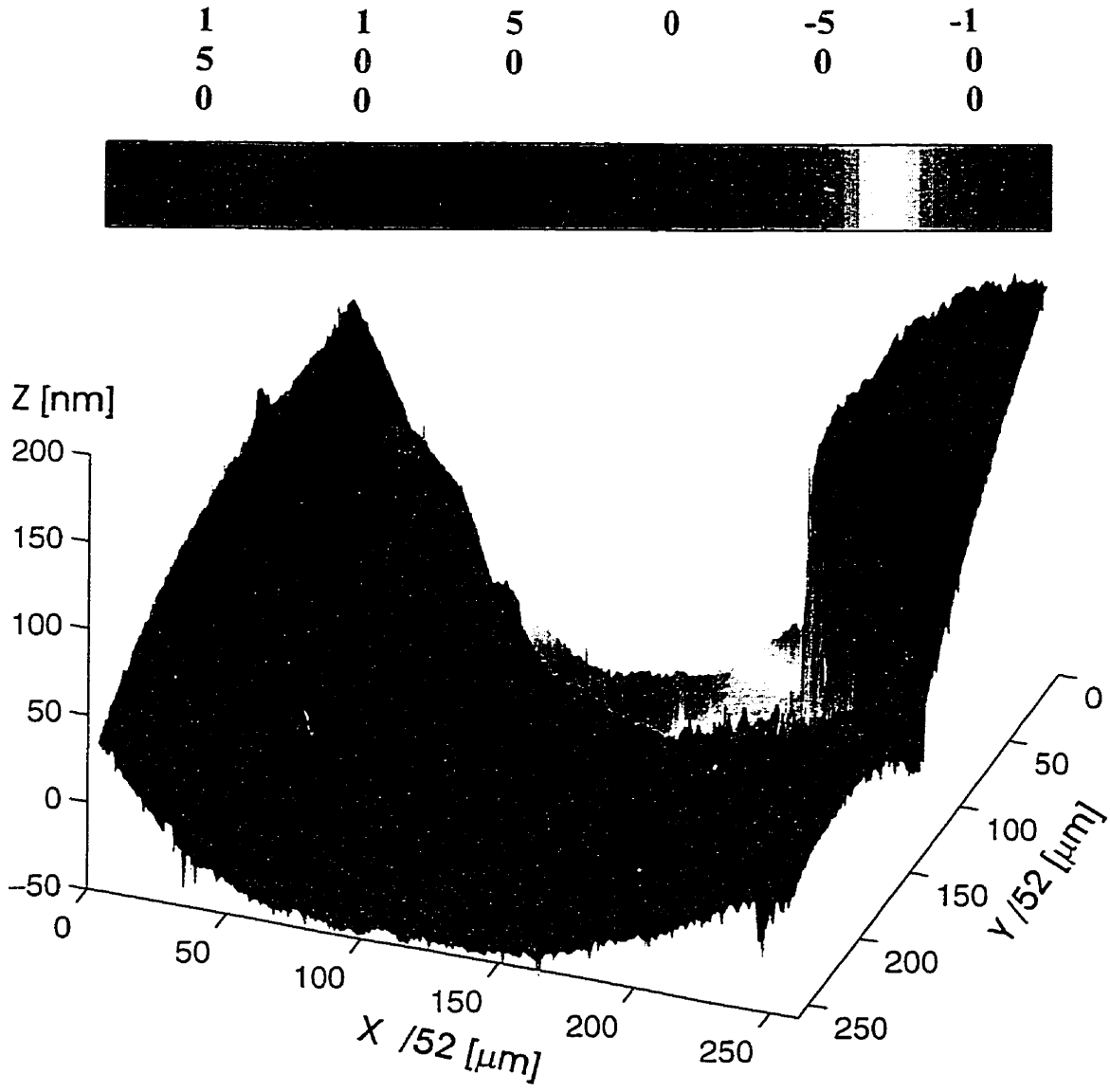

Figure 5.100 The same image as in Fig.5.99c but showing the height levels.

Note: the "zero" reference level in Fig.5.100 is not the level of undeformed material outside of the plastic zone.

5.8 Powders

5.8.1 Morphology and Microstructure of Powders

The only milled powders were alloys #14 and #15 in Table 5.1 whose chemical composition corresponds to the "base" 9Mn-25Ti composition. They were milled according to the procedures described in section 4.3.1. Figure 5.101 (and also K.1, K.2 and K.3 in Appendix K) shows scanning electron micrographs of titanium trialuminide powders milled for various times. After a relatively short milling time the shape of the particles is approximately globular although some of them are still far from being equiaxed as if they were composed of smaller pieces of material cold- welded to the main particle (Fig.5.101a). The morphology of short- time milled particles resembles closely a "popcorn ball" appearance, characteristic of mechanically milled brittle powders and, in particular, intermetallics [106]. With increasing milling time the shape of particles becomes more equiaxed and the surface appears much smoother although it still retains its "popcorn ball" appearance (Fig.5.101b,c). However, the most interesting features of the microstructure of milled powders are revealed by the optical microscopy of the cross- sections of powders (Fig.5.102 and also K.4, K.5 and K.6 in Appendix K).

The internal microstructure of powders milled up to 208-236 h is composed of a core (brighter on the micrographs) surrounded by an outer layer (greyish and dotted). The outer layer in powders milled for only 20 h is relatively thin, of the order of 1 to 5 μm and not quite evenly distributed around the core. Increasing milling time leads to two important microstructural developments. First, in some particles the outer layer becomes much thicker, reaching about 20 μm, in powders milled for 208 h (Figs.5.102a). Second, there is a gradual formation and increase of

the volume fraction of particles that do not contain any core (Fig.5.102b). These particles are referred to as the "no core" particles. Eventually, after 282- 386 h of milling practically all particles are of this type (Fig.5.102c). It seems that with

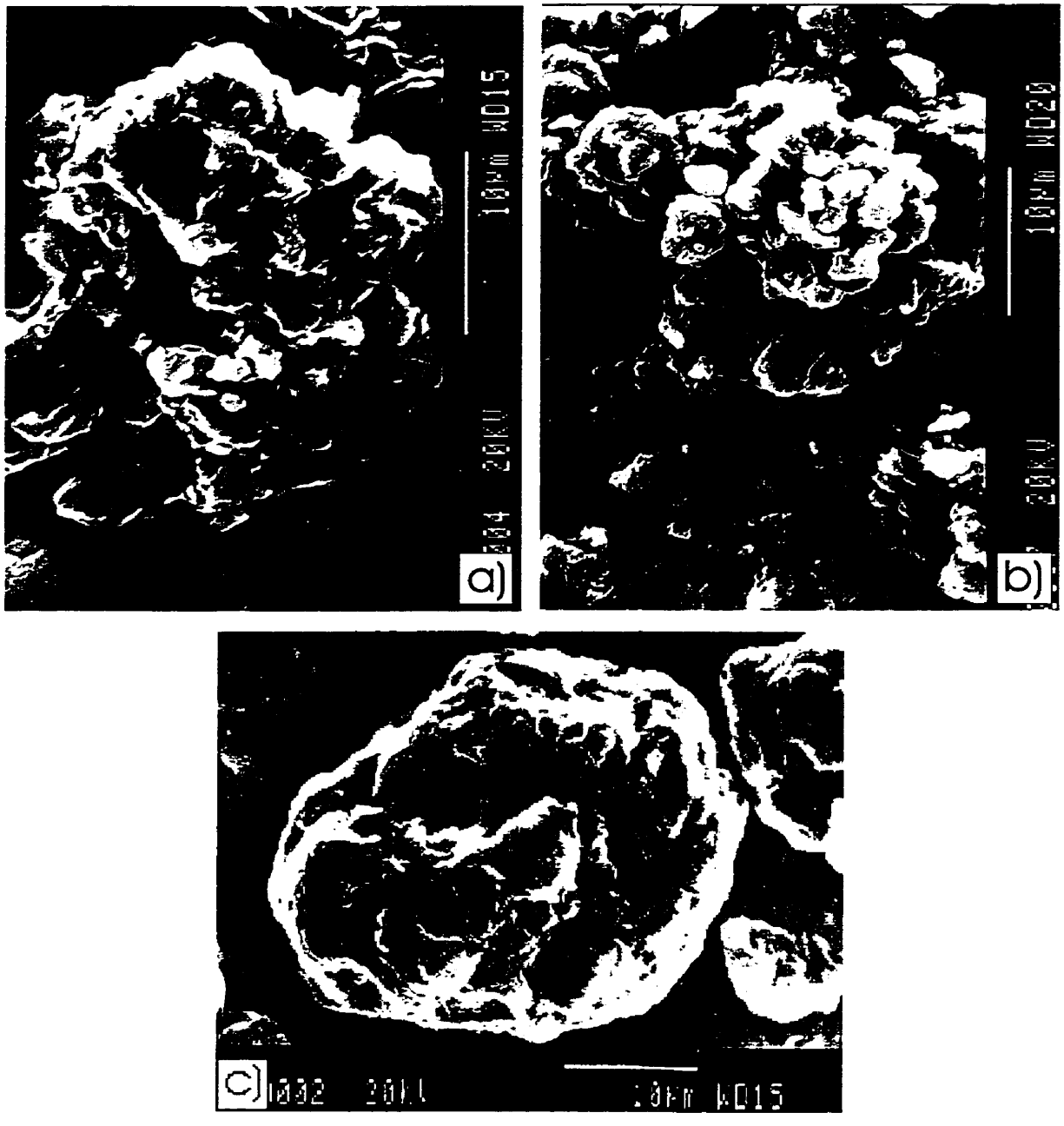

Figure 5.101 SEM micrographs of powder milled for a) 47 h (Ingot #14), b) 209 h (Ingot #15), c) 215 h (Ingot #15).

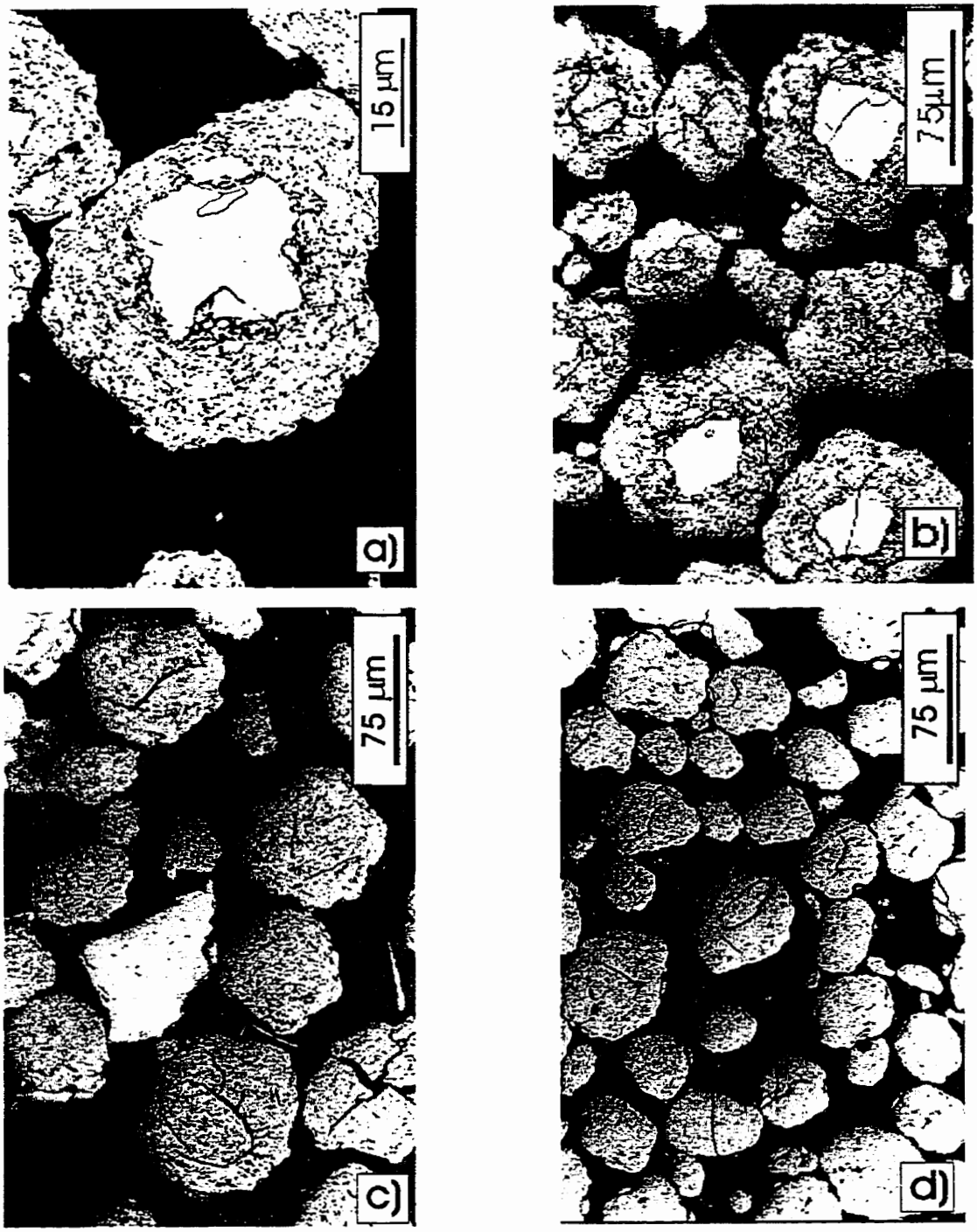

Figure 5.102 Optical micrographs of powder milled for a) 208 h (Ingot #14), b) 236 h (Ingot #14), c) 282 h (Ingot #15), d) 386 h (Ingot #14).

increasing milling time, the cores of the particles are gradually converted into the same, probably highly deformed structure, as occurs in the outer layer. Microhardness data of selected powders milled for increasing milling times and their corresponding crystallite sizes (Table 5.8) are listed in Table K.1. Somehow the average microhardness of "no core" particles after the longest milling time of 386 h (only "no core" particles exist in this powder), is much higher (HV 728) than the microhardness of both the outer layer (HV 611) and "no core" particles (HV 601) in powder milled for 208 h. This is despite the fact that the estimated crystallite size is the same (~3 nm) in powders milled for 208 and 386 h, respectively. The reason for this result is not known but might be related to the different grain boundary structure of nanocrystals formed in powders milled for 208 and 386 h. As seen in Table K.1 the microhardness of the cores of particles exhibiting both the core and outer layer (in powders milled for 19, 105 and 208 h) also increases with increasing milling time. As a result of prolonged milling the average microhardness of the cores increased from 296±20 HV, characteristic of a well- annealed ingot, up to 453±100 HV for the powder milled for 208 h. In general, quite large standard deviations of average microhardness value of milled powders observed in Table K.1 indicate that the microstructure of the powder particles is rather nonuniformly hardened exhibiting local soft and hard (or even extremely hard) spots. Nevertheless, the trends in the average microhardness values are quite clear.

5.8.2 Crystallite Size from X- ray Diffraction

As the milling time increases, all the Bragg peaks in the X-ray spectra broaden in width and decrease in intensity. These changes in the peak characteristics are attributed to the development of both nanocrystals and internal lattice strain in the

ball milled powders [150]. Table 5.8 shows the crystallite (grain) size calculated by both the simple Scherrer formula for the (111) peak and approximation of nanocrystalline size broadening by Cauchy/Gaussian function. It is seen that for milling times up to approximately 100 h the approximation by Cauchy/Gaussian function gives slightly different crystallite size values than does the Scherrer equation. For longer milling times both methods result in almost identical values although the approximation by Cauchy/Gaussian function gives more consistent values.

Table 5.8 Crystallite size and internal lattice strain of milled powders calculated from the Scherrer formula for the (111) FCC peak and approximation of nanocrystalline size broadening by a Cauchy function and approximation of strain broadening by a Gaussian function vs. milling time [151]

Milling time (h)	Crystallite size (nm)		Lattice- strain (Cauchy/Gaussian) (%)	Remarks
	Scherrer (111)FCC	Cauchy/Gaussian (Sec.4.3.1, Eq.4.2)		
19	37	24	0.22	Ingot#14
23	23	20	0.26	Ingot#15
42	23/26(R)	29/19(R)	0.26/0.20(R)	Ingot#14
65	23	30	0.43	Ingot#14
72	22	26	0.23	Ingot#14
96	6	5	0.94	Ingot#15
105	18	6	?	Ingot#14
160	5	6	1.20	Ingot#14
208	3	3	?	Ingot#14
209	6	3	1.21	Ingot#15
215	3	3	0.87	Ingot#15
236	5	3	1.27	Ingot#14
282	2	3	1.51	Ingot#15
386	3	3	0.49	Ingot#14

In general, the crystallite size remains relatively unchanged up to 100 h of milling and then quite drastically decreases reaching a saturation value of about 3 nm after

approximately 200 h of milling. The internal lattice strain is very modest and seems to increase only slightly with milling time although it never increases much beyond 1% (the question marks in Table 5.8 indicate cases where the intercept $16e^2$ in Eq. (2.2) resulted in an infinitesimally small negative value and the lattice strain could not be calculated).

5.8.3 Powder Processing

The very intriguing questions whether and how fracture toughness depends on the grain size when the grains are of the nanometer scale demanded that the next step be taken in elucidating this unknown area of material properties. For this purpose the powders were processed using various procedures in order to obtain the best microstructure for the fracture toughness testing. Only powders milled for 208h (Ingot #14) were used for compaction.

The simplest method of producing bulk specimens was by cold- pressing powders at RT. Various pressures were applied for ~3 min. The results are shown in Fig.K.7 (Appendix K). Tables showing the details of powder processing, microhardness and porosity measurements are also presented in the Appendix K. Applying higher cold- pressures causes that powder becomes increasingly densified. Up to 2400 MPa the particles still seem to be loose. At 2400 MPa these particles start to merge by cold welding, although unpolished surface of such a compressed button still resembles loose, evenly distributed powder particles (Figs.K.7e and f). Photographs i, j and k of the same figure show the powder compressed at the nominal pressure of 2580 MPa. That was the first and last trial of applying such a high pressure for long time (~20 min.). Unfortunately, after ~20 min. of applying this pressure the WC plungers broke into pieces. Resulting densification of the broken button is very

non- uniform. High, localized pressures caused that powder was 100% densified in small spots of the button. It is believed that in order to cold-compact the powder completely the nominal pressure of at least 3 GPa should be applied.

To find out whether sintering in air would give desired results, the cold pressed buttons were subsequently given various sintering treatments (Fig.K.8). The results of microhardness measurements and porosity are given in Table K.3 in Appendix K. In the temperature range 900°C- 1100°C, porosity remains on the same level of 23- 29%. With increasing temperature, porosity increases to 39% and 42% at 1150°C and 1200°C, respectively. Long holding time (3 hr) at 1100°C results in porosity level of 53% (Figs.K.8g and h). SEM photographs in Fig.K.9 show that sintering in air does not result in bonding of the powder particles.

Starting from the lowest sintering temperature (900°C), the cores of the powder particles started to recrystallize. The boundaries of the newly formed grains were initially barely visible under SEM. However, with increasing temperature, the recrystallization was more evident and grain boundaries more pronounced (Figs.5.103 and K.10). Interestingly enough, the heavily deformed regions (the outer layers) did not show the occurrence of recrystallization at least under the resolution used. In further discussion, an expression "recrystallization" (or "recrystallized" structure) will be used with respect to the microstructure of the outer layer and "no core" annealed powders. It is to be pointed out that it is impossible to discern unambiguously whether either recrystallization or growth of pre-existing nanocrystalline grains (from milling) has occurred in the annealed powders. Therefore, in this context, "recrystallized" can also mean microstructure containing micrometer grains formed due to nanocrystalline growth.

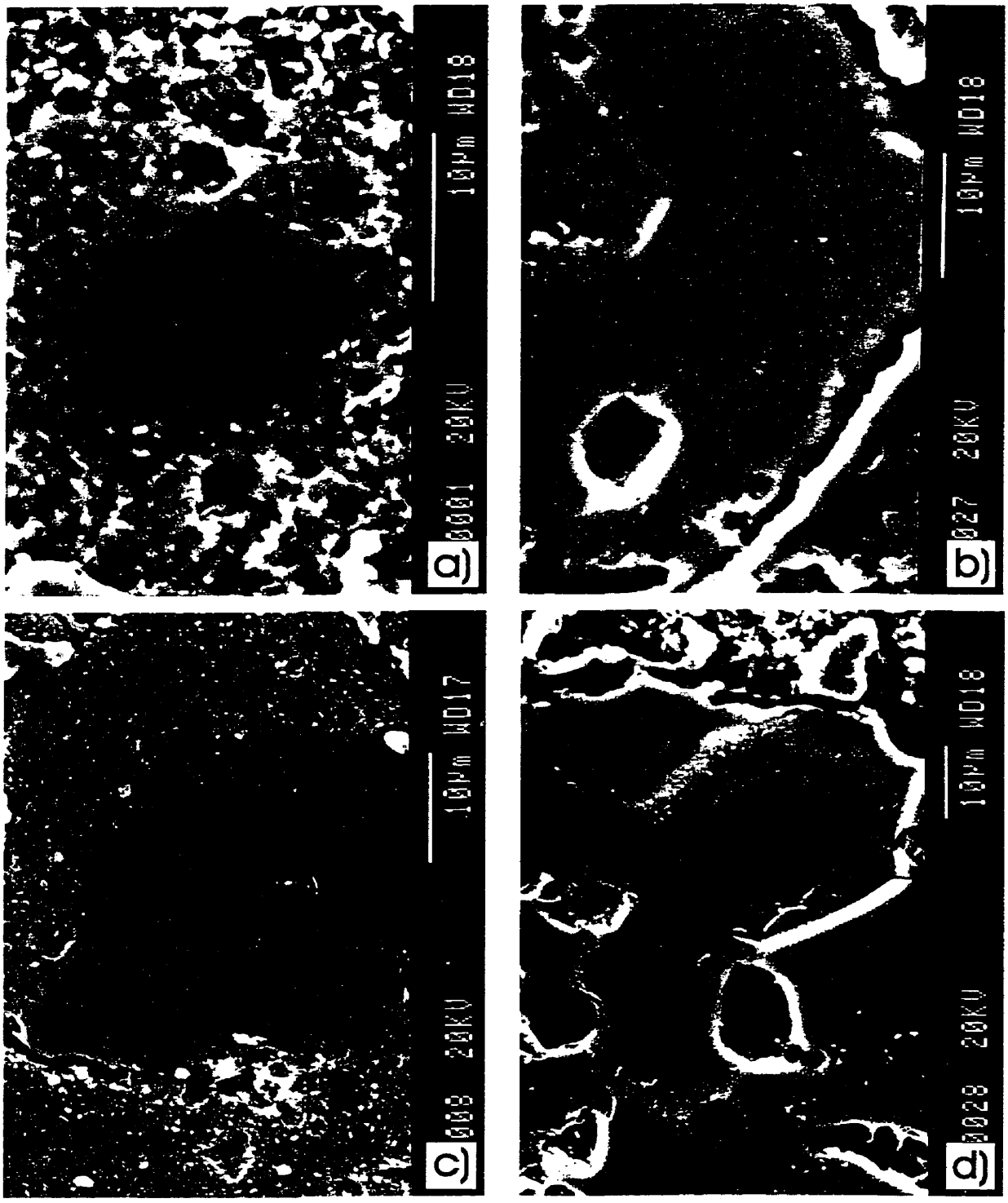

Figure 5.103 SEM micrographs of the recrystallized grains in specimens cold pressed under 2400 MPa and subsequently sintered at: a) 900°C; b) 1000°C; c) 1100°C; d) 1200°C.

Next step in seeking the right production method involved both cold and hot pressing at various temperature and pressure combinations. A series of six compaction experiments were conducted at the University of Wollongong (Australia). Powders were compacted with a hydraulic press under load control mode. RT compaction pressure was 450 MPa and high temperature pressure of 210 MPa was used. The cylindrical buttons of diameter of 8 mm were kept under constant pressure right from the RT, through the proper compaction temperature until the specimens reached ~150°C upon cooling after the process was completed. The results of the experiments are presented in Table K.4 (Appendix K). The best results were obtained by using single hot compaction procedure with the highest temperature used of 900°C. Porosity level was minimal, ~0.6%, although not uniformly distributed throughout the specimen volume (Figs.K.11c, d, e and f) (see also Table K.4 in Appendix K).

Applying two- steps of hot compaction, first at 700°C for 1h and the other at, again, 900°C for 15 min resulted in the second lowest porosity level (Figs.K.11a and b) (also Table K.4). Therefore, it seems that high compaction temperature is desirable.

The obtained material was in the form of small pieces whose size prevented bulk fracture toughness testing.

The compaction experiments were repeated in this work in the hope of obtaining the needed specimen bulk. The parameters used, microhardness results and porosity level are shown in Table K.5 (Appendix K). Here, in contrast to the previous tests conducted in Australia, the load for high temperature compression was applied after the pre- compacted button was heated to the desired temperature. The time of reaching the compaction temperature of 900°C was ~5min in the

experiments conducted in Australia, whereas in this work it was ~45min. Effects of this difference in heating time will be discussed later on.

Main characteristic feature of the microstructure of the compacted powders obtained according to the parameters given in Table K.5 (Appendix K) and shown in Fig.K.12, is the dark network of lines formed along the boundaries of the powder particles. They were not observed in the previous specimens compacted in Australia. One specimen showed unusual feature- a ring of fully condensed powder (Figs.K.12c, d and e). In general, the appearance of specimens obtained by these two sets of experiments is different.

Surprisingly, even though that both cold and hot compaction pressures in the present work were much higher (e.g. CP 2400 MPa, HP 470 MPa for compact K.5.4 in Table K.5) than those for tests conducted in Australia (CP 450 MPa, HP 210 MPa) the obtained material was worse. However, very similar morphology to that of the best obtained in previous tests (in Australia) was achieved in the last experiment in which the load for high- temperature compression was applied, similarly to the previous case (in Australia), right from the beginning of heating. Heating rate was relatively slow- the time to reach compaction temperature of 915°C was ~45min (the tubular radiant furnace was used) but unfortunately, the Al_2O_3/Si_3N_4 ceramic composite supports (inserts) (Fig.4.7) were destroyed due to superposition of high stresses and temperature gradients. It happened at relatively low temperature, ~400- 500°C, but the experiment was conducted further due to unawareness of that fact. On the basis of the results, the conclusion can be drawn that the dark lines forming along powder particle boundaries are the oxide films preventing the fusion of the particles. The compaction ratios were high when compared to the specimens compacted in Australia. The only drawback was the lack of fusion.

On the one hand, the high pressure applied from the beginning of heating substantially lowered the degree of oxidation and on the other, it allowed the plastic flow to take place at the lowest possible temperature, decreasing at the same time the amount of common interparticle surface (exposed to oxidation) over which the fusion should take place.

The heating rate was slow enough as to allow nanocrystallite growth. By comparing the microhardness values in Table K.4 for compacts obtained in Australia where the heating rate was very fast (4–5min to reach 900°C) to those obtained in this work it seems that the only reasonable explanation for substantially lowered microhardness of the outer layer (Table K.5) is the nanocrystallite growth.

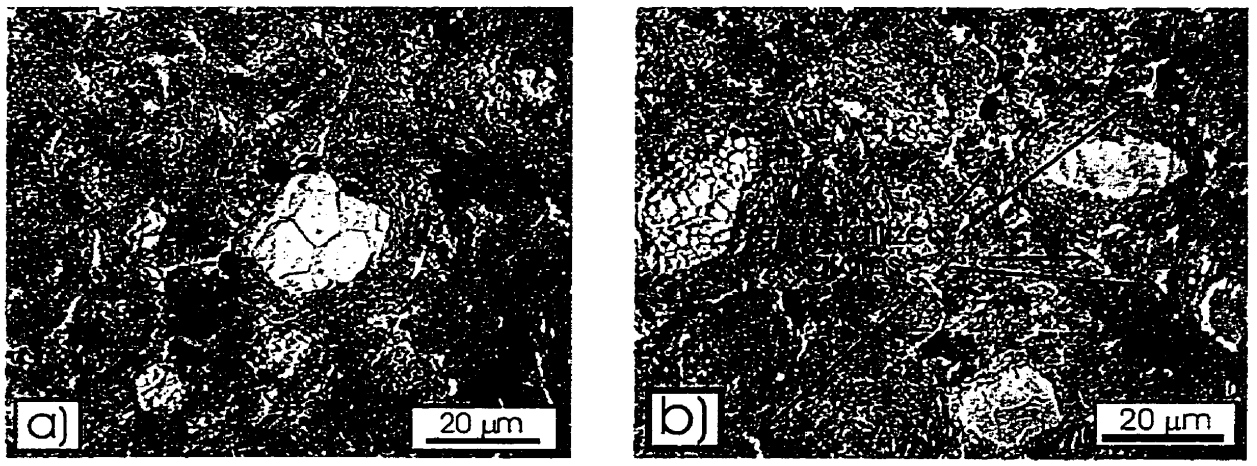

Figure 5.104 Optical micrographs of the powder compact obtained in Australia showing recrystallized "cores": a) heavily etched, b) lightly etched (K.4.2 powder in Table K.4).

Fig.5.104 (and also Figs.K.13 and K.14) shows the grains in the particles' cores in the powder compacted in Australia. It can be seen that the microstructure of the compacts obtained in Australia is composed of the relatively soft and recrystallized particle cores, very hard outer layers (727±93, Table K.4) and soft areas with recrystallized grains usually filling out the spaces between the particles' outer layers. These interparticle regions appear being squeezed out by much harder outer

layers. No recrystallized grains were observed by optical microscopy in the outer layers (Figs.5.104 and K.14) which suggests that grains remained in the submicron size range.

The microstructure of the powder compacts obtained in the present work is composed of recrystallized particle cores and partially-recrystallized outer layers (Figs.5.105, K.15 and K.16). The bright areas (Fig.5.105a and K.16) represent the recrystallized grains with the size ~1-2μm. The darker regions are comprised of grains which are still in submicron size range. It can be seen that the average grain size of the particle cores is bigger in compacts obtained in this work. Correspondingly, the microhardness of the cores is 243±30 (Table K.4) vs. 199±23 (Table K.5) for compacts obtained in Australia and in this work, respectively.

An example of the plastic flow distribution over the cross section of the hot-pressed powder button is shown in Fig.5.106. The microhardness values measured at the points marked in Fig.5.106 are shown in Table 5.8 and the corresponding indentations in Fig.K.17. The axis of symmetry of the compacted disc is also shown in Fig.5.106 (but this axis is not the axis of symmetry of the optical image of the disc in this figure). It can be seen that the deformation is almost symmetrical about the axis of symmetry of the disc- the volume of the disc between points 0 and 1 resembles a mirror image of the volume of the disc between points 1 and 3. The particles experienced the lowest deformation in the central portion of the button and the highest in the regions close to the external surface far from the axis of symmetry. Microhardness measurements, however, did not reveal any pattern in hardness meaning that work hardening due to plastic deformation is absent (most probably due to high deformation temperature). Indentations in Fig.K.17 confirm that there is just a small difference in microhardness in specimen parts plastically

deformed by different amounts. Interestingly enough, the big particle (Fig.K.17d) (most probably not milled chunk) which is much softer than the surrounding, remained undeformed, whereas the closest surrounding has been plastically and heavily deformed.

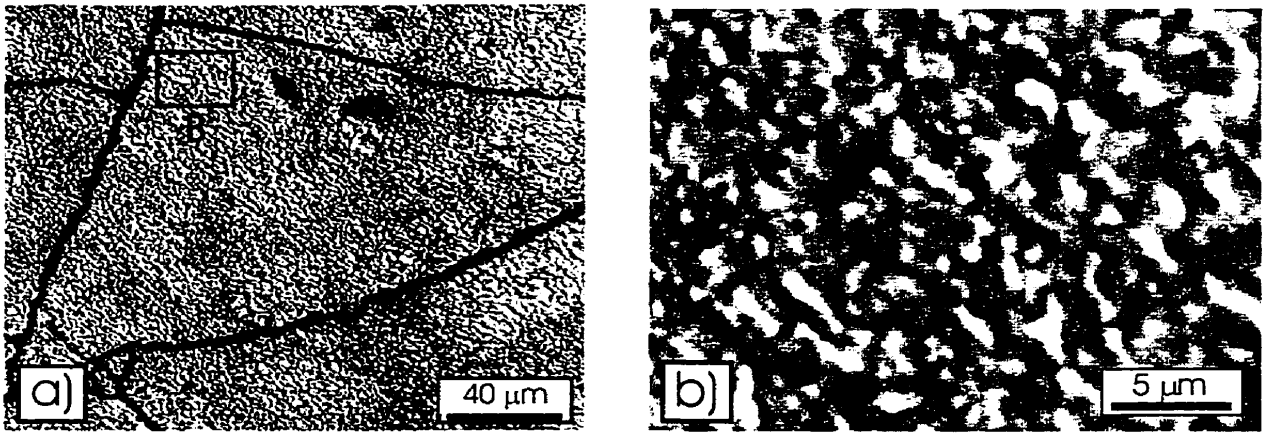

Figure 5.105 a) optical micrographs of the microstructure of the compact obtained in the present work (etched), b) higher magnification of the recrystallized grains.

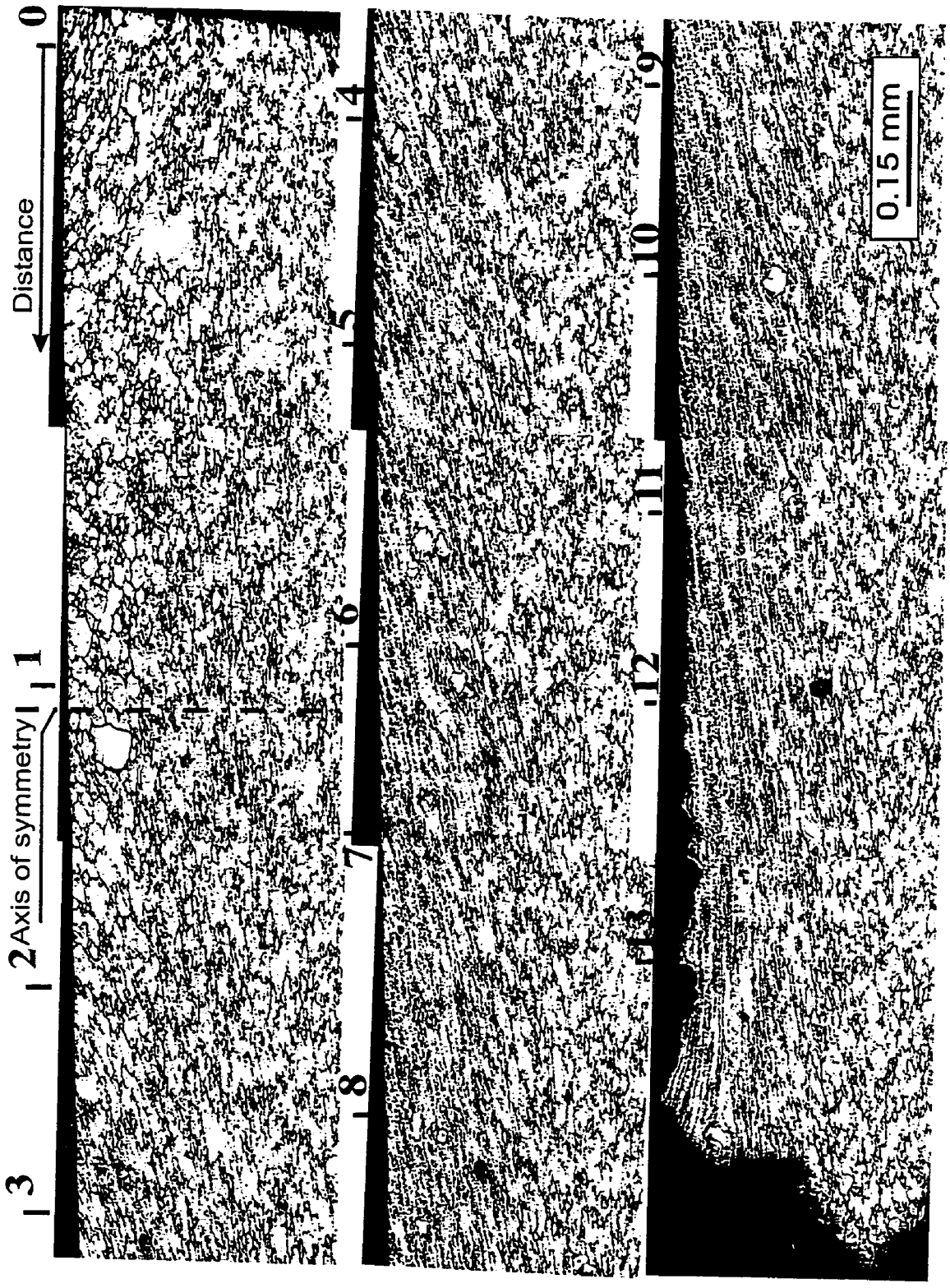

Figure 5.106 Cross- section of compacted powder, cold- pressed at 2400 MPa, hot- pressed at 360 MPa at 900°C for 20min.

Table 5.8 Microhardness (HV 0.01) (10g load) distribution along the transverse direction of the hot- pressed button.

Position Number	Distance [μm]	Microhardness (HV 0.01) [kg/mm²]
0.	0	320±50
1.	850	289±20
2.	1250	265±31
3.	1550	294±27
4.	1750	408±138
5.	2050	273±19
6.	2450	285±13
7.	2700	307±50
8.	3150	288±7
9.	3500	280±25
10.	3850	297±25
11.	4100	278±10
12.	4550	271±19
13.	4850	301±62

5.9 Indentation Microcracking Fracture Toughness

5.9.1 Indentation Microcracking Behavior

Indentation fracture toughness technique is based on the formation of well developed corner cracks at Vickers indent [152]. Therefore, it is important to investigate in the initial stage the nature of the indentation microcracking.

The powder compacted in Australia with the lowest porosity, no. K.4.2 in Table K.4 (Appendix K) was used for the observations of microcracks. The specimens were used in two states: etched and unetched. Unetched specimens better revealed the side cracks and surface distortions caused by indentations. Light etching on the

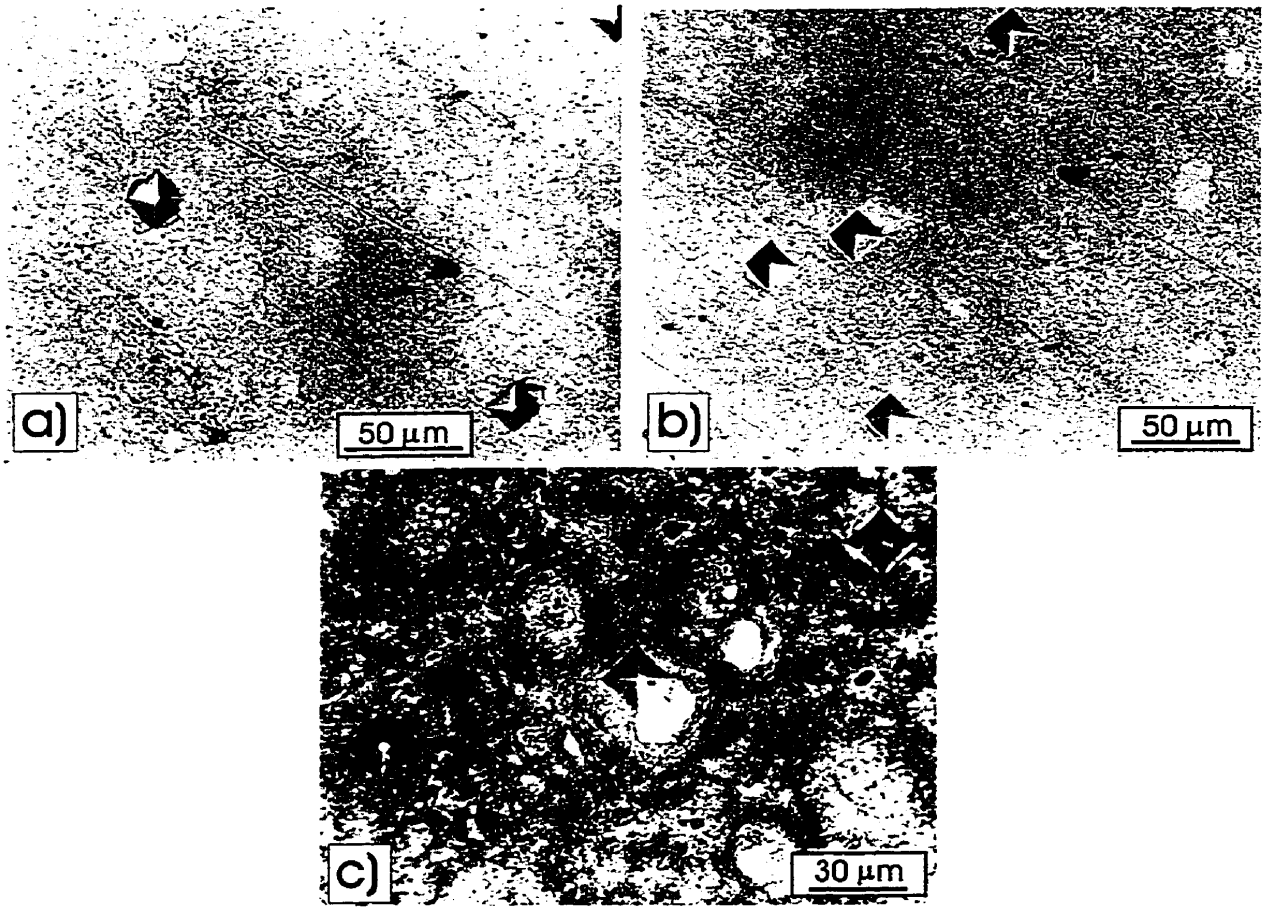

Figure 5.107 Optical micrographs of the indentations made under load: a) and b) 100 g; c) 200 g (powder compact no. K.4.2 in Table K.4).

other hand was applied to observe the behavior of cracks emanating from the indentation corners. Cracks were only occasionally observed at loads as low as 100 g (Fig.5.107). However, the lateral damage of the indentations was occurring more often than the radial cracks at this load (Fig.5.107a).

According to Lawn [153], the driving force for radial crack initiation comes from the residual field of the deformation zone induced by an indenter. It seems that the residual stresses are well accumulated (because of the low load threshold for crack initiation) in the material and their release is manifested by radial cracking. In order to obtain proper indents (i.e. four corner cracks) for toughness calculations at 200 g load, large number of indents had to be made. The 100 g load was omitted for toughness calculation purpose due to large number of indents required and high error involved in measurements. With increasing load, the number of proper indents also increased being over 90% for 500 g load.

Fig.5.108 shows the compact obtained in the present work with the lowest porosity (K.5.6 in Table K.5) and Fig.5.109 a gradual change in indentation size in this compact (see also Fig.K.19).

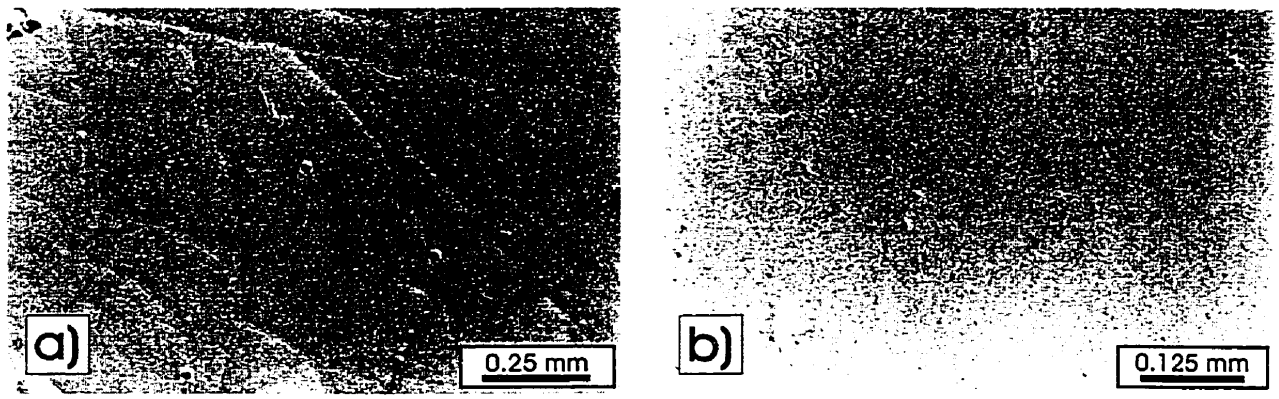

Figure 5.108 Optical micrographs of the hot- pressed powder obtained in this work (unetched) (powder compact no. K.5.6-Table K.5).

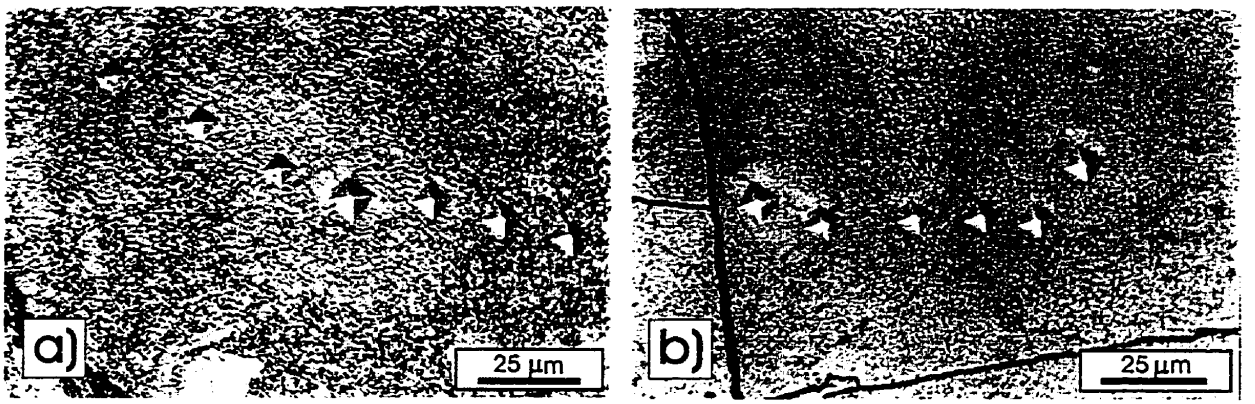

Figure 5.109 Optical micrographs of the hot– pressed powder (powder compact no. K.5.6–Table K.5) obtained in this work showing a gradual change in the indentation size (10g load).

Surprising behavior was observed when indentations were made under the highest load available of 2000 g. If the testing piece was small, substantial cracking of the specimen occurred (Figs.5.110a and b). However, when the test piece was larger, unlike the indentation corner cracks forming at low loads (Figs.5.107c, 5.111a,b, K.20 and K.21) in material made in Australia, the material obtained in this study neither fractured nor showed any evidence of plastic deformation (Fig.5.110c). Different behavior of the material obtained in Australia and in this work may result from a substantial difference in hardness for a particle outer layer (HV ~730 for the compacts obtained in Australia vs. ~310 for the compacts obtained in this work, Tables K.4 and K.5, respectively) and possibly different grain (crystallite) size. This problem will be discussed in more detail in the "Discussion" section. It is worth mentioning that still another behavior was exhibited by a cast material. At 2000 g there was no cracking but substantial plastic deformation occurred in the form of long slip lines.

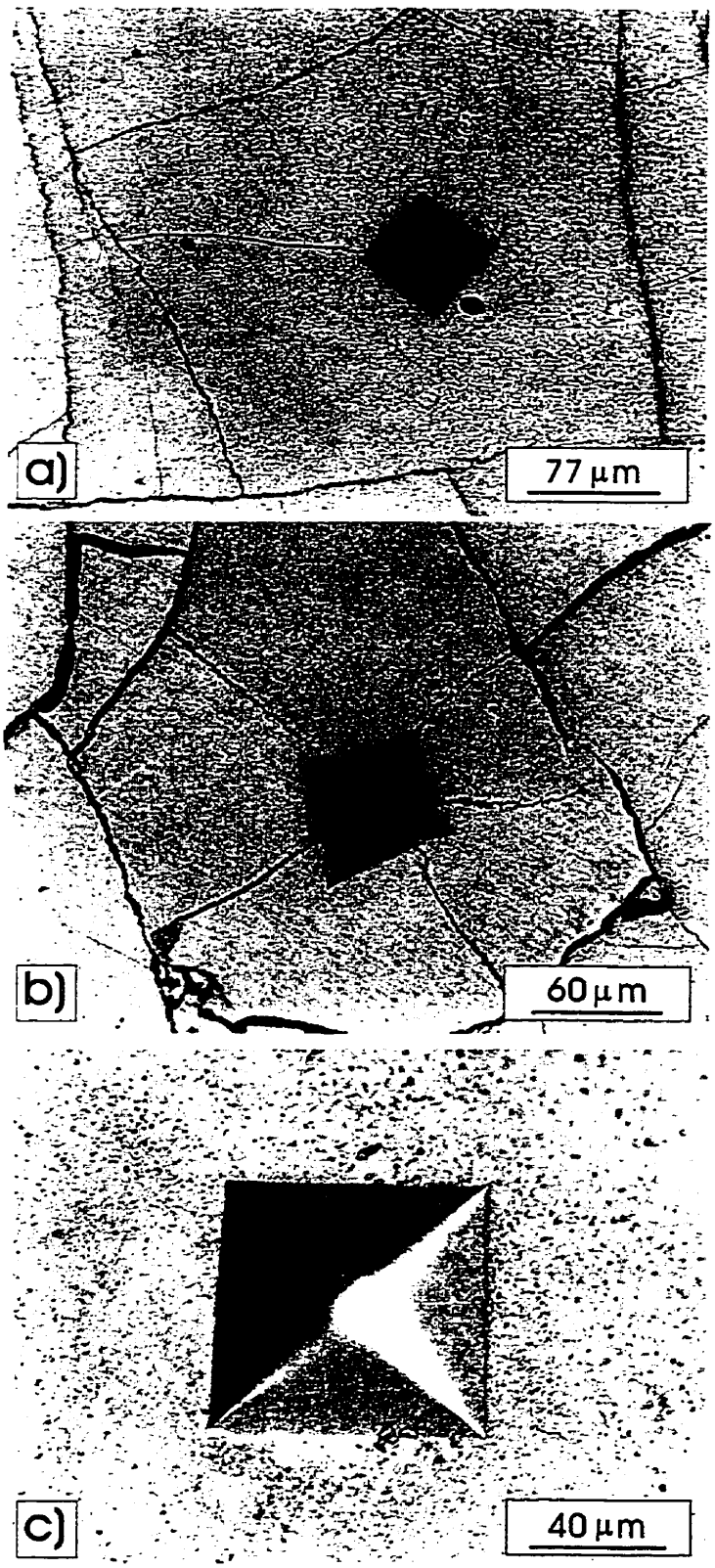

Figure 5.110 Optical micrographs of the indentations made under load: a) and b) 1000 g; c) 2000 g (powder compact no. K.5.6–Table K.5).

Figs.5.111, K.20, K.21, K.22 and K.23 show the interaction of radial cracks with microstructural features as a function of applied load. In most cases, the 300 g-load indents exhibited well defined radial cracks. Presence of softer "cores", either in the region adjacent to the indent's corner or partially indented completely prevented crack formation from that corner (Figs.K.20c, d, and e).

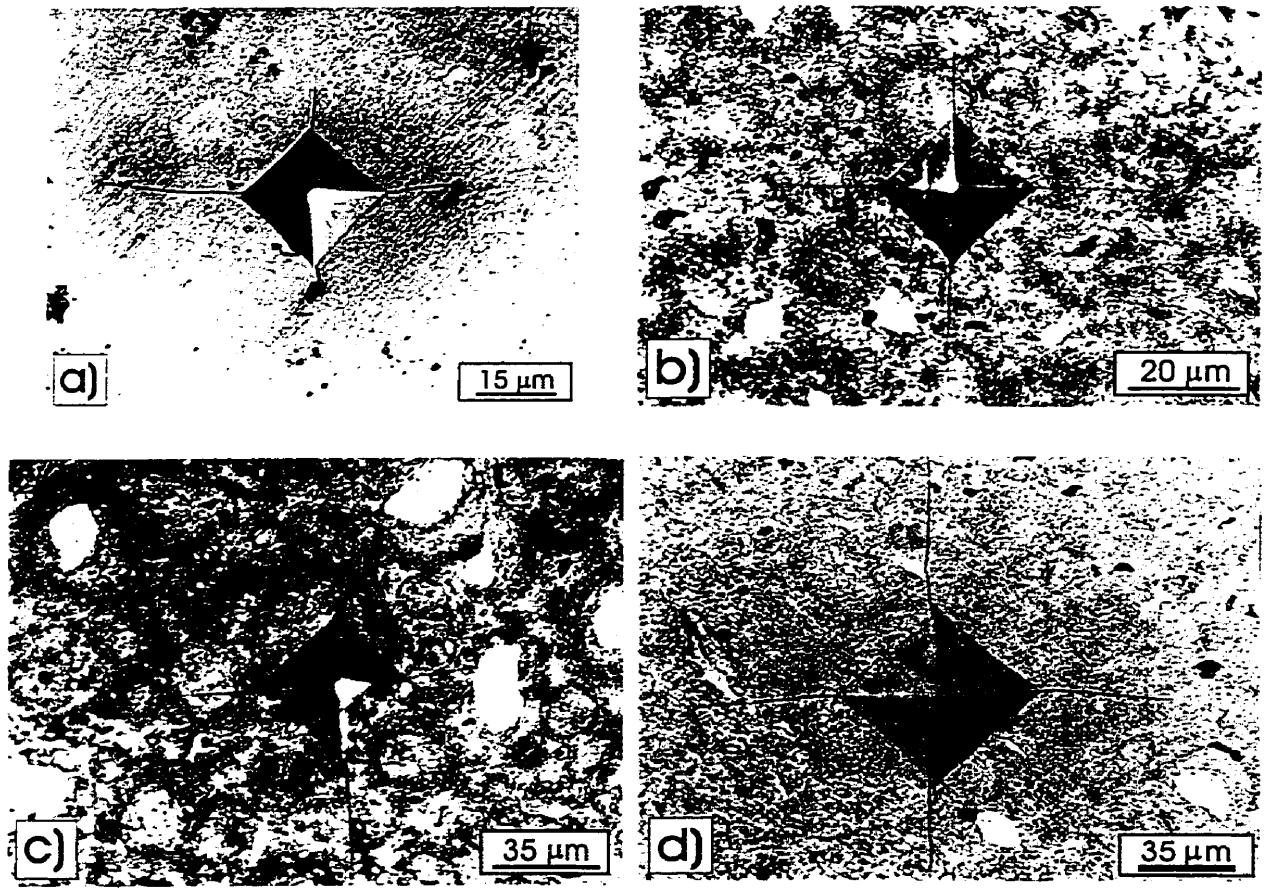

Figure 5.111 Optical micrographs of the indentations made under: a) 300g, b) 500g, c) 1000g, d) 2000g load (powder compact no. K.4.2- Table K.4).

At 500 g, where cracks are clearly visible, it becomes surprising that in such a heterogeneous microstructure (hardness and elastic modulus gradients) the cracking pattern resembles that in an isotropic material (Figs.5.111b and K.21). Most often the cracks are straight and aligned along indent's diagonal. Not even a single case was found where the soft core particle in obvious way changed the

crack path at loads equal to or higher than 500g. In contrast, 2000 g load in many instances was sufficient to make the crack propagate either underneath (Figs.K.23h,j) or cut through (Fig.K.23n) the large "core" particles located close to the corner of an indent or cut through the smaller particles being located in a remote position (Fig.K.23c). On the other hand, Figs.K.23o,p, and r show that these particles prevent crack propagation even though long cracks emanate from three other corners.

5.9.2 Measurements

Indentation fracture toughness tests were performed on several powder compacts fabricated in Australia (Table K.4 in Appendix K).

In order to determine the microcrack system (Palmqvist vs. half-penny) [154] developed at the Vickers indent, indentations at 2kg load were made. In almost all the cases, four cracks were emanating from the corners. Subsequently, the specimens were ground and repolished in order to observe the microcracks at various depths. Usually, below the indentation four microcracks were observed arranged as in Fig.5.112a giving the impression of the Palmqvist crack system. However, at greater depths, some additional microcracks were noted (Fig.5.112b). This microcracking behavior was identified [154] as a result of the formation of the "core zone" of the compressed material below the indent. This compressively stressed zone prevents the development of the microcracks. Below this zone, in the stress-free material, cracks were often observed (Fig.5.112b,c). Therefore, it seems that the powder compact is prone to exhibit "pseudo-half-penny" microcracks. Nevertheless, the indentation fracture toughness was calculated for Palmqvist

microcrack system. It was shown [154] that indentation microcracking toughness was very similar for both Palmqvist and half-penny crack systems.

The indentation fracture toughness was calculated using equation developed for a Palmqvist crack system [155]:

$$K_{IC} = \left[\frac{1}{3(1-\nu^2)(2^{1/2}\pi^{5/2}\tan\theta)^{1/3}}\right]\left[\frac{HP}{4l}\right]^{1/2} \qquad (5.1)$$

where ν- Poisson's ratio, 2θ- the angle of the opposite faces of Vickers indenter, H- is the mean indentation pressure exerted by the Vickers indenter, P- applied load, l- the average crack length.

By taking ν=0.11 and θ=68° and substituting H with $1.078H_V$ (where H_V is the Vickers hardness), the equation (5.1) can be written as:

$$K_{IC} = 0.0889\left[\frac{H_V P}{4l}\right]^{1/2} \qquad (5.2)$$

The results of toughness measurements are presented in Appendix L. The highest load of 2000 g, available on the testing instrument was also applied to the material obtained in this work (specimen K.5.6). However, there were no cracks appearing at the corners of the indentations, under condition that a testing piece was of sufficient size.

Graphs of fracture toughness vs. load are shown in Figs.5.113 and 5.114. The toughness values of specimens K.4.1, K.4.3, K.4.4, K.4.5, and K.4.6 are very similar, ~2 MPa√m. Average toughness of specimen K.4.2 seems to be slightly lower, ~1.8 MPa√m, even though it has the lowest porosity level. It can be seen from Table L.10 that toughness is independent of porosity level.

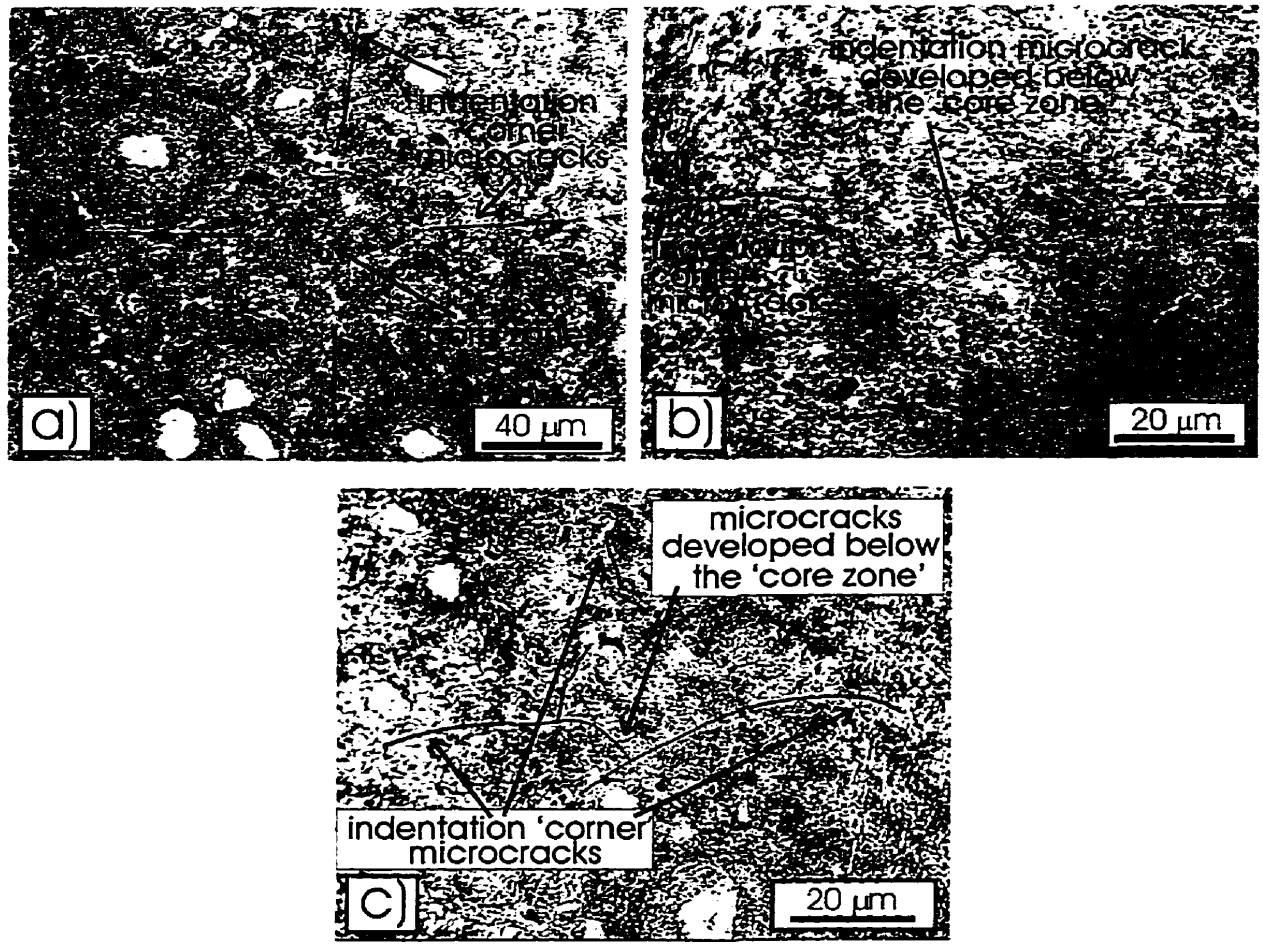

Figure 5.112 "Pseudo-penny" microcrack system developed at the Vickers indent under 2kg load; a) directly below the indent vertex, b) at the greater depth below the "core zone", c) at still greater depth.

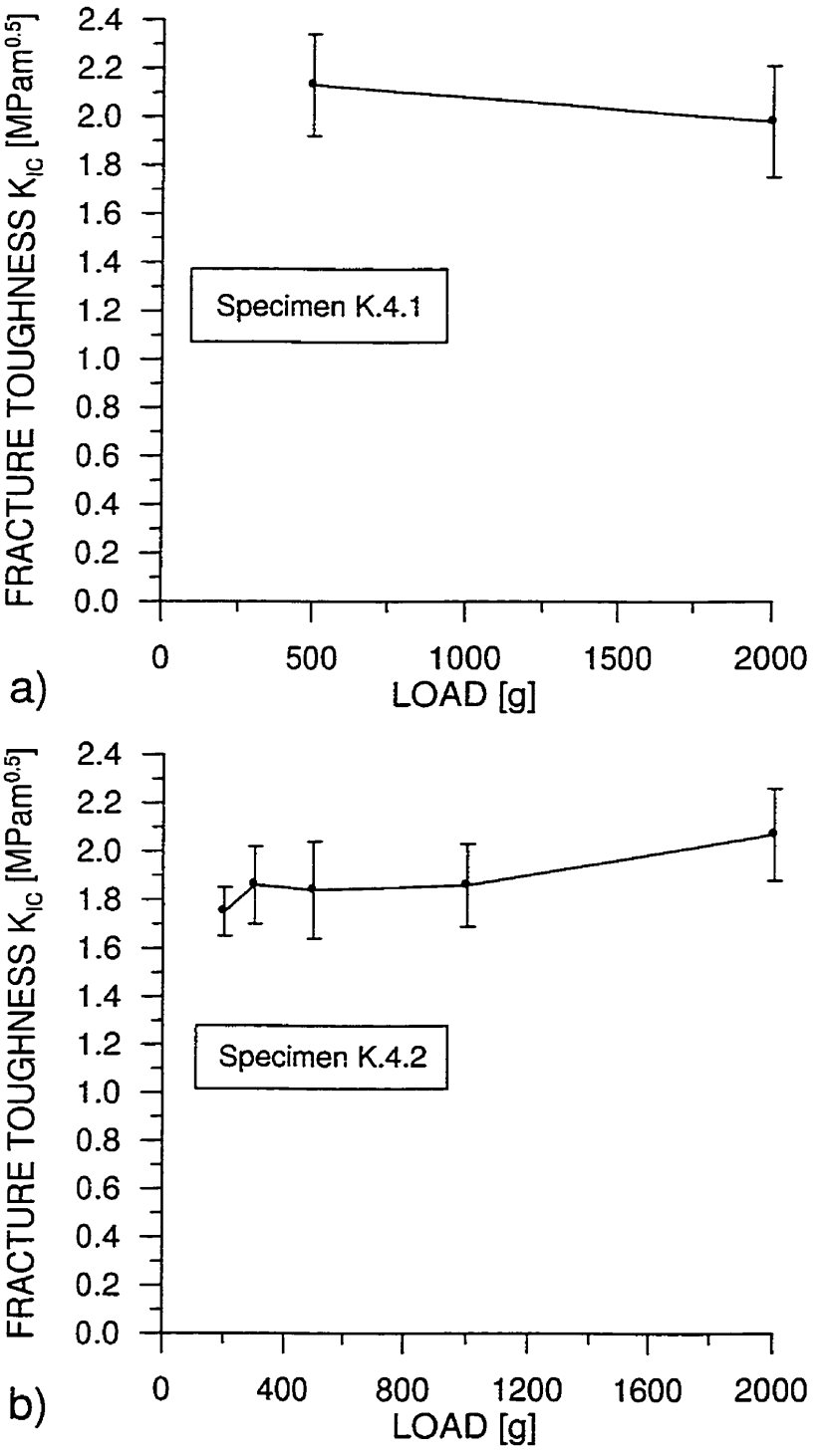

Figure 5.113 Indentation fracture toughness vs. load for specimen: a) K.4.1; b) K.4.2.

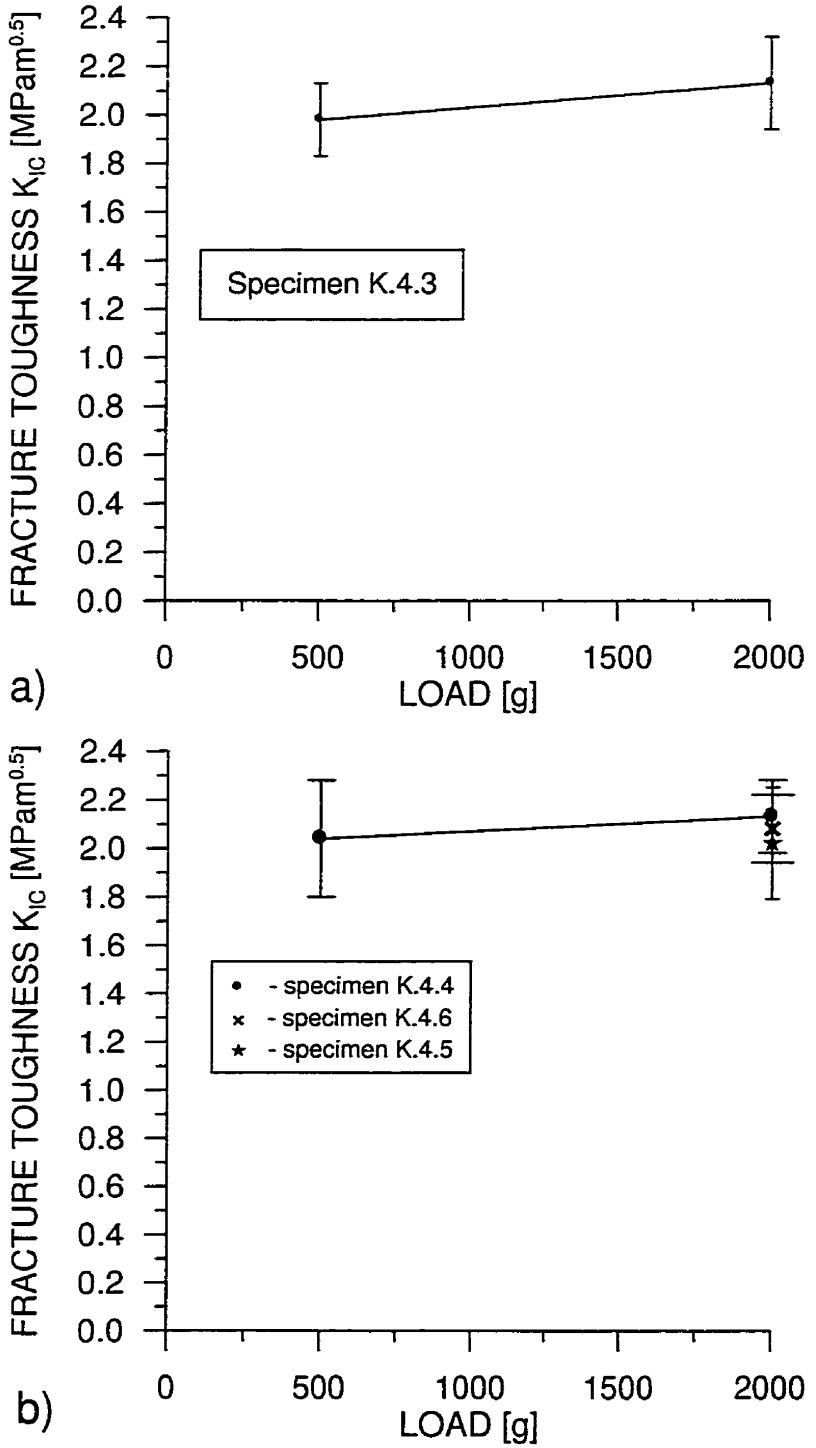

Figure 5.114 Indentation fracture toughness vs. load for specimen: a) K.4.3; b) K.4.4, K.4.5, and K.4.6.

6 Discussion

6.1 The Microstructure of HIP-ed and Dynamically Recrystallized Material

The single phase $L1_2$ region at 1473 K (this region corresponds most probably to much lower temperature than 1473 K because the cooling time in this experiment was ~30 min) determined by Zhang and Mikkola [107] (Fig.B1 in Appendix B) is much larger than that reported by Mabuchi for 1273 K [10]. This region in Al- Ti- Mn system is also larger than those at 1473 K for the Al- Ti- Ni and Al- Ti- Fe systems [156] but is somewhat smaller than that given for Al- Cu- Ti [156]. It appears that the size of the $L1_2$ region decreases with decreasing temperature in these Al- Ti- X systems [4].

The geometric center of the $L1_2$ phase region in Fig.B1 occurs at about 11 at. % Mn, 25 at. % Ti, and 64 at. % Al, covering a range of about 8 at. % in Mn and about 4 at. % in Ti. In order to ensure a single phase $L1_2$ structure the Ti content has to remain above 23 at. % on the low Ti side, but also to contain no more than 27 at. % on the high Ti side. This narrow Ti range and the general shape of the region, suggest that Mn substitutes preferentially for Al [10,107,157]. A tendency to develop higher porosity, despite remaining single phase is attributed to increasing Mn content with simultaneous decrease in Ti [10]. This porosity appears to form during the dissolution of Mn- rich second phases upon subsequent homogenization and is considered to form by Kirkendall effect [158,159].

The established goal of obtaining the essentially single phase $L1_2$ in Ti trialuminides was achieved. The compositions of the 9Mn-25Ti type alloys (alloys

numbers 1-7 and 14-19 in Table 5.1) fall into the $L1_2$ field in Fig.B1. Homogenization dissolved some amount of the second phase present in the as-cast material. However, some needle- like particles are still left. Their small width (~1 μm) prevented the compositional analysis. Similar difficulties were encountered in [107]. However, they were tentatively identified using SEM/WDX in Cr- modified Al_3Ti alloy [14] as Ti_2AlC and as Ti_2AlN in Fe- modified $L1_2$ trialuminides [133]. Content of these whisker or rod- like particles seems to be slightly higher in high Mn (14 at.% Mn) than in low Mn (9 at.% Mn) alloy but still is below 1%. Porosity content in low Mn and in B- doped (0.001 % B) low Mn alloys after HIP-ing was measured to be below 1 %, whereas in high Mn alloy it remained below 2 % (Table 5.2).

Hot working of 9Mn-alloys at 1000°C neither decreased the already low porosity nor did it change the morphology of these pores, leaving them round in shape.

If the rule that "the lower the stacking fault energy, the more the recovery process is inhibited and that recrystallization takes place readily" also holds for ordered intermetallics, the present 9Mn-type alloy must have a high stacking fault energy. A high stacking fault energy for the 8Mn-25Ti alloy was verified by the formation of the deformation cells during hot- working [160]. In addition, it has been shown that after annealing at 900°C of the 70 % deformed at 1000°C specimens, the hardness remained constant, at the same level as that of the hot- pressed sample and that the microstructure did not change [160]. Recrystallization began at a temperature higher than 900°C and was very sluggish. Annealing at 900°C resulted in 18 % volume recrystallization and at 1040°C (after 20 min) in 96 % recrystallized volume. A high microstructural stability of the material at high temperature is

attributed to the recovery processes which reduce the driving force for recrystallization.

The hot- pressed alloys in this study deformed extremely well, exhibiting virtually no edge cracking. Similar observation was made in 70 % deformed Mn- and Cr- modifications of Al_3Ti intermetallic [11]. However, the Mn- containing $L1_2$ compound exhibited better fabricability than the Cr- containing counterpart. The resultant grain size was ~50 μm which is very similar to 45 μm grain size obtained in this study. This ability to successfully forge such materials promises a viable processing route for near- net- shape components such as blades and compressors in engines.

Small amount of second phase was found in the high-Mn alloy doped with 0.66 at.% B. Its content was measured to be 1%±0.9%. The details of the microstructure of the alloys tested are given in Table 5.2. The composition of this phase corresponds to γ_1 phase in Fig.B1.

Boron doping with a level of 0.24 at.% and 0.66 at.% resulted in formation of borides whose content combined with needles was higher for higher doping level.

The work on boron- doping of $L1_2$ Al_3Ti- based intermetallics [32] indicated that 1600 ppm of boron introduced to Al_3Ti (Cu12.5) alloy formed various types of aluminum and titanium borides, whereas when added at the level of 500 ppm (level of up to 25 ppm was investigated) the existence of borides was not detected. Boron doping level at 0.004 at.% (~10ppm) in the present study also did not result in formation of borides.

The intention of introducing boron was its segregation to grain boundaries at elevated temperatures to prevent IGF. Windowless EDS analysis (Fig.5.18) shows no peaks from boron in the matrix which might be due to the fact that boron level was

below the detection limit . For the same reason, the presence of boron at the grain boundaries could not be checked. However, it is known that in Ni_3Al intermetallic alloy boron preferably resides at grain boundaries rather than in the lattice [134].

6.2 Microstructure of Powders and Resulting Grain Size

RT compaction did not lead to full densification of powder. With increasing applied pressure, however, the degree of densification also increased and so did the microhardness. At 2400 MPa powder particles started to cold weld to each other. Nominal pressure of 2580 MPa kept for longer time caused the failure of the WC plungers which resulted in the partial pressures exerted probably much in excess of 2600 MPa. Such a high pressure cold welded powder particles almost completely in small areas, leading to very low porosity level. Additional sintering in air of cold compacted powders did not lead to densification.

The best results were obtained by hot pressing of cold, pre- compacted buttons. Two different schemes of high temperature loading resulted in different microstructures. On the one hand, when the cold pre- compacted buttons were allowed to achieve the required temperature and then loaded, the resulting microstructure was highly compacted but with one main drawback. The oxidation of particle surfaces prevented their fusion and resulted in the network of thin oxide film along the particles' boundaries observed on the cross-section of the compact. These oxide envelopes were counted by the Java system as porosity resulting in an overestimated value of porosity for this specimens (Table K.5; specimens K.5.1-K.5.5). Such apparent "porosity" actually reflects the surface fraction of such oxide film on the polished specimen surface but not "real" porosity. Therefore, it is recommended to use high vacuum or an inert gas for hot compaction. When

compressed in vacuum or in argon, the load could probably be applied upon reaching the desired temperature. This option of loading is less aggressive and detrimental for inserts, since most of the ceramic materials cannot withstand the simultaneously imposed high pressure and high temperature gradients. On the other hand, applying pressure right from the beginning of heating prevented oxidation of powder particles. The lowest porosity level of ~0.4% was obtained at the highest temperature used of 900°C.

Specimens made in Australia retained their microhardness level. The time to reach the compaction temperature of 900°C was ~4–5 min. In contrast, those made in this study lost ~50% of their original microhardness due to prolonged time ~45 min to reach the compaction temperature. This difference of microhardness, most probably originates from different grain size and/or possible segregation of interstitial impurities such as C and/or N to the nanocrystalline grain boundaries upon heating and causing grain-boundary age hardening [161]. The grain size in the recrystallized areas of the outer layer of the present compacted powders still is estimated from Fig.5.105 as 0.5–2 μm in size. Some particle cores recrystallized with the grain size ~2– 20 μm (Figs.K.15 and K.16). The grain size in the unrecrystallized areas of the outer layers (Figs.5.105 and K.16) could be roughly assessed based on the data presented in Ref. [161]. The same powder as used in the present work (milled for 208h) when annealed at 600°C for 60 min exhibited the 29 nm grain size, whereas annealing for 240 min resulted in 35 nm grain size. In the present work, powders were heated for ~45 min from RT to 900°C before pressing, and for 15 min at 900°C during pressing. Therefore, the grain size could be assessed to be in the range ~0.1–1.0 μm. Correspondingly, the grain size in the compact obtained in Australia is assessed to be in the range 0.05–0.10 μm.

Therefore, the principal difference between the microstructure of the powder compacts obtained in Australia and in the present work is that there was no recrystallization and/or grain growth in the outer layers in compacts obtained in Australia (Figs.5.104, K.13 and K.14). Only particle cores and some interparticle regions recrystallized (Fig.5.104). On the other hand, compact produced in this work exhibited a relatively large volume (~50%) of recrystallized grains within the size range ~0.5–2 μm (Figs.5.105 and K.16). The diffused boundaries between unrecrystallized and recrystallized regions cause the observed gradual transition of indentation size (and corresponding microhardness) from one region to the other (Fig.5.109).

The plastic flow of powder particles observed in the compacts obtained in the present work was very inhomogenous (Fig.5.106). The lowest deformation was in the vicinity of loading axis and the highest in the regions far from the center and at the external surface. However, different amounts of plastic deformation did not cause large differences in microhardness throughout cross section of a button meaning that the material was well annealed.

6.3 Fracture Toughness

6.3.1 Important Aspects of Fracture Toughness Testing Methodology

The limited plasticity requirement established by the ASTM E399 Standard [114] was satisfied for each specimen tested in this work. Almost always, the P–LLD curves for both SEPB and CNB type specimens of the boron-free, "base" 9Mn–25Ti alloys were linear up to the maximum load P_M (Figs.5.19 and 5.20). Only at the

highest temperatures, a few specimens showed non-linear behavior before maximum load (Figs.5.19a no.6 and 5.20a no.6).

The fracture of high- Mn (boron doped and undoped) and low- Mn (boron-doped) material, on the other hand, was characterized by numerous pop- ins, before and in the peak load region (Figs.5.21a, 5.22, 5.24 and 5.26). The events were evidenced by audible clicks. These crack jumps were less often encountered in low-Mn alloy, especially at low and ambient temperature and also they were "weaker" (very often not audible). The occurrence of these pop-ins is beneficial because they provide a very sharp crack tip.

At low and ambient temperatures a specific pattern of fracturing was observed. In this temperature range, cleavage is a predominant mode of fracture. When the fracture origin was placed close to the notch tip, the load had a tendency to drop more gradually. If the "river" markings or cleavage steps were well developed and of substantial relative dimensions, the fracturing usually exhibited pop- in events before reaching maximum load. Short pop- ins were also often occurring when small cleavage planes were substantially misoriented one with respect to the other. However, even at 1000°C, when the cleaved planes were bigger (~500 μm in diameter due to large grains), highly misoriented and placed at the notch tip, rapid load drop commenced and further crack advance was halted by intergranular fracture. It seems that it is much easier for the specimens to pop- in the region of maximum load than completely suppress rapid load drop. If cleavage originated from a few weak spots in the vicinity of the notch tip, the crack advance seemed to be smoother. Also, when there was one cleavage center and placed some distance (for example as observed 400- 500 μm) from the notch vertex the fracture was rapid and large load drop resulted. It was also observed that large and deep

secondary cracking usually did not help preventing catastrophic fracture at low temperature.

An important fact that the toughness is independent of the geometrical relations (S_1/S_2 and S_1/W) (in the range of dimensions tested) is confirmed in Figs.5.50b and 5.79. CNB specimens of the 9Mn (Fig.5.50) and 9Mn-0.004B (Fig.5.79) alloys were tested in the temperature range from RT-1000°C. Subsequently these specimens were cut into halves and tested again in the same temperature range. The toughness results for both large specimens and their halves gave the same bound of scatter of fracture toughness values.

The only toughness tests conducted in this work that produced unreasonably high toughness values and huge scatter are those on CNB specimens tested in 3pt. bending. The substantial difference in toughness values obtained in 4 pt. and 3 pt. bending of CNB specimens could possibly be explained by the different shape of the geometrical function, Y^*, with crack length. Since the toughness values are calculated from the maximum load during the test and since there are usually no subcritical crack growths, the required "timing" between occurrence of maximum load event and minimum value Y^*_{min} of the geometrical function, is doubtful. The values of α_{min}, which designate the nondimensional crack lengths at which the geometrical function, Y^*, reaches its minimum values, are considerably higher in 3 pt. bending than in 4 pt. bending. If the maximum load and Y^*_{min} do not occur simultaneously there is an error introduced in calculations of fracture toughness. The bigger the α_{min} the greater the magnitude of that error which might be the case for 3 pt. bending. Notwithstanding the above mechanism of error in CNB specimen, the toughness values obtained in 3 pt. bending are much higher, instead of being lower than the true toughness values.

Other approach could also be applied to explain the values obtained in 3 pt. bending. Generally, the catastrophic failure of CNB specimens is treated with caution, due to possible overloading, e.g. the maximum load obtained in testing can be higher than that required for crack initiation and further its stable propagation [115]. However, similar reasoning could be applied to 4 pt. tests, yet in this case the catastrophic failure does not imply the overloading because the fracture toughness values are similar to those obtained on SEPB specimens. On the other hand, the amount of possible overloading should be smaller in more compliant specimens (assuming similarity in notch accuity) which is related to the rate of increase in the elastic energy stored in the specimen before onset of fracture. 3 pt. bending configuration is more preferable from this point of view. In summary, there was no reasonable explanation for persistently higher toughness values obtained in 3 pt. bending. Therefore, they are presented here only to show that the results of tests on CNB specimens that fractured in catastrophic manner should be confirmed by other test methods (for example SEPB specimen type).

6.3.2 Toughness of Coarse- Grained Boron-Free, "Base" 9Mn-25Ti Alloy in Air and Crack Tip Plasticity Observations

To date, only one study on the fracture toughness of the $L1_2$ Al_3Ti modified intermetallics has been reported by Brown and Kumar [49]. In that study, the fracture toughness tests were carried out on SENB type specimens (with notch root radius 50 μm) and only up to 700°C.

Fracture toughness results conducted on SEPB specimens (in the present study) at RT conformed surprisingly well to the plain strain condition requirement. Toughness shows steep increase for remaining ligament lengths (RLL) that are

below the required minimum. For longer RLL the toughness levels off and is in the range 4- 4.5 MPa$\sqrt{m}$ which is taken as representative, plane strain fracture toughness at RT. In contrast, work of fracture does not show this type of dependence (at least in the range of RLL tested).

The interpretation of the results becomes more complex for tests conducted at higher temperature. Raising temperature affects not only the toughness and work of fracture but also directly influences the mode of fracture. This change in mode of fracture with temperature is also most probably the principal source of scatter of the results. The observed tendency is that for the specimens which exhibited much different fracture modes at the same temperature, the tested properties also showed large scatter. However, very similar modes do not imply similar mechanical properties when tested at given temperature. At ambient temperature it seems that toughness shows a similar tendency to decrease with larger RLL, similar to that at RT. However, for temperature above 500°C there is no such a dependence. Suggestive explanation could be that changes of fracture mode with temperature from TGC to IGF can destroy the stress- strain field at the crack tip representative of that at room temperature and the grain boundary cracking can release stresses at the tip of the crack causing the plastic zone decrease in size. Such small plastic zones seem not to interact with specimen boundaries and have no effect on toughness.

Again, as it was at RT, work of fracture does not show dependence on the RLL. The lack of this dependency for work of fracture indicates that there is no correlation between this property and the initiation fracture toughness, K_{IC} and it is also well reflected in the fact that none of the assumptions of linearity for the test specimen are made for calculations of work of fracture. This property could be determined in

the absence of any information on stress intensity factor K, and the notch tip accuity [130].

One of the most striking observations is the occurrence of a broad fracture toughness peak in 200°C- 500°C temperature range and a subsequent decrease of toughness to its RT value ~4.5 MPa$\sqrt{m}$ at 1000°C. Some K_Q values in the peak temperature range lie above the plane strain validity line in Fig.5.49. However, the K_{QVM} values obtained from the valid 4pt. large CNB specimens are in almost exactly the same range of toughness as the "invalid" K_Q values from the 3pt. SEPB specimens in the 200°C- 600°C temperature range. It seems, therefore, that the observed toughness peak is true and that the formal plane strain validity criterion does not seem to be fully applicable to the material tested. One reason for that might be again a continuously changing mode of fracture with increasing temperature, from TGC to IGF. Since Brown and Kumar [49] carried out their fracture toughness tests only up to 700°C they assumed that the toughness increased continuously with increasing temperature which is to a certain extent in contradiction to the results in Figs.5.49 and 5.50. It must also be pointed out that there is no difference in fracture toughness behavior of equiaxed and columnar grained specimens. Finally, the fracture toughness values obtained in this work and the modes of fracture are consistent with those reported by Brown and Kumar [49] up to 700°C.

For that matter, one may conclude that there is no difference in fracture toughness between coarse- and medium size- grained $L1_2$ titanium trialuminides if one compares coarse grain sizes observed in the present material with those reported by Brown and Kumar (~50 μm). The fracture toughness behavior vs. temperature in Fig.5.49 does not correlate with increase in tensile ductility of the cubic $L1_2$ Mn-

and Cr- modified titanium trialuminides with increasing temperature [14,15] although the gradual change in the fracture mode in tension from cleavage to intergranular observed in [14,15] is the same as observed in the present work.

Work of fracture, in contrast to toughness, increases continuously with temperature. It rises slowly to ~800°C and then abruptly increases. Similar dependence on temperature is shown by the "average" stress intensity factor since it is calculated from the work of fracture. It does not have a strict physical meaning, but still, it is used in the literature for characterization of complex fractures.

Cleavage fracture at low temperature always resulted in a very low γ_{WOF}. It must be kept in mind that the grain morphology (equiaxed vis- a vis columnar) does not have any effect on K_Q. However, the highest values of work of fracture observed at very high temperature (intergranular fracture IGF) correspond to the equiaxed grained specimens and the lowest ones correspond to the columnar grained specimens (Fig.5.66).

For every test temperature the stress intensity factor calculated from the γ_{WOF} is larger than the stress intensity factor calculated from the maximum load, $K_{IWOF}>K_Q$ (or K_{QVM}). The magnitude of their separation becomes larger and larger with increasing temperature. According to Rodeghiero et al. [142] and Jenkins et al. [138] this is a significant observation indicating non- linear fracture process or so-called R- curve behavior. Moreover, the increasing separation of K_Q (K_{QVM}) and K_{IWOF} as a function of increasing temperature suggests a more extensive R- curve behavior for the higher temperature. It must be pointed out that the increase of γ_{WOF} and K_{IWOF} with temperature correlate well with a gradual change in the mode of fracture from TGC to IGF. Physical meaning of high work of fracture is attributed to the pull- out of highly interlocked grains which are designated 1-2-3-4 in the

schematic in Fig.6.1. It is assumed here that some grain boundaries are weaker than the others and the crack path will appear as shown in Fig.6.1. Substantial forces, not only at the onset of fracture but also at long cracks, must be applied to overcome grain boundary friction to pull-out grains 2-4 from in between 1-3. Some plastic deformation and the pull-out of the interlocked grains affect the propagation of cracks in many different and complex ways, and one of the important effects is the relaxation, or reduction of stress, which they produce at the tip of the crack. This effect which has been referred to as the "shielding" of the crack from a remote stress has been recognized and considered by many research workers in terms of the reduction of the stress intensity factor K [162,163]. This stress reduction lowers the local value of both the crack extension force G, and the stress intensity factor, K, so that the critical condition for crack instability is more difficult to achieve.

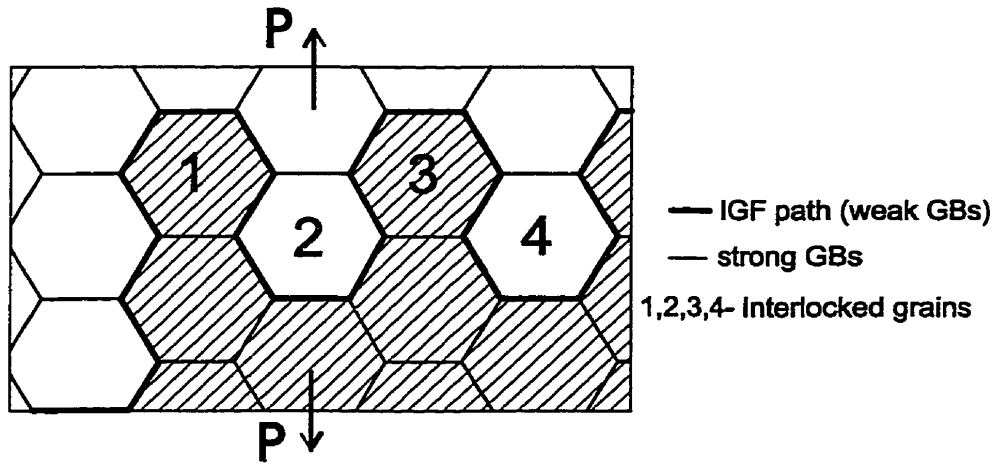

Figure 6.1 Schematic presentation of the interlocked grains. Shaded grains represent the portion (lower) of the polycrystal which is being pulled-out from the unshaded portions (upper) of the polycrystal.

A correlation between toughness and mode of fracture gave a hint for direction in designing tougher but still single phase material. However, it must be recognized

that, as was observed, the toughness is not a unique function of fracture mode and as will be confirmed later (section 6.3.5) is not the only function of fracture mode in the studied alloy.

An interesting feature is the nature of crack advance noticed in the present work. At some crack tips, high magnification, SEM observations of the step-wise loaded SEPB specimen revealed that a sharp precrack advances by formation of a few crack branches, and that a "cloud" of tiny microcracks is formed in the tip region. No signs of slip lines were observed. This type of crack advance very often occurs in ceramics where no dislocation activity is present due to a high energy barrier for dislocation emission even at high temperature. Also, very often, such bridging (in certain limits [148]) leads to increase in toughness with crack extension. Shear ligaments formation was also clearly observed during loading (Fig.5.90b). Such ligaments are known to increase the toughness for extending cracks and work of fracture but not the initiation toughness.

Still another characteristic feature at some crack tips was also observed. It is the localized deformation confined to the parallel bands (Fig.5.96). The plastically deformed region ahead of the crack tip appears entirely different in another $L1_2$ intermetallic alloy, Ni_3Al (and Ni_3Al+B) (Fig.5.97). It can be seen that in Ni_3Al, a larger volume of the material undergoes plastic deformation, which is more uniform and plane stress region at the tip is evident.

From the observations made in this study it can not be determined under what conditions the crack tips in low-Mn alloy develop localized plastic deformation and under what conditions microcrack zone forms without noticeable plastic deformation. However, an important conclusion could be that in order to increase

the fracture toughness of the 9Mn-25Ti alloy some degree of dispersion of the localized deformation at the crack tip should be achieved.

6.3.3 Effect of Grain Size and Grain Orientation on Fracture Toughness of "Base" 9Mn-25Ti Alloy.

As presented in Section 2.5 Armstrong [94] developed a model relating the critical stress intensity factor, K_C, to grain size, d. The dependence is a Hall-Petch type:

$$K_c = Cs^{1/2}[\sigma_0 + kd^{-1/2}] \qquad (2.2)$$

where C is a constant of proportionality, s is the plastic zone size, σ_0 is a measure of the lattice frictional stress and k is the microstructural stress intensity.

A reasonable agreement with this dependence was achieved in a number of investigations [95,96] on steel materials tested at relatively low temperatures. Recently, Mercer and Soboyejo [98] have tested gamma titanium aluminides (TiAl) and their results also clearly showed that a direct linear relationship exists between fracture toughness and $d^{-1/2}$, indicating a Hall-Petch behavior.

The goal of the powder processing in the present work was to obtain a bulk material appropriate for fracture toughness testing with the retained nanocrystalline structure of the powder to the largest extent possible in order to check whether the fracture toughness of cubic titanium trialuminide also increases with decreasing grain size as predicted by Hall-Petch relationship.

There were no radial cracks emanating from indentation corners (even at 2000 g load) for both- bulk material obtained by casting, homogenizing and HIP-ing and for hot compacted powders obtained in this study (powder compact no. K.5.6 in Table 5). Also lateral damage of indentations was not observed in either case. However, even though there were no cracks the material region close to the

indentation appeared different in both cases. The as-cast bulk material exhibited extensive plastic deformation with slip lines parallel to the sides of indentation. Such configuration of dense slip lines did not result in plastically induced microcracking. On the other hand, hot compacted powder "absorbed" and "spread" the plastic deformation in such a way that no slip lines were noticeable at the indentation sides and the surface at the indentations remained perfectly flat. It must be pointed out that the bulk material was much softer than that prepared from powder (163 HV 2- Table 5.4 vs. 310 HV 0.01- Table K.5).

Powder compacts obtained in Australia (compacts no. K.4.2 in Table K.4) behaved differently. Their microcracking at loads as low as 100 g could be attributed to high microhardness retained after processing (~730 HV0.01- Table K.4). Unfortunately, the small disk- bend method [164] of toughness measurement could not be applied to this material since it was available in very small pieces. Instead, indentation fracture toughness was used successfully. Contrary to the hopeful expectations, the material with such a small grain size (probably still much below 1 μm) resulted in the fracture toughness barely half that of the cast and coarse grained material (~2 MPa$\sqrt{m}$).

According to the model developed by Armstrong [94] (eq.2.2, section 2.5), toughness follows the Hall-Petch dependence on the grain size. In this model, a consequence of reaching the lower limit of grain size (approximately equal to the plastic zone size) is the triggering of the reversed negative slope of the Hall-Petch dependence (eq.2.3). Fig.6.2 shows the fracture toughness dependence on the inverse square root of grain size (similar to the Hall-Petch dependence) determined in the present work. For the partially recrystallized powder compact obtained in the present work the recrystallized grain size was assessed to be in the range 0.5-2

μm. This material did not show any corner microcracks around a Vickers indent made under 2 kg load and therefore the indentation fracture toughness could not be calculated at this load. To roughly assess the upper limit of fracture toughness of this material it is assumed that a 10 kg load could cause the total crack length around the Vickers indent to be equal to that caused by 2 kg load in the compact obtained in Australia (~62 μm x4, the average crack length from Table L.5). This assumption leads to the upper bound of fracture toughness of ~4.6 MPa√m. In a similar way, the lower bound of toughness can be calculated at the 3 kg load. This results in toughness of 2.5 MPa√m for the lower bound. The estimated average could be ~3.5 MPa√m. This value is indicated in Fig.6.2. The exact formula correlating the toughness to the grain size could not be found in the present work due to the rough estimate of the grain size of powder compacts and a broad band of toughness assessed for the powder compact obtained in the present work. However, it can be seen from Fig.6.2 that below certain critical grain size, the toughness clearly decreases. In this aspect, the results confirm the Armstrong's model [94] (eq.2.3). It can also be seen from Fig.6.2 that toughness seems to be independent of grain size for grains larger than 45 μm. This lack of dependence is in contradiction to the Armstrong's model. According to Morris [101], for a material exhibiting toughness 3-5 MPa√m and the Hall-Petch exponent n of 0.5, the brittle to ductile transition takes place for the grain size in the range 300-30 μm. The analysis was based on the assumption that if the critical crack length is less than the grain size the material fails, while if this length is greater than the grain size the material is stable and able to deform plastically. Unfortunately, the data in the present study can not be analyzed using Morris' model [101] since toughness is practically independent of grain size in the range 1270-45 μm in the present study.

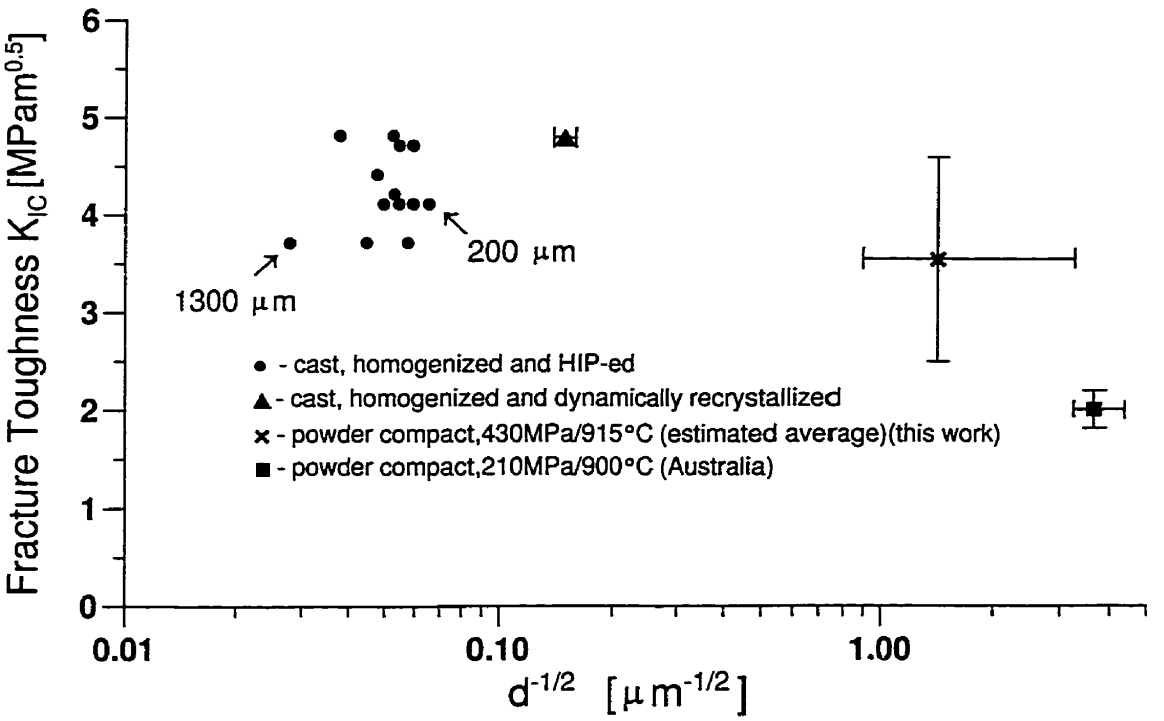

Figure 6.2 Fracture toughness dependence on grain size of 9Mn-25Ti alloy.

The inverse square root dependence of toughness on average grain/lamellar colony size in gamma based titanium aluminides was reported by Mercer and Soboyejo [98]. On the other hand, a lack of toughness dependence on grain size for gamma based titanium aluminides was reported by Gnanamoorthy [99]. In the latter study, however, the equiaxed grains of a single phase Ti-50Al were tested instead. Therefore, it seems that the Hall-Petch dependence reported by Mercer and Soboyejo was caused by some extrinsic toughening mechanism like for example shear ligament toughening typical for two-phase titanium aluminides [165]. Similar dependence of toughness on grain size for two phase ($\gamma+\alpha_2$) TiAl alloys to that obtained in the present study was reported by Morris and Leboeuf [102]. Fracture

toughness decreased slightly (12-10 MPa$\sqrt{m}$) as the grain size was reduced over the 100-5 μm range, and then fell rapidly (10-5 MPa$\sqrt{m}$) for smaller grain sizes. Lewandowski et al. [166] reported that the fine-grained, heavily deformed structure of NiAl resulting from the low-temperature hydrostatic extrusion processing produced the fracture toughness ~12 MPa$\sqrt{m}$ with the resistance curve behavior. However, the removal of the beneficial dislocation substructure via annealing at 973K returned the flow and fracture properties to that obtained in the NiAl conventionally extruded at high (1173K) temperature. Their hydrostatically extruded material had 12 μm grains in the transverse section with subgrains less than 1 μm in size and a dislocation density in the range 10^{11}-10^{12} cm^{-2}. It was also shown [167] that simply refining the grain size of NiAl has not significantly increased the toughness nor significantly changed the fracture mechanism, although the compressive yield strength was enhanced somewhat. Lewandowski et al. [166] suggested that their results could be explained by the model proposed by Ashby and Embury [66] (see section 2.4.2.1) in which a certain dislocation density is required in order for a BCC material to be ductile. In the present study, the recrystallized material exhibited a microhardness of 170±0.7 (HV 1kg) and 174±3 (HV 1kg) (Table C.1) for the partially and fully recrystallized material, respectively. The microhardness of the cast, homogenized and HIP-ed material is ~163 (HV 2kg) (Table 5.6) which is just a little lower than for the recrystallized alloy. These results suggest that the recrystallized material is free of substructure and the dislocation density is low. Therefore, according to Lewandowski et al. [166] such a material will not show increased fracture toughness with respect to the coarse grained material.

The effect of prestraining of cubic Al_3Ti on fracture behavior was reported by Kumar and Brown [56] (section 2.4.2). It was found that prestraining the

polycrystalline $L1_2$ compound, either at low (298K) or elevated temperature (1273K) was unsuccessful in improving the bend ductility; instead the available ductility in the well-annealed material was lost. The authors argued that the dislocations produced during prestraining may be immobile and do not contribute to enhanced plasticity. Similar conclusion was reached by Farkas [85] in her atomistic simulations on NiAl of crack response. It was shown that when the emitted dislocations are sessile and stay in the immediate vicinity of the crack tip the emitted dislocations can actually lead to brittle failure. Therefore, it seems that increasing the initial dislocation density in the Mn-modified Al_3Ti alloy might not produce beneficial effects on fracture toughness.

It is also worth mentioning that at 1000°C the fracture toughness for the partially dynamically recrystallized material with the average grain size ~45 μm was 7.8 MPa$\sqrt{m}$ which is substantially higher than average toughness for coarse-grained material (4-5 MPa$\sqrt{m}$) at this temperature. Therefore, it seems that the grain refinement could result in a continuous increase of toughness with temperature.

6.3.4 Effect of Environment

Fracture toughness shows no clear dependence on the environment at ambient and liquid nitrogen temperature (Fig.5.57). Therefore, there is no moisture effect on fracture toughness of 9Mn-25Ti alloy.

The disappearance of the toughness peak in argon at the intermediate temperature range (Fig.5.56) cannot be explained by the change in the mode of fracture since there is practically no difference in mode of fracture vs. temperature in air and argon. The K_Q fracture toughness numbers indicated in Fig.5.46 show that there is no dependence of fracture toughness on the fraction of intergranular (or cleavage)

mode of fracture for specimens tested in air and argon. It must also be pointed out that the K_Q values obtained at higher temperature in both air and argon do not exhibit any dependence on the remaining ligament length, (W-a), (Fig.5.58) as observed at RT (Fig.5.57a). It is clearly seen that K_Q data obtained in argon are independent of the remaining ligament length in the 800- 2500 μm range. The scatter of data obtained in air is the effect of the existence of a K_Q peak at intermediate temperatures (Figs.5.49 and 5.50). It has also been found that in both air and argon the fracture toughness at various temperatures is independent of whether the grains are equiaxed or columnar. Also, the orientation of columnar grains being either perpendicular or parallel to the direction of loading does not have any measurable influence on the obtained values of K_Q or K_{QVM}. This has been carefully checked for specimens tested in air and argon by either examining in SEM the fracture surface of those SEPB and CNB specimens which exhibited largely an intergranular failure or by etching the sides of the specimens which failed by cleavage and noticing in both cases the orientation of columnar grains with respect to the loading axis. Also, the cleavage fracture areas on the fracture surface of specimens tested in air and argon at temperature of 400, 500 and 600°C which correspond to the K_Q or K_{QVM} peak range in air, were carefully examined in SEM under various magnifications with the objective of revealing differences (if any) in the cleavage behavior during testing in air and argon that could explain the disappearance of the K_Q peak during testing in argon. Typical examples of cleavage surface appearance after fracture toughness test at 500°C in both air and argon are shown in Figs.5.37c and d and 5.42b and c. Each large cleavage facet (area) contains numerous parallel cleavage planes joined by tearing steps approximately perpendicular to the cleavage planes. The tearing step lines form the "river

patterns" on the cleavage facet. Unfortunately, there is no discernible difference between cleavage facets obtained in air and argon. They look quite alike. One might speculate that the elimination of the intermediate temperature fracture toughness peak in argon might be somehow related to the trapping of the argon gas at the crack tip. This might lead to a build up of a localized argon pressure at the crack tip and assisting in easier crack propagation. Unfortunately, the exact mechanism is unclear. Therefore, the origin of the fracture toughness peak in air at the intermediate temperature range and its elimination during testing in argon does not have any immediate explanation.

6.3.5 Effect of Boron and (Manganese+Titanium) Concentrations on Microhardness

Table 5.6 in section 5.6 shows the average microhardness values (HV2) of the alloys studied. In an earlier study, Winnicka and Varin [168] showed a nearly linear increase of HV with increasing Ti concentration in the $L1_2$ $Al_3Ti(X)$ alloys where X=Cr, Mn, Fe, and Cu. No microstructural studies by TEM were conducted in [168] and it was not clear whether the observed increase in HV could be the result of the existence of fine Al_2Ti precipitates or simply the effect of increased Ti concentration in the $L1_2$ matrix. The very fine Al_2Ti precipitates have been frequently observed by TEM in low-Mn, high-Ti trialuminides [4,5,133,169]. However, more recent studies of microhardness of the Al_2Ti precipitate-free zones (PFZs) in $L1_2$ $Al_3Ti(Ni)$ by Biswas and Varin [170], showed clearly that Vickers microhardness of PFZs (plain $L1_2$ matrix) increased with increasing concentration of Ti, Ni and/or (Ni+Ti) in the PFZs. Nakayama and Mabuchi [157] reported that microhardness of the $L1_2$ matrix in $Al_3Ti(X)$, where X=Cr, Mn, Ag, Cu, and Ni, increased with increasing Ti concentration and the most pronounced effect was observed in the Ni-bearing

alloy. This result confirms the results obtained by Winnicka and Varin [168] and Biswas and Varin [170]. Furthermore, Mabuchi et al. [36] reported that Vickers microhardness of the $L1_2$ matrix in $Al_3Ti(Mn)$, was nearly independent of the Mn content in the range 9–18 at%, but increased with increasing Ti content. They concluded that the microhardness of the $L1_2$ phase might be dependent on an off-stoichiometry for the titanium composition in the matrix, but was independent of the Mn concentration in the matrix. The microhardness results obtained in the present work (Table 5.6) and those obtained by other researchers, indicate very clearly that in the Mn and Cr alloyed trialuminides with high-Mn (or Cr) and Ti concentrations, the increase in Vickers microhardness of the $L1_2$ matrix is not the result of Al_2Ti precipitates. Rather, this is the effect of the increased Ti concentration (off-stoichiometry for titanium). This is also in agreement with the ternary Al–Mn–Ti phase diagram reported by Zhang and Mikkola [107] because at the composition of ~(14–15) at% Mn and ~(29–31) at% Ti, the Al_2Ti precipitates cannot form according to the phase diagram. In trialuminides alloyed with Ni the increase of microhardness may be the combined effect of Ni+Ti concentration [157,170]. It must also be pointed out that XRD studies conducted in the present work did not reveal the existence of any additional phase in the investigated 14Mn-type alloys. Even the X-ray peaks from phases such as γ_1, borides and needle (fibrous)-like Ti_2AlC (or Ti_2AlN) which are observed under optical/ scanning microscope, were not represented in the XRD scans. This confirms their very low volume fractions. The only XRD peaks observed beside oxides are those from the $L1_2$ matrix.

On the one hand, the mechanisms that might be responsible for the increase of hardness with increasing Ti content, could be an increase in the number of antisite

defects. Kogachi and Kameyama [171] reported that in a $L1_2$ $Al_3Ti(Cr)$ the number of the Cr atoms substituted on the Ti sites (Cr_{Ti}) and the Ti atoms substituted on the Al sites (Ti_{Al}) increased substantially with increasing Cr and Ti concentrations. On the other hand, however, the strengthening efficiency of antisite defects in intermetallics seems to be quite modest. Chang et al. [172] have estimated for B2 FeAl intermetallic that the dislocation–point defect interaction coefficient is about fourty–fold lower for antisite defects than vacancies. It is, therefore, not clear whether such a relatively weak mechanism might be indeed responsible for the observed increase in microhardness.

6.3.6 Effect of Boron and (Manganese+Titanium) Concentrations on Fracture Toughness

The major purpose of boron doping was to strengthen the weak grain boundaries at high temperatures which would possibly lead to higher toughness. Unusual feature of boron is that its segregation is stronger at grain boundaries than at free surfaces [134], in contrast to most embrittling solutes, which segregate more strongly to free surfaces. Boron has been found to be the most effective in improving the tensile ductility of Ni_3Al (<25 at.% Al) tested in air at RT [134,173]. Ductilizing effect of boron in Ni_3Al at room temperature is, for example, attributed to enhancement of grain boundary cohesion [51,174,175] and possibly permission of slip transmission across grain boundaries by means of grain boundary partial dislocations that are generated at the head of a pileup [176,177].

Table 6.1 shows a summary of the observed percentage improvement of fracture toughness with respect to the toughness of boron–free "base" 9Mn–25Ti alloy (Figs.5.79 and 5.80 in section 5.6), at various temperature ranges. The

microstructural factors such as the TGC/IGF transition temperature and fractions of IGF at 800–1000°C, accompanying fracture, are also shown. Various aspects of fracture toughness improvement are discussed in the following sections based on data summary in Table 6.1.

Table 6.1 A summary of the observed fracture toughness increase in percent with respect to boron-free 9Mn–25Ti alloy at various temperature ranges and microstructural factors accompanying fracture.

Alloy (at.%)	Fracture toughness increase (%)			TGC/IGF TT (°C)	Fraction of IGF at 800-1000°C (%)
	RT	200-600°C	1000°C		
9Mn-25Ti-0.004B	25-50	None	50-100	200	80-100
9Mn-25Ti-0.25B	25-50	None	50-100	200	80-100
9Mn-25Ti-0.66B	25-50	None	50-100	200	80-100
14Mn-29Ti	None	None	100-200	600	30-50
14Mn-29Ti-0.24B	100	50-100	100-200	600	20-80
14Mn-30Ti-0.65B	100	50-100	100-200	600	30-80

Fracture Toughness at Room Temperature

At room temperature, a very small addition of boron (0.004 at%) improves moderately (25–50%) the fracture toughness of 9Mn–25Ti alloy. Larger amounts of boron do not seem to benefit toughness of this alloy. The observed improvement is not accompanied by any changes in the fracture mode, which remains TGC (Fig.5.79). High-(Mn+Ti) concentration in boron-free 14Mn alloy does not improve toughness at room temperature. This result is to a certain extent contrary to the result of Mabuchi et al. [36] who reported a greater bend ductility of high-(Mn+Ti) cubic trialuminides. However, boron doping of high-(Mn+Ti), 14Mn-type alloys is very beneficial for the improvement of fracture toughness at room temperature, which increases by 100% (Table 6.1, Fig.5.80b,c). However, the mode of fracture is still TGC. Apparently, a combination of the boron addition and high concentration of (Mn+Ti) enhances fracture toughness with respect to that observed for both boron-free and boron-doped low-(Mn+Ti) alloys. Since the volume fraction of

second phase particles in boron-doped 9Mn-25Ti and 14Mn-type alloys is very similar and rather quite small (<5%) (Table 5.2) this effect does not seem to be related to the presence of these particles (which might affect toughness through, for example, crack bridging and/or crack deflection). In addition, the improvement of fracture toughness of boron-doped high-(Mn+Ti) alloys at room temperature seems not to be related to an increased hardness of these alloys as compared to 9Mn-type alloys. Boron-free 14Mn exhibits an increased hardness (Table 5.6) but no improvement of fracture toughness (Table 6.1 and Fig.5.80a). More likely, there might be some interactive effect of boron and high concentration of (Mn+Ti) on TGC at room temperature. As mentioned before, Kogachi and Kameyama [171] reported an increase of antisite defect numbers with increasing titanium and alloying element concentrations in cubic titanium trialuminides. It can be speculated that the boron atoms may interact with antisite defects, affecting the cleavage crack tip and leading to improved fracture toughness. However, the exact mechanism is not well understood and further studies are required. An alternative model of the toughness increase at room temperature could be outlined in the following way:

- Boron segregates to grain boundaries (GB)
- GB are strengthened
- Crack at RT propagates as TGC crack until it encounters a strong GB. It stops there and it must renucleate on the other side of strong GB but it propagates further still as TGC because the matrix is not strengthened by boron. Again it encounters another GB and the process is repeated.

Fracture Toughness at Intermediate and High Temperatures

As can be seen in Table 6.1 and Fig.5.79 for 9Mn-type alloys, a very small addition of boron (0.004 at%) improves moderately (50-100%) the fracture toughness at 1000°C. Larger amounts of boron (0.25 and 0.66 at%) benefit slightly the fracture toughness at 800°C but not at any other temperature. It does not seem to affect, however, the fracture toughness in the intermediate temperature range 200-600°C. The observed boron-induced improvements of toughness at 800-1000°C are not accompanied by any changes in the fracture mode. The variations in the mode of fracture remain the same with temperature as those for boron-free "base" 9Mn-25Ti alloys (section 5.6), i.e. TGC at room temperature with a gradual increase in IGF as temperature increases (Fig.5.81).

In boron-free 14 Mn alloy, an increased concentration of Mn+Ti improves fracture toughness only at 1000°C (Fig.5.80a). No improvement at the intermediate temperature range 200-600°C is observed. This is accompanied by a substantial suppression of IGF mode at the temperatures above TGC/IGF TT (Fig.5.82a). It seems that the IGF suppression resulting from high (Mn+Ti) is the major mechanism of toughness improvement at 1000°C of boron-free 14Mn alloy.

In boron-doped 14Mn-type alloys, at the intermediate temperature range 200-600°C, the effect of boron is more complex. Only the alloy with 0.24 at% B shows quite obvious toughness improvements with a relatively small scatter of results. Higher boron concentrations result in a larger scatter and do not increase fracture toughness any further (Table 6.1, Fig.5.80b,c). At temperatures above TGC/IGF TT (~600°C) the boron doping seems to increase the fraction of IGF with respect to that for boron-free 14Mn alloy (Fig.5.82b,c). However, as can be seen in Table 6.1, the fraction of IGF in boron-doped 14Mn-type alloys is still lower than that in 9Mn-

type alloys. Simultaneously, boron improves fracture toughness at 1000°C, mainly by eliminating experimental scatter, rendering the fracture toughness values more consistent (Fig.5.80b,c).

An important observation is that for 14Mn-type alloys the TGC/IGF TT is shifted to a much higher temperature of 600°C. However, boron doping does not affect the TGC/IGF TT (Fig.5.82). That implies that the shift can solely be attributed to the increased concentration of (Mn+Ti). A question arises whether or not the TGC/IGF TT shift is responsible for an improvement of fracture toughness at elevated temperatures. Boron- free 14Mn alloy exhibits the TGC/IGF TT shift (Fig.5.82a) but its fracture toughness up to 800°C is not improved. It seems, therefore, that the mere shift of TGC/IGF TT to higher temperatures is not a primary cause of fracture toughness improvement at elevated temperatures.

From a discussion above some factors emerge which, at present, can be related in only a qualitative manner to the fracture toughness improvements at intermediate (200-600°C) and very high temperatures (800-1000°C). In boron-doped 9Mn-25Ti (i.e. low-(Mn+Ti)) alloys, the improvement seems to be mostly due to the presence of boron at the grain boundaries (strongly suggesting that boron indeed segregated towards grain boundaries), without changing IGF mode. As seen in Table 6.1 this effect is moderate (50-100% toughness improvement).

In 14Mn-type alloys (i.e. high-(Mn+Ti)), a complex combination of an increased concentration of (Mn+Ti), suppression of IGF and boron doping (with most likely segregation at the grain boundaries) seems to be responsible for fracture toughness improvement. Thus, in boron-free high (Mn+Ti) alloys a profound suppression of IGF by about 50% (Fig.5.82a) seems to be the major mechanism of fracture toughness improvement at 800-1000°C. In boron-doped high (Mn+Ti)

alloys, fracture toughness improvement at 800-1000°C can be attributed to the combined effect of the possible presence of boron at the grain boundaries and the suppression of IGF. These proposed qualitative mechanisms are listed in Table 6.2. As shown in Figs.5.40 (9Mn alloy tested in air), 5.44 (9Mn alloy tested in argon), and 5.83c,d (boron-doped 14Mn alloy) dimples have been observed on the exposed grain boundary facets in specimens fractured at 1000°C. This kind of fracture progressing by the linking of voids but to assume an intergranular fracture path is quite common mode of fracture of many engineering alloys at high temperatures [178]. Knott [179] classified this mode of high temperature fracture as an "intergranular fibrous fracture" and Ashby et al. [180] called it an "intergranular creep fracture". Usually, intergranular (fibrous) creep fracture is observed under tensile testing conditions at lower stresses and high temperatures of deformation.

Table 6.2 An outline of the proposed qualitative mechanisms which might be responsible for the observed fracture toughness improvements.

Alloy	Mechanism at the Temperature Range (°C)		
	RT-200	200-600	800-1000
Boron-doped 9Mn-25Ti	Unknown	No benefit of boron doping	Boron segregation to GBs (?)
Boron-free 14Mn-29Ti	No benefit of high (Mn+Ti)	No benefit of high (Mn+Ti)	Suppression of IGF
Boron-doped 14Mn-29Ti	Interaction of ASD+boron atoms (?)	Boron segregation to GBs+suppression of IGF	

The nucleation of dimples at the grain boundary facets is attributed to grain boundary sliding with subsequent diffusional growth under the action of applied tensile stress, in the association with the presence of some second phase particles at the grain boundaries [179,180]. The nucleation criterion is one of a critical

amount of shear required to decohere the particle/matrix interface [179]. In the present work, second phase particles have not been observed at the grain boundary facets. Thus, the nucleation mechanism of dimples is not well understood. Nevertheless, their formation in the specimens fractured at 1000°C, at the lower portion of the chevron notch, i.e. at its base, where the crack propagation rate is the lowest one, correlates well with the requirements of low stresses and high temperatures [178–180]. It must be pointed out that the formation of dimples at the grain boundary facets do not affect the measured fracture toughness because it occurs later in the process of crack propagation, which corresponds to the "tail" portion of the P–LLD curve. As discussed in the preceding section, the fracture toughness is estimated from P_M on the P–LLD curve.

It is also instructive to discuss the present results in the view of models associated with the emission of dislocations at the crack tip.

As was presented in the section on crack tip plasticity, the incorporation of modified Rice and Thomson's dislocation emission model to intermetallic alloys (characterized by dissociated nature of dislocations) led Bartholomeusz and Wert [73] to the very practical conclusion that lowering the {111} APB energy in $Al_{67}Ni_8Ti_{25}$ below 330 mJ/m² and in Al_3Sc below 270 mJ/m² would allow sufficient spontaneous or thermally- activated emission of dissociated superlattice dislocations to avoid cleavage fracture at room temperature. According to this model, only changes in G, b, ν, Γ (γ^{APB} and/or γ^{SISF}) or γ (surface energy) can influence the fracture mode and of these, Γ is the most susceptible to manipulation by variation of chemical composition. Furthermore, the energy barrier for dislocation emission was only strongly dependent on γ^{APB} and was insensitive to γ^{SISF}.

It has been shown that the calculated $\xi(T)$ parameter [73] in the BW model (see section 2.4.2.2) corresponds well with the observed fracture modes for a number of intermetallics. However, further and more comprehensive experimental evidence is needed to confirm the usefulness and general application of the model. Just as a reminder, the $\xi(T)$ parameter in the BW model was established in a semiempirical way (similar to that in which the border value of Gb/γ was established in the Rice-Thomson model).

A matter that could raise some concerns is that the interpretation of Dislocation Emission Models (DEM) [77] was based on the idea that a fracture-mode transition occurs because the material becomes resistant to cleavage fracture as temperature increases, or alternately, a fracture-mode transition could result from a mechanism that promotes intergranular fracture as temperature increases. This assumption was applied to analyzing the fracture behavior of $Al_{67}Cr_8Ti_{25}$ alloy with temperature by Meng et al. [77]. As was mentioned earlier (section 2.4.2.2), a central result of the BW model for mode I loading is the identification of a critical value of $\xi(T)$, the normalized solid-angle range of slip system orientations corresponding to spontaneous or thermally activated dislocation emission at temperature T. Therefore, the $\xi(T)$ parameter is the border value for the dislocation emission/ cleavage fracture competition. The same authors [77] determined that the fracture mode of $Al_{67}Cr_8Ti_{25}$ alloy changed from predominantly TGC at ambient temperatures, to a mixture of TGC and IGF at intermediate temperatures, and then to predominantly IGF at high temperatures. More importantly, the fracture surfaces were not suggestive of increased plasticity at higher test temperatures. The authors also pointed out that this was consistent with the results showing a modest increase in fracture toughness with increasing temperature over the range of 298 to

873 K [49]. However, there is no conclusive comment given [77] on correlating these two conflicting facts: the assumption of the BW model (the competition between cleavage and dislocation emission which automatically is related to a change in fracture mode from cleavage to intergranular) and lack of any plastic deformation on grain boundary facets (but according to the BW model a change in the fracture mode is related to a change from brittle to ductile behavior). The correlation between the fracture mode change from TGC to IGF with the brittle to ductile transition, however, could be obscured by the limited test temperature (873 K) of $Al_{67}Cr_8Ti_{25}$ alloy [49]. In the present study, the Mn-modified (9Mn) Al_3Ti alloy exhibited very similar fracture mode change with temperature to that of its Cr-modified counterpart. However, for the Mn-modified alloy it is obvious that the change in fracture mode from TGC to IGF is not associated with the brittle- ductile transition. It should be pointed out that for 50% TGC + 50% IGF the low Mn (9Mn), boron-free alloy exhibited a toughness peak and further increase in % IGF caused the toughness drop to its RT value. Even more pronounced results contradicting the BW model assumption were obtained in the present study on the nearly- single phase, boron-free high Mn (14Mn) alloy. In this case the toughness increased monotonically with temperature up to 1000°C, and the IGF mode was suppressed to ~50% at the highest temperatures (vs. 100% IGF at 1000°C for boron-free low-Mn alloy). Therefore, it seems that a direct application of the BW model to the results obtained in the present work is not possible. It can be seen that application of the BW model even to single phase materials could lead to improper results. The interpretation of the results could be even more difficult and incorrect in case of two-, and multi-phase materials where some other toughening mechanisms can intervene.

Also the model proposed by Wang [78] (see section 2.4.2.2) seems not to be fully adequate to interpret the brittle- ductile transition in intermetallic alloys. The model suggests that in order to obtain ductile intermetallic alloys the a/6<112> type dissociation of superdislocation should be promoted. Although this dissociation scheme is mathematically correct and gives low energy barrier for dislocation emission, still it can be argued that CSF-coupled dissociation distance of the Shockley partials is so small due to high energy γ^{CSF} that both partials would have an effect on energy balance equal to that of undissociated superpartial leading to high energy barrier for dislocation emission. The TEM observations of the image contrast due to overlapping dislocation strain fields for dislocations dissociated over a small distance [90] were reported even for the APB-coupled dissociations. It is known that γ^{CSF} energy is higher than γ^{APB} energy which would lead to even smaller dissociation distance for CSF-coupled dislocations than for APB-coupled dislocations.

The Khantha, Pope, Vitek (KPV) model [84] (see section 2.4.2.2) can not be used to interpret the results of the present study at all. There are no assumptions made in this model which would take into account the continuous change in the fracture mode from TGC at low temperatures to IGF at higher temperatures. The same problem was encountered in the BW model. However, the authors [77] admitted that as a consequence of the strong influence of crystal and boundary orientations on the fracture and dislocation emission processes, it did not appear to be possible to formulate a general conclusion about the relative critical strain-energy release rates for the intergranular fracture and associated dislocation emission processes. Therefore, it was assumed [77] that a grain either cleaves when $G_{fract}<G_{disl}$ or exhibits a fracture mode other than cleavage when $G_{disl}>G_{fract}$, where G_{fract} and G_{disl}

are the critical strain energy release rate to propagate a crack and to cause the dislocation emission, respectively.

To summarize, all the models describing the brittle- to- ductile transition consider the emission of dislocations from crack tips. There must be a low energy barrier for such a process, the dislocations must be emitted in large quantities and the emitted dislocations must be free to move easily away from the crack tip under applied stresses. From the literature review presented in chapter 2 it seems that the dislocation emission is not a controlling step in fracture behavior of cubic $L1_2$ titanium trialuminides. The limiting factor could be the strain localization (compare plastic deformation ahead of the crack tips in the present study on 9Mn alloy and Ni_3Al [35] in Figs.5.96 and 5.97, respectively) and insufficient mobility of dislocations to move far away from the crack tip. This requirement was confirmed by atomistic study on NiAl of crack response [85] which showed that large density of immobile dislocations in the vicinity of the crack tip leads to cleavage fracture. It could be the case for $L1_2$ Al_3Ti alloys since it was shown that prestrain had detrimental effect on ductility of Cr-modified Al_3Ti [56], whereas prestrain in NiAl alloy had a beneficial effect on toughness. In this context the hypothetical interaction between ASD and the boron atoms in boron-doped 14Mn-type alloys might somehow lead to higher mobility of dislocations at the crack tip and associated improvement in fracture toughness.

7 Summary

1. Small amount of second phase in the as-cast low Mn-alloy dissolved during homogenization but there remained needle-like particles, most probably Ti_2AlC [14] and/or Ti_2AlN [133] with volume fraction <1%.

2. The content of needle-like particles is slightly higher in high-Mn alloy than in its low-Mn counterpart but is still below 1%. Porosity after HIP-ing remained ~2%. Addition of boron at the levels 0.25 and 0.66 % to the low- and high-Mn alloys caused formation of borides. Boron is partially chemically bound in boride particles. Total content of needle-like particles + boride particles ranged from 2.2-4.3%.

3. All the ingots showed similar, dual-grain morphology. Columnar grains were formed perpendicular to the mold walls and equiaxed ones were found in the central portion of the ingots. The grain size of all ingots falls into the wide range, which is ~0.2-0.5 mm for equiaxed and ~0.15-0.3 mm in thickness and ~2-5 mm in length for columnar grains.

4. The highest amount of second phase (0.96±0.87%) was found in high-Mn and high-boron alloy (beside needle-like and boride particles. This phase was identified as γ_1 phase $Al_{42}Mn_{25}Ti_{33}$ (at.%) which is in agreement with the phase diagram (Fig.B.1 in Appendix B).

5. Hot work at 1000°C at the deformation rate ~10^{-4} s^{-1} induced dynamic recrystallization of the low-Mn alloy. Material deformed to ~70% recrystallized completely, whereas when deformed to ~50% partially recrystallized. The average recrystallized grain size was ~45μm.

6. P-LLD curves look similar for CNB and SEPB specimens. They are also similar for SEPB type specimens tested in air, water, argon and vacuum. Fracture is catastrophic at ambient temperature and becomes more gradual at the highest temperature 800-1000°C. In liquid nitrogen P-LLD curves have the saw-toothed appearance.

7. Pop-ins observed during fracture toughness testing are caused by transgranular cleavage. When the cleavage origins are placed very close to the tip, the fracture is more gradual. Intergranular mode also usually results in more gradual fracture.

8. High-Mn alloy shows higher propensity for pop-ins than its low Mn-counterpart even if the fracture is 100% transgranular cleavage in both cases.

9. No crack stability (for SEPB and CNB specimens) was obtained at RT even in the most compliant specimens.

10. Fracture toughness results are in agreement for SEPB specimens loaded in 3 pt. bending and for CNB specimens loaded in 4 pt. bending. CNB specimens loaded in 3 pt. bending showed unreasonably high values of toughness and the origin of this could not be established unambiguously.

11. To ensure that results on CNB specimens represent valid K_{QVM} values, comparative tests on SEPB specimens are recommended, especially when CNB specimens fail catastrophically. Not complying with the recommended geometrical relations can lead to overestimation of fracture toughness.

12. Fracture toughness of coarse-grained (columnar and equiaxed) specimens of boron-free, "base" low-Mn 9Mn-25Ti alloy tested in air and vacuum measured as a function of temperature and calculated from the maximum load, exhibits a broad peak (7-10 MPa$\sqrt{m}$) at the intermediate 200-500°C temperature range and subsequently decreases reaching its room temperature value ~4.5 MPa$\sqrt{m}$ at 1000°C.

13. Regardless of alloy composition, during testing in air, vacuum and argon there is a gradual transition in the mode of fracture with increasing temperature from completely transgranular cleavage (TGC) at room temperature to completely intergranular failure (IGF) at 1000°C. Dimples have been observed on the grain boundary facets exposed by intergranular failure at 1000°C for grains located at the lower portion (base) of the chevron notch; their formation may be attributed to the occurrence of intergranular creep failure in the final stage of chevron-crack propagation (stable).

14. Fracture toughness of coarse-grained "base" 9Mn-25Ti alloy is not affected by testing in various environments such as air, vacuum (~1.5×10^{-7} Torr), argon, oxygen, water and liquid nitrogen. The low fracture toughness appears to be a fundamental response and not a consequence of the test environment.

15. Testing in argon of coarse-grained 9Mn-25Ti alloy eliminates the appearance of the fracture toughness peak at the intermediate temperature range and the low-Mn alloy exhibits approximately the same fracture toughness $K_Q \approx 5$ MPa$\sqrt{m}$ in the entire room to 1000°C temperature range.

16. At room temperature, fracture toughness measured using SEPB specimens depends on the remaining ligament length in air, vacuum and water. Toughness dependence on the remaining ligament length is somehow much weaker at higher temperature than that at room temperature.

17. The work of fracture does not show a dependence on the remaining ligament length in any of the environments. It increases with increasing temperature and especially at high temperature ~800-1000°C increases abruptly. At RT (cleavage fracture), the work of fracture in air, vacuum, water and liquid nitrogen is in the same range of values (100-800 J/m^2). The highest values of work of fracture are exhibited by specimens with very well developed and highly non-planar fracture surface (equiaxed grains).

18. The stress intensity factor calculated from the work of fracture (K_{IWOF}) is always higher than K_Q calculated from the maximum load, for every test temperature. The magnitude of the separation becomes larger with increasing temperature. This suggests an R-curve behavior.

19. For 9Mn-25Ti alloys there is no initiation toughness dependence on the grain size and morphology in the range of grain sizes tested, 50 μm-1300 μm. However, for the nanostructured 9Mn-25Ti compacts (~50-100 nm) the toughness is equal to half (2.1 MPa$\sqrt{m}$) that of the cast and HIP-ed alloy.

20. A very small boron doping of 0.004at.% increases fracture toughness of "base" 9Mn-25Ti trialuminide alloy by 25-50% at room temperature and 50-100% at 1000°C. No improvement is observed at the intermediate temperature range of 200-600°C. Larger doping with 0.25 and 0.66at.% B does not bring about further improvement of fracture toughness.

21. The evolution of fracture mode of boron-doped 9Mn-25Ti alloy as a function of temperature is unchanged with respect to boron-free "base" 9Mn-25Ti alloy, i.e. transgranular cleavage (TGC) at room temperature and a gradual transition to intergranular failure (IGF) with increasing temperature. For boron-doped 9Mn-25Ti alloys the TGC/IGF transition temperature (TGC/IGF TT) at which IGF starts to appear as a fracture mode is equal to ~200°C.

22. High (Mn+Ti) concentration in boron-free 14Mn-29Ti trialuminide alloy does not affect fracture toughness at room temperature but increases it by 100-200% at 1000°C with relatively high scatter of experimental data points.

23. Higher concentration of (Mn+Ti) in all the 14Mn-type alloys shifts the TGC/IGF transition temperature to ~600°C.

24. The occurrence of IGF mode in boron-free 14Mn alloy with high (Mn+Ti) concentration, at high temperatures above TGC/IGF TT (~600°C), is profoundly suppressed, rendering at 1000°C just 50% IGF, as compared to 100% IGF for boron-free "base" 9Mn-25Ti alloy. The observed increase (100-200%) of fracture toughness of boron-free 14Mn alloy at 1000°C seems to be due to the suppression of IGF.

25. A boron doping of 0.24 at.% results in a 100% increase of fracture toughness of 14Mn-type alloys at room temperature with respect to fracture toughness of both boron-free "base" 9Mn-25Ti and boron-free 14Mn alloys. It also increases 100-200% fracture toughness of 14Mn-type alloys at the intermediate temperature range of 200-600°C. At 1000°C boron eliminates largely the experimental scatter of fracture toughness data, rendering the data more consistent, but does not bring about any further toughness improvement as compared with that of boron-free 14Mn alloy. Higher boron concentration of 0.65 at.% does not provide more beneficial effect on toughness.

26. Boron does not affect the TGC/IGF TT for boron-doped 14Mn-type alloys, which remains at ~600°C.

27. The improvement of fracture toughness of boron-doped 9Mn-25Ti alloys at both room temperature and 1000°C seems to be due to the presence of boron. A combined effect of boron and a high (Mn+Ti) concentration in 14Mn-(29-

31)Ti alloys may be responsible for even more pronounced toughness improvements in the entire range from room temperature to 1000°C.

28. The average microhardness (HV2) of boron-free and boron-doped 14Mn-(29-31)Ti alloys with high (Mn+Ti) concentration is 50-70% higher than that of their boron-free and boron-doped, 9Mn-25Ti counterparts. However, higher microhardness seems to be unrelated to improvements of fracture toughness.

29. Some plastic deformation is present along the crack path in the locations where some branching occurs and whenever the crack deviates from straight line.

30. SEM observations of the step-wise loaded SEPB specimen showed that some crack tips form a "cloud" of tiny microcracks and that they advance in a manner similar to ceramics, e.g. by bridging, without signs of any plasticity.

31. Pre-alloyed ingots of the low-Mn alloy, as-cast, homogenized and subsequently crushed into coarse-particle powdered material were successfully mechanically milled into fine powders with nanocrystalline structure by controlled ball-milling under shearing mode.

32. X-ray spectra obtained from powders milled at various times show that all the Bragg peaks broaden in width and decrease in intensity which is attributed to formation of nanocrystals and internal lattice strains upon milling. The calculated internal lattice strain is in most cases less than 1%.

33. The morphology of powders upon ball-milling, observed under SEM, evolves from a typical "popcorn ball" within the first 100 h of milling into more equiaxed, globular shape.

34. The internal microstructure (cross-section) of a large fraction of powder particles milled up to 200 h is composed of a core and an outer layer. For milling times in the range 200 to 380 h the core/outer layer particles are gradually converted into "no core" particles. After milling for 386 h practically all particles do not exhibit a core.

35. The size distribution of powder particles milled for up to 200 h is bimodal. Between 200 and 380 h of milling, the particle size distribution becomes uniform, eventually approaching ~50 μm mean diameter.

36. The microhardness of the core increases with increasing milling time from the mean HV 296 for as-cast and homogenized ingot to HV 453 after 208 h of milling. This microhardness increase is most likely due to work hardening of the core.

37. The results of X-ray, microstructural and microhardness studies clearly indicate that nanometer sized grains are formed in the outer layer of particles with a core and throughout cross-section of the "no core" particles. The cores, most probably, retain the initial ingot structure, substantially work-hardened upon ball milling.

38. There is no indentation microcracking even at loads as high as 2000 g in both powders consolidated using long heating time (~40 min to reach 900°C) and in bulk (cast) specimens. Four-corner cracking pattern is occurring at loads as low as 100 g in powders consolidated using short heating time (~5 min to reach 900°C). Resulting indentation fracture toughness is ~half that of bulk material determined by bending of notched specimens and is equal to ~2.1 MPa$\sqrt{m}$.

References:

1. P.K. Wright, in: Structural Intermetallics, ed. by R. Darolia, J.J. Lewandowski, C.T. Liu, P.L. Martin, D.B. Miracle and M.V. Nathal, The Minerals, Metals and Materials Society, 1993, p.885.

2. Yamaguchi, M. and Inui, H., in Intermetallics Compounds: Practice, vol.2, ed. J.H. Westbrook and R.L. Fleisher, John Wiley & Sons, Chichester, 1995, p.147.

3. R.A. Varin, I. Virk, and M.B. Winnicka, in: Mechanical Behavior of Materials- VI, vol.3, ed. M. Jono and T. Inoue, p.179, Tokyo: Pergamon Press.

4. K.S. Kumar, (1993), in Structural Intermetallics, ed. by R. Darolia, J.J. Lewandowski, C.T. Liu, P.L. Martin, D.B. Miracle, and M.V. Nathal, The Minerals, Metals and Materials Society, p.87.

5. D.G. Morris, S. Gunter, R. Lerf, and J.C. Joye, (1993), in Structural Intermetallics, ed. by R. Darolia, J.J. Lewandowski, C.T. Liu, P.L. Martin, D.B. Miracle, and M.V. Nathal, The Minerals, Metals and Materials Society, p.97.

6. R.A. Varin, M.B. Winnicka, and I.S. Virk, (1993), in Structural Intermetallics, ed. by R. Darolia, J.J. Lewandowski, C.T. Liu, P.L. Martin, D.B. Miracle, and M.V. Nathal, The Minerals, Metals and Materials Society, p.97.

7. E.P. George, D.P. Pope, C.L. Fu, and J.H. Schneibel, ISIJ International, vol. 31, no.10, 1063(1991).

8. D.E. Mikkola, J.P. Nic, S.Zhang, and W.W. Milligan, ISIJ International, 31, 1076(1991).

9. H. Mabuchi, K. Hirukawa, H. Tsuda, and Y. Nakayama, Scripta Metall. Mat., 24(3), 505(1990).

10. H. Mabuchi, K. Hirukawa, and Y. Nakayama, Scripta Metall. 23(10), 1761(1989).

11. S.A. Brown, K.S. Kumar and J.D. Whittenberger, Scripta Met. Mater., vol. 24, 2001(1990).

12. D.J. Whittenberger, K.S. Kumar, S. Brown, M.S. DiPietro, and S.C. Farmer, 1991, in: Lightweight Alloys for Aerospace Applications II, ed. E.W. Lee and N.J. Kim, Warrendale, PA: The Minerals, Metals and Materials Society, p.327.

13. J.H. Schneibel, J.A. Horton, and W.P. Porter, 1992, Mat. Sci. Eng., Special issue: Proceeding of the International Conference on High- Temperature Aluminides and Intermetallics in San Diego, CA. Sept. 1991, A 152(1-2):126.

14. K.S. Kumar and S.A. Brown, Acta metall. mater., 26, 1923(1992).

15. K.S. Kumar and S.A. Brown, Phil. Mag. A, 65, 91(1992).

16. K.Hirukawa, H. Mabuchi, and Y. Nakayama, 1991, Scr. Metall. Mater. 25(5), 1211(1991).

17. L.J. Parfitt, J.L. Smialek, J.P. Nic, and D.E. Mikkola, 1991, Scr. Metall. Mat. 25(3):727.

18. J.L. Smialek, 1991, Private communication (also presented at the ASM-sponsored AEROMAT 1991 meeting in Long Beach, CA in May 1991).

19. C.D. Turner, W.O. Powers and J.A.Wert, Acta metall. 37, 2635(1989).

20. J. Tarnacki and Y.W. Kim, in Dispersion Strengthened Aluminum Alloys, ed. By Y.W. Kim and W.M. Griffith, The Minerals, Metals & Materials Society, 1988.

21. E.P. George, J.A. Horton, W.D. Porter and J.H. Schneibel, J. Mater. Res. 5, 1639(1990).

22. C.L. Fu, J. Mater. Res., 5, 971(1990).

23. R.W. Hyland, Jr. and R.C. Stiffler, Scr. Metall., 25, 473

24. K.S. Kumar and S.A. Brown, Scripta Metall. Mater., 26, 197(1992).

25. S. Zhang, J.P.Nic, W.W. Milligan and D.E. Mikkola, Scripta Metall., 24, 1441.

26. J.H. Schneibel and E.P. George, Scripta Met. Mater., 24, 1069(1990).

27. Z.L. Wu, D.P. Pope, and V. Vitek, Scripta Met. Mater., 24, 218(1990).

28. M.B. Winnicka and R.A. Varin, Metall. Trans. A, 24A, 935(1993).

29. S. Zhang, J.P. Nic, and D.E. Mikkola, Scripta Met. Mater., 24, 57(1990).

30. J.P. Nic, S. Zhang, and D.E. Mikkola, Scripta Metall., 24, (1989)

31. M.B. Winnicka and R.A. Varin, Scripta Met. Mater., 23, 1199(1989).

32. M.B. Winnicka and R.A. Varin, Scripta Met. Mater., 24, 611(1990).

33. K.S. Kumar and J.R. Pickens, (1989), Proc. Symp. on Dispersion Strengthened Aluminum Alloys, ed. by Kim Y.W. and Griffith W.M., TMS, Warrandale, 763.

34. I.S. Virk, M.B. Winnicka, and R.A. Varin, Scripta Metall., 24, 2181(1990).

35. J.D. Rigney and J.J. Lewandowski, Mat. Sci. Eng., A149, 143(1992).

36. H. Mabuchi, A. Kito, M. Nakamoto, H. Tsuda, and Y. Nakayama, Intermetallics, 4, S193, 1996.

37. C.T. Liu, in High Temperature Ordered Intermetallic Alloys II, vol. 86, ed. by N.S. Stoloff, C.C. Koch, C.T. Liu, and O. Izumi (Pittsburg: MRS), 355(1987).

38. T. Takasugi, O. Izumi, Acta Metall., 33, 39; Acta Metall, 33, 1247(1985).

39. C.T. Liu and C.L. White, Acta Metall., 35, 643(1987).

40. K.S. Kumar and J.R. Pickens, (1988), Scripta Metall., 22, 1015.

41. Z.L. Wu, D.P. Pope, and V. Vitek, (1990), Scripta Metall., 24, 2191.

42. K.S. Kumar, S.A. Brown, and J.D. Whittenberg, (1991), in High Temp. Intermetallic Alloys IV, ed. by Johnson, L., Pope, D.P., and Stiegler, J.O., MRS Symp. Proc., vol. 213, MRS, Pittsburgh, 481.

43. Z.L. Wu, D.P. Pope, and V. Vitek, (1991) in High Temp. Intermetallic Alloys IV, ed. by Johnson, L., Pope, D.P., and Stiegler, J.O., MRS Proc., vol. 213, 487.

44. A.N. Stroh, Adv. Phys. 6, 418(1957).

45. E. Smith and J.T. Barnby, Metal Sci. J., 1, 56(1967).

46. R.A. Varin and M.B. Winnicka, Scripta Metall. Mater., 28, 17(1993).

47. M.F. Ashby, Acta Metall. Mater., 37, 1273(1989).

48. M.R. Jackson, B.P. Bewlay, R.G. Rowe, D.W. Skelly, and H.A. Lipsitt, JOM, 48, 39(1996).

49. S.A. Brown and K.S. Kumar, J. Mater. Res. 8, 1763(1993).

50. H. Vehoff, in Ordered Intermetallics– Physical Metallurgy and Mechanical Behavior, ed. by Liu, C.T., Cahn, R.W., and Sauthoff, G., NATO Advanced Research Workshop, Irsee Germany, (1991), NATO ASI Series E: Applied Sciences, vol.213, Kluwer Academic, Boston (1992), 299.

51. C.T. Liu and C.L. White, in High Temp. Ordered Intermetallic Alloys, NV, ed. by C.C. Koch et al., MRS Sym. Proc., 35, 1533(1985)(1988).

52. N.S. Stoloff and C.T. Liu: Intermetallics, 2, 75(1994).

53. E.P. George, C.T. Liu, and D.P. Pope: Acta Mater., 44, 1757(1996).

54. J.C.M. Li, Scr. Metall., vol.20, 1477(1986).

55. R.D. Noebe, J.T. Kim, and R. Gibala, (1987) in High Temp. Ordered Intermetallic Alloys II, vol. 81, ed. by Stoloff, N.S., Koch, C.C., Liu, C.T., and Izumi, O., (Pittsburgh: MRS), 473.

56. K.S. Kumar and S.A. Brown, Intermetallics 4, 231(1996).

57. D.G. Morris, M.A. Morris, and M. Leboeuf, Acta Metall. Mater, 41, 2077(1993).

58. V. Vitek, G.J. Ackland and J.Cserti, MRS Symp. Proc., 186, 237(1991).

59. C.T. Liu et al. Ordered Intermetallics- Physical Metallurgy and Mechanical Behavior, 699.

60. Y. Liu, T. Takasugi, O. Izumi, and T. Takahashi, Philos. Mag. A, 59, 423(1989).

61. F.P. Bullen, F. Henderson, M.M. Hutchinson, and H.L. Wain, Phil. Mag., 9, 285(1964).

62. H. Inui, D.E. Luzzi, W.D. Porter, D.P. Pope, V. Vitek, and M. Yamaguchi, Philos. Mag. A, v.65, No 1, 245(1992).

63. J.R. Rice and R. Thomson, Philos. Mag., 29 (1974) 73.

64. J. Weertman, Dislocation Based Fracture Mechanics, World Scientific Publishing Co. Pte. Ltd., 1996.

65. G. Schoeck, Phil. Mag. A, vol. 63, no.1, 111(1991).

66. M.F. Ashby and J.D. Embury, Scripta Metall., 19, 557(1985).

67. V.K. Vasudevan, R. Wheeler, and H.L. Fraser: in High Temperature Ordered Intermetallic Alloys III, MRSS Proc., C.T. Liu, A.I. Taub, N.S. Stoloff, and C.C. Koch, eds., MRS, Pittsburg, PA, 705(1989).

68. M.J. Marcinkowski: in Electron Microscopy and Strength of Crystals, G.Thomas and J. Washburn, eds., Wiley Interscience, New York, NY, 333(1963).

69. N.S. Stoloff and R.G. Davies, Prog. Mat. Sci., vol.13, 1(1966).

70. M.J. Marcinkowski: Treatise on Materials Science and Technology, vol.5, 181(1974).

71. M. Yamaguchi, V. Vitek, and D.P. Pope: Phil. Mag., vol.43, 1027(1981).

72. D.P. Pope and S.S. Ezz: Inter. Met. Rev., vol.29, 136(1984).

73. M.F. Bartholomeusz and J.A. Wert, Acta metall. mater., vol. 40, no.4, 673(1992).

74. M.F. Bartholomeusz, W. Meng, and J.A. Wert, (1993), Mater. Res. Soc. Symp. Proc., ed. by Baker, I., Darolia, R., Whittenberg, J.D., and Yoo, M.H., MRS, Pittsburgh.

75. M.F. Bartholomeusz, W. Meng and J.A. Wert, M.R.S. Sym. Proc., vol. 288, Boston, MA, USA, eds. I. Baker, R. Darolia, J.D. Whittenberger, M.H. Yoo, 1992.

76. M.F. Bartholomeusz and J.A. Wert, J. Mater. Res., vol.7, no.4, 919(1992).

77. W.G. Meng, M.D. Vaudin, M.F. Bartholomeusz, and J.A. Wert, Metall. Mater. Trans. A, vol. 26A, 329(1995).

78. J.S. Wang, Acta mater., 46, no.8, 2663(1998).

79. P.M. Hazzledine and Q.S. Sun, in High-Temperature Ordered Intermetallic Alloys IV, 213, ed. L.A. Johnson, D.T. Pope and J.O. Stiegler. MRS Proc., 1991, p.209.

80. F. Fang, E.M. Shulson and I. Baker, Phil. Mag., A70, 1013(1994).

81. C.T. Liu and D.P. Pope, Intermetallics Compounds: Practice, vol.2, ed. J.H. Westbrook and R.L. Fleisher, John Wiley & Sons, Chichester, 1995, p.17.

82. N.S. Stoloff, International Materials Reviews, vol.34, 153(1989).

83. C.T. Liu, in Structural Intermetallics, ed. By R. Darolia, J.J. Lewandowski, C.T. Liu, P.L. Martin, D.B. Miracle and M.V. Nathal, The Minerals, Metals & Materials Society, 1993, p.365.

84. M. Khantha, D.P. Pope, V. Vitek, Mat. Sci. Eng., A192/193, 435(1995).

85. D. Farkas, Scr. Mater., 39, 533(1998).

86. E.P. George, W.D. Porter, H.M. Henson, W.C. Oliver, and B.F. Oliver, J. Mater. Res., vol.5, 1639(1991).

87. X. Wu, Y. Rong, S. Chen, and G. Hu, Scripta Metall. Mater., 28, 1519(1993).

88. M.H. Yoo, and C.L. Fu, (1991), Iron and Steel Inst. Japan International, 31, 1049.

89. S.F. Pugh, Phil. Mag., 45, 823(1954).

90. M. Kumar and K.J. Hemker, J. Mater. Res., vol. 13, no. 5, (1998), p.610.

91. Y. Miura and N. Watanabe, Scr. Metall. Mater., 29, 139, 1993.

92. D.P. Pope, (1992) in Ordered Intermetallics- Physical Metallurgy and Mechanical Behavior, eds Liu, C.T. et al., Kluwer Academic Publishers, 143.

93. M.L. Jokl, V. Vitek, C.J. McMahon, Jr.P. Burgers, Acta Metall., 37, 87(1989).

94. R.W. Armstrong, Eng. Fract. Mech., 28, no.5/6, 529(1987).

95. W.W. Gerberich, V.F. Zackay, E.R. Parker, and D. Porter, in Ultrafine-Grain Metals (ed. By J.J. Burke and V. Weiss), Syracuse Univ. Press, N.Y., (1970), p.259.

96. D.A. Curry and J.F. Knott, Metal Sci., 10, 1(1976).

97. R.J. Klassen, M.N. Bassim, M.R. Bayoumi, and H.G.F. Wilsdorf, Mater. Sci. Engng 80, 25(1986).

98. C. Mercer and W.O. Soboyejo, Scripta Mater., 35, no.1, 17(1996).

99. R. Gnanamoorthy, Y. Mutoh, N. Masahashi, and Y. Mizuhara, Metall. Mater. Trans. A, 26A, 305(1995).

100. K.S. Chan, Scr. Metall. Mater., 24, 1725(1990).

101. D.G. Morris, Mechanical Behavior of Nanostructured Materials, (1998), Trans Tech Publications Ltd., Switzerland.

102. M.A. Morris, M. Leboeuf, Mater. Sci. Engng., A224, 1(1997).

103. M. Hoffman and R. Birringer, Acta Mater., 44, 2729(1996).

104. M. Mayo, R.W. Siegel, A. Narayanasamy, and W.D. Nix, J. Mater. Res., 5, 1073(1990).

105. H.P. Klug and L. Alexander, X- ray Diffraction Procedures for Polycrystalline and Amorphous Materials, John Wiley and Sons, New York, 2nd Edition, 1992, p.661.

106. C.C. Koch and J.D. Whittenberger, Intermetallics, 4, 339(1996).

107. S. Zhang and D.E. Mikkola, Scripta Metall. Mater., vol. 26, 1315(1992).

108. A. Calka and A.P. Radlinski, Mater. Sci. Eng., A134, 1350(1991).

109. S.K. Pradhan, T. Chakraborty, S.P. Sen Gupta, C. Suryanarayana, A. Frefer and F.H. Froes, NanoStructured Mater., 5, 53(1995).

110. A.G. Evans, Fracture Mechanics of Ceramics, vol.1, Plenum Press, New York (1974).

111. L.M. Barker, Engng. Fract. Mech., 9, 361(1977).

112. J. Nakajama, J. Am. Cer. Soc., 48, 583(1965).

113. H.G. Tettersall and G.Tappin, J. Mat. Sci., 1, 296(1966).

114. ASTM E399-90, Standard Test Method for Plane- Strain Fracture Toughness of Metallic Materials.

115. Standard Test Method for Plane- Strain (Chevron- Notch) Fracture Toughness of Metallic Materials: E 1304- 97.

116. T.Nose and T.Fuji, J. Am. Cer. Soc., 71, 328(1988).

117. G. Albinger, Java Jandel Video Analysis Software, Jandel Scientific, Corte Madera, CA, 1988.

118. M. Sakai and R.C. Bradt, Intern. Mat. Rev., vol. 38, no. 2, 53(1993).

119. D. Munz, R.T. Bubsey, and J.L. Shannon, Jr, J. Am. Cer. Soc., vol. 63, no. 5-6, 300(1980).

120. D. Munz, J.L. Shannon, Jr. and R.T. Bubsey, Intern. Journal of Fracture, 16(1980), R137.

121. J.I. Bluhm, Eng. Fr. Mech. 7, 593(1975).

122. Sh.-X. Wu, Eng. Fracture Mech. 19, 221(1984).

123. D. Munz, R.T. Bubsey, and J.E. Srawley, International Journal of Fracture, vol. 16, no.4, 359(1980).

124. W. Chizhi, thesis, Chongqing University, May 1982.

125. L.M. Barker, Fracture Mechanics of Ceramics, 3, 483(1978).

126. Sh.-X. Wu, in Chevron-Notched Specimens: Testing and Stress Analysis, ASTM STP 855, eds. J.H. Underwood, S.W. Freiman, and F.I. Baratta, ASTM, Philadelphia, PA, 1984, p.176-192.

127. I. Bar-On, F.R. Tuler, and I. Roman, ibid, p.98.

128. I. Merkel and U. Messerschmidt, Materials Science and Engineering A, A151, 131(1992).

129. H.Nakamura and H. Kobayashi, Mater. Sci. Eng. A143. 119(1991).

130. B.Cotterell, E. Lee and Y.W. Mai, International Journal of Fracture, 20, 243(1982).

131. M. Sakai, K. Urashima, and M. Inagaki, J. Am. Cer. Soc., 868 (1983).

132. M. Sakai and H. Ichikawa, Int. J. Fracture 55, 65(1992).

133. Z.L. Wu and D.P. Pope, Acta Metall. Mater., 42, 519(1994).

134. C.T.Liu, C.L. White, and J.A. Horton, Acta Metall., 33, 213(1985).

135. P. Zhongjie, Z. Dong, Z. Dunxu, and Z. Zengyong, Scr. Metall. Mater., 26, 213(1992).

136. P.A. Whithey and P. Bowen, Int. Journal of Fracture 46, R55, 1990.

137. J. Sung and P.S. Nicholson, J. Am. Cer. Soc., 72, 1033(1989).

138. M.G. Jenkins, M.K. Ferber, A. Gosh, Peussa, and J.A. Salem, Chevron- Notch Fracture Test Experience: Metals and Nonmetals, ASTM STP 1172, K.R. Brown and F.I. Baratta, eds., ASTM, Philadelphia, 159, 1992.

139. J.A. Smith, P. Limthongkul and S.L. Sass in Processing and Fabrication of Advanced Materials IV, ed. by T.S. Srivatsan and J.J. Moore, TMS, Warrendle, PA, 1996.

140. E.D. Rodeghiero, O.K. Tse, B.S. Wolkenberg, and E.P. Gianuelis, in Processing and Fabrication of Advanced Materials IV, ed. by T.S. Srivatsan and J.J. Moore, TMS, Warrendale, PA, 775(1996).

141. M. Nakamura in Intermetallic Compounds Vol. 1 Principles, ed. by J.H. Westbrook and R.L. Fleischer (John Wiley and Sons Ltd., Chichester, 1995), p.873.

142. C.S. Barrett and T.B. Massalski, Structure of Metals, 3rd revised edition, Pergamon Press, (1980).

143. L.M. Barker, International Journal of Fracture, 15, 515(1979).

144. J.C. Newman, in Chevron-Notched Specimens: Testing and Stress Analysis, ASTM STP 855, eds. J.H. Underwood, S.W. Freiman, and F.I. Baratta, ASTM, Philadelphia, PA, 1984, p.5.

145. L. Chuck, Jr. E.R. Ruller, and S.W. Freiman, ibid, p.167.

146. A. Ghosh, M.G. Jenkins, K.W. White, A.S. Kobayashi, and R.C. Bradt, in Ceramic Materials and Components for Engines, ed. V.J. Tennery, The American Ceramic Society, Westerville, OH, 1989, p.562.

147. K.S. Kumar and S.A. Brown, in High-Temperature Ordered Intermetallic Alloys V, eds. I. Baker, R. Darolia, J.D. Whittenberger and M.H. Yoo, MRS Symp. Proc. vol.288, MRS, Pittsburgh, PA, 1993, p.781.

148. L.X. Han, R.Warren and S. Suresh, Acta metall. mater. vol. 40, no.40, 259(1992).

149. M.Goken, H.Vehoff, and P.Neumann, Scripta Met. Mater., vol.33, 1187(1995).

150. H.-J. Fecht, NanoStructured Mater., 6, 33(1995).

151. R.A. Varin, D. Wexler, A. Calka, and L. Zbroniec, Intermetallics 6, 547(1998).

152. S. Palmqvist, Jernkontorets Ann. 141, 300(1957).

153. B. Lawn, Fracture of Brittle Solids, eds. E.A. Davis, I.M. Ward, Cambridge University Press. 1975, (1993).

154. Y.K. Song and R.A. Varin, Intermetallics 6, 379(1998).

155. D.K. Shetty, I.G. Wright, P.N. Mincer, A.H. Clauer, J. Mat. Sci., 20, (1873)1985.

156. S. Mazdiyasni, D.B. Miracle, and D.M. Dimidiuk, Scripta Met., 23, 327(1989).

157. Y. Nakayama and H. Mabuchi, Intermetallics 1, 41(1993).

158. S. Zhang, W.W. Milligan, and D.E. Mikkola, J. Mater. Res., vol.9, no. 3, (1994), p.553.

159. D.D. Mysko, J.B. Lumsden, W.O. Powers, and J.A. Wert, Scripta Metall., 23, 1827(1989).

160. X. Chen, S. Chen, X. Wu, L. Fang and G.H., Materials Science and Engineering, A153, 370(1992).

161. R.A. Varin, J. Bystrzycki, A. Calka, Intermetallics, in press (1999).

162. R. Thomson, Solid state physics, 39, 1(1986).

163. R.O. Ritchie, Mater. Sci. & Eng. A103, 15(1988).

164. J. Zhang and A.J. Ardell, J. Mater. Res., vol. 6, no. 9, 1950(1991).

165. K.S. Chan, Metall. Trans. A, 22A, 2021(1991).

166. J.J. Lewandowski, B. Berger, J.D. Rigney, and S.N. Patankar, Phil. Mag. A, 78, no.3, 643(1998).

167. D.B. Miracle, Acta metall., 41, 649(1993).

168. M.B. Winnicka and R.A. Varin, Scr. Mater., 25, 2297(1991).

169. L. Potez, A. Loiseau, S. Naka, and G. Lapasset, J. Mat. Res., 7, 876(1992).

170. S. Biswas and R.A. Varin, Metall. Mater. Trans A, 27A, 71(1996).

171. M. Kogachi and A. Kameyama, Intermetallics, 3, 327(1995).

172. Y.A. Chang, L.M. Pike, C.T. Liu, A.R. Bilbrey, and D.S. Stone, Intermetallics, 1, 107(1993).

173. K. Aoki and O. Izumi, Nippon Kinzoku Gakkaishi, 43, 1190(1979).

174. J.R. Rice, Effect of Hydrogen on Behavior of Materials, ed. by A.W. Thomson and I.M. Bernstein, 455, New York, Metall. Society of AIME. 110(1976).

175. S.P. Chen, A.F. Voter, R.C. Albers, A.M. Boring, and P.J. Hay, Scripta Metall., 23, 217(1989).

176. I. Baker, E.M. Schulson, and J.A. Horton, Acta Metall., 35, 1533(1987).

177. G.M. Bond, I.M. Robertson, and H.K. Birnbaum, J. Mater. Res., 2, 436(1987).

178. A. Gysler and G. Lutjering, in Advances in Research on the Strength and Fracture of Materials, vol.2A- The Physical Metallurgy of Fracture, ed. D.M.R. Taplin, Pergamon Press, 1977, p.585.

179. J.F. Knott, in Fracture 1977-Proc. of the Fourth Int. Conf. on Fracture, ed. D.M.R. Taplin, University of Waterloo Press, 1977, vol.1, p.61.

180. M.F. Ashby, C. Gandhi, and D.M.R. Taplin, Acta Metall., 27, 699(1979).

Appendices

A Fracture Toughness Calculations for SEPB Specimens

Fracture toughness calculated for SEPB according to ASTM Standard [196]:

$$K_Q = \frac{P_Q S}{BW^{3/2}} f\left(\frac{a}{W}\right)$$

where

$$f\left(\frac{a}{W}\right) = \frac{3\left(\frac{a}{W}\right)^{1/2}\left[1.99 - \left(\frac{a}{W}\right)\left(1-\frac{a}{W}\right)\left(2.15 - 3.93\frac{a}{W} + 2.7\left(\frac{a}{W}\right)^2\right)\right]}{2\left(1+2\frac{a}{W}\right)\left(1-\frac{a}{W}\right)^{3/2}}$$

Fracture toughness calculated for SEPB (for $S_2/W \neq 4$) [102]:

$$K_Q = \frac{P}{BW^{1/2}} f\left(\frac{a}{W}\right)$$

where

$$f\left(\frac{a}{W}\right) = \left[(S_1 - S_2)/W\right]\left[\frac{3\left(\frac{a}{W}\right)^2}{2\left(1-\left(\frac{a}{W}\right)^{3/2}\right)}\right] x$$

$$\left\{1.99 - 1.33\frac{a}{W} - \left(3.49 - 0.68\frac{a}{W} + 1.35\left(\frac{a}{W}\right)^2\right)\left[\frac{\frac{a}{W}\left(1-\frac{a}{W}\right)}{\left(1+\frac{a}{W}\right)^2}\right]\right\}$$

For 3pt. bending $S_1=0$.

B Ternary, Al- Mn- Ti Phase Diagram

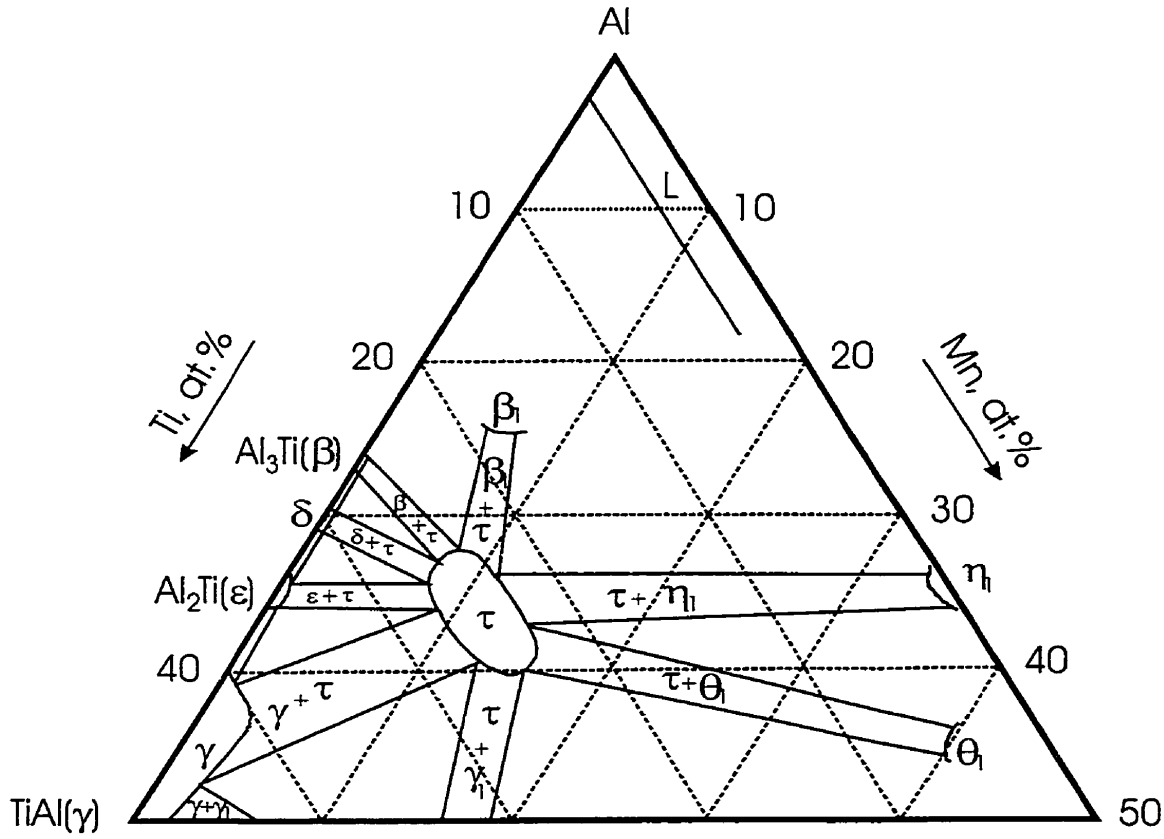

Figure B.1 Isothermal section of the Al- Mn- Ti system near the $L1_2$ phase region at 1473 K, according to Ref.[107] (cooling time from 1473 K to RT was ~30 min).

γ_1 - Al- 42, Mn- 25, Ti- 33 (at.%)

η_1 - Al- 65, Mn- 33, Ti- 2 (at.%)

θ_1 - Al- 54, Mn- 5, Ti- 30 (at.%)

Table C.1 Hot- worked specimens.

	DESIG-NATION	T [°C]	NOTCH [μm]	PREC-RACK [μm]	LIGA-MENT [μm]	B [mm]	W [mm]	a/W	f(a/W)	P_{max} [kG]	K_Q [MPam$^{0.5}$]
PARTIALLY RECRYSTALLIZED MATERIAL (~50% DEFORMATION), SEPB,S=16mm, 170±0.7 (HV 1kg)											
1.	RECRAL1	RT	1135	1979	1006	3.45	4.12	0.756	7.990	3.5	4.8
2.	RECRAL2	RT	1106	1608	1086	3.33	3.80	0.714	6.297	4.9	6.2
3.	RECRAL3	RT	1160	1038	1892	3.57	4.09	0.537	3.01	11.0	5.6
4.	RECRAL4	RT	1184	2562	644	3.50	4.39	0.8533	17.262	2.8	7.4
RECRYSTALLIZED MATERIAL (~70% DEFORMATION), SEPB, S=16mm, 174±2.6 (HV 1kg)											
5.	RECRAL1A	RT	1169	924	1407	3.88	3.50	0.598	3.743	5.5	4.0
6.	RECRAL2A	RT	1219	1764	1017	3.22	4.0	0.746	7.516	4.8	6.9
7.	RECRAL3A	RT	1145	2407	528	3.75	4.08	0.870	20.867	2.9	9.7
8.	RECRAL4A	RT	1120	2464	516	3.85	4.10	0.874	21.766	2.8	9.5
PARTIALLY RECRYSTALLIZED MATERIAL (~50% DEFORMATION), CNB, S_1=16mm, S_2=4mm											
	DESIG-NATION	T [°C]	B [mm]	W [mm]	a_0	a_1	Y_{min}		P_{max} [kG]		K_{QVM} [MPam$^{0.5}$]
9.	RECRAL5A	1000	3.7	3.34	0.166	0.966	14.7		11.52		7.8

Table C.2 SEPB specimens tested in 3pt bending (S=16mm).

	DESIG-NATION	T [°C]	NOTCH [μm]	PREC-RACK [μm]	LIGA-MENT [μm]	B [mm]	W [mm]	a/W	f(a/W)	P_{max} [kG]	K_Q [MPam$^{0.5}$]	W_F [J/m^2]
1.	1sh16	RT	506	1288.5	2406	4.16	4.2	0.4273	2.1397	12.39	3.7	246
2.	2sh26	RT	1078	1956.6	3345	3.9	6.38	0.4757	2.46	13.05	4.1	
3.	12sh16	RT	1290	881.25	1609	3.7	3.78	0.5744	3.428	7.702	4.8	770
4.	18sh16	RT	1054	2016.5	1049	3.90	4.12	0.745	7.48	4.556	5.2	109
5.	19sh16	RT	1100	1608	1212	3.80	3.92	0.691	5.59	5.879	5.5	243
6.	20sh16	RT	812	1633	1495	3.82	3.94	0.6207	4.093	6.15	4.2	184
7.	21sh16	RT	1141	1914.6	964	3.94	4.02	0.76	8.2	5.439	7.0	177
8.	5sh16	200	857	913	2030	3.6	3.8	0.466	2.39	19.02	8.5	1107
9.	13sh16	200	1015	1489	1376	3.8	3.8	0.645	4.54	9.195	7.0	487
10.	30sh16	200	1088	1783.4	1029	3.68	3.9	0.7362	7.108	6.054	7.5	193
11.	31sh16	200	1021	1555.6	1743	4.08	4.32	0.5964	3.748	13.38	6.8	602
12.	6sh16	400	1013	1243	1364	3.76	3.62	0.623	4.13	9.76	7.7	662
13.	15sh16	400	1502	1171.9	986	3.58	3.66	0.73	6.86	6.795	9.1	1548
14.	22sh16	400	979.4	1671.2	1389	3.86	4.04	0.6561	4.75	11.09	8.3	792
15.	29sh16	400	1141.3	1862.5	1136	4.1	4.14	0.7255	6.694	6.591	6.3	355
16.	9sh16	500	996	1342	1322	3.6	3.66	0.639	4.4	10.58	9.2	1260
17.	14sh16	500	1671	1371.7	697	3.54	3.74	0.8136	12.01	4.35	10.1	519
18.	23sh16	500	914	1086.7	2119	3.82	4.12	0.4856	2.54	17.26	6.8	997
19.	16sh16	600	1416	1011.3	1313	3.84	3.74	0.649	4.6	10.29	8.5	2054
20.	24sh16	600	1113	1458.9	1508	3.9	4.08	0.63	4.26	13.54	8.9	1976
21.	27sh16	600	1034.3	1047.4	2098	3.77	4.18	0.4979	2.645	14.93	6.1	871
22.	25sh16	700	1163.5	789.2	2067	3.47	4.02	0.4857	2.54	16.78	7.6	1900
23.	8sh16	800	1036	1428	1356	3.46	3.82	0.645	4.528	7.962	6.9	4093
24.	17sh16	800	1905	907	908	3.56	3.72	0.7478	7.608	4.027	5.9	615
25.	28sh16	800	1001.7	913.1	2265	3.62	4.18	0.458	2.34	14.81	5.6	3658
26.	4sh16	1000	974.2	818	2108	3.7	3.9	0.4595	2.39	11.4	4.7	2820
27.	11sh16	1000	1118	1102	2100	3.94	4.32	0.514	2.79	11.36	4.4	5785

Table C.3 CNB large specimens and their halves tested in 4pt bending.

CHEVRON- NOTCHED, LARGE SPECIMENS (4pt bending, S_1=25mm, S_2=9mm)											
	DESIGNATION	T [°C]	B [mm]	W [mm]	a_0	a_1	A [mm²]	Y_{min}	P_{max} [kG]	K_{QVM} [MPam$^{0.5}$]	W_F [J/m²]
1.	ALTIL1	RT	5.14	6.60	0.193	0.79	15.8924	7.9530	22.13	4.1	350
2.	ALTIL9	RT	4.14	4.92	0.414	1.0	5.762	25.136	5.538	4.7	121
3.	ALTIL2	200	5.14	6.60	0.191	0.879	16.9855	9.1585	42.71	9.2	865
4.	ALTIL10	300	4.66	5.50	0.1796	0.937	11.5804	12.1	22.5	7.6	615
5.	ALTIL5	400	5.14	6.60	0.104	0.792	11.669	6.806	54.37	8.7	1870
6.	ALTIL7	600	5.06	6.44	0.201	0.899	10.0185	9.8658	26.18	6.2	1442
7.	ALTIL12	800	4.62	5.06	0.2087	0.787	11.889	10.92	25.03	8.2	5004
8.	ALTIL14	800	4.82	4.96	0.048	0.842	13.5717	9.11	30.87	8.1	8189
9.	ALTIL11	900	4.66	4.9	0.224	0.858	10.7434	12.9	15.1	5.9	1857
10.	ALTIL6	1000	5.08	6.5	0.188	0.868	17.4901	9.0874	20.54	4.5	1860
11.	ALTIL13	1000	4.86	5.0	0.028	0.8216	13.5814	8.43	23.95	5.8	7632
Cut From Large CNB (4pt bending, S_1=16mm, S_2=4mm)											
	DESIGNATION	T [°C]	B [mm]	W [mm]	a_0	a_1	Y_{min}	P_{max} [kG]	K_{QVM} [MPam$^{0.5}$]		
1.	AlTi161	RT	4.64	4.86	0.234	1	12.22	12.75	4.7		
2.	AlTi162	RT	4.68	4.94	0.299	1	13.84	8.98	3.7		
3.	AlTi163	200	5.0	5.06	0.27	1	12.67	14.43	5.0		
4.	AlTi164	400	4.94	5.42	0.323	1	13.33	21.1	7.6		
5.	AlTi165	600	4.8	4.9	0.293	1	13.76	19.64	7.9		
6.	AlTi166	800	4.9	5.4	0.324	1	13.42	15.92	5.8		
7.	AlTi167	1000	4.9	5.0	0.284	1	13.84	9.91	3.7		
8.	AlTi168	1000	4.68	4.88	0.30	1	14.04	11.31	4.8		
9.	AlTi169	1000	4.84	4.96	0.288	1	13.45	12.31	4.8		

Table C.4 CNB small specimens tested in 4pt bending (S_1=25mm, S_2=9mm).

	DESIGNATION	T [°C]	B [mm]	W [mm]	a_0	a_1	A [mm²]	Y_{min}	P_{max} [kG]	K_{QVM} [MPam$^{0.5}$]	W_F [J/m²]
1.	ALTI2	RT	2.42	5.28	0.337	1.0	4.236	18.7959	4.242	4.4	213
2.	ALTI3	RT	2.48	5.5	0.35	1.0	5.0376	18.6106	4.118	4.1	127
3.	ALTI8	200	2.56	5.64	0.372	1.0	5.6408	19.145	10.88	10.6	393
4.	ALTI10	200	2.60	5.50	0.344	0.958	5.07088	17.9175	11.39	10.4	446
5.	ALTI5	400	2.46	5.2	0.362	1.0	4.69798	20.2568	10.49	11.7	555
6.	ALTI9	400	2.58	5.1	0.375	1.0	4.13262	21.3202	5.221	5.9	327
7.	ALTI11	400	2.50	5.28	0.344	0.958	4.31433	17.7937	8.309	8.0	528
8.	ALTI16	600	2.68	5.4	0.037	0.929	5.56046	9.27	19.99	9.3	1168
9.	ALTI14	750	2.52	5.16	0.302	1.0	4.79304	17.7478	8.459	8.1	1308
10.	ALTI19	800	2.36	4.9	0.288	1.0	4.1103	18.68	6.813	7.6	2462
11.	ALTI17	1000	2.6	5.04	0.304	1.0	4.6875	18.82	6.094	6.1	2413
12.	ALTI18	1000	2.6	5.14	0.19	0.961	5.29789	13.69	9.766	7.0	

Table C.5 CNB specimens tested in 3pt bending.

1.	**A3ALTI1**	RT	4.0	5.46	0.236	0.862	9.842	32.487	8.993	9.7	174
2.	**A3ALTI2**	RT	4.1	5.54	0.261	0.891	9.6285	33.704	6.322	6.8	145
3.	**A3ALTI3**	200	4.1	5.32	0.344	0.867	8.6018	38.672	10.5	13.3	391
4.	**A3ALTI4**	300	4.12	5.46	0.241	0.92	9.4348	35.459	8.389	9.6	226
5.	**A3ALTI5**	400	4.12	5.6	0.241	0.868	10.2835	33.159	15.72	16.8	958
6.	**A3ALTI7**	500	4.02	5.52	0.257	0.896	9.3965	34.005	12.61	14.1	954
7.	**A3ALTI8**	600	4.3	5.4	0.303	1.0	8.0947	45.347	7.487	10.3	939
8.	**A3ALTI6**	700	4.06	5.44	0.24	0.9	9.4984	34.612	14.96	17.0	1823
9.	**A3ALTI9**	800	5.0	5.48	0.094	0.886	13.975	29.101	17.81	13.7	1816
10.	**A3ALTI10**	900	4.0	5.6	0.184	0.816	11.256	27.617	11.83	10.7	1660
11.	**A3ALTI11**	1000	4.36	5.0	0.064	0.812	12.256	31.299	14.84	14.8	3605

Table C.6 9Mn-0.004B CNB specimens (4pt. bending, S_1=25mm, S_2=4.5mm).

	DESIG-NATION	T [°C]	B [mm]	W [mm]	a_0	a_1	Y_{min}	P_{max} [kG]	K_{QVM} [MPam$^{0.5}$]
1.	AlTiB1	RT	5.8	8.34	0.451	1	19.16	16.19	5.7
2.	AlTiB2	200	5.74	8.34	0.419	1	18.77	18.21	6.4
3.	AlTiB3	400	5.8	8.32	0.421	1	18.91	18.9	6.6
4.	AlTiB4	600	5.78	8.34	0.431	1	19.45	18.82	6.8
5.	AlTiB5	800	5.8	8.32	0.428	1	19.27	20.1	7.2
6.	AlTiB6	1000	5.76	8.34	0.444	1	20.07	22.5	8.4
7.	AlTiB7	1000	5.76	8.34	0.435	1	19.58	19.3	7.0
8.	AlTiB8	1000	5.76	8.34	0.427	1	19.16	22.5	8.0
9.	AlTiB9	1000	5.78	8.34	0.426	1	19.14	18.3	6.5

Table C.7 9Mn-0.004B CNB specimens cut from those in Table C.6 (4pt. bending, S_1=16mm, S_2=4mm).

	DESIG-NATION	T [°C]	B [mm]	W [mm]	a_0	a_1	Y_{min}	P_{max} [kG]	K_{QVM} [MPam$^{0.5}$]
1.	AlTiBB1	RT	3.74	5.74	0.247	1	10.7	11.2	4.1
2.	AlTiBB2	200	4.22	5.80	0.291	0.9776	11.2	15.2	5.2
3.	AlTiBB3	400	4.12	5.74	0.3174	1	12.4	15.7	5.8
4.	AlTiBB4	600	3.76	5.70	0.3281	1	12.9	19.0	8.4
5.	AlTiBB5	600	3.46	5.76	0.2764	0.9477	10.4	15.8	6.2
6.	AlTiBB6	900	4.06	5.70	0.3231	0.9838	12.4	14.9	5.9
7.	AlTiBB7	1000	3.70	5.74	0.2136	0.9815	9.7	15.3	6.0
8.	AlTiBB8	1000	4.14	5.74	0.1063	0.9836	7.8	35.4	8.6

Table C.8 High- Mn (14Mn) CNB specimens- series I (4pt. bending, S_1=16mm, S_2=4mm).

	DESIG-NATION	T [°C]	B [mm]	W [mm]	a_0	a_1	Y_{min}	P_{max} [kG]	K_{QVM} [MPam$^{0.5}$]
1.	AlTiHM1	RT	4.14	4.1	0.24	1	14.62	7.58	4.1
2.	AlTiHM2	RT	4.1	4.1	0.26	1	15.26	7.05	4.0
3.	AlTiHM3	200	4.12	4.14	0.25	1	14.79	11.04	6.0
4.	AlTiHM4	200	4.1	4.12	0.27	1	15.53	9.58	5.5
5.	AlTiHM5	400	4.2	4.1	0.23	1	14.31	10.02	5.2
6.	AlTiHM6	500	4.06	4.12	0.25	1	14.86	10.12	5.7
7.	AlTiHM7	500	4.1	4.14	0.27	1	15.45	8.76	5.0
8.	AlTiHM8	600	4.12	4.12	0.25	1	14.87	10.26	5.7
9.	AlTiHM9	600	4.12	4.08	0.29	1	16.39	7.7	4.7
10.	AlTiHM10	700	4.12	4.1	0.32	1	17.46	12.69	8.2
11.	AlTiHM11	700	4.14	4.1	0.27	1	17.46	9.69	6.3
12.	AlTiHM12	800	4.08	4.12	0.29	1	16.23	10.56	6.4
13.	AlTiHM13	800	4.18	4.12	0.27	1	15.53	8.72	4.9
14.	AlTiHM14	1000	4.06	4.12	0.32	1	17.37	17.1	11.2
15.	AlTiHM15	1000	4.12	4.12	0.24	1	14.55	20.97	11.3
16.	AlTiHM16	1000	3.62	4.2	0.32	1	16.9	11.22	7.9
17.	AlTiHM17	1000	4.1	4.2	0.29	1	15.92	16.79	9.9
18.	AlTiHM18	1000	4.16	4.1	0.26	1	15.27	12.89	7.2
19.	AlTiHM19	1000	3.68	4.16	0.37	1	19.19	10.68	8.5
20.	AlTiHM20	1000	3.64	4.18	0.39	1	20.48	8.79	7.5

Table C.9 High- Mn (14Mn) CNB specimens- series II (4pt. bending, S_1=16mm, S_2=4.5mm).

	DESIG-NATION	T [°C]	B [mm]	W [mm]	a_0	a_1	Y_{min}	P_{max} [kG]	K_{QVM} [MPam$^{0.5}$]
1.	HM1	RT	4.2	5.12	0.348	1	14.36	10.08	4.7
2.	HM2	RT	4.12	5.08	0.332	1	13.93	10.06	4.7
3.	HM3	RT	4.2	5.0	0.333	1	14.19	9.09	4.3
4.	HM4	RT	4.18	5.22	0.28	1	12.06	9.404	3.7
5.	HM5	200	4.22	5.08	0.351	1	14.57	13.03	6.2
6.	HM6	200	4.08	5.0	0.338	1	14.36	12.3	6.0
7.	HM7	200	4.18	5.08	0.353	1	14.64	11.22	5.4
8.	HM8	200	4.12	5.08	0.369	1	15.21	12.35	6.3
9.	HM9	400	4.18	5.2	0.333	1	13.65	13.73	6.1
10.	HM10	400	4.2	5.12	0.332	1	13.83	18.78	8.5
11.	HM11	400	4.12	5.1	0.342	1	14.21	17.61	8.3
12.	HM12	400	4.06	5.04	0.368	1	15.3	11.72	6.1
13.	HM13	600	4.18	5.06	0.368	1	15.23	13.88	7.0
14.	HM14	600	4.1	5.08	0.348	1	14.47	15.35	7.4
15.	HM15	600	4.12	5.2	0.354	1	14.34	17.42	8.2
16.	HM28	700	4.2	5.1	0.362	1	14.89	13.65	6.6
17.	HM29	700	4.16	5.0	0.306	1	13.33	14.85	6.6
18.	HM16	800	4.18	5.08	0.308	1	13.19	15.17	6.6
19.	HM17	800	4.22	5.12	0.324	1	13.57	15.73	6.9
20.	HM18	800	4.08	5.0	0.347	1	14.67	17.29	8.6
21.	HM19	800	4.08	5.1	0.364	1	14.98	15.24	7.7
22.	HM20	800	4.1	5.1	0.340	1	14.14	17.28	8.2
23.	HM21	800	4.22	5.1	0.283	1	12.42	17.28	7.0
24.	HM26	900	4.22	5.12	0.336	1	13.96	14.36	6.5
25.	HM27	900	4.4	5.18	0.325	1	13.6	21.5	9.1
26.	HM22	1000	4.12	5.0	0.35	1	14.77	18.8	9.3
27.	HM23	1000	4.08	5.12	0.351	1	14.46	22.94	11.1
28.	HM24	1000	4.16	5.08	0.368	1	15.19	18.72	9.4
29.	HM25	1000	4.2	5.1	0.309	1	13.16	15.26	6.6

Table C.10 Specimens of 14Mn-0.24B alloy (no.12 in Table 5.1) (4pt. bending, S_1=25mm, S_2=4.5mm), microhardness - 246±7 HV (at 2kg).

	Specimen	Grain Size [μm]	Test Temperature [°C]	α_0	α_1	B [mm]	W [mm]	Y_{min}	P_{max} [kG]	K_{QVM} [MPa√m]
1.	A10	176±47	RT	0.403	0.924	4.44	5.9	22.109	12.5	7.9
2.	A1	220±65	RT	0.420	0.981	4.46	5.84	25.937	9.9	7.4
3.	A12	147±40	200	0.406	0.939	4.52	5.9	22.885	14.9	9.7
4.	A11	309±102	200	0.390	0.939	4.50	5.9	22.084	14.8	9.3
5.	A13	183±51	400	0.405	0.937	4.40	5.8	23.030	13.0	8.7
6.	A7	351±144	400	0.402	0.938	4.42	5.9	22.674	12.3	8.0
7.	A6	286±89	600	0.419	0.930	4.42	5.94	23.070	15.1	10.0
8.	A5	123±28	600	0.421	0.950	4.36	5.84	24.499	11.5	8.3
9.	A2	403±153	600	0.396	0.950	4.44	5.80	23.224	18.5	12.4
10.	A14	469±119	800	0.398	0.933	4.46	5.80	22.959	12.2	11.6
11.	A4	156±36	800	0.417	0.968	4.46	5.84	25.079	11.7	8.5
12.	A3	306±177	800	0.367	0.919	4.56	5.82	20.457	13.7	7.9
13.	A17	265±72	800	0.399	0.922	4.44	5.88	21.904	17.3	10.9
14.	A15	348±123	1000	0.402	0.948	4.46	5.78	23.561	14.7	10.0
15.	A18	298±163	1000	0.411	0.952	4.62	4.68	15.866	16.9	11.0
16.	A8	287±89	1000	0.404	0.945	4.46	5.88	23.147	17.4	11.6

Table C.11 Specimens of 14Mn-0.65B alloy (no.13 in Table 5.1) (4pt. bending, S_1=25mm, S_2=4.5mm), microhardness - 294±12 HV (at 2kg).

	Specimen	Grain Size [μm]	Test Temperature [°C]	α_0	α_1	B [mm]	W [mm]	Y_{min}	P_{max} [kG]	K_{QVM} [MPa√m]
1.	B1	143±54	RT	0.454	0.981	4.30	5.4	30.654	12.5	6.9
2.	B2	116±34	RT	0.385	0.914	4.42	5.9	20.766	9.9	7.6
3.	B3	264±65	RT	0.424	0.923	4.52	5.9	23.194	14.9	7.6
4.	B4	211±68	200	0.390	1.000	4.54	5.9	24.630	14.8	9.9
5.	B5	276±72	200	0.314	0.946	4.54	5.34	18.810	13.0	5.7
6.	B6	301±82	400	0.386	0.961	4.58	5.86	22.894	12.3	9.4
7.	B7	422±39	400	0.389	0.961	4.56	5.72	23.587	15.1	5.7
8.	B8	286±89	600	0.415	0.928	4.54	5.90	22.899	11.5	8.5
9.	B9	69±8	600	0.381	0.949	4.56	5.88	22.487	18.5	7.3
10.	B13	323±94	800	0.151	0.901	4.62	4.68	15.866	12.2	8.3
11.	B10	125±65	800	0.314	0.942	4.50	5.52	19.981	11.7	9.2
12.	B11	147±42	1000	0.436	0.948	4.28	5.90	25.028	13.7	10.7
13.	B12	160±40	1000	0.351	0.944	4.50	5.40	22.201	17.3	9.7
14.	B14	173±58	1000	0.390	0.986	4.62	5.82	24.341	14.7	9.5

Table C.12 Specimens of 9Mn-0.25B alloy (no.10 in Table 5.1) (4pt. bending, S_1=25mm, S_2=4.5mm), microhardness - 170±7 HV (at 2kg).

	Specimen	Grain Size [μm]	Test Temperature [°C]	α_0	α_1	B [mm]	W [mm]	Y_{min}	P_{max} [kG]	K_{QVM} [MPa√m]
1.	C4	500±166	RT	0.350	0.974	4.76	5.84	21.593	8.8	5.1
2.	C5	742±215	RT	0.379	0.931	4.40	5.80	21.537	9.5	6.0
3.	C1	167±36	200	0.342	1.000	4.76	5.86	22.039	12.2	7.2
4.	C2	389±142(col.)	200	0.408	0.939	4.30	5.68	23.873	7.9	5.7
5.	C3	839±278	400	0.404	0.945	4.46	5.88	23.164	14.2	9.4
6.	C6	750±203(col.)	400	0.373	0.942	4.50	5.82	21.630	10.4	6.4
7.	C11	651±278(col.)	600	0.393	0.948	4.52	5.80	22.943	10.7	7.0
8.	C12	576±175	600	0.332	0.904	4.74	5.90	21.795	14.5	8.5
9.	C7	458±81(col.)	800	0.492	0.974	4.44	5.80	31.312	9.9	9.0
10.	C10	314±53	800	0.337	0.934	4.68	4.80	19.704	13.6	7.4
11.	C8	495±192	1000	0.408	0.902	4.56	5.88	21.490	11.6	7.0
12.	C9	412±97	1000	0.455	0.905	4.42	5.62	25.282	16.3	12.2
13.	C13	611±193	1000	0.384	0.939	4.56	5.84	21.988	10.7	6.6

col. - columnar grains (the number indicates the average cross- section grain size)

Table C.13 Specimens of 9Mn-0.66B alloy (no.11 in Table 5.1) (4pt. bending, S_1=25mm, S_2=4.5mm), microhardness - 171±4 HV (at 2kg).

	Specimen	Grain Size [μm]	Test Temperature [°C]	α_0	α_1	B [mm]	W [mm]	Y_{min}	P_{max} [kG]	K_{QVM} [MPa√m]
1.	D11	305±99	RT	0.381	0.918	4.54	5.70	21.452	9.5	5.8
2.	D12	136±23(col.)	RT	0.380	0.929	4.60	5.88	21.230	8.4	5.0
3.	D1	286±92(col.)	200	0.422	0.965	4.46	5.90	25.020	6.8	4.9
4.	D1A	301±128(col.)	200	0.434	0.980	4.54	5.64	27.751	6.1	4.9
5.	D13	502±228	200	0.405	0.957	4.56	5.88	23.658	8.5	5.6
6.	D3	570±194(col.)	400	0.400	0.944	4.52	5.76	23.310	8.0	5.3
7.	D4	615±240	400	0.406	0.955	4.50	5.88	23.663	12.2	8.2
8.	D14	71±25(col.)	400	0.370	0.943	4.60	5.78	21.640	10.2	6.2
9.	D5	716±340	600	0.387	0.959	4.46	5.62	23.817	13.4	9.4
10.	D6	653±164	600	0.384	0.923	4.80	5.72	21.742	11.9	7.0
11.	D7	530±144	800	0.413	0.973	4.54	5.76	25.428	8.0	5.8
12.	D8	99±22(col.)	800	0.377	0.948	4.58	5.76	22.267	10.2	6.4
13.	D15	364±110	800	0.397	0.952	4.50	5.88	23.034	15.6	10.2
14.	D17	536±158	800	0.388	0.921	4.52	5.68	22.043	9.3	5.9
15.	D19	480±130	800	0.210	0.918	4.54	4.90	17.432	18.5	10.0
16.	D9	550±155(col.)	1000	0.395	0.904	4.52	5.86	21.065	16.9	10.0
17.	D10	622±158(col.)	1000	0.381	0.939	4.60	5.60	22.687	10.6	6.9
18.	D16	792±334	1000	0.328	0.926	4.54	5.90	18.767	13.1	6.9
19.	D18	600±200(col.)	1000	0.425	0.966	4.50	5.80	25.742	8.5	6.3
20.	D20	640±189	1000	0.234	0.918	4.46	5.02	17.850	18.5	10.3
21.	D21	611±170	1000	0.219	0.928	4.52	4.88	18.077	10.9	6.1

col. - columnar grains (the number indicates the average cross- section grain size)

D Results of Fracture Toughness in Various Environments-Boron-Free "Base" 9Mn-25Ti Alloy

Table D.1 SEPB specimens tested in vacuum (3pt. S=16mm).

	DESIG-NATION	T [°C]	NOTCH [μm]	PREC-RACK [μm]	LIGA-MENT [μm]	B [mm]	W [mm]	a/W	f(a/W)	P_{max} [kG]	K_Q [MPam$^{0.5}$]	W_F [J/m^2]
1.	VAC3SH3	RT	1959	616	1205	3.74	3.78	0.6812	5.339	6.131	5.9	303
2.	VAC3SH4	RT	944	1920	976	3.86	3.84	0.7458	7.5	6.142	7.9	220
3.	VAC3SH5	RT	1589	774	1357	3.66	3.72	0.6352	4.335	6.381	5.2	190
4.	VAC3SH7	RT	1112	1130	2078	4.1	4.32	0.519	2.83	14.14	5.4	-
5.	VAC3SH8	RT	1156	1063	1481	3.42	3.7	0.6	3.765	8.352	6.4	229
6.	VAC3SH9	RT	1640	1515.5	525	3.52	3.68	0.857	17.97	2.032	7.3	109
7.	VAC3SH10	RT	1007	2475	898	3.54	4.38	0.795	10.39	6.188	9.8	399
8.	VAC3SH11	RT	1081	2147	882	3.34	4.11	0.785	9.68	4.752	8.2	227
9.	VAC3SH13	RT	1030	779	2511	3.46	4.32	0.4187	2.088	13.56	4.5	361
10.	VAC3SH14	RT	1260	1373	1547	3.26	4.18	0.6299	4.251	6.66	5.0	200
11.	VAC3SH15	RT	1030	1496	1694	3.22	4.22	0.5986	3.75	8.199	5.5	495
12.	VAC3SH16	RT	1132	1314	1154	3.48	3.6	0.6794	5.285	5.042	5.6	200
13.	VAC3SH17	RT	1064	2050	806	3.74	3.92	0.7944	10.386	4.829	8.6	287
14.	VAC3SH18	RT	1443	1669	1128	3.7	3.94	0.7137	6.2759	8.596	9.2	387
15.	VACTEM1	200	948	1225	1707	3.55	3.88	0.56	3.25	9.125	5.4	210
16.	VACTEM2	400	1033	802	1085	3.37	3.82	0.4804	2.504	16.07	7.9	1306
17.	VACTEM3	600	1319	1043	1618	3.74	3.96	0.612	3.9526	10.24	6.8	457
18.	VACTEM4	800	957	1332	1411	3.34	3.7	0.6187	4.0756	6.899	5.9	1440
19.	VACTEM5	950	858	1250	1732	3.84	3.84	0.549	3.1314	11.83	6.4	1798

Table D.2 SEPB specimens tested in argon (3pt. S=16mm).

	DESIG-NATION	T [°C]	NOTCH [μm]	PREC-RACK [μm]	LIGA-MENT [μm]	B [mm]	W [mm]	a/W	f(a/W)	P_{max} [kG]	K_Q [MPam$^{0.5}$]	W_F [J/m^2]
1.	ARGON12	RT	1122.4	1280.5	1497.1	3.7	3.9	0.6161	4.02	6.966	4.9	
2.	ARGON13	100	1065	1674.4	1260.6	3.74	4.0	0.6848	5.427	5.071	4.6	1405
3.	ARGON14	200	1125	903.3	2071.7	3.35	4.1	0.4948	2.62	10.82	5.1	858
4.	ARGON16	200	1261.5	1029.5	1549.0	3.58	3.84	0.5966	3.7228	6.70	4.6	118
5.	ARGON15	300	1280.6	1725.5	831.9	3.90	3.84	0.7833	9.572	3.404	5.5	258
6.	ARGON6	400	1098.2	749.8	2452	4.07	4.3	0.4296	2.1535	18.02	5.3	758
7.	ARGON8	400	1141.1	1074.5	1814.4	3.36	4.03	0.5498	3.14	8.835	5.1	1037
8.	ARGON9	500	1071	1426	1583	3.81	4.08	0.612	3.953	8.76	5.5	1611
9.	ARGON1	600	1070.7	763.3	2166	3.76	4.0	0.4585	2.3437	11.16	4.3	745
10.	ARGON10	600	1091.8	837	2011	4.0	3.94	0.4895	2.576	13.19	5.4	1311
11.	ARGON2	700	1118.7	1410	1391.3	3.83	3.92	0.6451	4.53	6.91	5.2	1155
12.	ARGON3	800	1136.2	704	2319.8	3.76	4.16	0.4423	2.23	11.88	4.1	2653
13.	ARGON11	800	1079.2	811.35	2169.5	3.94	4.06	0.4656	2.394	13.56	5.0	1139
14.	ARGON4	900	1008	1179	2033	4.04	4.22	0.5182	2.823	12.72	5.1	3233
15.	ARGON5	1000	1223.8	1021	1935.2	3.88	4.18	0.537	3.01	9.799	4.4	3113

Table D.3 SEPB specimens tested in water and liquid nitrogen (3pt. S=16mm).

	DESIG-NATION	T [°C]	NOTCH [μm]	PREC-RACK [μm]	LIGA-MENT [μm]	B [mm]	W [mm]	a/W	f(a/W)	P_{max} [kG]	K_Q [MPam$^{0.5}$]	W_F [J/m^2]
WATER												
1.	WATER1	RT	1057	2009.4	873.6	3.84	3.94	0.7782	9.244	5.259	8.0	424
2.	WATER2	RT	917.2	1828.5	1254.3	3.92	4.0	0.6864	5.469	9.232	8.0	436
3.	WATER3	RT	1000	1830	1150	3.82	3.98	0.711	6.19	6.969	7.1	259.5
4.	WATER4	RT	1080.9	635	2164.1	3.66	3.88	0.4422	2.23	10.75	4.3	182.2
5.	WATER5	RT	1111.9	1223.9	1844.2	3.8	4.18	0.5588	3.24	8.204	4.1	141.5
LIQUID NITROGEN												
1.	NITR1	-196	1158	1050.6	1871.4	3.88	4.08	0.5413	3.0499	14.53	6.9	525.4
2.	NITR2	-196	927.6	1500	1632.4	3.76	4.06	0.5979	3.7417	7.769	4.7	781.5
3.	NITR3	-196	1136.3	1141.2	1802.5	3.74	4.08	0.558	3.234	9.498	4.9	429.9

E Results of Complimentary Testing of CNB and SEPB Specimens in Air at Room Temperature

Table E.1 Complimentary SEPB and pre- cracked CNB specimens.

Sp. #	B [mm]	W [mm]	α_0	α_l	α_{pr}	Y_{min}	$Y_{\alpha pr}$	P_{max} [kG]	K_{QVM} [MPa√m]
Alloy composition: Al 65.7±0.2%; Ti 25.2±0.1%; Mn 9.2±0.2% Mode of Loading: 4 pt. bending, S_1=16 mm; S_2=4 mm; Specimen Type: CNB									
1	4.06	5.32	0.062	0.971	$<\alpha_m$	7.59	-	26.9	6.8
2	3.94	5.56	0.12	1.0	$<\alpha_m$	8.49	-	21.5	6.1
3	3.98	5.54	0.122	1.0	0.585	8.416	12.27	12.9	5.2
4	4.08	5.32	0.067	0.959	0.292	7.55	7.61	23.3	5.8
Mode of Loading: 4 pt. bending, S_1=35 mm; S_2=4 mm;									
5	3.1	6.72	0.297	0.972	0.72	25.05	42.21	4.2	6.8
6	3.62	5.84	0.427	0.943	0.725	37.03	50.8	4.3	7.7
Alloy composition: Al 65.8±0.1%; Ti 25.5±0.1%; Mn 8.8±0.1%; B 0.004 ±0.001% Mode of Loading: 4 pt. bending, S_1=16 mm; S_2=4 mm; Specimen Type: CNB									
1	3.72	5.74	0.202	0.911	0.645	8.56	13.03	11.3	5.1
2	4.06	5.76	0.237	0.944	0.708	9.60	17.08	10.6	5.8
3	4.0	5.8	0.246	0.947	0.736	9.76	19.24	10.1	6.3
4	4.32	5.74	0.293	0.946	0.700	10.86	17.05	8.9	4.5
Alloy composition: Al 65.8±0.1%; Ti 25.5±0.1%; Mn 8.8±0.1%; B 0.004 ±0.001% Mode of Loading: 3 pt. bending, S=16 mm; Specimen Type: SEPB									
Sp. #	Notch [μm]	Precr. [μm]	Lig. [μm]	B [mm]	W [mm]	a/W	f(a/W)	P_{max} [kG]	K_Q [MPa√m]
1	2179	1629	1950	3.9	5.76	0.661	14.01	18.96	8.8
2	2417	1548	1810	3.96	5.78	0.686	15.64	19.48	9.9
3	1306	1250	3180	3.64	5.74	0.445	6.681	25.06	5.9
4	1296	1132	3310	3.64	5.74	0.423	6.281	23.4	5.2

F Fracture Modes of Toughness Specimens

Table F.1 Fracture mode of CNB specimens (9Mn) tested in air (4pt.).

Specimen	Temp. [°C]	% Intergranular Fracture
AlTiL9	RT	0
AlTiL2	200	5
AlTiL15	200	10
AlTiL5	400	27
AlTiL16	400	33
AlTiL17	500	55
AlTiL18	500	48
AlTiL7	600	70
AlTiL12	800	78
AlTiL14	800	85
AlTiL6	1000	100
AlTiL13	1000	99

Table F.2 Fracture mode of SEPB (3pt.) and CNB (4pt.) specimens.

AIR, Low-Mn (9Mn), 3pt bending (SEPB)			ARGON, Low-Mn (9Mn), 3pt bending (SEPB)		
Specimen	Temp. [°C]	% Intergranular Fracture	Specimen	Temp. [°C]	% Intergranular Fracture
2sh26	RT	0	ARGON12	RT	0
5sh16	200	15	ARGON13	100	5
6sh16	400	60	ARGON14	200	5
9sh16	500	50	ARGON16	200	10
14sh16	500	65	ARGON15	300	15
16sh16	600	80	ARGON6	400	30
27sh16	600	85	ARGON8	400	18
25sh16	700	80	ARGON9	500	35
17sh16	800	90	ARGON1	600	50
11sh16	1000	100	ARGON10	600	80
			ARGON2	700	85
			ARGON3	800	85
			ARGON11	800	95
			ARGON5	1000	100
High Mn (14Mn), 4pt bending (CNB)			9Mn-0.004B, 4pt bending (CNB)		
Specimen	Temp. [°C]	% Intergranular Fracture	Specimen	Temp. [°C]	% Intergranular Fracture
AlTiHM1	RT	0	AlTiB1	RT	0
AlTiHM2	RT	0	AlTiB2	200	5
AlTiHM3	200	0	AlTiB3	400	30
AlTiHM4	200	0	AlTiB4	600	75
AlTiHM5	400	0	AlTiB5	800	90
AlTiHM6	500	0	AlTiB6	1000	95
AlTiHM7	500	5	AlTiB7	1000	100
AlTiHM8	600	0	AlTiB8	1000	100
AlTiHM9	600	5			
AlTiHM10	700	20			
AlTiHM11	700	15			
AlTiHM12	800	25			
AlTiHM13	800	30			
AlTiHM14	1000	50			
AlTiHM15	1000	50			
AlTiHM16	1000	50			
AlTiHM17	1000	40			
AlTiHM18	1000	40			

Table F.3 Fracture mode of CNB Low- and High- Mn, B-doped specimens (4pt.).

14Mn-0.24B (no.12 in Table 5.1)			14Mn-0.65B (no.13 in Table 5.1)		
Specimen	Temp. [°C]	% Intergranular Fracture	Specimen	Temp. [°C]	% Intergranular Fracture
A10	RT	0	B1	RT	0
A1	RT	0	B2	RT	0
A12	200	0	B3	RT	0
A11	200	0	B4	200	0
A13	400	0	B5	200	0
A7	400	0	B6	400	0
A6	600	10	B7	400	0
A5	600	15	B8	600	0
A2	600	5	B9	600	0
A14	800	20	B13	800	30
A4	800	50	B10	800	40
A3	800	30	B11	1000	80
A17	800	30	B12	1000	85
A15	1000	85	B14	1000	90
A18	1000	60			
A8	1000	40			
9Mn-0.25B (no.10 in Table 5.1)			9Mn-0.66B (no.11 in Table 5.1)		
Specimen	Temp. [°C]	% Intergranular Fracture	Specimen	Temp. [°C]	% Intergranular Fracture
C4	RT	0	D11	RT	0
C5	RT	0	D12	RT	0
C1	200	5	D1	200	5
C2	200	10	D1A	200	10
C3	400	20	D13	200	3
C6	400	90	D3	400	30
C11	600	40	D4	400	50
C12	600	30	D14	400	70
C7	800	80	D5	600	70
C10	800	85	D6	600	80
C8	1000	100	D7	800	90
C9	1000	90	D8	800	85
C13	1000	90	D15	800	80
			D17	800	85
			D19	800	80
			D9	1000	100
			D10	1000	100
			D16	1000	90
			D18	1000	95
			D20	1000	95
			D21	1000	90

G Pole Figures

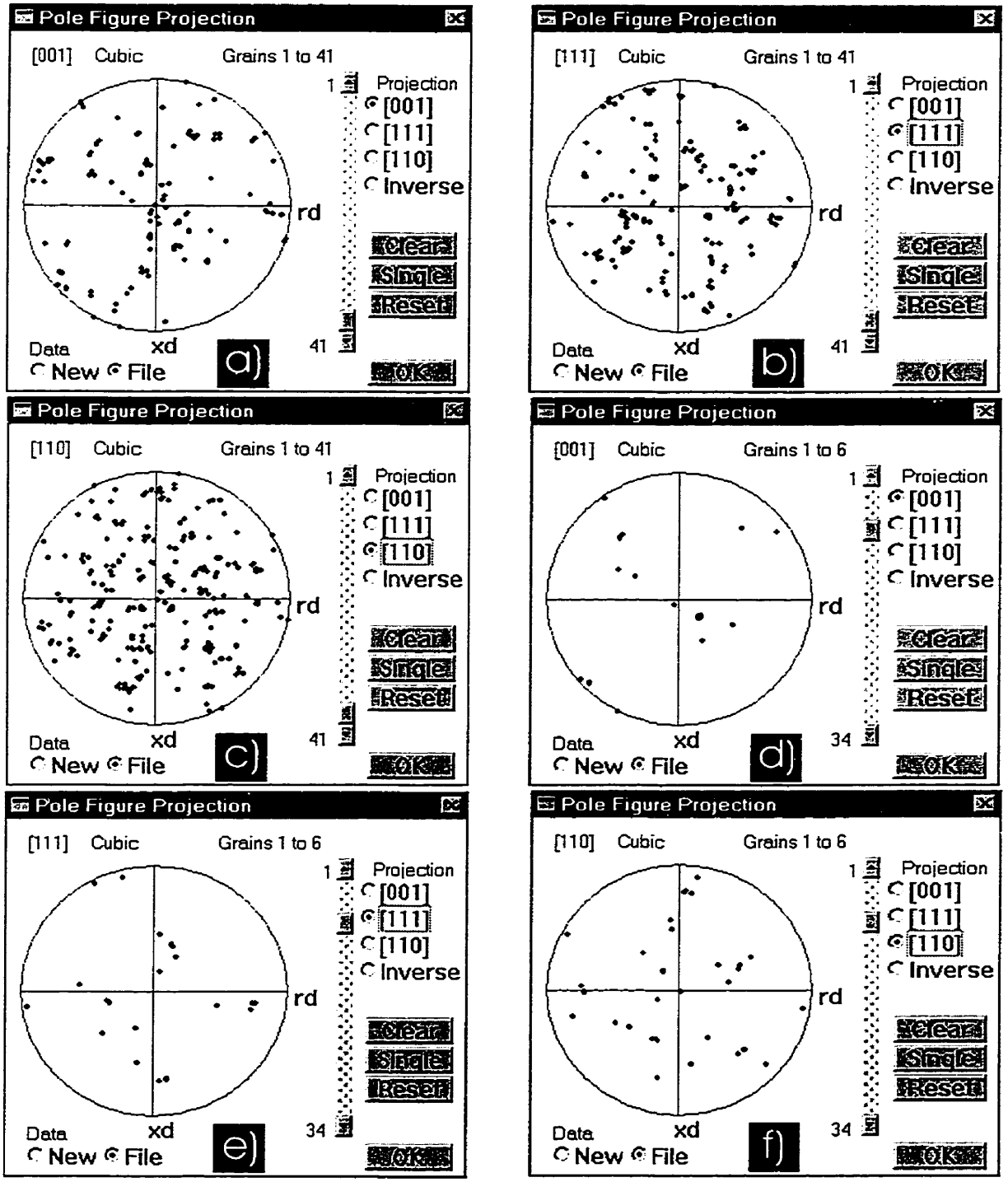

Figure G.1 Pole figures for grains in the specimen of the 9Mn alloy tested at 200°C; a), b), and c) for all the grains measured; d), e), and f) for the fractured grains.

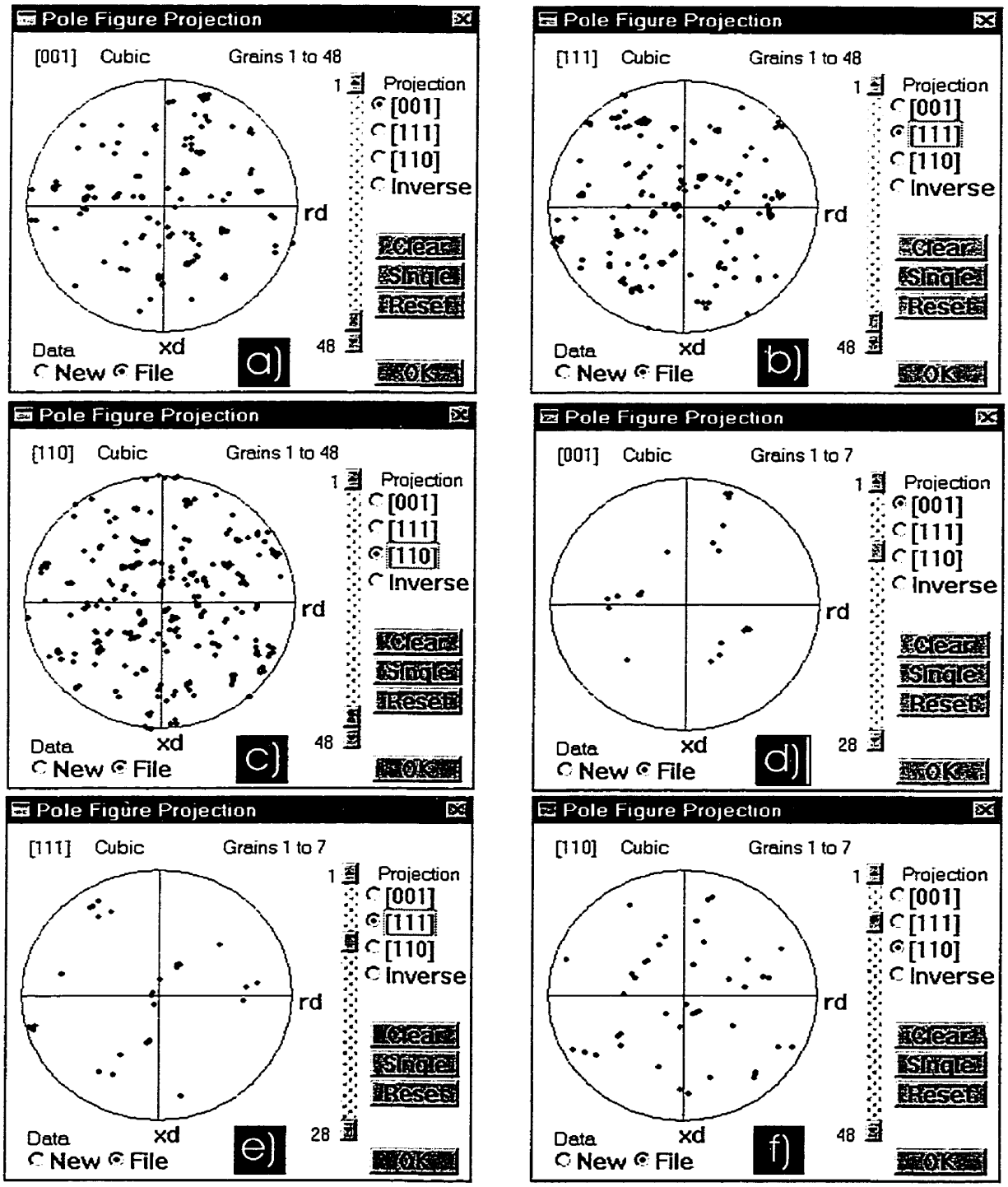

Figure G.2 Pole figures for grains in the specimen of the 9Mn alloy tested at 400°C; a), b), and c) for all the grains measured; d), e), and f) for the fractured grains.

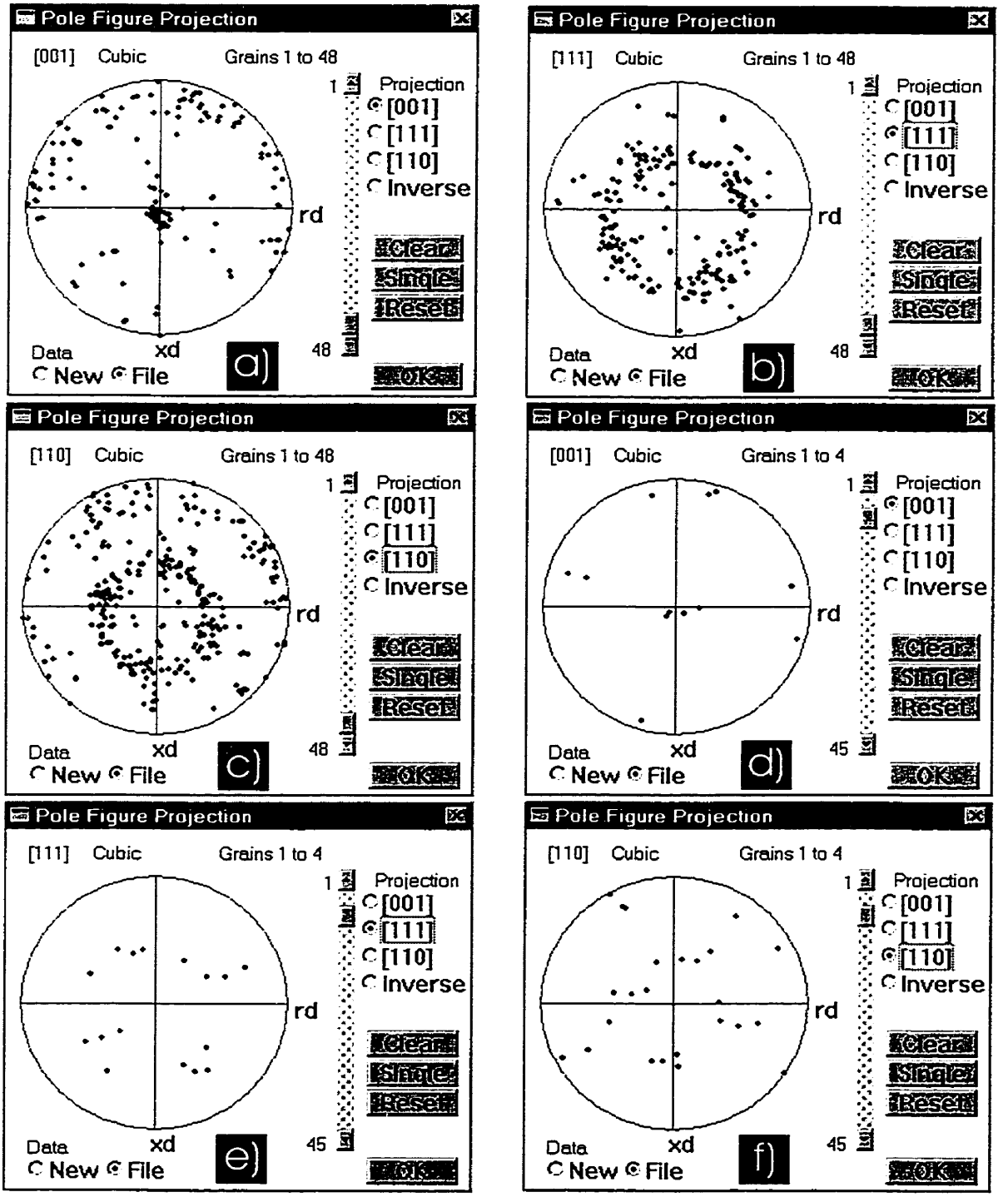

Figure G.3 Pole figures for grains in the specimen of the 9Mn alloy tested at 600°C; a), b), and c) for all the grains measured; d), e), and f) for the fractured grains.

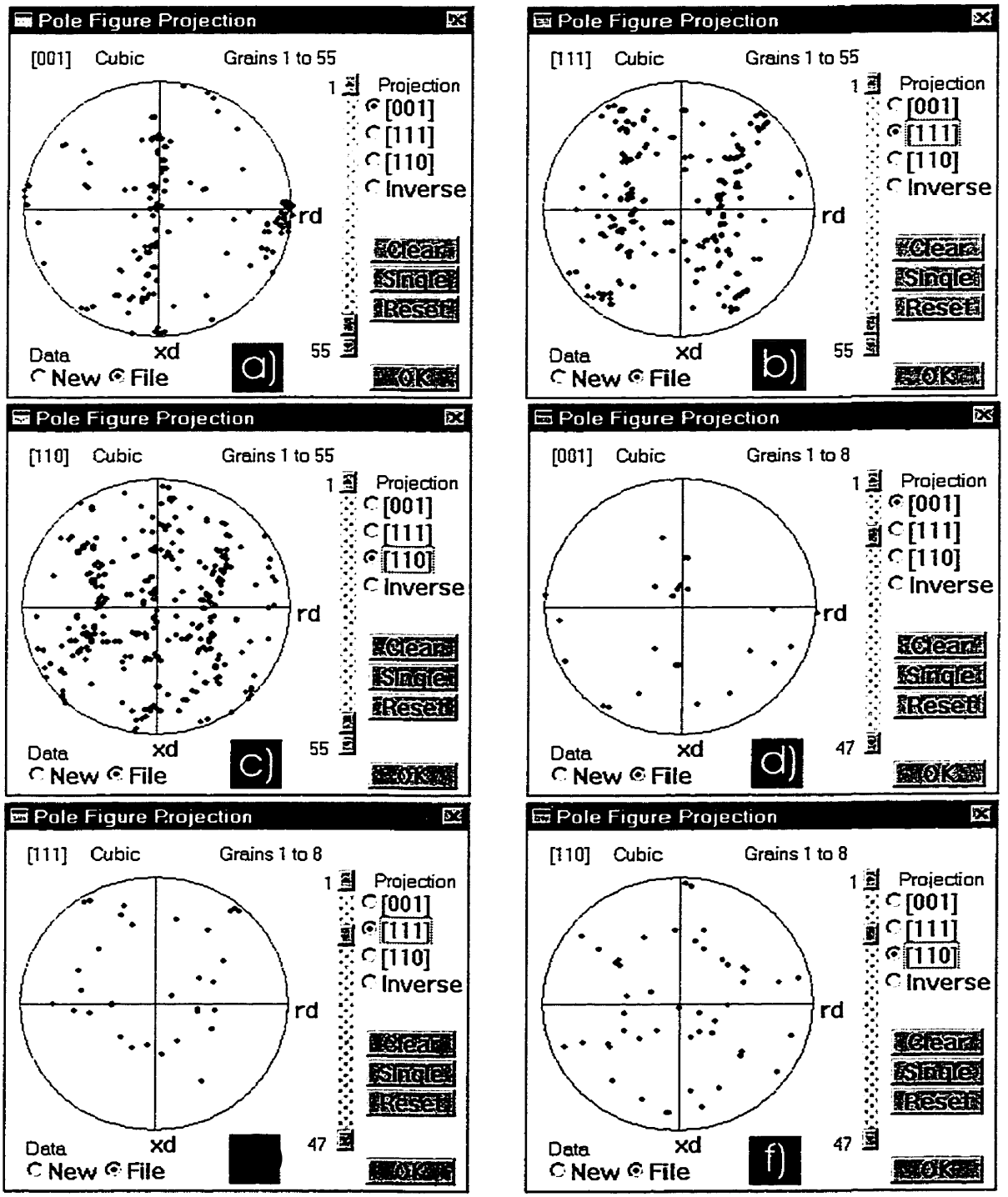

Figure G.4 Pole figures for grains in the specimen of the 9Mn alloy tested at 800°C; a), b), and c) for all the grains measured; d), e), and f) for the fractured grains.

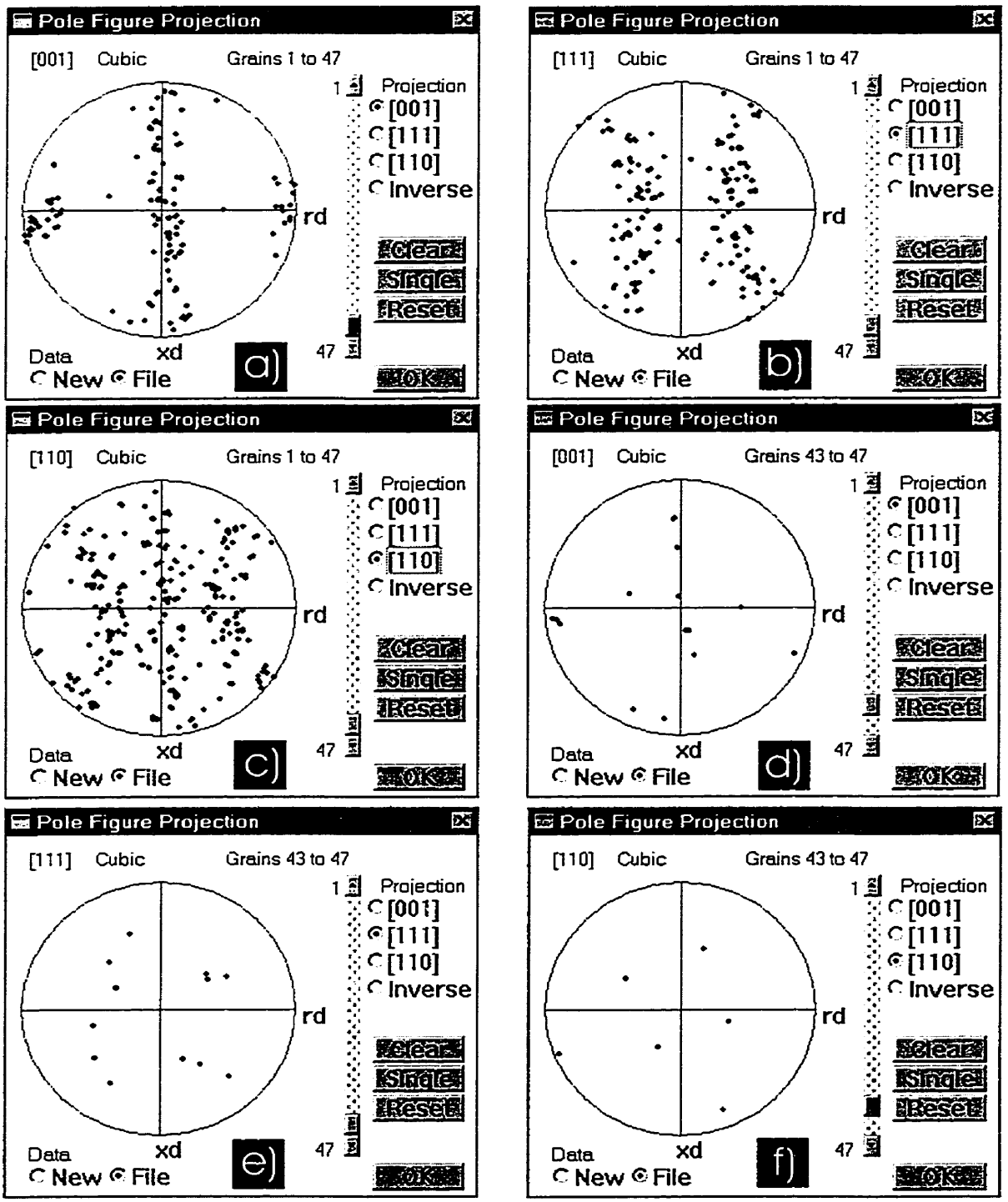

Figure G.5 Pole figures for grains in the specimen of the 9Mn alloy tested at 1000°C; a), b), and c) for all the grains measured; d), e), and f) for the fractured grains.

H Optical Micrographs of Surface Cracks

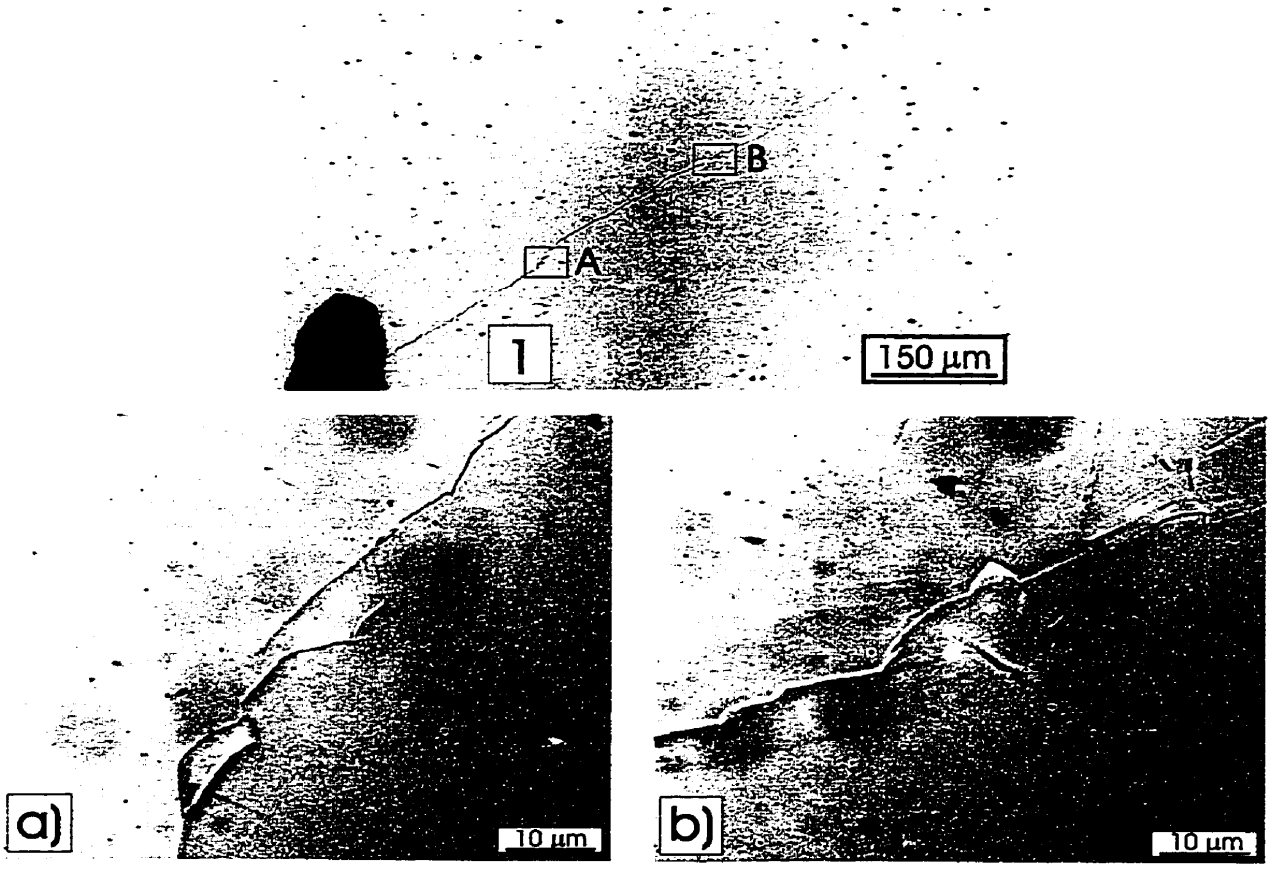

Figure H.1 a) Plastic deformation between closely spaced cracks, b) plastic deformation along crack path irregularities.

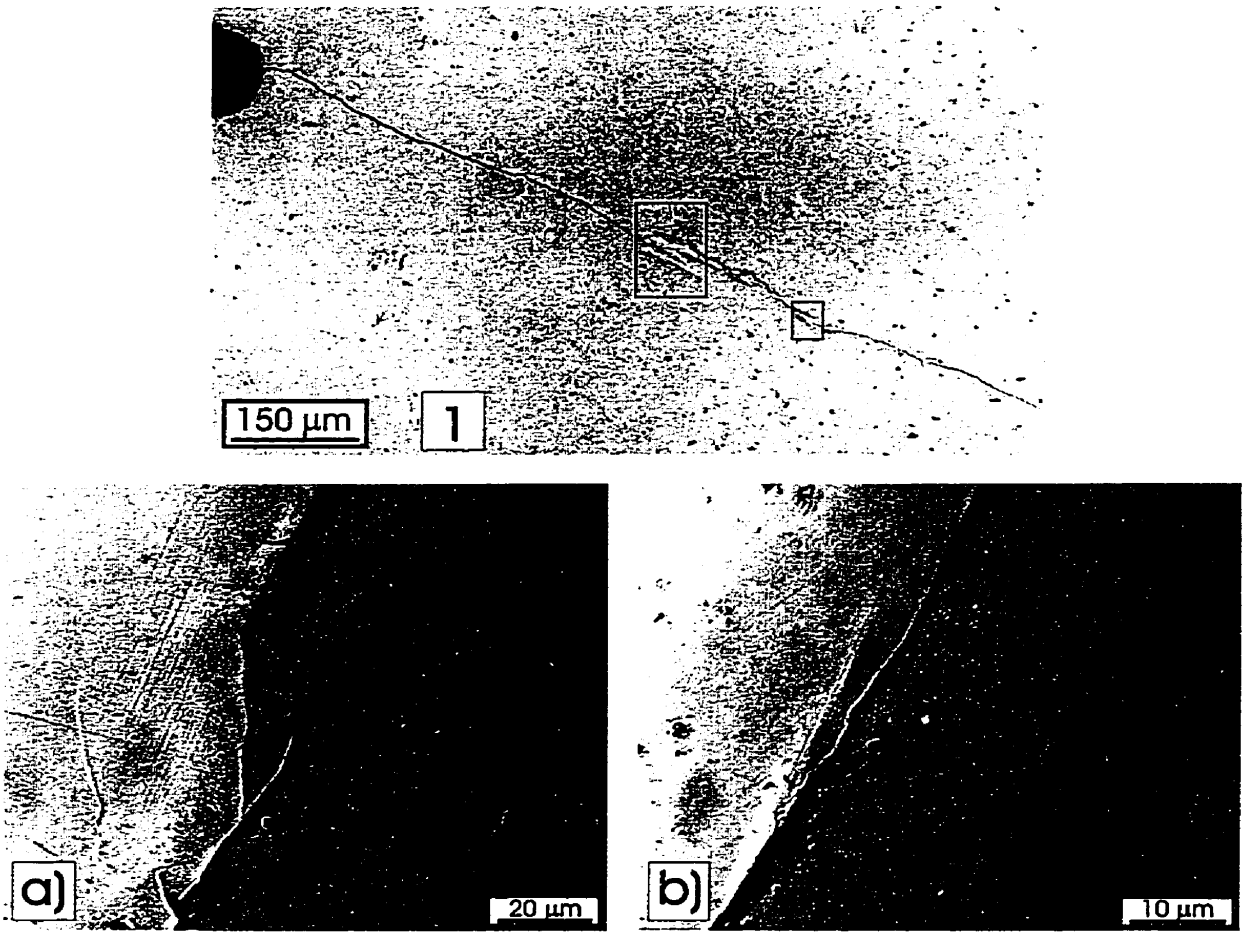

Figure H.2 a) Plasticity developed in the region of crack deviation from its main path, b) slip lines symmetrical about the main, straight crack (very rarely occurring).

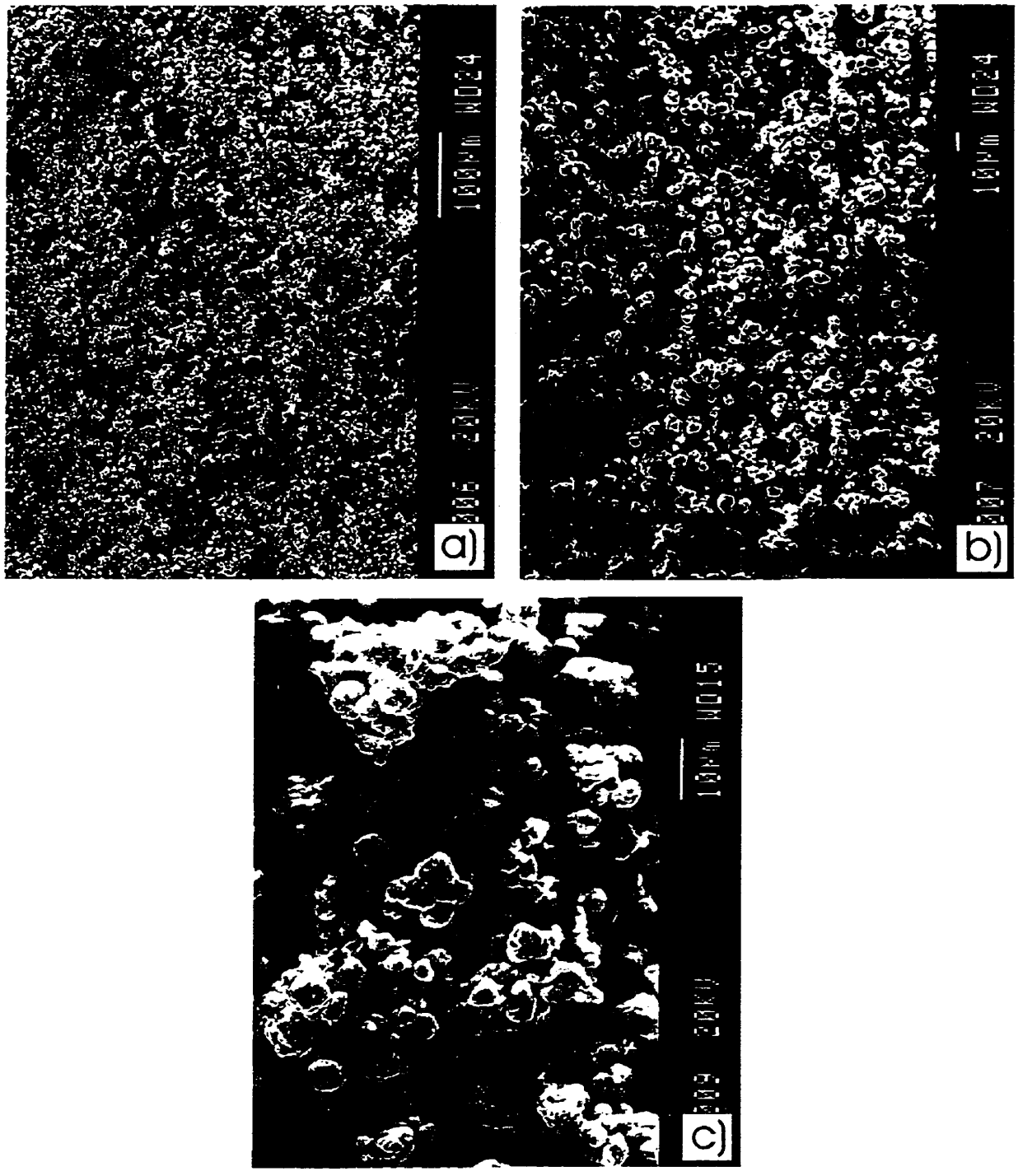

Figure K.1 SEM micrographs of powder milled for 47 h (Ingot #14).

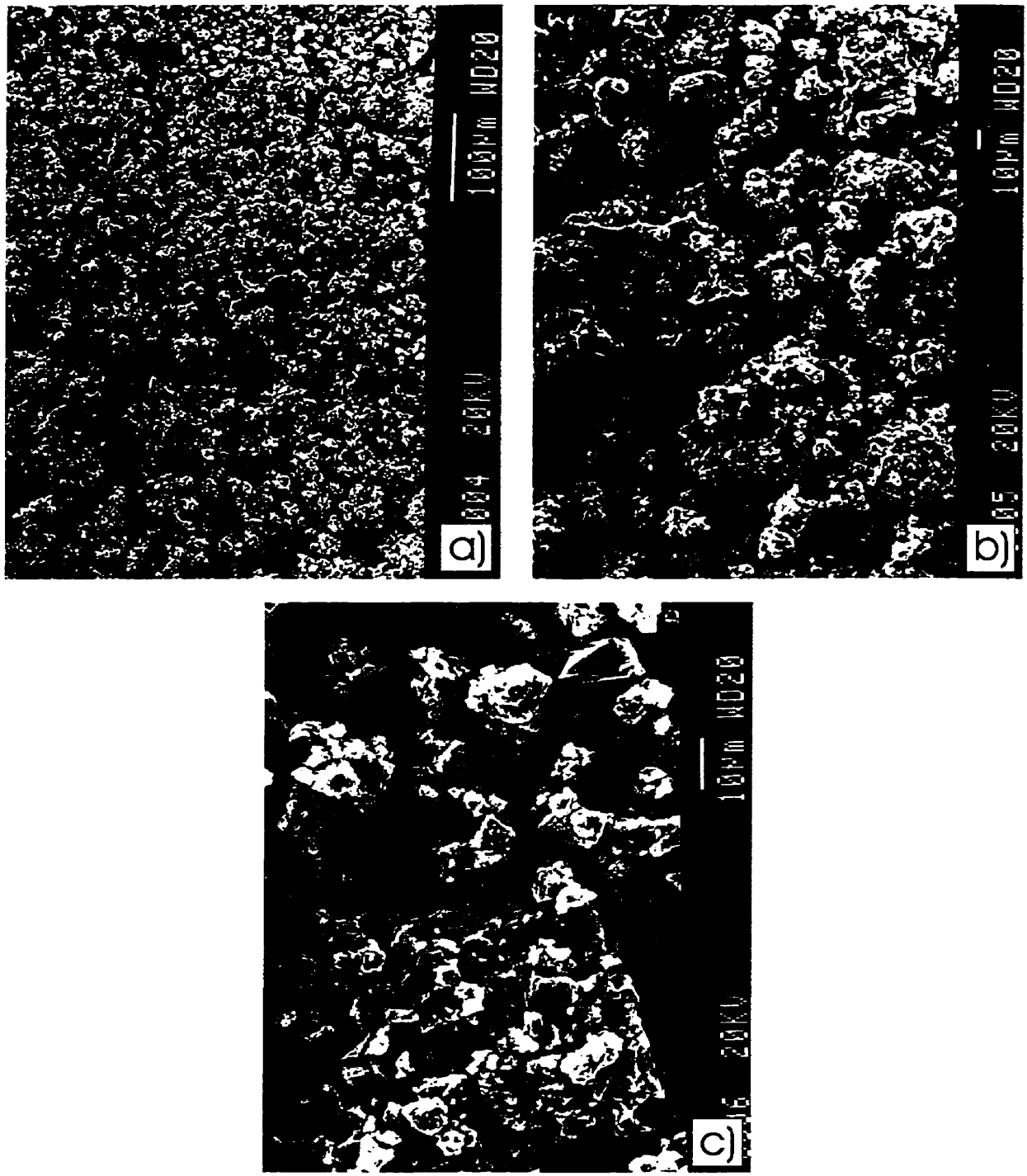

Figure K.2 SEM micrographs of powder milled for 209 h (Ingot #15).

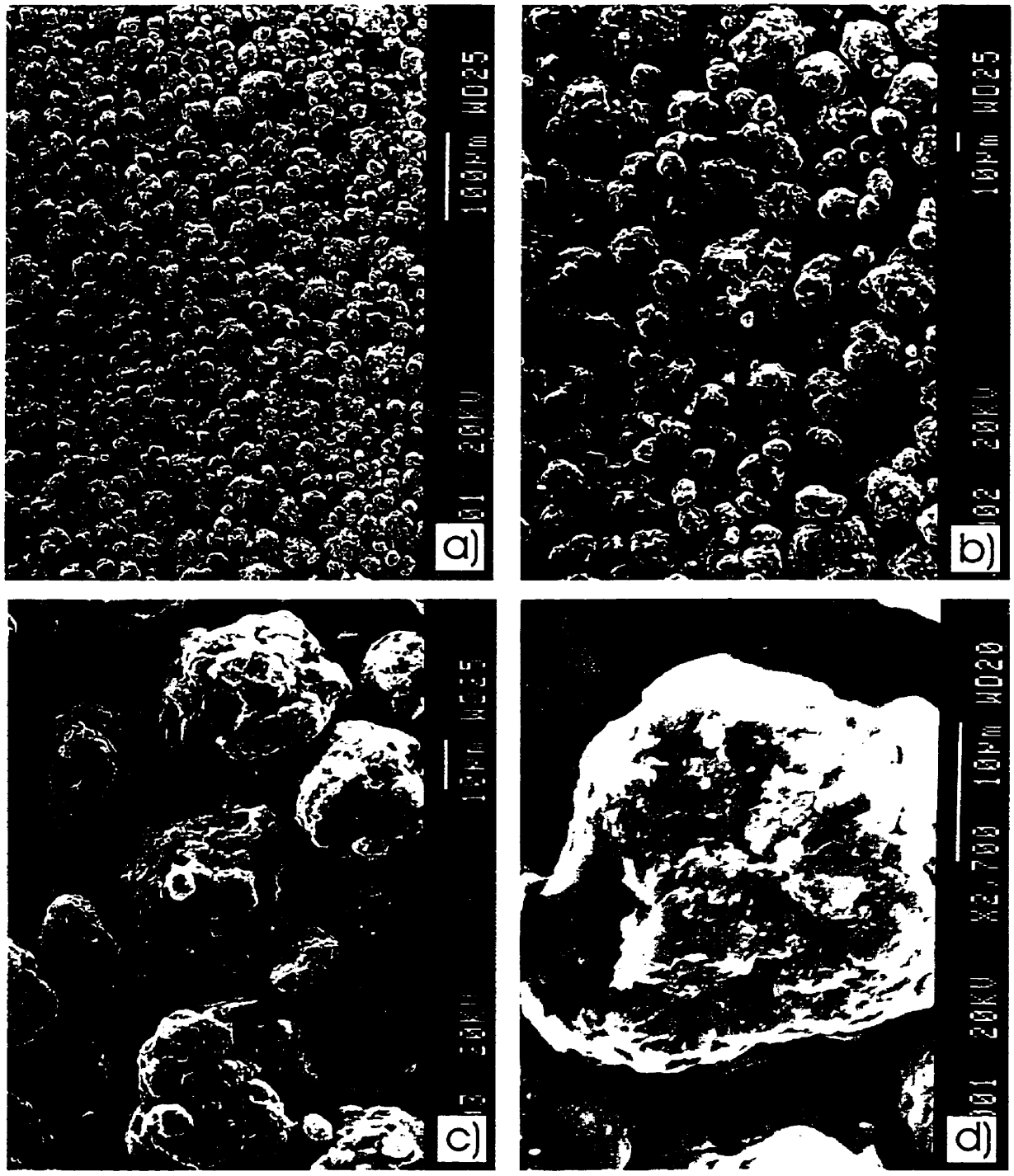

Figure K.3 SEM micrographs of powder milled for 215 h (Ingot #15).

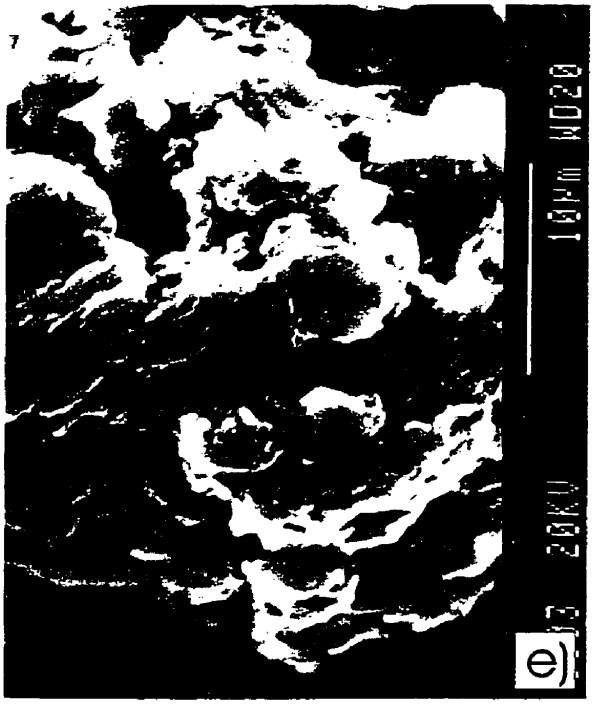

Figure K.3 Contd.

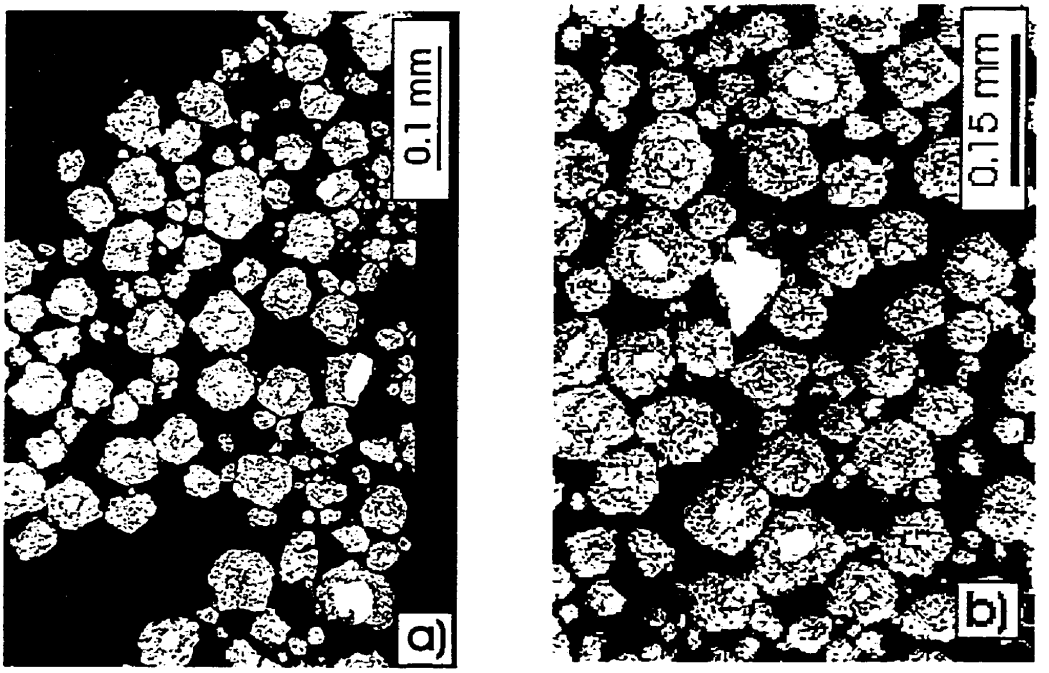

Figure K.4 Optical micrographs of powder milled for a) 208 h, b) 236 h (Ingot #14)

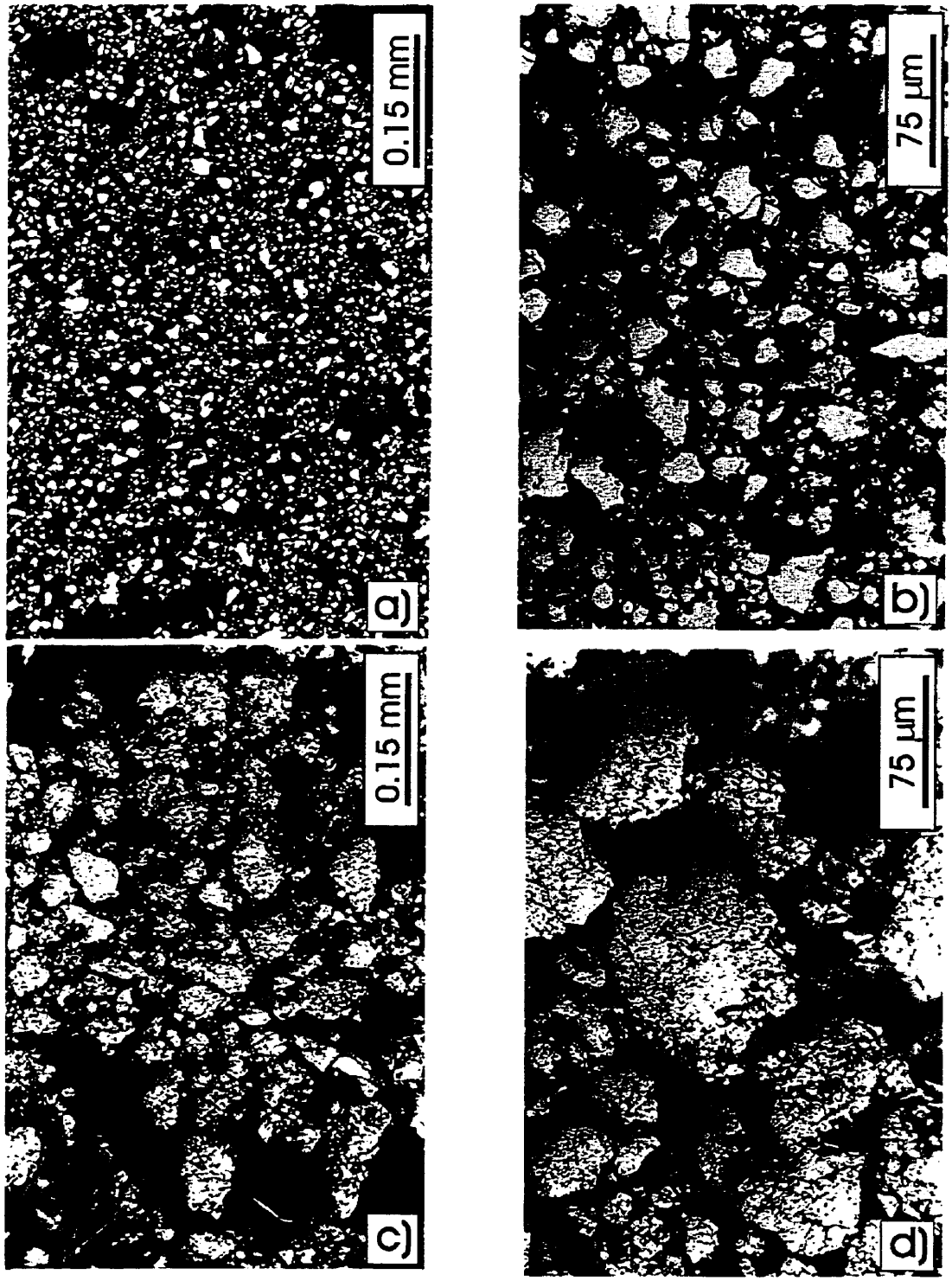

Figure K.5 Optical micrographs of powder milled for: a) and b) 19 h (Ingot #14); c) and d) 209 h (Ingot #15); e) and f) 215h (Ingot #15).

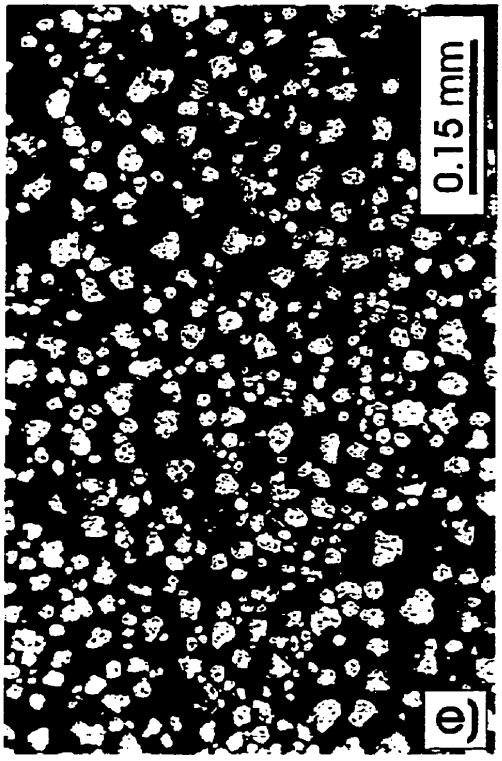

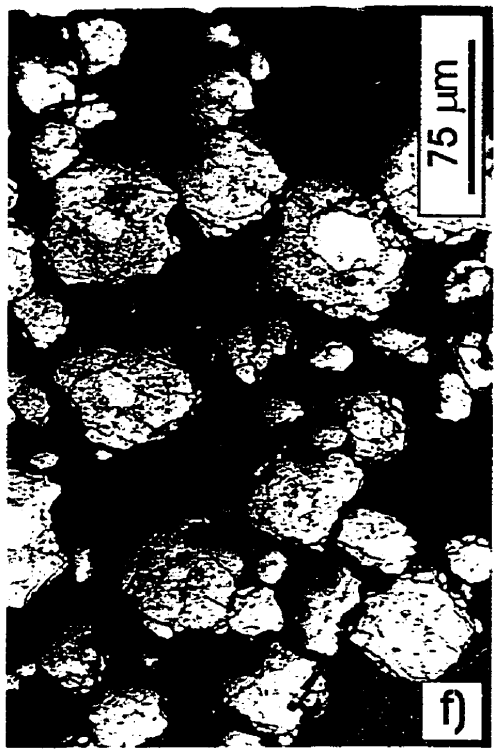

Figure K.5 Contd.

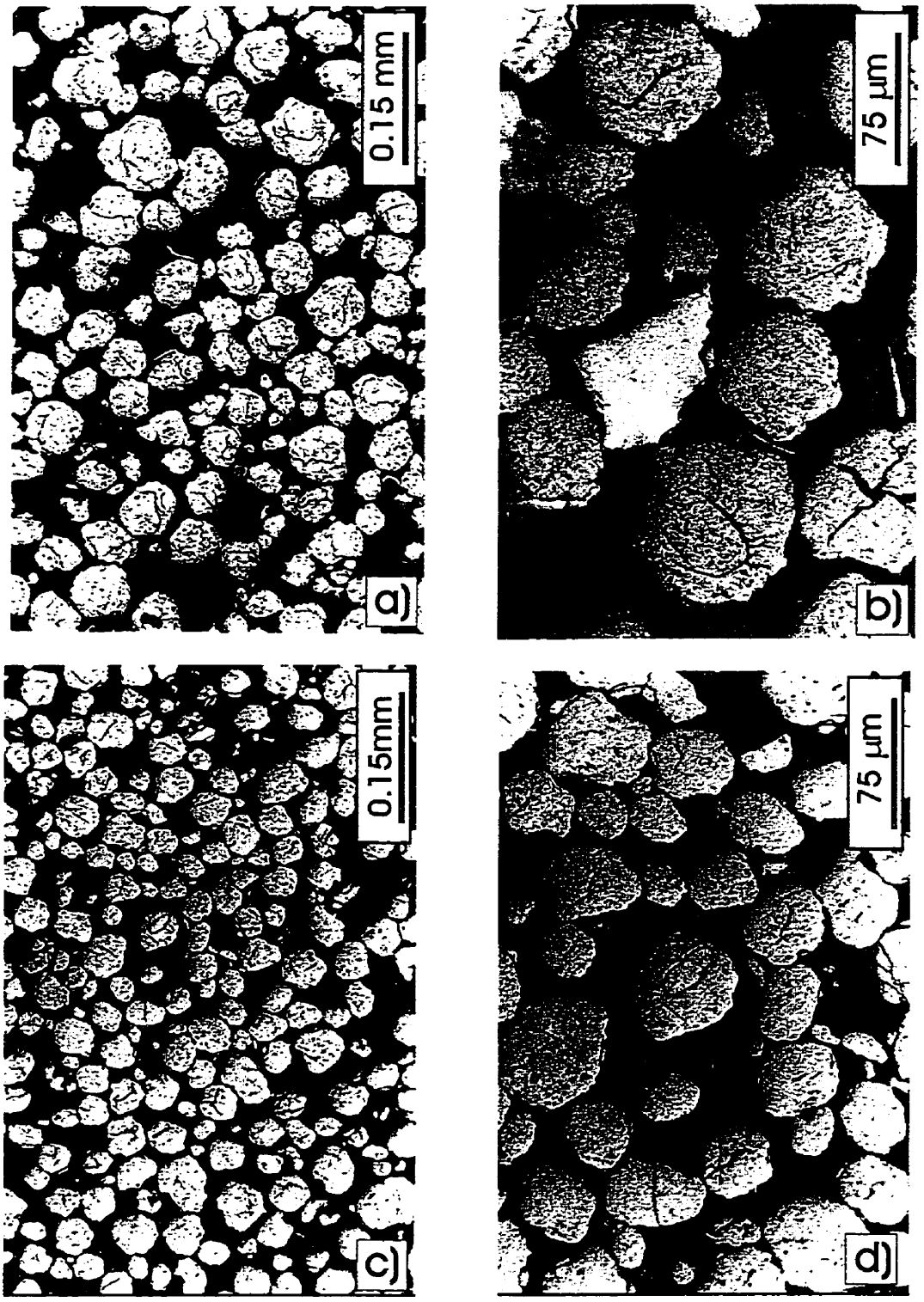

Figure K.6 Optical micrographs of powder milled for: a) and b) 282 h (Ingot #15); c) and d) 386 h (Ingot #14).

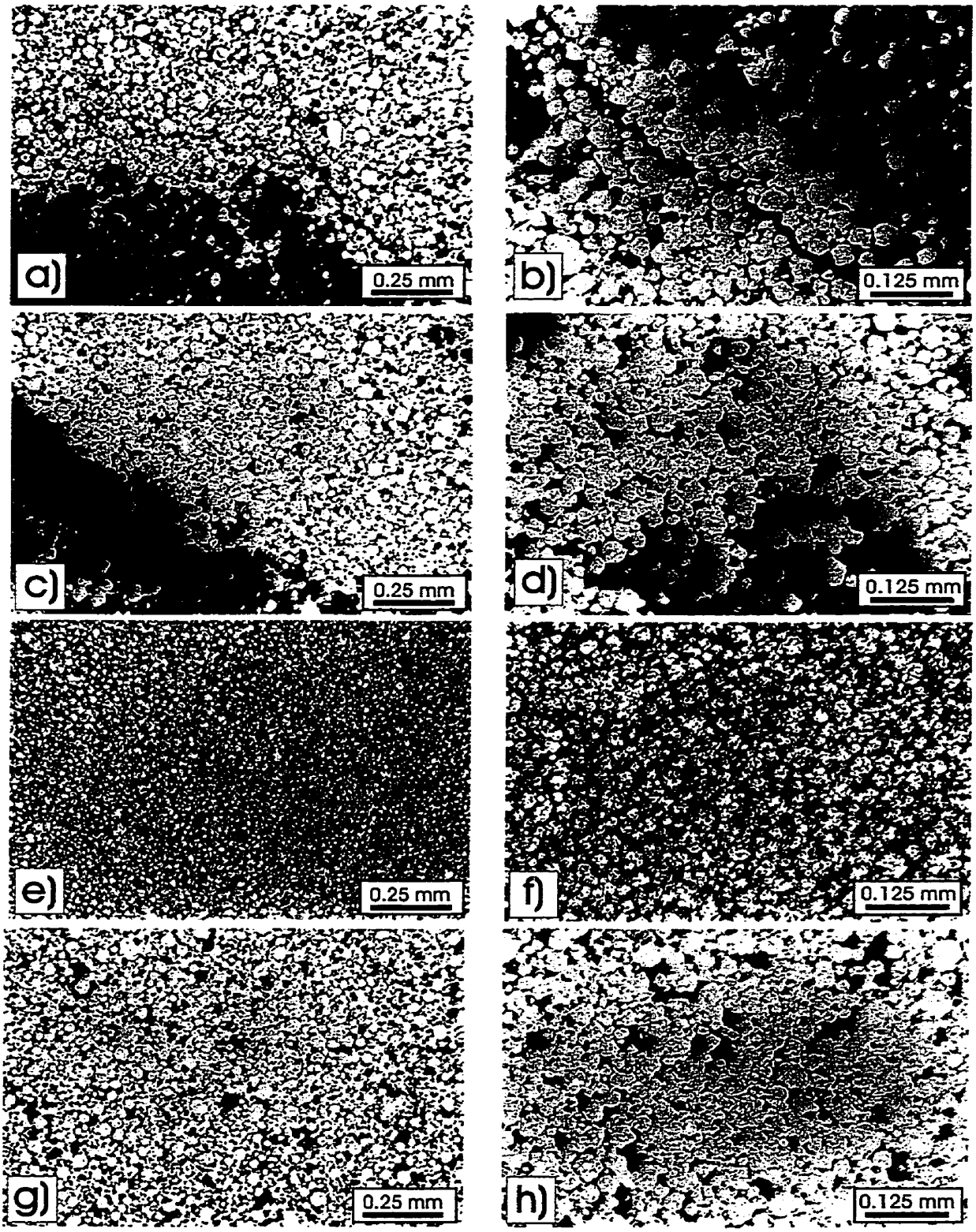

Figure K.7 Optical micrographs of powder pressed at RT at pressures: a) and b) 1980 MPa; c) and d) 2180 MPa; e) and f) 2400 MPa (not polished); g) and h) 2400 MPa (polished); i), j) and k) 2580 MPa.

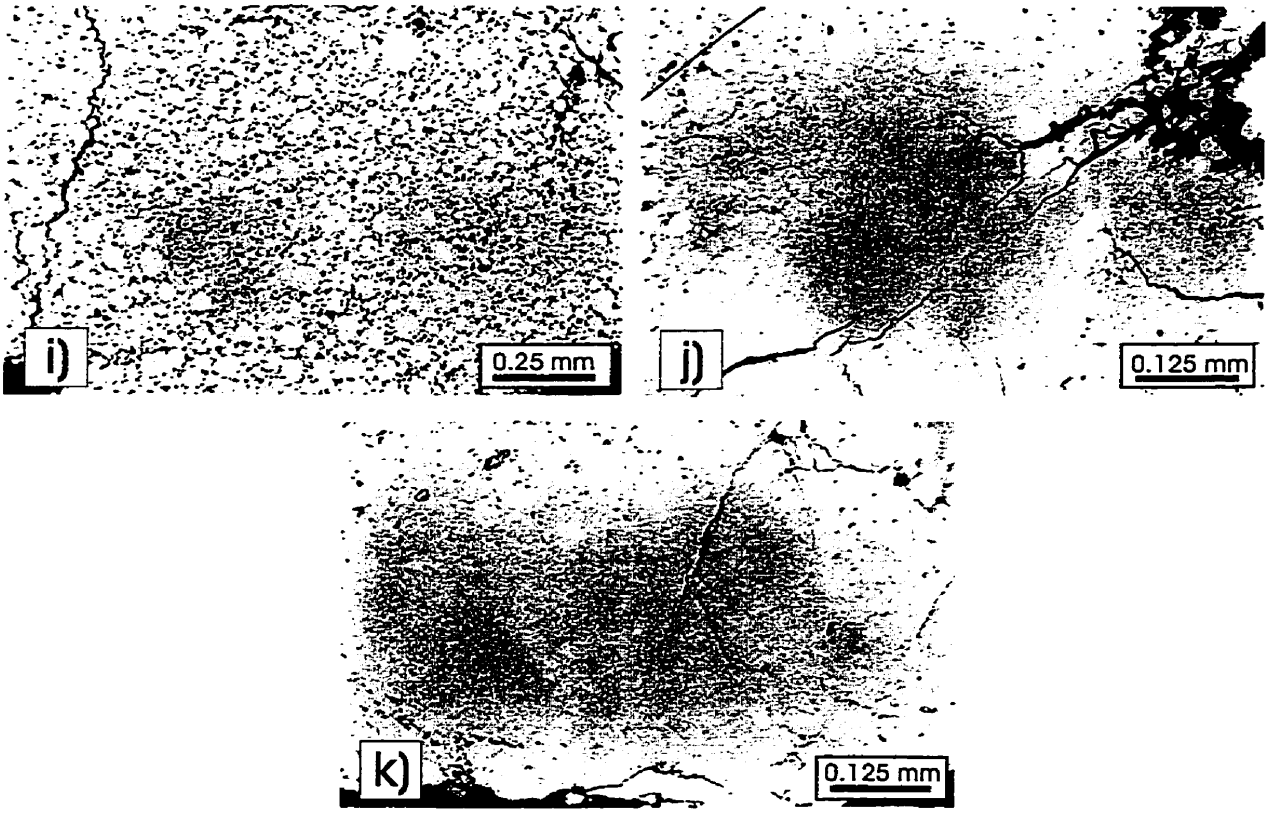

Figure K.7 Contd.

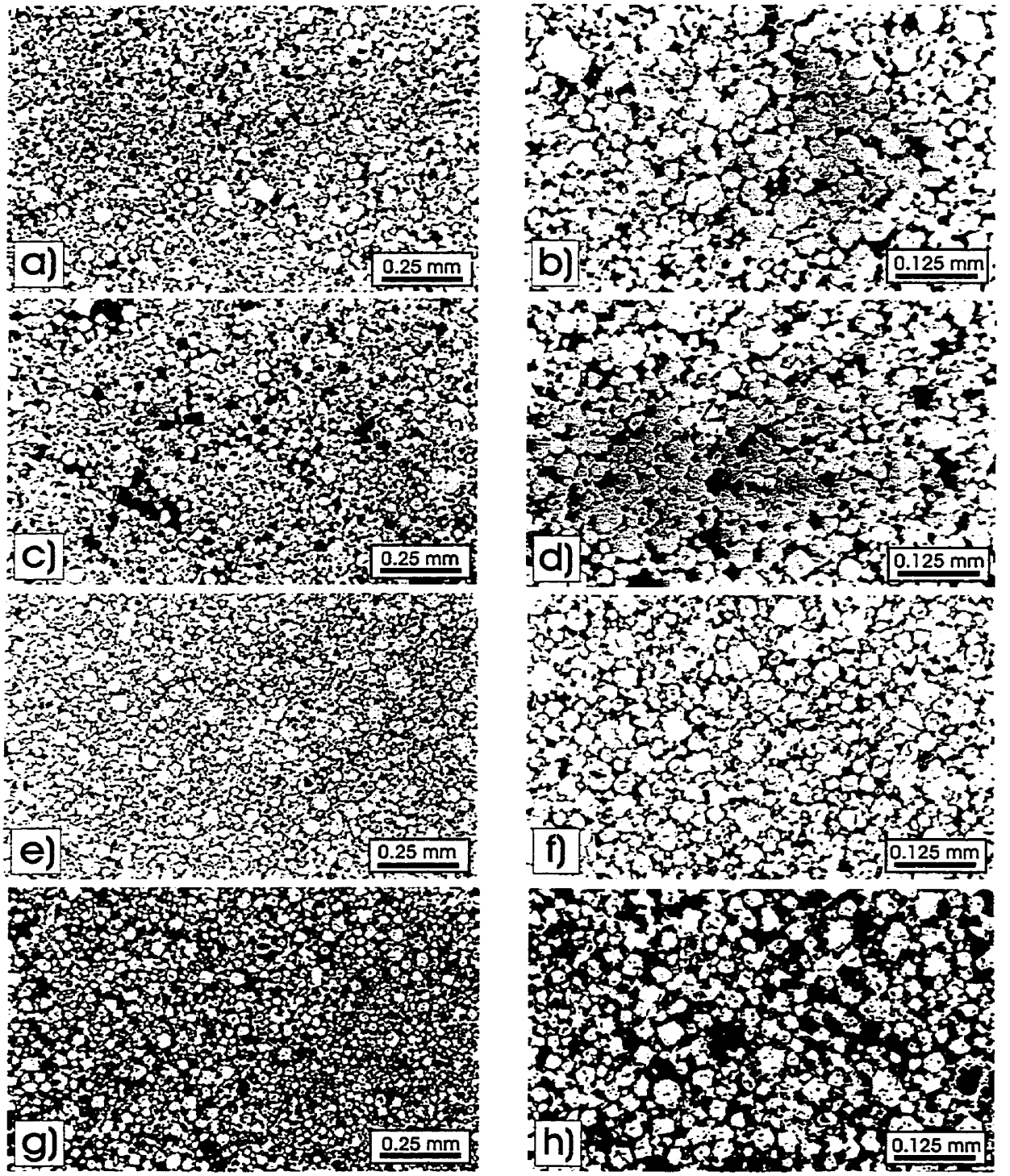

Figure K.8 Optical micrographs of powder, cold pressed at 2400 MPa and sintered at: a) and b) 900°C for 15 min; c) and d) 1000°C for 15 min; e) and f) 1100°C for 15 min; g) and h) 1100°C for 3hr; i) and j) 1150°C for 15 min (not polished); k) and l) 1150°C for 15 min (polished); m) and n) 1200°C for 15 min.

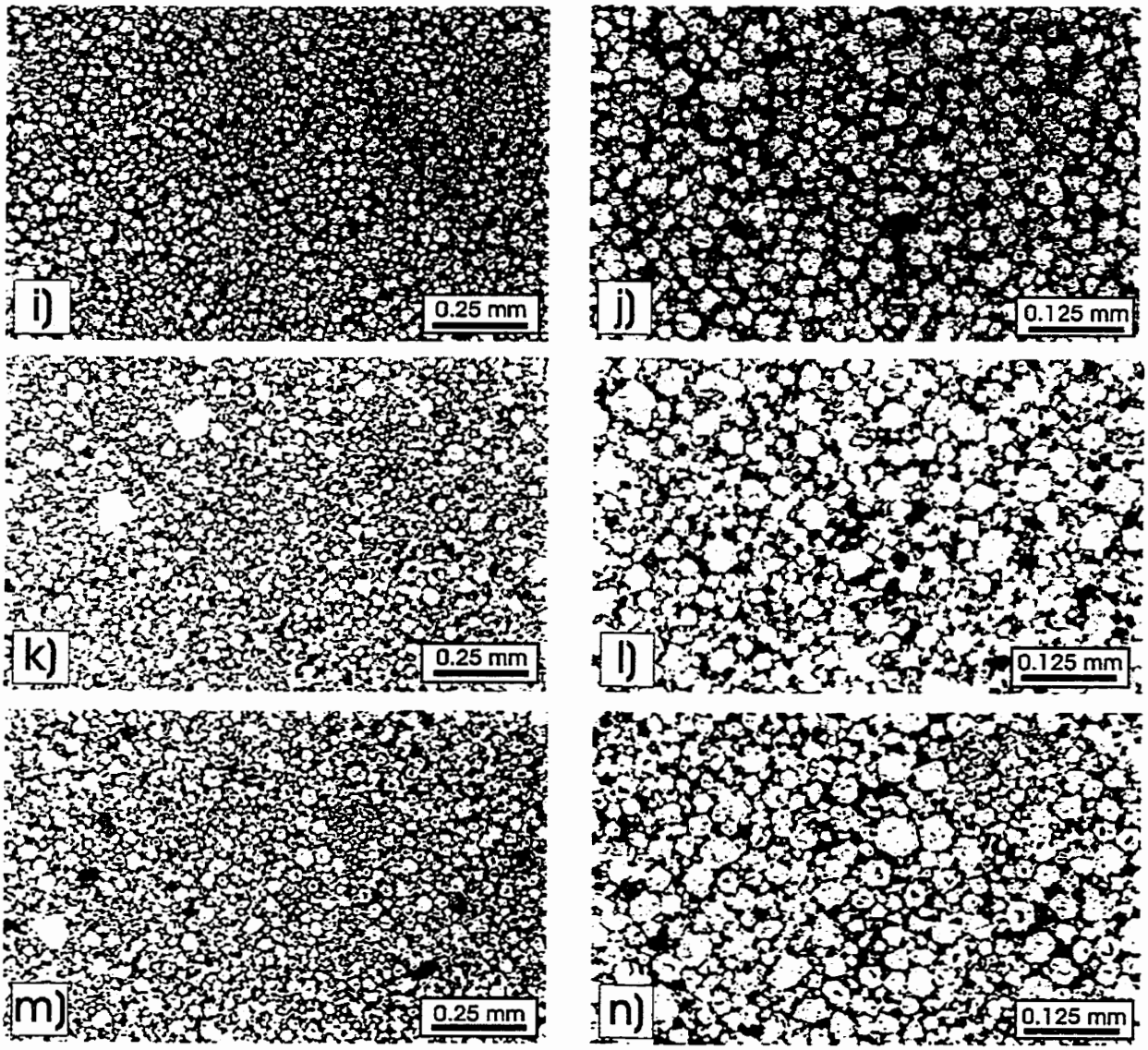

Figure K.8 Contd.

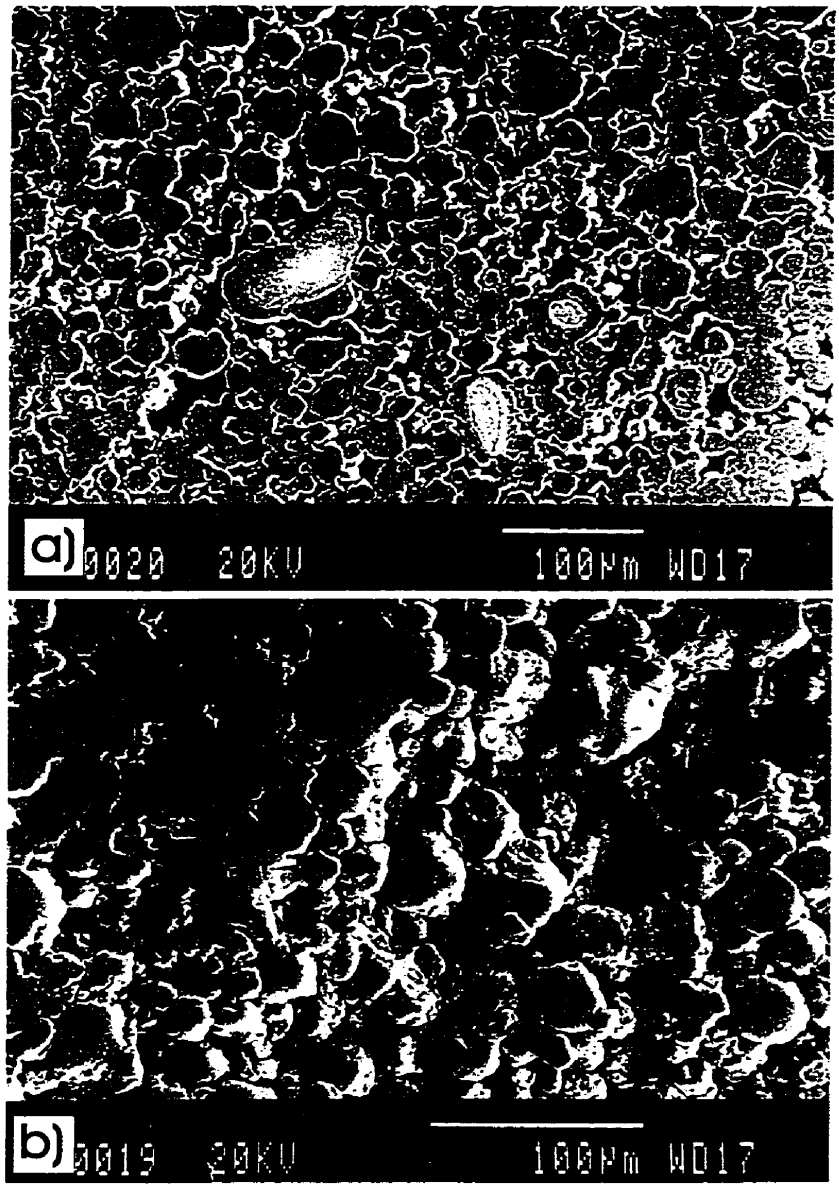

Figure K.9 SEM micrographs of powder, cold pressed under 2400 MPa and subsequently sintered for 15 min at: a) 900°C; b) 1000°C.

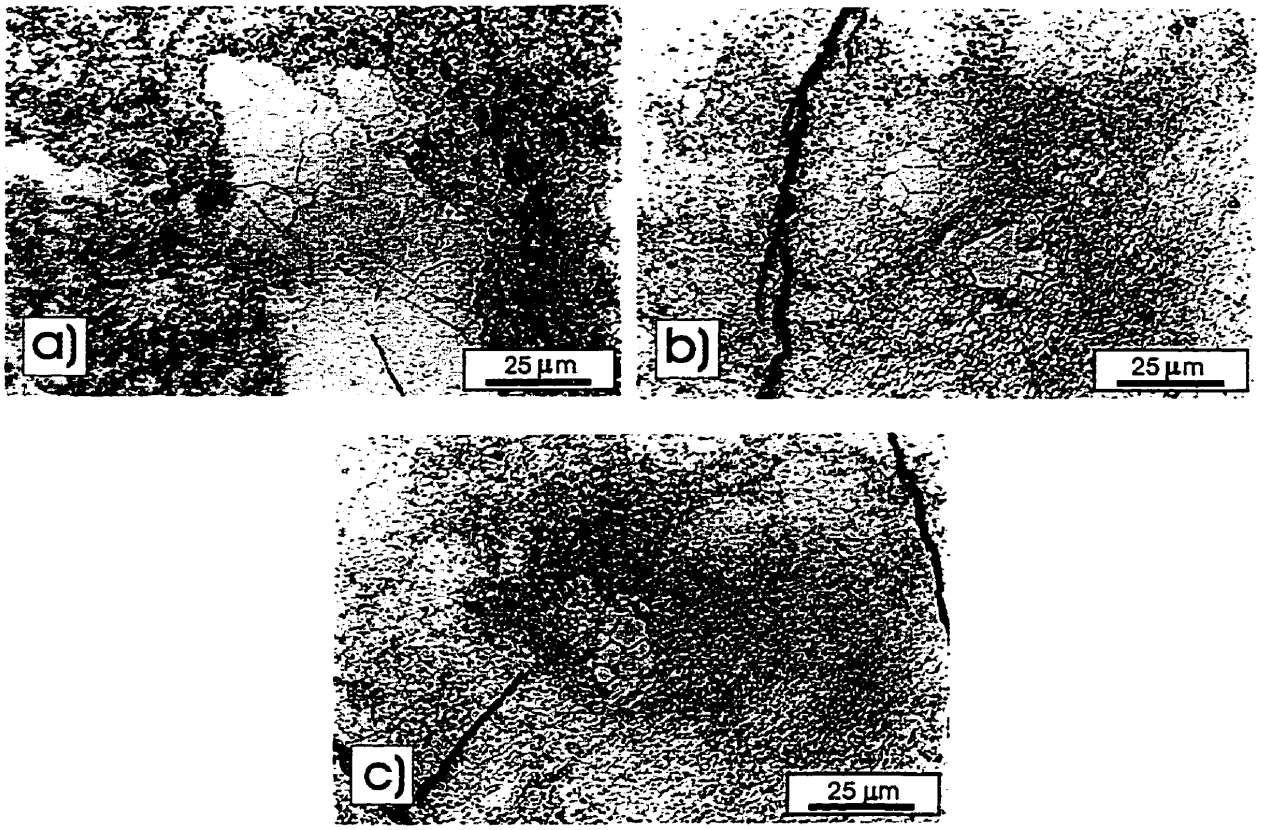

Figure K.10 Optical micrographs of the recrystallized grains in specimens cold-pressed under 2400 MPa and subsequently sintered at: a) 1000°C; b) 1100°C; c) 1150°C.

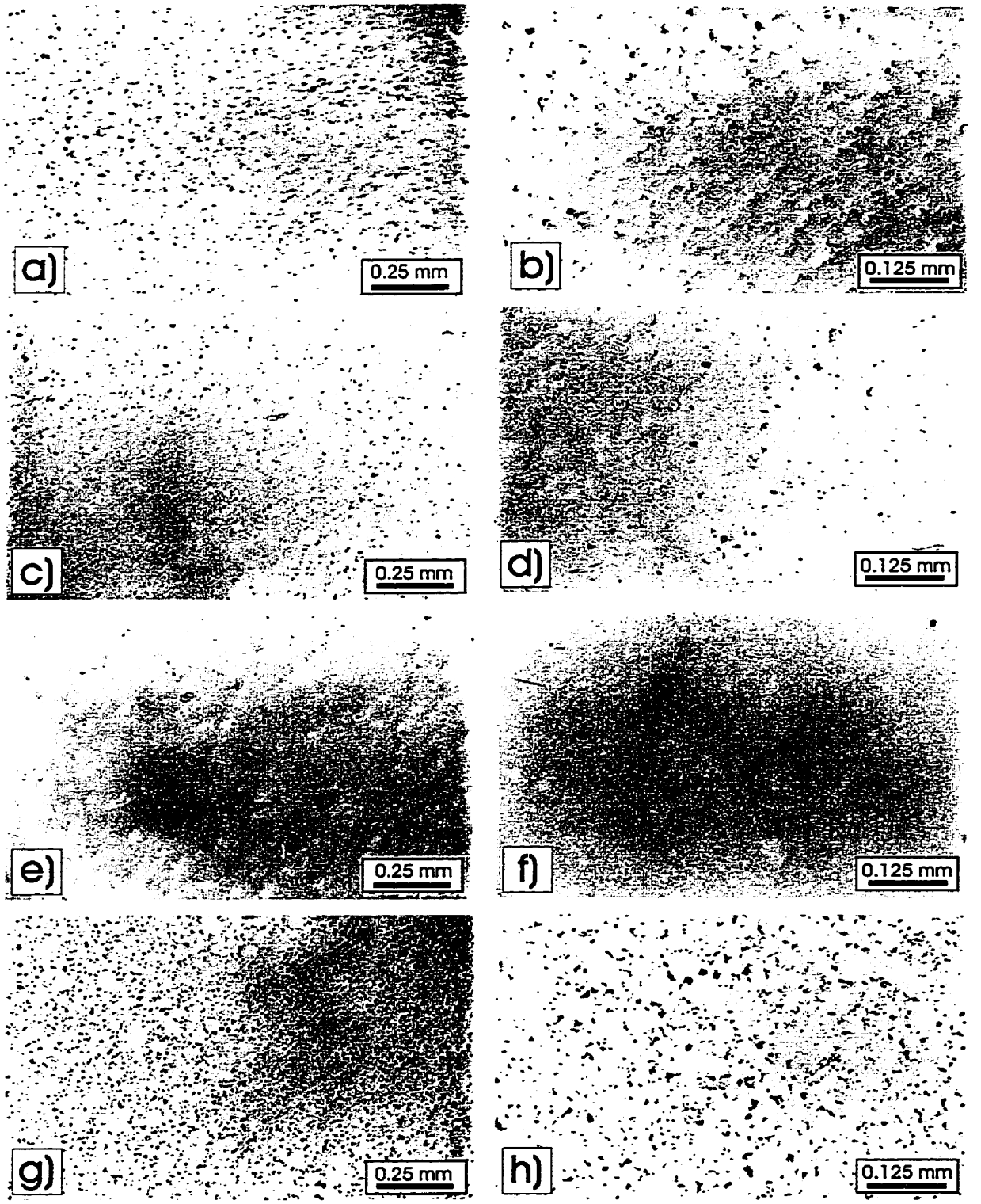

Figure K.11 Optical micrographs of cold and hot compacted powders: a) and b) K.4.1; c), d), e) and f) K.4.2; g) and h) K.4.3; i) and j) K.4.4; k) and l) K.4.5; m) and n) K.4.6 (Table K.4 in Appendix K).

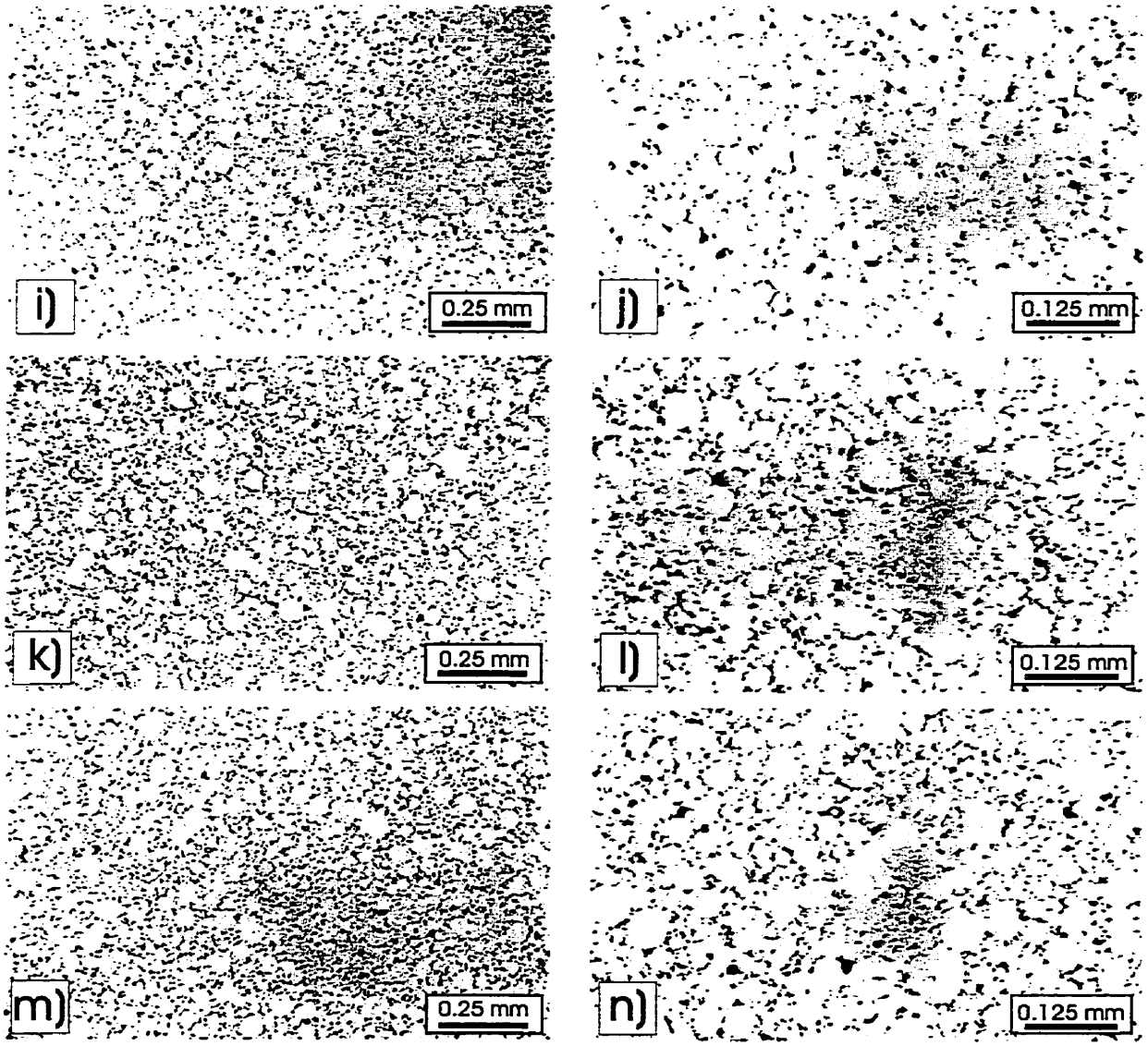

Figure K.11 Contd.

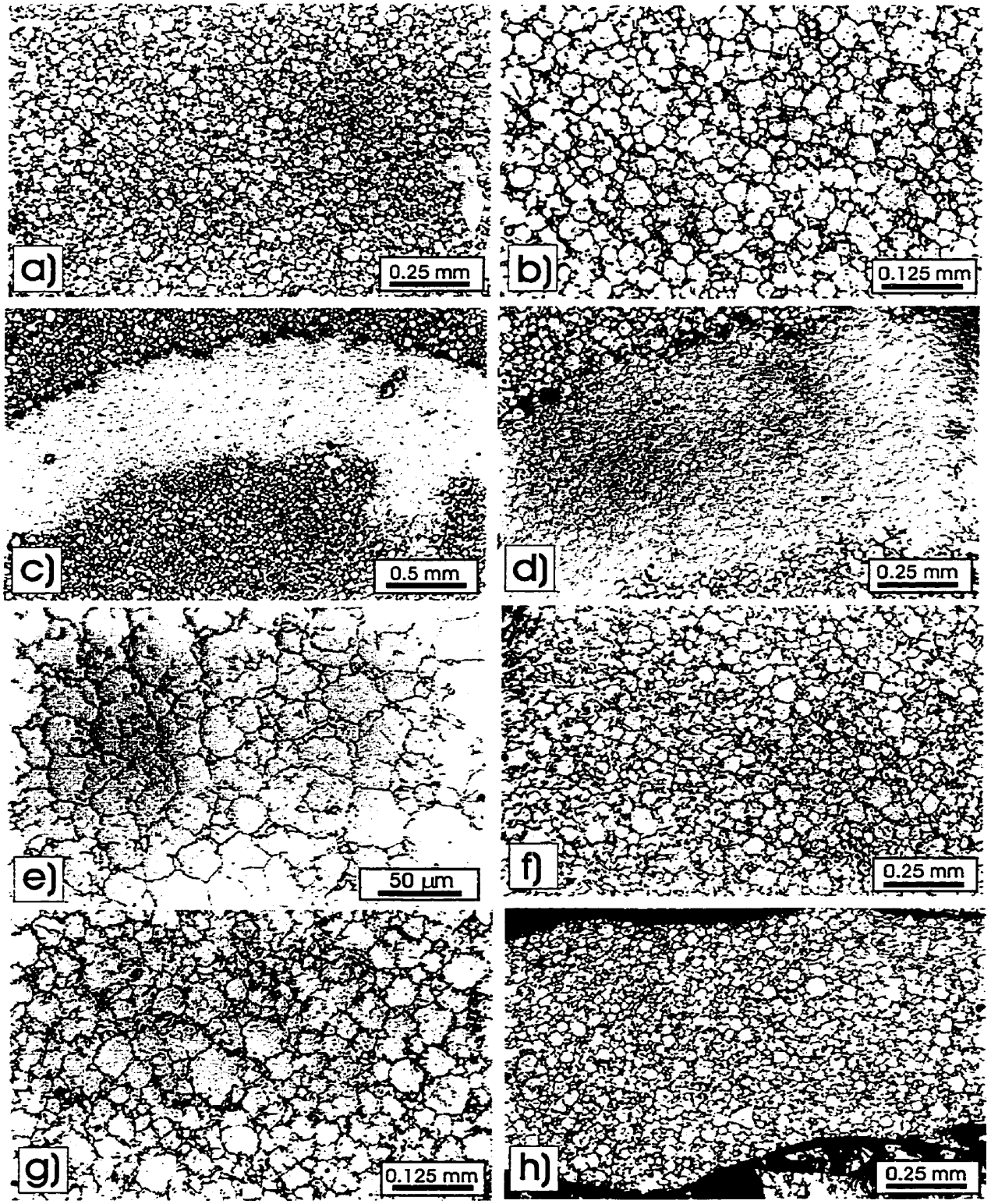

Figure K.12 Optical micrographs of cold and hot compacted powders: a) and b) K.5.1; c), d) and e) K.5.2; f) and g) K.5.3; h) and i) K.5.4; j) and k) K.5.5; l) and m) K.5.6 (Table K.5 in Appendix K).

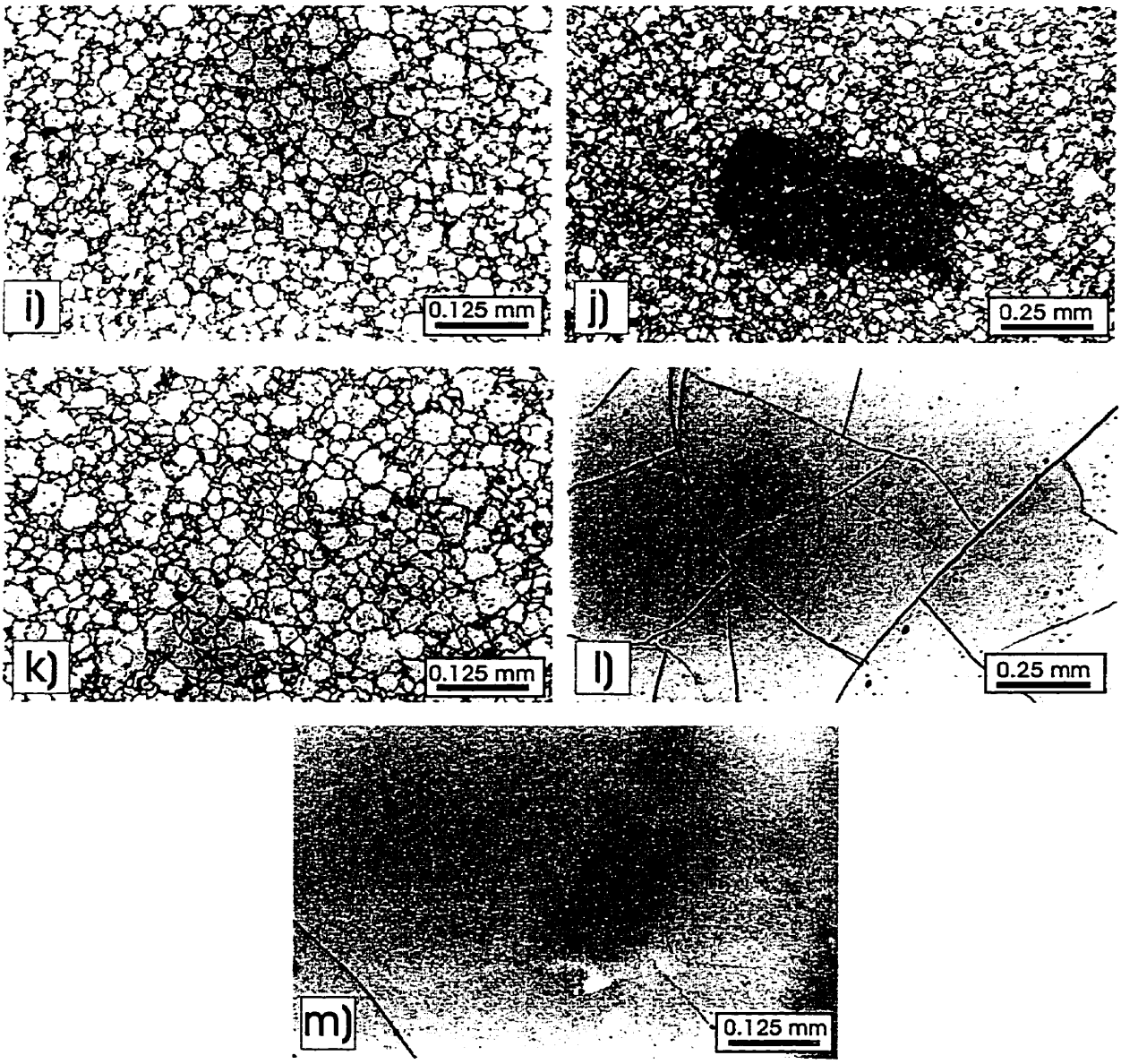

Figure K.12 Contd.

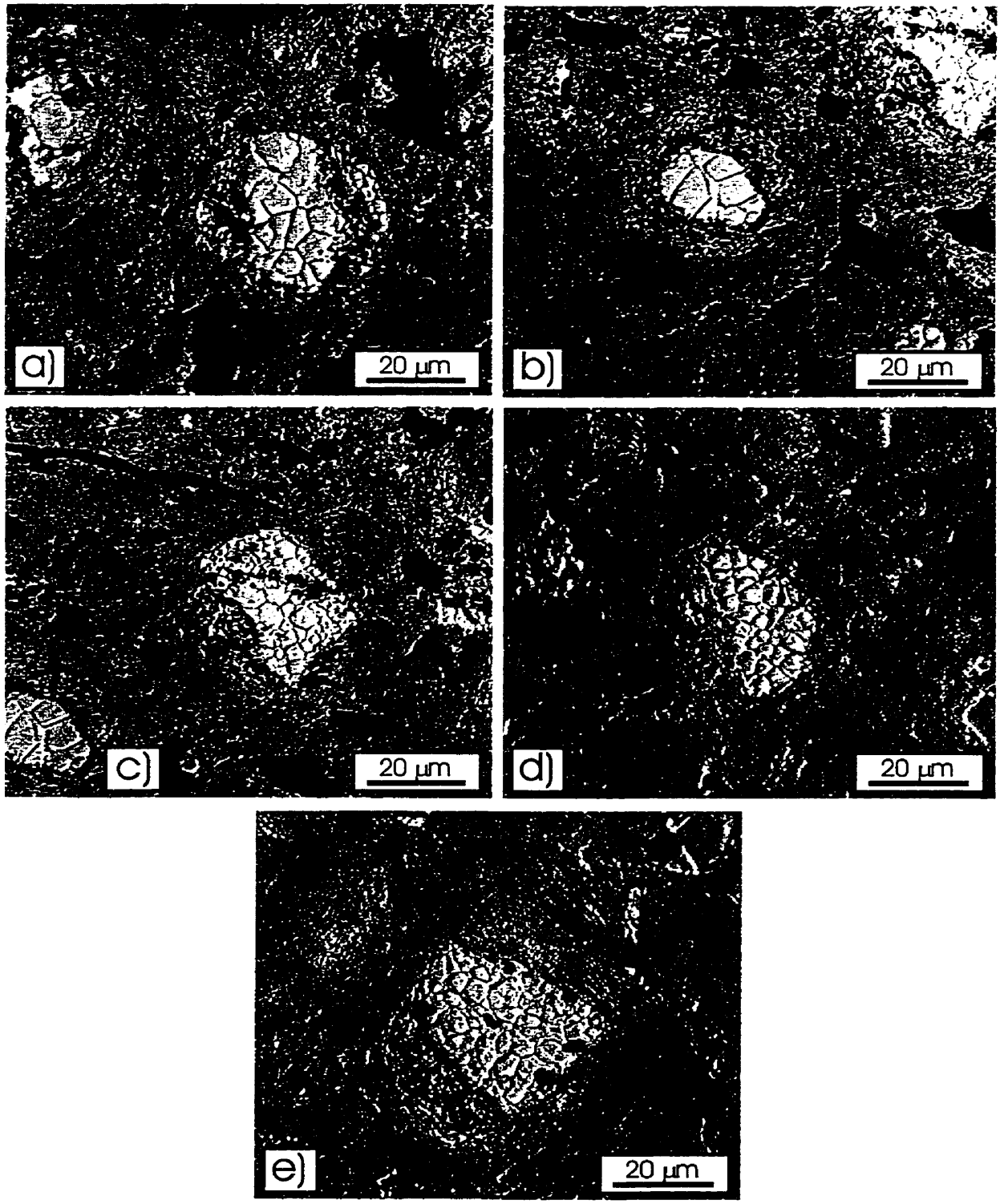

Figure K.13 Optical micrographs of the powder compact obtained in Australia showing recrystallized "cores" (heavily etched) (K.4.2 powder in Table K.4).

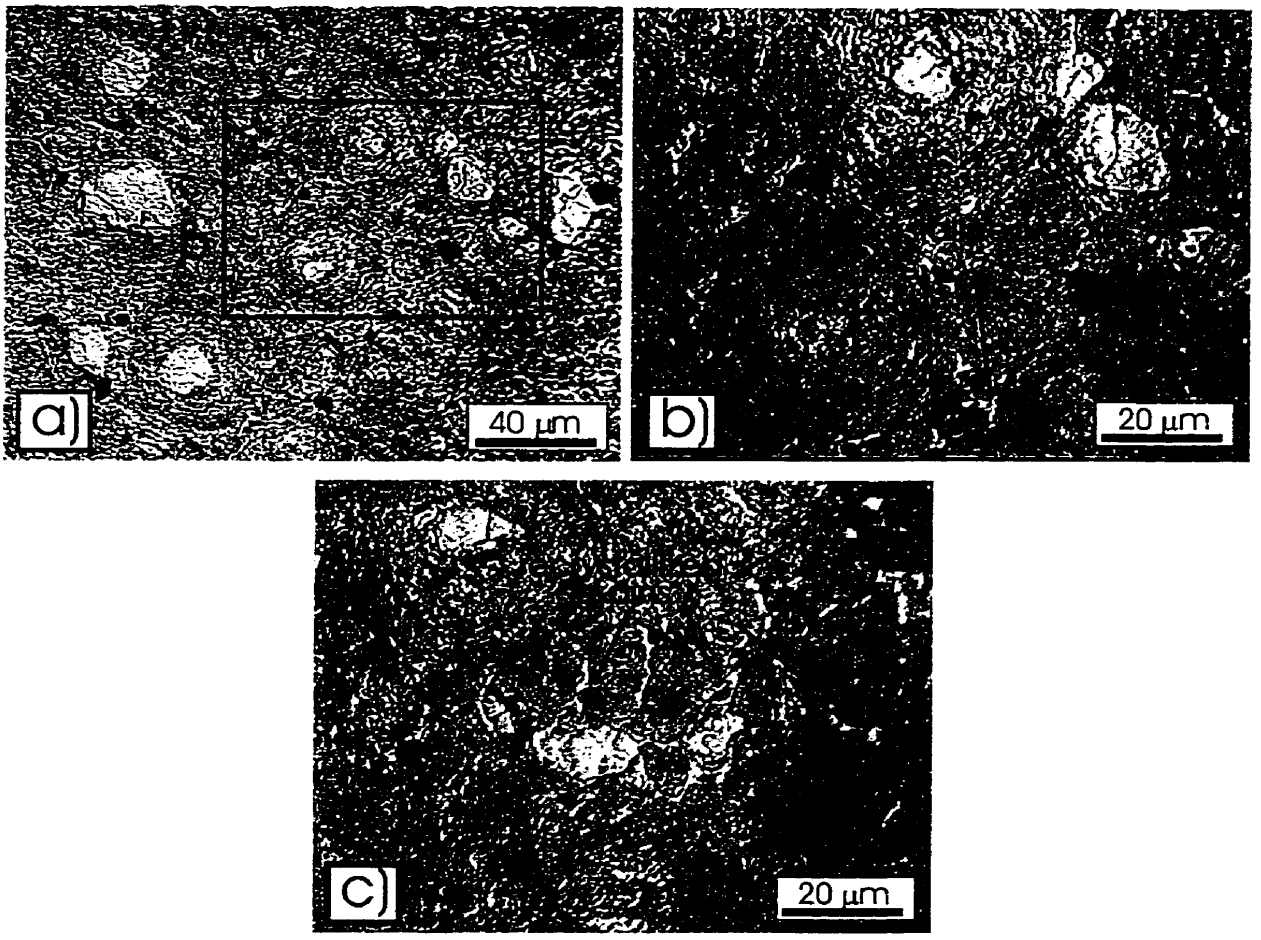

Figure K.14 Optical micrographs of the microstructure of the compact obtained in Australia (lightly etched).

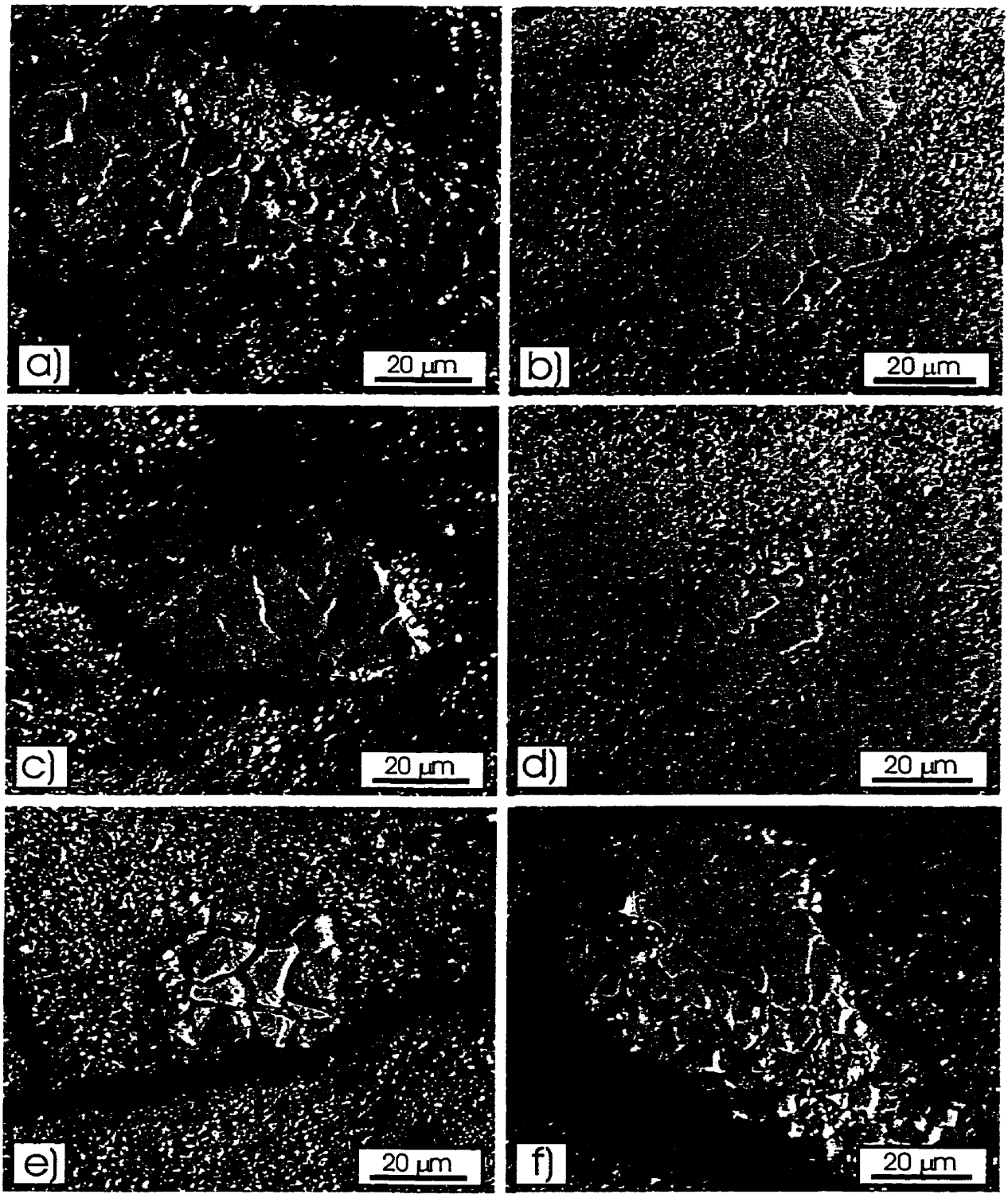

Figure K.15 Optical micrographs of the powder compact obtained in this work showing recrystallized cores (heavily etched) (compact K.5.6 in Table K.5).

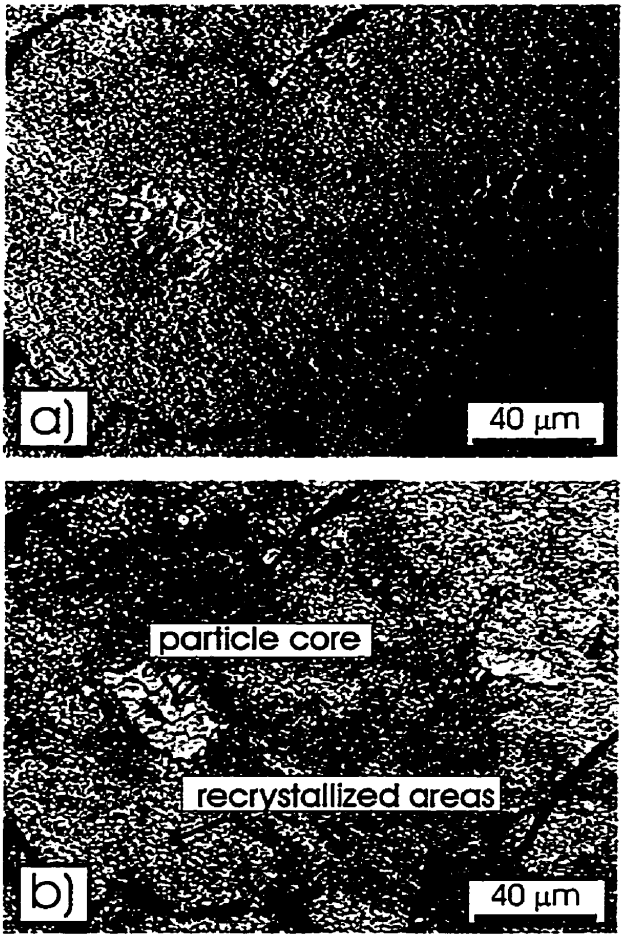

Figure K.16 Optical micrographs of the microstructure of the compact obtained in the present work (etched); pictures (a) and (b) were obtained under different illumination conditions to show the non-uniformity of recrystallization.

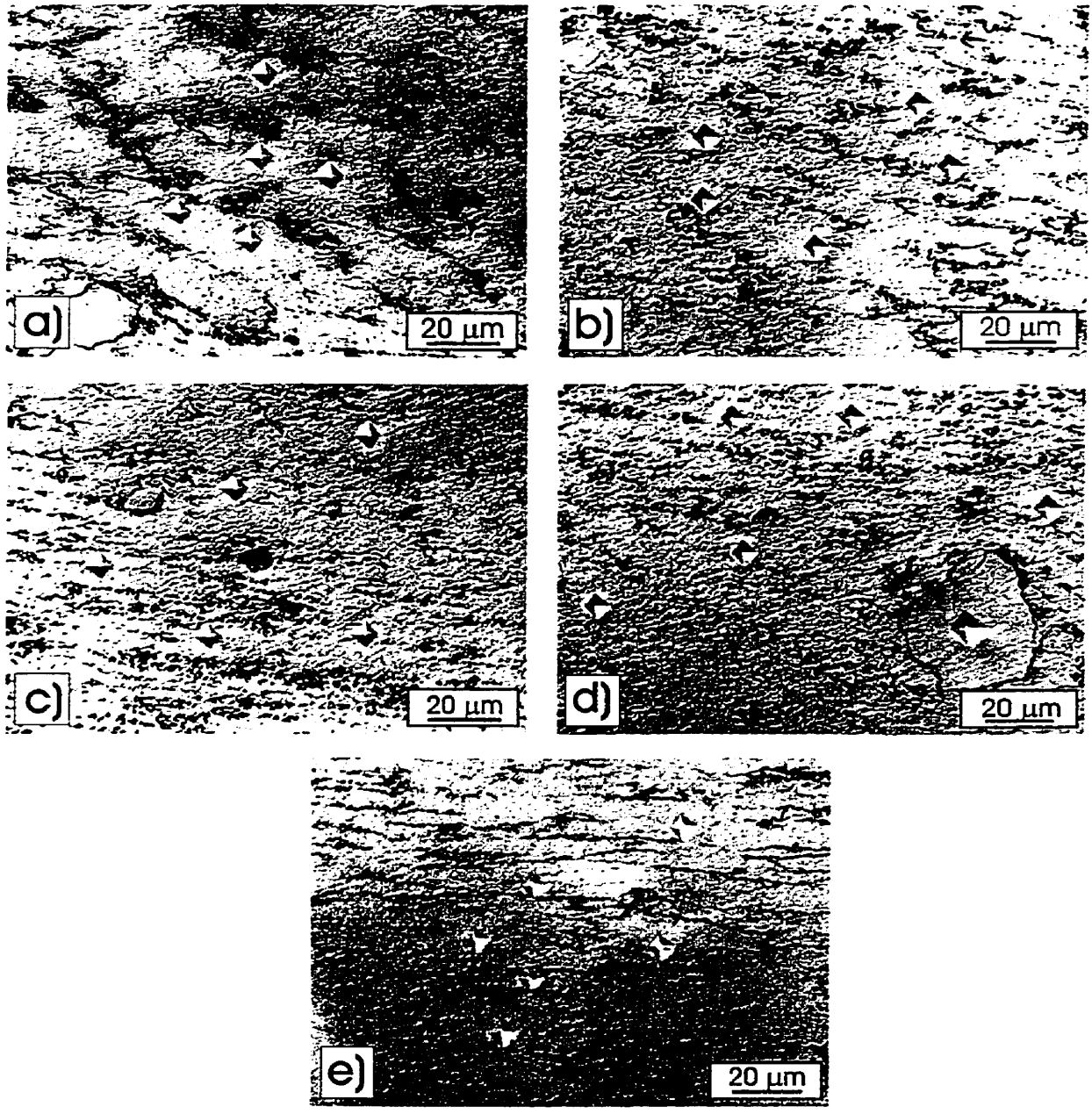

Figure K.17 Optical micrographs of microhardness indentations in the location number: a) 6; b) 9; c) 10; d) 11, and e) 13 in Fig.5.106.

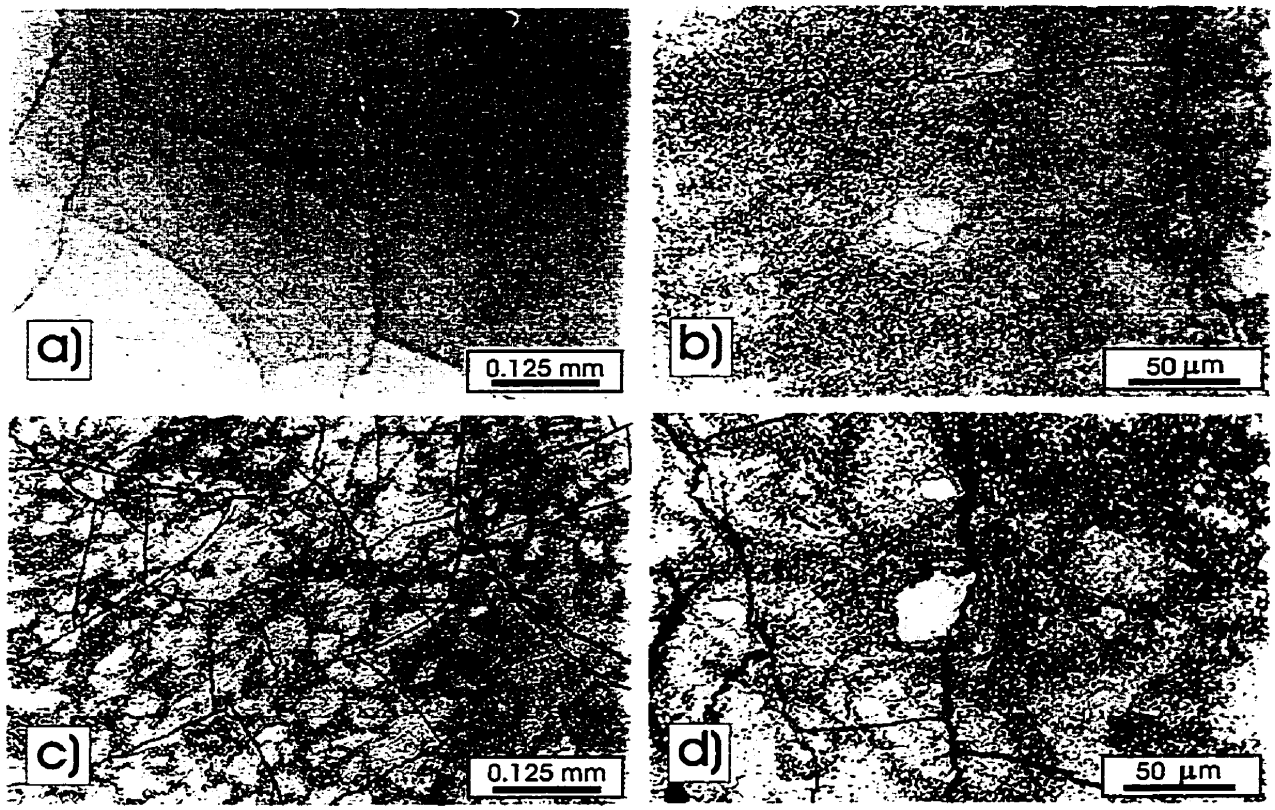

Figure K.18 Optical micrographs of the hot-pressed powder obtained in this work: a) unetched; b), c) and d) etched and showing recrystallized regions (bright areas) (powder compact no. K.5.6- Table K.5).

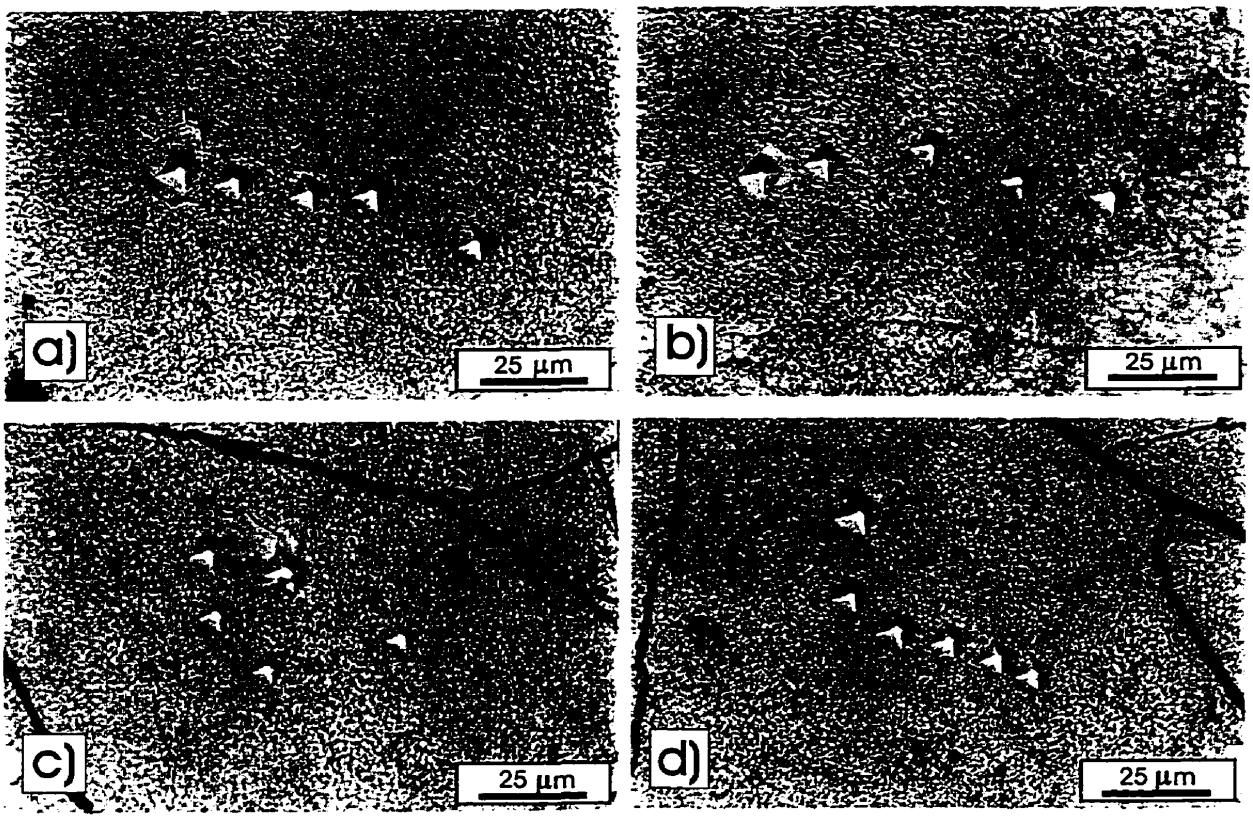

Figure K.19 Optical micrographs of the hot-pressed powder (powder compact no. K.5.6- Table K.5) obtained in this work: a), b) and d) a gradual change in indentation size, c) abrupt indentation size change at the particle (unmilled) boundary (10g load).

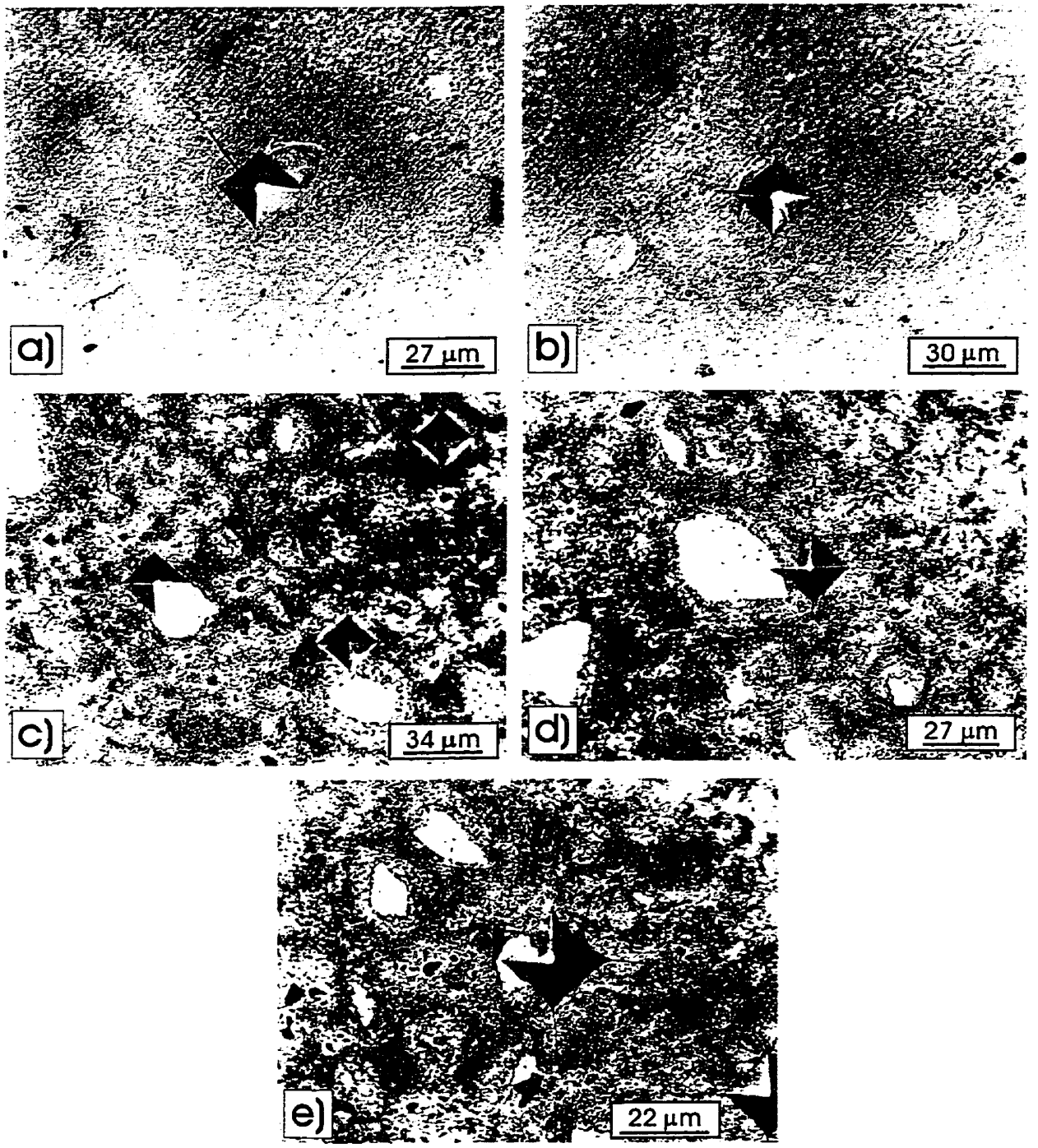

Figure K.20 Optical micrographs of the indentations made under 300g load (powder compact no. K.4.2– Table K.4).

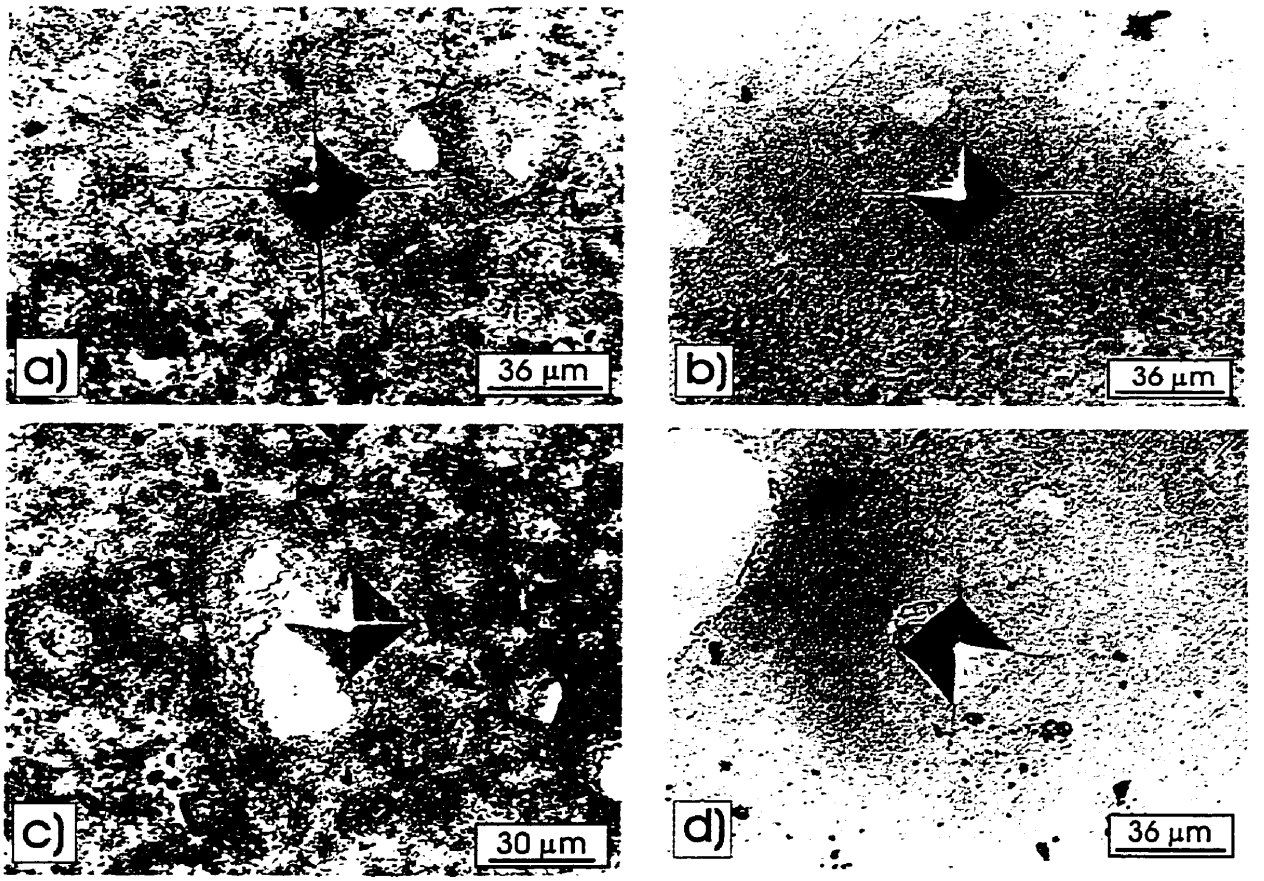

Figure K.21 Optical micrographs of the indentations made under 500g load (powder compact no. K.4.2– Table K.4).

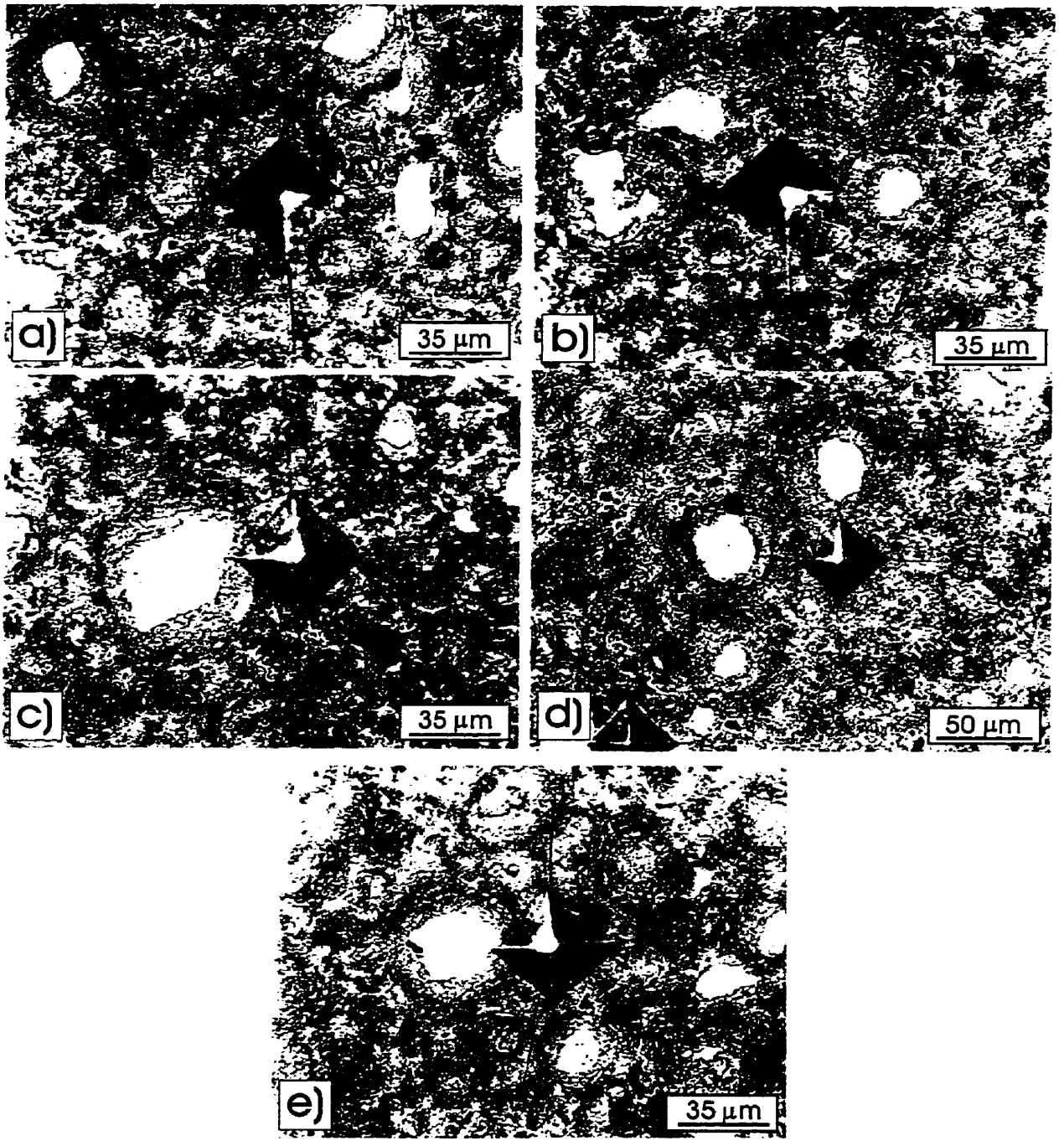

Figure K.22 Optical micrographs of the indentations made under 1000g load (powder compact no. K.4.2– Table K.4).

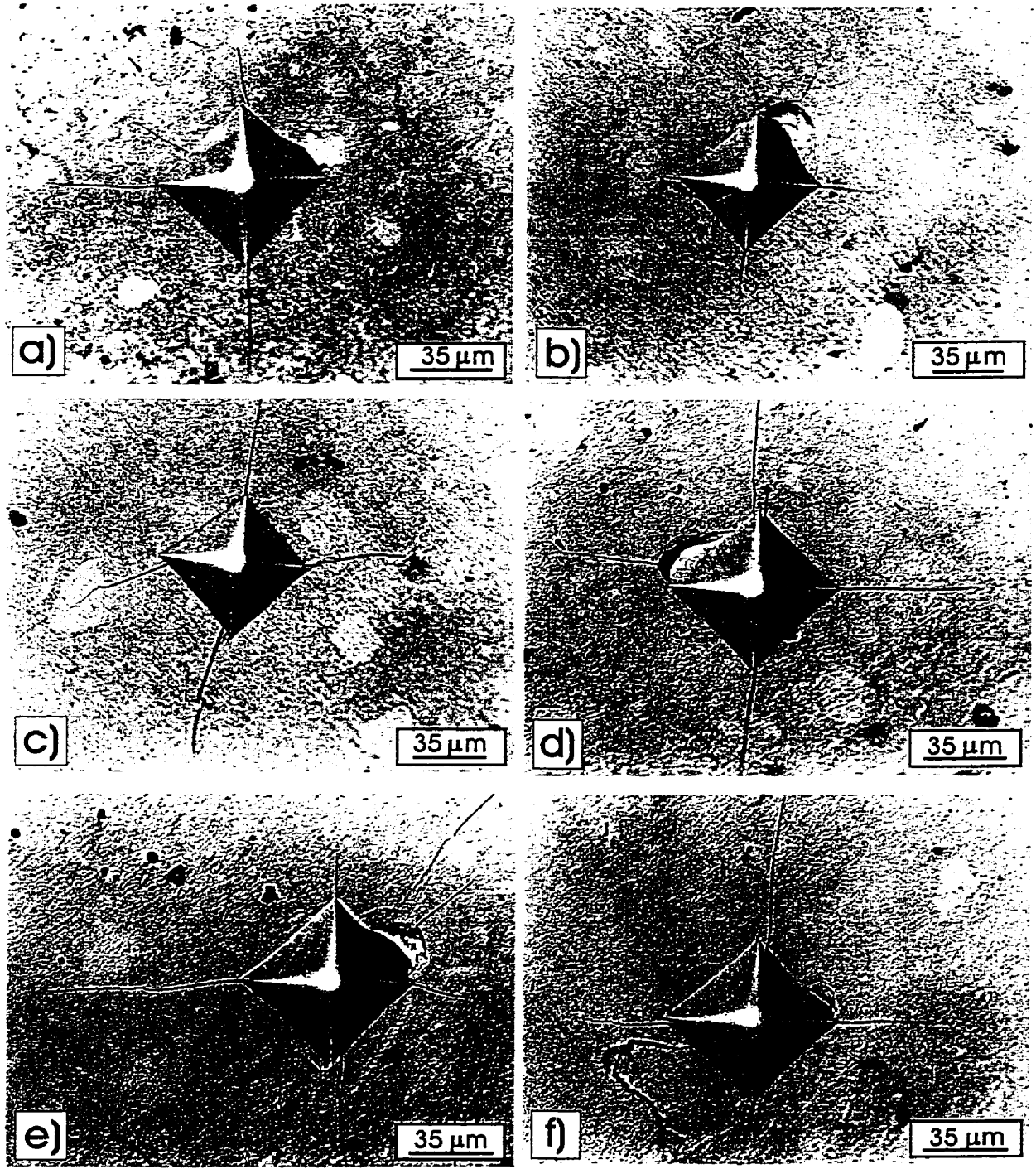

Figure K.23 Optical micrographs of the indentations made under 2000g load (powder compact no. K.4.2– Table K.4).

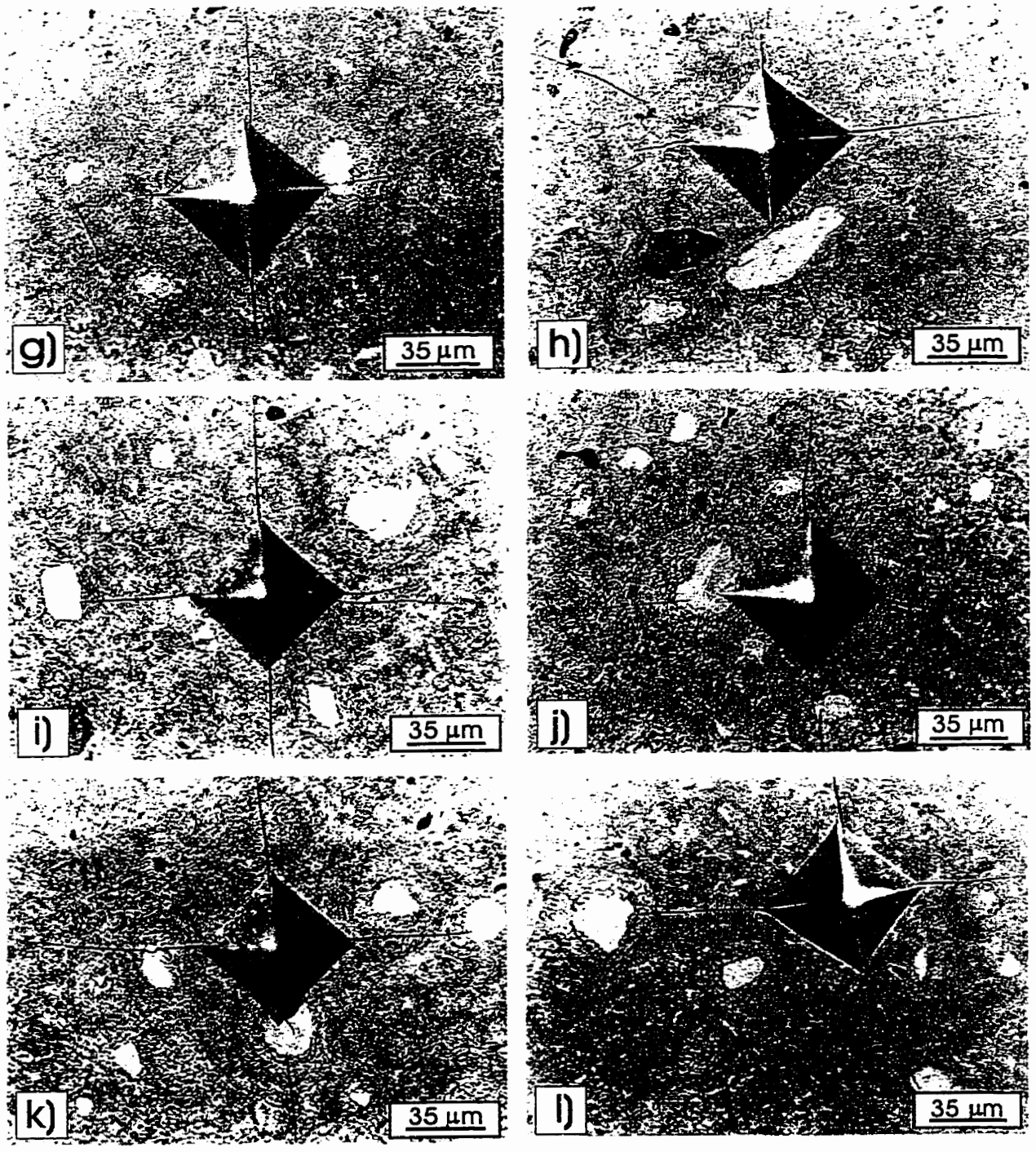

Figure K.23 Contd.

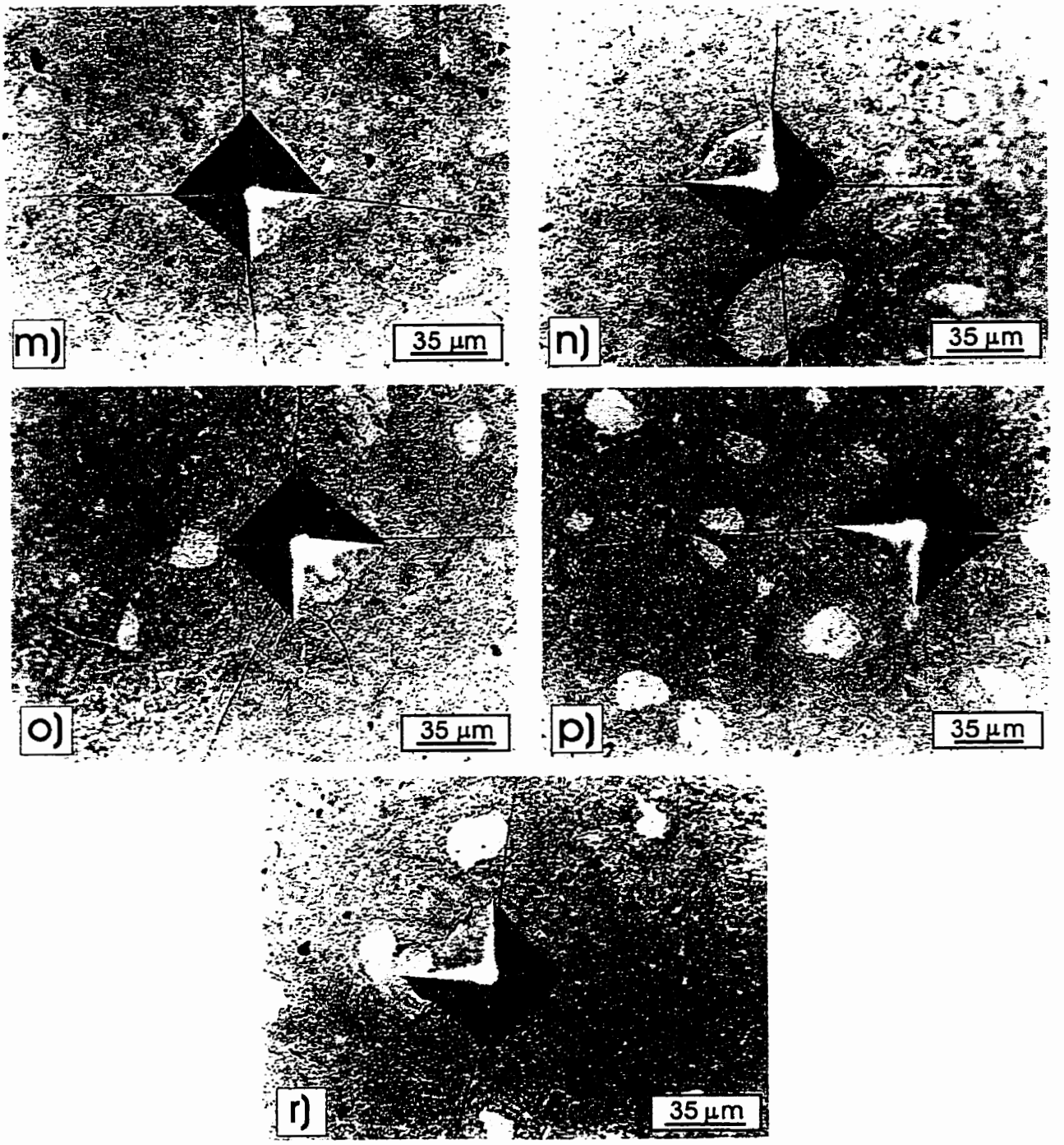

Figure K.23 Contd.

Table K.1 Microhardness (HV 0.01) (10g load) of selected powders and corresponding crystallite size as a function of milling time.

Milling Time [h]	Crystallite Size [nm] (Cauchy approx.)	Microhardness (HV 0.01) [kg/mm²]		
		Core	Outer Layer	No Core
0 (as-cast homogenized ingot)	---	296±20(20)	---	---
19	24	386±47(27)	489±82(17)	---
105	6	430±62(23)	615±80(20)	613±70(25)
208	3	453±100(39)	611±80(72)	601±75(34)
386	3	---	---	728±71(26)

Table K.2 Microhardness (HV 0.01) of powder milled for 208h compacted at room temperature under various compaction pressures (ten measurements were made for the average).

Spec. No.	Specimen description	Microhardness (HV 0.01) [kg/mm²]		Porosity [%]
		Core	Outer layer	
1.	CP 1980 MPa	414±67	577±73	32±3.2
2.	CP 2180 MPa	440±55	617±80	26±3.5
3.	CP 2400 MPa	429±39	618±59	29±2.0
4.	CP 2580 MPa	454±36	693±119	16±3.3

Table K.3 Microhardness (HV 0.01) of powders compacted at room temperature and subsequently sintered in air (ten measurements were made for the average).

Spec. No.	Specimen description	Microhardness (HV 0.01) [kg/mm²]		Porosity [%]
		Core	Outer layer	
1.	CP 2400 MPa sintered at 900°C for 15 min	267±27	347±26	28±3.1
2.	CP 2400 MPa sintered at 1000°C for 15 min	245±35	343±40	23±5.3
3.	CP 2400 MPa sintered at 1100°C for 15 min	242±30	320±25	29±3.6
4.	CP 2400 MPa sintered at 1100°C for 3 hr	238±24	314±32	53±1.6
5.	CP 2400 MPa sintered at 1150°C for 15 min	194±15	254±16	39±4.3
6.	CP 2400 MPa sintered at 1200°C for 15 min	158±13	262±18	42±7.2

Table K.4 Microhardness at various loads of powders milled for 208h compacted at room and high temperatures (in the University of Wollongong, Australia) (ten measurements were made for the average).

Spec. No	Powder processing	Porosity [%]	Microhardness [kg/mm²]					
			Core 10 g	Outer layer		"average"		
				10 g	200 g	500 g	1000 g	2000 g
K.4.1	CP, HP 700°C for 1 h 900°C for 15 min	2.0±0.8	209±17	574±42	679±45	695±33	641±33	699±37
K.4.2	CP, HP 900°C for 15 min	0.6±0.2	243±30	727±93	753±40	684±47	684±23	698±31
K.4.3	CP, HP 700°C for 1 h 850°C for 15 min	7.5±1.4	197±18	732±77	794±89	686±46	642±21	675±42
K.4.4	CP HP 850°C for 15 min	8.3±2.2	280±19	866±84	754±83	664±49	609±34	681±64
K.4.5	CP HP 800°C for 15 min	12.5±1.7	307±46	924±102	732±52	594±51	574±19	600±30
K.4.6	CP, HP 700°C for 1 h 800°C for 15 min	10.9±1.1	227±33	646±71	769±78	612±51	590±41	578±23

Heating time to achieve compaction temperature was ~5 min.

Full load was kept on the samples right from the beginning of heating and until temperature reached ~150°C upon cooling after the test.

CP - cold pressed (at RT) at 450 MPa

HP - hot compacted at 210 MPa

Table K.5 Microhardness (HV 0.01) of powders compacted at room and high temperatures (in this work) (ten measurements were made for the average).

	Specimen description	Microhardness (HV 0.01) [kg/mm²]		Porosity [%] (includes oxide layer)
		Core	Outer layer	
K.5.1	CP 2400 MPa HP 320 MPa at 900°C for 10 min	317±43	401±37	20±2.2*)
K.5.2	CP 2400 MPa HP 350 MPa at 900°C for 15 min	179±16	306±16	19±1.4*)
K.5.3	CP 2400 MPa HP 360 MPa at 900°C for 20 min	255±19	383±45	17±2.1*)
K.5.4	CP 2400 MPa HP 470 MPa at 915°C for 15 min	232±31	384±47	19±1.3*)
K.5.5	CP 450 MPa HP 430 MPa at 915°C for 15 min	220±28	347±24	22±2.2*)
K.5.6	CP 450 MPa HP 430 MPa at 915°C for 15 min	199±23	310±45	0.4±0.1 (real)

Heating time to achieve compaction temperature was ~45 min.

Specimens K.5.1- 5.5 were loaded once they reached the hot compaction temperature and unloaded right after the compaction

Specimen K.5.6 was fully loaded from the beginning of heating, pressed for 15 min under that load and kept fully loaded until it reached ~150°C on cooling after the test.

*)- Numbers are overestimated because interparticle boundaries (dark lines) were counted by the Java system as additional porosity.

L Microhardness and Indentation Fracture Toughness of Hot-Compacted Powders

Table L.1 Microhardness and indentation fracture toughness of hot compacted powder K.4.1 in Table K.4 (at 500 g).

	Load 500 [g]		
	Microhardness [HV] [kg/mm²]	Crack length l [μm]	Fracture toughness K_{Ic} [MPa√m]
1.	683	16.7	2.0
2.	692	11.8	2.4
3.	719	11.9	2.4
4.	661	11.6	2.3
5.	740	15.4	2.1
6.	674	17.8	1.9
7.	685	18.6	1.9
8.	690	13.6	2.2
9.	675	18.5	1.9
10.	732	12.0	2.4
11.	704	14.7	2.1
12.	717	14.2	2.2
13.	597	18.6	1.7
14.	702	17.4	2.0
15.	674	17.7	1.9
16.	694	12.7	2.3
17.	696	14.5	2.1
18.	686	15.3	2.1
19.	645	15.1	2.0
20.	727	12.0	2.4
21.	725	11.7	2.4
22.	690	17.4	1.9
23.	685	10.7	2.5
24.	702	14.7	2.1
25.	685	11.4	2.4
26.	763	15.6	2.2
27.	704	19.6	1.8
28.	647	21.1	1.7
29.	685	10.5	2.5
30.	663	12.5	2.3
31.	665	16.3	2.0
32.	621	12.7	2.1
33.	704	18.1	1.9
34.	707	12.5	2.3
35.	732	14.5	2.2
36.	729	13.6	2.2
37.	729	15.4	2.1

Table L.2 Microhardness and indentation fracture toughness of hot compacted powder K.4.1 in Table K.4 (at 2000 g).

	Load 2000 [g]		
	Microhardness [HV] [kg/mm²]	Crack length l [μm]	Fracture toughness K_{Ic}[MPa√m]
1.	654	69	1.9
2.	613	86	1.6
3.	730	69	2.0
4.	686	81	1.8
5.	729	92	1.7
6.	757	58	2.2
7.	720	54	2.2
8.	726	38	2.7
9.	673	68	1.9
10.	718	79	1.9
11.	723	58	2.2
12.	685	70	1.9
13.	729	50	2.3
14.	682	63	2.0
15.	757	59	2.2
16.	715	67	2.0
17.	672	59	2.1
18.	696	77	1.9
19.	646	88	1.7
20.	651	55	2.1
21.	741	81	1.9
22.	743	91	1.8
23.	670	57	2.1
24.	717	82	1.8
25.	700	67	2.0
26.	642	85	1.7

Table L.3 Microhardness and indentation fracture toughness of hot compacted powder K.4.2 in Table K.4 (at 200 and 300 g).

Load [g]					
200			300		
Microhardness [HV] [kg/mm²]	Crack length l [μm]	Fracture toughness K_{Ic}[MPa√m]	Microhardness [HV] [kg/mm²]	Crack length l [μm]	Fracture toughness K_{Ic}[MPa√m]
746	8.5	1.8	746	11.7	1.9
674	8.9	1.7	749	10.5	2.0
810	9.6	1.8	730	13.2	1.8
742	9.8	1.7	685	10.0	2.0
806	10.2	1.7	741	14.8	1.7
759	10.1	1.7	757	12.8	1.8
770	10.1	1.7	733	13.3	1.8
780	9.1	1.8	722	12.8	1.8
795	7.9	1.9	671	15.0	1.6
749	10.4	1.6	702	11.4	1.9
770	8.2	1.9	700	14.9	1.6
695	9.1	1.8	733	12.7	1.8
763	7.1	2.0	766	10.0	2.1
777	10.6	1.7	786	9.0	2.2
710	9.8	1.7	733	13.8	1.7
723	8.0	1.8	757	15.0	1.7
766	11.3	1.6	705	11.4	1.9
710	10.1	1.6	685	10.7	1.9
680	9.6	1.6	725	14.5	1.7
784	8.8	1.8	722	13.9	1.7
825	8.4	1.9	807	16.5	1.7
729	9.4	1.7	807	12.8	1.9
759	8.7	1.8	728	11.3	1.9
			780	10.9	2.0
			755	11.1	2.0
			786	12.3	1.9
			746	13.2	1.8
			682	11.3	1.9
			789	8.4	2.3
			749	11.1	2.0
			786	10.0	2.1
			722	15.6	1.6
			746	15.4	1.7
			780	12.1	1.9
			777	11.8	1.9

Table L.4 Microhardness and indentation fracture toughness of hot compacted powder K.4.2 in Table K.4 (at 500 and 1000 g).

500 [g]			1000 [g]		
Microhardness [HV] [kg/mm²]	Crack length l [μm]	Fracture toughness K_{Ic}[MPa√m]	Microhardness [HV] [kg/mm²]	Crack length l [μm]	Fracture toughness K_{Ic}[MPa√m]
770	20.7	1.9	726	27	2.0
746	16.0	2.1	751	25	2.4
740	15.3	2.1	655	28	2.1
736	24.2	1.7	737	40	2.1
766	17.7	2.0	696	31	2.1
740	32.1	1.5	709	31	2.1
679	22.0	1.7	705	48	1.7
672	11.5	2.3	628	48	1.6
679	24.5	1.6	682	44	1.7
702	21.7	1.7	664	30	2.0
704	16.7	2.0	660	33	1.9
717	16.0	2.1	687	38	1.8
706	20.6	1.8	678	37	1.9
639	23.3	1.6	696	47	1.7
688	16.6	2.0	700	59	1.5
732	19.1	1.9	637	37	1.8
715	22.7	1.7	675	33	2.0
649	20.3	1.7	702	37	1.9
677	20.3	1.8	670	58	1.5
647	26.0	1.5	700	38	1.9
692	19.9	1.8	739	43	1.8
622	19.2	1.7	690	38	1.8
717	16.8	2.0	706	45	1.7
746	21	1.8	713	36	1.9
702	22.5	1.7	665	34	1.9
672	14.9	2.1	703	34	2.0
721	13.2	2.3	687	35	1.9
692	15.6	2.0	692	31	2.0
686	17	2.0	688	38	1.9
709	22.1	1.7	675	36	1.9
709	21.3	1.8	706	38	1.9
715	18.7	1.9	674	34	1.9
685	26.2	1.6	700	34	2.0
635	20.4	1.7	639	29	2.0
675	20.8	1.7	695	39	1.8
			654	39	1.8
			690	46	1.7
1000 [g] contd.			700	37	1.9
655	39	1.8	703	42	1.8
702	38	1.9	649	46	1.6
674	45	1.7	706	40	1.8

Table L.5 Microhardness and indentation fracture toughness of hot compacted powder K.4.2 in Table K.4 (at 2000 g).

Load 2000 [g]					
Microhardness [HV] [kg/mm²]	Crack length l [μm]	Fracture toughness K_{Ic}[MPa√m]	Microhardness [HV] [kg/mm²]	Crack length l [μm]	Fracture toughness K_{Ic}[MPa√m]
654	69	1.9	675	67	2.0
613	86	1.6	674	57	2.1
730	69	2.0	680	45	2.4
686	81	1.8	725	63	2.1
729	92	1.7	671	51	2.2
757	58	2.2	714	63	2.1
720	54	2.2	701	51	2.3
726	38	2.7	694	57	2.1
673	68	1.9	694	61	2.1
718	79	1.9	699	57	2.1
723	58	2.2	671	49	2.3
685	70	1.9	671	65	2.0
729	50	2.3	686	60	2.1
682	63	2.0	683	53	2.2
757	59	2.2	668	43	2.4
715	67	2.0	668	59	2.1
672	59	2.1	672	58	2.1
696	77	1.9	675	60	2.0
646	88	1.7	673	48	2.3
651	55	2.1	649	58	2.1
741	81	1.9	625	46	2.3
743	91	1.8	662	45	2.3
670	57	2.1	677	56	2.1
717	82	1.8	700	51	2.3
700	67	2.0	664	54	2.1
642	85	1.7	703	52	2.3
671	60	2.0	703	53	2.2
703	71	1.9	668	63	2.0
655	71	1.9	667	66	2.0
737	73	1.9	706	53	2.3
652	68	1.9	663	66	2.0
692	59	2.1			

Table L.6 Microhardness and indentation fracture toughness of hot compacted powder K.4.3 in Table K.4 (at 500 g).

	Load 500 [g]		
	Microhardness [HV] [kg/mm²]	Crack length l [μm]	Fracture toughness K_{Ic} [MPa√m]
1.	772	21.5	1.8
2.	683	16.7	2.0
3.	661	22.5	1.7
4.	681	16.3	2.0
5.	668	14.8	2.1
6.	657	13.5	2.1
7.	668	14.3	2.1
8.	675	14.2	2.1
9.	777	18.7	2.0
10.	709	17.0	2.0
11.	675	20.3	1.8
12.	717	15.0	2.1
13.	663	17.6	1.9
14.	666	20.6	1.7
15.	696	14.4	2.1
16.	591	12.5	2.1
17.	761	22.4	1.8
18.	681	19.7	1.8
19.	704	15.9	2.0
20.	779	19.1	2.0
21.	656	15.3	2.0
22.	629	14.2	2.0
23.	637	12.6	2.2
24.	692	13.5	2.2
25.	639	21.1	1.7
26.	593	15.5	1.9
27.	717	19.2	1.9
28.	709	13.7	2.2
29.	692	14.5	2.1
30.	727	15.3	2.1

Table L.7 Microhardness and indentation fracture toughness of hot compacted powders: K.4.3, K.4.4, and K.4.5 in Table K.4 (at 2000 g).

	Microhardness [HV] [kg/mm²]	Crack length l [μm]	Fracture toughness K_{Ic}[MPa√m]
Specimen K.4.3			
1.	659	67	1.9
2.	716	59	2.1
3.	589	60	1.9
4.	662	52	2.2
5.	677	57	2.1
6.	634	50	2.2
7.	728	41	2.6
8.	692	62	2.1
9.	715	62	2.1
Specimen K.4.4			
1.	779	81	1.9
2.	746	72	2.0
2.	736	60	2.1
3.	790	62	2.2
4.	710	47	2.4
5.	697	67	2.0
6.	686	55	2.2
7.	583	54	2.0
8.	718	59	2.1
9.	691	59	2.1
10.	644	57	2.1
11.	612	44	2.0
12.	583	54	2.0
13.	621	55	2.1
14.	593	50	2.1
15.	666	49	2.3
16.	595	50	2.1
17.	691	41	2.5
18.	725	53	2.3
Specimen K.4.5			
1.	624	39	2.5
2.	528	51	2.0
3.	554	86	1.6
4.	621	45	2.3
5.	612	60	2.0
6.	628	70	1.8
7.	590	55	2.0
8.	610	69	1.8
9.	632	54	2.1
10.	594	55	2.0
11.	620	50	2.2
12.	584	64	1.9

Table L.8 Microhardness and indentation fracture toughness of hot compacted powder K.4.4 in Table K.4 (at 500 g).

	Load 500 [g]		
	Microhardness [HV] [kg/mm²]	Crack length l [μm]	Fracture toughness K_{Ic} [MPa√m]
1.	674	19.8	1.8
2.	736	18.5	1.9
3.	637	12.3	2.2
4.	666	13.2	2.2
5.	647	11.0	2.4
6.	656	18.6	1.8
7.	637	14.8	2.0
8.	654	20.7	1.7
9.	795	19.0	2.0
10.	578	18.4	1.7
11.	642	16.5	1.9
12.	717	11.7	2.4
13.	723	10.8	2.5
14.	719	15.6	2.1
15.	649	13.4	2.1
16.	649	21.5	1.7
17.	640	14.6	2.0
18.	661	11.7	2.3
19.	779	20.5	2.0
20.	711	14.0	2.2
21.	738	16.8	2.0
22.	654	11.0	2.4
23.	702	10.5	2.5
24.	677	21.6	1.7
25.	661	19.2	1.8
26.	593	11.6	2.2
27.	634	14.0	2.1
28.	609	11.9	2.2
29.	609	20.8	1.7
30.	670	11.5	2.3
31.	632	18.0	1.8
32.	681	14.9	2.1
33.	674	15.5	2.0
34.	629	11.7	2.3
35.	584	13.0	2.1
36.	677	17.9	1.9
37.	622	14.0	2.0
38.	600	20.6	1.6
39.	630	15.2	2.0

Table L.9 Microhardness and indentation fracture toughness of hot compacted powder K.4.6 in Table K.4 (at 2000 g).

	Load 2000 [g]		
	Microhardness [HV] [kg/mm²]	Crack length l [μm]	Fracture toughness K_{Ic}[MPa√m]
1.	574	48	2.1
2.	563	39	2.3
3.	614	60	2.0
4.	589	68	1.8
5.	603	51	2.1
6.	551	44	2.2
7.	552	47	2.1

Table L.10 Average indentation fracture toughness of hot compacted powders (in Table K.4) at various indentation loads.

SPECIMEN#	Porosity [%]	Fracture toughness [MPa√m]				
		200 [g]	300 [g]	500 [g]	1000 [g]	2000 [g]
K.4.1	2			2.1±0.21		2.0±0.23
K.4.2	0.6	1.8±0.10	1.9±0.16	1.8±0.20	1.9±0.17	2.1±0.19
K.4.3	7.5			2.0±0.15		2.1±0.19
K.4.4	8.3			2.0±0.24		2.1±0.15
K.4.5	12.5					2.0±0.23
K.4.6	10.9					2.1±0.14